Physics of the Solid State, Vol. 42, No. 6, 2000, pp. 1009–1016. Translated from Fizika Tverdogo Tela, Vol. 42, No. 6, 2000, pp. 979–985.

METALS AND SUPERCONDUCTORS

Effect of the Electron and Phonon Mutual Drag on the Thermomagnetic and Thermoelectric Phenomena in Conductors with Degenerate Carrier Statistics

I. G. Kuleev

Institute of Metal Physics, Ural Division, Russian Academy of Sciences, ul. S. Kovalevskoĭ 18, Yekaterinburg, 620219 Russia
e-mail: kuleev@imp.uran.ru

Received August 5, 1999

Abstract—The transport coefficients of conductors with degenerate carrier statistics in a magnetic field have been calculated with the inclusion of the mutual electron and phonon drag. The calculation is carried out in the linear approximation in the degeneracy parameter. A study has been made of the mutual drag on the thermomagnetic and thermoelectric phenomena in conductors, in both isothermal and adiabatic conditions. © *2000 MAIK "Nauka/Interperiodica".*

Investigating the influence of electron-phonon drag on the thermomagnetic phenomena in conductors is not only more interesting than studying galvanomagnetic effects, but more complex as well [1–14]. Thermomagnetic (TM) phenomena, such as the longitudinal and transverse Nernst–Ettingshausen effects, are much finer probes to study the carrier scattering mechanism than mobility [2]. When the dominant scattering mechanism changes, the carrier mobility changes only in magnitude, whereas TM effects, which are proportional to the energy derivative of the relaxation time, can reverse their sign [2, 13]. Therefore, the investigation of their dependences on the magnetic field and temperature yields more complete information, both on the mechanisms of carrier and phonon relaxation and on the spectrum of quasiparticles in the compounds under study.

This work aimed to study the influence of the mutual electron and phonon drag on the thermomagnetic and thermoelectric effects in metals and semiconductors with degenerate carrier statistics. The theory developed in [7, 8] in zeroth approximation in the degeneracy parameter $k_BT/\zeta \ll 1$ (ζ is the Fermi energy) cannot be used to analyze these phenomena, because in this approximation diffusion fluxes, as well as the Nernst–Ettingshausen effects, vanish. Therefore, in order to study TM effects, one should solve coupled transport equations for nonequilibrium distribution functions of the electron-phonon systems, taking into account the higher terms of the expansion in the k_BT/ζ parameter. This solution, with due account of the mutual electron-phonon drag, was found in our work [15] in a linear approximation in the degeneracy parameter.

In this work, we shall use this solution, calculate the charge and heat fluxes, and analyze the role played by the mutual electron-phonon drag in thermomagnetic and thermoelectric effects in degenerate conductors with an isotropic carrier spectrum. In Section 1, the conduction current in a nonequilibrium electron-phonon system is calculated, and the transverse and longitudinal Nernst–Ettingshausen effects are considered. Section 2 deals with a calculation of the heat flux and analyzes the magnetic-field dependence of the heat conductivity and the Maggi–Righi–Leduc effect in a linear approximation in the degeneracy parameter. Thermomagnetic and thermoelectric phenomena in degenerate conductors in adiabatic conditions are studied in Section 3 with the inclusion of the mutual electron-phonon drag.

1. TRANSVERSE AND LONGITUDINAL NERNST–ETTINGSHAUSEN EFFECTS

The transverse Nernst–Ettingshausen (NE) effect consists in the generation of an electric field in a sample in the direction perpendicular to the temperature gradient $\nabla T = (\nabla_x T, 0, 0)$ and to the magnetic field $\mathbf{H} = (0, 0, H)$. The magnitude of this effect is determined by the coefficient $Q(H)$ [3]

$$Q(H) = -H\nabla_x T / E_y. \tag{1}$$

The coefficient of the longitudinal NE effect $\Delta\alpha(H)$ characterizes the variation of the electric field along the temperature gradient induced by the magnetic field; it is actually the variation of the thermopower in a magnetic field

$$\begin{aligned} E_x(\mathbf{H}) - E_x(0) &= (\alpha(H) - \alpha(0))\nabla_x T \\ &= \Delta\alpha(H)\nabla_x T. \end{aligned} \tag{2}$$

1063-7834/00/4206-1009$20.00

In isothermal conditions $j_x = 0$, $j_y = 0$, $\nabla_y T = 0$, and in order to find the $Q(H)$ and $\Delta\alpha(H)$ coefficients, it is sufficient to calculate the conduction current $\mathbf{j}$.

We separate the part of the conduction current proportional to the nonequilibrium extra terms in the electron distribution function, $\delta f_{\mathbf{k}}^{(1)}$ and $\delta f_{\mathbf{k}}^{(2)}$ [15]. Then, for a conductor with an isotropic carrier dispersion law, we obtain

$$\begin{aligned}
\mathbf{j} &= -\frac{en}{m_{\mathrm{F}}}\int_0^\infty d\varepsilon\left(-\frac{\partial f_0}{\partial\varepsilon}\right)\frac{(\tilde{k}(\varepsilon))}{\tilde{m}(\varepsilon)}(\boldsymbol{\chi}_{1H}(\varepsilon)+\boldsymbol{\chi}_{2H}(\varepsilon)) \\
&= \mathbf{j}_1 + \mathbf{j}_2, \\
\boldsymbol{\chi}_{2H}(\varepsilon) &= \frac{\tilde{m}^2(\varepsilon)\psi(\varepsilon)}{\tilde{k}^3}\mathbf{Q}_H(\varepsilon), \\
\mathbf{Q}_H(\varepsilon) &= \mathbf{Q}(\varepsilon) + \gamma(\varepsilon)(\mathbf{h}\times\mathbf{Q}(\varepsilon)), \\
\psi(\varepsilon) &= \frac{\tau(\varepsilon)}{1+\gamma^2(\varepsilon)},
\end{aligned} \tag{3}$$

$$\boldsymbol{\chi}_{1H}(\varepsilon) = \{\boldsymbol{\chi}_1(\varepsilon) + \gamma(\varepsilon)(\mathbf{h}\times\boldsymbol{\chi}_1(\varepsilon))\}(1+\gamma^2(\varepsilon))^{-1},$$

$$\boldsymbol{\chi}_1(\varepsilon) = -e\tau(\varepsilon)\left(\mathbf{E} + \frac{k_{\mathrm{B}}}{e}\left(\frac{(\tilde{m}(\varepsilon))^2}{\tilde{k}^3}A_{\mathrm{ph}}(\varepsilon) + \frac{\varepsilon-\zeta}{k_{\mathrm{B}}T}\right)\nabla T\right),$$

$$A_{\mathrm{ph}}(\varepsilon) = \sum_\lambda \frac{m_{\mathrm{F}}s_\lambda}{k_{\mathrm{B}}T}\int_0^{2^{z_{2k}^\lambda}} dz_q^\lambda \frac{\nu_{\mathrm{eph}}^\lambda(k_{\mathrm{F}}, q)}{\nu_{\mathrm{ph}}^\lambda(q)}.$$

Here, $\tilde{m}(\varepsilon) = m(\varepsilon)/m_{\mathrm{F}}$, m_{F} is the effective electron mass at the Fermi level, $\tilde{k} = k/k_{\mathrm{F}}$, $\hbar k_{\mathrm{F}}$ is the Fermi momentum, $\gamma(\varepsilon) = \Omega\tau(\varepsilon)$, where Ω is the cyclotron frequency, $\tau(\varepsilon)$ is the total electron relaxation time, $\tau^{-1}(\varepsilon_k) = \nu_{\mathrm{e}}(k) = \nu_{\mathrm{ei}}(k) + \nu_{\mathrm{e,\,ph}}(k)$, $\nu_{\mathrm{ei}}(k)$ and $\nu_{\mathrm{e,\,ph}}(k)$ are the electron relaxation rates at impurities and phonons, respectively, and the function $\mathbf{Q}(\varepsilon)$ is defined in [15]. The current $\mathbf{j}_1$ is caused by the direct action of the electric field and of the temperature gradient on the electron subsystem and also includes the phonon drag of electrons. It can be expressed in the well-known way [3]

$$\begin{aligned}
\mathbf{j}_1 &= \sigma_{xx}^0\{\mathbf{E}_{j11} + \gamma_{\mathrm{F}}(\mathbf{h}\times\mathbf{E}_{j12})\}, \\
\mathbf{E}_{j1N} &= \mathbf{E}_A + \frac{k_{\mathrm{B}}}{e}\frac{\pi^2}{3}D_{jN}\nabla T, \\
\mathbf{E}_A &= \mathbf{E} + \frac{k_{\mathrm{B}}}{e}A_{\mathrm{ph}}(\zeta)\nabla T,
\end{aligned} \tag{4}$$

$$D_{jN} = k_{\mathrm{B}}T\frac{d}{d\varepsilon}\left[\ln\left(\frac{k^3(\varepsilon)\psi(\varepsilon)(\psi(\varepsilon))^{N-1}}{m(\varepsilon)}\right)\right]_{\varepsilon=\zeta},$$

$$\sigma_{xx}^0 = \frac{e^2 n_e \tau_F}{m_{\mathrm{F}}(1+\gamma_{\mathrm{F}}^2)}.$$

The charge flux $\mathbf{j}_2$ takes into account the interaction of nonequilibrium electrons with the phonon subsystem. The only contribution to it in the linear approximation in $k_{\mathrm{B}}T/\zeta$ comes from the symmetric part $\mathbf{Q}_s(\varepsilon)$ of the function $\mathbf{Q}(\varepsilon)$. Substituting the solution of the integral equation for the $\mathbf{Q}(\varepsilon)$ function found in [15] into (3) and integrating over the parameter ε yields

$$\begin{aligned}
\mathbf{j}_2 &= \frac{\sigma_{xx}^0\Gamma}{(1-\Gamma)^2+\gamma_{\mathrm{F}}^2}\{\mathbf{E}_{j22} + \gamma_{\mathrm{F}}(\mathbf{h}\times\mathbf{E}_{j12})\}, \\
\mathbf{E}_{j2N} &= \beta_{j2N}\mathbf{E}_A + \mathbf{E}_{T2N}, \\
\beta_{j21} &= 1-\Gamma-\gamma_{\mathrm{F}}^2 - \frac{C_1 D_\Phi(1+\gamma_{\mathrm{F}}^2)(1-\tilde{\gamma}_{\mathrm{F}}^2)}{1+\tilde{\gamma}_{\mathrm{F}}^2}, \\
\beta_{j22} &= 2-\Gamma-\frac{2C_1 D_\Phi(1+\gamma_{\mathrm{F}}^2)}{(1-\Gamma)(1+\tilde{\gamma}_{\mathrm{F}}^2)}, \\
\mathbf{E}_{T21} &= \frac{k_{\mathrm{B}}}{e}\frac{\pi^2}{3}[(1-\Gamma)D_{Q1} - \gamma_{\mathrm{F}}^2 D_{Q2}]\nabla T, \\
\mathbf{E}_{T22} &= \frac{k_{\mathrm{B}}}{e}\frac{\pi^2}{3}[D_{Q1} - (1-\Gamma)D_{Q2}]\nabla T, \\
D_{QN} &= k_{\mathrm{B}}T\frac{d}{d\varepsilon}[\ln[m(\varepsilon)\psi(\varepsilon)(\gamma(\varepsilon))^{N-1}\Phi^{1/2}(\varepsilon)]]_{\varepsilon-\zeta}, \\
D_\Phi &= k_{\mathrm{B}}T\frac{d}{d\varepsilon}[\ln(\Phi(\varepsilon))]_{\varepsilon=\zeta},
\end{aligned} \tag{5}$$

where $\Phi(\varepsilon) = \sum_\lambda \langle \nu_{\mathrm{e,\,ph}}^\lambda(k_{\mathrm{F}}, q)\nu_{\mathrm{ph}}^\lambda(k_{\mathrm{F}}, q)/\nu_{\mathrm{ph}}^\lambda(q)\rangle_{z_{2k}^\lambda}$, $C_1 = \ln(2) + J_1$ by [14], and $J_1 = 0.31$. The $\Gamma = \tau_{\mathrm{F}}\Phi(\zeta)$ parameter characterizes the extent of the mutual effect of the deviation of the electrons and phonons from equilibrium in the absence of a magnetic field. It is equal to the ratio of the electron mean free time to the time required for the momentum imparted by electrons to phonons to transfer back to the electron system [14]. As seen from (5), in strong magnetic fields for $\gamma_{\mathrm{F}} \gg 1$, as well as for $\Gamma \ll 1$, we have $\mathbf{j}_2 \ll \mathbf{j}_1$, so that the mutual drag effects may be neglected. The significance of the $\mathbf{j}_2$ current increases with increasing the parameter Γ, and for $\Gamma > 1/2$ disregarding the mutual drag in weak magnetic fields will produce qualitatively inaccurate results in the interpretation of experimental data. It should be pointed out that the drift current (which is proportional to the electric field $\mathbf{E}$) and the drag current (proportional to $A_{\mathrm{ph}}\nabla T$ renormalize in the same way due to the influence of the nonequilibrium electron distribution on the electrons through the phonon system. Expressing the total current $\mathbf{j}$ in terms of the tensor components of

the electrical conductivity $\sigma_{\mu\nu}$ and thermoelectric coefficients $\beta_{\mu\nu}$,

$$j_\mu = \sum_\nu (\sigma_{\mu\nu}E_\nu - \beta_{\mu\nu}\nabla_\nu T), \quad (6)$$

we can write the $\sigma_{\mu\nu}$ and $\beta_{\mu\nu}$ components as

$$\sigma_{xx} = \tilde{\sigma}^0_{xx}\left\{1 - \frac{C_1\Gamma D_\Phi(1-\tilde{\gamma}_F^2)}{(1-\Gamma)(1+\tilde{\gamma}_F^2)}\right\},$$

$$\sigma_{yx} = -\sigma_{xy} = \tilde{\sigma}^0_{xx}\tilde{\gamma}_F\left\{1 - \frac{2C_1\Gamma D_\Phi}{(1-\Gamma)(1+\tilde{\gamma}_F^2)}\right\},$$

$$\beta_{xx} = \beta_{yy} = -\frac{k_B}{e}\left\{\sigma_{xx}A_{ph}(\zeta) + \frac{\pi^2}{3}\sigma^0_{xx}[D_{j1} + D^{(1)}_\Gamma]\right\}, \quad (7)$$

$$D^{(1)}_\Gamma = \frac{\Gamma[(1-\Gamma)D_{Q1} - \gamma_F^2 D_{Q2}]}{(1-\Gamma)^2 + \gamma_F^2},$$

$$\beta_{yx} = -\beta_{xy} = -\frac{k_B}{e}\left\{\sigma_{yx}A_{ph}(\zeta) + \frac{\pi^2}{3}\sigma^0_{yx}[D_{j2} + D^{(2)}_\Gamma]\right\},$$

$$D^{(2)}_\Gamma = \frac{\Gamma[D_{Q1} + (1-\Gamma)D_{Q2}]}{(1-\Gamma)^2 + \gamma_F^2},$$

where $\tilde{\sigma}^0_{xx} = e^2 n_e \tilde{\tau}_F / m_F(1 + \tilde{\gamma}_F^2)$ and $\tilde{\sigma}^0_{yx} = \tilde{\gamma}_F\tilde{\sigma}^0_{xx}$. For $H \longrightarrow 0$, the expression for σ_{xx} coincides with the result given in [14]. In zero the approximation in degeneracy, the effect of mutual drag on the conductivity tensor components reduces to replacing τ_F by $\tilde{\tau}_F = \tau_F/(1-\Gamma)$. In this approximation, the diffusion terms in the tensor components of the thermoelectric coefficients $\beta_{\mu\nu}$ vanish, and Equations (7) reduce to the results quoted in [7, 8]. The extra term linear in the k_BT/ζ parameter in the tensor components $\sigma_{\mu\nu}$ can become significant in the case of a strong drag, where $1 - \Gamma \ll 1$.

In isothermal conditions, the coefficient of the transverse Nernst–Ettingshausen effect $Q(H)$ and the thermopower $\alpha(H)$ can be expressed through the tensor components $\sigma_{\mu\nu}$ and $\beta_{\mu\nu}$ in the following way [3]:

$$Q(H) = \frac{\sigma_{yx}\beta_{xx} - \sigma_{xx}\beta_{yx}}{H(\sigma^2_{xx} + \sigma^2_{yx})},$$
$$\alpha(H) = \frac{\sigma_{xx}\beta_{xx} + \sigma_{yx}\beta_{yx}}{\sigma^2_{xx} + \sigma^2_{yx}}. \quad (8)$$

Inserting (7) in (8) yields

$$Q(H) = -\frac{\pi^2 k_B\gamma_F}{3eH(1+\gamma_F^2)} \times [D_{j1} - D_{j2} - \Gamma(D_{Q2} - D_{j2})], \quad (9)$$

$$\alpha(H) = -\frac{k_B}{e} \times \left\{A_{ph}(\zeta) + \frac{\pi^2}{3(1+\gamma_F^2)}[D_{j1} + \gamma_F^2 D_{j2} + \Gamma(D_{Q1} - D_{j1})]\right\} = \alpha_{ph} + \alpha_{dif}. \quad (10)$$

We note, first of all, that the mutual influence of the electron and phonon nonequilibrium distributions does not lead to renormalization of the contribution of phonon drag to the thermopower, because the drift current and the drag current renormalize in the same way [see (5)]. The appearance of the extra term in the diffusion component of thermopower is also physically clear. Because the average velocity of the ordered electron motion is zero, the momentum transfer from electrons to the phonon subsystem occurs owing to the dependence of the electron effective mass, electron quasimomentum, and scattering parameters on the electron energy near the Fermi level; hence, this contribution should be proportional to the derivative of the above-mentioned parameters with respect to the electron energy. This is what follows from (5). Note that, in their calculation of the thermopower, the authors of [7, 8] limited themselves to the zeroth approximation in electron-gas degeneracy, and therefore both the diffusion contribution and the contribution of mutual drag to the thermopower were disregarded. In zero magnetic field, the expression for the thermopower $\alpha(0)$ coincides with the one derived in [14]. Taking into account that

$$D_{j2} - D_{j1} = D_0 = k_BT\frac{d}{d\varepsilon}\left[\ln\left(\frac{\tau(\varepsilon)}{m(\varepsilon)}\right)\right]_{\varepsilon=\zeta},$$

$$D_{QN} - D_{jN} = D_{Qj} = k_BT\frac{d}{d\varepsilon}\left[\ln\left(\frac{(m(\varepsilon))^2\Phi^{1/2}(\varepsilon)}{k^3(\varepsilon)}\right)\right]_{\varepsilon=\zeta},$$

we finally come to

$$Q(H) = \frac{\pi^2 k_B\gamma_F}{3eH(1+\gamma_F^2)}[D_0 + \Gamma D_{Qj}],$$
$$\Delta\alpha(H) = \frac{\pi^2 k_B\gamma_F^2}{3eH(1+\gamma_F^2)}[D_0 + \Gamma D_{Qj}]. \quad (11)$$

For $\Gamma = 0$, the expressions for the $Q(H)$ and $\Delta\alpha(H)$ coefficients coincide with those obtained in [16, 17]. As follows from (11), taking into account the mutual drag of

electrons and phonons does not change the magnetic-field dependence of the transverse and longitudinal Nernst–Ettingshausen coefficients, but affects only the magnitude of the effects through the terms proportional to the mutual drag parameter Γ. The magnitude of $\Delta\alpha(H)$ grows quadratically with the magnetic field in the weak-field domain, where $\gamma_F \ll 1$, and tends to saturation for $\gamma_F \gg 1$, as in the case when no mutual drag is present [17]. The $Q(H)$ coefficient decreases slowly in absolute value for $\gamma_F \ll 1$ and tends to zero for $\gamma_F \gg 1$. Thus, the inclusion of the mutual drag within the generally accepted approximations [7–15] cannot account for the experimentally observed sign reversal of the $Q(H)$ coefficient and the absence of saturation of the $\Delta\alpha(H)$ quantity [18].

2. HEAT CONDUCTIVITY AND THE MAGGI–RIGHI–LEDUC EFFECT

Calculate the electronic, $\mathbf{W}_e$, and phonon, $\mathbf{W}_{ph}$, heat fluxes by separating them into parts proportional to the nonequilibrium terms in the distribution functions of electrons, $\delta f_{\mathbf{k}}^{(1)}$ and $\delta f_{\mathbf{k}}^{(2)}$, and of phonons, $g_\lambda^{(1)}(\mathbf{q})$ and $g_\lambda^{(2)}(\mathbf{q})$. We obtain

$$\mathbf{W}_e = \frac{n_e}{m_F}\int_0^\infty d\varepsilon\left(-\frac{\partial f_0}{\partial\varepsilon}\right)(\varepsilon-\zeta)\frac{\tilde{k}^3}{\tilde{m}(\varepsilon)} \times(\boldsymbol{\chi}_{1H}(\varepsilon)+\boldsymbol{\chi}_{2H}(\varepsilon)) = \mathbf{W}_e^{(1)}+\mathbf{W}_e^{(2)}, \tag{12}$$

$$\mathbf{W}_{ph} = \frac{1}{V}\sum_{q,\lambda}\hbar\omega_{q\lambda}\vartheta_q^\lambda(g_\lambda^{(1)}(\mathbf{q})+g_\lambda^{(2)}(\mathbf{q})) = \mathbf{W}_{ph}^0+\mathbf{W}_{ph,e}. \tag{13}$$

The contribution $\mathbf{W}_{ph}^0$ is due to the direct action of the temperature gradient on the phonon subsystem

$$\mathbf{W}_{ph}^0 = -\kappa_{ph}^0\nabla T,$$
$$\kappa_{ph}^0 = \sum_\lambda\frac{k_B s_\lambda^2 q_T^3}{6\pi^2}\int_0^{z_d^\lambda}dx_q^\lambda\frac{(z_q^\lambda)^4}{v_{ph}^\lambda(q)}N_{q\lambda}^0(N_{q\lambda}^0+1), \tag{14}$$

where $z_q^\lambda = \hbar\omega_{d\lambda}/k_BT$ and $\omega_{d\lambda}$ is the Debye frequency for phonons of polarization λ. The second part, $\mathbf{W}_{ph,e}$, appears due to the action of nonequilibrium electrons on phonons. It results in the renormalization of both the electronic and phonon heat fluxes, and can also be divided in two parts proportional to the nonequilibrium terms added to the electron distribution functions $\delta f_{\mathbf{k}}^{(1)}$ and $\delta f_{\mathbf{k}}^{(2)}$:

$$\mathbf{W}_{ph,e} = \frac{1}{V}\sum_{\mathbf{q},\lambda}s_\lambda^2\hbar\mathbf{q}g_\lambda^{(2)}(\mathbf{q}) = \frac{k_BT}{m_F}\frac{2}{V}\sum_{\mathbf{k}}\frac{\tilde{m}(\varepsilon_k)}{\tilde{k}^3}A_{ph}(\varepsilon_k)\hbar\mathbf{k}(\delta_{\mathbf{k}}^{(1)}+\delta_{\mathbf{k}}^{(2)}) = \mathbf{W}_{ph,e}^{(1)}+\mathbf{W}_{ph,e}^{(2)}. \tag{15}$$

The flux $\mathbf{W}_e^{(1)}$ is due to a direct action of the electric field and temperature gradient on the electronic subsystem and also includes the phonon drag of electrons. The expression for the latter has the form [3]

$$\mathbf{W}_e^{(1)} = -\frac{e}{k_B}L_0\sigma_{xx}^0\{\mathbf{E}_{W11}+\gamma_F(\mathbf{h}\times\mathbf{E}_{W12})\},$$
$$\mathbf{E}_{W1N} = \left\{D_{jN}\mathbf{E}+\frac{k_B}{e}(A_{ph}D_{AN}+1)\nabla T\right\}, \tag{16}$$
$$D_{AN} = k_BT\frac{d}{d\varepsilon}(\ln[\psi(\varepsilon)m(\varepsilon)A_{ph}(\varepsilon)(\gamma(\varepsilon))^{N-1}])_{\varepsilon=\zeta},$$

where $L_0 = (\pi^2/3)(k_B/e)^2$. One can readily verify that the Onsager relations for the thermoelectric coefficients in the fluxes of heat (16) and charge (4) are not satisfied. As shown in [14], one has to take into account the heat flux $\mathbf{W}_{ph,e}$, which is transported by phonons but is due to the nonequilibrium electrons. Calculation of the flux $\mathbf{W}_{ph,e}^{(1)}$ connected with the nonequilibrium term $\delta f_{\mathbf{k}}^{(1)}$ yields

$$\mathbf{W}_{ph,e}^{(1)} = -\frac{k_BT}{e}\sigma_{xx}^0A_{ph}(\zeta)\{\mathbf{E}_{ph,e1}+\gamma_F(\mathbf{h}\times\mathbf{E}_{ph,e2})\},$$
$$\mathbf{E}_{ph,eN} = \mathbf{E}_A+\frac{\pi^2}{3}\frac{k_B}{e}D_{AN}\nabla T. \tag{17}$$

As in [14], we include the drift and diffusion components of the heat flux $\mathbf{W}_{ph,e}^{(1)}$, which are related to the effect of the nonequilibrium electron distribution, into the electronic heat flux. The term

$$\Delta\mathbf{W}_{ph,e}^{(1)} = -\left(\frac{k_B}{e}\right)^2 \times T\sigma_{xx}^0(A_{ph}(\zeta))^2\{\nabla T+\gamma_F(\mathbf{h}\times\nabla T)\} \tag{18}$$

in (17) appears as a result of nonequilibrium phonons acting on phonons through the conduction electron subsystem. It should be included into the phonon heat flux

[14]. We finally obtain for the heat conductivity tensor components $\kappa^{(1)}_{\mathrm{ph}\mu\nu}$

$$\mathbf{W}_{\mathrm{ph}\mu} = -\sum_{\nu}\kappa^{(1)}_{\mathrm{ph}\mu\nu}\nabla_\nu T,$$

$$\kappa^{(1)}_{\mathrm{ph}yx} = \left(\frac{k_\mathrm{B}}{e}\right)^2 T\sigma^0_{yx}(A_{\mathrm{ph}}(\zeta))^2, \quad \sigma^0_{yx} = \gamma_\mathrm{F}\sigma^0_{xx}, \tag{19}$$

$$\kappa^{(1)}_{\mathrm{ph}\mu\mu} = \kappa^0_{\mathrm{ph}} + \left(\frac{k_\mathrm{B}}{e}\right)^2 T\sigma^0_{\mu\mu}(A_{\mathrm{ph}}(\zeta))^2.$$

Thus, taking into account the effect of nonequilibrium phonons acting on phonons through the conduction electrons gives rise to the appearance of off-diagonal components in the phonon heat conductivity tensor. Note that expressions (19) for $\kappa^{(1)}_{\mathrm{ph}\mu\nu}$ are applicable when the phonon relaxation rate in normal scattering processes, $\nu^{\lambda}_{\mathrm{ph}N}(q)$, is substantially lower than that involving momentum loss, $\nu^{\lambda}_{\mathrm{ph}R}(q)$ [19]. Here and in what follows, into the electronic heat flux $\mathbf{W}_{\mathrm{et}}$

$$W_{\mathrm{et}\mu} = \sum_{\nu}(\gamma_{\mu\nu}E_\nu - \kappa^e_{\mu\nu}\nabla_\nu T), \tag{20}$$

besides the heat flux $\mathbf{W}_\mathrm{e}$, we include the drift and diffusion components of the flux $\mathbf{W}_{\mathrm{ph,\,e}}$. In this case, the Onsager relations for the thermoelectric coefficients $\gamma^{(1)}_{\mu\nu}$ and $\beta^{(1)}_{\mu\nu}$ are satisfied:

$$\gamma^{(1)}_{xx} = T\beta^{(1)}_{xx} = -\sigma^{(0)}_{xx}T\frac{k_\mathrm{B}}{e}\left\{A_{\mathrm{ph}}(\zeta) + \frac{\pi^2}{3}D_{j1}\right\},$$
$$\gamma^{(1)}_{xy} = T\beta^{(1)}_{xy} = -\sigma^0_{xy}T\frac{k_\mathrm{B}}{e}\left\{A_{\mathrm{ph}}(\zeta) + \frac{\pi^2}{3}D_{j2}\right\}, \tag{21}$$

and the expression for the components of the electronic heat conductivity tensor $\kappa^{e(1)}_{\mu\nu}$ takes on the form

$$\kappa^{e(1)}_{\mu\nu} = L_0\sigma^0_{xx}T\{1 + A_{\mathrm{ph}}(\zeta)(D_{j1} + D_{A1})\},$$
$$\kappa^{e(1)}_{xy} = L_0\sigma^0_{xy}T\{1 + A_{\mathrm{ph}}(\zeta)(D_{j2} + D_{A2})\}. \tag{22}$$

Thus, in order for the relations of microscopic reversibility to be met, when calculating the total electronic heat flux, one must take into account the heat transported by phonons and originating from the electrons being not in equilibrium; note that all three fluxes $\mathbf{j}$, $\mathbf{W}_\mathrm{e}$, and $\mathbf{W}_{\mathrm{ph,\,e}}$ should be calculated using the same nonequilibrium electron distribution function. In this case, they are calculated with the function $\delta f^{(1)}_{\mathbf{k}}$ taking into account the phonon drag of electrons. As we shall see later on, this conclusion is also valid when taking into account the mutual drag. Note that the Onsager relations for the transport coefficients calculated with inclusion of the electron-phonon drag [3] are not met, because the $\mathbf{W}^{(1)}_{\mathrm{ph,\,e}}$ flux was disregarded.

The heat flux $\mathbf{W}^{(2)}_\mathrm{e}$ is calculated similar to the manner this was done for the $\mathbf{j}^{(2)}$ current. We substitute the expression for $\mathbf{Q}(\varepsilon)$ in (12) and integrate over ε, limiting ourselves to the linear approximation in the degeneracy parameter:

$$\mathbf{W}^{(2)}_\mathrm{e} = -\frac{e}{k_\mathrm{B}}\Gamma L_0\sigma^0_{xx}T\{\mathbf{E}_{W21} + \gamma_\mathrm{F}(\mathbf{h}\times\mathbf{E}_{W22})\},$$
$$\mathbf{E}_{W1N} = \frac{\mathbf{E}_A[(1-\Gamma)D_{Q1} - \gamma^2_\mathrm{F}D_{Q2}]}{(1-\Gamma)^2 + \gamma^2_\mathrm{F}} + \frac{k_\mathrm{B}}{e}\frac{1-\gamma^2_\mathrm{F}}{1+\gamma^2_\mathrm{F}}C_2D_\Phi\nabla T,$$
$$C_2 = \ln 2 - \frac{3}{\pi^2}J_3 \cong 0.577, \tag{23}$$
$$\mathbf{E}_{W2N} = \frac{\mathbf{E}_A[D_{Q1} + (1-\Gamma)D_{Q2}]}{(1-\Gamma)^2 + \gamma^2_\mathrm{F}} + \frac{k_\mathrm{B}}{e}\frac{C_2D_\Phi}{1+\gamma^2_\mathrm{F}}\nabla T,$$
$$J_3 = \int_0^\infty d\eta\left(-\frac{\partial f_0}{\partial\eta}\right)\eta f_2(\eta) \cong 0.381.$$

On calculating the heat flux $\mathbf{W}_\mathrm{e}$ from (15) and (23) and comparing the transport coefficients in the fluxes $\mathbf{j}$ and $\mathbf{W}_\mathrm{e}$, we can see that they do not satisfy the Onsager relations. Obviously enough, one has to take into account the heat flux $\mathbf{W}^{(2)}_{\mathrm{ph,\,e}}$ transported by phonons but originating from the nonequilibrium extra term added to the electron distribution function $\delta f^{(2)}_{\mathbf{k}}$. In a linear approximation in the degeneracy parameter, we obtain for this flux

$$\mathbf{W}^{(2)}_{\mathrm{ph,\,e}} = -\frac{k_\mathrm{B}}{e}TA_{\mathrm{ph}}(\zeta)\mathbf{j}_2. \tag{24}$$

As a result, the total flux $\mathbf{W}_{\mathrm{ph,e}}$ acquires the form

$$\mathbf{W}_{\mathrm{ph,\,e}} = -\frac{k_\mathrm{B}}{e}TA_{\mathrm{ph}}(\zeta)\left\{\sigma_{xx}\mathbf{E}_A + \sigma_{yx}(h\times\mathbf{E}_A) + \frac{\pi^2}{3}\frac{k_\mathrm{B}}{e}\sigma^0_{xx}\{D_{\mathrm{ph,\,e1}}\nabla T + \gamma_\mathrm{F}D_{\mathrm{ph,\,e2}}(\mathbf{h}\times\nabla T)\}\right\}, \tag{25}$$
$$D_{\mathrm{ph,\,e1}} = D_{A1} + D^{(1)}_\Gamma, \quad D_{\mathrm{ph,\,e2}} = D_{A2} + D^{(2)}_\Gamma.$$

Next we include the drift and diffusion components of the heat flux $\mathbf{W}_{\mathrm{ph,e}}$ into the electronic heat flux, while the term taking into account the effect of nonequilib-

rium phonons on phonons through the conduction electrons, into the phonon heat flux. After this separation, we obtain the following expressions for the transport coefficients

$$\gamma_{\mu\nu} = T\beta_{\mu\nu}, \quad \gamma_{\mu\nu}(H) = \gamma_{\mu\nu}(-H), \quad \mu \neq \nu,$$

$$\kappa^e_{xx} = \kappa^e_{yy}$$

$$= L_0\sigma^0_{xx}T\left\{1 + 2A_{\rm ph}(\zeta)[D_{A1} + D^{(1)}_\Gamma] + \Gamma C_2 D_\Phi \frac{1-\gamma_{\rm F}^2}{1+\gamma_{\rm F}^2}\right\},$$

$$\kappa^e_{yx} = -\kappa^e_{xy} \tag{26}$$

$$= L_0\sigma^0_{yx}T\left\{1 + 2A_{\rm ph}(\zeta)[D_{A2} + D^{(2)}_\Gamma] + \frac{2C_2\Gamma D_\Phi}{1+\gamma_{\rm F}^2}\right\},$$

$$\kappa_{{\rm ph}xx} = \kappa_{{\rm ph}yy} = \kappa^{(0)}_{\rm ph} + \frac{3}{\pi^2}L_0T\sigma_{xx}(A_{\rm ph}(\zeta))^2,$$

$$\kappa_{{\rm ph}yx} = -\kappa_{{\rm ph}xy} = \frac{3}{\pi^2}L_0T\sigma_{yx}(A_{\rm ph}(\zeta))^2,$$

where the thermoelectric tensor components $\beta_{\mu\nu}$ are given by relations (7). Thus, we have verified by direct calculation that the Onsager relations for the transport coefficients $\sigma_{\mu\nu}$, $\beta_{\mu\nu}$, and $\gamma_{\mu\nu}$, as determined in a linear approximation in the degeneracy parameter including the mutual electron and phonon drag, are satisfied. This gives us grounds to believe that we have consistently taken into account both the mutual influence of nonequilibrium electrons on electrons through the phonon subsystem and the mutual effect of the nonequilibrium state of phonons on phonons through the conduction electrons.

Calculate now the isothermal heat conductivity $\kappa(H)$. To do this, we substitute into the expression

$$\kappa(H) = \kappa^{\rm e}_{xx} + \kappa^{\rm ph}_{xx} - T\beta_{xx}\alpha(H) - TH\beta_{yx}Q(H) \tag{27}$$

the results obtained above for the transport coefficients to find

$$\kappa(H) = \kappa^0_{\rm ph} + L_0\sigma^{(0)}_{xx}T$$

$$\times\left\{1 + 2A_{\rm ph}(\zeta)[D_{A1} - D_{j1}] + \Gamma C_2 D_\Phi \frac{1-\gamma_{\rm F}^2}{1+\gamma_{\rm F}^2}\right\}. \tag{28}$$

Equation (28) can be used to obtain the expression for the Maggi–Righi–Leduc effect

$$\Delta\kappa(H) = \kappa(H) - \kappa(0) = -\frac{L_0\sigma_0 T\gamma_{\rm F}^2}{1+\gamma_{\rm F}^2}$$

$$\times\left\{1 + 2A_{\rm ph}(\zeta)[D_{A1} - D_{j1}] + \Gamma C_2 D_\Phi \frac{3+\gamma_{\rm F}^2}{1+\gamma_{\rm F}^2}\right\},$$

$$\kappa(0) = \kappa^0_{\rm ph} \tag{29}$$

$$+ L_0\sigma_0 T\{1 + 2A_{\rm ph}(\zeta)[D_{A1} - D_{j1}] + \Gamma C_2 D_\Phi\}$$

$$= \kappa^0_{\rm ph} + \kappa_{\rm e}(0).$$

In isothermal conditions, mutual drag contributes only to the diffusion component of the electronic heat conductivity, which is small in degenerate conductors at low temperatures where $k_{\rm B}T/\zeta \ll 1$. If the function $\Phi(\varepsilon)$ does not exhibit an anomalous dependence on the electron energy near the Fermi level on the $k_{\rm B}T$ scale, then mutual drag will not affect the dependence of the Maggi–Righi–Leduc effect on the magnetic field.

3. THERMOMAGNETIC AND THERMOELECTRIC EFFECTS IN DEGENERATE CONDUCTORS IN ADIABATIC CONDITIONS

The preceding sections were devoted to TM effects in isothermal conditions. TM effects are measured, however, in close-to-adiabatic conditions [2], because it turns out to be simpler to isolate side faces of a sample by placing it in vacuum and ensuring zero transverse heat flux than to experimentally realize the condition $\nabla_y T = 0$. Therefore, we shall consider TM effects in adiabatic conditions, namely, $j_x = 0$, $j_y = 0$, and $\nabla_y \mathbf{W} = 0$. To do this, we have first to analyze the Righi-Leduc effect, because the adiabatic corrections to the TM effect are directly expressed through the $S(H)$ coefficient characterizing the latter [3]. The Righi-Leduc effect consists in the formation of a transverse temperature gradient $\nabla_y T$ in the presence of the gradient $\nabla_x T$ and of a magnetic field perpendicular to it in the sample:

$$S(H) = \frac{\nabla_y T}{H\nabla_x T} = \frac{1}{H\kappa(H)} \tag{30}$$

$$\times\{\kappa_{yx} - T\beta_{yx}\alpha(H) + TH\beta_{yy}Q(H)\}.$$

We make use of (7), (8), (10), (26), and (28) to obtain

$$S(H) = \frac{L_0\sigma^0_{yx}T\{1 + 2A_{\rm ph}(\zeta)[D_{A2} + D_{j2}] + (2C_2\Gamma D_\Phi)/(1+\gamma_{\rm F}^2)\}}{H\{\kappa^{(0)}_{\rm ph} + L_0\sigma^{(0)}_{xx}T[1 + 2A_{\rm ph}(D_{A1} - D_{j1}) + 2C_2\Gamma D_\Phi(1-\gamma_{\rm F}^2)/(1+\gamma_{\rm F}^2)]\}}. \tag{31}$$

As is seen from (31), mutual drag contributes only to the diffusion components of the effects in both isothermal and adiabatic conditions. The smallness of these contributions to the $S(H)$ coefficient is due to the smallness of the degeneracy parameter, $k_{\rm B}T/\zeta \ll 1$. Therefore, in our subsequent analysis of the adiabatic correc-

tions to the TM effect, we shall restrict ourselves to the approximation

$$S(H) = \frac{\gamma_F \xi}{H(1+\xi+\gamma_F^2)}, \quad \xi = \frac{\kappa_e(0)}{\kappa_{ph}^0}. \tag{32}$$

Using the expressions [3]

$$\begin{aligned} Q_{ad}(H) &= Q(H) + S(H)\alpha(H), \\ \alpha_{ad}(H) &= \alpha(H) - H^2 S Q(H), \end{aligned} \tag{33}$$

for the transverse or longitudinal NE effects in adiabatic conditions we obtain

$$Q_{ad}(H) = \frac{\pi^2 k_B \gamma_F}{3eH(1+\xi+\gamma_F^2)} \times \left\{ D_0 + \Gamma D_{Qj} + \xi \left[\frac{3}{\pi^2} A_{ph} + 3k_B T \left[\frac{k'(\varepsilon)}{k(\varepsilon)} \right]_{\varepsilon=\zeta} \right] \right\}, \tag{34}$$

$$\Delta\alpha_{ad}(H) = -\frac{\pi^2 k_B \gamma_F}{3eH(1+\xi+\gamma_F^2)} [D_0 + \Gamma D_{Qj}].$$

The magnitude of the adiabatic correction to the longitudinal NE effect is determined by the ξ parameter. If the electronic heat conductivity is not too small compared to the phonon one, it will affect both the magnitude of the longitudinal NE effect and its magnetic-field dependence. Any deviation from isothermality more strongly influences the transverse NE effect. In contrast to the isothermal contribution, the adiabatic correction to this effect does not contain the degeneracy parameter. For $3\xi A_{ph}/\pi^2 > |D_0|$, it will determine both the magnitude and the sign of the effect, with the $Q_{ad}(H)$ coefficient being positive throughout the magnetic field range covered, irrespective of the dominant carrier scattering mechanism. It should be taken into account that, for a parabolic dispersion law, we have $D_0 \approx ak_BT/\xi$, where a is about –3/2 for electron scattering from a random charged-center system and $a \sim 1/2$ for scattering from acoustic phonons [16]. In the case where electron scattering from acoustic phonons is dominant, $Q_{ad}(H) > 0$ for all magnetic fields. If electron scattering from charged impurities predominates, one can conceive two possible magnetic-field dependences of the $Q_{ad}(H)$ coefficient, depending on the relative magnitude of the diffusion and phonon drag contributions. For $3\xi A_{ph}/\pi^2 < 3k_BT/2$, the coefficient $Q_{ad}(H)$ is negative, and in the opposite case we have $Q_{ad}(H) > 0$ throughout the magnetic-field range covered. Thus, in degenerate conductors and at low temperatures, the nonisothermality of the transverse NE effect substantially affects both the magnitude and sign of the effect and changes its dependence on the magnetic field.

Equations (28) and (32) can be used to find the heat conductivity in adiabatic conditions

$$\begin{aligned} \kappa_{ad}(H) &= \kappa(H)(1+H^2S^2) \\ &= \left(\kappa(0) - \frac{\gamma_F^2 \kappa_e(0)}{1+\gamma_F^2} \right) \left(1 + \frac{\gamma_F^2 \xi^2}{(1+\xi+\gamma_F^2)^2} \right). \end{aligned} \tag{35}$$

It can be reduced to the expression for the Maggi–Righi–Leduc effect:

$$\Delta\kappa_{ad}(H) = -\xi \left\{ \left(\frac{\gamma_F^2}{(1+\gamma_F^2)(1+\xi)} \right) \left(1 + \frac{\xi^2 \gamma_F^2}{1+\xi+\gamma_F^2} \right) - \frac{\xi \gamma_F^2}{1+\xi+\gamma_F^2} \right\}. \tag{36}$$

A numerical analysis of this relation showed that the magnetic-field dependence of $\Delta\kappa_{ad}(H)$, similar to $\Delta\kappa(H)$, follows a characteristic pattern with saturation in the strong magnetic-field domain, $\gamma_F \gg 1$. The magnitude of the adiabatic correction in weak fields is controlled by the ξ parameter, but in strong fields the role it plays decreases in inverse proportion to the squared magnetic field.

In conclusion, we present an expression for the Ettingshausen effect, which consists in the onset of a transverse temperature gradient $\nabla_y T$ in a conductor with current j_x placed in a magnetic field $\mathbf{H} = (0, 0, H)$ in the absence of transverse flows $j_y = 0$, $\nabla_y \mathbf{W} = 0$, as well as for a zero longitudinal temperature gradient $\nabla_x T = 0$:

$$P = \frac{TQ(H)}{\kappa(H)} \approx \frac{\pi^2 k_B T \gamma_F (D_0 + \Gamma D_{Qj})}{eH\kappa_{ph}^0 (1+\xi+\gamma_F^2)}. \tag{37}$$

Mutual drag does not result in a change of the magnetic-field dependence of the Ettingshausen effect, as well as of the isothermal Nernst–Ettingshausen and Maggi–Righi–Leduc effects, while affecting the magnitude of the phenomenon itself through the term proportional to the mutual drag parameter.

Thus, we have considered thermomagnetic and thermoelectric phenomena in conductors with degenerate carrier statistics in both isothermal and adiabatic conditions. We have calculated the transport coefficients for nonequilibrium electron-phonon systems by including the mutual drag of electrons and phonons in a linear approximation in the degeneracy parameter. It has been shown that in isothermal conditions, mutual drag considerably influences the magnitude of the Nernst–Ettingshausen effects while not changing their dependences on the magnetic field. The contribution of the mutual drag to the isothermal Maggi–Righi–Leduc effect turns out to be proportional to the degeneracy parameter.

We calculated the Righi-Leduc effect and analyzed the adiabatic corrections to the TM effect. It was shown that the contribution of mutual drag to the Righi-Leduc effect is proportional to the degeneracy parameter and should be small in the case of strong degeneracy. The magnitude of the adiabatic correction to the longitudinal NE effect is determined by the ratio of the electronic to phonon heat conductivity, and it decreases in inverse proportion to the squared magnetic field in the strong magnetic-field domain. The influence of nonisothermality is strongest on the transverse NE effect. In contrast to the isothermal contribution, the adiabatic correction to this effect does not contain the degeneracy parameter. In degenerate conductors and at low temperatures, it strongly influences both the magnitude and sign of the effect, and is capable of changing the magnetic-field dependence of the transverse NE effect.

Note that this work has been performed within the commonly accepted approach [7–15] to the consideration of effects associated with the mutual drag of electrons and phonons. This approach assumes that the phonon relaxation rate in normal scattering processes, $\nu^{\lambda}_{\mathrm{ph}N}(q)$, is much less than that involving momentum loss, $\nu^{\lambda}_{\mathrm{ph}R}(q)$ [19], and that the momentum relaxation of a nonequilibrium phonon system can be described with a single parameter, the total phonon-momentum relaxation rate ν_{ph}. In the conditions where $\nu^{\lambda}_{\mathrm{ph}N}(q) \geq \nu^{\lambda}_{\mathrm{ph}R}(q)$, one has to take into account the specific role of the normal phonon-scattering processes, which result in the relaxation of the phonon system to a locally equilibrium distribution with an average drift rate. In this case, the momentum relaxation in the nonequilibrium phonon system should be described by three parameters, namely, two relaxation rates and the drift velocity. Note that the drift velocity should be found by solving coupled transport equations for nonequilibrium electronic and phonon distribution functions. This approach should permit a better description of momentum relaxation in a nonequilibrium electron-phonon system and, accordingly, of the transport phenomena in degenerate conductors.

ACKNOWLEDGMENT

The author is grateful to A.P. Tankeev and V.I. Okulov for fruitful discussions.

This work was supported by the Russian Foundation for Basic Research (project no. 00-02-16299).

REFERENCES

1. L. É. Gurevich, Zh. Éksp. Teor. Fiz. **16**, 193 (1946); *ibid.*, **16**, 416 (1946).
2. I. M. Tsidil'kovskiĭ, *Thermomagnetic Phenomena in Semiconductors* (Nauka, Moscow, 1960).
3. V. M. Askerov, *Electronic Transport Phenomena in Semiconductors* (Nauka, Moscow, 1985).
4. F. J. Blatt, P. A. Schroeder, C. L. Foiles, and D. Greig, *Thermoelectric Power of Metals* (Plenum, New York, 1976; Metallurgiya, Moscow, 1980).
5. R. N. Gurzhi, Usp. Fiz. Nauk **94**, 689 (1968); R. N. Gurzhi and A. I. Kopeliovich, Usp. Fiz. Nauk **133**, 33 (1981).
6. P. S. Zyryanov and M. I. Klinger, *Quantum Theory of Electronic Transport in Crystalline Semiconductors* (Nauka, Moscow, 1976).
7. L. É. Gurevich and I. Ya. Korenblit, Fiz. Tverd. Tela (Leningrad) **6**, 856 (1964).
8. I. G. Lang and S. T. Pavlov, Zh. Éksp. Teor. Fiz. **63**, 1495 (1972) [Sov. Phys. JETP **36**, 793 (1972)].
9. I. I. Hanna and E. H. Sondheimer, Proc. R. Soc. London, Ser. A **239**, 247 (1957).
10. E. H. Sondheimer, Proc. R. Soc. London, Ser. A **234**, 391 (1956).
11. J. E. Parrott, Proc. Phys. Soc. London, Sect. B **70**, 590 (1957).
12. J. Appel, Z. Naturforsch. A **12**, 410 (1957); *ibid.*, **13**, 386 (1958).
13. I. M. Tsidilkovskiĭ and I. G. Kuleyev, Semicond. Sci. Technol. **11**, 625 (1996).
14. I. G. Kuleev, Fiz. Met. Metalloved. **87** (6), 5 (1999); Fiz. Tverd. Tela (St. Petersburg) **41**, 1753 (1999).
15. I. G. Kuleev, Fiz. Tverd. Tela (St. Petersburg) **42**, 415 (2000) [Phys. Solid State **42**, 423 (2000)].
16. I. G. Kuleev, I. I. Lyapilin, A. T. Lonchakov, and I. M. Tsidilkovski, Zh. Éksp. Teor. Fiz. **103**, 1447 (1993) [JETP **76**, 707 (1993)].
17. I. G. Kuleev, I. I. Lyapilin, A. T. Lonchakov, and I. M. Tsidilkovskiĭ, Fiz. Tekh. Poluprovodn. **28**, 937 (1994) [Semiconductors **28**, 544 (1994)].
18. I. G. Kuleev, I. I. Lyapilin, A. T. Lonchakov, and I. M. Tsidilkovskiĭ, Zh. Éksp. Teor. Fiz. **106**, 1205 (1994) [JETP **79**, 653 (1994)].
19. J. Callaway, Phys. Rev. **113**, 1046 (1959).

Translated by G. Skrebtsov

Physics of the Solid State, Vol. 42, No. 6, 2000, pp. 1017–1022. Translated from Fizika Tverdogo Tela, Vol. 42, No. 6, 2000, pp. 986–991.

METALS AND SUPERCONDUCTORS

Thermal Conductivity and Lorentz Number of the "Golden" Phase of the $Sm_{1-x}Gd_xS$ System with Homogeneous Variable Valence of Samarium

A. V. Golubkov[1], A.V. Gol'tsev[1], L. S. Parfen'eva[1], I. A. Smirnov[1], H. Miserek[2], J. Mucha[2], and A. Jezowski[2]

[1] *Ioffe Physicotechnical Institute, Russian Academy of Sciences, Politekhnicheskaya ul. 26, St. Petersburg, 194021 Russia*

[2] *Institute for Low Temperatures and Structural Studies, Polish Academy of Sciences, 53-529 Wroclaw, Poland*

Received November 4, 1999

Abstract—The thermal conductivity and electrical resistivity are measured in the temperature range 160–300 K for two compositions of the "golden" phase of the $Sm_{1-x}Gd_xS$ system with $x = 0.14$ and 0.3, in which a homogeneous variable valence of samarium ions is observed. It is found that, in this temperature range, the experimentally obtained Lorentz number L appearing in the electron component of thermal conductivity for these compositions exceeds the theoretical Sommerfeld value $L_0 = 2.45 \times 10^{-8}$ WΩ/K^2 typical of metals and highly degenerate semiconductors. It is also proved that the value of L increases with temperature in the interval 160–300 K starting from 160 K. A theoretical model capable of explaining the obtained experimental results is discussed. © *2000 MAIK "Nauka/Interperiodica".*

The physical properties of the $Sm_{1-x}Gd_xS$ system of solid mixtures have been investigated since 1973 [1], and many papers devoted to the study of this system have been published. Unfortunately, the thermal conductivity κ of $Sm_{1-x}Gd_xS$ was investigated only in [2], where the value of κ was measured in the temperature range 80–300 K for two compositions with $x = 0.1$ and 0.14, pertaining to the so-called "black" phase of this system. At the same time, the data on $\kappa(T)$ provide interesting information on the scattering mechanisms for charge carriers and phonons in the substance, as well as the information on the electron band structure of a material under investigation.

Let us first recall the main features of the $Sm_{1-x}Gd_xS$ system.

(1) In $Sm_{1-x}Gd_xS$ with $x = 0.16$, a first-order isostructural (NaCl–NaCl) phase transition occurs from a strongly degenerate semiconductor (or "poor" metal) to a metal in which samarium ions are in the state with a homogeneous variable valence ($Sm^{2.6+}$) [1, 3–6]. During the phase transition ($x = 0.16$), the crystal lattice constant (at 300 K) changes from $a_{x<0.16} = 5.85$ Å to $a_{x>0.16} = 5.68$ Å [7, 8]. The phase transition occurs due to the intrinsic "chemical compression" of samarium ions, emerging due to a difference in the ionic radii of Sm^{2+} and Gd^{3+} ions.

(2) Samples are black in the composition range $x =$ 0–0.16 ("black" phase *B*), but acquire golden-yellow color after the phase transition at $x > 0.16$ ("golden" phase *G*).[1]

(3) The samples of $Sm_{1-x}Gd_xS$ with $x = 0.16$ (up to $x \sim 0.3$–0.35) at $T \lesssim 120$–150 K undergo a $G \longrightarrow B$ phase transition with a change in the lattice constant from ~5.68 to 5.83–5.85 Å. The transition (which is reversible in temperature) occurs jumpwise, the bulk sample being transformed into a powder. As the temperature increases from 300 to 900 K, a "gradual" phase transition is observed from a metal to a strongly degenerate semiconductor (*B*). The lattice constant at 900 K becomes 5.53–5.85 Å. The transition is reversible in temperature, and the sample is not destroyed as a result of thermal cycling (Fig. 1) [5, 7, 9, 10].

(4) Under a hydrostatic pressure $P_{cr} \sim 6.5$ kbar (300 K), SmS experiences an isostructural (NaCl $\longleftrightarrow$ NaCl) first-order semiconductor–metal phase transition ($B \longrightarrow G$) with the lattice constant changing from 5.95 to 5.68–5.7 Å. After the removal of pressure, the reverse transition ($G \longrightarrow B$) takes place, with a considerable pressure hysteresis. The reverse transition is accompanied by sample cracking and pulverization [5, 6, 11].

In the $Sm_{1-x}Gd_xS$ system, compositions with x up to 0.16 under a hydrostatic pressure for $P_{cr}(Sm_{1-x}Gd_xS) <$

[1] For the sake of brevity, we shall henceforth denote by the $B \longrightarrow G$ and $G \longrightarrow B$ transitions the isostructural phase transitions from a strongly doped semiconductor ("poor" metal) to a metal in which Sm ions are in a state with a homogeneous variable valence ($Sm^{2.6+}$), as well as the reverse phase transition, respectively.

1063-7834/00/4206-1017$20.00

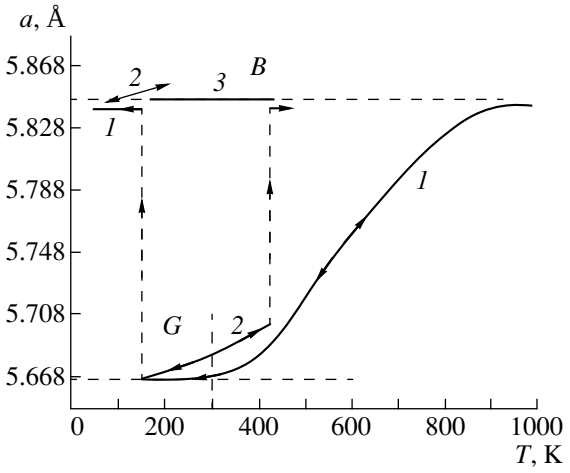

Fig. 1. Dependence of the crystal lattice constant on the composition in the $Sm_{1-x}Gd_xS$ system: (*1*) $x = 0.17$ (*G*) [5, 7, 9, 10], (*2*) $x \sim 0.13$ (*G*) (after the application of a hydrostatic pressure ~4 kbar [7, 14, 15]), and (*3*) $x = 0.15$ (*B*) [7, 9, 10].

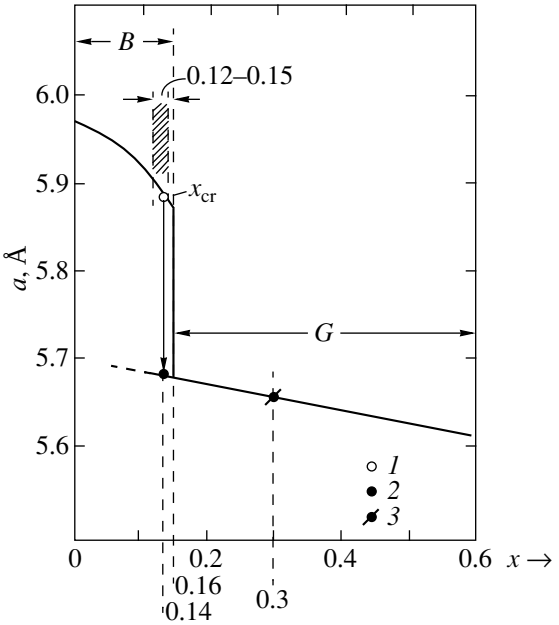

Fig. 2. Dependence of the crystal lattice constant on the composition in the $Sm_{1-x}Gd_xS$. The solid curve describes the results obtained in [8], and symbols are experimental results for compositions with $x = 0.14$: (*1*) "black" *B* phase [2]; (*2*) "golden" *G* phase (after the hydrostatic compression of the sample with $x = 0.14$ (*B*) to ~4 kbar); x_{cr} is the critical concentration of Gd for which the $B \longrightarrow G$ phase transition takes place; (*3*) $x = 0.3$ ("golden" *G* phase); *B* and *G* are the regions of "black" and "golden" phases, respectively.

$P_{cr}(SmS)$[2] also undergo a $B \longrightarrow G$ transition similar to that observed in SmS [5–7]. After the removal of pressure, the reverse phase transition $G \longrightarrow B$ takes place. The only exception in the $Sm_{1-x}Gd_xS$ system are compositions with $x = 0.12$–0.15. The samples of such compositions can be transformed into the "golden" phase *G* under a hydrostatic pressure of ~4 kbar (300 K). After the removal of pressure, the state with a homogeneous variable valence of Sm ions is preserved in these samples in the temperature range ~150–400 K for an indefinitely long time (Fig. 1) [5, 7, 12–17]. After the removal of pressure, the samples do not crack, and the changes in the sample structure are insignificant: after the treatment by pressure, monocrystalline blocks in them are broken into fragments having a size of ~100 μm and disoriented by 4° [14]. The reversible $G \longrightarrow B$ phase transition can be induced in such samples by temperature [7, 14, 15]. A transition accompanied by the sample breakdown occurs at $T \sim 150$ and 400 K (Fig. 1).

(5) The conduction band of $Sm_{1-x}Gd_xS$ is constructed from the "heavy" *d* and "light" *s* subbands for the "black" phase and *s*, *d*, and *f* ("superheavy") subbands in the "golden" phase [5, 18, 19].

Let us now describe the results obtained in the present research.

The aim of this work is (1) to determine the magnitude and temperature dependence of κ of the "golden" phase for compositions with $x = 0.3$ and 0.14 (of the sample subjected to a hydrostatic pressure) of the $Sm_{1-x}Gd_xS$ system in the temperature range 160–300 K, and (2) to find out whether the Lorentz number is affected by the presence of a homogeneous variable valence of samarium ions in the "golden" phase.

The samples for experiments were prepared as follows. SmS and GdS were synthesized from the elements [20, 21]. The obtained material was used to prepare melted polycrystalline or monocrystalline $Sm_{1-x}Gd_xS$ samples with $x = 0.14$ and 0.3. The synthesis and melting of the samples were carried out in sealed tantalum containers [20, 21] in an induction furnace. Material losses were reduced to a minimum, owing to the reliable sealing of the containers in which the melting and annealing of the samples were carried out.

The samples with $x = 0.14$ were subjected to hydrostatic compression in special bombs up to pressures of ~4 kbar which led to a $B \longrightarrow G$ phase transition in them. The "golden" phase remained stable at 300 K indefinitely.

We measured the crystal lattice constants (*a*) at 300 K, the thermal conductivity (κ) and the resistivity (ρ) in $Sm_{1-x}Gd_xS$ samples with $x = 0.3$ and 0.14 in the temperature range 160–300 K (in the "black" and "golden" phases).

The x-ray diffraction analysis was carried out on a DRON-2 setup (in the CuK_α radiation), and the values of κ and ρ were measured on a setup similar to that used in [22].

The results of measurements are presented in Figs. 2–5.

[2] $P_{cr}(Sm_{1-x}Gd_xS) < P_{cr}(SmS)$ in view of the presence of an additional intrinsic "chemical compression" in the solid mixture.

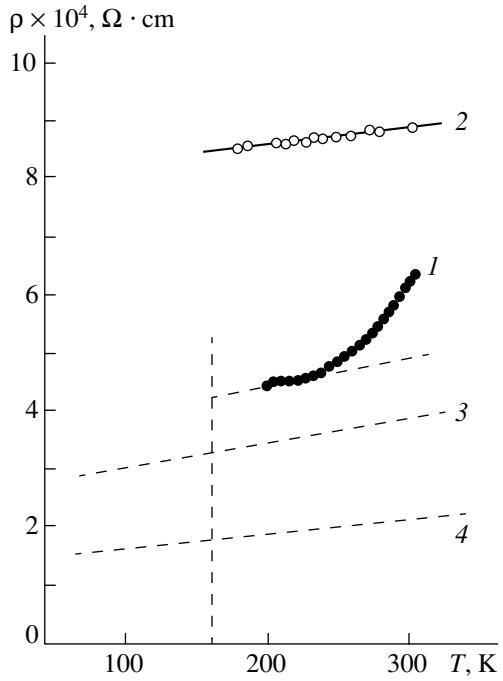

Fig. 3. Temperature dependence of ρ for $Sm_{1-x}Gd_xS$ for various values of x: (*1* and *4*) $x = 0.14$ for the *B* and *G* phases respectively, (*2*) $x = 0.3$ (*G* phase), (*3*) $x = 0.1$ (*B* phase). The data for the dependences *3* and *4* are borrowed from [2].

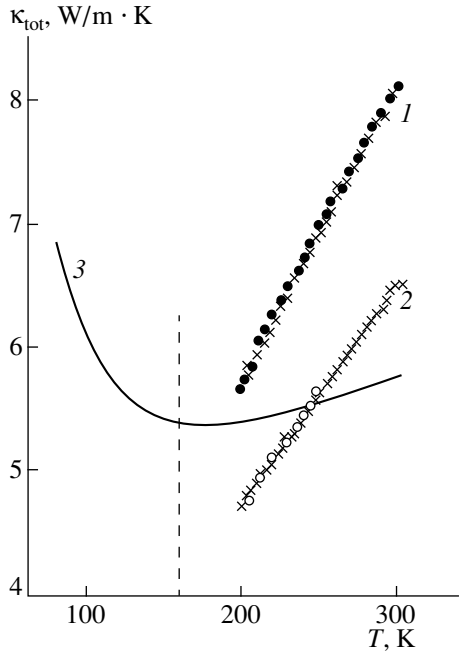

Fig. 4. Temperature dependence of the total thermal conductivity κ_{tot} for $Sm_{1-x}Gd_xS$ with various values of x: (*1* and *3*) $x = 0.14$ for the *G* and *B* phase, respectively, (*2*) $x = 0.3$ (*G* phase). The data described by curve (*3*) are borrowed from [2]. The crosses and circles on curves *1* and *2* correspond to measurements with the temperature decreasing from 300 to 200 K and increasing from 200 to 300 K, respectively.

Figure 2 shows the crystal lattice constants for a number of compositions of $Sm_{1-x}Gd_xS$ compositions. The value of a for a composition with $x = 0.3$ (*G* phase) agreed with the available data [8]. The values of a for $x = 0.14$ (*G* phase) fit to the $a(x)$ dependence extrapolated from the region with $x > 0.16$ to that with $x < 0.16$. The same figure also shows the results obtained for $x = 0.14$ (*B* phase) in [2].

Figure 3 presents the data on $\rho(T)$. For both compositions of the *G* phase with $x = 0.3$ and 0.14, the $\rho(T)$ dependence is of the metallic type. For comparison, Fig. 3 shows the values of $\rho(T)$ obtained in [2] for the *B* phase with the compositions $x = 0.1$ and 0.14. It should be noted that the $\rho(T)$ curve for $x = 0.14$ (*G* phase) exhibits a behavior differing from that of $\rho(T)$ for the compositions of the $Sm_{1-x}Gd_xS$ system presented in Fig. 3. A similar behavior of $\rho(T)$ was observed in [8] for $Sm_{1-x}Gd_xS$ with a composition $x = 0.17$ (*G* phase) in the vicinity of the "critical" concentration $x_{cr} \sim 0.16$. The difference in the values of ρ for samples with $x = 0.14$ (*B*) and 0.14 (*G*) is probably due to a lower mobility of samples with the "golden" phase as compared to those with the "black" phase. This also refers to the sample with the composition $x = 0.3$ (*G*).

Figure 4 presents the experimental data for the measured total thermal conductivity (κ_{tot}) for the "golden"

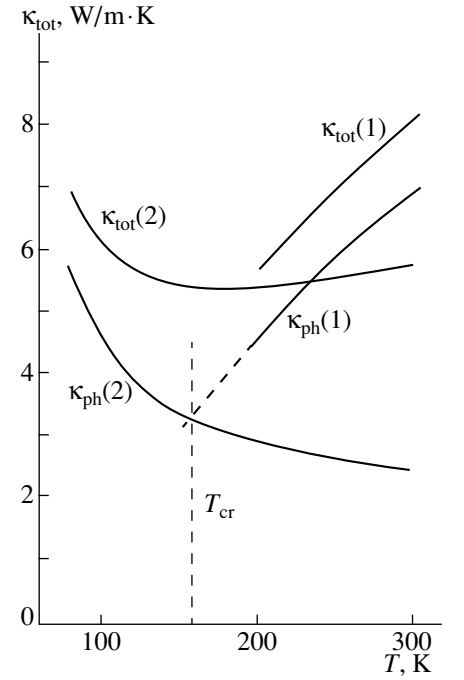

Fig. 5. Temperature dependences of the total thermal conductivity (κ_{tot}) and lattice conductivity component (κ_{ph}) for $x = 0.14$ in the *B* and *G* phases of $Sm_{1-x}Gd_xS$: (*1*) *G* phase, (*2*) *B* phase [2]. While calculating the electron component of thermal conductivity (κ_e), we assumed that $L = L_0$, T_{cr} is the temperature of the inverse phase transition $G \longrightarrow B$ for a sample with $x = 0.14$ (*G*).

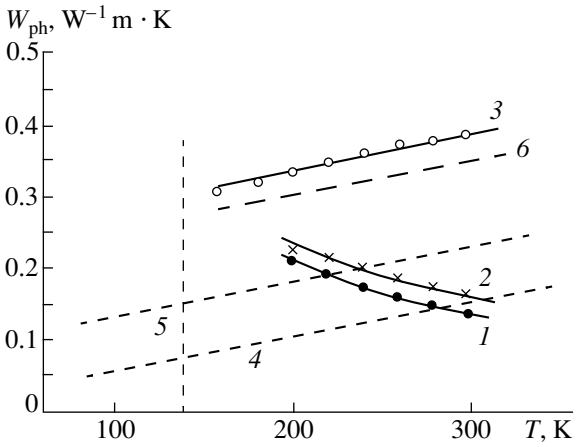

Fig. 6. Temperature dependence of the thermal resistance of the crystal lattice for various values of x in $Sm_{1-x}Gd_xS$: curves *1* and *3* correspond to $x = 0.14$ for the *G* and *B* phase, respectively [2], curve *2* corresponds to $x = 0.3$ (*G* phase), and curves *4–6* represent data obtained for SmS, $Sm_{1.015}S$ [23, 24], and $Sm_{0.9}Gd_{0.1}S$ (*B* phase) [2]. Points on curves *1*, *2*, and *3* are taken from the averaged experimental curves. While calculating κ_e, we assumed that $L = L_0$.

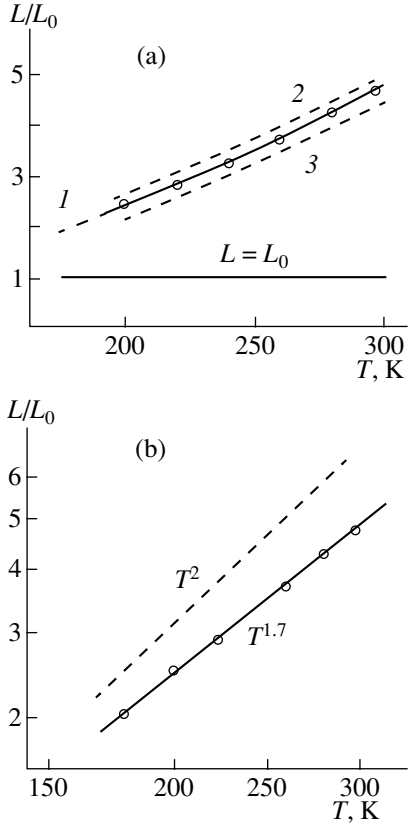

Fig. 7. (a) Experimental value of $L/L_0(T)$ for $Sm_{0.86}Gd_{0.14}S$ (*G* phase), points represent dependence *1*; curves *2* and *3* correspond to $L/L_0(T)$ for $\kappa_{ph}(G)$ smaller or greater than $\kappa_{ph}(B)$, respectively; (b) temperature dependence of L/L_0; points correspond to experimental values for $Sm_{0.86}Gd_{0.14}S(G)$. Dashed curve describes the dependence $L/L_0 \sim T^2$ according to [29] [(see formula (7)], given to compare the slopes of the theoretical and experimental curves.

($x = 0.14$ and 0.3) and "black" ($x = 0.14$ [2]) phases of the system under investigation:

$$\kappa_{tot} = \kappa_{ph} + \kappa_e, \tag{1}$$

where κ_{ph} and κ_e are the lattice and electron components of thermal conductivity, respectively.

The value of κ_e can be calculated from the Wiedemann–Franz law

$$\kappa_e = L\rho/T. \tag{2}$$

For metals and strongly degenerate semiconductors with elastic scattering of charge carriers, we have

$$L = L_0 = 2.45 \times 10^{-8}\ \mathrm{W\Omega/K^2}. \tag{3}$$

Figure 5 shows the values of κ_{tot} and κ_{ph} for the composition $x = 0.14$ in the *G* and *B* phases. The values of κ_e were calculated by formula (2) taking into account (3). The data for the composition $x = 0.14$ in the *B* phase were borrowed from [2].

Finally, Fig. 6 depicts thermal resistances $W_{ph}(T) = 1/\kappa_{ph}(T)$ for samples of the *G* phase with $x = 0.14$ and 0.3, for which κ_e was calculated by (2) and (3). For the sake of comparison, the same figure gives information for samples of the *B* phase with $x = 0.1$ [2] and SmS [23, 24].

Let us try to interpret the obtained experimental data. The results presented in Figs. 5 and 6 lead to the conclusion that the behavior of $\kappa_{ph}(T)$ and $W_{ph}(T)$ for samples of the "black" phase [($x = 0.1$ (*B*) and 0.14 (*B*)] when κ_{ph} is separated from the total thermal conductivity κ_{tot} under the assumption that $L = L_0$ in the Wiedemann-Franz law for κ_e does not contradict the basic theory for the lattice thermal conductivity: $\kappa_{ph} \sim T^{-1}$ for $T \geq \Theta$, where Θ is the Debye temperature [25]. This does not apply to samples of the "golden" phase [($x = 0.14$ (*G*) and 0.3 (*G*)]. In this case, the parameters exhibit anomalous behavior upon a change in temperature. What is the reason behind the observed anomaly? It is hard to assume that this is associated with $\kappa_{ph}(T)$. In all probability, this anomaly appears because of incorrect determination of κ_e. In other words, $L \neq L_0$ for samples of the "golden" phase of $Sm_{1-x}Gd_xS$.

Let us consider in greater detail the results obtained for the composition with $x = 0.14$ (*G*). Considerable difficulties are encountered in separating κ_{ph} from the data on κ_{tot} in the case when $\kappa_{ph} \simeq \kappa_e$. In our situation, we tried to solve this problem by using a not quite standard technique. As the first approximation, we assumed that $\kappa_{ph}(G)$ is equal to $\kappa_{ph}(B)$. Then the actual value of L for the composition $x = 0.14(G)$ can be calculated from the following relation:

$$L = \frac{[\kappa_{tot}(G) - \kappa_{ph}(B)]\rho(G)}{T}. \tag{4}$$

The values of $L/L_0(T)$ obtained according to (4) are presented in Fig. 7a. The value of $L/L_0(T)$ can be smaller or greater than that in Fig. 7a (curve *1*) if the value of $\kappa_{ph}(G)$ is respectively smaller than $\kappa_{ph}(B)$ (curve *2* in Fig. 7a) due to the emergence of defects in the formation of defects in the sample after the $B \longrightarrow G$ phase transition (although, as mentioned above, only a small rotation of crystallites is observed during the formation of the metallic phase in this sample due to hydrostatic compression [14]), or if $\kappa_{ph}(G)$ is greater than $\kappa_{ph}(B)$ (curve *3* in Fig. 7a) due to the crystal lattice "compaction" as a result of a decrease in the lattice parameter during the phase transition (see Fig. 2). Our calculations proved, however, that in both cases, the value of $L/L_0(T)$ for reasonably chosen parameters does not differ significantly from the values depicted by curve *1* in Fig. 7a. It should be noted that in all cases, the value of L/L_0 increases with temperature.

On the basis of the data presented in Fig. 4, one can expect similar behavior of $L/L_0(T)$ for a composition with $x = 0.3$ (*G*).

Let us try to interpret theoretically the obtained experimental results.

The temperature dependence of the Lorentz number $L(T)$ in the "golden" phase can be explained in the theory of first-order isostructural valence transitions in compounds with a variable valence, which was proposed in a recent publication by Goltsev and Bruls [26]. Although this theory was developed thoroughly for describing the isostructural valence transition in the compounds $YbIn_{1-x}Ag_xCu_4$, its general results can also be applied to $Sm_{1-x}Gd_xS$. The main physical idea underlying this theory lies in the fact that a nonmagnetic metallic state of rare-earth ions with a fractional valence (such ions in $Sm_{1-x}Gd_xS$ are Sm ions; as noted above, Gd ions here play the role of a "chemical press", their valence before and after the phase transition remaining unchanged and equal to +3) is a result of coherence stabilization in the Kondo scattering of conduction electrons (holes) at the electrons localized in 4*f* shells of rare-earth ions. As a result of this effect, quasiparticle excitations are of a hybrid nature, being a quantum-mechanical superposition of states from the conduction band and localized 4*f* states. Such quasiparticles are usually referred to as "heavy fermions". In the framework of the theory [26], the isostructural transition in $Sm_{1-x}Gd_xS$ should be treated as a transition from a strongly degenerate semiconductor and a heavy-fermion metal, i.e., the "golden" phase is a state with heavy fermions. This conclusion could be confirmed by a fairly large value of the linear coefficient of specific heas (γ) observed for many typical heavy-fermion compounds. However, the information on γ for $Sm_{1-x}Gd_xS$ obtained from heat capacity measurements is not available. There are data on γ for the "golden" phase in $Sm_{1-x}Y_xS$ in which Y, like Gd in $Sm_{1-x}Gd_xS$, ensures, due to the difference in the ionic radii of Sm^{2+} and Y^{3+}, a "chemical compression" of samarium, which is sufficient for its transition to a state with a variable valence of $Sm^{2.6+}$ for $x \gtrsim 0.2$. For a composition of $Sm_{1-x}Y_xS$ with $x = 0.33$, $\gamma = 50$ mJ/mole K^2 [27].[3] We can assume that the value of γ for compositions of the "golden" phase of $Sm_{1-x}Gd_xS$ investigated by us will be of the same order of magnitude.

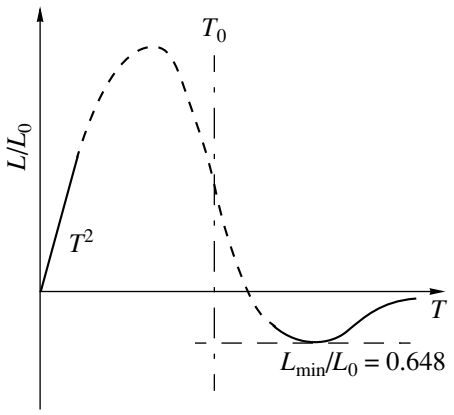

Fig. 8. Theoretical dependence of L/L_0 on T [29]. The solid curve describes the low-temperature segment corresponding to dependence (7) and the high-temperature segment corresponds to numerical calculations [29]. The dashed curve represents a possible dependence $L/L_0(T)$. The formulas for calculating this segment are not given in [29]; T_0 is the low-temperature Kondo scale.

Another argument in favor of the above assumption is the enhanced paramagnetic susceptibility of the electron liquid in $Sm_{1-x}Gd_xS$ of the "golden" phase, in contrast to the Curie–Weiss susceptibility of Sm^3 ions in the "black" phase [5, 6, 23].

In the framework of such a physical interpretation of the "golden" phase, one can explain the behavior of $L(T)$ presented in Fig. 7. Indeed, according to [29], the collisions between heavy fermions in the heavy-fermion state at $T < T_0$ lead to the following expression for the Lorentz number:

$$L(T) = L_0 + \alpha(T/T_0)^2, \tag{5}$$

where α is a certain numerical coefficient and T_0 is the low-temperature Kondo scale (Fig. 8). The value of T_0 can be estimated from the data on the magnetic susceptibility χ at $T = 0$:

$$\chi(T = 0) = \frac{C(1 - \Delta n_f)}{T_0} \tag{6}$$

(where C is the Curie–Weiss constant for Sm^{3+} ions, and Δn_f is the deviation of the valence of Sm ions from

[3] For the "golden" phase of SmS obtained under hydrostatic compression of the sample up to 7–12 kbar, the value of γ obtained from heat capacity measurements amounted to ~145 mJ/mole K^2 [28].

the integral value +3) and from the data for the linear coefficient of specific-heat

$$\gamma = \frac{1/3\pi^2 k_B^2 N_f}{T_0}, \quad (7)$$

where $N_f = 1 - \Delta n_f$.

The estimation of the value of T_0 on the basis of formula (7) for $\gamma \sim 50$ mJ/mole · K^2 gives the value $T_0 \geqslant 500$ K. Such a value of T_0 fits well to the description of the behavior of $L/L_0(T)$ in a system with heavy fermions [29]. The application of this model is justified by the closeness of the experimental dependence $L/L_0 \sim T^{1.7}$ to the quadratic law [cf. formula (5)] [29].

The main conclusion of this work can be formulated as follows. For samples in the "golden" phase of $Sm_{1-x}Gd_xS$ exhibiting a homogeneous variable valence of samarium ions, $L > L_0$ in the temperature range 160–300 K, the value of L/L_0 increasing with temperature. Such a behavior of $L/L_0(T)$ can be explained on the basis of the theory [29], in which the isostructural phase transition $B \longrightarrow G$ is regarded as a transition from a strongly degenerate semiconductor to a heavy-fermion metal.

ACKNOWLEDGMENTS

The authors are grateful to N. F. Kartenko for carrying out x-ray diffraction experiments with the samples.

This research was carried out in accordance with a bilateral agreement between the Russian Academy of Sciences and the Polish Academy of Sciences, with the financial support of the Russian Foundation for Basic Research, grant nos. 99-02-18078 and 98-02-18299.

REFERENCES

1. A. Jayaraman, E. Bucher, P. Dernier, and L. D. Longinotti, Phys. Rev. Lett. **31** (11), 700 (1973).
2. A. V. Golubkov, L. S. Parfen'eva, I. A. Smirnov, *et al.*, Fiz. Tverd. Tela (St. Petersburg) **41** (1), 26 (1999) [Phys. Solid State **41** (1), 22 (1999)].
3. V. A. Shaburov, A. I. Egorov, G. A. Krutov, *et al.*, Zh. Éksp. Teor. Fiz. **68** (1), 326 (1975) [Sov. Phys. JETP **41**, 158 (1975)].
4. A. I. Egorov, E. V. Petrovich, Yu. P. Smirnov, *et al.*, Izv. Akad. Nauk SSSR, Ser. Fiz. **40** (2), 395 (1976).
5. I. A. Smirnov and V. S. Oskotskiĭ, Usp. Fiz. Nauk **124** (2), 241 (1978) [Sov. Phys. Usp. **21**, 117 (1978)].
6. D. I. Khomskiĭ, Usp. Fiz. Nauk **129** (3), 443 (1979) [Sov. Phys. Usp. **22**, 879 (1979)].
7. A. Jayaraman, P. Dernier, and L. D. Longinotti, Phys. Rev. B **11** (8), 2783 (1975).
8. M. Ohashi, T. Kaneko, H. Yoshido, and S. Abe, Physica B **86-88**, 224 (1977).
9. S. P. Nikanorov, Yu. A. Burenkov, A. B. Lebedev, *et al.*, Phys. Status Solidi A **105**, K103 (1988).
10. Yu. A. Burenkov, A. V. Golubkov, V. V. Zhdanova, *et al.*, Fiz. Tverd. Tela (Leningrad) **33** (8), 2350 (1991) [Sov. Phys. Solid State **33** (8), 1322 (1991)].
11. A. Jayaraman, V. Narayanamurti, E. Bucher, and R. G. Maines, Phys. Rev. Lett. **25**, 368 (1970).
12. I. L. Aptekar', V. I. Rashchupkin, and E. Yu. Tonkov, Fiz. Tverd. Tela (Leningrad) **23** (6), 1589 (1981) [Sov. Phys. Solid State **23** (6), 930 (1981)].
13. V. I. Rashchupkin, I. L. Aptekar', V. K. Gartman, and E. Yu. Tonkov, Fiz. Tverd. Tela (Leningrad) **20** (3), 799 (1978) [Sov. Phys. Solid State **20** (3), 463 (1978)].
14. B. A. Abdikamalov, I. L. Aptekar', V. M. Sergeeva, and E. Yu. Tonkov, Fiz. Tverd. Tela (Leningrad) **21** (1), 187 (1979) [Sov. Phys. Solid State **21** (1), 108 (1979)].
15. I. A. Smirnov, J. Phys. Colloq. **41** (6), 143 (1980).
16. A. V. Golubkov, A. I. Egorov, T. S. Orlova, *et al.*, Fiz. Tverd. Tela (Leningrad) **29** (12), 3683 (1987) [Sov. Phys. Solid State **29** (12), 2107 (1987)].
17. A. V. Golubkov, V. M. Egorov, T. S. Orlova, *et al.*, Phys. Status Solidi A **105**, K93 (1988).
18. E. V. Shadrichev, L. S. Parfen'eva, V. I. Tamarchenko, *et al.*, Fiz. Tverd. Tela (Leningrad) **18** (8), 2380 (1976) [Sov. Phys. Solid State **18** (8), 1388 (1976)].
19. O. V. Farberovich, Fiz. Tverd. Tela (Leningrad) **21** (11), 3434 (1979) [Sov. Phys. Solid State **21** (11), 1982 (1979)].
20. A. V. Golubkov, T. B. Zhukova, and V. M. Sergeeva, Izv. Akad. Nauk SSSR, Neorg. Mater. **2** (11), 77 (1966).
21. A. V. Golubkov and V. M. Sergeeva, Preprint of Institute of Metal Physics, UNTS AN SSSR (Sverdlovsk, 1977).
22. A. Jezowski, J. Mucha, and G. Pompe, J. Phys. D: Appl. Phys. **20**, 1500 (1987).
23. V. S. Oskotskiĭ and I. A. Smirnov, in *Rare-Earth Semiconductors*, Ed. by V. P. Zhuze and I. A. Smirnov (Nauka, Leningrad, 1977).
24. V. P. Zhuze, E. V. Goncharova, N. F. Kartenko, *et al.*, Phys. Status Solidi A **18**, 63 (1973).
25. V. S. Oskotskiĭ and I. A. Smirnov, *Defects in Crystals and Thermal Conduction* (Nauka, Leningrad, 1972).
26. A. V. Goltsev and G. Bruls, submitted to Phys. Rev. B.
27. S. Von Molnar, T. Penney, and F. Holtzberg, J. Phys. Colloq. **37** (10), 241 (1976).
28. S. D. Bader, N. E. Phillips, and D. B. McWhan, Phys. Rev. B **7**, 4686 (1973).
29. V. I. Belitsky and A. V. Goltsev, Physica B **172**, 459 (1991).

Translated by N. Wadhwa

Physics of the Solid State, Vol. 42, No. 6, 2000, pp. 1023–1025. Translated from Fizika Tverdogo Tela, Vol. 42, No. 6, 2000, pp. 992–994.

METALS AND SUPERCONDUCTORS

Microwave Studies of Bi(2212) HTSC Single Crystals at Nitrogen Temperatures

A. V. Prikhod'ko and N. M. Shibanova

St. Petersburg State Technical University, Politekhnicheskaya ul. 29, St. Petersburg, 195251 Russia

Received September 7, 1999; in final form, November 29, 1999

Abstract—Absorption of microwave power by single-phase Bi(2212) crystals with a broad (15 K) phase transition has been studied. A temperature-localized drop of microwave power absorption at the beginning of the superconducting transition at 80 K has been established. A possible mechanism of this absorption feature based on the concept of synchronization of Josephson junctions near T_c is discussed. *© 2000 MAIK "Nauka/Interperiodica".*

Two main directions can be singled out in the experimental studies of coherent effects associated with the formation of the superconducting state. One of them deals with the so-called coherent effects II [1], which are directly related to the coherent Cooper-pair interaction. The other involves the investigation of macroscopic quantum effects associated with the existence of a multiply connected Josephson medium [2]. Our earlier microwave studies of coherent effects were carried out on Bi(2212) single crystals in the mm-wavelength range [3]. We observed effects of two types, namely, the existence of a coherent conduction peak, which is anisotropic in single-phase crystals, and a change in the standing-wave profile near the sample surface. The latter effect was attributed by us to the existence of Josephson junctions in single- and multiphase crystals. The threshold condition for the manifestation of Josephson effects is the Josephson frequency

$$\omega_J = \frac{2eV}{\hbar} = 10^{11}\ \mathrm{s}^{-1},$$

which is of the order of 100 GHz (for a voltage of 10^{-4} V [2], if one takes into account rectification at inhomogeneities in the sample). At the same time, the threshold condition for coherent effects II is

$$\omega_S = \frac{2\Delta}{\hbar},$$

which amounts to 2.4×10^{11} s^{-1} for a binding energy of 10^{-3} eV.

To study the coherent conduction peak, one should naturally perform measurements in the mm-wavelength range, because the generation of quasiparticle pairs occurs at frequencies starting with the threshold value. Note that the coherence factor is manifested most strongly at the energies of the pair localized near the gap edge.

This work deals with the absorption of microwave power by single-phase HTSC crystals $Bi_2Sr_2CaCu_2O_8$ [Bi(2212)] in the 10-cm wavelength range, where the condition $\omega < \omega_J$ is satisfied. The idea underlying the experiment is based on the assumption that individual Josephson junctions become synchronized near the phase transition [2]. An analysis of the Josephson current in the reverse Josephson effect indicates that odd harmonics do appear, even in the absence of a constant potential difference. Hence, the temperature dependence of the power absorbed by a sample should have a feature similar to the formation of harmonics in ceramic HTSC samples near T_c. This work is devoted to searching for such features.

1. SAMPLES AND TECHNIQUE

The samples used by us were $Bi_2Sr_2CaCu_2O_8$ single crystals prepared by spontaneous crystallization from the melt in air [4]. The sample dimensions in the (*ab*) plane were 4×3 mm. In contrast to the samples studied earlier [3], these samples were not annealed after the growth at 800–820°C in air and, hence, had a composition differing more strongly from the optimum cation oxidation for this material [4]. The deviation in composition is also accompanied by lower temperatures of transition to the superconducting state and a wider transition width for the samples compared to those studied in [3]. The superconducting transition temperature was determined from the appearance of a microwave absorption signal in the EPR experiment [5]. The transition to the

1063-7834/00/4206-1023$20.00

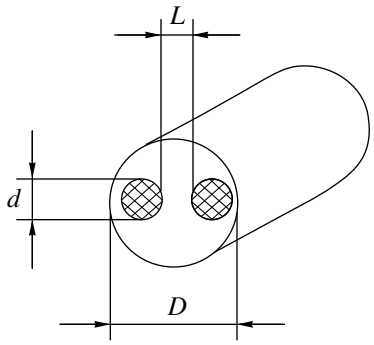

Fig. 1. Segment of the resonator probe scanning the sample surface.

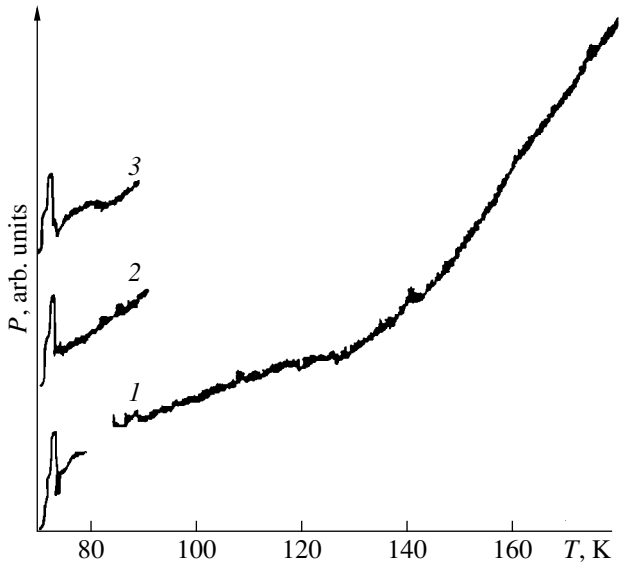

Fig. 2. Temperature dependence of power P for a $Bi_2Sr_2CaCu_2O_8$ single crystal (curve *1*) and reproduction of the peak in two consecutive thermal cycles (curves *2* and *3*).

superconducting state started at 80 K. The width of the phase transition was not less than 15 K; i.e., the transition was broad and terminated at 65 K. The existence of a broad superconducting transition in a single crystal is a key factor in experiments aimed at revealing specific features of a Josephson medium, because it is well known that the transition width is determined primarily by the size distribution of the Josephson network [2].

The microwave properties were studied on a setup based on a coaxial quarter-wave resonator probe made of a symmetrical twin line [6]. The sample was placed at the antinode of the electric field at the center of a rectangular waveguide. Figure 1 shows a segment of the probe scanning the sample surface. The probe dimensions were $D = 1$ mm, $d = 0.16$ mm, and $L = 0.5$ mm. The resonance frequency of the probe was 0.942 GHz. Measurements were made in the temperature interval from 78 to 300 K. The resonator probe was used to measure the power P related inversely to the microwave power absorbed by the sample. The microwave power absorbed by the sample decreased with increasing signal P.

2. RESULTS AND DISCUSSION

Figure 2 shows the temperature dependences of the signal P obtained from the probe when the basal plane of the sample is parallel to the electric field. As seen from Fig. 2, a well-reproducible peak appears at the beginning of the superconducting transition, at approximately 80 K, (the temperature corresponding to the onset of the transition coincides with the peak). In our opinion, the presence of this peak may indicate a manifestation of coherence effects in a Josephson medium with a broad network-size distribution. The existence of coherence effects in a medium with a narrow size distribution (the transition width did not exceed 5 K) was reported in [3].

It may be surmised that, using ceramics as an analogy [2], the key factor in the onset of superconducting state in the case of single-crystal samples with a broad Josephson-network size distribution is the existence of a superconducting network; at temperatures close to critical, the network breaks up into separate contours with built-in Josephson junctions, and the process is accompanied by a sharp drop in the microwave power absorbed by the sample (the peak of the signal in Fig. 2).

Note that the process of breakup and formation of a Josephson network is reversible, which is evidenced by a persistent recurrence of the peak of signal P upon thermal cycling (curves *1–3* in Fig. 2).

The origin of the coherent interaction among a large number of Josephson junctions in the field of an electromagnetic wave remains obscure. It is conjectured that the so-called "effective junctions" play a dominant role [2]. In the case of monocrystalline Bi(2212) samples, it can be assumed that superconducting currents produce loops at the defects associated with compositional nonstoichiometry, including oxygen deficiency, or at twinning boundaries, which can exist in single-phase samples. The relation between the character of structural defects and the parameters of the observed sharp drop in microwave power absorbed by a sample will be the subject of future study.

ACKNOWLEDGMENTS

Support of the Ministry of Science and Technology, program "Superconductivity," is gratefully acknowledged.

REFERENCES

1. M. Tinkham, *Introduction to Superconductivity* (McGraw-Hill, New York, 1975; Atomizdat, Moscow, 1980).
2. V. F. Masterov, in *High-Temperature Superconductivity*, Ed. by A. A. Kiselev (Mashinostroenie, Leningrad, 1990), p. 405.
3. M. N. Kotov, V. F. Masterov, V. V. Potapov, *et al.*, Int. J. Infrared Millimeter Waves **14** (8), 1679 (1993).
4. N. M. Shibanova, V. V. Potapov, N. M. Baranova, *et al.*, Sverkhprovodimost: Fiz., Khim., Tekh. **6** (12), 597 (1993).
5. V. F. Masterov, I. L. Likholit, A. V. Fedorov, *et al.*, Sverkhprovodimost: Fiz., Khim., Tekh. **5** (12), 2235 (1992).
6. V. F. Masterov, A. V. Prikhod'ko, O. I. Kon'kov, and A. A. Shaklanov, Fiz. Tverd. Tela (St. Petersburg) **39** (1), 97 (1997) [Phys. Solid State **39** (1), 84 (1997)].

Translated by G. Skrebtsov

Physics of the Solid State, Vol. 42, No. 6, 2000, pp. 1026–1035. Translated from Fizika Tverdogo Tela, Vol. 42, No. 6, 2000, pp. 995–1003.

METALS AND SUPERCONDUCTORS

Intercalated Hydrogen in Yttrium Barium Cuprate: The State and Mobility of a "Guest" and Modification of the "Host" Properties

Yu. M. Baĭkov

Ioffe Physicotechnical Institute, Russian Academy of Sciences, Politekhnicheskaya ul. 26, St. Petersburg, 194021 Russia
e-mail: shadr.solid@pop.ioffe.rssi.ru

Received November 22, 1999

Abstract—The electric, magnetic, and physicochemical properties of yttrium barium hydrocuprate ($H_2YBa_2Cu_3O_7$) and its oxidized form ($H_2YBa_2Cu_3O_{7.8}$) are governed, to a large measure, by poorly studied behavior of hydrogen atoms in the lattice. The crystal chemical state and the mobility of a proton intercalated into yttrium barium cuprate have been investigated by the isotope exchange and inelastic neutron scattering techniques. By their behavior in the process of inelastic neutron scattering, a substantial fraction of protons can be considered mechanically free particles without chemical bonding with oxygen ions. The self-diffusion coefficient of a proton is estimated to be several orders of magnitude larger than that of oxygen ions, the latter coefficient being equal to 10^{-13} cm^2 s^{-1} at 490 K. Considerable changes in the lattice parameters and local charge distribution in the copper–oxygen subsystem are revealed by the x-ray powder diffraction analysis and nuclear quadrupole resonance (NQR). Discrete changes in the interplanar spacings along the *c* axis and in the Cu NQR frequencies with a gradual variation in the degrees of hydration and oxidation indicate the formation of hydrocuprate and (or) oxyhydrocuprate in the matrix of the initial material. © *2000 MAIK "Nauka/Interperiodica".*

1. INTRODUCTION

Yttrium barium cuprate of composition $YBa_2Cu_3O_y$, $6 \le y \le 7$, (hereafter, $YBCO_y$) was synthesized in February 1987 [1] almost immediately after the discovery of high-temperature superconductivity in complex oxides. Investigations into the influence of hydrogen on the properties of $YBCO_7$ (and the "nearest related compounds" in which yttrium is replaced by rare-earth elements) have already been started in summer 1987. The history and results of these investigations were described in detail in the reviews [2, 3]. The main objective of researches in this field of high-temperature superconductivity physics was to modify the electronic subsystem of an oxide by electrons of intercalated hydrogen atoms. Nuclei of these atoms (protons) were assigned the role of a probe sensitive to local features of magnetic fields in the lattice. These explorations were carried out with a wide variety of physical methods at different laboratories in Europe, America, Japan, and Israel. However, the results obtained were not universally unambiguous. Some effects, for example, the direction of variations in the lattice parameters or the T_c temperature upon hydrogen incorporation (see [2, 3]), differed qualitatively. It has become evident that there are uncontrollable "nonphysical" factors, among which the process of hydrogen intercalation is of decisive importance, as it was demonstrated in the review [2] prepared with the author's participation. At present, chemical aspects of the interaction between hydrogen and $YBCO_7$ have been studied in sufficient detail [4–6]. The conditions for hydrogen intercalation were established with due regard for the competition of three processes. One of these processes—deintercalation of oxygen—does not lead to hydrogen incorporation but accompanies two other processes—the formation of hydride-like "hydrogen bronze" at a low hydrogen content (less than 10 at. %) and the formation of a hydrogenated form in the initial cuprate matrix at a hydrogen content as much as two atoms per formula units. (In what follows, $H_xYBa_2Cu_3O_y = H_x\ldots O_y$ will be referred to as hydrocuprate at $y \le 7$ and as oxyhydrocuprate at $y > 7$.) In the vast majority of research works, the wide diversity of hydrogen (proton) forms occurring in yttrium barium cuprate were disregarded in studies of physical phenomena, which resulted in the discrepancy of the data obtained. Moreover, the investigation into chemical aspects of the hydrogen intercalation revealed that the intercalated proton is an extremely active "guest," so that the hydrogen-containing derivatives of yttrium barium cuprate with the empirical formula $H_xYBa_2Cu_3O_y$ ($0 < x \le 2$ and $6.9 < y < 7.8$) represent new members of the Y–Ba–Cu–O (or, more precisely, H–Y–Ba–Cu–O) family. These compounds possess some interesting physical properties, but in a manner that is different from those of superconductivity. In particular, among these compounds are antiferromagnets, semiconductors, and proton conductors [3, 7, 8]. Of crucial importance in the understanding of the physical properties of new members in the H–Y–Ba–Cu–O family is having information on the state and mobility of a

1063-7834/00/4206-1026$20.00

proton (guest) in the crystal lattice and the interaction of the proton with ionic and electronic subsystems of the "host."

The fact that yttrium barium cuprate is a "hospitable host" for hydrogen is undisputed, but the question of the chemical structure of the proton (hydrogen) incorporated into yttrium barium hydrocuprate and yttrium barium oxyhydrocuprate remains open for discussion. The contrary viewpoints are represented by the "hydride" and "hydroxide" hypotheses. They were thoroughly considered by the author and his colleagues in the review [2]. Actually, these hypotheses can also be formulated in a somewhat different way: (i) hydrogen can exist as a "free" monoatomic particle (H^-, H^0, or H^+) in the crystal lattice, and (ii) hydrogen can form the chemical bond with an oxygen ion (OH^- or H_2O). The latter statement seems more "natural" for oxides. However, the hydride hypothesis historically appeared first and was more popular for a long time. For this reason, the problems concerning the localization of a proton in the YBCO lattice and its mobility (including self-diffusion, chemical diffusion, and electromigration) have remained controversial or completely unsolved up to this time. In order to obtain further insight into these problems, in the present work, we employed the isotope exchange and inelastic neutron scattering techniques. Both methods are characterized by the selective sensitivity just to hydrogen, its mobility, and the state of hydrogen in crystal lattice. It was necessary to answer the principal question: How much is the degree of proton delocalization if oxygen serves as a proton "trap"?

Another aspect of the "hydrogen–yttrium barium cuprate" problem concerns the influence of intercalated hydrogen on the oxide properties. According to the available data [8–10], the proton turns out to be an extremely active guest modifying the crystal and, especially, electronic structures of the oxide host. Electrons carried by hydrogen atoms fill the hole states of the initial cuprate, as a result of which it loses the metallic and superconducting properties and becomes antiferromagnet and semiconductor. Changes observed in the charge states of copper ($Cu^{2+} + e^- \longrightarrow Cu^{1+}$) and oxide sites ($O^{2-} + H^+ \longrightarrow OH^-$), along with the appearance of an interstitial proton, bring about changes in the interatomic interactions (Coulomb and covalent) and manifest themselves in variations of the crystal lattice parameters. These changes, as a rule, were ignored in studies of the samples with a relatively low hydrogen content. Analysis of the correctness of this approach is beyond the scope of the present work. Our attention was focused on high hydrogen concentrations when we really dealt with new compounds in the Y–Ba–Cu–O family at a high hydrogen content and an increased oxygen content. From the data available in the literature by the time our explorations started (1997), it has become clear that the YBCO compounds with a high hydrogen content (up to two atoms per formula unit) have been studied only by three research groups—two groups in Germany (under the guidance of R. Schöllhorn at Berlin Technical University and A. Weidinger at Hahn–Meitner University) and our group (Ioffe Physicotechnical Institute, Russian Academy of Sciences). The investigations performed revealed the universal feature of variations in the lattice parameter, irrespective of means for intercalating hydrogen into $YBa_2Cu_3O_7$, namely, the appearance of an intense peak of x-ray scattering at small angles corresponding to the interplanar spacings in the range 1.25–1.35 nm, which exceed the "standard" parameter $c \sim 1.17$ nm for $YBCO_7$. In the light of the available data for metal hydrides (a relative increase in the volume per one hydrogen atom is as much as 17% [11]), the lattice expansion upon hydrogen intercalation did not appear as an anomalous phenomenon; however, the cause of variations in the lattice parameter upon hydrogenation of YBCO remained unknown. It could be assumed that the above variations are primarily caused by changes in the copper–oxygen subsystem, specifically in its charge state and coordination. In order to examine these changes, we chose the copper nuclear quadrupole resonance (Cu NQR) technique, because its efficiency was proved in studies of nonhydrogenated members of the family $LnBa_2Cu_3O_{7-\delta}$ (Ln = Y, Gd, Nd, La, etc.; $0 \le \delta \le 1$) [12–14]. The combined employment of the x-ray powder diffraction analysis and Cu NQR technique for the study of the same samples made it possible to perform a reliable comparison between averaged and local changes in the lattice of yttrium barium cuprate. The main purpose of the present work was to trace the evolution of variations in the lattice parameters and NQR spectra in going from the initial nonhydrogenated $YBCO_7$ cuprate to the $H_2YBa_2Cu_3O_7$ hydrocuprate and its oxidized form. For lack of theoretical methods for analyzing a very complex system, the investigation into the evolution of the lattice parameters in going from the well-known compound to the new system seems to be most justified.

2. EXPERIMENTAL TECHNIQUES

Yttrium barium hydrocuprate with the empirical formula $H_2YBa_2Cu_3O_7$ was used as the main object in the investigation of the state and mobility of a proton. (Here, for brevity, the hydrogen and oxygen stoichiometric indices are integers, even though they actually vary in the ranges $1.9 < x < 2.05$ and $6.85 < y < 6.95$). It should be noted that the hydrogen modification of the cuprate properties was studied with due regard for the evolution of the x-ray diffraction patterns and Cu NQR spectra under variations in the content of both hydrogen and oxygen. The technological aspects of hydrogen and oxygen treatments were reported in [4, 6].

The basic principles of the experimental techniques and their features specific for the object under investigation—yttrium barium cuprate—were described in the other works, including those of the author of the present paper.

The inelastic neutron scattering technique for proton conductors was considered generally, for example,

Table 1. Degrees of isotope exchange F for hydrogen (columns F–Hydr) and oxygen (columns F–Ox) in the $H_2YBa_2Cu_3O_7$–water vapor system at 413, 443, and 490 K

T, K	413		443		490	
P_{water}, Pa	7		44		460	
Q_{solid}, mg	6		35		70	
t, min	413 K		443 K		490 K	
	F–Hydr[a)]	F–Ox[b)]	F–Hydr[a)]	F–Ox[b)]	F–Hydr[a)]	F–Ox[b)]
5	–	–	0.60	0.05	–	–
15	0.12	0.00	0.92	0.12	1.00	0.29
30	0.22	0.05	0.98	0.25	1.00	0.47
60	0.39	0.12	1.00	0.32	–	0.62
150	0.78	0.19	–	0.51	–	0.87
300	0.92	0.25	–	0.64	–	–
600	1.00	0.36	–	0.81	–	–
1400	1.00	0.48	–	–	–	–

Note: Specific surface area, 1 $m^2\ g^{-1}$; mean grain size, 1 μm. P_{water} is the partial pressure of water vapor, and Q_{solid} is the amount of solid phase.

[a] The mean accuracy of determination $\Delta F = \pm 0.03$.

[b] The mean accuracy of determination $\Delta F = \pm 0.05$.

in [15], and more specifically for hydrocuprate in [16]. The experiment was carried out on a TFXA backscattering spectrometer (resolution $\Delta\omega/\omega \geq 2\%$) with the use of an ISIS pulsed neutron source (Rutherford Appleton Laboratory, Chilton, UK).

The Cu NQR technique as applied to the exploration of cuprate superconductors was described in considerable detail in many works. The measurements were performed on a setup at the Julich Research Center. The experimental details, specific for our investigation, were reported, for example, in [13].

The x-ray powder diffraction analysis was carried out on a STADI diffractometer (Stoe & CIE GmbN, Germany) at the Julich Research Center.

The isotope exchange technique was thoroughly described in [5, 17]. The features, essential for the understanding and analysis of the experimental data obtained for the given system, are reported below. In the present work, unlike our earlier work [17], the isotopically substituted water vapor species $D_2^{16}O$, $H_2^{18}O$, and $D_2^{18}O$ brought to physicochemical equilibrium with hydrocuprate were chosen as counterparts. This allowed simultaneous observation of the behavior of both oxygen and hydrogen. In the experiment, an equilibrium water vapor pressure (for example, 460 Pa at 490 K) was first established in a small closed volume (~100 cm^3) over the studied sample. Then, this volume was connected through a circulating pump to a large vessel (~ 3000 cm^3) containing a gas mixture. In this mixture, nitrogen or argon served as a gas carrier and the partial pressure of isotopically substituted water vapors was equal to the vapor pressure in the small closed volume over the sample. The above experimental technique made impossible variations in the chemical composition of the solid phase, i.e., the appearance of chemical concentration gradients for hydrogen and oxygen, which could lead to the chemical diffusion. According to the experimental conditions (volume of gas phase, partial pressure of water vapors, and amount of solid phase), the content of D and (or) ^{18}O in the gas phase upon attainment of an equilibrium should be halved and amount to ~ 45 at. % D and 28 at. % ^{18}O. This estimate was obtained under the assumption that all the intercalated hydrogen atoms are involved in the exchange and only oxygen atoms that occupy the Cu(1) plane are capable of participating in the exchange (~ one atom per formula unit or ~ 14% of the total oxygen content in $YBCO_7$) (see review [18]). Since a set of peaks corresponding to masses in the range from 16 to 22 in the mass spectrum virtually elude analysis, the isotopic composition of selected vapor phase samples was determined by the decomposition of vapor on hot carbon to hydrogen (H_2, HD, and D_2) and carbon monoxide ($C^{16}O$ and $C^{18}O$). This considerably improved the accuracy of analysis but drastically decreased the number of points in the kinetic curve.

3. RESULTS AND DISCUSSION

3.1. Mobility and State of Proton in Yttrium Barium Cuprate

3.1.1. Isotope exchange. In the first experiments, it was found that the dependences of the degree of isotope exchange F on the time t for hydrogen and oxygen cannot be described by the same equations. As a rule, the $F(t)$ curves are fitted to the appropriate mathematical models, which enables one to determine two main parameters of the process: (i) the rate of chemical conversion J of water vapor atoms into oxygen ions and (or) protons of a solid on the surface and (ii) the diffusion coefficients of oxygen D_O and (or) hydrogen D_H in the bulk of a grain. As can be seen from Table 1, the exchange rate of hydrogen in the temperature range studied is considerably higher than that of oxygen. However, these differences cannot be completely judged from comparison of the observed degrees of isotope exchange. The matter is that the kinetic curves $F(t)$ for hydrogen and oxygen differ in shape. This suggests that the rates of the process are controlled by different stages. Figure 1 displays the kinetic curves on the generalized coordinates. It can be seen from the figure that all the data for oxygen well fit the model curve corresponding to the diffusion-controlled rate in the bulk of a grain when the ratio between the numbers of exchanging atoms in the gas and the solid is equal to 1 : 1. The shape of this curve is determined by the parameter $G = d^2/\pi^2 D_O$. At temperatures of 413, 443, and 490 K, the values of G are equal to 140, 14, and 3 h, respectively. By assuming that the grain sizes are identical at all the temperatures, we obtain the temperature dependence of the diffusion coefficient for oxygen in the hydrocuprate under consideration, which is characterized by an activation energy of approximately 1 eV. This value falls in the range of energies presented in the review [18]. As regards the absolute value of D_O, it can be determined only with the knowledge of the grain sizes. The grain-size analysis proved to be not suitable for their determination, because the hydrogenation resulted in the refinement of the initial grains down to micron and submicron sizes. According to the data on the specific surface area obtained by the krypton adsorption technique (~ 1 m^2/g instead of 0.05 m^2/g in the initial sample), the mean size of the hydrocuprate grains is equal to ~ 1 μm. Then, $D_O = 2 \times 10^{-15}$, 2×10^{-14}, and 10^{-13} cm^2/s at 413, 443, and 490 K, respectively. These values are close to those determined by the extrapolation of the D_O coefficients for yttrium barium cuprate toward the high-temperature range [18]. Yoshimura *et al*. [19] obtained a somewhat lesser value of the diffusion coefficient for the hydroxide ion in yttrium barium cuprate treated with water (10^{-15} cm^2/s at 470 K); however, this coefficient actually characterizes the chemical diffusion into the sample with a low hydrogen content.

Since the kinetic curve for the isotope exchange of hydrogen on the $\ln(1 - F)$–t coordinates is represented as a straight line, the factor responsible for the rate of the process in this case is the chemical reaction at the vapor–hydrocuprate interface. Then, the lower limit of the diffusion coefficient at these conditions can be estimated from the relationship $A = Jd/DN$, where d is the characteristic grain size, and N is the concentration of diffusing particles. The exchange rate J at the interface was evaluated taking into account the characteristic grain size or, what is the same—the specific surface area of powder. The value of J is equal to 10^{-12} mol cm^{-2} s^{-1} and only slightly depends on temperature. Hence, $AD_H = 10^{-14}$ cm^2 s^{-1}. The linearity of the $\ln(1 - F)$–t curve signifies that $A < 0.1$ [5, 17, 18]; i.e., $D_H > 10^{-13}$ cm^2 s^{-1}. Undeniably, in order to evaluate the diffusion coefficient D_H, it was necessary to use considerably more large-sized crystalline grains, which we did not have at our disposal in this experiment.

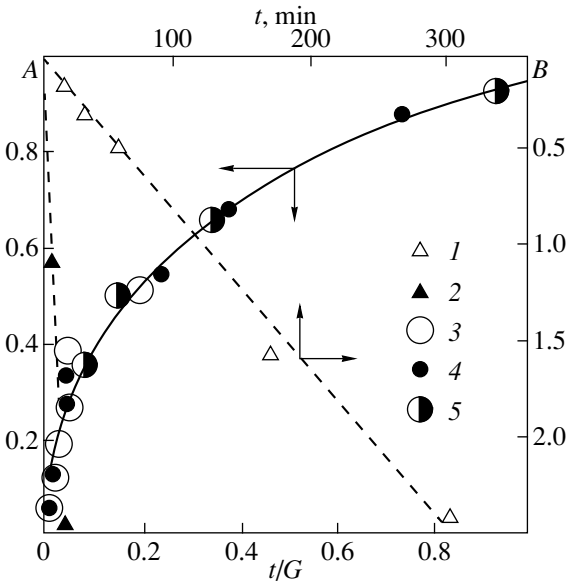

Fig. 1. Experimental and model dependences of the degree of isotope exchange F on the time t for (*1*, *2*) H–D and (*3*–*5*) ^{18}O–^{16}O exchanges in the $H_2YBa_2Cu_3O_7$–H_2O system. Temperature, K: (*1*, *3*) 413, (*2*, *4*) 443, and (5) 490. $A = F$, and $B = -\ln(1 - F)$. The solid line represents the results of calculations within the model determining the diffusion rate in the bulk of a grain when the ratio between numbers of exchanging atoms in a gas and a solid is equal to 1 : 1. G specifies the time scale (see text). Dashed lines are drawn for the benefit of clarity and correspond to the model determining the rate of hydrogen exchange at the interface.

Despite the semiquantitative character of the data obtained, they unambiguously indicate that a proton migrates in the hydrocuprate lattice "independently" of oxygen, rather than together with it. Although the oxygen ions are not proton "carriers," their participation in the migration of a proton is of crucial importance, because it is these ions that form the network of sites in which the proton executes a hopping motion. Certainly, this does not follow immediately from our experiments on isotope exchange, but it is the universally accepted concept used in analysis of the proton migration in

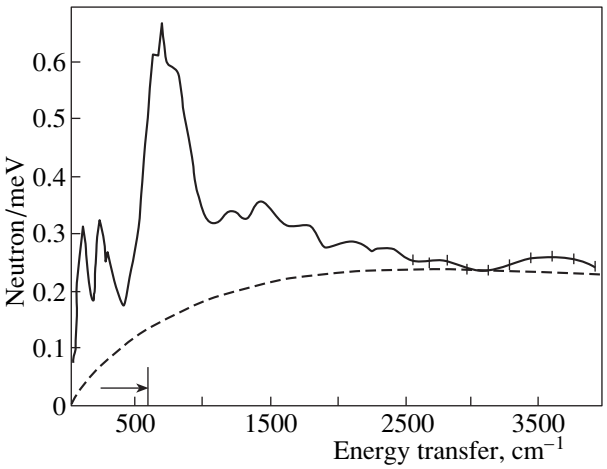

Fig. 2. The inelastic neutron scattering spectrum of $H_{1.92}YBa_2Cu_3O_{6.92}$ at a temperature of 20 K. Low-energy spectral details are not shown. Absolute error of measurements is shown in the range characteristic of the O–H stretching vibrations (2000–3500 cm^{-1}) for assessment of the reliability of the increase in intensity. The arrow indicates the upper bound of the phonon spectrum of $YBa_2Cu_3O_7$. The region below the dashed line can be defined as a continuum of "mechanically free protons" (proton gas).

oxides [20]. Note, for comparison, that a considerable difference between the mobilities of hydrogen and oxygen was also revealed in our earlier works by the isotope exchange technique for another perovskite, namely, fused crystalline $H_{0.04}BaCe_{0.8}Y_{0.2}O_{3-\alpha}$ at 920 K ($D_O = 4.2 \times 10^{-9}$ cm^2 s^{-1} and $D_H = 3.8 \times 10^{-7}$ cm^2 s^{-1}) [21], and also for solid KOH at 600 K ($D_O = 10^{-9}$ cm^2 s^{-1} and $D_H = 10^{-7}$ cm^2 s^{-1}) [22].

3.1.2. Inelastic neutron scattering. In addition to the traditional approach to the proton migration through a "crew" (together with oxygen) or hopping mechanism, we consider the probability of the migration of a free proton along appropriate channels running in the Cu(1)O and Y planes in the YBCO structure. This migration can be realized with monoatomic hydrogen forms ("free protons," atoms, or hydride ions). The arguments in favor of the existence of these forms were obtained by using the inelastic neutron scattering technique. An idea of invoking the incoherent inelastic neutron scattering technique for the investigation into the proton dynamics arose from considerable progress achieved in this field of spectroscopy in studying the behavior of protons in solids (see, for example, the review [15]). Since neutrons, unlike electrons and protons, interact only with nuclei of ions constituting the lattice, the observed energy and intensity of scattering are closely connected with the lattice dynamics. At the same time, compared to any nuclei, protons exhibit an anomalously large incoherent inelastic neutron scattering cross-section, which noticeably manifests itself in the intensity of vibrational modes connected with protons in one or another way. One can expect not only changes in the intensity of the observed lines, but also the appearance of new lines and the shift of the lines attributed to the nonhydrogenated samples. A detailed analysis of the experimental data will be the subject matter of a separate paper. In the present work, the main attention was concentrated on the general conclusions concerning the behavior of a proton in $H_2YBa_2Cu_3O_7$.

Figure 2 demonstrates the overall inelastic neutron scattering spectrum at 20 K (the total hydrogen content in the sample is 8×10^{22} atoms). The sample was prepared in the form of two ceramic plates $35 \times 35 \times 3$ mm in size. The stoichiometry of the sample is described by the empirical formula $H_{1.92}YBa_2Cu_3O_{6.92}$.

From general considerations, the inelastic neutron scattering spectrum of the studied hydrocuprate can exhibit about 40 lines due to the vibrational modes of the crystal lattice. However, many of these lines correspond to the motion of heavy atoms (Y, Ba, and Cu), and their contribution to the inelastic neutron scattering spectrum is virtually unnoticeable. Initially, the features in the inelastic neutron scattering spectrum of $H_2YBa_2Cu_3O_7$ can be interpreted using the known analogues. In actual fact, this approach touches on the discussion of the chemical state of hydrogen in $H_xYBa_2Cu_3O_7$, which, in essence, reduces to the "competition" between the hydroxide and monoatomic models. The former model suggests the presence of the O–H bond and rests on the general chemical concepts of protophilic properties of an oxide ion. The latter model is based on the metal-like properties of the $YBa_2Cu_3O_7$ compound. Although the metallic character of conductivity—the negative derivative with respect to temperature—is observed only at a low hydrogen content (< 0.2 at. %), its electronic character is retained at a high hydrogen content [7]. In a number of works [15, 20], it was noted that the O–H stretching vibrations do not manifest themselves in the inelastic neutron scattering spectrum of electron-conducting oxides, because the O–H bond is broken under the action of conduction electrons. A similar explanation seems to be reasonable in the case of hydrocuprate. However, at 20 K (the temperature at which the inelastic neutron scattering spectrum was recorded), the conductivity of $H_2\cdots O_7$ is likely to be extremely low (below room temperature, the conductivity is far less than 10^{-12} S cm^{-1}). Therefore, the breaking of the O–H bond subject to conduction electrons can hardly be responsible for the lack of indicators of this bond in the observed inelastic neutron scattering spectrum of $H_2YBa_2Cu_3O_7$. Another possible reason is a strong broadening of the line attributed to the O–H bond, which is observed, for example, for hydrogen-containing $BaCe_{1-x}Y_xO_3$ [23]. In this case, the IR absorption that corresponds to the line of the O–H bond is observed in the range 3500–2000 cm^{-1} and exhibits three submaxima. The traditional explanation of this broadening—the formation of a strong hydrogen bond at the O–O distances of shorter than 250 pm—is in con-

tradiction with the absence of so very short O–O bond lengths according to the crystallographic data: the shortest O–O distance (312 pm) is observed in $BaCeO_3$. However, in the $YBa_2Cu_3O_7$ structure, there are the shorter O–O distances, for example, the apical oxygen–"chain" oxygen or oxygen–oxygen bond lengths (~270 pm) in the BaO and Cu(2)O planes. As follows from the data on the muon–spin rotation, only the position between former oxygens can be occupied by the intercalated proton at high hydrogen concentrations (more than 0.7 atom per formula unit).

The third reason for the lack of indications of the O–H bond in the inelastic neutron scattering spectrum can be a broadening of the line assigned to the O–H bond and, correspondingly, a decrease in its intensity due to the short lifetime of a proton near the oxygen ion. The short lifetime of a proton near the oxygen ion can be explained by the presence of a "competitive" position for localization of the proton, namely, in certain crystallographic interstices as a specific potential box. This hypothesis is confirmed by the second feature observed in the inelastic neutron scattering spectra, namely, the peaks in the range 800–1000 cm^{-1}. The lines in the range of 1000 cm^{-1} are characterized by a sufficiently high intensity, and, hence, they cannot be treated as the second harmonics of modes in the range of 500 cm^{-1}. These lines could be assigned to the bending vibrations of OH^- or H_2O, but the aforementioned absence of the relevant O–H stretching vibrations permits one to propose an alternative explanation for this group of lines. The proposed approach is based on an analogy with transition metal hydrides [11], in which the lines observed in the inelastic neutron scattering spectra in the range 600–1200 cm^{-1} are attributed to the vibrations of monoatomic hydrogen forms (H^+, H^-, and H^0) in tetrahedral and (or) octahedral interstices formed by metal cations. A proton in these interstices experiences a complex combination of attractive and repulsive forces. In this respect, the actual role of these interstices as "traps" of a mechanically free proton and the character of hopping between the traps (providing a high migration mobility of the proton) call for special theoretical consideration. Moreover, the intercalation of hydrogen results in an anisotropic expansion of the YBCO lattice, and a change in the interatomic distances can essentially affect this analysis. Nonetheless, the concept of the interstitial position of a proton in yttrium barium hydrocuprate is in good qualitative agreement with the data obtained from analysis of the inelastic neutron scattering spectrum.

The third feature of the inelastic neutron scattering spectrum—a structureless continuum observed up to 4000 cm^{-1} (and above)—is of special interest. The existence of free protons in solids has long been the subject of discussions, and until recently, no experimental evidence has been put forth. The regularities of neutron scattering by an ideal gas of free particles were considered in [24]. The spectrum of HYBCO is characterized by an intensity continuum observed over the entire energy transfer range. The free proton gas can be responsible for this continuum, but, in fact, the forward inelastic neutron scattering cannot be observed upon recording of the backscattering. This is explained by the fact that the angular momentum and energy conservation laws hold true only for forward scattered neutrons. However, in the case of samples characterized by a sizable probability of secondary (elastic) scattering, the continuum observed can be associated with the multiple scattering, including the scattering by free protons.

3.2. Hydrogen-Induced Modification of $YBa_2Cu_3O_7$ Properties

3.2.1. Structural changes according to the x-ray diffraction analysis. The unit cell parameter *c* most considerably changes upon hydrogenation of samples. The *a* and *b* parameters also vary with an obvious tendency for the larger parameter to be retained and the smaller parameter to increase until they become equal (tetragonalization). However, these changes do not exceed 2%, whereas the *c* parameter varies by 10–17%. In the range of scattering angles usually observed for YBCO, the diffraction patterns are characterized by the disappearance of many peaks and a broadening of the remaining peaks; however, the location of the latter peaks changes insignificantly [25]. This evolution is most clearly observed with an increase in the hydrogen content *x* up to one hydrogen atom per formula unit. In our opinion, these findings argue for retaining the cationic skeleton of the initial cuprate. Hence, ignoring the ortho–tetra transformations, hereafter, we will use the line assignment corresponding to the $YBa_2Cu_3O_7$ structure. However, the question arises about the assignment of peaks at small diffraction angles, which correspond to the interplanar spacings in the range 1.20–1.77 nm. For the initial YBCO, the (001) peak in this range corresponds to ~ 1.17 nm, and its intensity is less than 1% of the intensity of the most intense peak (013). Upon hydrogenation, the x-ray diffraction pattern in this range changes in an intricate way (Table 2) [9, 26]. To the zeroth approximation, the main tendencies are the shift toward smaller scattering angles and a relative increase in the intensity. Closer examination of this evolution demonstrates that an increase in the degree of hydrogenation leads to discrete changes in the interplanar spacings in the following order: 1.17–1.25–1.35 nm. Note that the "mixing" of the 1.25-nm line with the 1.17-nm line characteristic of O_7 ($YBa_2Cu_3O_7$) is observed only at small degrees of hydrogenation. (Here, we will not discuss the lines observed in the range 1.55–1.70 nm for oxygen-deficient samples.) In this range, the evolution of x-ray diffraction patterns upon hydrogenation of films with a small step in the film composition was investigated in [9, 10]. It was clearly shown that the interplanar spacings change in a discrete manner, and, as the measurements were per-

Table 2. Characteristic interplanar distances (nm) corresponding to small diffraction angles for the $H_xYBa_2Cu_3O_y$ samples

x	y		
	6.4–6.7	6.8–7.0	7.4–7.8
<0.5	1.68*a* 1.17*s* 1.24*s* 1.77*s* 1.24*s* 1.55*w*	1.17*s* 1.25*s* [19] 1.26*s* 1.25*s*	
0.8–1.4	1.25 1.26*s* 1.34*w*	1.25 [9] 1.26*s* 1.29*w*	1.35 1.18
		[9], [10], [25]	[9], [25]
1.8–2.0		1.35 ±0.03	1.35 ±0.02

Note: x is the number of hydrogen atoms per formula unit; y is the number of oxygen atoms per formula unit; *s* indicates that the intensity of lines is higher than 20% of the intensity of the (013) line; and *w* designates a weak, more often broad line. Distance denoted by *a* is observed in the samples with $x \approx 0$ and $y \sim 6.5$, prepared by low-temperature treatment [2]. Two values united by curly brackets refer to the same sample.

Table 3. Frequencies (MHz) of the ^{63}Cu(1) nuclear quadruple resonance in the $H_2YBa_2Cu_3O_7$ samples

x	y				
	6.0	6.5	7.0	7.4	7.8
0	30*s*	22*w* 24	22*s*		
0.5		27*w* 30	27*w* 30*a*		
1.0		27 30	20*b* 27 30		
1.4			27 30*w*	20 24	
2.0			27*s* 30*w*	30	20*s* 30*vw*

Note: *s* indicates a strong line; *w* refers to a weaker line in the given pair; and *vw* designates a very weak but observable, more often broad line. Line denoted by *a* is broadened and overlaps with the ^{63}Cu(2) line at 31.5 MHz. Line designated by *b* is observed after oxidation of the sample (6.5/1.0). Cu NQR frequency for Cu_2O is 27 MHz.

formed with the *c*-oriented films, the assignment of the above lines to the (00*l*) reflections is beyond question.

3.2.2. Comparison of hydrogen-induced changes in the coordination sphere of copper and the lattice parameters of yttrium barium cuprate. Although the aforementioned data of x-ray diffraction analysis indicate structural transformations observed upon hydrogenation of cuprate and subsequent oxidation of hydrocuprate, they give no way of revealing the reasons for crystal chemical changes in the lattice. For instance, the case in point is the correlation between an increase in the *c* parameter and a decrease in the copper valence as a result of the reducing action of hydrogen. Qualitatively, this correlation also manifests itself upon a decrease in the copper valence due to oxygen elimination, but the quantitative changes in this case are substantially less than those upon intercalation of hydrogen: the parameter *c* is equal to 1.168 nm in $YBCO_7$, 1.187 nm in $YBCO_6$, and 1.35 nm in H_2YBCO_7.

Let us consider this phenomenon in more detail. The intercalation of two hydrogen atoms is equivalent in the reducing action to the removal of one oxygen atom and leads to a decrease in the formal copper valence from 2.33 for $YBCO_7$ to 1.67 for $YBCO_6$ or $H_2\cdots O_7$, which was experimentally established in [5, 6]. According to more detailed approaches, the elimination of oxygen brings about the formation of Cu^{1+} at the Cu(1) site. Further elaborated models treat a complex process of changes in the charge state of the copper–oxygen subsystem with the charge redistribution between Cu(1) and apical oxygen. However, in any case, variations in the charge state of Cu(1) upon elimination of oxygen are associated with the oxygen-induced change of the Cu(1) coordination from a "square" in $YBCO_7$ to a "dumbbell" in $YBCO_6$. At an intermediate oxygen content (from O_7 to O_6), there exist the Cu(1) threefold-coordinated ions; i.e., there is one vacant site in the square [13, 14]. The intercalation of hydrogen does not affect the oxygen content, but causes the charges of copper ions and (or) their environment to change. The chemical dissociation of hydrogen atoms gives rise to electrons filling the hole states of the electronic subsystem and protons forming either OH^- ions at the oxygen site or quasi-free protons in the region close to the Cu(1) plane. Since the electric field gradient on nuclei is responsible for the Cu NQR frequency, the latter quantity is sensitive to changes in both the outer electron shell and the coordination sphere of copper ions. Therefore, the investigation into the evolution of Cu NQR spectra upon intercalation of hydrogen makes it possible to elucidate the origin of crystal chemical changes on the atomic level.

At present, the Cu NQR spectra of LnBCO (Ln = Y, Cd, Nd, La, etc.) have been interpreted by separating the lines attributed to both different crystallographic sites [Cu(1) and Cu(2)] and the isotope doublet (^{63}Cu and ^{65}Cu). In the subsequent discussion, we will deal with the lines associated with ^{63}Cu(1). In the case when

some doubts were cast upon the assignment of lines to the Cu(1) or Cu(2) sites, we determined the relaxation time T_2, which considerably differed for these two sites [13]. Furthermore, in some cases, the spectrum of $H_xGdBa_2Cu_3O_y$ was studied at a temperature of 1.2 K (rather than at the conventional temperature of 4.2 K). Then, the ordering of Gd spins produced a considerable effect on the Cu(2) NQR response and did not affect the Cu(1) NQR response, which served as a basis for the assignment of the observed lines to a particular site [13].

Table 3 presents our experimental results and the data available in the literature on Cu NQR frequencies for the YBCO compounds of different oxygen and hydrogen content. Only one tendency is clearly traced: the smaller the copper valence, the higher the Cu NQR frequency. Since Cu^{1+} has the closed electron shell, only surrounding ions contribute to the electric field gradient at nuclei in the case of $YBCO_6$, $H_2\cdots O_7$, and Cu_2O. The difference in frequencies for $YBCO_6$ and Cu_2O can be explained by the small difference in the Cu–O distances (0.181 and 0.185 nm at room temperature, respectively). The coincidence of the Cu NQR frequencies for Cu_2O and $H_2\ldots O_7$ most likely is accidental. The assumption that Cu_2O arises as a product of the chemical decomposition is ruled out, because the formation of Cu_2O in appreciable amounts is not observed. For $H_2\cdots O_{7.8}$ and $YBCO_7$ with a higher oxidation state of copper, the electron shell of the copper ion also makes a contribution to the electric field gradient. This is likely the reason why the Cu NQR frequencies for these compounds are less than those for the Cu^{1+}-containing samples of $YBCO_6$ and $H_2\cdots O_7$ by approximately the same value (8 and 7 MHz, respectively). The coordination numbers for the hydrogen-containing samples were not determined experimentally. It can be assumed that, upon hydrogenation, the coordination number of Cu(1) with respect to oxygen remains equal to four, but the charge of this coordination sphere decreases owing to the proton incorporation. Upon oxidation of hydrocuprate, "excess" oxygen (i.e., above seven atoms per formula unit) fills "empty" sites in the Cu(1)–O plane. Therefore, the unit cell can contain eight atomic oxygen ions (or OH^-), and the oxygen octahedron can be formed around Cu(1) (coordination number is six).

Since the Cu(1) coordination sphere undergoes a considerable change due to the influence of intercalated hydrogen, according to the Cu NQR data, we can argue that the protons and electrons carried by hydrogen atoms are localized in the crystal lattice region near the Cu(1)–O basal plane. This conclusion is in complete agreement with the data obtained in the muon–spin investigations [27, 28].

It should be emphasized that only the NQR frequencies listed in Table 3 manifest themselves in the spectra with a gradual change in the composition $YBCO_6 \longrightarrow YBCO_7$, $YBCO_7 \longrightarrow H_2\cdots O_7$, and $H_2\cdots O_7 \longrightarrow H_2\cdots O_{7.8}$. No shift in these frequencies is observed, even though the broadening of peaks (attended by a decrease in the intensity at a maximum) is a "typical" situation. In essence, the evolution of the Cu NQR spectra is similar to the above-described evolution of the x-ray diffraction patterns in the case when the appearance of particular peaks, rather than their regular shift, is observed in the x-ray diffraction patterns at small angles. The coincidence in the behavior of local (NQR) and macroscopically averaged (x-ray diffraction) characteristics can be explained in the simplest way by the formation of new phases in the matrix of the initial compound, for example, $H_2\cdots O_7$ in $YBCO_7$ or $H_2\cdots O_{7.8}$ in $H_2\cdots O_7$. Note that the ratio "new phase : initial phase" varies with absorption of hydrogen or oxygen. This brings up the question as to which form of the mixed state of initial and new phases is realized. Reasoning from numerous investigations into the phase state of $YBCO_y$ samples with an intermediate oxygen content ($6 < y < 7$), most likely, the case in point is the microheterogeneity, domain structure, and "phase separation" in the electronic subsystem. In any case, according to the x-ray powder diffraction analysis, no macroscopically detectable separation of the material into components occurs. At the same time, it should be remarked that the term "initial phase" does not reflect the essence of the matter. The line at 31.5 MHz, which is characteristic of $^{63}Cu(2)$ in $YBa_2Cu_3O_7$, is retained (even if broadened) in the spectrum only at small degrees of hydrogenation (less than one atom per formula unit). Consequently, in a certain sense, we are dealing with a partial retention of the $YBCO_7$ initial phase. An argument, even if indirect, in support of this inference is the observation of superconductivity with $T_c \sim 70$–80 K in the hydrogenated samples containing to 0.8–1 hydrogen atom per formula unit. However, at a higher hydrogen content, the spectrum of Cu(2) is observed only in the frequency range 70–110 MHz due to the antiferromagnetic ordering in the Cu(2)–O planes, which implies the disappearance of the $YBCO_7$ initial phase. This correlates with the fact that the peaks corresponding to the interplanar spacings in the range 1.17–1.19 nm, characteristic of the $YBCO_7$ phase, are not observed in the x-ray diffraction pattern. Upon oxidation of hydrocuprate to $H_2YBa_2Cu_3O_{7.8}$, the high-frequency spectrum of Cu(2) "disappears," which also is typical of superconducting $YBa_2Cu_3O_7$. Note also that, according to the diamagnetic measurements, oxyhydrocuprate is the superconductor with T_c in the range 60–70 K. However, the NQR spectrum of oxyhydrocuprate exhibits only one intense line at 20 MHz, which, according to the relaxation measurements, was assigned to Cu(1). The necessary special investigations are beyond the scope of the present work.

By summing up the discussion of the results obtained in the investigation of hydrogen in yttrium barium cuprate, it should be mentioned that the hydro-

gen intercalation is a complex "double-edged" process involving the mutual influence of the host oxide and guest hydrogen.

The active role of the $YBa_2Cu_3O_7$ oxide macroscopically manifests itself in the chemisorption of molecular hydrogen. At the microscopic level, this process is treated as the dissociation of H_2 molecule into atoms ($H_2 \longrightarrow 2H$) and a spatial separation of H atoms into electrons and protons in the lattice ($H \longrightarrow H^+ + e^-$).

At the macroscopic level, the active role of hydrogen shows itself in the modification of the physical and chemical characteristics of oxide. In particular, it is revealed that the metal-like superconducting cuprate transforms into the semiconductor antiferromagnet, which was earlier observed for oxygen-deficient samples. Moreover, after the hydrogenation, yttrium barium cuprate acquires two quite new properties: (i) the ability to increase oxygen content up to eight atoms per formula unit and (ii) the occurrence of highly mobile protons migrating in the lattice independently of oxygen ions. At the microscopic level, the modifying role of hydrogen is associated with the changes in the copper–oxygen subsystem of cuprate. The intercalated protons transform the charge distribution in the coordination sphere of copper cations, which, in turn, fulfill the function of acceptors of the incorporated "hydrogen" electrons. These transformations are most clearly pronounced in the evolution of the Cu NQR spectra. The fact that the Cu NQR frequencies change in a discrete, rather than gradual, manner indicates the localization of the observed transformations in a certain region of the crystal lattice. Analysis of our experimental results and available data makes it possible to assign these transformations to the Cu(1) ("chain") ions. Furthermore, the case in point is the region near the Cu(1)–O plane, judging the location of protons from the data of the muon–spin rotation [27, 28]. By their behavior in the process of inelastic neutron scattering, a substantial fraction of protons can be considered mechanically free particles occupying interstices in the crystal lattice. The fraction of protons that take part in the formation of strong O–H bonds in $H_2YBa_2Cu_3O_7$ is likely to be insignificant.

The discreteness of changes in the local characteristics determined by the NQR technique and the macroscopically averaged characteristics obtained by x-ray diffraction analysis suggests that the formation of stoichiometric compounds, for example, $H_2YBa_2Cu_3O_7$, occurs through the stage of their solid solutions in the matrix of the initial materials.

ACKNOWLEDGMENTS

I am grateful to V.M. Egorov, I.N. Zimkin, Yu.P. Stepanov, and B.T. Melekh (Ioffe Physicotechnical Institute), H. Lütgemeier†, Ch. Freiborg, and P. Menfells (FZ Julich, Germany), Ph. Colomban and R. Baddour-Hadjean (LADIR-CNRS, Thiais, France), and F. Parker (RAL, Chilton, UK) for their assistance in performing the experiments and fruitful discussions of the results.

This work was supported by the Russian Foundation for Basic Research, project nos. 95-03-08001a and 97-03-33466a.

† Deceased.

REFERENCES

1. C. W. Chu, D. H. Hor, L. Meng, *et al.*, Phys. Rev. Lett. **58**, 405 (1987).
2. E. K. Shalkova, Yu. M. Baikov, and T. A. Ushakova, Superconductivity **5** (1), 22 (1992).
3. T. Hirata, Phys. Status Solidi **156** (2), 227 (1996).
4. Yu. M. Baĭkov, Sverkhprovodimost: Fiz., Khim., Tekh. **7** (7), 1208 (1994).
5. Yu. M. Baikov and S. E. Nikitin, Solid State Ionics **86–88**, 673 (1996).
6. Yu. M. Baĭkov, Zh. Neorg. Khim. **43** (1), 22 (1998).
7. Yu. M. Baĭkov, S. E. Nikitin, Yu. P. Stepanov, and V. M. Egorov, Fiz. Tverd. Tela (S.-Peterburg) **39**, 823 (1997) [Phys. Solid State **39**, 729 (1997)].
8. Yu. M. Baikov and S. E. Nikitin, in *Proceedings of the Third International Symposium on Ionic and Mixed Conducting Ceramics, Paris, France, 1997*, Ed. by T. A. Ramanarajanan (Electrochemical Society Inc. Proc. **97-24**, 1997), p. 390.
9. W. Gunther and R. Schöllhorn, Physica C **271**, 241 (1996).
10. R. Borner, W. Paulus, R. Schöllhorn, *et al.*, Adv. Mater. **7** (1), 55 (1995).
11. P. V. Gel'd, R. A. Ryabov, and L. P. Mokhracheva, *Hydrogen and Physical Properties of Metals and Alloys: Transition Metal Hydrides* (Nauka, Moscow, 1985).
12. H. Yasuoka, T. Shimizu, T. Imai, *et al.*, Hyperfine Interact. **49**, 167 (1989).
13. I. Heinemaa, H. Lütgemeier, S. Pekker, *et al.*, Appl. Magn. Reson. **3**, 689 (1992).
14. H. Lütgemeier, S. Schmenn, P. Menffels, *et al.*, Physica C **267**, 191 (1996).
15. Ph. Colomban and J. Tomkinson, Solid State Ionics **97**, 123 (1997).
16. Yu. M. Baikov, W. Gunther, V. P. Gorelov, *et al.*, Ionics **4** (5/6), 347 (1998).
17. Yu. M. Baĭkov, Zh. Neorg. Khim. **43** (2), 192 (1998).
18. Yu. M. Baikov, E. K. Shalkova, and T. A. Ushakova, Superconductivity **6** (3), 349 (1993).
19. M. Yoshimura, S. Inoue, and Y. Ikuma, Solid State Ionics **49**, 39 (1991).
20. K. D. Kreuer, Chem. Mater. **8** (3), 610 (1996).
21. Yu. M. Baikov and E. K. Shalkova, J. Solid State Chem. **97**, 224 (1992).

22. Yu. M. Baĭkov, B. S. Nikolaev, T. A. Perevalova, *et al.*, Izv. Akad. Nauk SSSR, Neorg. Mater. **24**, 615 (1988).

23. K. D. Kreuer, W. Muench, M. Ise, *et al.*, Phys. Chem. **101** (9), 1344 (1997).

24. J. Tomkinson, Spectrochim. Acta, Part A **48** (3), 329 (1992).

25. Yu. M. Baĭkov, V. M. Egorov, I. N. Zimkin, and Yu. P. Stepanov, Zh. Neorg. Khim. **42** (10), 1620 (1997).

26. Sh. Edo and T. Takama, Jpn. J. Appl. Phys. **37**, 3956 (1998).

27. H. Glückler, Ch. Niedermaier, G. Nowitzke, *et al.*, J. Less-Common Met. **164–165**, 1016 (1990).

28. W. K. Dawson, C. Boekema, L. Lichti, and D. W. Coone, Physica C **183–189**, 1221 (1991).

Translated by O. Borovik-Romanova

Physics of the Solid State, Vol. 42, No. 6, 2000, pp. 1036–1040. Translated from Fizika Tverdogo Tela, Vol. 42, No. 6, 2000, pp. 1004–1008.

SEMICONDUCTORS AND DIELECTRICS

Electrical Properties of the High-Pressure Phases of Gallium and Indium Tellurides

V. V. Shchennikov, K. V. Savchenko, and S. V. Popova

Institute of Metal Physics, Ural Division, Russian Academy of Sciences, ul. S. Kovalevskoĭ 18, Yekaterinburg, 620219 Russia

e-mail: phisica@ifm.e-burg.su

Received November 1, 1999

Abstract—A study has been made of the resistance ρ, the thermopower *S*, and magnetoresistance MR of Ga_2Te_3 and α-In_2Te_3 single crystals at pressures *P* up to 25 GPa. It is found that the resistance ρ and |*S*| sharply decrease at ~0–5 and 1.5–3 GPa, respectively. The semiconductor–metal phase transitions in the temperature range from 77 to 300 K are established from the sign reversal of the temperature coefficient of ρ to occur at $P > 4.4$ and > 1.9 GPa. The values $S \approx +(10–20)\mu V/K$ for the metallic phases with a Bi_2Te_3-type structure agree with those for liquid In_2Te_3 and Ga_2Te_3. Negative MR is revealed in In_2Te_3 at $P \approx 1.9$ GPa. No MR is observed in Ga_2Te_3 up to 25 GPa. The variation of the electronic structure of In_2Te_3 and Ga_2Te_3 under pressure is discussed. © *2000 MAIK "Nauka/Interperiodica".*

1. INTRODUCTION

The $A_2^{III}B_3^{VI}$ semiconductors (A = Ga or In; B = S, Se, or Te), which in the A^NB^{8-N} series occupy a place between the $A^{II}B^{VI}$ and $A^{III}B^V$ compounds [1], are promising materials for nuclear power engineering (due to their high radiation strength), optoelectronics, etc. [1–6]. The Ga_2Te_3 and In_2Te_3 compounds have a sphalerite-type defect crystalline structure with a statistical (β phase) or ordered (α phase) vacancy distribution [1, 5, 7], in which Te atoms form the closest-packed cubic lattice, and Ga(In) atoms occupy 2/3 of the sites in the tetrahedral voids [1, 5–7]. The Ga(In) and Te atoms are bound through covalent sp^3 bonds, and the lone electron pairs distributed among the four neighboring Te atoms are directed toward the vacancy; formally, a vacancy is bonded to anions as a conventional cation [1, 7]. This scheme accounts for the semiconducting properties and electrical neutrality of the vacancies in the cation lattice [1, 8] and a low carrier mobility μ for sphalerite crystals [1, 7].

It was found that In_2Te_3 [9–11] and Ga_2Te_3 [10] undergo phase transitions to a Bi_2Te_3-type structure at pressures $P \approx 2$ and 5 GPa, respectively. The Bi_2Te_3-type structure was obtained [9] after subjecting In_2Te_3 to a pressure of 3.2 GPa at 400 K ($a = 4.27$ Å, $c = 29.65$ Å). The $\alpha \longrightarrow \beta$ transition was also found in In_2Te_3 at $P \approx 1.9$ GPa [10]. Above ~4 and ~7 GPa, In_2Te_3 and Ga_2Te_3 were observed to transform to phases with a high electric conductivity [2], but no study was made of their carrier parameters and conductivity type. The variation in the electronic structure upon phase transformations can be retraced by studying the behavior of the thermopower *S* and magnetoresistance MR, which characterize the carrier concentration and μ [12–14]. The purpose of this work was to use these effects to examine the variation of the electronic structure of Ga_2Te_3 and In_2Te_3 under pressure.

2. EXPERIMENTAL TECHNIQUE

The measurements of ρ, *S*, and MR were made in anvil-type chambers of steel (for *P* up to 5 GPa), VK6 hard alloy ("toroid" anvil [12], pressures up to 10 GPa), and synthetic diamond (up to 30 GPa) [13, 14]. The magnitude of *P* in the pressure-transmitting medium (katlinite) was estimated to within ~10% from calibration graphs based on phase transitions in reference substances Bi, GaP, etc. [13–15]. Platinum–silver ribbons 5 μm thick were used as hold-down electrical probes. The anvils, whose temperature was monitored by thermocouples, served as current contacts, as well as a heater and a cooler [13, 14, 16]. The $\rho(P)$ and $\rho(T)$ dependences were measured in the dc mode with the current through the sample switched. The MR effect at 77 and 293 K was determined by averaging the results of the measurements upon switching the current through the sample and the magnetic field [14]. The relative errors of measurements (without taking into account the change of sample shape under compression) were ~3% for ρ and ~20% for *S*.

The samples were prepared by the Bridgman–Stockbarger method [16]. The x-ray characterization was performed on a STADI-P setup (STOE, Germany) with CuK_{α_1} radiation. Polycrystalline silicon was used as an internal standard [$a_k = 5.43075(5)$ Å]. The Ga_2Te_3 and In_2Te_3 single crystals had a cubic zincblende lattice with $a = (5.9000 \pm 0.0004)$ Å and $a = (18.4778 \pm 0.0019)$ Å, respectively, which corresponded to Ga_2Te_3 with a disordered vacancy distribution [2, 7] and α-In_2Te_3 with a superstructure (ordered vacancies) [7].

1063-7834/00/4206-1036$20.00 © 2000 MAIK "Nauka/Interperiodica"

3. RESULTS AND DISCUSSION

The resistance and S of the Ga_2Te_3 samples decreased with an increase in P up to ~5 GPa; note that, unlike [2], where ρ monotonically decreased by ~ three orders of magnitude from 1 to 7 GPa, our measurements showed the pressure coefficient of ρ to increase in absolute magnitude within the range ~3–5 GPa. The data obtained in different chambers agree satisfactorily with one another (Fig. 1a) and with the values $S \approx 0.5$–1 mV/K at $P = 0$ [7]. The $\rho(P)$ and $S(P)$ dependences measured for In_2Te_3 (Fig. 1b) revealed a sharp drop at $P \sim 2$ GPa. We are unaware of any such data available for α-In_2Te_3, but the resistance of β-In_2Te_3 (a = 6.158 Å) also decreased by about six orders of magnitude in the range ~ 2–3.5 GPa [2]. Near $P = 0$, S was not measured because of the high sample resistance; as quoted in [7], $S \approx -(0.6–1)$ mV/K. The low values of ρ and of $S \approx +(10–20)$ μV/K, and their weak dependence on P above ~5 and ~2 GPa (see Fig. 1), argue for the metallic conductivity in Ga_2Te_3 and In_2Te_3, which was supported by the measurements of $\rho(T)$ (Fig. 2). As is seen from the thermopower data, the high-pressure phases have a hole-type conductivity. According to [10], the metallic phases have a Bi_2Te_3 structure.

The semiconducting behavior of $\rho(T)$ for Ga_2Te_3 (curve *1* in Fig. 2a) was replaced with an increase in P by the metallic pattern at $P_1 = 4.4$ GPa (curve *2* in Fig. 2a), which indicated a semiconductor–metal transition. The conduction activation energy ε_a estimated from the $\rho(T)$ dependence is less than ~0.01 eV (at $P = 0$, $\varepsilon_a \approx 0.5$ eV [3]). At $T \geq 270$ K, ρ follows a nonmonotonic course at $P = 17.5$ and 24 GPa (Fig. 2), which is possibly associated with another phase transition. In In_2Te_3, the semiconductor–metal transition took place in the range $P \approx 1.9$–2.9 GPa (curves *1*, *2* in Fig. 2b). At $T \geq 220$ K, $\rho(T)$ retained a negative temperature coefficient within the range $P = 1.9$–3.6 GPa. As was shown in [3], the charge carrier concentration in In_2Te_3 decreases, and μ increases with an increase in the temperature to 350 K, and, as a result, ε_a increases from 0.16 eV at $T \leq 250$ K to 0.55 eV at $T \geq 250$ K [3, 4]. The same nonmonotonic $\rho(T)$ dependences, but with lower energies ε_a, are observed in the semiconducting phase at $P = 1.9$ GPa and in the high-pressure phase at $P \leq 3.6$ GPa (Fig. 2).

The MR of Ga_2Te_3 and In_2Te_3 was measured at the same P as $\rho(T)$. In most cases, the magnitude of the effect was found to be below 0.01%, which did not even permit establishing its sign. The absence of MR indicates a low hole mobility [8, 17], which is in accord with the values $\mu \leq 50$ cm²/Vs for Ga_2Te_3 at atmospheric pressure [7]. In In_2Te_3 at $T = 293$ K, when the hole mobility is substantially higher, $\mu \sim 200$ cm²/Vs [3], we have succeeded in measuring the field dependence of MR, which was found to be negative at $P = 1.9$ GPa (Fig. 3). One of the possible mechanisms which could result in a negative MR is the carrier scat-

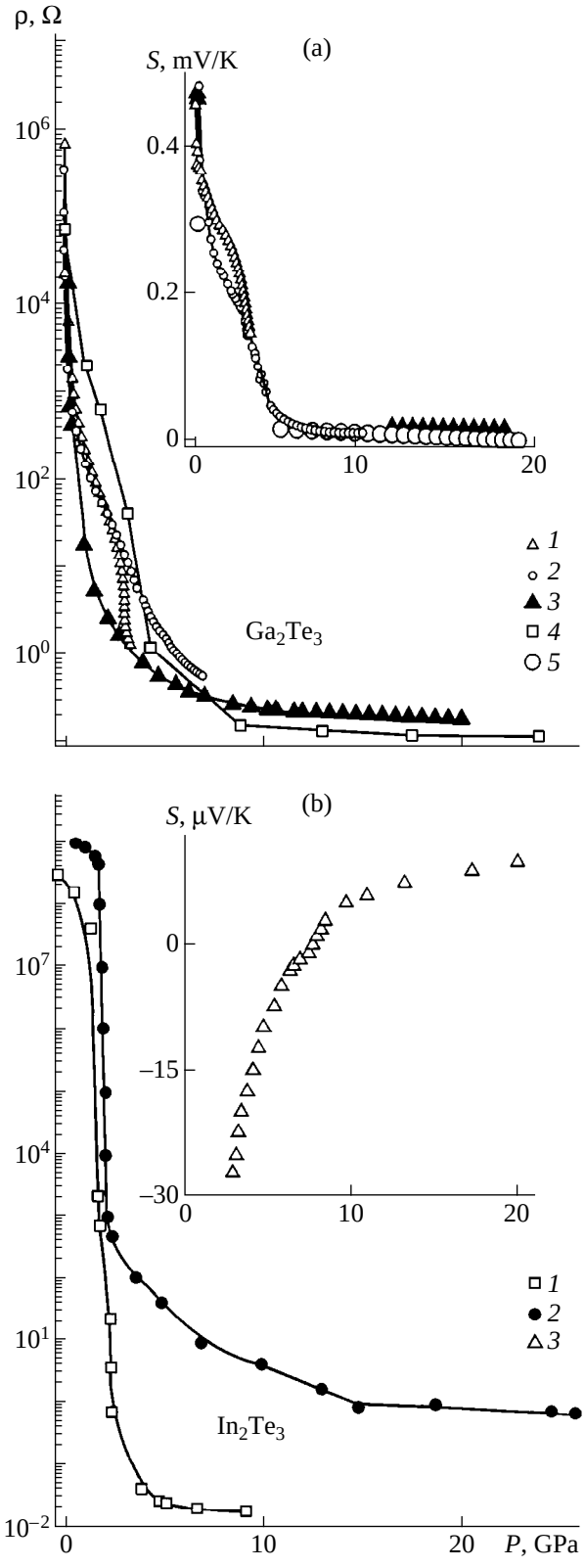

Fig. 1. Pressure dependences of the electrical resistance ρ and the thermopower S (insets) obtained at $T = 293$ K for samples of (a) Ga_2Te_3 and (b) In_2Te_3. The data were obtained in steel and hard-alloy toroid-type chambers (a) *1*, *2* and (b) *1*, and in diamond chambers (a) *3*, *4*, *5* and (b) *2*, *3*.

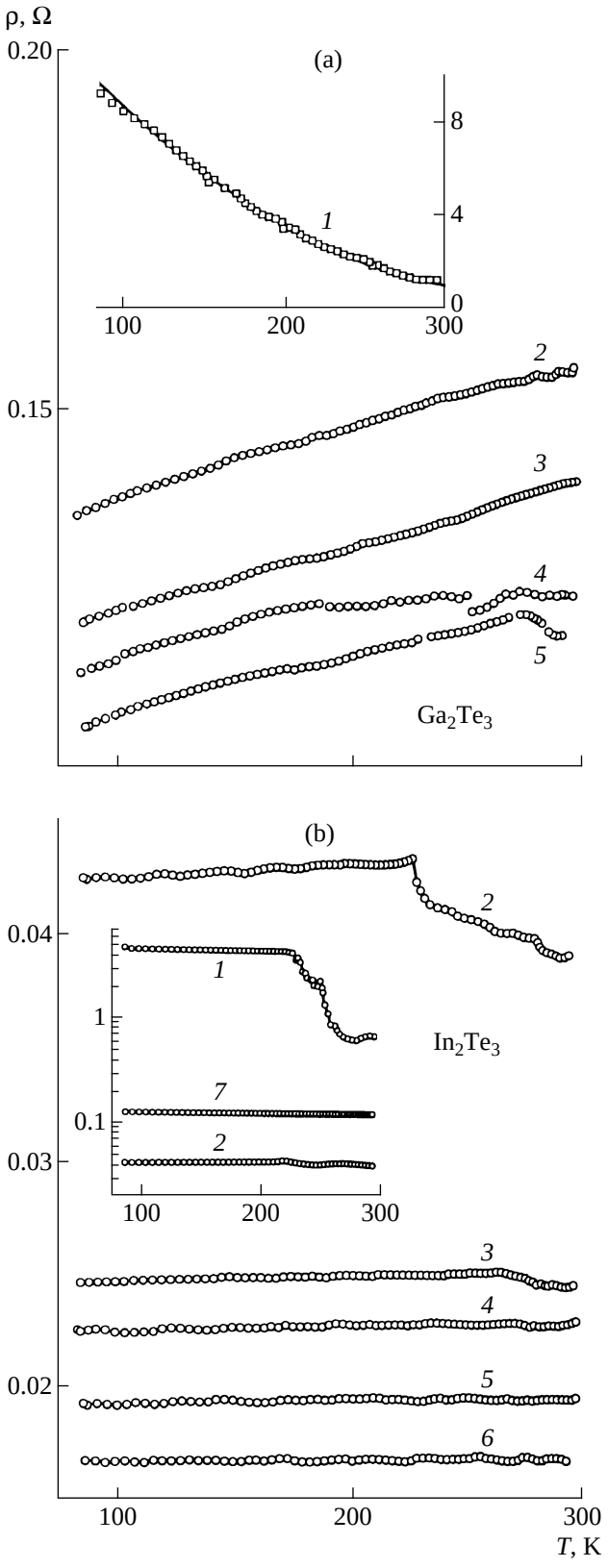

Fig. 2. Temperature dependences of the resistance ρ for (a) Ga_2Te_3 and (b) In_2Te_3 at a fixed pressure P (GPa): (a) (inset, *1*) 4.4, (*2*) 8.8, (*3*) 13, (*4*) 17.5, and (*5*) 24; (b) (inset, *1*) 1.9, (*2*) 2.95 (inset and the main panel), (*3*) 3.6, (*4*) 3.8, (*5*) 4.8, (*6*) 6, and (*7*) 1.2 (after a pressure drop, inset).

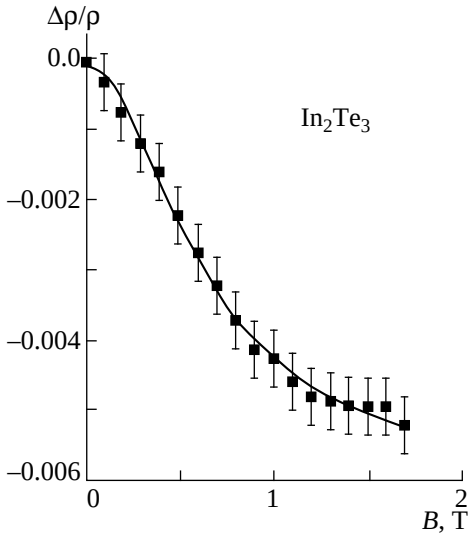

Fig. 3. Dependence of transverse magnetoresistance of an In_2Te_3 sample on the magnetic field B at P = 1.9 GPa (T = 293 K).

tering from magnetic impurities, when the spin polarization of impurity atoms reduces the probability of electron spin-flip scattering and, hence, reduces the total scattering probability and ρ [17, 18]. It is known that impurity atoms in In_2Te_3 remain unionized and possess a magnetic moment [6, 7]. For this mechanism, the field dependences of the negative MR are proportional to $\sim B^2$ in weak fields B and tend to saturation in strong fields [14, 17, 18], which is actually observed in In_2Te_3 (Fig. 3). In the high-pressure metallic phases, MR was less than 0.01%.

The melting of In_2Te_3 and Ga_2Te_3 at $T \geq 1000$ K also brings about an increase in ρ by two or three orders of magnitude and a semiconductor–metal transition in the liquid phase [8]. The values of S for the liquid phases (+30 μV/K for In_2Te_3 and +45 μV/K for Ga_2Te_3 [8]) agree with those for the high-pressure phases (Fig. 1). The electronic-structure model that describes the melting of In_2Te_3 and Ga_2Te_3 (Fig. 4) [8] is also applicable to the pressure-induced semiconductor–metal transition. The semiconducting gap in a tetrahedral structure of the sphalerite forms between the bonding and antibonding states obtained upon hybridization of the In (Ga) *s* states with the Te *p* states (Fig. 4). The melting suppresses the hybridized states, and the Fermi level occurs in the Te *p* band overlapping with the In *s* band (Fig. 4a) [8], which corresponds to the electronic structure of a metal. When pressure induces the phase transformation to the Bi_2Te_3 structure, which can be considered a distorted NaCl lattice [11, 19], the coordination number increases, $Z = 4 \longrightarrow 6$; i.e., the tetrahedral sp^3 bonds are also broken [15]. In the ionic bonding approximation, the electronic structure in the NaCl cubic lattice has the same form as that of melts [8] (Fig. 4a).

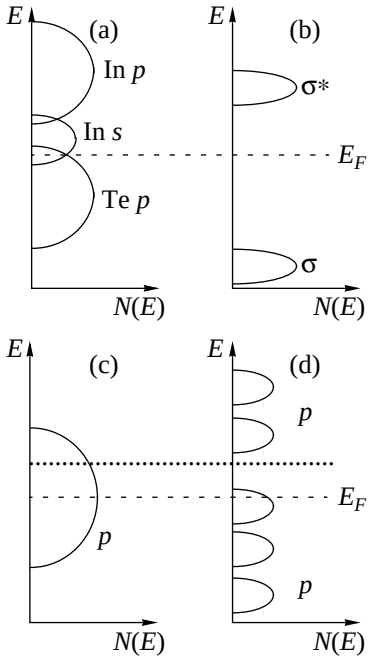

Fig. 4. Models of the electronic structure of In_2Te_3 and Ga_2Te_3 in (a) liquid state, (b) ZnS phase [8], (c) hypothetical NaCl praphase [11, 19], and (d) high-pressure phase with a Bi_2Te_3 structure [11, 19]. Low temperatures and pressures favor formation of covalent sp^3 bonds transferring (a) the In *s* and Te *p* states into (b) the σ and σ* states [8]. E_F is the chemical potential level. Dotted lines in Figs. 4c and 4d show the position of E_F in Bi_2Te_3 (see text).

In the model that assumes a dominant role of the *p* electrons in bonding in materials with an unfilled *p* shell [11, 19, 20], In_2Te_3, Ga_2Te_3, and Bi_2Te_3 in the cubic NaCl phase should also act as metals (Fig. 4c). This model qualitatively explains the formation of the electronic spectrum and crystal structure of Group V, VI, and VII elements [20], as well as the Group IV, II, and V chalcogenides [11, 19]. The metallic nature of the spectrum of cubic phases of these substances is accounted for by its consisting of three overlapping bands p_x, p_y, and p_z, which are partially filled [19]. In the cubic praphase, the Bi_2Te_3 *p* band is 3/5 filled [11, 19], and the *p* bands of In_2Te_3 and Ga_2Te_3, filled to 7/15 (Fig. 4c). The structure of Bi_2Te_3 differs from the NaCl lattice in that it consists of Te–Bi–Te–Bi–Te layers; i.e., the structure parameter increases fivefold (a = 4.3835 Å, c = 30.487 Å) [11]. This increase (caused by the Peierls distortion) of the lattice spacing gives rise to a fivefold *p*-band splitting as compared to the cubic praphase, and the Fermi level E_F for Bi_2Te_3 occurs in the opening gap [11, 19], whereas in In_2Te_3 and Ga_2Te_3, it remains in the allowed state band (Fig. 4d). Therefore, unlike Bi_2Te_3, which is a semiconductor, the high-pressure phases of In_2Te_3 and Ga_2Te_3 should be metals [11].

The calculations performed for Group V–VII elements showed that the ion-core repulsion makes the Peierls lattice distortion energetically unfavorable at some critical *P*, which accounts for the decrease in the energy gap and the transition of these substances to the metallic form [20]. At $P \approx 6$ GPa, Bi_2Te_3 undergoes a transition to the metallic phase with a layered structure close to the initial one [11, 12]. The metallic phases of Bi_2Te_3 [12, 21], In_2Te_3, and Ga_2Te_3 have equal *S*, which suggests a similarity of their electronic structures.

Other Ga compounds with a sphalerite structure, namely, Ga_2S_3 (a = 5.17 Å) and Ga_2Se_3 (a = 5.429 Å) [7], under pressure can undergo the same electronic structure rearrangement as Ga_2Te_3 (see Fig. 4). Indeed, Ga_2Se_3 at $P \sim 14$ GPa exhibited a drop in its electrical resistance and the thermopower [16], as well as a structural transformation [5], with its high-pressure phase probably having a Bi_2Te_3-type structure (a = 3.99 Å, c = 27.8 Å) [22].

ACKNOWLEDGMENTS

The authors are grateful to A.P. Tyutyunnik for assistance in x-ray measurements and B.N. Goshchitskiĭ for interest in this work.

This study was supported in part by the State Program for Leading Scientific Schools (project no. 96-15-96515) and the Russian Foundation for Basic Research (project no. 98-03-32656).

REFERENCES

1. V. P. Zhuze, V. M. Sergeeva, and A. I. Shalykh, Fiz. Tverd. Tela (Leningrad) **2** (11), 2858 (1960) [Sov. Phys. Solid State **2**, 2545 (1960)].
2. D. N. Bose, S. Sen, D. K. Joshi, and S. N. Vaidya, Mater. Lett. **1** (2), 61 (1982).
3. S. Sen and D. N. Bose, Solid State Commun. **50** (1), 39 (1984).
4. A. T. Nagat, M. M. Nassary, and H. A. El-Shaikh, Semicond. Sci. Technol. **6** (10), 979 (1991).
5. M. Takumi, Y. Koshio, and K. Nagata, Phys. Status Solidi B **211** (1), 123 (1999).
6. Y. G. Gurevich, V. M. Koshkin, and I. N. Volovichev, Solid-State Electron. **38** (1), 235 (1995).
7. N. Kh. Abrikosov, V. F. Bankina, L. V. Poretskaya, E. V. Skudnova, and S. N. Chizhevskaya, *Semiconductor Chalcogenides and Their Alloys* (Nauka, Moscow, 1975).
8. M. Cutler, *Liquid Semiconductors* (Academic Press, New York, 1977; Mir, Moscow, 1980).
9. S. Geller, A. Jayaraman, and G.W. Hull, Jr., J. Phys. Chem. Solids **26** (2), 353 (1965).
10. N. R. Serebryanaya, Powder Diffr. **7** (2), 99 (1992).
11. P. B. Littlewood, CRC Critical Rev. Solid State Mater. Sci. **11** (3), 229 (1984).
12. L. G. Khvostansev, A. I. Orlov, N. Kh. Abrikosov, *et al.*, Phys. Status Solidi A **71** (1), 49 (1982).

13. I. M. Tsidil'kovskiĭ, V. V. Shchennikov, and N. G. Gluzman, Fiz. Tekh. Poluprovodn. (Leningrad) **17** (5), 958 (1983) [Sov. Phys. Semicond. **17**, 604 (1983)].
14. V. V. Shchennikov, Fiz. Tverd. Tela (Leningrad) **35** (3), 783 (1993) [Phys. Solid State **35**, 401 (1993)].
15. L. F. Vereshchagin and S. S. Kabalkina, *X-Ray Diffraction Studies at High Pressures* (Nauka, Moscow, 1979).
16. K. V. Savchenko and V. V. Shchennikov, Can. J. Phys. **72** (9–10), 681 (1994).
17. A. A. Abrikosov, *Fundamentals of Metal Physics* (Nauka, Moscow, 1987).
18. S. A. Obukhov, Preprint of the Physicotechnical Institute, USSR Acad. Sci., Leningrad, 1991, no. 1459.
19. B. A. Volkov, O. A. Pankratov, and S. V. Pakhomov, Zh. Éksp. Teor. Fiz. **86** (6), 2293 (1984) [Sov. Phys. JETP **59**, 1336 (1984)].
20. J. P. Gaspard, F. Marinelli, and A. Pellegatti, Europhys. Lett. **3** (10), 1095 (1987).
21. V. A. Kul'bachinskiĭ, V. V. Shchennikov, J. Horak, and P. Loshtyak, Fiz. Tverd. Tela (S.-Peterburg) **36** (2), 526 (1994) [Phys. Solid State **36**, 292 (1994)].
22. W. Becker, K.-J. Range, and A. Weiss, Z. Naturforsch. B **23** (11), 1545 (1968).

Translated by G. Skrebtsov

Physics of the Solid State, Vol. 42, No. 6, 2000, pp. 1041–1044. Translated from Fizika Tverdogo Tela, Vol. 42, No. 6, 2000, pp. 1009–1012.

SEMICONDUCTORS AND DIELECTRICS

Polarization-Dependent Inhomogeneous Broadening of the Edge Luminescence Band of Hexagonal Gallium Nitride

M. E. Kompan, I. Yu. Shabanov, and Yu. V. Zhilyaev

Ioffe Physicotechnical Institute, Russian Academy of Sciences, Politekhnicheskaya ul. 26, St. Petersburg, 194021 Russia

Received November 15, 1999

Abstract—A correlation of the shape of the edge luminescence band for hexagonal gallium nitride and the polarization of exciting light is revealed. The effect is explained by the existence of microregions with different directions of deformation in the plane perpendicular to the sixfold axis. *© 2000 MAIK "Nauka/Interperiodica".*

1. INTRODUCTION

A wide-gap semiconductor—gallium nitride—is a promising material whose properties have been extensively investigated in recent years. A substantial part of these studies are concerned with the luminescence of this material. These works are of great theoretical and practical importance, specifically for possible applications of GaN in optoelectronics [1].

Since the main (hexagonal) modification of this material possesses an optical anisotropy, the studies of polarization effects in luminescence present certain difficulties, and the polarization properties of gallium nitride luminescence have not been considered in the majority of the research works dealing with the luminescence. At the same time, the investigations of $A^{III}B^{V}$ semiconductors demonstrate that the luminescence polarization and the character of its dependence on the polarization of excitation can provide a nontrivial information on the properties of fluorescent materials and the nature of recombination processes.

In the general case, the influence of light polarization on the luminescence parameters can be treated as the polarization memory of luminescence. In the case when the material under study is isotropic with respect to polarized light modes, which are used for exciting the luminescence, the manifestations of optical polarization memory are nontrivial. The memory effect of the circular polarization of excitation in an isotropic material is referred to as the "optical orientation" and has been studied with a large number of semiconductor materials [2]. The memory for the linear polarization of excitation was observed in studies of the so-called "hot luminescence" [3]. Recently, the memory for the linear polarization of excitation was revealed for a fluorescent porous silicon [4]. The latter effect was interpreted as a manifestation of the internal structure of the material consisting of individual anisotropic nanometer elements. In all the aforementioned cases, the polarization memory manifested itself in the polarization of the recombination radiation, and no changes in the spectral characteristics were found.

The purpose of the present work was to investigate the linearly polarized edge luminescence of hexagonal gallium nitride upon linearly polarized excitation. This study is a part of the program on the search for and investigation of spin-dependent phenomena in gallium nitride. Until presently, no observations of these effects have been reported.

2. SAMPLE PREPARATION AND EXPERIMENTAL TECHNIQUE

The samples to be studied were prepared by chloride epitaxy on silicon and sapphire substrates at a temperature of ~900°C with the use of ammonia as a nitrogen source. The most perfect samples with a low dislocation density of $\sim 10^7$ cm^{-2} were produced by the lateral overgrowth technology. The material obtained represents single crystals grown together along the side surfaces in the form of hexagonal columns with the *C* axis perpendicular to the substrate plane. The sizes of individual single crystals ranged from 1 to 200 μm. In the case when the samples separated from the substrates, they were in the shape of flat plates 0.4–0.5 mm thick. Deviations of the hexagonal axis of the material from the normal to the sample plane were about 5–10 angular minutes. Such an orientation of the material made it possible to eliminate the manifestation of trivial effects in the dependence of the luminescence parameters on the polarization of excitation.

Upon nonpolarized excitation, the samples exhibited typical edge luminescence parameters of this material: the location of the band maximum was 3.47 (3.22) eV and the full width at half maximum (FWHM) was equal to 25 (50) meV at 78 (300) K.

The luminescence was excited by a pulsed molecular nitrogen laser with a wavelength of 337 nm (3.69 eV) and a pulse duration of 6 ns. The experiments were carried out at temperatures of 78 and 300 K. The lumines-

1063-7834/00/4206-1041$20.00

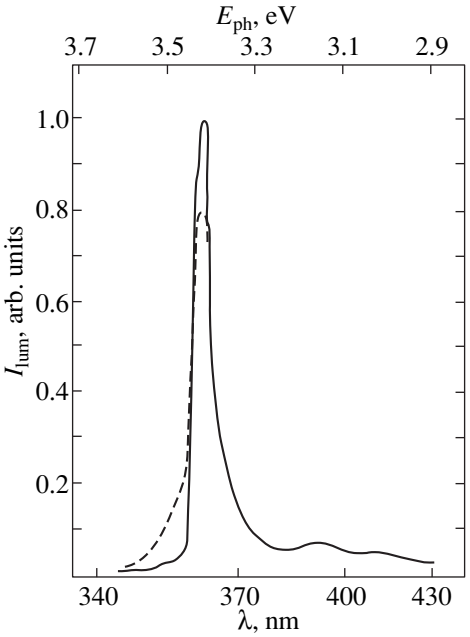

Luminescence spectra of hexagonal gallium nitride at 78 K for parallel (solid line) and mutually perpendicular (dashed line) orientations of an analyzer and a polarizer. The first curve is normalized to unity at a maximum of the intensity, and the scale of the second curve remains unchanged with respect to the first one.

cence signals were recorded using a boxcar-type device with a time resolution of 10^{-8} s. By this means, for gallium nitride with its subnanosecond scale of recombination processes, the experimental conditions corresponded to the stationary conditions of excitation and detection.

3. RESULTS

The experiments revealed that the shape of the edge luminescence band at 78 K depends on the mutual orientation of the polarization of the exciting light and the analyzer in the detection channel. When the linear polarizer and analyzer were crossed relative to each other (in the channels of excitation and detection, respectively), the band had a non-Gaussian shape with a broad base (about 39 meV at a level of 0.1 of the maximum). The change in the mutual orientation of the analyzer and polarizer to the parallel one led to a noticeable change in the band shape: the short-wavelength edge became shorter with the disappearance of the broad base (to 3–5 meV at a level of 0.1). In some cases, a considerable narrowing of the short-wavelength edge of the band was also observed at a level 0.5. This narrowing of the short-wavelength edge was accompanied by a certain increase in the band intensity at a maximum. At the same time, the shape and intensity of the long-wavelength edge of the luminescence band remained unchanged. A typical shape of the spectra is shown in the figure.

It should be noted that different shapes of the luminescence band at different polarizations immediately indicate a partial linear polarization of this band, which is different for its various spectral components. The effect was not revealed in the experiments at room temperature.

To our knowledge, neither observations of similar effects in other materials nor data on the memory effects for the polarization of excitation in gallium nitride have been reported.

4. DISCUSSION

Let us consider mechanisms that can be responsible for the effect observed.

It is unlikely that the effect under consideration is related to effects such as optical orientation or alignment [2, 3], when the memory for the polarization of exciting photons remains owing to the orientation of quasi-particles involved in the recombination processes. According to the existing concepts, the linear polarization of luminescence can arise upon recombination of carriers when their total angular momentum is equal to $h/2\pi$ and more. Since gallium nitride has a simple conduction band with spin 1/2, the linear polarization of luminescence can be caused only by the hole orientation. However, taking into account that the energy of excitation is about 250 meV higher than that of the band location in the luminescence spectrum and also an extremely high efficiency of the relaxation of the hole angular momentum in scattering events, it is very unlikely that the holes can retain the "memory" of the direction of the starting angular momentum from the instant of generation of an electron–hole pair by the light to the instant of its recombination.

The key to the explanation of this effect can be found from analysis of the spectral properties of luminescence. The effect under study implies a change in the non-Gaussian wings of the band (upon variation in the mutual orientation of the light polarization of excitation and detection); i.e., it is in the change of the inhomogeneous broadening contour. A decrease in the band wing is observed only for the short-wavelength edge and occurs with an increase in the intensity at a maximum (i.e., for the dominant component of the band). With due regard for the physical meaning of the inhomogeneous broadening, the changes observed in the spectrum can be interpreted as follows: under certain conditions, the excitations can migrate from some regions whose energy gap E_g is higher than that of the host material into the regions in which E_g corresponds to the bulk of the material.

Note that the above interpretation did not require additional model assumptions. Nonetheless, the formulation of the effect in terms of the inhomogeneous broadening directly explains the most specific features

observed experimentally. A decrease in the intensity of the high-energy wing and an increase in the peak intensity correspond to the migration of excitations toward lower energies E_g (into the host material), whereas the retention of the shape and intensity of the low-energy wing means that the excitations do not migrate from the regions with an energy gap below E_g for the host material into the regions with higher energies E_g. Moreover, this approach provides an immediate explanation for the fact that the effect under study is not observed at room temperature. The width of the band wings is about 30 meV. At 300 K, the states with an energy of 30 meV above the energy of the ground state can be permanently occupied at the expense of thermal injection. Therefore, the luminescence from these higher-lying states is recorded in the experiment at 300 K.

It is necessary to refine the concepts: when interpreting the experiment in terms of inhomogeneous broadening, we proceed from the fact that the changes observed refer to the components in the band wings of the edge luminescence, and with a high probability, these components have the same nature as the central components of the band. We assume that the difference between the wavelength of components in the band wings and the wavelength at a maximum is due to the presence of inhomogeneous deformation in the sample. The influence of this deformation on E_g for gallium nitride is well known and has been studied in many works (see, for example, [5]). The bulk gallium nitride formed by single crystals grown together *a fortiori* involves inhomogeneous deformations. Their presence was confirmed experimentally in [6]. Thus, the assumption of the inhomogeneous deformations in the samples under study is rather justified.

Now, we should elucidate how the polarization relationships are connected with the presence or absence of excitation migration. Since the structure of deformed regions is unknown, detailed interpretation of this fact is impossible. However, the effect observed can be qualitatively explained from general considerations.

Recall that the experiment was performed with samples in which the C axis was oriented parallel to the optical axis of the experiment and perpendicular to the sample plane. This implies that the sample, as a whole, is isotropic in the plane normal to the light propagation. Moreover, as mentioned above, the probability of the loss of orientation by holes is very high. For this reason, the material likely does not exhibit micro- and macroscopic factors of anisotropy that could give rise to the polarization of recombination radiation.

However, the deformation can be observed in a local region of the material in the sample plane. In this case, the different directions of the linear polarization of exciting light and luminescence are nonequivalent. For the band of edge luminescence, both the excitation and recombination are associated with the valence band–conduction band transitions, the selection rules for optical transitions being identical for absorption and emission. It follows that the predominant polarization of the luminescence should coincide with the polarization of the excitation. (Note once again that we assume not the memory of the initial direction of the hole angular momentum, but the relationships between the selection rules for absorption and emission in local regions that can be characterized by additional anisotropy). Experimentally, the luminescence of deformed regions should be efficiently observed in the same polarization in which the exciting light was polarized; the corresponding components should be shifted from the center of the spectral band.

For the regions with a weak deformation, the polarization relationships are of little significance (according to the above considerations). Moreover, by reason of weak deformation, the emission of these regions corresponds to the central, weakly shifted components of the luminescence bands. This provides an explanation for the fact that the migration of excitations from the regions with an increased value of E_g into the host material affects the shape of the spectra at the parallel orientation of an analyzer and a polarizer and leaves the band shape unchanged when the polarizations are orthogonal. When recording the luminescence in the polarization parallel to the polarization of excitation, the migration toward lower energies E_g manifests itself but only between the regions with identical (or close) directions of the deformation. In this case, the migration can be realized within the small spatial region, which is characterized by the deformation gradient, within one crystallite included.

If the spectrum is recorded with an analyzer positioned perpendicular to a polarizer, the observation of the migration manifestation should mean that the migration occurs between the regions with different directions of deformation. However, the assumption of the migration between the regions, which are deformed along different directions, implies that the migrating excitations should traverse the boundary between these regions. Since these boundary regions often coincide with the intercrystalline boundaries, or, at least, have a high density of defects, this migration should be hampered. If it is assumed that such a compact boundary does not exist and considerable deformation gradients are absent in the sample, the migration path should be long enough for the local deformation to significantly change, specifically in direction. In this case, even the length of the required path is an obstacle to migration.

As a whole, the effect is caused by the following factors: the material is not entirely homogeneous, and the central band corresponds to the bulk with respect to the perfect material. The defect regions are characterized, first, by the deviation of E_g from the value typical of the bulk of the material and, second, by the direction of deformation. The excitation in the regions with a decreased value of E_g remain and undergo recombination at the point of generation. The excitations can migrate from the regions with an increased value of E_g

into the host material (toward lower energies E_g). However, the migration between the regions with different directions of the deformation is suppressed, because the path of migration in-between should include a highly defective region with an inhomogeneous deformation (of the type of intercrystalline boundary), or these regions should be widely separated.

Thus, the effect of polarization memory in gallium nitride crystals was experimentally observed for the first time. This effect manifested itself as a polarization-dependent inhomogeneous broadening of the edge luminescence band. The effect is associated with the specific features of the migration of excitations in hexagonal gallium nitride crystals. Actually, in the framework of this interpretation, the experiment represents a new version of the so-called "site-selected" luminescence spectroscopy on revealing defect regions and can be used in studies of materials with local inhomogeneities.

ACKNOWLEDGMENTS

This work was supported by the Russian Foundation for Basic Research, project no. 97-02-18088.

REFERENCES

1. H. Morkoc, S. Strite, G. B. Gao, *et al.*, J. Appl. Phys. **76**, 1363 (1994).
2. *Optical Orientation*, Ed. by B. P. Zakharchenya and F. Maĭer (Nauka, Leningrad, 1989).
3. B. P. Zakharchenya, D. N. Mirlin, V. I. Perel', and I. I. Reshina, Usp. Fiz. Nauk **136** (3), 459 (1982) [Sov. Phys. Usp. **25**, 143 (1982)].
4. D. Kovalev, M. Ben Chorin, J. Diener, *et al.*, Appl. Phys. Lett. **67**, 1585 (1995).
5. K. C. Zeng, J. Y. Lin, and H. X. Jiang, Appl. Phys. Lett. **74**, 1227 (1999).
6. F. A. Ponce, MRS Bull. **22** (2), 51 (1997).

Translated by T. Galkina

Physics of the Solid State, Vol. 42, No. 6, 2000, pp. 1045–1048. Translated from Fizika Tverdogo Tela, Vol. 42, No. 6, 2000, pp. 1013–1016.

SEMICONDUCTORS AND DIELECTRICS

Heat Conductivity of Gd_2S_3 with Excess Gadolinium

S. M. Luguev[1], N. V. Lugueva[1], and V. V. Sokolov[2]

[1] *Institute of Physics, Dagestan Scientific Center, Russian Academy of Sciences, ul. 26 Bakinskikh Komissarov 94, Makhachkala, 367003 Russia*

[2] *Institute of Inorganic Chemistry, Siberian Division, Russian Academy of Sciences, pr. Akademika Lavrent'eva 3, Novosibirsk, 630090 Russia*

E-mail: kamilov@sinol.ru

Received September 23, 1999

Abstract—An experimental study of the heat conductivity of Gd_2S_3 with excess Gd content has been carried out in the temperature range from 80 to 400 K. It is shown that, as the concentration of excess Gd increases, the heat conductivity of the samples initially drops sharply to reach a minimum at ~0.25 at.% Gd, after which it increases only slightly. The reasons for such an anomalous variation of the heat conductivity of Gd_2S_3 with composition are discussed. The temperature dependence of the thermal resistance of the samples displays breaks characteristic of structural transformations in the temperature range 170–185 K. © *2000 MAIK "Nauka/Interperiodica".*

Heat conductivity is not only a vital characteristic of structural materials, but also provides valuable information on crystal lattice defects [1]. Rare-earth (RE) sesquichalcogenides crystallizing in the Th_3P_4-type structure (γ modification) are promising materials for use in optoelectronics, laser technology, and piezoelectric transducers [2, 3]. In contrast to thorium phosphide, each ninth site in the cation sublattice of stoichiometric Ln_2X_3 (Ln stands here for an RE element, and X for a chalcogen) is vacant, and the compound is an insulator. Deviation of the composition from stoichiometry in either direction leaves the anion chalcogen sublattice unchanged, but causes an excess or deficiency of the metal in the cation sublattice. The excess metal atoms fill the cation vacancies, thus reducing their concentration. As a result, electrons that are not involved in chemical bond formation appear, which entails a change of the physical properties of the crystal [2]. It is known that cation vacancies are efficient phonon-scattering centers [1], and therefore a decrease in their concentration should bring about an increase in the heat conductivity of the crystal. In samples with excess RE content, one may expect that free electrons which are not involved in chemical bond formation also make a certain contribution to heat transport. However, heat conductivity studies made on a number of RE sesquichalcogenides (La_2Te_3, Pr_2Te_3, La_2S_3) and compositions with partially filled cation vacancies [4–7] do not lead to the unambiguous conclusion that introducing excess RE atoms in them does indeed result in an enhancement of the heat conductivity. In order to establish the character of heat conductivity variation upon a slight deviation from stoichiometry and to investigate the influence of various types of defects on the phonon heat conductivity κ_p, we experimentally studied the heat conductivity of gadolinium sulfide (Gd_2S_3) and of a number of compositions with excess Gd in the temperature range 80–400 K. The available experimental data on the heat conductivity of Gd_2S_3 and nonstoichiometric compositions are scarce [8–11]. The heat conductivity of stoichiometric Gd_2S_3 was investigated in [8], and the compositions studied in [9–11] are essentially nonstoichiometric.

The samples studied in this work were prepared by melt crystallization in a controllable sulfur-vapor atmosphere [12]. The homogeneity of the sample composition was checked by thermopower measurements with a thermal probe along the ingot. The sample composition was measured by the gas chromatographic method [13] to within 0.015 wt.% S. X-ray diffraction measurements showed all samples to be single phase having a Th_3P_4 structure. The samples intended for the heat conductivity studies measured $5 \times 5 \times 10$ mm and were cut from polycrystalline ingots. Stoichiometric Gd_2S_3 samples (which is equivalent to $GdS_{1.50}$) were yellowish-brown in color and transparent, while samples with excess Gd (GdS_x, where $x < 1.50$) were dark gray and opaque. The table lists the compositions studied and some characteristics of the samples determined experimentally at 300 K.

The heat conductivity κ was measured in the range 80–400 K in a vacuum of ~1.39×10^{-3} Pa by the absolute steady-state method on a type-A setup discussed in [14]. The measurements of κ were complemented by studying the electrical conductivity (σ) and thermopower (α) on the same samples, which made it possible to determine the electronic component of the heat conductivity κ_e and elucidate its role in the heat transport in the samples studied.

1063-7834/00/4206-1045$20.00

Properties of GdS_x samples at 300 K

Sample no.	Composition (x in GdS_x)	n, 10^{19} cm^{-3}		σ, $\Omega^{-1} \cdot$ cm^{-1}	α, μV/K
		exp.	calc.		
1	1.500		–	$<10^{-6}$	–
2	1.4989		3.98	0.9	407
3	1.4980	1.94	7.24	3.2	373
4	1.4971		10.5	5.1	335
5	1.4965		12.7	8.2	295
6	1.4960	5.04	14.5	11.8	270
7	1.4954		16.7	15.5	238

Figure 1 shows the results of measurements of the heat conductivity of GdS_x samples. The general form of the temperature dependence of κ of the samples does not differ substantially from the $\kappa(T)$ dependence obtained for lanthanum sulfide [6] and lanthanum telluride [4, 7], which are isostructural with gadolinium sulfide. The only difference is in the absolute value of κ, which is due to the difference in their molecular weights. The main contribution to heat transport in all the samples studied is due to lattice vibrations. The contribution κ_e to the total heat conductivity is negligible because of small values of σ (see the data on σ in the table). The value of κ_e for the sample with the largest σ is less than 1% of the total heat conductivity. It should be pointed out that the temperature dependence of κ for sample *1* at temperatures $T > 200$ K differs substantially from $\kappa(T)$ for other samples. It may be conjectured that because of optical transparency of sample *1*, electromagnetic radiation makes the largest contribution to its total heat conductivity at $T > 200$ K.

Figure 2 displays the concentration dependences of the lattice heat conductivity of the investigated samples at a number of fixed temperatures. The values of κ_p for sample *1* at 250, 300, and 400 K were obtained by extrapolating the low-temperature dependence $\kappa \sim T^{-1}$ to higher temperatures under the assumption that κ_p is governed by phonon–phonon and phonon–defect scattering in the entire temperature range. An unusual feature in Fig. 2 is the decrease of κ_p for nonstoichiometric compositions. It is believed [2] that metal atoms which are in excess compared to Ln_2X_3 in such compounds fill cation vacancies, whose concentration in Gd_2S_3 is

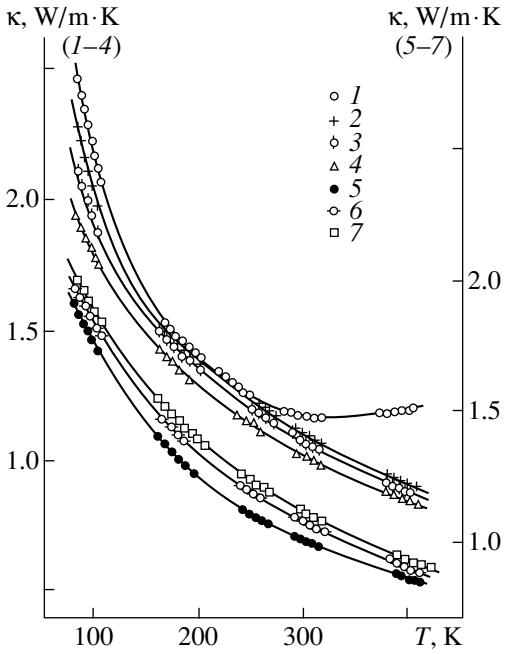

Fig. 1. Temperature dependences of the heat conductivity κ of GdS_x samples in the 80–400 K range. (*1–7*) Sample numbers (the samples are numbered as in the table).

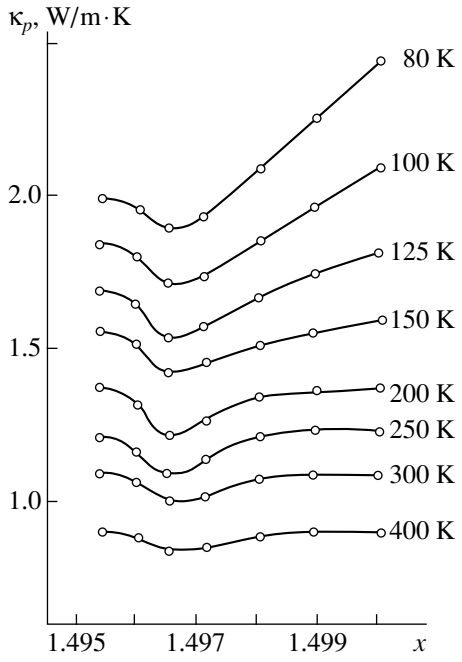

Fig. 2. Lattice heat conductivity κ_p vs. GdS_x composition for fixed temperatures.

2.08×10^{21} cm^{-3}. Filling of cation vacancies in nonstoichiometric samples should have increased κ_p, which is not observed in the experimental data in Fig. 2. The presence of a minimum in the $\kappa_p(x)$ dependence is also unusual.

It was pointed out earlier that, by occupying vacancies in the metal sublattice, the excess gadolinium reduces the cation vacancy concentration, which should reduce the number of phonon scattering centers as well. This should increase the value of κ_p. The observed anomalous dependence $\kappa_p(x)$ (Fig. 2) can be attributed to the formation of new phonon scattering centers as the Gd_2S_3 composition deviates from stoichiometry. The nature of these defects remains unclear. Such phonon scattering centers could be interstitial atoms in the presence of excess gadolinium in Gd_2S_3. This conjecture is also supported by the fact that the carrier concentration n derived experimentally from Hall coefficient measurements is substantially lower than the theoretical value (see the table). The concentration was calculated by assuming that the filling of cation vacancies releases one electron per structural unit to the conduction band [2]. It can be seen from the $\kappa_p(x)$ dependence that, as the composition deviates from the stoichiometry, the contribution of new defects to the decrease in heat conductivity becomes more significant than the possible increase in κ_p due to the cation vacancy filling. Starting with a certain excess gadolinium concentration (sample *5*), further filling of the cation vacancies and the corresponding decrease in their concentration results in an increase in κ_p (samples *6* and *7*). The variation of $\kappa_p(x)$ becomes weaker with increasing temperature. This is due to the relative enhancement of the role of phonon–phonon scattering with increasing temperature compared to phonon–defect processes in the decrease of the heat conductivity. Therefore the decrease in heat conductivity upon a deviation from stoichiometry is not as pronounced at $T > 200$ K as at lower temperatures.

Figure 3 shows the heat resistivity $W = 1/\kappa$ of four GdS_x samples studied. Since the contribution κ_e to the total heat conductivity is small, the data presented can be considered as the temperature dependences of the lattice heat resistance. The $W(T)$ dependence for sample *1* in the high-temperature region ($T > 200$ K) differs from that for other samples, which can be attributed to the appearance of an additional heat-conductivity component $\Delta\kappa$. The calculations made under the assumption that the temperature dependence of the lattice heat conductivity of sample *1* follows the relation $\kappa_p \sim T^{-1}$ similar to the $\kappa_p(T)$ dependence for samples *2* and *3* which are closest in composition to Gd_2S_3 suggest that the additional component of heat conductivity has a temperature dependence $\Delta\kappa \sim T^{3.1}$. The $\Delta\kappa$ singled out in this way from experimental data is close in terms of temperature dependence to the photon heat conductivity ($\kappa_{phot} \sim T^3$). Samples *2–7* do not reveal any contribution of $\kappa_p$hot to heat conductivity, because free carriers absorb electromagnetic radiation in the presence of excess Gd.

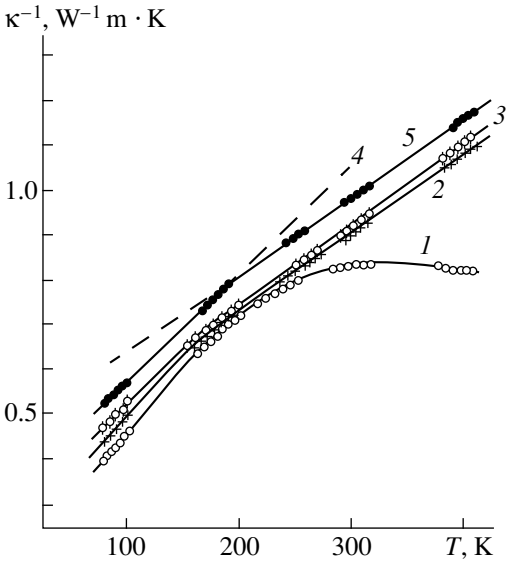

Fig. 3. Temperature dependences of the heat resistivity ($W = \kappa^{-1}$) for a number of GdS_x compositions. Sample numbers are the same as in Fig. 1.

In the temperature interval studied by us, the $W(T)$ plots for the samples (except sample 1) exhibit breaks, which divide each plot into two linear parts with different slopes. This break is not seen in the $W(T)$ dependence for sample *1* against the background of the κ_{phot} contribution to heat transport at $T > 200$ K. It should be pointed out that the position of the break on the temperature scale changes with the composition. For example, the break for sample *2* with the lowest Gd excess lies at 170 K, while for sample *5* it is at 185 K. The breaks in the $W(T)$ dependence for the investigated samples are possibly of the same nature as the anomalies observed near 200 K in the temperature dependence of the specific heat of La_2Se_3 [15], La_2Te_3 [16], and Nd_2Se_3 [17], which are isostructural with Gd_2S_3. The same region of anomalous behavior in the interval 160–240 K was observed in the temperature dependence of the linear thermal expansion coefficient of γ-Nd_2S_3 [18].

The experimental results obtained permit the following conclusions. Besides filling the cation vacancies, gadolinium atoms present in Gd_2S_3 in excess of the stoichiometric content, produce new defect states in the lattice, whose nature is not fully clear. The decrease in heat conductivity due to these defects is more substantial (particularly at $T < 200$ K) than the possible increase in κ_p expected from the filling of cation vacancies by gadolinium. In the case of 0.25% Gd excess, the effects of the two mechanisms on κ_p cancel out. The temperature dependence $W(T)$ for all samples displays breaks characteristic of structural transformations. As the excess gadolinium concentration in the substances

studied increases, the transition temperature T_c ($170 < T_c < 185$ K for different compositions) shifts toward higher temperatures.

ACKNOWLEDGMENTS

The authors are indebted to A. É. Ramazanov for performing the Hall measurements.

Partial support of the Russian Foundation for Basic Research (grant no. 99-02-16823) is gratefully acknowledged.

REFERENCES

1. V. S. Oskotskiĭ and I. A. Smirnov, *Defects in Crystals and Thermal Conductivity* (Nauka, Leningrad, 1972).
2. *Physical Properties of Rare-Earth Chalcogenides* (Nauka, Leningrad, 1973).
3. V. P. Zhuze and A. I. Shelykh, Fiz. Tekh. Poluprovodn. (Leningrad) **23** (3), 393 (1989) [Sov. Phys. Semicond. **23** (3), 245 (1989)].
4. S. M. Luguev, V. S. Oskotskiĭ, V. M. Sergeeva, and I. A. Smirnov, Fiz. Tverd. Tela (Leningrad) **17** (11), 3229 (1975) [Sov. Phys. Solid State **17** (11), 2126 (1975)].
5. L. N. Vasil'ev, S. M. Luguev, V. S. Oskotskiĭ, and I. A. Smirnov, Fiz. Tverd. Tela (Leningrad) **18** (3), 906 (1976) [Sov. Phys. Solid State **18** (3), 524 (1976)].
6. S. M. Luguev, N. V. Lugueva, V. V. Sokolov, and Yu. N. Malovitskiĭ, Neorg. Mater. **21** (5), 878 (1985).
7. S. M. Luguev, Synopsis of Ph.D. Thesis (Ioffe Physicotechnical Institute, Leningrad, 1978).
8. S. M. Luguev, N. V. Lugueva, and V. V. Sokolov, Fiz. Tverd. Tela (Leningrad) **30** (3), 873 (1988) [Sov. Phys. Solid State **30** (3), 504 (1988)].
9. G. G. Gadzhiev, S. M. Luguev, V. V. Sokolov, *et al.*, *Charge and Heat Transport in Semiconductors* (Makhachkala, 1986).
10. G. G. Gadzhiev, Sh. M. Ismailov, M. A. Aĭdamirov, *et al.*, Neorg. Mater. **33** (4), 404 (1997).
11. S. M. A. Taher and J. B. Gruber, Phys. Rev. B **16** (4), 1624 (1977).
12. A. A. Kamarzin, K. E. Mironov, V. V. Sokolov, *et al.*, J. Cryst. Growth **52** (2), 619 (1981).
13. L. S. Chuchalina, I. G. Vasil'eva, A. A. Kamarzin, and V. V. Sokolov, Zh. Anal. Khim. **33** (1), 190 (1978).
14. E. D. Devyatkova, A. V. Petrov, I. A. Smirnov, and B. Ya. Moĭzhes, Fiz. Tverd. Tela (Leningrad) **2** (4), 738 (1960) [Sov. Phys. Solid State **2** (4), 681 (1960)].
15. I. E. Paukov, V. V. Nogteva, and E. I. Yarembash, Zh. Fiz. Khim. **40** (12), 3094 (1966).
16. V. V. Nogteva, I. E. Paukov, and E. I. Yarembash, Zh. Fiz. Khim. **43** (8), 2118 (1969).
17. V. V. Nogteva, I. E. Paukov, and E. I. Yarembash, Zh. Fiz. Khim. **42** (1), 232 (1968).
18. O. A. Nabutovskaya, V. V. Nogteva, V. V. Sokolov, and A. A. Kamarzin, Fiz. Tverd. Tela (Leningrad) **24** (5), 1464 (1982) [Sov. Phys. Solid State **24** (5), 834 (1982)].

Translated by G. Skrebtsov

Physics of the Solid State, Vol. 42, No. 6, 2000, pp. 1049–1051. Translated from Fizika Tverdogo Tela, Vol. 42, No. 6, 2000, pp. 1017–1019.

SEMICONDUCTORS AND DIELECTRICS

Electric-Field Effect and Orientational Relaxation of Gd^{3+}–F^- Dipole Complexes in BaF_2

V. A. Vazhenin, V. B. Guseva, and M. Yu. Artemov

Institute of Physics and Applied Mathematics, Ural State University, Yekaterinburg, 620083 Russia

e-mail: vladimir.vazhenin@usu.ru

Received October 19, 1999

Abstract—The relaxation parameters of the orientational kinetics of trigonal Gd^{3+}–fluorine complexes in BaF_2 have been determined by a method based on the electric-field effect in paramagnetic resonance. © *2000 MAIK "Nauka/Interperiodica".*

1. Apart from the methods based on thermally stimulated depolarization (TSD) [1–3], dielectric [4–9] and inelastic [5, 6] losses, as well as the temperature dependence of EPR linewidth [4, 7, 8], the method based on the electric-field effect (EFE) can be used to study the orientational relaxation of dipole complexes formed by impurity centers and charge compensating defects [10–13]. Unlike the other methods, it does not require additional data and ensures the unambiguous identification of activation energy with the type of a relaxing complex. When an external electric field is applied to the crystal, two dipole complexes related through the inversion operation are no longer magnetically equivalent, and the EPR signal splits into two components, whose intensity ratio is determined by the difference in the energies of these complexes

$$I_+/I_- = \exp(2dE/kT), \qquad (1)$$

where d is the dipole moment of the complex [12], and E is the electric field.

By studying the time dependence of the pseudo-Stark component intensities immediately after the application of the field or after its reversal, one can measure the dipole-complex reorientation time [12, 13].

The purpose of this work was to use this method to study the relaxation of the Gd^{3+}–F^- dipole trigonal complexes in BaF_2 [14], as well as to attempt to discover the tetragonal centers in this crystal.

2. The measurements were carried out on BaF_2 single crystals doped with Gd^{3+} having a concentration of 0.1 wt.% in the charge. We studied for $\mathbf{E} \parallel \mathbf{H} \parallel C_3$ the $5/2 \longleftrightarrow 7/2$ transition (producing the largest electric-field effect) of the parallel trigonal-center spectrum (0.371 T at a frequency of 9.4 GHz, the Gd^{3+} excess charge is compensated by the F^- ion occupying the interstice closest to the C_3 axis [14]). For the sample thickness of 0.05 cm, the field strength reached 100–150 kV/cm.

Since the electric fields used are not strong enough to attain total splitting of the signal into two separate components, we were only able to observe a broadening of the signal upon the application of an electric field, and a shift of the broadened signal as a result of field reversal. This shift is caused by an interchange of the unresolved pseudo-Stark components of different intensities. Ultimately, the EPR signal regains its original position, thus reflecting the relaxation of the intensities of unresolved components.

It was shown [12] that the relaxation of the trigonal Gd^{3+}–fluorine centers in SrF_2 takes place through tetragonal interstices, at which equilibrium is attained much more rapidly. The high intensity of the tetragonal complexes is due to a higher (by 0.06 eV compared to trigonal ones) energy of coupling with the compensator. It can be expected that the relaxation of the 3*mm* centers in BaF_2 follows the same pattern as in SrF_2, except for the change in sign of the difference in energies of coupling with the compensator, which is indicated by the absence of noticeable tetragonal-center lines in the EPR spectrum. In this case, the relaxation involves the transfer of a fluorine ion from a trigonal to a tetragonal site (Fig. 1), and the relaxation times of the pseudo-Stark components are identical.

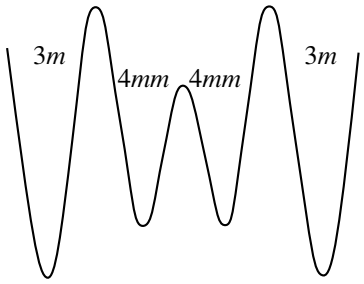

Fig. 1. Qualitative energy relief profile (in zero electric field) for interstitial fluorine motion near Gd^{3+} in BaF_2.

1063-7834/00/4206-1049$20.00

Relaxation parameters of Gd^{3+}–F^- complexes in fluorites obtained by various methods

Crystal	CaF_2		SrF_2				BaF_2	
Type of center	4*mm*		4*mm*		3*mm*		3*mm*	
Dielectric relaxation								
τ_0, 10^{-13} s	2.22	[7]	2.0	[8]	1.3	[8]	0.77	[8]
U, eV	0.395(5)	[7]	0.454	[8]	0.640	[8]	0.610	[8]
EPR line broadening								
τ_0, 10^{-13} s	2.22	[7]	3.6	[8]	0.25	[8]	2.9	[8]
U, eV	0.395(5)	[7]	0.429	[8]	0.680	[8]	0.535	[8]
TSD								
τ_0, 10^{-13} s	0.02	[13]	0.1	[13]	0.4	[13]	0.1	[1]
U, eV	0.42(1)	[13]	0.45(1)	[13]	0.62(2)	[13]	0.60	[1]
EFE								
τ_0, 10^{-13} s	0.195(9)	[13]	0.40(5)	[13]	0.3(1)	[13]	0.3	[*]
U, eV	0.412(5)	[13]	0.455(5)	[13]	0.64(1)	[13]	0.63(2)	[*]

* This work.

We assume that the broadened signal is the sum of two close components $I(t, B) = I_+(t, B) + I_-(t, B)$ (B is the magnetic-field induction) with equal relaxation rates

$$I_+(t, b) = f(B_+, B)[(A - C)\exp(-t, \tau) + C],$$
$$I_-(t, b) = f(B_-, B)[(C - A)\exp(-t, \tau) + A], \quad (2)$$

where $f(B_+, B)$ is the shape function of a line centered at B_+, and A and C are the steady-state intensities of the component. In this case, we find that after the electric field switching, the time dependence of the intensity of this signal at any point will be described by the same exponential (the same parameter τ) as that of the intensities of the individual components.

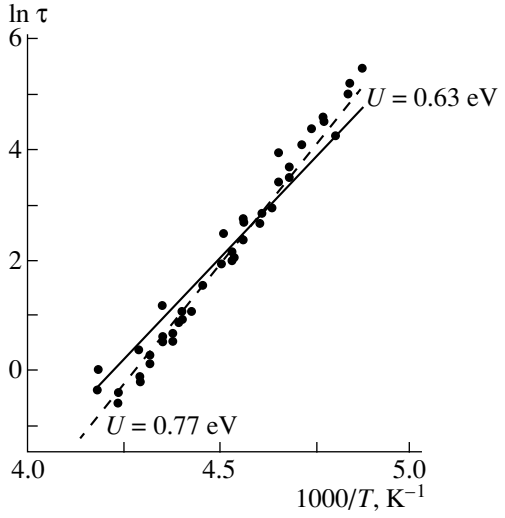

Fig. 2. Temperature dependence of the relaxation time of Gd^{3+}–F^- trigonal dipole complexes in BaF_2.

The time dependence of the intensity of the first derivative of the signal near the center of the broadened line after the reversal of the electric field was measured in the 205–239 K range. With the exclusion of the initial portion of the curve distorted by the charge reversal in the sample, the time dependence was approximated by an exponential function. The dependence of τ on the temperature T thus obtained (Fig. 2) yielded the following values for the activation energy and the preexponential factor in the equation

$$\tau = \tau_0 \exp(U/kT), \quad (3)$$

$U = 0.77$ eV and $\tau_0 = 2.5 \times 10^{-17}$ s. One of the reasons for obtaining such an underestimated value of τ_0 could be an error in temperature measurement, which increases upon cooling and is caused by the impossibility of measuring the temperature directly in the sample (which is under a high voltage) placed in liquid-nitrogen vapor. Assuming τ_0 to be equal to the corresponding parameter for SrF_2 yields an optimum value $U = 0.63(2)$ eV (see the table). With this choice, the fitting straight line passes satisfactorily through the experimental points (see Fig. 1), and the standard error increases only slightly.

3. By extrapolating the data on the EPR spectrum of Gd^{3+}–fluorine tetragonal centers in CaF_2 [15] and SrF_2 [16] to BaF_2, we determined for this crystal the magnetic-field regions free of trigonal-center signals, where one could expect the existence of transitions of the 4*mm* centers. Assuming the relaxation times of the tetragonal centers in BaF_2 and SrF_2 to be similar, one can predict that cooling of the sample in an electric field to temperatures below 150 K should produce a spectrum of tetragonal centers with signals broadened or splitted by the electric-field effect into two unequal (1) compo-

nents, which should shift or vary in component intensity, respectively, as a result of field reversal, thus revealing a very slow relaxation. No signals exhibiting such behavior were found among the weak lines in the above-mentioned magnetic-field regions. Taking into account the ratio S/N = 50 observed for a trigonal center, it can be stated that the binding energy of Gd^{3+} in BaF_2 with a 3*mm* compensator is higher than that with a 4*mm* one by at least 0.1 eV.

REFERENCES

1. E. L. Kitts, Jr., M. Ikeya, and J. H. Crawford, Jr., Phys. Rev. B **8** (12), 5840 (1973).
2. B. P. Lenting, J. A. J. Numan, E. J. Bijvank, and H. W. den Hartog, Phys. Rev. B **14** (5), 1811 (1976).
3. G. Eric Matthews, Jr. and J. H. Crawford, Jr., Phys. Rev. B **15**, 55 (1977).
4. A. D. Franklin and S. Marzullo, J. Phys. C: Solid State Phys. **3** (9), L171 (1970).
5. A. D. Franklin and J. Crissman, J. Phys. C: Solid State Phys. **4**, L239 (1971).
6. A. D. Franklin, J. M. Crissman, and K. F. Young, J. Phys. C: Solid State Phys. **8**, 1244 (1975).
7. A. Edgar and H. K. Welsh, J. Phys. C: Solid State Phys. **8**, L336 (1975).
8. A. Edgar and H. K. Welsh, J. Phys. C: Solid State Phys. **12**, 703 (1980).
9. P. Varotsos and K. Alexopoulos, J. Phys. Chem. Solids **41**, 443 (1979).
10. Yu. A. Sherstkov, V. A. Vazhenin, and K. M. Zolotareva, Fiz. Tverd. Tela (Leningrad) **16**, 2080 (1974) [Sov. Phys. Solid State **16**, 1352 (1974)].
11. Yu. A. Sherstkov, V. A. Vazhenin, and K. M. Zolotareva, Fiz. Tverd. Tela (Leningrad) **17**, 2757 (1975) [Sov. Phys. Solid State **17**, 1830 (1975)].
12. Yu. A. Sherstkov, V. A. Vazhenin, N. V. Legkikh, and K. M. Zolotareva, Fiz. Tverd. Tela (Leningrad) **18**, 2614 (1976) [Sov. Phys. Solid State **18**, 1526 (1976)].
13. Yu. A. Sherstkov, V. A. Vazhenin, and N. V. Legkikh, in *Abstract of the All-Union Conference on Physics of Dielectrics, Karaganda, 1978*.
14. L. A. Boatner, R. W. Reynolds, and M. M. Abraham, J. Chem. Phys. **52**, 1248 (1970).
15. Yu. E. Pol'skiĭ, *Radiospectroscopy of Solids* (Atomizdat, Moscow, 1967).
16. A. Edgar and D. J. Newman, J. Phys. C: Solid State Phys. **8**, 4023 (1975).

Translated by G. Skrebtsov

Physics of the Solid State, Vol. 42, No. 6, 2000, pp. 1052–1057. Translated from Fizika Tverdogo Tela, Vol. 42, No. 6, 2000, pp. 1020–1025.

SEMICONDUCTORS AND DIELECTRICS

Recombination-Assisted Creation of Cation Excitons and Cross-Luminescence Quenching in CsCl Crystals at High Excitation Densities

Ch. B. Lushchik[1], F. A. Savikhin[1], V. N. Makhov[2], O. V. Ryabukhin[3], V. Yu. Ivanov[3], A. V. Kruzhalov[3], and F. G. Neshov[3]

[1] *Institute of Physics, Tartu University, EE2400 Tartu, Estonia*

[2] *Lebedev Physical Institute, Russian Academy of Sciences, Leninskiĭ pr. 53, Moscow, 117924 Russia*

[3] *Ural State Technical University, ul. Mira 19, Yekaterinburg, 620002 Russia*

e-mail: rov@dpt.ustu.ru

Received November 15, 1999

Abstract—At high excitation densities, recombination-assisted creation of cation excitons, which transfer energy efficiently to the anion sublattice to initiate the luminescence of anion excitons and impurity centers, has been observed in CsCl crystals. At the same time, the creation of cation excitons competes with the electron recombination with cation holes and quenches the cross-luminescence. The intensity ratio of the cross-luminescence to exciton-impurity luminescence is different for crystal irradiation with γ rays and heavy particles. © *2000 MAIK "Nauka/Interperiodica".*

Three kinds of intrinsic luminescence are known to exist in regular regions of wide-gap metal halides, namely, luminescence of self-trapped excitons (STE), intraband luminescence (IBL), and cross-luminescence (CL). The luminescence of the STEs, which are formed as a result of direct optical creation, as well as in recombination of electrons with self-trapped holes, shows the highest quantum yield (η) at low temperatures (4–80 K) [1, 2]. The radiative transitions of electrons between conduction- or valence-band levels in irradiated crystals (electron IBL and hole IBL) [3, 4] occur over a period of the order of picoseconds and are observed in a broad temperature range, but with a low integrated efficiency (about 10^{-4} photon per electron–hole (*e*–*h*) pair).

Radiative transitions between electrons in the anion valence band and holes generated by short-wavelength radiation in the core cation zone have also been studied comprehensively in the recent years. This so-called cross-luminescence or core-valence luminescence in the VUV spectral region was described for LiF in the pioneering work [5]. Cross-luminescence was identified in the 2–8 eV spectral region convenient for practical applications from characteristic CL excitation spectra produced by synchrotron radiation in BaF_2 [6] and CsBr [7], and after that, in many simple and complex metal halides [8–15]. It was found that the CL efficiency in BaF_2 is substantially lower for irradiation by α particles than by electrons or photons [13]. This feature of the CL, as well as the simultaneous detection of the cross-luminescence and of the STE luminescence, which had different characteristic times in $LiBaF_3$, were used to develop a technique for the selective measurement of γ-rays and heavy particles in mixed γ-neutron fluxes [14, 15]. But the mechanism of decrease in the CL efficiency upon irradiation by heavy particles, which is important for practical applications, has not been established.

The present work aims to study the mechanism of a sharp decrease in the cross-luminescence efficiency in crystals irradiated by protons, α-particles, and ions compared to their excitation by VUV radiation and x- and γ-rays. We will consider the problem of selective cross-luminescence efficiency of crystals exposed to various kinds of radiation for the specific case of CsCl crystals that were earlier studied in considerable detail [16–27].

1. SUBJECTS OF THE STUDY. MEASUREMENT TECHNIQUES

Single crystals of CsCl were grown at the Institute of Physics (Tartu) of the Estonian Academy of Sciences by a modified Stockburger method (see [19] for details). Plates measuring $15 \times 15 \times 2.5$ mm cut from the prepared crystal were annealed at 690 K to remove the dislocations and point defects introduced during preparation. The luminescence spectra of CsCl crystals excited by x-rays in the energy range 2–6 eV at 5 K also showed, in addition to the three intrinsic luminescences described in [22, 24] (see below), impurity luminescence bands at 3.15 and 3.7 eV, for which the Rb^+ and Br^- ions are primarily responsible.

1063-7834/00/4206-1052$20.00 © 2000 MAIK "Nauka/Interperiodica"

Three main experimental setups were employed for the excitation and study of the luminescence in the crystals. A GIN-600 electron accelerator designed by Mesyats and Koval'chuk provided solitary 3 ns electron-beam pulses (300 keV, 1–120 A cm^{-2}). Irradiation by heavy charged particles was done on the cyclotron of Ural State Technical University. The channel used makes it possible to study the optical properties of solids irradiated by heavy charged particles (H^+, He^+, C^{3+}, N^{3+}, O^{4+}, and Ar^{6+}) with energies of up to 1 MeV/nucl and flux densities of 9.7×10^9–4.7×10^{11} s^{-1} cm^{-2} in the temperature range from 80 to 600 K. The spectral range investigated using an MSD-1 monochromator and a FÉU-106 PM tube is 200–800 nm (1.5–6.0 eV). The use of a vacuum monochromator (600 mm^{-1}, $R = 0.5$ m grating) combined with a FÉU-142 PM tube extends the range to 11 eV [28]. The ion beams of H^+ with energies of 0.7, 1, 3, and 6.7 MeV, He^+ with 3 MeV, and N^{+3} with 16 MeV were used in the experiment. Standard x-ray sources (40–50 keV), VUV radiation (6–14 eV) [19, 22], and synchrotron radiation of the MAX-LAB storage ring in Lund, Sweden were also used [22, 24]. The STE luminescence (2.9 eV) and the two principal cross-luminescence bands (4.6 and 5.2 eV) isolated by the monochromators were recorded in the photon counting mode. The luminescence excitation spectra were corrected for the quantum efficiency of the VUV radiation during measurements.

2. CsCl LUMINESCENCE UNDER EXCITATION AND IONIZATION OF ANIONS AND CATIONS

It was shown in [19, 20] that the STE π luminescence band in CsCl has a maximum at 2.9 eV and a halfwidth of 0.7 eV, and that heating the crystal to 45 K weakens this luminescence. At high temperatures, the dominant luminescences are the impurity luminescence of the Br^- (3.7 eV) and Rb^+ (3.15 eV) centers, as well as the tunneling luminescence of F^-, V_K pairs (2.7 eV) and the luminescence of halogens near vacancy associations (3–4 eV) [19, 20].

Preliminary observations of fast (~2 ns) luminescence at 4.6 and 5.1 eV, which were identified as STE σ luminescence, were reported for the electron-beam irradiation of CsCl at 5 K [2, 29]. It turned out, however, that this luminescence was not excited in the case of the direct creation of anion excitons (7.8–8.3 eV). Similar to the short-wavelength fast radiation in CsBr [7], the excitation spectrum of the 4.6 and 3.1 eV luminescence bands in CsCl was found to be unusual. The threshold excitation energy for these luminescence bands, both at 115 and at 8 K, turned out to be ~14 eV [22, 23], thus permitting their identification as two cross-luminescence components.

Figure 1 presents the emission spectrum of our CsCl crystal excited by a weak x-ray flux (40 keV, 2 mA, W anode) at 5 K. The 3.0 eV band is due to the STE π-luminescence, while the 4.6 and 5.15 eV bands correspond to cross-luminescence. Optical generation of *e*–*h* pairs by 9 eV photons excites only the STE π luminescence and weak impurity luminescence. The luminescence intensity at 3.7 eV due to the Br^- ions increases by several factors when excited by 7.8–8.3 eV photons during the direct optical production of high-mobility excitons at 5 K.

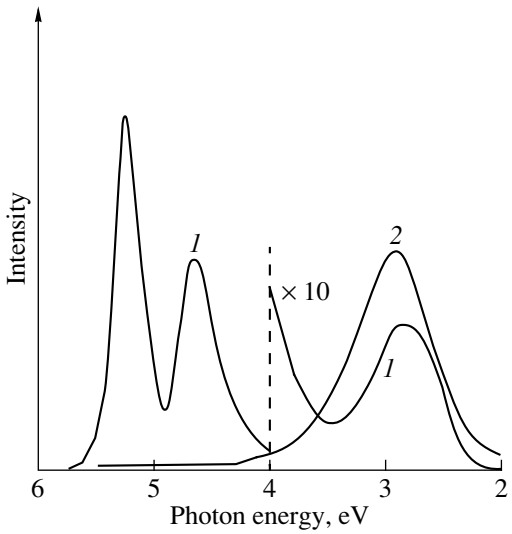

Fig. 1. Emission spectra of CsCl crystals measured under excitation by x-rays (curve *1*) and 9 eV photons (curve *2*) at 5 K.

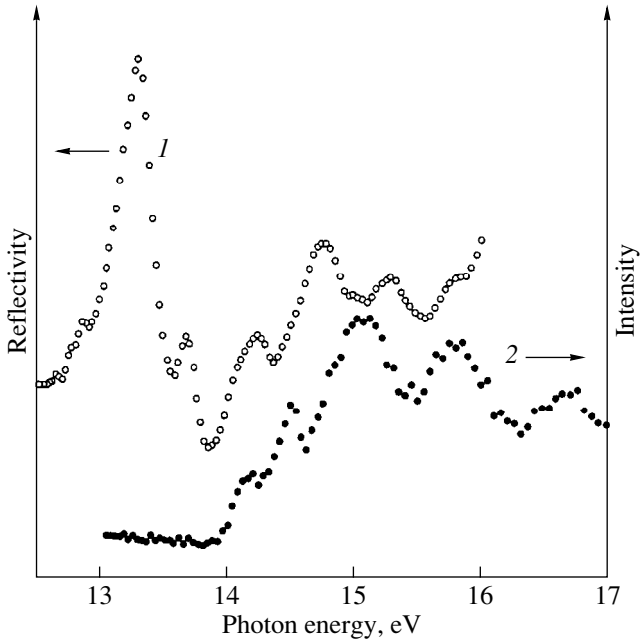

Fig. 2. Spectra of reflectance at 78 K (curve *1*) and 5.17 eV luminescence excitation at 8 K (curve *2*) for CsCl. The residual background luminescence in the excitation spectrum in the region 12.5–14 eV is due to a weak impurity luminescence and superposition of second-order synchrotron radiation.

Figure 2 presents the CsCl reflectance spectra measured on the MAX-LAB synchrotron at 8 K for photon

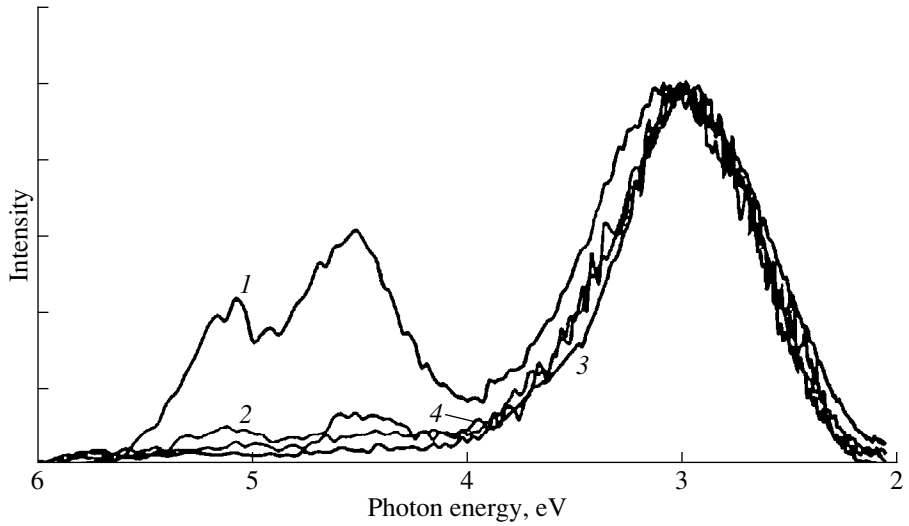

Fig. 3. Emission spectra of CsCl crystals measured at 295 K under irradiation by x-rays (curve *1*), 1 MeV protons (curve *2*), 4.6 MeV He^+ ions (curve *3*), and 16 MeV N^{3+} ions (curve *4*).

energies from 12.5 to 16 eV. The peaks at 13.2 and 13.5 eV correspond to the creation of cation excitons. Also shown is the excitation spectrum of the 5.2 eV cross-luminescence, which is practically not excited up to 14 eV in pure CsCl crystals. Even direct generation by 13–14 eV photons of cation complexes, which were first studied from reflectance spectra (at 290 K in [16], and at 20 K in [18]), does not give rise to cross-luminescence. According to [18], the ionization of Cs^+ ions in CsCl is identified with a step in the reflectance spectrum at 14.1 eV. It is in this region that the threshold energy of excitation of the 5.2 eV cross-luminescence at 8 K lies (see Fig. 2).

As in BaF_2 [6] and CsBr [7] crystals, the formation of cation excitons in CsCl does not practically excite the cross-luminescence. In the region where 13–14 eV photons produce cation excitons, the anion exciton luminescence (2.9 eV) is excited in CsCl at 8 K. This fundamentally important fact remained unexplained for a long time. In spite of repeated attempts, the specific luminescence of cation excitons in their direct creation by 13–14 eV photons could not be detected in cesium halides, although the spectral region investigated in Tartu extended from 2 to 12 eV. In CsI crystals, where the band gap E_g = 6.2 eV, decay of the cation exciton into two *e–h* pairs was detected [16]. However, this process can occur only at temperatures of $T \geq 300$ K in CsBr crystals, and it is ruled out in CsCl, because $2E_g$ = 16.8 eV far exceeds the cation exciton energy. It was recently shown that the photoelectron emission characteristic of photoionization in the lower part of the CsCl valence band is greatly enhanced when irradiated by 13.2 eV photons, which create cation excitons in CsCl [30]. This implies that the energy of the cation excitons created by 13.2 eV photons is transferred in a nonradiative way to the neighboring anions, thus causing their ionization, and ultimately resulting in the formation of the STE and impurity luminescences.

3. LUMINESCENCE EXCITED BY PROTONS AND IONS

Figure 3 shows the emission spectra of CsCl crystals measured at 295 K under excitation by x-rays, as well as under irradiation by protons (1 MeV), He^+ ions (3 MeV) and N^{3+} ions (16 MeV). At room temperature, x-rays effectively excite impurity luminescence in the 2.5–3.3 eV interval and both characteristic cross-luminescence bands at 4.6 and 5.2 eV with a CL duration of 1.2 ns for CsCl [12]. It was assumed in the very first study of the cross-luminescence in CsBr [7] that part of the cation holes become self-trapped before recombining with the electrons of the neighboring anions. Recent precision measurements of the CL band profiles in CsCl carried out over a broad temperature range provide evidence supporting this assumption [25, 26]. Self-trapping of cation holes should increase the effective cross section of their recombination with the electrons of the neighboring anions. However, the intensity ratio of the cross-luminescence to impurity anion luminescence excited by 1 MeV protons and helium and nitrogen ions is much smaller than that for irradiation by x-rays.

Figure 4 presents emission spectra of CsCl crystals irradiated by protons with energies of 0.7, 1.0, and 6.7 MeV. It can be readily seen that the decrease of the CL efficiency (compared to the excitation by x-rays) becomes less pronounced with increasing proton energy, and 6.7 MeV particles already excite the cross-luminescence. Such a strong dependence of CL intensity on the type of excitation can be associated with the difference between the volume excitation densities created in CsCl in the various conditions of irradiation. This assumption is also supported by the fact that bombardment of a crystal with heavy particles (protons, α particles, fission fragments) not only decreases the CL intensity, but also shortens the decay time. Indeed, the CL characteristic time in CsF exposed to γ rays and

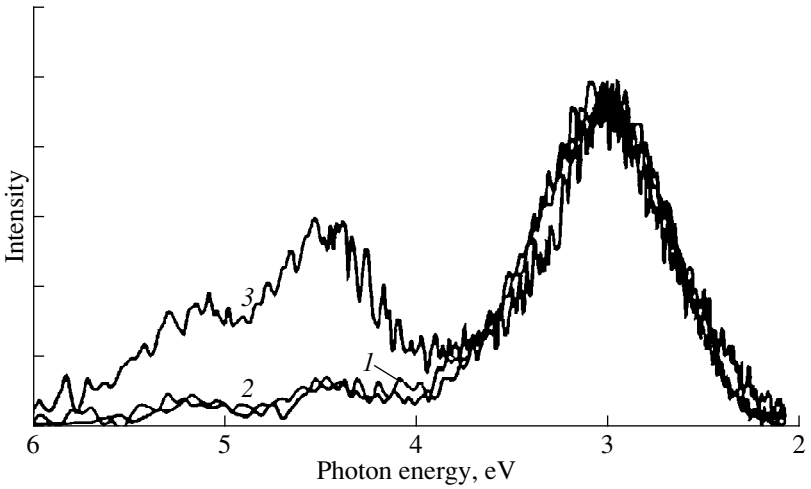

Fig. 4. Emission spectra of CsCl crystals measured at 295 K under irradiation by protons with energies (MeV) 0.7 (curve *1*), 1 (curve *2*), and 6.7 (curve *3*).

electrons, is τ = 4 ns [12], while bombardment by α particles gives τ = 0.2 ns for weak CL [31].

An estimate of the excitation density for the irradiation regime used by us (40 kV, 10 mA, W anode) was made using standard relations for x-rays and tabulated data for x-ray attenuation in CsCl. It was found to be 3×10^{17} eV cm^{-3} s^{-1}. It follows from an analysis of the averaged excitation densities produced by protons with energies of 1 and 6 MeV [32] that the effective proton track radius in CsCl at a particle energy of 2–8 MeV is independent of the energy and equal to 7.5 nm. According to estimates, the volume excitation densities in tracks of protons of the above energies can be as high as 10^{20} and 3×10^{19} eV $\cdot$ cm^{-3}, respectively, which is about two orders of magnitude higher than in the case of x-irradiation. It should be noted that, according to [32], in tracks of α particles with velocities considerably higher than those of orbital electrons, i.e., with energies above 1 MeV, the volume excitation density is only 1.5–2 times higher than that in the tracks of protons having the same energies.

The above results show that if the excitation densities in CsCl crystals are high enough, they can initiate processes leading to the suppression of cross-luminescence without any weakening (or even with some enhancement) of the anion luminescence.

4. DEPENDENCE OF CROSS-LUMINESCENCE EFFICIENCY ON ELECTRON IRRADIATION DENSITY

An attempt was made to simulate a high e-h pair generation density by using powerful solitary electron-beam pulses from the GIN-600 accelerator by varying the current density from 10 to 130 A cm^{-2}. Such pulses produced volume excitation densities from 2×10^{18} to 2.6×10^{19} eV/cm^3 in CsCl. Figure 5 presents the luminescence spectrum excited in CsCl by fast (3 ns) electron-beam pulses at 295 K (for more details, see [21]). The dependence of the intensities of two luminescence bands at 4.5 and 5.15 eV singled out by the double monochromator on the current density was measured. As seen from Fig. 6, the intensity of both cross-luminescence bands increases linearly with the current density in the region from 10 to 60 A cm^{-2} (2×10^{18}–1.2×10^{19} eV/cm^3). However, in the 90–140 A cm^{-2} region (1.8×10^{19}–2.6×10^{19} eV/cm^3) a characteristic sublinear behavior is observed, which suggests a strong decrease in the efficiency of cross-luminescence excitation under these conditions. The situation observed in the case of irradiation by a powerful electron pulse of 130 A cm^{-2} was found to be similar to that in the case of irradiation by high-energy (6 MeV) protons. At high electron-beam densities, we observe the initial stage of the effect occurring in the case of bombardment of

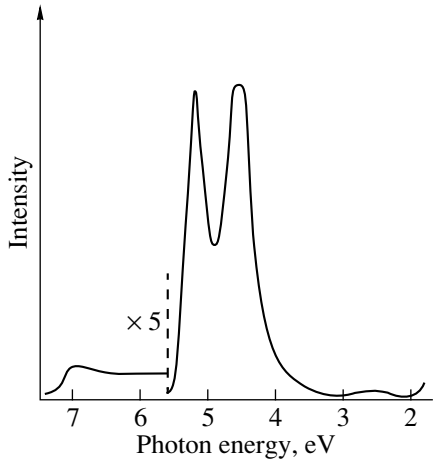

Fig. 5. Fast luminescence spectra ($\tau \leq 2$ ns) of a CsCl crystal obtained under pulsed electron-beam irradiation (300 keV, 90 A cm^{-2}, 3 ns) at 295 K.

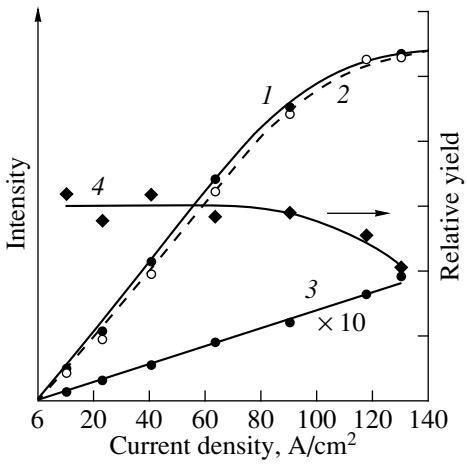

Fig. 6. Intensities of the cross-luminescence bands at 4.5 eV (curve *1*) and 5.15 eV (curve *2*) and of intraband luminescence at 2.5 eV (curve *3*) as functions of current density in electron-beam pulse measured at 295 K. Curve *4* presents the relative cross-luminescence yield determined as the ratio of intensities of the cross-luminescence (4.5 eV) and intraband luminescence (2.5 eV).

CsCl by protons and helium and nitrogen ions (see Fig. 3). Note that the weak intraband fast ($\tau < 10^{-10}$ s) luminescence of CsCl crystals [21] detected over a broad spectral range (from 1.8 to 7.2 eV) depends linearly on current density (Fig. 6). Figure 6 also shows the efficiency of 4.5 eV CL as a function of current density. At the current density of 130 A/cm^2, it decreases by a factor 1.5. According to estimates obtained in [21], the energy efficiency of the cross-luminescence in CsCl irradiated by electron pulses is 3–10^{-3} eV/eV.

5. RECOMBINATION-ASSISTED CREATION OF CATION EXCITONS AND THE POSSIBILITY OF SELECTIVE DETECTION OF PARTICLES AND PHOTONS

The obtained results can be used to discuss the mechanism of the selective response of the various intrinsic and impurity luminescences to irradiation by particles (protons, neutrons, α particles, ions) and photons (x- and γ-rays) in ionic crystals capable of cross-luminescence. This problem has been a subject of discussion for many years (see, e.g., reviews [26, 33–35]), but remains unsolved for systems with cross-luminescence. The large amount of data available on the dependence of the intensity of luminescence of various kinds on volume excitation density I_{ex} shows a linear dependence of I on I_{ex} (first linear region) at low I_{ex}, when the excited regions of the crystal still do not overlap. As I_{ex} increases to the level when the regions of the crystal excited by individual particles overlap, a superlinear dependence of I on I_{ex} is frequently observed. The superlinear region is well pronounced in crystals where radiative or nonradiative recombination channels compete with the electron and hole radiative recombination channel studied here. For relatively high values of I_{ex}, the impurity and defect-related competing channels attain saturation, after which a part of the intrinsic luminescences is found to be proportional to I_{ex} (second linear region). Accepting the rough estimates of the excitation densities obtained in the preceding sections according to which the CL efficiency decreases sharply under excitation by protons (1 MeV, Fig. 3) and nanosecond electron-beam pulses (250 keV) at current densities above 90 A cm^{-2} (Fig. 6), one can estimate the number of the *e–h* pairs produced in 1 cm^3 under these conditions. Electrons with an average energy of 250 keV lose their energy in a CsCl crystal over a layer of thickness ~250 μm. For a current of 130 A cm^{-2}, the energy transferred to the crystal during the pulse duration (3×10^{-9} s) is 2.6×10^{19} eV cm^{-3}. Accepting the rough assumption, based on the rich experience in the investigation of alkali halide crystals that the energy required to create one anion electron-hole pair, does not exceed $2E_g$ on average, it can be concluded that one electron-beam pulse with a current density of 130 A cm^{-2} produces not less than 1.4×10^{18} anion electron-hole pairs in 1 cm^3 of CsCl. Because the energy expended to create one cation hole in CsCl is not less than 14 eV, one electron-beam pulse (130 A cm^{-2}) will produce not more than 2×10^{18} cation holes in 1 cm^3 of CsCl. On the other hand, an analysis of characteristic losses in CsCl crystals [36] suggests that the number of cation *e–h* pairs created by electrons close in energy to the δ electrons as well as by bombardment with 1 MeV protons is two to three times smaller than that of the anion *e–h* pairs.

For a volume ionization density of about 10^{18} cm^{-3} of Cs^+ ions in CsCl, conduction electrons recombine with cation holes to form cation excitons in a time $\tau_R \ll 1$ ns. Note that self-trapping of a part of the cation holes [25, 26] significantly increases the effective recombination cross section of conduction electrons with fixed cation holes and undoubtedly facilitates recombination-assisted creation of cation excitons. As regards the time of radiative recombination with the cation holes of electrons bound to the anions adjacent to the hole, it is substantially longer. For CsCl, the cross-luminescence time is 1.2 ns, and for CsF it is even 4 ns [12]. Thus, the processes of recombination-assisted creation of cation excitons taking place at high volume ionization densities induced in CsCl by protons, α particles, nitrogen ions, and heavy-current ns-long electron-beam pulses, which were not considered earlier, are capable of competing with cross-luminescence. Cross-luminescence is not excited even in the direct optical creation of cation excitons. The energy of the cation excitons is spent for creating anion excitations. In our opinion, recombination-assisted creation of cation excitons at high excitation densities is a major (if not the primary) reason for the selective response of the cross-luminescence to irra-

diation of CsCl by photons, as well as by low-current electron beams, on the one hand, and by protons, neutrons, α particles, and ions, on the other.

In conclusion, we note that the recombination-assisted creation of excitons in recombination of electrons and holes under heavy-current irradiation by nanosecond electron pulses was also observed recently in Al_2O_3 crystals, where recombination luminescence of self-trapped excitons (7.6 eV) is found to occur in the absence of self-trapping of electrons and hole effects in a crystal [35, 37].

ACKNOWLEDGMENT

Support of the Estonian Science Foundation (grants nos. 3867 and 3868) and Ministry of Science of the Russian Federation for financing the 120 cm cyclotron of Ural State Technical University (regn. no. 06-02), is gratefully acknowledged.

REFERENCES

1. Ch. B. Lushchic, in *Excitons*, Ed. by E. I. Rashba and M. D. Sturge (North-Holland, Amsterdam, 1982), Chap. 12.
2. K. S. Song and R. T. Williams, *Self-Trapped Excitons* (Springer-Verlag, Berlin, 1993).
3. D. I. Vaĭsburd and B. N. Semin, Izv. Ross. Akad. Nauk, Ser. Fiz. **37** (2), 103 (1992).
4. Ch. B. Lushchik, A. Ch. Lushchik, E. A. Vasil'chenko, and F. A. Savikhin, Fiz. Tverd. Tela (St. Petersburg) **37** (2), 525 (1995) [Phys. Solid State **37** (2), 284 (1995)].
5. A. L. Maĭste, A. A. Saar, and M. A. Élango, Fiz. Tverd. Tela (Leningrad) **16** (6), 1720 (1974) [Sov. Phys. Solid State **16** (6), 1118 (1974)].
6. Yu. M. Aleksandrov, V. N. Makhov, P. A. Rodnyĭ, *et al.*, Fiz. Tverd. Tela (Leningrad) **26** (9), 2865 (1984) [Sov. Phys. Solid State **26** (9), 1734 (1984)].
7. Yu. M. Aleksandrov, I. L. Kuusmann, P. Kh. Liblik, *et al.*, Fiz. Tverd. Tela (Leningrad) **29** (4), 1026 (1987) [Sov. Phys. Solid State **29** (4), 587 (1987)].
8. V. N. Makhov, Nucl. Instrum. Methods Phys. Res. A **308**, 187 (1991).
9. I. Kuusmann, T. Kloiber, W. Laasch, and G. Zimmerer, Radiat. Eff. Defects Solids **119–121**, 21 (1991).
10. P. A. Rodnyĭ, Fiz. Tverd. Tela (St. Petersburg) **34** (7), 1975 (1992) [Sov. Phys. Solid State **34** (7), 1053 (1992)].
11. V. Makhov, J. Becker, L. Frankenstein, *et al.*, Radiat. Eff. Defects Solids **135**, 349 (1995).
12. M. Kamada and N. Ohno, J. Phys. Soc. Jpn. **66**, 2502 (1997).
13. S. Kubota, N. Kanai, and J. Ruan, Phys. Status Solidi B **139** (2), 635 (1987).
14. C. W. E. van Eijk, Nucl. Instrum. Methods Phys. Res. A **392**, 285 (1997).
15. C. M. Combes, P. Dorenbos, R. W. Hollander, and C. W. E. van Eijk, Nucl. Instrum. Methods Phys. Res. A **416**, 364 (1998).
16. É. R. Il'mas, R. A. Kink, G. G. Liĭd'ya, and Ch. B. Lushchik, Tr. Inst. Fiz. Akad. Nauk Ést. SSR **23**, 221 (1963); Izv. Akad. Nauk SSSR, Ser. Fiz. **29** (1), 28 (1965).
17. N. E. Lushchik and E. A. Vasil'chenko, Tr. Inst. Fiz. Ést. SSR **35**, 150 (1969).
18. V. Saile and M. Skibowski, Phys. Status Solidi B **50**, 661 (1972).
19. K. U. Ibragimov, A. Ch. Lushchik, Ch. B. Lushchik, *et al.*, Fiz. Tverd. Tela (St. Petersburg) **34** (11), 3421 (1992) [Sov. Phys. Solid State **34** (11), 1831 (1992)].
20. M. Itoh, K. Tanimura, and N. Itoh, J. Phys. Soc. Jpn. **62**, 2904 (1993).
21. K. U. Ibragimov and F. A. Savikhin, Fiz. Tverd. Tela (St. Petersburg) **35** (6), 1474 (1993) [Phys. Solid State **35** (6), 744 (1993)].
22. Y. M. Aleksandrov, V. N. Makhov, T. T. Syreischikova, and M. N. Yakimenko, Nucl. Instrum. Methods Phys. Res. A **261**, 153 (1987).
23. A. Lushchik, E. Feldbach, A. Frorip, *et al.*, J. Phys.: Condens. Matter **6**, 2357 (1994).
24. A. Lushchik, E. Feldbach, A. Frorip, *et al.*, J. Lumin. **63**, 273 (1995).
25. V. N. Makhov, M. A. Terekhin, I. H. Munro, *et al.*, J. Lumin. **72-74**, 114 (1997).
26. V. N. Makhov, L. Kuusmann, J. Becker, *et al.*, J. Electron. Spectrosc. Relat. Phenom. **101–103**, 817 (1999).
27. M. Itoh, Y. Bokumoto, and H. Yoshida, J. Phys. Soc. Jpn. **68** (5), 1731 (1999).
28. A. V. Kruzhalov, V. Yu. Ivanov, F. G. Neshov, *et al.*, in *Proceedings of the International Conference on Radiation Physics of Solids State, 1998*, p. 180.
29. D. Pooley and W. A. Runciman, J. Phys. C: Solid State Phys. **3**, 1815 (1970).
30. M. Kamada, Y. Fujii, and K. Fukui, in *Proceedings of the 10th International Conference VLV Radiation Physics*, Paris, 1992.
31. M. Moszynski, C. Gresset, J. Vacker, and R. Ordy, Nucl. Instrum. Methods **179** (2), 271 (1981).
32. D. I. Vaĭsburd, A. A. Vorob'ev, and L. A. Melikyan, At. Énerg. **30** (6), 538 (1971).
33. Ch. B. Lushchik and T. A. Soovik, Tr. Inst. Fiz. Akad. Nauk Ést. SSR **34**, 68 (1966).
34. I. Jaek, F. Savikhin, and H. Kaambre, in *Proceedings of the 4th International Conference on Solid State Dosimetry, Krakow, 1974*, p. 565.
35. Ch. Lushchik and F. Savikhin, in *Solid State Detectors of Ionizing Radiation*, Ed. by V. S. Kortov, B. N. Shulgin, and A. J. Kuznetsov (Ural. Techn. Univ., Yekaterinburg, 1998), p. 13.
36. M. Kreuzburg, Z. Phys. **196**, 433 (1966).
37. M. Kirm, G. Zimmerer, A. Lushchik, *et al.*, Phys. Rev. B **60** (1), 502 (1999).

Translated by G. Skrebtsov

Physics of the Solid State, Vol. 42, No. 6, 2000, pp. 1058–1065. Translated from Fizika Tverdogo Tela, Vol. 42, No. 6, 2000, pp. 1026–1033.

DEFECTS, DISLOCATIONS, AND PHYSICS OF STRENGTH

Nonlinear Multimode Dynamics of the Formation of Deformation Defect Mesostructures in Crystals under Radiation

V. I. Emelyanov and I. M. Panin

Moscow State University, Vorob'evy gory, Moscow, 119899 Russia

Received in final form December 15, 1999

Abstract—Two-stage dynamics of the self-organization of three-dimensional cluster- and periodic deformation defect mesostructures in cubic crystals under radiation is considered and the criteria of mesostructure self-organization are formulated. © *2000 MAIK "Nauka/Interperiodica".*

1. INTRODUCTION

In [1, 2], the theory of the formation of a stationary one-dimensional deformation defect (DD) mesostructure hierarchy in crystals under irradiation with energetic beams was developed. The Landau functional of DD-system free energy was obtained. Its minimization leads to a nonlinear equation for a spatially nonhomogeneous order parameter of a phase transition, which proceeds as a self-consistent longitudinal deformation of a cubic crystal along a direction of the [100] type. It was shown that, when the control parameter, which is the spatially homogeneous defect concentration n_{d0}, becomes higher than certain threshold values, first stationary localized DD mesostructures (nanoclusters) and then periodic mesostructures are formed.

This paper is concerned with the dynamics of the formation of three-dimensional DD mesostructures in cubic crystals. A set of three-dimensional kinetic equations for the Fourier amplitudes of self-consistent deformation is derived, including elastic anisotropy of the cubic crystal, nonlocal interactions of lattice atoms between each other (with an interaction length l_0) and with lattice defects (with an interaction length l_d, such that $l_d > l_0$ [2]), and lattice anharmonicity. This set of equations describes the dynamics of coupled unstable DD modes, which is characterized by two stages.

The first stage is related to the collapse of the angular spectrum of DD modes of wave vectors $\mathbf{q}$ ($|\mathbf{q}| \equiv q$ = const). This results in the formation of three independent continua of DD modes with wave vectors $\mathbf{q}$ that are oriented along the three axes of the [100] type.

Interaction between modes in each independent continuum determines the dynamics at the second stage of DD self-organization; when n_{d0} exceeds certain threshold values, the q-mode spectrum either broadens and localized DD mesostructures (clusters) are formed, or the q-mode spectrum degenerates into a δ function, which leads to the formation of periodic DD mesostructures.

The transformation of the DD-mode distributions in the q-space occurs independently in each of the three continua of self-consistent longitudinal deformation modes along the three axes of the [100] type. Superposing the resultant ordered one-dimensional DD structures produces three-dimensional stationary cluster or periodic DD mesostructures.

In this paper, it is shown that the problem of description of three-dimensional stationary DD mesostructures in cubic crystals can be reduced to a one-dimensional problem, which was solved in [1, 2]. Studying the dynamics of the formation of DD mesostructures, we formulate criteria of the self-organization of cluster and periodic DD mesostructures.

The preliminary results of this work were reported in [3].

2. KINETIC EQUATIONS FOR THE FOURIER AMPLITUDES OF A SELF-CONSISTENT DEFORMATION IN AN EFFECTIVE DD-MODE PAIRWISE-INTERACTION APPROXIMATION

The deformation and the concentration of defects in a three-dimensional cubic crystal, which are of interest to us, may be thought of as coupled angular packets of quasi-longitudinal waves, being characterized by wave vectors $\mathbf{q}$ located in the neighborhood of one of the directions of the [100] type (which coincides with the z axis)

$$\xi(\mathbf{r}) = \xi_0 + \xi_1(\mathbf{r}), \quad \xi_1(\mathbf{r}) = \sum_{\mathbf{q}} \xi_{\mathbf{q}} e^{i\mathbf{qr}}, \qquad (1a)$$

$$n_d(\mathbf{r}) = n_{d0} + n_{d1}(\mathbf{r}), \quad n_{d1}(\mathbf{r}) = \sum_{\mathbf{q}} n_{\mathbf{q}} e^{i\mathbf{qr}}, \qquad (1b)$$

where n_{d0} and ξ_0 are spatially homogeneous parts of the defect concentration and medium deformation, respectively, while $n_{d1}(\mathbf{r})$ and $\xi_1(\mathbf{r})$ are nonhomogeneous ones.

1063-7834/00/4206-1058$20.00

Under the condition that $\xi(\mathbf{r}, t) \approx \partial U_z(r, t)/\partial z$, the equation for the cubic crystal deformation, which follows from equations for the x, y, and z components (U_x, U_y, U_z) of the medium-displacement vector [4], takes the form

$$\rho\partial^2\xi/\partial t^2 = c_{11}\Delta\xi + Ac_{11}(\Delta\xi - \partial^2\xi/\partial z^2), \quad (2)$$

where ρ is the medium density; $A = (c_{12} + 2c_{44} - c_{11})/c_{11}$ is the elastic anisotropy constant; and c_{12}, c_{44}, c_{11} are the elastic stiffness constants of the cubic crystal.

Now, in (2), in the same manner as in the one-dimensional case [2], let us take into account the nonlocal lattice atom interaction, anharmonicity, and the interaction between deformation and defects.

Using (1a), we obtain the following equation for Fourier amplitudes of quasi-longitudinal deformation:

$$\begin{aligned}\frac{\partial^2\xi_{\mathbf{q}}}{\partial t^2} &= -q^2c_l^2(\theta)(1 - q^2l_0^2)\xi_{\mathbf{q}} \\ &+ |\alpha|q^2c_l^2(\theta)\sum_{\mathbf{q}_1}\xi_{\mathbf{q}_1}\xi_{\mathbf{q}-\mathbf{q}_1} \\ &- \beta q^2c_l^2(\theta)\sum_{\mathbf{q}_1,\mathbf{q}_2}\xi_{\mathbf{q}_1}\xi_{\mathbf{q}_2}\xi_{\mathbf{q}-\mathbf{q}_1-\mathbf{q}_2} + \frac{\theta_d}{\rho}q^2n_{\mathbf{q}}.\end{aligned} \quad (3)$$

Here, $\alpha < 0$ and $\beta > 0$ are the elastic anharmonism constants;

$$c_l^2(\theta) = c_{l0}^2(1 + A\theta^2), \quad (4)$$

where $\cos\theta = \mathbf{qz}/|\mathbf{q}|$, $\mathbf{z}$ is the unit vector along the z axis, $c_{l0}^2 = c_{11}/\rho$ is the velocity of longitudinal sound in the direction [100], θ_d is the potential of the deformation defect ($d = i$ for an interstitial atom and $d = v$ for a vacancy).

To close equation (3), let us derive the equation for $n_{\mathbf{q}}$. Taking into account a deformation-induced flow of defects in the continuity equation, we obtain the equation of defect diffusion that includes nonlocality of the defect–atom interaction (cf. [2])

$$\begin{aligned}\partial n_d/\partial t &= D_d\Delta n_d \\ &- (D_d\theta_d/k_BT)\nabla n_d\nabla(\xi + l_d^2\Delta\xi),\end{aligned} \quad (5)$$

where D_d is the diffusivity of defects of d type and T is temperature. Substituting (1) into (5), we obtain the desired equation for the Fourier amplitude of the defect concentration

$$\begin{aligned}\frac{\partial n_{\mathbf{q}}}{\partial t} &= -D_dq^2n_{\mathbf{q}} + \frac{D_d\theta_d}{k_BT} \\ &\times\sum_{\mathbf{q}_1}n_{\mathbf{q}_1}\xi_{\mathbf{q}-\mathbf{q}_1}\mathbf{q}(\mathbf{q}-\mathbf{q}_1)(1 - l_d^2(\mathbf{q}-\mathbf{q}_1)^2).\end{aligned} \quad (6)$$

Equations (3) and (6) constitute a closed set of equations for the Fourier amplitudes of the deformation $\xi_{\mathbf{q}}$ and concentration $n_{\mathbf{q}}$.

Substituting in (6) the expression for $n_{\mathbf{q}}$ that follows from (3) in the adiabatic approximation, after some mathematical manipulation, we obtain a kinetic equation for the Fourier amplitude of the self-consistent deformation. In the DD-mode pairwise-interaction approximation, this equation takes the form

$$\begin{aligned}\frac{\partial\xi_{\mathbf{q}}}{\partial t} &= \lambda_q(\theta)\xi_{\mathbf{q}} + \frac{D_dq^2}{1 - l_0^2q^2} \\ &\times\sum_{\mathbf{q}_1\neq 0}\xi_{\mathbf{q}_1}\xi_{\mathbf{q}-\mathbf{q}_1}\left\{|\alpha| - 3\beta\xi_0 + \frac{\theta_d}{k_BT}(1 - l_d^2q^2)\left(1 - \frac{\mathbf{qq}_1}{q^2}\right)\right\}\end{aligned} \quad (7)$$

Since nonequilibrium defects in a crystal under radiation are formed in pairs of vacancies ($\theta_d = \theta_v < 0$) and interstitials ($\theta_d = \theta_i > 0$) with $|\theta_i| \gg |\theta_d|$ [5], we have $\xi_0 = \theta_i n_{d0}/\rho c_{l0}^2 > 0$ in (7).

The growth rate of DD modes in (7) is

$$\lambda_q(\theta) = D_dq^2\left(\frac{1 - l_d^2q^2}{1 - l_0^2q^2}\frac{\theta_d^2n_{d0}}{\rho c_l^2(\theta)k_BT} - 1\right) \approx \lambda_m - \delta_a\theta^2, \quad (8)$$

where λ_m is the maximal value of the growth rate,

$$\lambda_m = D_dq^2\left(\frac{n_{d0}}{n_{dc}}\left(\frac{1 - l_d^2q^2}{1 - l_0^2q^2}\right) - 1\right) \quad (9)$$

and λ_a is the steepness of the $\lambda_q(\theta)$ curve at the point $\theta = 0$,

$$\delta_a = \frac{1}{2}\partial^2\lambda(\theta)/\partial\theta^2 = D_dq^2A\frac{n_{d0}}{n_{dc}}\left(\frac{1 - l_d^2q^2}{1 - l_0^2q^2}\right). \quad (10)$$

In (9), the critical defect concentration $n_{dc} = \rho c_{l0}^2 k_BT/\theta_d^2$ is introduced.

Let us now consider the first stage of the DD self-organization.

3. ASCENDING ANGULAR DIFFUSION IN THE VECTOR **q** SPACE AND COLLAPSE OF THE DD-MODE ANGULAR SPECTRUM

As it is evident from (7), owing to the mode–mode interaction, the harmonic $\xi_{\mathbf{q}-\mathbf{q}_1}$ transforms into the harmonic $\xi_{\mathbf{q}_1}$. In this process, both the direction and magnitude of the initial vector $\mathbf{q} - \mathbf{q}_1$ are changed.

Let us consider the first stage of this process, when $|\mathbf{q} - \mathbf{q}_1| = |\mathbf{q}| = \text{const}$. At this stage, the ends of the Fourier-harmonics wave vectors are located on the sphere $|\mathbf{q}| = \text{const}$ in the $\mathbf{q}$ space. Furthermore, we will limit

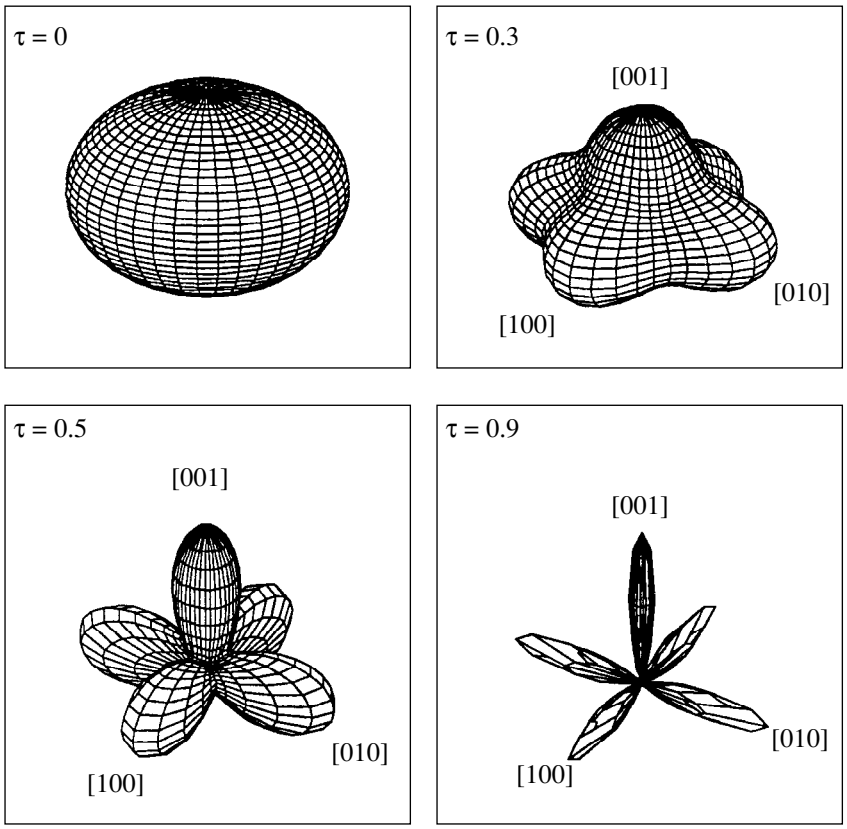

Fig. 1 Collapse of DD-mode angular spectrum. Polar diagram of the relative Fourier amplitude $\xi_q(\theta, \tau)/\xi_q(\theta, \tau = 0) = \exp[\Lambda\tau - (\tau\Delta\theta^2/(1-\tau^2))]/\sqrt{1-\tau^2}$ versus an angle θ, where θ is the angle between the vector **q** and the [001] direction. According to (16), at $\tau = t/t_q$, we have $\Lambda = \lambda_m t_q = 0.2$ and $\Delta = \delta_a t_q = 5$ (the second peak along the [001] direction is not shown). The similar collapses also take place along the directions [100], [010].

our consideration to small jumps of $\mathbf{q} - \mathbf{q}_1$ vectors in the meridional direction ϕ = const, when only the polar angle θ is changed in the neighborhood of one direction of the [100] type, for which θ = 0. This consideration is also true for the other directions of the [100] type.

Expanding $\xi_{\mathbf{q}-\mathbf{q}_1}$ in a series in $\mathbf{q}_1$ ($q_1 \ll q$) in spherical coordinates to within the terms of the second order and assuming ϕ = const, we obtain from (7) the equation of diffusion and drift including the DD-mode amplitude growth in the θ space. If the angular drift is ignored, the equation of angular diffusion takes the form

$$\frac{\partial \xi_{\mathbf{q}}(\theta, t)}{\partial t} = \lambda_{\mathbf{q}}(\theta)\xi_{\mathbf{q}}(\theta, t) + D_{\mathbf{q}}\frac{\partial^2 \xi_{\mathbf{q}}(\theta, t)}{\partial \theta^2}, \qquad (11)$$

where the angular diffusion constant in the **q** space is

$$D_{\mathbf{q}} = \frac{9}{2}\frac{D_d}{1 - l_0^2 q^2} \times \left\{(|\alpha| - 3\beta\xi_0) + \frac{\theta_d}{k_B T}(1 - l_d^2 q^2)\right\}\sum_{\mathbf{q}_1 \neq 0}\xi_{\mathbf{q}_1}\mathbf{q}_1^2, \qquad (11a)$$

and the growth rate $\lambda_{\mathbf{q}}(\theta)$ is given by (8).

Studying the angular DD self-organization, we will suppose that the long-wave spectrum components ($|\mathbf{q}_1| \ll |\mathbf{q}|$) in (11a) are given ($\xi_{\mathbf{q}_1} \approx$ const) and that $\xi_{\mathbf{q}_1} > 0$ (which corresponds to the self-consistent deformation induced by interstitials).

The angular DD-spectrum self-organization (degeneration) occurs at $\lambda_{\mathbf{q}}(\theta) > 0$, $D_{\mathbf{q}} < 0$ (see below). Let us consider the conditions where this is the case.

As was shown in [2], there is the following hierarchy of DD mesostructures, which are formed as the defect concentration n_{d0} increases: first DD clusters and then periodic DD mesostructures appear. These two types of DD structure occupy different regions in **q** space.

For clusters, in the vicinity of the formation threshold (see [2]), the following condition is fulfilled:

$$l_d^2 q^2 \gg 1, \quad l_0^2 q^2 \gg 1. \qquad (12)$$

In the cluster region of **q** space (12), the maximal growth rate (9) becomes positive at $n_{d0} > n_{dc1} =$

$n_{dc} l_0^2 / l_d^2 < n_{dc}$. It was shown in [2] that $n_{d0} = n_{dc1}$ is the threshold value for the formation of stationary three-dimensional cluster DD mesostructures.

From (11a) and (10), we obtain the following expressions for the angular-diffusion coefficient and steepness in the cluster region (12):

$$D_{\mathbf{q}} = 9 D_d \theta_d l_d^2 \sum_{\mathbf{q}_1 \neq 0} \xi_{\mathbf{q}_1} q_1^2 / 2 k_B T l_0^2 < 0 \quad \text{at} \quad \theta_d < 0, \tag{13a}$$

$$\delta_a = D_d q^2 A \frac{n_{d0}}{n_{dc}} \frac{l_d^2}{l_0^2}. \tag{13b}$$

Thus, at $\theta_d = \theta_v < 0$ (for vacancies), the equation of the angular diffusion (11) describes the transformation (degeneration) of the starting uniform distribution of the vector $\mathbf{q}$ over a sphere $|\mathbf{q}| = \text{const}$ into a cone around the z axis (see (16) and Fig. 1). For interstitials ($\theta_d = \theta_i > 0$), we have $D_d > 0$ in the cluster region, i.e., there is no angular spectrum self-organization.

For periodical structures near their generation threshold, the condition

$$l_d^2 q^2 \ll 1, \quad l_0^2 q^2 \ll 1 \tag{14}$$

is fulfilled (see [2]).

From (9), we obtain that the maximum growth rate $\lambda_m = D_d q^2 (n_{d0}/n_{dc} - 1) > 0$ at $n_{d0} > n_{dc}$. In [2], it was shown that the value $n_{d0} = n_{dc}$ is the threshold for the formation of one-dimensional stationary periodic DD mesostructures.

In the region of the formation of periodic structures (14), in the case of interstitials ($\theta_d > 0$), from (11a) and (10) at $n_{d0} > n_{dc}$, the angular-diffusion coefficient and the steepness parameter are found to be

$$D_{\mathbf{q}} = -27 \beta D_d k_B T n_{d0} \times \sum_{\mathbf{q}_1 \neq 0} \xi_{\mathbf{q}_1} q_1^2 / 2 \theta_d n_{dc} \equiv -|D_{\mathbf{q}}| < 0, \tag{15a}$$

$$\delta_a = D_d q^2 A n_{d0} / n_{dc}. \tag{15b}$$

At $\lambda_m > 0$ and $D_{\mathbf{q}} \equiv -|D_{\mathbf{q}}| < 0$, the solution of (11) has the form:

$$\xi_{\mathbf{q}}(\theta, t) = \xi_{\mathbf{q}}(\theta, t = 0) \exp(\lambda_m t) \times \exp\{-\theta^2 / (\delta_a t)^{-1} - 4|D_q| t\} / \sqrt{1 - 4|D_{\mathbf{q}}| \delta_a t^2}, \tag{16}$$

where $\xi_{\mathbf{q}}(\theta, t = 0) = \text{const}$ is the initial value of the deformation Fourier amplitude, which corresponds to the initial uniform $\mathbf{q}$-vector distribution over the angle θ range in the wave packet (1). The expressions for δ_a and $|D_{\mathbf{q}}|$ for the cluster region (12) are given by formulas (13), while for the periodic region (14), they are given by (15). The validity of solution (16) may be verified by immediate substitution into (11).

Formula (16) describes the dynamics of narrowing and collapse of the initially uniform angular DD-mode spectrum with time-increased amplitudes at a fixed value of $|\mathbf{q}| = q$. In this case, the defects that take part in the self-organization in the angular spectrum are vacancies in the region of cluster structures (12) ($\theta_d < 0$), while in the region of periodic structures (14) ($\theta_d > 0$), they are interstitials.

By the instant $t = t_\theta(q)$, the spectrum collapses to the δ function

$$\xi_{\mathbf{q}}(\theta, t = t_{\mathbf{q}}) = \xi_{\mathbf{q}}(\theta, t = 0) \times \exp(\lambda_m t_\theta(q)) (\pi^2 \delta_a / 4|D_q|)^{1/4} \delta(\theta), \tag{17}$$

where the time it takes for the angular collapse to occur

$$t_\theta(q) = 1 / \sqrt{4|D_{\mathbf{q}}| \delta_a} \tag{18}$$

depends on q.

The similar collapse of cones of angular distribution q also takes place for two other axes of the [100] type (Fig. 1).

For periodic interstitial DD mesostructures, we have $q = 2\pi/d$, where d is the period of the structure (see [2]). Thus, from (18), we obtain the characteristic collapse time for the angular spectrum of interstitial-deformation modes (ID modes) to be

$$\tau_\theta \equiv t_\theta(q = 2\pi/d) = \frac{d^2}{D_d} \frac{n_{dc}}{n_{d0}} C,$$
$$C = (12\pi^2)^{-1} \left(6 \frac{k_B T}{\theta_d} \beta A \sum_{q_1 \neq 0} \xi_{q_1} (q_1/q)^2 \right)^{-1/2}. \tag{19}$$

Due to the angular DD-mode self-organization, three independent continua of ID modes appear, which are characterized by vectors $\mathbf{q}$ oriented along one of the three orthogonal directions of the [100] type.

4. DIFFUSION IN THE ONE-DIMENSIONAL $\mathbf{q}$ SPACE AND THE TRANSFORMATION OF THE SPATIAL DD-MODE SPECTRUM

4.1. Equations for Amplitudes and Phases of Fourier Harmonics

Now, let us consider the second stage of the DD-mode self-organization, when, due to mode–mode interaction, the transformation of $\xi_{\mathbf{q}-\mathbf{q}_1}$ harmonics into the $\xi_{\mathbf{q}}$ harmonic takes place.

Let us consider the continuum of $\xi_{\mathbf{q}}$ modes with wave vector $\mathbf{q}$ oriented along one of the [100]-type directions in a cubic crystal (e.g., along the z axis), for which $\xi_{\mathbf{q}} = \xi_{q_z} \equiv \xi_q$ ($-\infty < q < +\infty$). Our consideration is also true for the other directions of the [100] type.

The kinetic equation for $\xi_{\mathbf{q}}$ follows from (7) at $|\mathbf{q}| = q$, $|q_1| = q_1$, $\mathbf{q} \uparrow\uparrow \mathbf{q}_1$:

$$\frac{\partial \xi_q}{\partial t} = \lambda(q)\xi_q + \frac{D_d q^2}{1 - l_0^2 q^2} \times \sum_{q_1 \neq 0} \xi_{q_1}\xi_{q-q_1}\left\{|\alpha| - 3\beta\xi_0 + \frac{\theta_d}{k_B T}(1 - l_d^2 q^2)\left(1 - \frac{q_1}{q}\right)\right\}, \quad (20)$$

where the growth rate is given by

$$\lambda(q) = D_d q^2[(1 - l_d^2 q^2)n_{d0}/(1 - l_0^2 q^2)n_{dc} - 1]. \quad (21)$$

Let us represent the complex Fourier amplitude in the form

$$\xi_q = A_q \exp(i\varphi_q), \quad (22)$$

where A_q and φ_q are the real amplitude and phase, respectively. Substituting (22) in (20) and separating the real and imaginary parts, we obtain a set of coupled kinetic equations for the real amplitudes A_q and phases φ_q

$$\frac{\partial A_q}{\partial t} = \lambda(q)A_q + \frac{D_d q^2}{1 - l_0^2 q^2}\sum_{q_1 \neq 0} A_{q_1}A_{q-q_1} \times\left\{|\alpha| - 3\beta\xi_0 + \frac{\theta_d}{k_B T}(1 - l_d^2 q^2)\left(1 - \frac{q_1}{q}\right)\right\}\cos(\Delta\varphi(q, q_1)), \quad (23)$$

$$\frac{\partial \varphi_q}{\partial t} = \frac{D_d q^2}{1 - l_0^2 q^2}\sum_{q_1 \neq 0}\frac{A_{q_1}A_{q-q_1}}{A_q}\left\{|\alpha| - 3\beta\xi_0 + \frac{\theta_d}{k_B T}(1 - l_d^2 q^2)\left(1 - \frac{q_1}{q}\right)\right\}\sin(\Delta\varphi(q, q_1)), \quad (24)$$

where $\Delta\varphi(q, q_1) = \varphi_{q_1} + \varphi_{q-q_1} - \varphi_q$.

Let us simplify this set of equations. As before, we assume that there is a set of long-wave harmonics with wave vectors $q_1 \ll q_m$ (where q_m is the characteristic wave number of the DD mesostructure), which we may consider as given and also put $\varphi_{q_1} = 0$. Moreover, let us take into account that, as it will become evident later, during a characteristic time τ_{phase}, which is substantially shorter than the characteristic time interval of amplitude-A_q spectrum change, the phase locking takes place: $\varphi_{q_1} = \varphi_q$ (see (28)). Therefore, at $t > \tau_{\text{phase}}$, putting $\cos(\Delta\varphi(q, q_1)) = 1$, we obtain from (23) the kinetic equation for A_q. Expanding A_{q-q_1} in powers of q_1 up to the second–power term in this equation, we obtain a diffusion equation for the amplitudes of Fourier harmonics $A_q = A(q, t)$, which describes the amplification and drift in $\mathbf{q}$ space

$$\frac{\partial A(q, t)}{\partial t} = \lambda(q)A(q, t) + K(q)\frac{\partial A(q, t)}{\partial q} + D(q)\frac{\partial^2 A(q, t)}{\partial q^2}, \quad (25)$$

where $\lambda(q)$ is given by (21) and the following notation has been introduced: the drift coefficient

$$K(q) = D_d q((1 - l_d^2 q^2)/(1 - l_0^2 q^2)) \times (\theta_d/k_B T)\sum_{q_1 \neq 0} A_q q_1^2 \quad (26a)$$

and the diffusion coefficient in $\mathbf{q}$ space

$$D(q) = \frac{1}{2}\frac{D_d q^2}{1 - l_0^2 q^2} \times\left\{|\alpha| - 3\beta\xi_0 + \frac{\theta_d}{k_B T}(1 - l_d^2 q^2)\right\}\sum_{q_1 \neq 0} A_{q_1} q_1^2. \quad (26b)$$

From (24), using approximations $\varphi_{q_1} = 0$, $A_{q-q_1} \cong A_q$, and $\sin(\varphi_{q-q_1} - \varphi_q) \approx \varphi_{q-q_1} - \varphi_q$, we obtain the kinetic equation for φ_q

$$\frac{\partial \varphi_q}{\partial t} = \frac{D_d q^2}{1 - l_0^2 q^2}\sum_{q_1 \neq 0} A_{q_1}\left\{|\alpha| - 3\beta\xi_0 + \frac{\theta_d}{k_B T}(1 - l_d^2 q^2)\left(1 - \frac{q_1}{q}\right)\right\}(\varphi_{q-q_1} - \varphi_q). \quad (27)$$

Later, on the basis of (25) and (27), we will study the DD self-organization dynamics for each of two regions in $\mathbf{q}$ space, where cluster and periodic DD mesostructures are formed.

4.2. Phase Locking and DD-Mode Spectrum Broadening: Cluster Formation

In the short-wave (cluster) region (12), from (27), we obtain the relaxation equation for φ_q

$$\frac{\partial \varphi_q}{\partial t} = D_d q^2 \frac{\theta_d}{k_B T}\frac{l_d^2}{l_0^2}\sum_{q_1 \neq 0} A_{q_1}(\varphi_{q-q_1} - \varphi_q). \quad (28)$$

As it follows from (28), the relaxation process of phase φ_q is accomplished ($\partial\varphi_q/\partial t = 0$) when harmonics phases become equal: $\varphi_q = \varphi_{q-q_1}$. This occurs for the phase locking time τ_{phase}, which may be derived from (28):

$$\tau_{\text{phase}} = \left(D_d \frac{\theta_d}{k_B T}\frac{l_d^2}{l_0^2}\sum_{q_1 \neq 0} A_{q_1}\right)^{-1}. \quad (29)$$

From (21), under condition (12), we obtain for the growth rate the expression

$$\lambda(q) = D_d q^2 (n_{d0} l_d^2 / n_{dc} l_0^2 - 1) \equiv D_d q^2 (n_{d0}/n_{dc1} - 1). \quad (30)$$

From (30), it is evident that $\lambda(q) > 0$ at $n_{d0} > n_{dc1} = l_0^2/l_d^2 n_{dc}$, i.e., all harmonics ξ_q are growing. In [2], it was shown that in the region $n_{d0} > n_{dc1}$, stationary cluster DD mesostructures are formed.

From (26b), we obtain for the diffusion coefficient in the cluster region (12)

$$D(q) = \frac{1}{2} D_d q^2 \frac{l_d^2}{l_0^2} \frac{\theta_d}{k_B T} \sum_{q_1 \neq 0} q_1^2 A_{q_1}. \quad (31)$$

As it follows from Section 3, the self-organization in the angular range in the cluster region leads to the collapse of the angular spectrum of the vacancy-deformation (VD) modes into the directions of the [100] type. Thus, in this case, the defects that are responsible for the self-organization in $|\mathbf{q}|$ space of DD modes with wave vectors along these directions are vacancies. For this reason, we assume that $A_{q_1} \approx \text{const}$ and $A_{q_1} < 0$ in (29) and (31) (which corresponds to self-consistent deformation produced by vacancies). Taking into account that $\theta_d = \theta_v < 0$ for vacancies, we obtain from (31) that, in the cluster region, $D(q) > 0$. (Moreover, on the basis of (26a), it can be shown that $K(q) > 0$ here). With a positive growth rate (30), drift coefficient (26a), and diffusivity (31), diffusion equation (25) describes both the growth (during the time λ^{-1}) and broadening of the spectrum of Fourier components ξ_q with locked phases φ_q. Let us estimate the characteristic times for these processes.

We will determine the characteristic time of the spectrum broadening by formula

$$\tau_b = q_0^2 / D(q), \quad (32)$$

where $q_0 = l_{\min}^{-1}$, $l_{\min}$ is the minimal cluster size. Using (30) and (31), we obtain that, at least near the threshold of the formation of localized structures, the following inequality is fulfilled:

$$\tau_b(q)/\lambda^{-1}(q) = 2(n_{d0}/n_{dc1} - 1)/(\theta_d/k_B T) \times (l_d/l_0)^2 \sum_{q_1 \neq 0} q_1^2/q_0^2 A_{q_1} < 1. \quad (33)$$

Thus, before the amplitudes grow enough, the diffusion spreading of the amplitude spectrum occurs and causes the amplitudes A_q to level off. In this process, the phases of harmonics ξ_q remain locked, because it follows from (29) and (32) that

$$\tau_{\text{phase}}/\tau_b = \sum_{q_1 \neq 0} A_{q_1} (q_1/q_0)^2 / 2 \sum_{q_1 \neq 0} A_{q_1} \ll 1, \quad (34)$$

since $q_1 \ll q_0$.

From (33) and (34), we obtain the following hierarchy of the characteristic times of the DD self-organization in short-wave region (12):

$$\tau_{\text{phase}} \ll \tau_b < \lambda^{-1}(q). \quad (35)$$

Thus, in the short-wave region, growth of ξ_q harmonics occurs, they have the same phases and leveled-off amplitudes due to spectral diffusion. The formation of a planar spectrum of harmonics with locked phases corresponds to the formation of localized (cluster) DD mesostructures. The stationary characteristics of a one-dimensional DD cluster were determined in [2]. Three-dimensional DD clusters are built up by the superposition of one-dimensional ones.

4.3. Collapse of q Spectrum of DD Modes: The Formation of Periodic Mesostructures

To describe the formation of periodic DD structures in the long-wave region (14), it is enough to consider the dynamics of the Fourier amplitude ξ_q. The corresponding equation can be derived from (20) in the same manner, as (25) was derived from (23). As a result, we obtain the equation of spectral diffusion

$$\frac{\partial \xi(q,t)}{\partial t} = \lambda(q)\xi(q,t) + K_1(q)\frac{\partial \xi(q,t)}{\partial q} + D_1(q)\frac{\partial^2 \xi(q,t)}{\partial q^2}, \quad (36)$$

with the growth rate

$$\lambda(q) = D_d q^2 \left(\frac{n_{d0}}{n_{dc}} (1 - l_d^2 q^2) - 1 \right), \quad (37)$$

the drift coefficient

$$K_1(q) = D_d q (1 - l_d^2 q^2)(\theta_d/k_B T) \sum_{q_1 \neq 0} \xi_{q_1} q_1^2 \quad (38)$$

and the spectral diffusivity

$$D_1(q) = \frac{1}{2} D_d q^2 \times \left\{ |\alpha| - 3\beta\xi_0 + \frac{\theta_d}{k_B T}(1 - l_d^2 q^2) \right\} \sum_{q_1 \neq 0} \xi_{q_1} q_1^2. \quad (39)$$

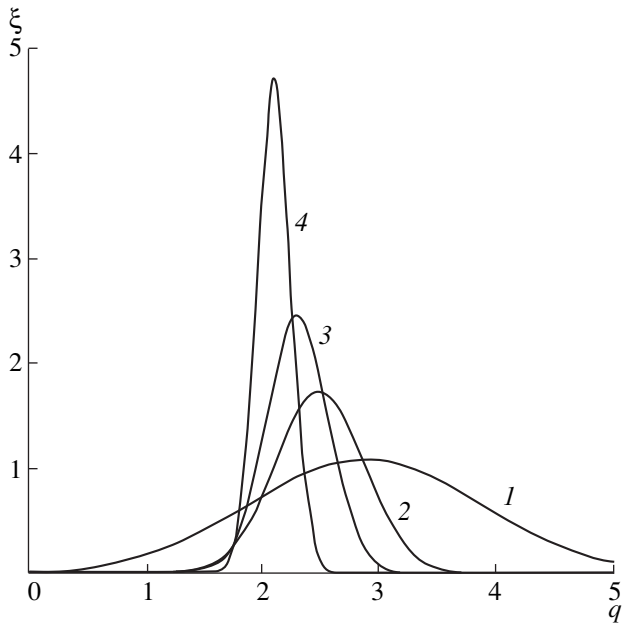

Fig. 2 Dynamics of the DD-mode spatial q-spectrum collapse. The diagram of the relative Fourier amplitude $\xi(q, \tau)/\xi(q, \tau = 0) = \exp[\Lambda\tau - (\tau\Delta(q - q_m + K\tau)^2/(1 - \tau^2))]/\sqrt{1 - \tau^2}$ versus q calculated from (43) at $\Lambda = \lambda_m t_q = 0.2$, $\Delta = \delta_m t_q = 5$, $q_m = 3$, $K = 1$, and different values of $\tau = t/t_q$: 0.1 (*1*), 0.5 (*2*), 0.7 (*3*), and 0.9 (*4*).

Since in the region (14) the angular-spectrum collapse is the case for ID modes, then $\xi_{q_1} > 0$, and, at $n_{d0} = n_{dc}$, we have from (39) that the diffusivity

$$D_1(q) = -3\beta D_d q^2 (k_B T/2\theta_d)(n_{d0}/n_{dc}) \times \sum_{q_1 \neq 0} \xi_{q_1} q_1^2 \equiv -|D(q)| < 0. \quad (40)$$

The maximum of the growth rate (37) is achieved at $q = q_m$, where

$$q_m = l_d^{-1}((n_{d0}/n_{dc} - 1)/2(n_{d0}/n_{dc}))^{1/2}. \quad (41)$$

Near $q = q_m$, the growth rate $\lambda(q) = \lambda_m - \delta_m(q - q_m)^2$, its maximal value is $\lambda_m = \lambda(q_m) = D_d(n_{d0}/n_{dc} - 1)^2/4l_d^2 n_{d0}/n_{dc}$, and, at the point $q = q_m$, the steepness parameter of the dependence $\lambda(q)$ is $\delta_m = 2D_d(n_{d0}/n_{dc} - 1)$. In the vicinity of $q = q_m$, diffusion equation (36) takes the form

$$\frac{\partial \xi(q, t)}{\partial t} = (\lambda_m - \delta_m(q - q_m)^2)\xi(q, t) + K_m \frac{\partial \xi(q, t)}{\partial q} - |D_m| \frac{\partial^2 \xi(q, t)}{\partial q^2}, \quad (42)$$

where the coefficients K_m and $|D_m|$ are given by formulas (38) and (40), respectively, at $q = q_m$. The initial and boundary conditions are given in the form $\xi_q(t)|_{t=0} = \xi(q, 0) = \text{const}$ and $\xi_q(t)|_{q \to \pm\infty} = 0$. The solution of (42) has the form

$$\xi_q(t) = \xi(q, 0) \frac{\exp(\lambda_m t)}{\sqrt{1 - 4|D_m|\delta_m t^2}} \times \exp\left\{ -\frac{(q - q_m + K_m t)^2}{\frac{1}{\delta_m t} - 4|D_m| t} \right\}. \quad (43)$$

Formula (43) describes the dynamics of narrowing of the spatial spectrum of DD modes with time-growing amplitudes (Fig. 2). After the time

$$t = \tau_m = 1/\sqrt{4|D_m|\delta_m} \quad (44)$$

the DD mode spectrum transforms to the δ function

$$\xi(q, t_m) = \xi(q, 0)\exp(\lambda_m \tau_m) \times \sqrt{\frac{\pi}{2}} \sqrt[4]{\frac{\delta_m}{|D_m|}} \delta(q - q_m + K_m \tau_m), \quad (45)$$

in **q** space, which implies the formation of the single DD mode ξ_{q_s} with the wave vector $q_s = q_m - K_m t_m$, i.e., of a periodic DD mesostructure with the period $d = 2\pi/q_s$.

From (44), we obtain the characteristic time after which the spatial spectrum of DD modes becomes monochromatic:

$$\tau_m = \frac{l_d^2}{D_d} \frac{(n_{d0}/n_{dc})^{1/2}}{(n_{d0}/n_{dc} - 1)^{3/2}} C_1, \quad C_1 = \left(\frac{k_B T}{\theta_d} \beta \sum_{q_1 \neq 0} \xi_{q_1} \frac{q_1^2}{q_m^2} \right)^{-1/2}. \quad (46)$$

The criterion of self-organization (collapse) of the spatial spectrum of DD modes may be formulated as inequality

$$\tau_m/\lambda_m^{-1} = C_1((n_{d0}/n_{dc} - 1)/(n_{d0}/n_{dc}))^{1/2}/4 < 1, \quad (47)$$

which is true at least near the threshold of the formation of periodic DD mesostructures.

When condition (47) is fulfilled, a single DD mode is formed, i.e., a periodic one-dimensional DD mesostructure arises. Its stationary characteristics were determined in [2]. The similar periodic DD mesostructures (superlattices) are concurrently formed in the two other [100]-type directions. The superposition of three DD superlattices with wave vectors directed along the [100]-type axes results in the formation of a three-dimensional cellular DD mesostructure.

5. CONCLUSIONS

The investigation of multimode dynamics of a three-dimensional DD mesostructure self-organization, which was carried out in this work, allows one to formulate the following criteria of self-organization in a DD system, where the external energy flow generates point defects.

When the defect concentration exceeds the first threshold value, $n_{d0} = n_{dc} l_0^2 / l_d^2 < n_{dc}$, the DD self-organization occurs in the short-wave region of the **q** space (12). It results in the VD-cluster formation, if the conditions $\tau_\theta < \tau_{\text{phase}} < \tau_b < \lambda_m^{-1}$ are obeyed, with τ_θ, τ_{phase}, τ_b, λ_m^{-1} being the characteristic values of angular-spectrum collapse time, phase-locking time, spectrum-broadening time, and time of VD-mode amplitude-spectrum growth, respectively.

When the defect concentration exceeds the second threshold value, $n_{d0} = n_{dc} \sim 10^{19}$ cm^{-3} [2], the DD self-organization occurs in the long-wave region of the **q** space. It results in the formation of periodic interstitial DD mesostructures, if the conditions $\tau_\theta < \tau_m < \lambda_m^{-1}$ are obeyed. Here, τ_θ, τ_m, and λ_m^{-1} are the characteristic values of the angular-spectrum collapse time, spatial-spectrum monochromatization time, and time of ID-mode amplitude growth.

The dynamics of the self-organization of DD nanostructure in the vector **q** space (DD-mode angular-spectrum collapse in directions of the [100] type with subsequent spreading or monochromatization of the mode spectrum in the one-dimensional |**q**| space), which was considered in our work, is quite similar to the dynamics of the self-organization of large-scale (micron) surface DD structures, which was investigated theoretically in [6]. The results of [6] agree well with the experimental results of [7], where the diffraction of probe radiation, with time resolution, from the surface of a Si(100) crystal exposed by power millisecond laser pulse was investigated. In [7], the dynamics of the angular selection of DD modes with subsequent mode-spectrum collapse in the |**q**| space was studied. The process gave rise to the surface DD-lattice formation of micron-order periods (see reviews [8, 9]).

The similar dynamics of DD mesostructure (nanostructure) self-organization, which was predicted in this work, may be studied by x-rays diffraction with time resolution. In this connection, we note that, in [10], using synchrotron radiation, the dynamics of the formation of Si surface-relief nanostructures was studied. The features of self-organization dynamics that were predicted in our work (amplitude growth with concurrent spectrum narrowing and its shifting to the long-wave region (Fig. 2)) agree with the experimental data of [10].

REFERENCES

1. V. I. Emel'yanov, Laser Phys. **6** (2), 423 (1996).
2. V. I. Emel'yanov and I. M. Panin, Fiz. Tverd. Tela (St. Petersburg) **39** (11), 2029 (1997) [Phys. Solid State **39** (11), 1815 (1997)].
3. V. I. Emel'yanov and I. M. Panin, in *Abstracts of Invited Lectures and Contributed Papers of the International Symposium on Nanostructures: Physics and Technology-97, Saint-Petersburg, Russia, 1997.*
4. C. Kittel, *Introduction to Solid State Physics* (Wiley, New York, 1976, 5th ed.; Nauka, Moscow, 1978).
5. S. T. Konobeevskiĭ, *Effect of Irradiation of Materials* (Atomizdat, Moscow, 1967).
6. V. I. Emel'yanov and Yu. G. Shlykov, Laser Phys. **4** (1), 1 (1994).
7. V. P. Veĭko, Ya. A. Imas, M. N. Libenson, *et al.*, Izv. Akad. Nauk SSSR, Ser. Fiz. **49** (6), 1236 (1985).
8. V. I. Emel'yanov, Laser Phys. **2**, 389 (1992).
9. V. I. Emel'yanov, Kvantovaya Élektron. (Moscow) **28**, 2 (1999).
10. S. Song, S. G. J. Mochrie, and G. B. Stephenson, in *Faceting Kinetics of Stepped Si Surfaces, Researches in Materials*, Annual Reports of Massachusets Technological Institute (1995), p. 309.

Translated by N. Ostrovskaya

Physics of the Solid State, Vol. 42, No. 6, 2000, pp. 1066–1069. Translated from Fizika Tverdogo Tela, Vol. 42, No. 6, 2000, pp. 1034–1037.

DEFECTS, DISLOCATIONS, AND PHYSICS OF STRENGTH

Low-Temperature Deformation of Nanocrystalline Niobium

V. V. Shpeĭzman*, V. I. Nikolaev*, B. I. Smirnov*, A. B. Lebedev*, and V. I. Kopylov**

** Ioffe Physicotechnical Institute, Russian Academy of Sciences, Politekhnicheskaya ul. 26, St. Petersburg, 194021 Russia*

*** Physicotechnical Institute, Belarussian Academy of Sciences, Minsk, 220730 Belarus*

e-mail: shpeizm.v@pop.ioffe.rssi.ru

Received December 1, 1999

Abstract—The strain characteristics of nanocrystalline niobium are measured in the temperature range 4.2–300 K. It is shown that the development of a strong local deformation with clearly delineated macroscopic slip bands occurs at 4.2 K and 10 K. The thermal effects at a stress jump observed upon transition of the sample (or a niobium strip placed close to the sample) from the superconducting state to the normal state are estimated. It is demonstrated that the temperature dependence of the yield point $\sigma_s(T)$ can be divided into three portions: two portions ($T < 10$ K and $T > 70$ K) with a slight change in σ_s and the third portion with a strong dependence $\sigma_s(T)$. The strain characteristics of polycrystals with nano- and larger-sized grains are compared with those of single crystals. © *2000 MAIK "Nauka/Interperiodica".*

1. INTRODUCTION

At present, the experimental data on the low-temperature mechanical properties of nanocrystalline materials are very limited. The specific features of the deformation of face-centered cubic (fcc) metals at helium temperature were discussed in our earlier works [1–3]. In particular, we studied copper, nickel, and the Cu–Zr alloy. As is known, the fcc metals retain the high plasticity down to the lowest temperatures. This is also true for pure niobium with a body-centered cubic lattice (bcc). In general, this behavior is not typical of bcc metals, which usually embrittle with a decrease in the temperature [4]. Another reason for the considerable interest in the low-temperature deformation of niobium is the superconducting transition at $T = 8.7$ K [5], which affects the strain characteristics of niobium [6, 7]. The low-temperature deformation of nanocrystalline niobium has not yet been investigated at all.

In the present work, the strain characteristics of nanocrystalline niobium were compared with those of coarser-grained and single-crystal niobium. This allowed us to judge the validity of the Hall–Petch relationship, which was repeatedly discussed with respect to the problem of nanocrystallinity [1, 8–10].

2. EXPERIMENTAL TECHNIQUE

The experiments were carried out using polycrystalline niobium samples of different grain sizes (200 nm and 100 μm) and single-crystal niobium samples. The nanostructure was obtained by multiple equichannel angular pressing, with a bar rotation through 90° after each cycle [11]. Electron microscopy showed that the grain size of the material was no more than 200 nm. An x-ray diffraction analysis revealed that the broadening of the lines is primarily associated with small-sized coherent scattering regions (about 30 nm), and the lattice distortion (the relative change of the lattice parameter $\Delta a/a$, which is caused by internal stresses) is equal to 1.1×10^{-3}. The values obtained are close to those measured earlier for nanocrystalline copper [1].

After the multiple equichannel angular pressing, we obtained the bars 50 mm long with a cross-section of 14×14 mm. The samples (height, 6 mm; cross-section, 2.5×2.5 mm) for mechanical testing were cut from a bar along its larger side. In addition, we used single-crystal and polycrystalline niobium samples (height, 8 mm; diameter, 3,5 mm), which were preliminarily treated under pressure and then were annealed. All the samples were subjected to compression on an Instron 1342 universal testing machine in liquid helium at 4.2 K, as well as at higher temperatures with the use of an ITC 4 controller. The experiments at temperatures below 77 K were carried out in an Oxford helium cryostat. The samples were cooled to 77 K with liquid nitrogen. Liquid helium was supplied to the cryostat by two pumps, which provided a slight evacuation in the cryostat. The strain rate was 4×10^{-4} s^{-1}.

3. RESULTS AND DISCUSSION

3.1. Mechanical Properties of Niobium at Helium Temperatures

The compression curves for single-crystal and nanocrystalline niobium samples are depicted in Fig. 1. As is seen from Fig. 1, the stress exhibits large jumps, which indicate a strong local deformation. The amplitude of jumps $\Delta\sigma$ increases with an increase in the strain, as was observed, for example, in [2, 7, 12]. At the strain $\varepsilon \approx 10$ % (for nanocrystals) and 20 % (for single crystals), the ratio of amplitude to working stress $\Delta\sigma/\sigma$ becomes equal to ≈ 40 and 60 %, respectively.

These deep stress jumps correspond to axial displacements of 0.5–0.7 mm, which, in turn, are due to a giant local deformation caused by macroscopic slip bands (Fig. 2) or cracks [2]. A similar deformation of single-crystal niobium at 4.2 K was observed earlier in [13, 14]; in this case, the surface relief was referred to as "the catastrophic slip bands." (In our opinion, this term is inadequate, because such a local slip is not a catastrophe). It follows from the data shown in Fig. 1 that the local deformation (jumps in the compression diagram) begins immediately after reaching the yield point σ_s. Note that the deformation observed between the jumps is almost completely elastic for single-crystal samples and exhibits a small, but appreciable, region of a uniform plasticity for nanocrystalline samples. The jumps were also observed in the compression diagrams for nanocrystalline samples at 10 K. However, no jumps were found at 20 K. The compression diagrams for coarser-grained polycrystals were similar to those shown in Fig. 1 and exhibited intermediate stress levels as compared to single crystals and nanocrystalline samples. The local slip for samples with a rectangular cross-section could occur parallel to one of the lateral faces of the sample (Fig. 2) or could be directed at the same angle to the faces and made an angle $\varphi \approx 45°$ with the sample axis.[1]

Compressive yield point for niobium with different initial structures (T = 4.2 K)

Material	Single crystal	Polycrystal after deformation and annealing	Nanocrystal
σ_s, MPa	1047	1338	1810

The compressive yield points σ_s for niobium with the different initial structures are presented in the table. It should be noted that σ_s for nanocrystalline niobium has the maximum value (among the known values for niobium). This is apparently caused by two factors, namely, a small grain size and a low testing temperature. We plotted the $\sigma_s(d)$ dependence from our data in the form of the Hall–Petch relationship: $\sigma_s = \sigma_s = \sigma_0 + kd^{-1/2}$, where d is the grain size, and σ_0 and k are constants. As can be seen (Fig. 3), the slope of the $\sigma_s(d^{-1/2})$ straight line for polycrystals proves to be close to that given in [4], whereas the point for the single-crystal sample lies below this straight line (the cross-section of the single crystal was taken as its grain size). Therefore, we can draw the following inferences. First, unlike copper and nickel [1–3], the applicability of the Hall–Petch relationship for niobium extends, at least, to a grain size of 200 nm. Second, there are no sufficiently strong obstacles to motion of dislocations such as subgrain boundaries, etc.

[1] Note that the use of short samples in the compression experiments (longer samples lost stability upon deformation) led to the emergence of one band edge on the sample end. This did not allow us to determine the slip angle with a higher precision and to relate it to the strain tensor.

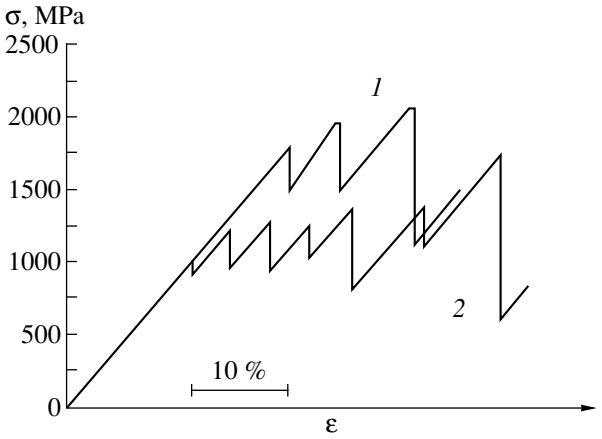

Fig. 1. Stress–strain (σ–ε) compression curves for (*1*) nanocrystalline and (*2*) single-crystal niobium at 4.2 K. Strain rate is 4×10^{-4} s^{-1}.

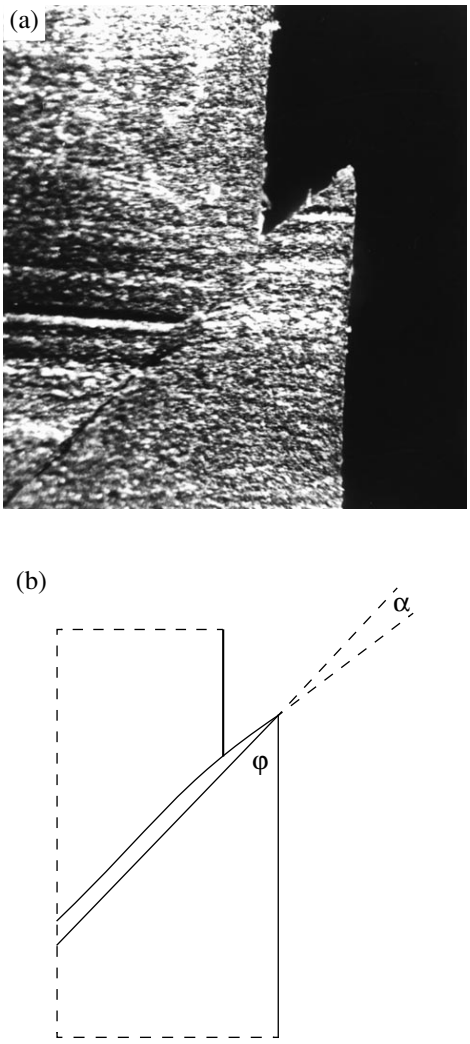

Fig. 2. (a) Local slip band upon deformation of nanocrystalline niobium (T = 4.2 K, ×20) and (b) its schematic representation for evaluating the slip strain.

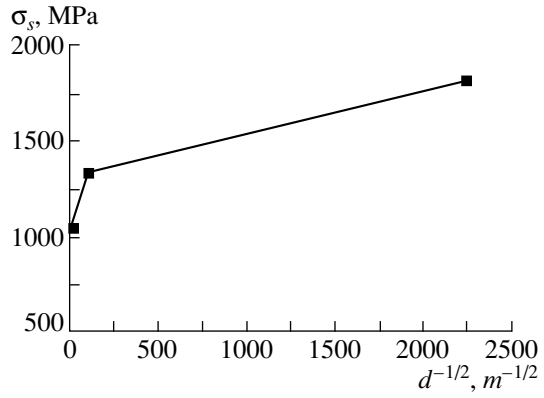

Fig. 3. Dependence of the yield point on the grain size for niobium. $T = 4.2$ K.

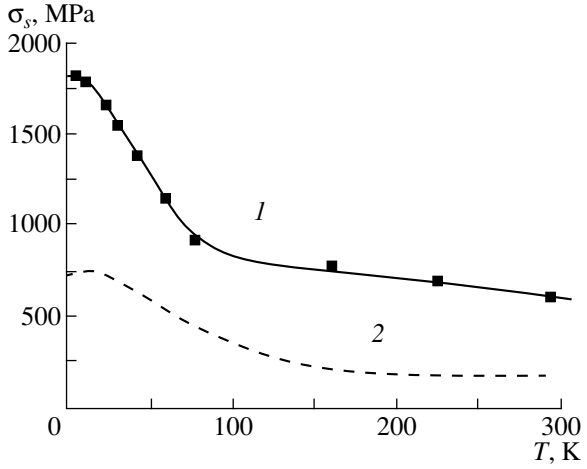

Fig. 4. Temperature dependence of the yield point for (*1*) nanocrystalline niobium and (*2*) conventional polycrystals (taken from [16]).

The temperature dependence of the yield point for nanocrystalline niobium is displayed in Fig. 4. The yield point was determined either immediately from the strain curve at a given temperature or by the technique of multiple stressing of a single sample at different temperatures [15]. The first method was used to determine the yield point on testing in liquid helium, liquid nitrogen, and at room temperature, whereas the second method was employed at intermediate temperatures. In the latter case, the change in the flow stress was determined at the temperature jump. Thereafter, the yield point change $\Delta\sigma_s$ was calculated from the hardening $\Delta\sigma$ for a given strain by using the known yield point values as the reference points to determine σ_s. Although this method is indirect, it has certain advantages. First, this method introduces no errors that can arise from testing of different samples. Second, the flow stress change (its sign and magnitude) is precisely fixed; hence, the possible slight deviations from the main law of the variation in $\sigma_s(T)$ should be considered the specific feature of deformation rather than the experimental error, as was noted in [1]. As is seen from Fig. 4, the $\sigma_s(T)$ dependence in the temperature range 4.2–300 K can be divided into three portions: at temperatures below 10 K and above 70 K, the dependence is rather weak, and, in the range from 10 K to 70 K, the yield point decreases almost two times. For comparison, Fig. 4 also depicts the $\sigma_s(T)$ dependence for coarser-grained niobium polycrystals [16]. This curve has similar three portions. However, the critical temperatures of the change in behavior of the $\sigma_s(T)$ dependence are shifted toward higher temperatures, and the stress level is less than half of that obtained in the present work for nanocrystals.

3.2. Nonuniformity of Niobium Deformation and Superconducting Transition

It is known that the local deformation, which manifests itself in the diagram as a stress jump, leads to sample heating [7, 13, 17, 18]. The deeper the jump in the diagram, the stronger the local deformation and, correspondingly, the stronger the sample heating. We assume that the deformation is an adiabatic process. Then, the estimates of the thermal effect give different heating temperatures: from several degrees to 100–200 K, depending on the degree of local deformation [13]. Attempts to measure the heating temperature have to do not with the time of passing through a local slip (10^{-5}–10^{-3} s according to different estimates [6–8, 13, 14, 17, 18]) but with a considerably longer time for which either the whole sample (or its part) or the environment becomes heated. These measurements are most often performed with a thermocouple kept against the sample or placed in a special recess in the sample. An original method for observing thermal effects upon deformation of the sample in liquid helium was used in [17]. This method is based on the helium boiling and bubble formation at sites of the emergence of slip bands on the sample surface. Niobium gives one more possibility of measuring thermal effects caused by local deformation. Since the superconducting transition temperature for niobium T_c is equal to 8.7 K, we can deform the sample, for example, at helium temperature, and measure the electrical resistance (or the instant of its onset) of the deformed sample itself or the emissary sample, which is placed in He close to the sample. These measurements make it possible to estimate the strain energy transferred into heat. The second variation is preferable for testing small samples, because, owing to the low heat capacity, the sample heating from 4.2 to 8.7 K requires a low energy; in this case, the He boiling in a certain volume around the sample and heating of gaseous He are the main thermal effects. Therefore, this method can be considered an extrapolation of the "bubble" method to a giant local deformation and, correspondingly, to a large volume of boiled He. The

limiting distance between the deformed and emissary samples, at which the resistance arises in the emissary sample at the instant of stress jump in the diagram, can be treated as the radius of helium heated to 8.7 K.

Let us now make numerical estimates. The integral heat effect of the local slip is determined as $Q = \eta\tau\gamma V$, where γ is the slip strain, τ is the in-plane slip stress, η is the fraction of the strain energy transferred into heat, and V is the volume of the slip zone. By its meaning, $0 < \eta < 1$, and different estimates give both small η values and the values close to unity. It seems likely that, for nanocrystals obtained through a strong plastic deformation, additional latent strain energy cannot be very high, and, hence, we can accept $\eta \approx 1$. The τ, γ, and V quantities can be calculated from the data presented in Figs. 1 and 2. Specifically, $\tau = \sigma_j \sin\varphi\cos\varphi$, where σ_j is the normal stress at a jump, $\sigma_j = 2100$ MPa, $\varphi \approx 45°$, $\gamma = \cot\alpha - \cot\varphi \approx 8$ (Fig. 2b), and $V \approx 6 \times 10^{-10}$ m^3, from which $Q \approx 5$ J. The conductivity measurements gave a distance of ≈1.5 cm from the deformed sample, at which He undergoes boiling and heating above the temperature of transition to the normal state. From these data, we obtain the energy necessary for He vaporization Q_v and its subsequent heating Q_t as follows: $Q_v = q\rho V_{\mathrm{He}} = 1.3$ J and $Q_t = c_v\rho V_{\mathrm{He}}\Delta T = 0.9$ J. Here, $q = 20.9 \times 10^3$ J/kg is the heat of vaporization for He, $\rho = 4.6$ kg/m^3 is the density of gaseous He [17], and $c_v = 3k/2m = 3.1 \times 10^3$ J/kg K, where k is the Boltzmann constant, m is the molecular mass of He, and $\Delta T = (T_c - 4.2)$ K. The Q_v and Q_t values are obviously underestimated. The reason is that the probable increased pressure of gaseous He and its overheating above T_c are not taken into account. However, even this rough estimate shows that the η value for nanocrystalline niobium is more than 0.5. Under the assumption that the deformation during the stressing separation is an adiabatic process, we can estimate the heating temperature from the formula $T \approx (4Q/C\rho_{\mathrm{Nb}}V)^{1/4}$. Here, $C = 1.55 \times 10^{-3}$ J/kg K^4 is the constant in the Debye formula for the heat capacity of niobium at a low temperature [13], and $\rho_{\mathrm{Nb}} = 8.4$ g/cm^3 is the density of niobium. Substituting V by the volume of the local share zone, we obtain $T = 225$ K. However, with the condition that Q is distributed throughout the volume of the sample, its temperature turns out equal to 70 K. At this temperature, the yield point σ_s is ≈ 1 GPa, which corresponds to the lowest point of the last jump in the compression diagram (Fig. 1). Thus, even these very rough estimates, which do not take into account many factors (for example, the real rate of local deformation, bending moments arising upon the slip, etc.), demonstrate the relation between thermal effects and the shape of the strain curve at helium temperatures.

ACKNOWLEDGMENTS

We thank I.N. Zimkin for performing x-ray investigations and G.A. Malygin for helpful discussion of the results.

This work is supported by the Scientific Council of the International Scientific and Technical Program (MNTP) "Physics of Solid-State Nanostructures," project no. 97-3006.

REFERENCES

1. V. V. Shpeĭzman, V. I. Nikolaev, B. I. Smirnov, *et al.*, Fiz. Tverd. Tela (S.-Peterburg) **40** (7), 1264 (1998) [Phys. Solid State **40** (7), 1151 (1998)].
2. V. V. Shpeĭzman, V. I. Nikolaev, B. I. Smirnov, *et al.*, Fiz. Tverd. Tela (S.-Peterburg) **40** (9), 1639 (1998) [Phys. Solid State **40** (9), 1489 (1998)].
3. V. V. Shpeĭzman, V. I. Nikolaev, B. I. Smirnov, A. B. Lebedev, V. V. Vetrov, S. A. Pul'nev, A. K. Markov, and V. I. Kopylov, in *Proceedings of the Second International Seminar on Topical Problems of Strength, Staraya Russa, Belarus, 1998* (Novgorod Gos. Univ., Novgorod, 1998), Vol. 2, p. 149.
4. V. I. Trefilov, Yu. V. Mil'man, and S. A. Firstov, *Physical Principles of the Strength of Refractory Metals* (Naukova Dumka, Kiev, 1975).
5. *Low-Temperature Physics*, Ed. by A. I. Shal'nikov (Berlin, 1956; Inostrannaya Literatura, Moscow, 1959).
6. G. Kostorz, Acta Metall. **35** (6), 813 (1973).
7. V. I. Startsev, V. Ya. Il'ichev, and V. V. Pustovalov, *Plasticity and Strength of Metals and Alloys at Low Temperatures* (Metallurgiya, Moscow, 1975).
8. G. A. Malygin, Fiz. Tverd. Tela (S.-Peterburg) **37** (8), 2281 (1995) [Phys. Solid State **37** (8), 1248 (1995)].
9. J. E. Carsley, J. Ning, W. W. Milligan, *et al.*, Nanostruct. Mater. **5** (4), 441 (1995).
10. M. Yu. Gutkin, Author's Abstract of Doctoral Dissertation in Mathematical Physics (Institute of Problems in Machine Science, Russian Academy of Sciences, St. Petersburg, 1997).
11. V. M. Segal, V. I. Reznikov, A. E. Drobyshevskiĭ, and V. I. Kopylov, Izv. Akad. Nauk SSSR, Met., No. 1, 115 (1981).
12. O. V. Klyavin and A. V. Stepanov, Fiz. Tverd. Tela (Leningrad) **1** (6), 955 (1959) [Sov. Phys. Solid State **1** (6), 873 (1959)].
13. A. R. Baraz and B. V. Molotilov, Fiz. Nizk. Temp. (Kiev) **3** (4), 514 (1977) [Sov. J. Low Temp. Phys. **3** (4), 249 (1977)].
14. A. M. Dolgin and V. Z. Benguz, Phys. Status Solidi A **94** (2), 529 (1986).
15. R. Kamada and I. Joshizawa, J. Phys. Soc. Jpn. **4**, 1056 (1971).
16. I. A. Gindin and Ya. D. Starodubov, Fiz. Met. Metalloved. **15** (5), 736 (1963).
17. O. V. Klyavin and A. V. Nikiforov, Izv. Akad. Nauk SSSR, Ser. Fiz. **27** (11), 2411 (1973).
18. T. Ogata, K. Ishikava, K. Nagai, *et al.*, Adv. Cryog. Eng. Mater. B **36**, 1249 (1990).

Translated by N. Korovin

Physics of the Solid State, Vol. 42, No. 6, 2000, pp. 1070–1074. Translated from Fizika Tverdogo Tela, Vol. 42, No. 6, 2000, pp. 1038–1042.

MAGNETISM AND FERROELECTRICITY

Effect of Orbital Ordering on the Magnetic-Structure Formation in the $LaMnO_3$ Jahn–Teller Magnet

L. É. Gonchar' and A. E. Nikiforov

Ural State University, pr. Lenina 51, Yekaterinburg, 620083 Russia

e-mail: lyudmila.gonchar@usu.ru

Received September 23, 1999

Abstract—A study is reported on the relation between orbital ordering and the magnetic structure of an $LaMnO_3$ crystal. The dependence of the exchange parameters on the orbital-structure angle Φ has been determined. Inclusion into the spin Hamiltonian of isotropic exchange interaction and single-ion anisotropy, which depends on the angle Φ and rotational distortions, results in a four-sublattice structure (A_X, F_Y, G_Z), with the sublattice magnetic moments oriented close to the long axis of the orthorhombic cell in the basal plane of the crystal ($A_X \gg G_Z, F_Y$). The effect of the rare-earth-ion size in $R\mathrm{MnO}_3$ manganites on the orbital and magnetic structures is considered. © *2000 MAIK "Nauka/Interperiodica".*

The discovery of colossal magnetoresistance in $LaMnO_3$-based compounds has stimulated renewed interest in this compound, followed by the appearance of a large number of publications dealing with this crystal.

$LaMnO_3$ is characterized by a strong coupling between the spin, charge, and orbital degrees of freedom. Revealing the specific features of this coupling in the parent compound $LaMnO_3$ would be an important step in interpreting the properties of doped compounds as well.

Experimental studies showed [1, 2] that below T_N = 140 K the crystal possesses type-A magnetic structure with the sublattice magnetic moments oriented along the long orthorhombic axis in the basal plane of the *O*' crystal structure (*Pnma* symmetry group). A qualitative analysis based on the Goodenough–Kanamori rules [3] permitted us to explain the ferromagnetic character (sign) of the isotropic exchange interaction in the basal plane, while the magnetic-moment orientation along the orthorhombic axis was associated with fourth-order single-ion anisotropy [1].

A number of publications dealing with experimental determination of exchange integrals for $LaMnO_3$ have recently appeared [4, 5]. This offers a possibility of studying the dependence of the exchange parameters on orbital structure with greater accuracy.

This work analyzes the dependence of the isotropic-exchange parameters on the angle of the orbital structure Φ. Taking into account the single-ion anisotropy, which likewise depends on this angle, we explain the magnetic structure without invoking the fourth-order anisotropic terms. The variation of the orbital structure and exchange integrals is studied for $R\mathrm{MnO}_3$ materials (R = La, Pr, Nd, Y).

1. ORBITAL STRUCTURE AND EXCHANGE COUPLING IN MANGANITES

The $LaMnO_3$ crystal possesses distorted perovskite structure [1, 2, 6, 7]. At low temperatures this substance is in the *O*' orthorhombic phase, and an increase of temperature or weak doping transfers it to the quasi-cubic phase *O**. The space group of both phases is $Pnma(D_{2h}^{16})$. They differ primarily in the primitive cell parameters

$$\begin{aligned} b/\sqrt{2} < c < a \text{ for } O', \\ b/\sqrt{2} \sim c \sim a \text{ for } O^*. \end{aligned} \quad (1)$$

The orthorhombic distortion of an ideal perovskite lattice can be presented in the form of three basic distortions [8, 9]:

1. The *R*-type distortion represents the rotation of the oxygen octahedra about the $[110]_p$ axis of the ideal perovskite with unit cell doubling along all three axes ($\{k_{13}\}\tau_9(C_1C_10)$ in Kovalev's notation [10] or (φ φ 0) in the notation of [11]). The angle φ = 12.3° [12].

2. The *M*-type distortion is the rotation of the oxygen octahedra about the $[001]_p$ axis with unit cell doubling along two axes ($\{k_{11}\}\tau_3(0\ 0\ C_2)$ in the notation of [10] or (0 0 ψ) by [11]). The angle ψ = 9.9° [12].

3. The ε-type distortion (Q_2) consists of an *e*-type deformation of the oxygen octahedron with cell doubling along two axes ($\{k_{11}\}\tau_5$ in the notation of [10] and with the arm chosen along $[1/2\ 1/2\ 0]_p$).

The corresponding basal distortions are accompanied by a lattice rearrangement.

In the *O** phase there is no ε distortion, whereas the rotational distortions remain. Simulation of the $LaMnO_3$ crystal in the pair-potential model [9] showed

1063-7834/00/4206-1070$20.00

that the ε distortion is connected with the electron-lattice interaction (the cooperative Jahn–Teller effect) and the rotations originate from lattice effects.

The ε distortion displayed in Fig. 1 is the most essential for our consideration. Local distortions of the oxygen octahedron are given by e_g-type symmetrized coordinates Q_θ, Q_ε (Q_3, Q_2), which are expressed through the lattice constants (a, b, c) and the displacement parameters of the oxygen sublattice (V_X, V_Z) in the primitive cell of the O' phase [9]:

$$Q_\theta = \frac{1}{\sqrt{12}}\left[b - \frac{1}{\sqrt{2}}(a + c)\right],$$
$$Q_\varepsilon = \sqrt{2}(V_X a + V_Z c). \quad (2)$$

These distortions can be conveniently characterized by the polar angle Φ,

$$\tan\Phi = \frac{Q_\varepsilon}{Q_\theta}. \quad (3)$$

As readily seen from Fig. 1, the angles of the e_g distortions of the oxygen octahedra surrounding the magnetic ions are related through

$$\Phi_1 = \Phi_2 = -\Phi_3 = -\Phi_4 = \Phi. \quad (4)$$

In the strong linear vibronic coupling approximation, the wave function of the lowest level of the nth Mn^{3+} ion in the O' phase is a linear combination of orbital functions of the ${}^5E(t_2^3 e)$ term

$$\psi_n = \sin\frac{\Phi_n}{2}\varphi_{n\theta} + \cos\frac{\Phi_n}{2}\varphi_{n\varphi}. \quad (5)$$

The effective Hamiltonian of spin-isotropic exchange interaction along the z_p axis for two manganese ions residing in orbitally degenerate states in an ideal perovskite lattice can be written as [13, 14]

$$H_{ex}^{z_p}(a, b) = [J + J_1(X_{a\theta} + X_{b\theta}) + J_2 X_{a\theta} X_{b\theta}](S_a S_b), \quad (6)$$

where $X_{\theta,\varepsilon}$ are orbital operators acting in the space of $(\varphi_\theta\varphi_\varepsilon)$ functions of the ground E term

$$X_\theta = \begin{pmatrix} -1 & 0 \\ 0 & 1 \end{pmatrix}, \quad X_\varepsilon = \begin{pmatrix} 0 & 1 \\ 1 & 0 \end{pmatrix}. \quad (7)$$

The exchange parameters J, J_1, and J_2 can be expressed in terms of one-electron superexchange parameters [13, 14].

For a pair of ions along the x_p (y_p) axis, one can write

$$H_{ex}^{x_p(y_p)}(a, b) = \left[J - \frac{1}{2}J_1(X_{a\theta} \pm \sqrt{3}X_{a\varepsilon} + X_{b\theta} \pm \sqrt{3}X_{b\varepsilon}) + \frac{1}{4}J_2(X_{a\theta} \pm \sqrt{3}X_{a\varepsilon})(X_{b\theta} \pm \sqrt{3}X_{b\varepsilon})\right](\mathbf{S}_a\mathbf{S}_b). \quad (8)$$

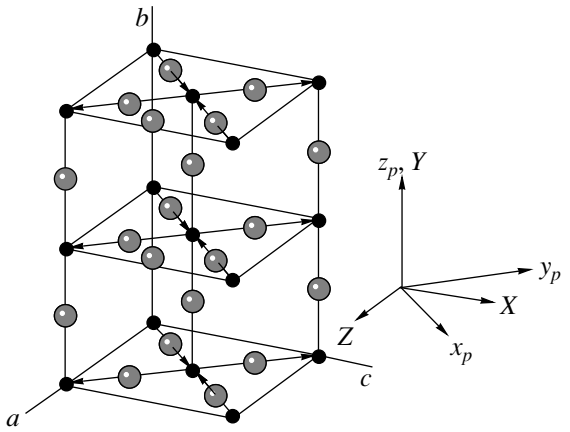

Fig. 1. Primitive cell of $LaMnO_3$ with ε-type distortion. The La^{3+} ions are omitted. X, Y, Z is the orthorhombic coordinate frame, x_p, y_p, and z_p is the quasi-cubic coordinate frame.

By averaging the orbital parameters with the use of wave functions (5) and taking into account the differences of the metal-ligand distances r_b, r_{ac} and superexchange bond angles φ_b, φ_{ac} between the pairs of interacting ions along the z_p axis and in the basal plane, respectively, we obtain the following expressions for the manganese-ion isotropic-exchange parameters $J_{12} = J_{34} = J_b$ and $J_{14} = J_{23} = J_{ac}$:

$$J_b = \frac{J_0\cos^2\varphi_b}{r_b^{10}}F_b(\Phi), \quad J_{ac} = \frac{J_0\cos^2\varphi_{ac}}{r_{ac}^{10}}F_{ac}(\Phi), \quad (9)$$

where

$$F_b(\Phi) = [1 + 2\alpha\cos(\Phi + \beta\cos^2\Phi)],$$
$$F_{ac}(\Phi) = \left[1 - \alpha\cos\Phi + \beta\left(\cos^2\Phi - \frac{3}{4}\right)\right], \quad (10)$$

and J_0, α, and β are parameters which can be extracted from experimental data; Φ is the Jahn–Teller distortion angle. The exchange integrals for $LaMnO_3$ can be found in the literature [4, 5]: $J_b = 13.4$ K, and $J_{ac} = -19.2$ K [4].

Unfortunately, no measurement data are presently available for the exchange integrals for other RMnO$_3$ manganites. We used the Néel temperatures for $PrMnO_3$ and $NdMnO_3$ to determine the third parameter in (9). Because the molecular-field model yields overestimated figures for T_N (207 in place of 140 K for $LaMnO_3$), we used in the fitting procedure the experimental values of the Néel temperature for $PrMnO_3$ ($T_N = 91$ K [15]) and $NdMnO_3$ ($T_N = 85$ K [16]) multiplied by 1.48.

The table presents structural data and exchange parameters for manganites obtained for the parameters $J_0 = 14372$ K × Å^{10}, α = 0.9, and β = 4.8. Thus, for $LaMnO_3$ the exchange parameters were found to be $J_b = 12.4$ K and $J_{ac} = -17.1$ K. Our result appears to be

Structural data and exchange parameters for some rare-earth manganites

Compound	Rare-earth ionic radius, Å [20]	Φ, deg	r_b, Å	$\bar{r}_{ac}$, Å	φ_b, deg	φ_{ac}, deg	J_b, K	J_{ac}, K
$LaMn_3$	1.06	107 [12]	1.96 [12]	2.04 [12]	155.1 [12]	153.8 [12]	12.4 (13.4 [4], 14.0 [5])	–17.1 (–19.2 [4], 19.4 [5])
$PrMnO_3^*$	1.01	121 [15]	1.94 [15]	2.07 [15]	154.4 [15]	148.3 [15]	20.4	–6.2
$NdMnO_3^{**}$	0.99	111 [16]	193 [16]	2.08 [16]	156.2 [16]	144.1 [16]	15.9	–10.3
Orthorhombic $YMnO_3$	0.97	134 [21]	2.01 [21]	2.05 [21]	133.0 [21]	146.5 [21]	13.1	2.9

Note: * *A*-type antiferromagnet [15], ** *A*-type antiferromagnet [16].

an underestimation compared to the experimental values (J_b = 13.4 K, J_{ac} = –19.2 K [4], J_b = 14.0 K, J_{ac} = –19.4 K [5]), which can be assigned to the use of the molecular-field approximation for the Néel temperature. The calculation made in terms of the microscopic model [17] yields overestimated exchange parameters (J_b = 30.5 K, J_{ac} = –29.2 K).

Figure 2 presents the dependence of the angular part of the exchange parameters on the Jahn–Teller angle Φ. We readily see that the exchange parameter can even reverse its sign in the basal plane. As follows from our calculations, this case is realized in the orthorhombic phase of $YMnO_3$ (see the table).

The possibility of the exchange parameter sign reversal and the characteristic orbital-structure angles φ at which this change occurs depend primarily on the relative magnitude of the α and β parameters.

For the ^2E state of copper ions, where only e_g holes participate in exchange interaction, the ratio $\alpha/\beta \approx -1$ (for instance, in $KCuF_3$ this ratio is 1.24 [18]).

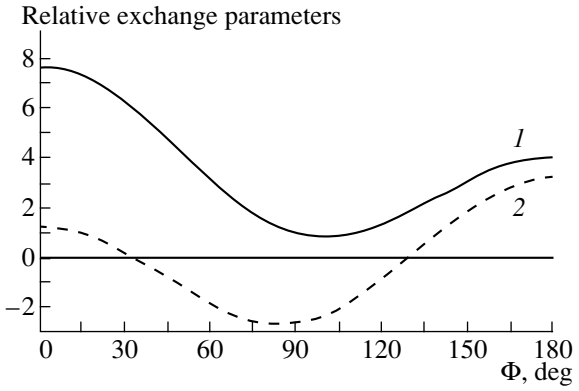

Fig. 2. Dependence of the angular part of the exchange integrals along the *b* axis and in the basal plane on the Jahn–Teller distortion angle (the angle of the orbital structure). (*1*) F_b, (*2*) F_{ac}.

In the ^5E state, a noticeable contribution to the exchange coupling comes not only from superexchange between the *e* orbitals, but also from that between the *e* and t_2 and between the t_2 orbitals. In this case, $|\alpha/\beta| < 1$, because exchange between the *e* and t_2 states reduces α and increases β. For instance, for $KCrF_3$, $\alpha/\beta = 0.59$ [13]. In our case, it is $\alpha/\beta = 0.19$.

This can be assigned to the fact that the ratio of the superexchange constants between the *e* and t_2 orbitals and between the *e* orbitals is larger if the interaction involves oxygen rather than in the case of interaction via fluorine. In our case, this ratio presupposes the presence of *A*-type magnetic ordering in the angular interval $33.5° < \Phi < 130.5°$, while the other Φ angles belong to the *G* structure (e.g., our calculations suggest that the orthorhombic $YMnO_3$ possesses a magnetic structure of the *G* type). For $KCrF_3$, this angular interval reduces to $57° < \Phi < 85°$, with the ferromagnetic exchange being considerably weaker than the antiferromagnetic one.

Single-ion anisotropy plays a substantial part for the high-spin state of Mn^{3+}. The corresponding term of second order in spin variables for the orbitally degenerate ^5E term has the form [19]

$$H_{an} = P[X_\theta(3S_{z_p}^2 - S(S+1)) + \sqrt{3}X_\varepsilon(S_{x_p}^2 - S_{y_p}^2)]. \quad (11)$$

This term appears in the second order of perturbation theory in spin–orbit interaction. The closest excited term is $^3T_1(t_2^4)$, separated from the ground term by a gap of $\Delta = 2800$ cm^{-1} [1]. For a free Mn^{3+} ion, ζ_{3d} = 380 cm^{-1} [19]. In this case, $P = -\zeta_{3d}^2/(12\Delta) = -3.0$ K. This figure exceeds noticeably in magnitude the value obtained in our work, because the ζ_{3d} constant for the manganese ion in the crystal is smaller. Accepting ζ_{3d} = 288 cm^{-1} [1], we come to $P = -1.7$ K.

Averaging the Hamiltonian (11) with functions (5) yields single-ion anisotropy in quasi-cubic axes, which

depends on the orbital-ordering angle

$$H_{\text{an}}^{(n)} = D_n S_{nz_p}^2 + E_n (S_{nx_p}^2 - S_{ny_p}^2), \quad (12)$$

where

$$D_n = 3P\cos\Phi_n, \quad (13)$$

$$E_n = \sqrt{3}P\sin\Phi_n. \quad (14)$$

The values of D_n turn out to be positive ($\cos\Phi_i < 0$, $P < 0$) and the same for all magnetic ions in the cell, while E_n reverses its sign as one crosses over to the adjacent magnetic ion in the basal plane.

The value of P was determined from the gap for the lowest spin-wave branch, $\Delta E = 2.7$ meV [4], and was found to be $P = -1.48$ K (see Fig. 3).

2. RESULTS AND DISCUSSION

The cooperative Jahn–Teller effect results in the onset of an orbital structure, i.e., a certain ordering of e orbitals of the Mn^{3+} ions in the crystal, and, because of the isotropic exchange coupling and single-ion anisotropy being dependent on the filling of the orbitals of the interacting ions, it leads to a certain magnetic structure.

Combining (9) and (12), we write the magnetic interaction Hamiltonian for $LaMnO_3$ in the form

$$H = J_b \sum_{n>m} (\mathbf{S}_n \mathbf{S}_m) + J_{\text{ac}} \sum_{n>m} (\mathbf{S}_n \mathbf{S}_m) + \sum_n H_{\text{an}}^{(n)}. \quad (15)$$

The single-ion anisotropy term for ions in the cell can be obtained from (12) by correspondingly turning the local axes to the common orthorhombic coordinate frame X, Y, Z. The orbital-structure angles and the angles of turn of the R and M lattice distortions for different Mn ions in the primitive cell relate to one another in the following way: Mn_1 (φ, ψ, Φ), Mn_3 ($-\varphi$, $-\psi$, $-\Phi$), Mn_4 ($-\varphi$, $-\psi$, $-\Phi$).

Minimizing the magnetic energy in model (15) results in a four-sublattice magnetic structure, which is noncollinear and is classified as (A_X, 0, G_Z) (see Fig. 4a) without taking into account the rotational distortions, and as (A_X, F_Y, G_Z) (Figs. 4a and 4b) if the turns are taken into account. The magnetic-moment projections are $\mu_X = 3.698\ \mu_B$, $\mu_Y = 0.063\ \mu_B$, and $\mu_Z = 0.105\ \mu_B$ (accepting $3.7\ \mu_B$ for the magnetic moment of the Mn^{3+} ion [12]). Experiment yields $\mu_Y \sim 0.1\ \mu_B$ [1]. Neutron scattering measurements cannot yield μ_Z [1, 4], and no other experiments have been made. The magnitude of μ_Y can be calculated more precisely by including into the Hamiltonian the antisymmetric Dzyaloshinski-Moriya exchange, which we neglected.

In paper [1], which considered the magnetic structure of $LaMnO_3$ in a similar model, the magnetic-moment orientation along the long axis was explained as being due to anisotropic terms of the fourth order in spin variables. The preferred orientation of the easy-magnetization axis in our model is associated with the orbital structure of the crystal.

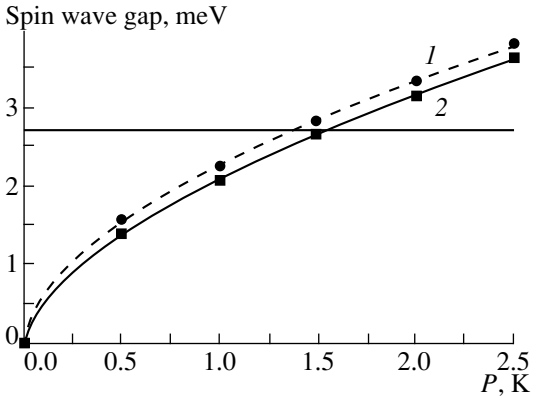

Fig. 3. Dependence of the energies of the two lowest spin-wave branches at the center of the magnetic Brillouin zone on single-ion anisotropy constant. (*1*) upper branch, (*2*) lower branch. The horizontal line specifies 2.7 meV [4].

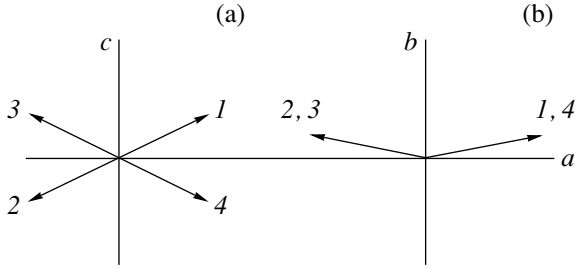

Fig. 4. Magnetic structure of $LaMnO_3$. (a) A_X and G_Z components. (b) A_X and F_Y components.

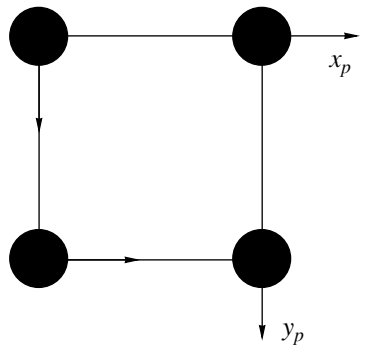

Fig. 5. Location of local easy magnetic axes in the basal plane.

Indeed, because $\sin\Phi_i$ reverses its sign at adjacent ions in the basal plane, local easy axes alternate from one ion to another and are mutually perpendicular (Fig. 5). Because the exchange interaction between magnetic ions in this plane is ferromagnetic, the spins of adjacent ions are attracted, as it were, to the diagonal of the octahedra, i.e., to the X or Z axes, without becoming at the same time totally aligned with either of these

axes (Fig. 4a). The projection of the moment on the Z axis will in this case be $\mu_Z = |E_n/(4J_{ac})|$. When including rotations, one has to take into account the orthorhombic nature of the crystal structure, and, therefore, the X and Z axes are already no longer equivalent, with a component of the structure appearing along the Y axis. The R-type rotational distortion, which occurs about the X axis, plays the major part here. It is this distortion that makes the long and the short orthorhombic axes inequivalent. Its inclusion into the Hamiltonian (15) accounts for the weak ferromagnetic component of the magnetic structure.

The formation of the Y component of the magnetic structure can be explained by assuming that rotation does not change the magnetic-moment direction relative to the local axes of each magnetic ion. Because the R rotation occurs about the X axis, the X component remains unchanged after the rotation, while the Z component is displaced relative the Y and Z axes. Because the Z components of the magnetic moment at adjacent ions reverse their sign, and because the R distortion changes the phase, the Y projection of the magnetic moment induced by the rotation possesses the same sign at all ions of the magnetic lattice.

We calculated the magnon energies for the Hamiltonian (15) in the linear spin-wave approximation. The dependences of the spin-wave frequencies at the Γ point of the magnetic Brillouin zone on the anisotropy constant P are presented graphically in Fig. 3. The experimental data were taken from [4]. While the single-ion anisotropy model accepted in [4], as in [5], had a simple phenomenological form, it nevertheless reproduced the dispersion curves well. In contrast to [4, 5], our model (15) predicts the absence of degeneracy in the dispersion relations (they are weakly split at the Γ point) and the magnetic-cell doubling. Model (15) fully describes the experimental dispersion relations.

In contrast to the previous models [1, 4, 5], our model permits taking into account the orbital ordering, which is a consequence of cooperative Jahn–Teller distortions, and explicitly following its role in magnetic ordering in Jahn–Teller magnetic crystals, of which the particular case is $LaMnO_3$.

REFERENCES

1. G. Matsumoto, J. Phys. Soc. Jpn. **29** (3), 606 (1970).
2. E. O. Wollan and W. C. Koehler, Phys. Rev. **100** (2), 545 (1955).
3. J. Goodenough, *Magnetism and the Chemical Bond* (Interscience Publ., New York, 1963).
4. F. Moussa, M. Hennion, J. Rodríguez-Carvajal, *et al.*, Phys. Rev. B **54** (21), 15149 (1996).
5. K. Hirota, N. Kaneko, A. Nishizawa, and Y. Endoh, J. Phys. Soc. Jpn. **65** (12), 3736 (1996).
6. P. Norby, I. G. K. Andersen, E. K. Andersen, and N. H. Andersen, J. Solid State Chem. **119** (1), 191 (1995).
7. J. Rodríguez-Carvajal, M. Hennion, F. Moussa, *et al.*, Phys. Rev. B **57** (6), R3189 (1998).
8. V. E. Naĭsh, Fiz. Met. Metalloved. **85** (6), 5 (1998).
9. A. E. Nikiforov, S. É. Popov, and S. Yu. Shashkin, Fiz. Met. Metalloved. **87** (2), 16 (1999).
10. O. E. Kovalev, *Irreducible Induced Representations and Corepresentations of Fedorov Groups* (Nauka, Moscow, 1986).
11. K. S. Aleksandrov, A. T. Anistratov, B. V. Beznosikov, and N. V. Fedoseeva, *Phase Transitions in Crystals of Halogen Compounds* (Nauka, Novosibirsk, 1981).
12. Q. Huang, A. Santoro, J. W. Lynn, *et al.*, Phys. Rev. B **55** (22), 14987 (1997).
13. M. V. Eremin and V. N. Kalinenkov, Fiz. Tverd. Tela (Leningrad) **20** (12), 3546 (1978) [Sov. Phys. Solid State **20** (12), 2051 (1978)].
14. A. E. Nikiforov, S. Yu. Shashkin, M. L. Levitan, and T. H. Agamalyan, Phys. Status Solidi B **118** (1), 419 (1983).
15. Z. Jirák, S. Krupicka, Z. Šinša, *et al.*, J. Magn. Magn. Mater. **53** (1-2), 153 (1985).
16. A. Oles, M. Kajzar, W. Kucab, *et al.*, Magnetic Structures Determined by Neutron Diffraction (Krakow Panstwowe Wydawnictwo Naukowe, Warszawa, 1976).
17. I. Soloviev, N. Hamada, and K. Terakura, Phys. Rev. Lett. **76** (25), 4825 (1996).
18. V. Ya. Mitrofanov, A. E. Nikiforov, and S. Yu. Shashkin, Solid State Commun. **104** (9), 499 (1997).
19. A. Abragam and B. Bleaney, *Electron Paramagnetic Resonance of Transition Ions* (Clarendon Press, Oxford, 1970; Mir, Moscow, 1973).
20. A. P. Babichev, N. A. Babushkina, A. M. Bratkovskiĭ, *et al.*, *Handbook on Physical Quantities*, Ed. by I. S. Grigor'ev and E. Z. Meĭlikhov (Énergoatomizdat, Moscow, 1991).
21. M. N. Iliev, M. V. Abrashev, H.-G. Lee, *et al.*, Phys. Rev. B **57** (5), 2872 (1998).

Translated by G. Skrebtsov

Physics of the Solid State, Vol. 42, No. 6, 2000, pp. 1075–1080. Translated from Fizika Tverdogo Tela, Vol. 42, No. 6, 2000, pp. 1043–1048.

MAGNETISM AND FERROELECTRICITY

Diffraction of Light from a Stripe Domain Structure with Tilted Domain Walls

I. F. Gismyatov and D. I. Sementsov

Ul'yanovsk State University, 432700 Ul'yanovsk, Russia

e-mail: Sements@quant.univ.simbirsk.ru

Received October 25, 1999

Abstract—The intensity and polarization parameters of light waves diffracted from a stripe domain structure with tilted domain walls and the magnetic moment in domains oriented parallel to the walls are determined in the approximation of thin layers and linear magnetooptical coupling. *© 2000 MAIK "Nauka/Interperiodica".*

In most publications devoted to magnetooptical diffraction (MOD) from stripe domain structures (SDSs) formed in thin layers of ferromagnetic dielectrics, a theoretical analysis is based on the approximation of binary magnetization distribution in the magnetic lattice [1–5]. In real SDSs, the thickness of domain walls is much less than the width of stripe domains, which justifies using this approximation to describe MOD from domain structures with vertical domain walls (DWs). However, the magnetization distribution does not explain all the features of diffraction of laser radiation from an SDS with tilted DWs [6, 7]. This is primarily due to the fact that the distribution of the Faraday magnetization component parallel to the direction of light propagation and responsible for the diffraction of light from SDS in the case of tilted DWs is more complicated than the binary distribution. For example, DWs in epitaxial garnet ferrite films are vertical only when one of crystallographic planes [e.g., (111)] coincides with the plane of the film. In view of various technological factors, a slight deviation of the crystallographic direction [111] from the normal to the film surface always takes place, leading to a deviation of DWs from the normal, which can exceed the corresponding deviation of the crystallographic axis [8, 9]. Here, we investigate the features of the intensity and polarization distributions of the light wave diffracted from an SDS, which are associated with domain wall tilting and the deviation of the distribution of the Faraday magnetization component in the SDS from the binary distribution.

1. DOMAIN STRUCTURE AND TYPES OF MAGNETIC LATTICES

For typical Bi-containing garnet-ferrite films, the exchange constant is $A \approx 3 \times 10^{-7}$ erg/cm, the axial anisotropy constant $K \approx 5 \times 10^4$ erg/cm^3, and the saturation magnetization is $4\pi M_0 \approx 10^3$ G. In this case, the thickness of domain walls is $\tau \cong \pi\sqrt{A/K} \approx 0.1$ μm, and the domain width $S \cong (2\pi L\sqrt{A/K}/M_0^2)^{1/2} \approx 5$ μm (for the film thickness $L \approx 10$ μm). Since $\tau \ll S$, we can assume that the spins are rotated stepwise through 180° upon a transition through a DW. Figure 1a schematically shows an SDS with tilted domain walls. The periodicity axis of the domain structure coincides with the *y* axis, and the normal to the surface, with the *z* axis. We shall assume that the magnetization within domains is oriented parallel to DWs and, in view of their tilting, forms the angles φ and π – φ, with the *y* axis in two groups of domains with opposite magnetizations. The rotation of spins in the SDS takes place at domain walls defined by the planes $z = \tan\varphi\,(y - nS)$, where φ is the angle formed by a DW with the plane of the film and *n* is the number of DWs. For the SDS type under investigation, the distribution of magnetization components averaged over the film thickness can be described by the expression

$$M_\alpha(y) = \frac{1}{L}\int_0^L M_\alpha(y,z)dz = M_0 g(y)\begin{cases}\cos\varphi, & \alpha = y,\\ \sin\varphi, & \alpha = z,\end{cases} \quad (1)$$

where $g(y)$ is a modulating function depicted in Figs. 1b and 1d. Its shape depends considerably on the ratio of the transition region width δ and the domain width *S*. For example, the trapezoidal type of the $M_\alpha(y)$ distribution in the SDS takes place if the transition region width $\delta = L/\tan\alpha < S$. If $\delta = S$, the trapezoidal distribution is transformed into a saw-tooth distribution. For $\delta > S$, the $M_z(y)$ distribution again becomes trapezoidal with the maximum value $M_\alpha = M_{\alpha 0}(1 - 2\Delta/\delta)$, the half-period $S' = \delta - \Delta$, and the transition region width $\delta' = \delta - 2\Delta$. For these types of magnetooptic grating, in the general case of different widths of oppositely magnetized

1063-7834/00/4206-1075$20.00

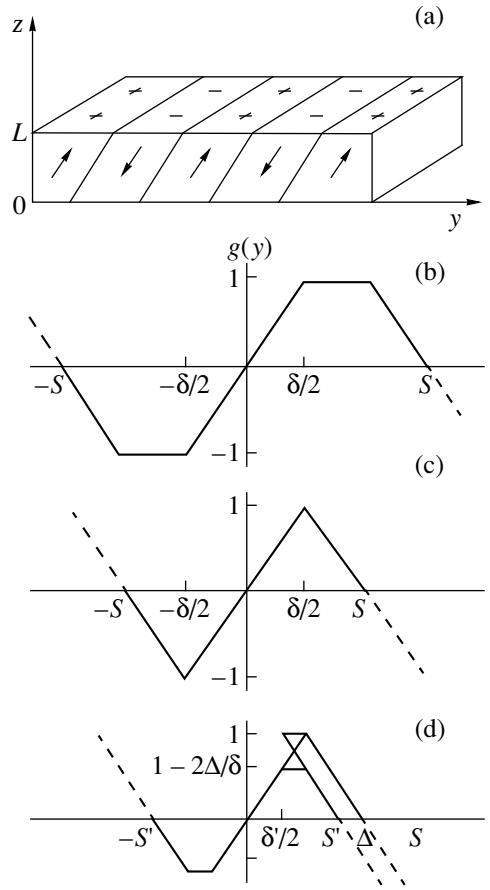

Fig. 1. (a) SDS with tilted DWs and (b–d) various types of modulating function distribution $g(y)$.

domains, the analytical dependence of the modulating function $g(y)$ can be presented as follows:

$$g(y) = \begin{cases} 2(S_2 - y)/\delta, & S_2 - \delta/2 \le y \le S_2, \\ 1, & \delta/2 \le y \le S_2 - \delta/2, \\ 2y/\delta, & -\delta/2 \le y \le \delta/2, \\ -1, & -S_1 + \delta/2 \le y \le -\delta/2, \\ -2(y + S_1)/\delta, & -S_1 \le y \le -S_1 + \delta/2, \end{cases} \quad (2)$$

where S_i is the width of the corresponding domain for an SDS with a period $D = S_1 + S_2$.

2. GENERAL RELATIONS

Let a linearly polarized plane monochromatic wave be incident along the normal to a monocrystalline layer with an SDS in which the distribution of the magnetization component M_z responsible for MOD is described by relation (2). In the thin-layer approximation ($L \ll D^2/\lambda$, where λ is the wavelength of light), the distribution of the far-zone field of the light transmitted through the layer is defined as follows [10]:

$$\mathbf{E}(y_0, z) = C_t \int \mathbf{E}(y, L) \exp(-2\pi i f y) dy. \quad (3)$$

Here, the factor $C_t = (1/\sqrt{\lambda z}) \exp[ik_0(z + y_0^2/2z)]$, $k_0 = 2\pi/\lambda$, $f = y_0/\lambda z$, y_0 is the coordinate in the plane of observation of the diffraction pattern, and y is the coordinate at the output surface of the film. The integration limits in (3) are determined by the size of the illuminated region, which is assumed to be equal to $a = (2N + 1)D$, where N is a large integer ($N \approx 100$ for a laser beam diameter $a \approx 2$ mm and $D \approx 10$ μm). The field at the output surface of the film can be presented in the form

$$\mathbf{E}(y, L) = \hat{T}(y, L)\mathbf{E}_0, \quad (4)$$

where $\hat{T}$ is the transmission matrix determined by the form of the magnetization distribution in the SDS, and $\mathbf{E}_0$ is the field at the input film surface.

In the chosen reference frame, the permittivity tensor of the film with an SDS has the following form in the linear magnetooptical (MO) coupling approximation [10]:

$$\hat{\varepsilon} = \begin{pmatrix} \varepsilon & i f_0 m_z & -i f_0 m_y \\ -i f_0 m_z & \varepsilon & 0 \\ i f_0 m_y & 0 & \varepsilon \end{pmatrix}, \quad (5)$$

where $m_\alpha = M_\alpha/M_0$ are direction cosines of the magnetization vector in the SDS, which are periodic in the coordinate ν, and f_0 is the linear MO parameter. For a wave in a medium whose optical properties are determined by tensor (5), the electric field components can be presented as a superposition of the field of two proper waves:

$$E_\alpha = A_{1\alpha} \exp(ik_1 z) + A_{2\alpha} \exp(ik_2 z). \quad (6)$$

Here, the propagation constants of the corresponding waves are defined as

$$k_{1,2} = \frac{k_0}{\sqrt{2}} [b_{xx} + b_{yy} \pm \sqrt{(b_{xx} - b_{yy})^2 + 4b_{xy}b_{yx}}]^{1/2}, \quad (7)$$

where $b_{\alpha\beta} = \varepsilon_{\alpha\beta} - \varepsilon_{\alpha z}\varepsilon_{z\beta}/\varepsilon_{zz}$, $\alpha, \beta = x, y$. The constants $A_{j\alpha}$ are determined from the boundary conditions and have the form

$$A_{jx} = (-1)^{j/2} 2 \frac{(n_{3-j}^2 - b_{xx})E_{0x} - b_{xy}E_{0y}}{(n_j + 1)(n_1^2 - n_2^2)},$$
$$A_{jy} = (-1)^j 2 \frac{(n_j^2 - b_{xx})[(n_{3-j}^2 - b_{xx})E_{0x} - b_{xy}E_{0y}]}{b_{xy}(n_j + 1)(n_1^2 - n_2^2)}, \quad (8)$$

where $j = 1, 2$; $n_j = k_j/k_0$; and $E_{0\alpha}$ are the amplitudes of the corresponding field components of the wave incident on the film. In accordance with formulas (6)–(8),

the transmission matrix elements for a magnetized layer of thickness L have the form

$$\begin{aligned}
T_{xx} &= \frac{2}{n_2^2 - n_1^2} \\
&\times \left(\frac{n_2^2 - b_{xx}}{1 + n_1} \exp(ik_1 L) - \frac{n_1^2 - b_{xx}}{1 + n_2} \exp(ik_2 L) \right), \\
T_{yy} &= \frac{2}{n_2^2 - n_1^2} \\
&\times \left(-\frac{n_1^2 - b_{xx}}{1 + n_1} \exp(ik_1 L) + \frac{n_2^2 - b_{xx}}{1 + n_2} \exp(ik_2 L) \right), \\
T_{xy} &= \frac{2b_{xy}}{n_2^2 - n_1^2} \left(-\frac{\exp(ik_1 L)}{1 + n_1} + \frac{\exp(ik_2 L)}{1 + n_2} \right), \\
T_{yx} &= \frac{2(n_1^2 - b_{xx})(n_2^2 - b_{xx})}{b_{xy}(n_2^2 - n_1^2)} \left(\frac{\exp(ik_1 L)}{1 + n_1} - \frac{\exp(ik_2 L)}{1 + n_2} \right).
\end{aligned} \tag{9}$$

It follows from (3) that the distribution of the far-zone field of the diffracted wave is determined by the Fourier transform of the field distribution at the output surface of the film. This field can be presented in the form

$$\mathbf{E}(y_0, z) = C_t \hat{D}(y_0, z) \mathbf{E}_0, \tag{10}$$

where the matrix $\hat{D}(y_0, z)$ is the Fourier transform of the transmission matrix and is determined by the form of the magnetization distribution in the SDS. The parameters n_i, k_i, and $b_{\alpha\beta}$ appearing in (9) are periodic functions of the coordinate y, the form of these functions being determined by the nature of the magnetization distribution in the SDS. In order to determine these functions explicitly, we take into account the smallness of the MO parameter ($f_0 \propto 10^{-3}$). Relation (7) leads to the following, relatively accurate expression for the propagation constants:

$$k_{1,2} = k(1 \pm f_0 m_z / 2\varepsilon), \tag{11}$$

where $k = k_0 \sqrt{\varepsilon}$ is complex-valued in the general case, its imaginary component determining the attenuation of the light wave in the film. Substituting (11) into (9), we obtain the following expressions for the transmission matrix elements:

$$\begin{aligned}
T_{xx} &= T_{yy} = 2(k_0/\nu) \\
&\times \exp(ikL)[\cos GL - i(G/\nu)\sin GL], \\
T_{xy} &= -T_{yx} = -2(k_0/\nu) \\
&\times \exp(ikL)[\sin GL + i(G/\nu)\cos GL],
\end{aligned} \tag{12}$$

where $\nu = k_0(1 + \sqrt{\varepsilon})$ and $G = (kf_0/2\varepsilon)g(y)\sin\varphi$. Substituting (12) into (3), we carry out the integration taking into account (2) and obtain the following expression for the elements of the diffraction matrix $\hat{D}$:

$$\begin{aligned}
D_{xx} &= D_{yy} = \frac{e^{ikL}}{1 + \sqrt{\varepsilon}} \frac{\sin \pi f a}{\sin \pi f D} \Big\{ P_1^+ + P_2^+ + R_1^+ + R_2^+ \\
&+ \frac{2}{\pi f} \left(\cos FL - i \frac{F}{\nu} \sin FL \right) \\
&\times [e^{i\pi f \Delta S} \sin \pi f (D - \delta) - \sin \pi f D] \Big\}, \\
D_{xy} &= -D_{yx} = \frac{ie^{ikL}}{1 + \sqrt{\varepsilon}} \frac{\sin \pi f a}{\sin \pi f D} \Big\{ P_1^- - P_2^- + R_1^- - R_2^- \\
&- \frac{2}{\pi f} \left(\sin FL + i \frac{F}{\nu} \cos FL \right) \\
&\times [e^{i\pi f \Delta S} \cos \pi f (D - \delta) - \cos \pi f D] \Big\},
\end{aligned} \tag{13}$$

where $\Delta S = S_1 - S_2$, and the following notation has been introduced:

$$P_i^+ = \delta \frac{\sin \beta_i}{\beta_i} \left(1 - \frac{iF}{2\nu\beta_i} \right) [e^{i\pi f \Delta S} \cos(\pi f D - \beta_i) \pm \cos \beta_i],$$

$$R_i^+ = \frac{iF\delta}{2\nu\beta_i} [e^{i\pi f \Delta S} \cos(\pi f D - 2\beta_i) \pm \cos 2\beta_i],$$

$\beta_{1,2} = (FL \pm \pi f \delta)/2$ and $F = F_0 \sin\varphi$, with $F_0 = kf_0/2\varepsilon$ being the specific Faraday rotation of the film material.

3. FIELD AT DIFFRACTION MAXIMA

An analysis of expressions (13) proves that, in the general case, the diffraction maxima in the MOD spectrum are located at the points $f = n/D$, where $n = 0, \pm 1, \pm 2, \ldots$; their angular position is determined by the relation $\sin\psi_n = n\lambda/D$, and their angular width is $\Delta\psi_n = \lambda/a$. We will analyze relations (13) for a linearly polarized incident radiation, assuming that the field $\mathbf{E}_0 = \boldsymbol{\tau}_x E_0$, i.e., is polarized along the x axis.

Let us determine the field at the zeroth diffraction maximum for the asymmetric SDS with tilted DWs. Assuming in (13) that the coordinate in the plane of observation is $y_0 = 0$, i.e., $f = 0$, we obtain

$$E_x^{(0)} = A \frac{e^{-\alpha L/2}}{1 + \sqrt{\varepsilon}} \left\{ 2 \frac{\delta}{D} \left(\frac{\sin FL}{FL} - \cos FL \right) + \cos FL \right.$$

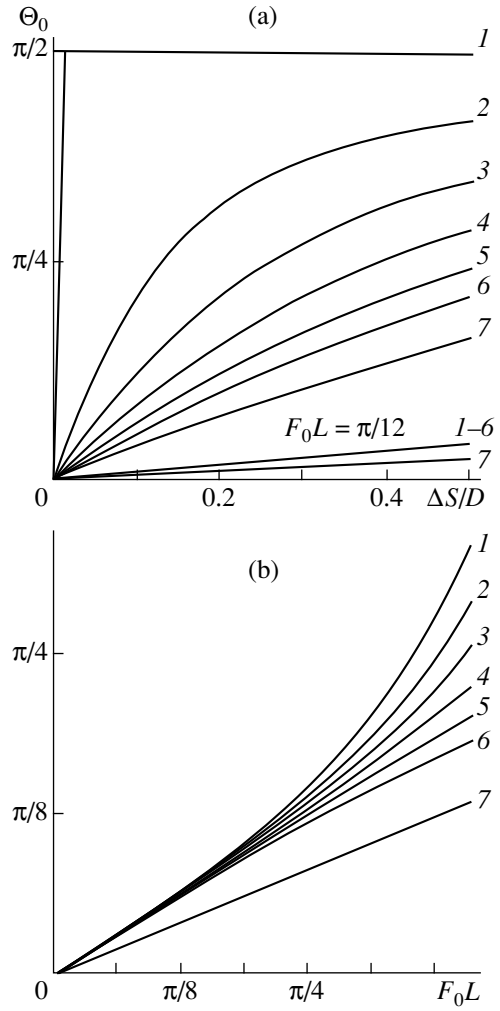

Fig. 2. Angle of rotation Θ_0 of the polarization plane at the zeroth diffraction maximum as a function (a) of the SDS asymmetry parameter $\Delta S/D$ for $F_0L = \pi/2$ and $\pi/12$ and (b) of the effective film thickness F_0L for $\Delta S/D = 0.5$ for the values of the parameter $\delta/D = 0, 0.1, \ldots, 0.6$ (curves *1–7*).

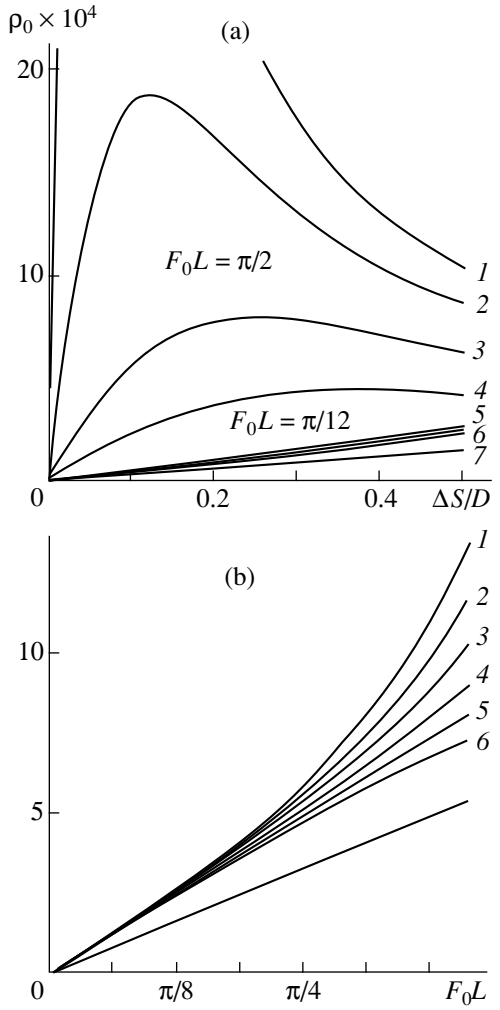

Fig. 3. Dependence of ellipticity ρ_0 at the zeroth diffraction maximum (a) on the parameter $\Delta S/D$ for $F_0L = \pi/2$ and $\pi/12$ and (b) on the parameter F_0L for $\Delta S/D = 0.5$ for $\delta/D = 0, 0.1, \ldots, 0.6$ (curves *1–7*).

$$+ i\frac{1}{\nu L}\left[2\frac{\delta}{D}\left(\cos FL - \frac{\sin FL}{FL}\right) - FL\sin FL\left(1 - 2\frac{\delta}{D}\right)\right]\Bigg\}, \quad (14)$$

$$E_y^{(0)} = -A\frac{e^{-\alpha L/2}}{1+\sqrt{\varepsilon}}\frac{\Delta S}{D}\left(\sin FL + i\frac{F}{\nu}\cos FL\right),$$

where $A = C_t 2e^{ik'L}E_0 a$, $k' = \mathrm{Re}k$, and $\alpha = \mathrm{Im}k$ is the optical absorption coefficient. In an analysis of the features of the magnetization distribution in a SDS, based on diffraction measurements, the knowledge of the angle of rotation of the polarization plane and the ellipticity of the light field at diffraction maxima is essential. For calculating the angle of rotation Θ of the polarization plane and the ellipticity ρ, we will use the following expressions [11]:

$$\tan 2\Theta = \frac{2|E_x||E_y|}{|E_x|^2 - |E_y|^2}\cos(\varphi_y - \varphi_x),$$
$$\tan 2\chi = \frac{2|E_x||E_y|}{|E_x|^2 + |E_y|^2}\sin(\varphi_y - \varphi_x), \quad (15)$$

where the amplitudes and phases of the corresponding components of the diffracted light field are introduced as follows: $E_\alpha = |E_\alpha|\exp(i\varphi_a)$, $\alpha = x, y$, and the auxiliary angle χ defines the ellipticity $\rho = \tan\chi$ as the ratio of the semiaxes of the polarization ellipse.

Figure 2 shows the dependences of the angle of rotation Θ_0 of the polarization plane at the zeroth diffraction maximum (a) on the asymmetry parameter $\Delta S/D$ of the domain structure for two values of the effective film

thickness $F_0L = \pi/2$ and $\pi/12$ and (b) on the effective film thickness F_0L for a fixed value of the asymmetry parameter $\Delta S/D = 0.5$. These dependences are given for various values of the transition region width $\delta/D = 0$, 0.1, …, 0.6 (curves *1–7*). For small film thicknesses ($E_0L \ll 1$), the effect of DW tilting on the rotational angle Θ_0 of the polarization plane is practically absent for an SDS in which the tilting of DWs does not lead to their overlapping. The corresponding dependences $\Theta_0(\Delta S/D)$ for $\delta/\Delta \le 0.5$ merge into one (curves *1–6*). In the case of DW overlapping (Fig. 1d), the angle Θ_0 decreases due to a reduced effective Faraday rotation. In thick layers, the DW tilt considerably affects the value of the angle Θ_0. It is interesting to note that, for $F_0L = \pi/2$ and vertical DWs, the angle $\Theta_0 = \pi/2$ and does not depend on the asymmetry parameter for $\Delta S/D \neq 0$. For a symmetric SDS, the rotation of the polarization plane at the zeroth diffraction maximum is absent for both tilted and vertical DWs, and the light field is polarized in the same way as the incident radiation.

Figures 3a and 3b show the dependences of the ellipticity ρ_0 of the light field at the zeroth diffraction maximum on the same parameters as in Fig. 2 and for the same fixed values of the parameters F_0L, $\Delta S/D$, and Δ/D. It can be seen that the DW tilt also considerably affects the ellipticity. However, the order of magnitude of the ellipticity for thin, as well as for thick, layers ($\rho_0 \propto 10^{-4}$–10^{-3}) is such that we have a virtually linear polarization of the light field at the zeroth maximum.

We will carry out the subsequent analysis for a symmetric SDS ($S_1 = S_2$, $\Delta S = 0$). The DW tilt considerably modifies the form of the diffraction spectrum. In contrast to a symmetric SDS with vertical domain walls, the spectrum in the present case contains, along with odd maxima of the *y* polarization ($fD = 2m + 1$), also even orders ($fD = 2m$) with the *x* polarization:

$$\frac{E_x^{2m}}{A} = \frac{e^{-\alpha L/2}}{1+\sqrt{\varepsilon}}\left[\frac{2\sin\pi n\delta/D}{\pi n}\left(i\frac{F}{\nu}\sin FL - \cos FL\right) + \frac{\delta}{2D}\left(2U_1 - i\frac{F}{\nu}V_1\right)\right],$$

$$\frac{F_y^{(2m+1)}}{A} = i\frac{e^{-\alpha L/2}}{1+\sqrt{\varepsilon}}\left[\frac{2\cos\pi n\delta/D}{\pi n}\left(i\frac{F}{\nu}\cos FL + \sin FL\right) + \frac{\delta}{4D}\left(2U_2 - i\frac{F}{\nu}V_2\right)\right], \quad (16)$$

$$U_j = \frac{\sin 2\beta_2}{\beta_2} - (-1)^j\frac{\sin 2\beta_1}{\beta_1},$$

$$V_j = \frac{\sin 2\beta_2}{\beta_2^2} - \frac{\cos 2\beta_2}{\beta_2} - (-1)^j\left(\frac{\sin 2\beta_1}{\beta_1^2} - \frac{\cos 2\beta_1}{\beta_1}\right),$$

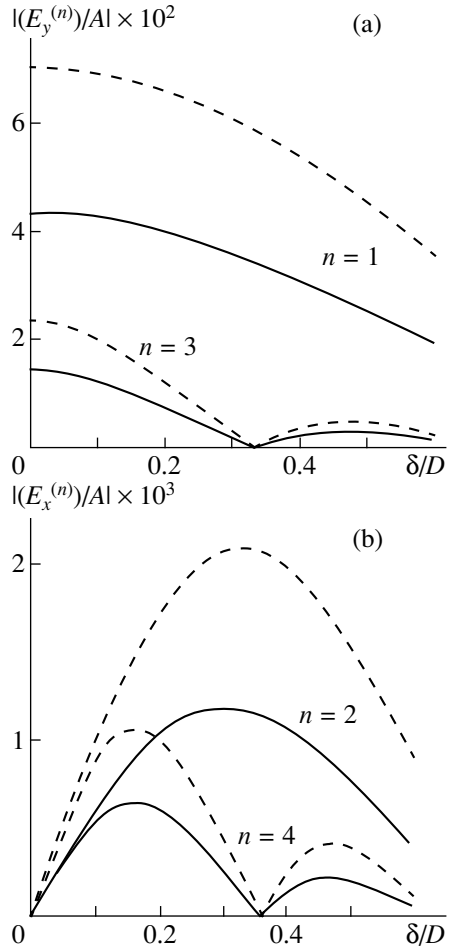

Fig. 4. Field amplitude at the first four diffraction maxima as a function of the transition region width δ/D for a symmetric SDS, $L = 8$ μm, $F_0 = 1$ deg/μm, and $\alpha = 500$ cm^{-1}.

where $2\beta_{1,2} = FL \pm \pi n\delta/D$. For $\delta = 0$, the diffraction spectrum contains, as expected [6], only odd diffraction orders with the *y* polarization, namely,

$$E_x^{(2m)} = 0,$$
$$E_y^{(2m+1)} = A\frac{e^{-\alpha L/z}}{1+\sqrt{\varepsilon}}\frac{2i}{\pi n}\left(\sin FL + i\frac{F}{\nu}\cos FL\right). \quad (17)$$

Figure 4 shows the field amplitude at (a) the first two odd and (b) two even diffraction maxima as functions of the width δ/D of the transition region for a film with a symmetric SDS, the thickness $L = 8$ μm, and the parameters $F = 1$ deg/μm and $\alpha = 500$ cm^{-1}. The curves show that in even orders, the field attains maximum values for $\delta \neq 0$, while in odd orders the amplitude is maximal for vertical DWs. Dashed curves obtained without the boundary conditions (8), i.e., in the absence of reflection of the wave incident on the film, are shown for comparison. The difference between these curves signifies the fraction of incident power of the light field that dissipates to the corresponding diffraction orders

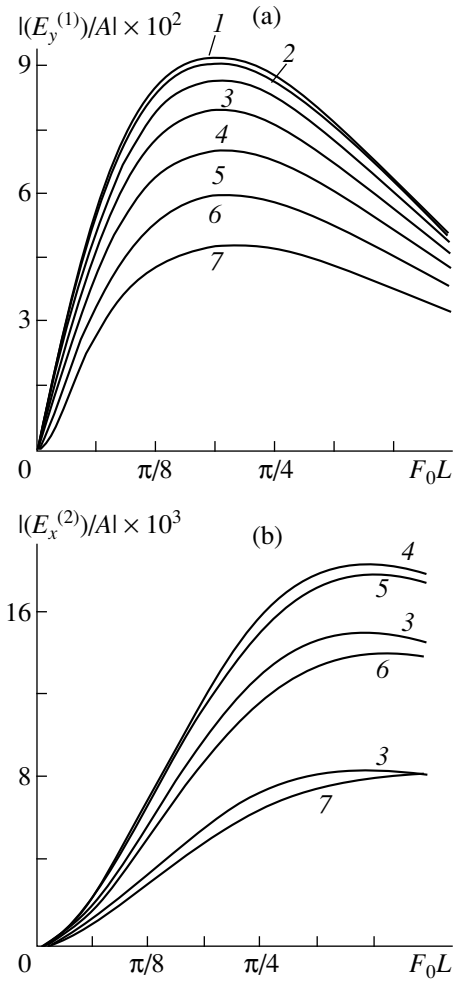

Fig. 5. Field amplitude at (a) the first and (b) the second diffraction maximum as a function of the film thickness for various values of the parameter $\delta/D = 0, 0.1, \ldots, 0.6$ (curves *1–7*).

of the reflected light field. Figure 5 gives the amplitudes of the field in the first two diffraction orders as functions of the film thickness for various values of the parameter δ/D. It can be seen that in the first diffraction order, $E_y^{(1)}$ (Fig. 5a), attains its maximum value for smaller film thicknesses than in the second order, $E_x^{(2)}$ (Fig. 5b). The maximum values of the amplitudes attained in the indicated diffraction orders greatly depend on the width δ of the transition region, i.e., on the slope of the DW.

The above analysis reveals that the DW tilt and the deviation of the distribution of the Faraday magnetization component from the binary distribution considerably affect the MOD characteristics. The diffraction pattern in this case differs from that for vertical DWs not only quantitatively, but also by the presence of even diffraction orders for a symmetric SDS. The polarization and intensity parameters of the field at diffraction maxima change with the DW slope, displaying typical dependences on the SDS parameters.

REFERENCES

1. G. S. Kandaurova and V. V. Zverev, Fiz. Tverd. Tela (Leningrad) **17** (4), 1061 (1975) [Sov. Phys. Solid State **17** (4), 676 (1975)].
2. D. I. Sementsov and A. M. Morozova, Mikroélektronika **8** (2), 99 (1979).
3. V. V. Katal'nikov, A. V. Kovalev, and V. N. Pavlov, Zh. Tekh. Fiz. **55** (2), 394 (1985) [Sov. Phys. Tech. Phys. **30** (2), 231 (1985)].
4. D. L. Sementsov and R. M. Grechishkin, Phys. Status Solidi A **118**, 271 (1988).
5. E. N. Il'icheva, A. V. Dubova, V. K. Peterson, *et al.*, Fiz. Tverd. Tela (St. Petersburg) **35** (5), 1167 (1993) [Phys. Solid State **35** (5), 594 (1993)].
6. G. S. Kandaurova, V. N. Mal'tsev, and V. Kh. Osadchenko, Opt. Spektrosk. **67** (2), 413 (1989) [Opt. Spectrosc. **67** (2), 241 (1989)].
7. Yu. N. Zubkov and I. M. Kozhemyakin, Izv. Vyssh. Uchebn. Zaved., Ser. Fiz., No. 9, 68 (1997).
8. A. M. Balbashov and A. Ya. Chervonenkis, *Magnetic Materials for Microelectronics* (Énergiya, Moscow, 1979).
9. O. L. Galkin and P. E. Zil'berman, Zh. Tekh. Fiz. **56** (7), 1379 (1986) [Sov. Phys. Tech. Phys. **31** (7), 810 (1986)].
10. G. A. Smolenskiĭ and V. V. Lemanov, *Ferrites and Their Technical Applications* (Nauka, Leningrad, 1975).
11. M. Born and R. Wolf, *Principles of Optics* (Pergamon Press, Oxford, 1969, 4th ed.; Nauka, Moscow 1970).

Translated by N. Wadhwa

Physics of the Solid State, Vol. 42, No. 6, 2000, pp. 1081–1086. Translated from Fizika Tverdogo Tela, Vol. 42, No. 6, 2000, pp. 1049–1054.

MAGNETISM AND FERROELECTRICITY

On the Interaction of a Shear Wave with a Moving Domain Wall in a Nonlinear Response of the Spin Subsystem

E. A. Vilkov[1], V. G. Shavrov[2], and N. S. Shevyakhov[1]

[1] *Institute of Radio Engineering and Electronics, Russian Academy of Sciences, 432011 Ul'yanovsk, Russia*
e-mail: ufire@mv.ru

[2] *Institute of Radio Engineering and Electronics, Russian Academy of Sciences, ul. Mokhovaya 18, Moscow, 103907 Russia*
e-mail: shavrov@mail.cplire.ru

Received July 9, 1999; in final form, October 29, 1999

Abstract—A solution of the problem of parametric interaction between a plane monochromatic shear wave and a uniformly moving 180°-domain wall of a garnet-ferrite crystal is obtained in the exchangeless magnetostatic approximation by using the perturbation method under the conditions of a nonlinear response of the spin subsystem. It is shown that in a ferromagnetic resonance with magnetostatic oscillation of stray fields, the nonlinearity of the spin subsystem leads to the excitation of shear waves of triple frequency, which may have amplitudes comparable with that of the incident wave for oscillations doubly localized by a domain wall. © *2000 MAIK "Nauka/Interperiodica".*

Magnetic crystalline dielectrics are known to possess a considerable nonlinearity associated with the spin subsystem and effective unharmonism of coupled acoustic and spin waves. The anharmonism of magnetoelastic waves is manifested most strongly in antiferromagnets [1]. In ferrites, the spin–phonon coupling is relatively weak, and it is the spin subsystem that serves as the main source of nonlinear effects (generation of harmonics, self-action of waves, etc.) [2, 3].

It was proved earlier [4] in the linear approximation that a reflection of a shear wave incident at an angle on a 180° domain wall (DW) uniformly moving in a crystal of the yttrium–iron garnet (YIG) type may induce an effective resonance response of the spin subsystem through magnetostatic stray fields excited in its neighborhood. Under these conditions, one can naturally expect that nonlinear properties of the spin subsystem will also be manifested most clearly. This work aims to verify this hypothesis. It is appropriate to note here that in the most convenient (for experimental realization) case of the normal incidence of a shear wave on a DW such a verification is ruled out in view of the absence of the response of the spin subsystem, since magnetostatic stray fields are not excited in this case [5, 6]. Another feature of the problem under consideration is that the localization of magnetostatic fields at DWs [4], whose resonance excitation we attribute to a possible manifestation of a noticeable nonlinearity of the spin subsystem, allows us to speak of a "boundary" nature of magnetic nonlinearity in the parametric interaction of an incident wave with a moving DW.

We assume that in the laboratory (crystallographic) reference frame *xyz*, shear waves propagate in the (001) plane of garnet ferrite with displacements $\mathbf{u}_j = (0, 0, u_z^{(j)})$ which are collinear with the spontaneous magnetizations $\mathbf{M}_0^{(j)}$ in domains ($\mathbf{M}_0^{(j)} \uparrow\downarrow \mathbf{M}_0^{(j)} \parallel [001]$, with $j = 1, 2$ being the number of a domain) separated in the (010) plane by a geometrically thin and structureless 180° DW with the running coordinate $y_d = V_d t$, where t is the time and V_d is the velocity of the DW. Spontaneous magnetizations $M_0^{(j)}$ and internal magnetic fields $H_i^{(j)}$ in the domains can accordingly be ascribed (taking into account magnetic anisotropy and the action of external, generally nonuniform, gradient magnetic fields controlling the DW displacement) the following values:

$$M_0^{(j)} = (-1)^{(j+1)} M_0, \quad H_i^{(j)} = (-1)^{(j+1)} H_i, \quad M_0 > 0, \quad H_i > 0, \tag{1}$$

where $j = 1$ for $y > y_d$ and $j = 2$ for $y < y_d$. Since we are using the exchangeless magnetostatic approximation, the adopted model of a DW will be quite satisfactory in the interval of "exchangeless" wave numbers $k < k^*$ (for example, $k^* \sim 10^5$ cm^{-1} for YIG) and frequencies ω up to values slightly exceeding the "forbidden" gap in the spectrum of exchangeless magnetoelastic waves [7]. Apart from the fulfillment of the condition $k\Delta \ll 1$ (Δ is the DW thickness) ensured by the above circumstances, we also presume a low structural sensitivity of domain walls to external controlling effects [8] that cause motion with a preset velocity, which is typical of garnet ferrites far from the phase transition. In order to exclude the Cerenkov instability manifested through the magnetostriction mechanism of DW instability [9], we impose the constraint $|\mathbf{V}_d| < c_t$, where c_t is the veloc-

ity of shear waves in the absence of magnetoelastic coupling.

We will use the equation of motion for magnetic moment disregarding losses [1, 2, 7]

$$\frac{\partial \mathbf{M}_j}{\partial t} = \gamma\left[\frac{\mathbf{M}_j}{M_0}, \frac{\partial \omega_j}{\partial(\mathbf{M}_j/M_0)}\right] \tag{2}$$

and the equation of motion in the theory of elasticity

$$\rho\frac{\partial^2 u_i^{(j)}}{\partial t^2} = \frac{\partial T_{ik}^{(j)}}{\partial x_k}, \quad T_{ik}^{(j)} = \frac{1+\delta_{ik}}{2}\frac{\partial w_j}{\partial u_{ik}^{(j)}}. \tag{3}$$

Here, $T_{ik}^{(j)}$ is the mechanical stress tensor, w_j is the energy density of the crystal within a domain, γ is the gyromagnetic ratio, ρ is the density, $u_{ik}^{(j)}$ is the strain tensor, and $x_k = x, y, z$ for $k = 1, 2, 3$, respectively. In the exchangeless magnetostatic approximation

$$w_j = w_U^{(j)} + w_{MU}^{(j)} + w_H^{(j)}, \tag{4}$$

where the elastic $w_U^{(j)}$, magnetoelastic $w_{MU}^{(j)}$, and Zeeman $w_H^{(j)}$ energies of interaction for the waves in question under the above assumptions are defined as

$$\begin{aligned} w_U^{(j)} &= \frac{\lambda_{44}}{2}(\nabla u_z^{(j)})^2, \\ w_{MU}^{(j)} &= 2b_{44}M_s(\mathbf{m}^{(j)}\nabla u_z^{(j)}), \\ w_H^{(j)} &= -\mathbf{M}_s^{(j)}\mathbf{H}_i^{(j)} - \mathbf{m}^{(j)}\mathbf{h}^{(j)}. \end{aligned} \tag{5}$$

Here, b_{44} is the active component of the magnetoelastic interaction tensor, λ_{44} is the elastic modulus, $\mathbf{m}^{(j)}$ is the magnetic-moment perturbation, $\mathbf{h}^{(j)}$ is the dynamic magnetic field, and ∇ is the nabla operator in the *xy* plane. Substituting expressions (4) and (5) into (2) and (3), retaining in (3) the terms characterizing the magnetic nonlinearity, and taking into account (1), we obtain

$$\rho\frac{\partial^2 u_z^{(j)}}{\partial t^2} = \lambda_{44}\nabla^2 u_z^{(j)} + (-1)^{j+1}\frac{\beta}{M_0^2}(\nabla \mathbf{M}_j)M_z^{(j)}, \tag{6}$$

$$\frac{\partial \mathbf{M}_j}{\partial t} = \left\{\mathbf{M}_j, \left[\frac{\beta}{M_0^2}(M_x^{(j)}\nabla u_z^{(j)}) - \mathbf{H}_i^{(j)} - \mathbf{h}^{(j)}\right]\right\}, \tag{7}$$

where

$$\mathbf{M}_j = (m_x^{(j)}, m_y^{(j)}, m_z^{(j)}), \quad M_z^{(j)} = m_z^{(j)} + (-1)^{j+1}M_0,$$

$\beta = 2b_{44}M_s^2$ being the magnetoelastic coefficient. Equations (6) and (7) should be supplemented with the magnetostatics equations

$$\nabla \mathbf{b}^{(j)} = 0, \quad \mathbf{b}^{(j)} = \mathbf{h}^{(j)} + 4\pi\mathbf{m}^{(j)}, \quad \mathbf{h}^{(j)} = -\nabla\varphi_j. \tag{8}$$

Here, φ_j is the magnetostatic potential and $\mathbf{b}^{(j)}$ is the dynamic magnetic induction vector.

The solution of the system of equations (6) and (7) satisfies the following boundary conditions at a DW:

$$\begin{aligned} u_z^{(1)}\big|_{y=y_d} &= u_z^{(2)}\big|_{y=y_d}, \quad T_{yz}^{(1)}\big|_{y=y_d} = T_{yz}^{(2)}\big|_{y=y_d}, \\ \varphi_1\big|_{y=y_d} &= \varphi_2\big|_{y=y_d}, \quad b_y^{(1)}\big|_{y=y_d} = b_y^{(2)}\big|_{y=y_d}, \end{aligned} \tag{9}$$

which reflect in the nonrelativistic ($|\mathbf{V}_d| \ll c$, $c_t \ll c$) case (without taking into account the corrections $|\mathbf{V}_d/c| \ll 1$, where c is the velocity of light) the continuity of shear displacements and stresses, as well as magnetic potentials and normal components of the magnetic induction. The weak nonlinearity of the spin subsystem is activated by the standard procedure of retaining only the lowest-order nonlinear terms in the expansion of $M_z^{(j)}$ in the parameter $(m_x^{(j)2} + m_y^{(j)2})/M_0^2$ [3, 11]; taking relation (1) into consideration, we obtain

$$M_z^{(j)} \approx (-1)^{j+1}M_0\left(1 - \frac{m_x^{(j)2} + m_y^{(j)2}}{2M_0^2}\right). \tag{10}$$

This formula shows that the correction to the spontaneous magnetizations, $m_z^{(j)}$, is of the second order of smallness. It does not appear in equations (7) for the components $m_x^{(j)}$ and $m_y^{(j)}$, which are transverse to the spontaneous magnetizations, so we can assume that the quantities $m_x^{(j)}$ and $m_y^{(j)}$ are known by solving the linear problem [4], while $m_z^{(j)}$ are determined by these components in accordance with (10). In this case, the component $u_{zA}^{(j)} = u_z^{(j)} - u_{z0}^{(j)}$ of the shear displacement field associated with the nonlinearity of the spin subsystem and supplementing the solution [4] $u_{z0}^{(j)}$ satisfies, in accordance with (6), (7), and (10), the equation

$$\begin{aligned} &\rho\frac{\partial^2 u_{zA}^{(j)}}{\partial t^2} - \lambda_{44}\nabla^2 u_{zA}^{(j)} \\ &\simeq \frac{\beta}{M_0^2}\left[\frac{\partial(m_x^{(j)}m_z^{(j)})}{\partial x} + \frac{\partial(m_y^{(j)}m_z^{(j)})}{\partial y}\right]. \end{aligned} \tag{11}$$

In terms of structure, it is a nonhomogeneous wave equation whose right-hand side contains the field sources $u_{zA}^{(j)}$ of magnetic origin, which are distributed over the volume of domains and are known from the linear solution [4].

In order to construct a solution of equation (11), we go over to the reference frame *xyz* in which the DW is at rest and which is connected with the laboratory reference frame *xyz* through the Galilei transformation $y = \tilde{y} = y - V_d t$, $\tilde{t} = t$, $\tilde{x} = x$, and $\tilde{z} = z$ in view of the nonrelativistic nature of the magnetostatic approxima-

tion. Typically, the frequency of oscillations and waves described by the linear solution in the intrinsic frame of reference of the DW is the time invariant of the phase:

$$\Omega = \omega - k_y V_d = \omega' - k'_y V_d \equiv \text{inv}, \qquad (12)$$

where ω and ω' are the frequencies and k_y, k'_y are the transverse (relative to the DW) components of the wave vectors of the incident (or transmitted directly) and reflected shear waves in the laboratory frame of reference. Condition (12) expresses the time synchronism of all oscillations appearing in the linear solution of the wave problem. It ensures, apart from the equality of the wave vector components at the DW to the quantity $k_x = k\sin\theta$, $k_x \geq 0$, (where k is the wave number of the incident shear wave and θ is the angle of incidence), the fulfillment of the boundary conditions (9) if we assume that $u_z^{(j)}$ stands for $u_{z0}^{(j)}$.

The nonlinear component of the solution can be presented as a purely elastic field $u_{zA}^{(j)}$ that is self-consistent to the nonlinear magnetostatic fields of the bulk sources on the right-hand side of equation (11). Bearing in mind a higher order of smallness of magnetic sources on the right-hand side of (11) in comparison with the magnetic nonlinearity of the solution taken into account by formula (10), we can assume that the field $u_{zA}^{(j)}$ satisfies the first pair of the boundary conditions (9), in which $u_z^{(j)}$ is automatically replaced by $u_{zA}^{(j)}$. In other words, the residual term associated with the field $u_{zA}^{(j)}$ in the complete mechanical boundary conditions (9) is negligible.

At the same time, the fact that $u_{zA}^{(j)}$ automatically satisfies the boundary conditions (9) indicates that $u_{zA}^{(j)} \sim m_{x,y}^{(j)} m_z^{(j)}\big|_{y=y_d}$ in accordance with the form of the right-hand side of equation (10). For this reason, in the intrinsic frame of reference of the DW (for $\tilde{y} = 0$), we have, in accordance with (12), $u_{zA}^{(j)} \sim \exp(-i3\Omega)\exp(i3k_x\tilde{x})$. Among solutions to the nonhomogeneous ordinary differential equation formed in this case from (11), only the particular solution for a nonzero right-hand side has a physical meaning. The formally existing general solution of the homogeneous differential equation is simply discarded, since the boundary conditions (9) alone are insufficient to determine the unique solution of equation (11) by taking this solution into account. It should be noted, however, that the general solution of the homogeneous differential equation might be required for analyzing the parametric effects of interaction between moving DWs and nonstationary fields (pulses) of shear waves, or in the interaction of monochromatic shear waves with abruptly accelerated or decelerated DWs. In the latter case, the additional term in the solution of equation (11), which is determined by the start/stop condition for the DW (initial condition), will describe transient acoustic processes that are possible under the conditions of "breakdown" or stabilization of the domain structure.

On the basis of the above arguments, we can present the nonlinear part of the solution $u_{zA}^{(j)}$ for a plane monochromatic shear wave having an amplitude U_0 and incident on a DW from the side of the domain with $j = 1$ at an angle θ in the laboratory frame of reference as follows:

$$u_{zA}^{(j)} = \exp(3ik_x x)\sum_{p=1}^{3} A_p^{(j)} \exp[i(ph_y^{(j)} y - \omega_p^{(j)} t)] \times \exp[(-1)^j (3-p)k_x (y - y_d)], \qquad (13)$$

where $k_y^{(1)} \equiv k'_y$, $k_y^{(2)} \equiv k_y$, and $\omega_p^{(j)}$ are the partial frequencies of wave oscillations, defined, in accordance with (10), by the relations

$$\omega_p^{(1)} = p\omega' + \Omega(3-p), \quad \omega_p^{(2)} = p\omega + \Omega(3-p). \qquad (14)$$

The amplitudes $A_p^{(1)}$ of waves described by solution (13) in the region $y > y_d$ have the form

$$A_1^{(1)} = U_0 R C^2 \zeta^* \frac{M_0^2}{\beta^2} \frac{\omega_0^3 k_x^2 \xi^2}{(\omega' - \omega_0)(\omega'^2 - \omega_k^2)} \times \left[\left(\frac{2V_d}{c_t}\xi_+ - \frac{3\omega'}{c_t} i\right)^2 + 3k'^2 + 2\xi_+^2\right]^{-1},$$

$$A_2^{(1)} = -U_0^2 R^2 C \zeta^* \frac{M_0}{\beta} \frac{\omega_0^3 k_x \xi_+}{(\omega'^2 - \omega_k^2)^2} \times \frac{(\omega' - \omega_0)\xi_+ k_x + (3\omega_0 + \omega')k'^2}{((V_d/c_r)\zeta_+ - 3(\omega'/c_t)i)^2 + 6k'^2 + 2\xi_+^2}, \qquad (15)$$

$$A_3^{(1)} = -U_0^3 R^3 \frac{\zeta}{6} \frac{\omega_0^2(\omega'^2 - \omega_0^2)}{(\omega'^2 - \omega_k^2)^2} k'^2.$$

In order to determine the amplitudes $A_p^{(2)}$ ($p = 1, 2, 3$), it is sufficient to carry out the following substitutions in formulas (15): $A_p^{(1)} \longrightarrow A_p^{(2)}$, $R \longrightarrow T$, $C \longrightarrow -D$, $\omega' \longrightarrow \omega$, $k'_y \longrightarrow -k_y$, $k_x \longrightarrow -k_x$, $k' \longrightarrow k$. It should be recalled that C and D are the amplitudes of oscillations of magnetostatic stray fields, R is the reflection coefficient, and T is the transmission coefficient of a shear wave through the DW, which are known from the solution of the linear problem [4]. In expressions (15), the following notation is introduced: $\zeta = \chi\lambda_{44}/\omega_0 M_0$, $\zeta^* = \zeta\chi$, $\chi = \gamma\beta^2/\lambda_{44}\omega_0 M_0$ is the magnetoelastic

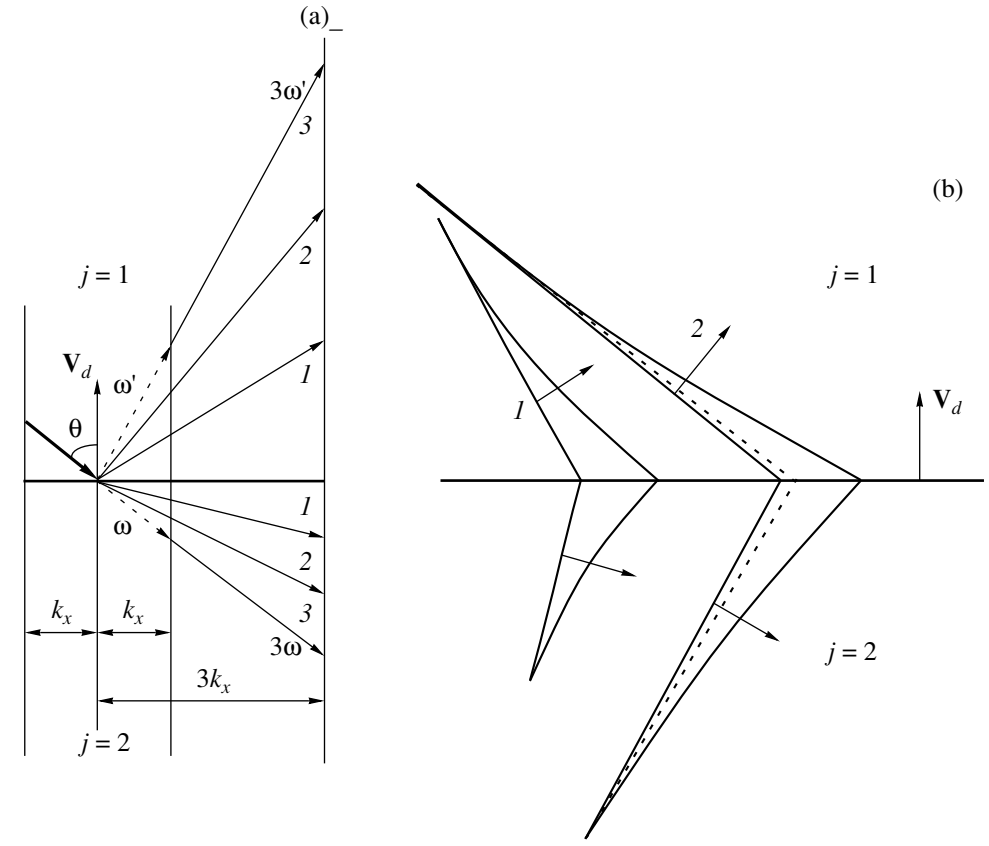

Fig. 1. Ray pattern of refraction of a shear wave at a moving DW, taking into account the magnetic nonlinearity of garnet ferrite (a) and the profiles of shear displacement distribution along the wavefronts of the third harmonic waves, localized by DW (b). The figures correspond to the numbers of $p = 1, 2, 3$ of the third-harmonic waves; arrows in (b) depict the vectors of wave normals for waves with the numbers $p = 1, 2$.

coupling constant, $\xi_\pm = k_x \pm ik_y$, $\omega_k = [\omega_0(\omega_0 + \omega_m)]^{1/2}$ is the magnetoacoustic resonance frequency, $\omega_0 = \gamma H_i$ is the uniform precession frequency, $\omega_m = 4\pi\gamma M_0$ is the magnetization frequency, and $k' = (k_x^2 + k_y'^2)^{1/2}$ is the wave number of the reflected wave. In accordance with (13), we conclude that, in addition to the first-harmonic waves of the fundamental frequency ω or of the Doppler-shifted frequency ω' (these waves have, respectively, the meaning of the directly transmitted or reflected shear wave of the linear solution [4]), a triplet of shear waves with the triple frequency 3Ω in the intrinsic frame of reference of a DW (referred to as third-harmonic waves) are formed in each domain under the effect of magnetic nonlinearity of the crystal. In the laboratory frame of reference, third-harmonic waves experience Doppler shifts due to the motion of the DW. If $V_d > 0$ (approaching DW), the limitations $k_y' > 0$ and $k_y < 0$ following from the radiation condition imply that, in accordance with (10), $\omega' > \Omega$ and $\omega < \Omega$, and it follows from (14) that the frequencies $\omega_p^{(1)}$ increase relative to 3Ω, while $\omega_p^{(2)}$ decrease. For $V_d < 0$ (moving away DW), the reverse inequalities are observed.

The largest Doppler shifts are experienced by third-harmonic waves with number $p = 3$, which are not localized by the DW. Their frequencies exceed those of the corresponding first-harmonic waves by a factor of three, and they propagate collinearly to the latter waves. Thus, the singled-out component of solution (13) is a collinear correction to the first-harmonic waves, which appears owing to magnetic nonlinearity.

Along with the multiplicity of transverse components of wave vectors, lower numbers of the third harmonic ($p = 2, 1$, respectively) also exhibit single and double localization at a DW, which can be estimated relative to magnetostatic stray fields. Figure 1 gives a visual idea of the structure of lower numbers of the third harmonic, where for the adopted configuration of rays of the first (dashed arrows) and third harmonics (solid arrows labeled according to $p = 1, 2, 3$), which is determined by the preset wave vector of the incident wave (light arrow) and the vector V_d (Fig. 1a), the positions of wavefronts and the distribution of shear displacements in the third-harmonic waves with numbers $p = 1, 2$ are depicted (Fig. 1b). The boundary nature of

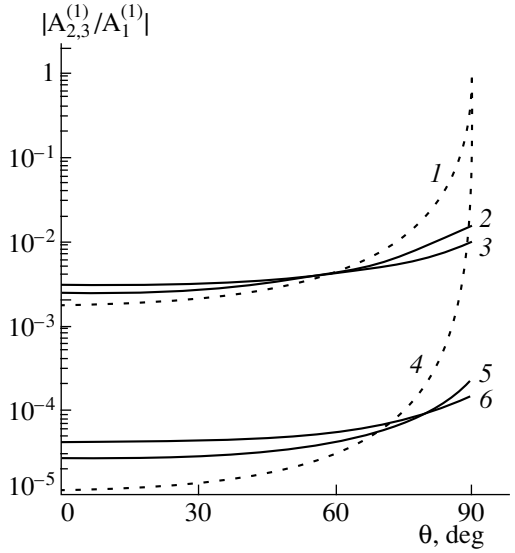

Fig. 2. Angular dependences of the quantities $\left|A_2^{(j)}/A_1^{(j)}\right|$ for $V_d/c_t = 0$ (curve *1*), 0.2 (curve *2*), and 0.3 (curve *3*) and angular dependences of the quantities $\left|A_3^{(j)}/A_1^{(1)}\right|$ for $V_d/c_t = 0$ (curve *4*), 0.2 (curve *5*), and 0.3 (curve *6*).

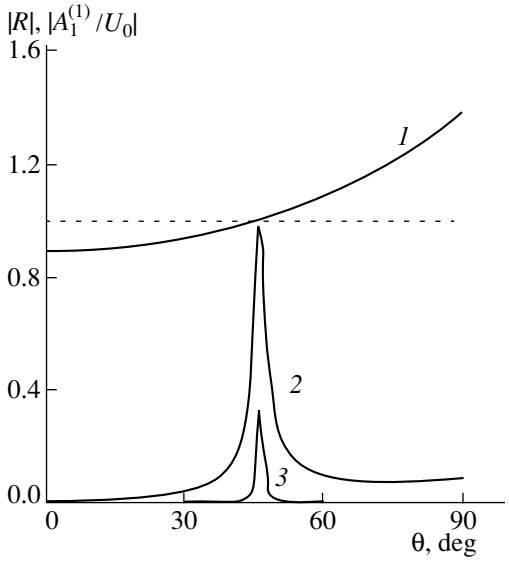

Fig. 3. FMR peaks for a reflected wave (curve *2* describes the dependence $|R(\theta)|$) and the third-harmonic wave for $j = 1$ (curve *3* describes the dependence of $\left|A_1^{(j)}/U_0\right|$ on θ) against the background of the intensified dependence of the ratio ω'_F/ω' on θ (curve *1*) for $V_d/c_t = 0.3$, $\omega = 1.5 \times 10^9$ rad/s, $U_0 = 5 \times 10^{-7}$ cm. The dashed straight line corresponds to the relative value equal to unity.

the manifestations of magnetic nonlinearity noted in the formulation of the problem should obviously be attributed to the latter waves.

In order to estimate the amplitudes $A_p^{(j)}$ by formulas (15), it is important to note that in the frequency range $\omega' < \omega_k$ under investigation (for $V_d < 0$), they do not display any singularities. For example, since $C \sim \omega'^2 - \omega_0^2$ and $D \sim \omega^2 - \omega_0^2$, the poles $\omega' = \omega_0$ ($j = 1$) and $\omega = \omega_0$ ($j = 2$) of the amplitudes $A_1^{(j)}$ turn out to be removable singularities, while the pole of the quantities $R(\omega'^2 - \omega_k^2)^{-1}$ and $T(\omega^2 - \omega_k^2)^{-1}$ attainable for $V_d = 0$ in the joint limit $\omega' \longrightarrow \omega_k$, and accordingly of all the amplitudes $A_p^{(j)}$, lies outside the frequency interval admissible according to the conditions of the exchangeless approximation. An analysis of the behavior of $A_p^{(j)}$ in the neighborhood of the point $\omega' = \omega_k$ requires not only the inclusion of the exchange term in the dispersion spectra of modes, but also a consistent examination of the effect of transformations between acoustic and spin wave branches [12], which is beyond the scope of the present paper.

Numerical calculations for a garnet ferrite of the YIG type with the parameters [2, 13] $M_0 = 140$ G, $\omega_0 = 2 \times 10^9$ rad/s^{-1}, $\omega_m = 3.5 \times 10^{10}$ rad/s^{-1}, $\beta = 7.4 \times 10^6$ erg/cm^3, and $c_t = 3.8 \times 10^5$ cm/s ($\chi \approx 5.1 \times 10^{-3}$ and $\zeta \approx 1.4 \times 10^{-2}$) proved that, except for doubly localized waves with the number $p = 1$, the amplitudes of the remaining third-harmonic waves are, as a rule, insignificant. The fulfillment of the inequalities $\left|A_1^{(j)}\right| \gg \left|A_2^{(j)}\right| \gg \left|A_3^{(j)}\right|$ is visually illustrated in Fig. 2 showing the angular dependences of the quantities $\left|A_{2,3}^{(1)}/A_1^{(1)}\right|$ for a number of positive values of the parameter V_d/c_t in the case when $j = 1$, $\omega = 1.5 \times 10^9$ rad/s, and $U_0 = 5 \times 10^{-7}$ cm. Thus, the assumption concerning the "boundary nature" of magnetic nonlinearity in the effects of the paramagnetic interaction of a shear wave with a moving DW is directly confirmed by the calculations. Taking this into account, we conclude that the real distribution of the amplitude along the front of singly localized waves with number $p = 2$ corresponds to the dashed, and not solid line in Fig. 1b.

The curves in Fig. 2 also show that with increasing θ, a weak mutual change in the amplitudes $A_p^{(j)}$ takes place, indicating approximately the same type of their angular behavior. With this in mind, and in view of the observed inequality $A_1^{(j)} \gg \left|A_{2,3}^{(j)}\right|$, we will concentrate our attention solely on the amplitude properties of doubly localized waves. First of all, the presence of a well-defined peak ($j = 1$, Fig. 3) or, conversely, a dip ($j = 2$, Fig. 4) in the angular dependence of the quantity $|A_1^{(j)}/U_0|$ deserves attention.

A comparison of curve *3* describing the angular dependence of $|A_1^{(j)}/U_0|$ in Fig. 3 with curve *2* describ-

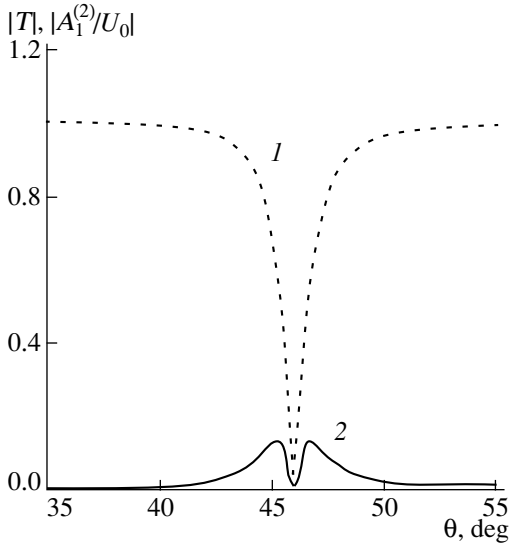

Fig. 4. FMR dips for directly transmitted wave (curve *1* describes the dependence $|T(\theta)|$) and the third-harmonic wave for $j = 2$ (curve *2* describes the dependence of $\left|A_1^{(1)}/U_0\right|$ on θ). The parameters of calculations are the same as in Fig. 3.

ing the $|R(\theta)|$ dependence and curve *1* for the ratio ω'_F/ω', where $\omega'_F = \omega_0 + \omega_m(\omega - \omega_0)[2(\omega - \omega_0) - \omega_m]^{-1}$ is the frequency of the ferromagnetic resonance (FMR) for the reflected wave indicates unequivocally that these peculiarities are definitely due to manifestations of the FMR at magnetostatic stray fields. Its typical feature is a change in the position of the resonance frequency ω'_F and accordingly new positions of peaks and dips of $|A_1^{(j)}/U_0|$ observed upon the reversal of spontaneous magnetization and intrinsic fields of domains. The latter is attained by the formal substitution $\omega \longrightarrow \omega'$, the duality of the results under such transformations indicating [2, 3, 13] the nonreciprocal nature of waves in magnetic materials under the FMR conditions.

The replacement of the FMR peaks of the third harmonic in Fig. 3 by the dips in Fig. 4 is a consequence of the relation $1 + R = T$ for the linear solution [4] and essentially reflects the well-known complementarity of angular reflection and transmission spectra of refracted waves. The maximum level of the third harmonic $\left|A_1^{(j)}/U_0\right|_{\max}$, which is estimated from the height of the FMR peak ($j = 1$, Fig. 3) or the depth of the dip ($j = 2$, Fig. 4) is determined to a considerable extent by the value of U_0^2. The choice of the admissible values of U_0 is limited from above by the verification of the smallness of the ratio m_z^j/M_0 ensuring the fulfillment of the approximate equality (8). In this connection, the value of $U_0 = 5 \times 10^{-7}$ cm adopted in Figs. 3 and 4 is close to optimum. An order-of-magnitude decrease in this value makes the height of the peak or the depth of the dip of the FMR of the third harmonic insignificant, while an increase in U_0 to 10^{-6} cm leads to a noticeable increase in $m_z^{(j)}$ relative to M_0. Figures 3 and 4 shows that, although the FMR peaks of the third harmonic are manifested less strongly than the principal peaks, they are quite accessible for observation. The main difficulty encountered in their detection apparently lies in the necessity to mount the detector in the immediate vicinity of a moving DW at the instant of signal recording.

It should be noted, in conclusion, that a change in the angular positions of the FMR peaks (dips) of the third harmonic depending on the velocity and direction of motion of a DW corresponds to the results described in [4].

ACKNOWLEDGMENTS

This research was carried out in accordance with project A0066 of the Federal Program “Integration”.

REFERENCES

1. V. I. Ozhogin and V. A. Preobrazhenskiĭ, Usp. Fiz. Nauk **155** (4), 593 (1988) [Sov. Phys. Usp. **31**, 713 (1988)].
2. B. A. Goldin, L. N. Kotov, L. K. Zarembo, and S. N. Karpachev, *Spin–Phonon Coupling in Ferrite Crystals* (Nauka, Leningrad, 1991).
3. A. G. Gurevich, in *Ferromagnetic Resonance* (GIFML, Moscow, 1961), p. 290.
4. N. S. Shevyakhov, Akust. Zh. **36** (4), 760 (1990) [Sov. Phys. Acoust. **36** (4), 427 (1990)].
5. B. A. Auld and C. S. Tsai, Appl. Phys. Lett. **9** (5), 192 (1966).
6. G. M. Nedlin and R. Kh. Shapiro, Fiz. Tverd. Tela (Leningrad) **18** (6), 1696 (1976) [Sov. Phys. Solid State **18** (6), 985 (1976)].
7. A. I. Akhiezer, V. G. Bar’yakhtar, and S. V. Peletminskiĭ, *Spin Waves* (Nauka, Moscow, 1967; North-Holland, Amsterdam, 1968).
8. V. S. Gornakov, L. M. Dedukh, and Yu. P. Kabanov, Fiz. Tverd. Tela (Leningrad) **26** (3), 648 (1984) [Sov. Phys. Solid State **26** (3), 391 (1984)].
9. V. G. Bar’yakhtar, S. A. Ivanov, and M. V. Chetkin, Usp. Fiz. Nauk **146** (3), 417 (1985) [Sov. Phys. Usp. **28**, 563 (1985)].
10. V. V. Lemanov and G. A. Smolenskiĭ, Usp. Fiz. Nauk **108** (3), 465 (1972).
11. A. D. Bordman and S. A. Nikitov, Fiz. Tverd. Tela (Leningrad) **31** (4), 143 (1989) [Sov. Phys. Solid State **31** (4), 626 (1989)].
12. R. L. Comstock and N. Kusnezov, J. Appl. Phys. **38** (9), 3740 (1967).
13. Yu. M. Yakovlev and S. Sh. Gendelev, *Ferrite Single Crystals in Radio Electronics* (Sovetskoe Radio, Moscow, 1975).

Translated by N. Wadhwa

Physics of the Solid State, Vol. 42, No. 6, 2000, pp. 1087–1093. Translated from Fizika Tverdogo Tela, Vol. 42, No. 6, 2000, pp. 1055–1061.

MAGNETISM AND FERROELECTRICITY

The Anion and Cation Effects in the Magnetic Anisotropy of Rare-Earth Compounds: Charge Screening by Conduction Electrons

Yu. P. Irkhin and V. Yu. Irkhin

Institute of Metal Physics, Ural Division, Russian Academy of Sciences, ul. S. Kovalevskoĭ 18, Yekaterinburg, 620219 Russia

e-mail: Valentin.Irkhin@imp.uran.ru

Received November 2, 1999

Abstract—The formation of magnetic anisotropy (MA) in rare-earth compounds with transition metals has been analyzed. The screening of the charges creating the crystal field by conduction electrons has been shown to play an important role. The calculations took into account the Friedel charge-density oscillations. The model used for RCo_5 is the point-charge crystal field including nonuniform screening by conduction electrons with an anisotropic Fermi surface. The mechanisms of strong MA due to light-element impurities (hydrogen and nitrogen) are considered. The effective charge of an impurity can heavily depend on its ionic radius and the characteristics of the Fermi surface (in particular, on the Fermi momentum k_F) of the screening electrons. The screening of the cation and anion charge in hydrides and nitrides based on the R_2Fe_{17} and $RFe_{11}Ti$ intermetallic compounds is discussed. *© 2000 MAIK "Nauka/Interperiodica".*

The main mechanism responsible for the magnetic anisotropy in rare-earth-based systems is known to be the crystal field (CF) (see, e.g., [1–3]). However, the simplest point-charge model often meets with difficulties and disagreements in experiments. For instance, the MA constants K_1 calculated by it for RCo_5 are very large and have the wrong sign [4]. Similar difficulties also arise for the $R_2Fe_{14}B$ system [5].

A number of studies have recently appeared that deal with the effect of embedded hydrogen and nitrogen atoms on the magnetic properties of rare-earth compounds with transition metals. Of particular interest is the unusual behavior of the MA. The doping effects turn out to be large and are capable of both decreasing and increasing the MA constants, up to reversing their sign. Likewise, using the nominal impurity atom charges does not lead to agreement with experimental data.

Thus, screening plays an important part in the CF model in all the above cases. It is often taken into account by introducing effective ionic charges Q^*, which may greatly differ from the bare ones. It should be stressed that CF theory should include nonuniform charge distribution around the ion, because it is the electric-field gradient that determines the magnitude of the CF.

Introducing effective charge parameters is not satisfactory, either from a theoretical or an experimental standpoint; indeed, the pattern obtained for metallic RE compounds is fairly irregular, with the values of Q^* being quite often negative. The most probable reason for these difficulties lies in not taking into account the CF screening by the conduction electrons. However, the treatment of such a screening in terms of the point-charge approximation does not seem a simple task. Daniel's model [6], which takes into account Friedel electron-density oscillations, appears to be more reasonable physically for a more detailed description of the spatial nonuniformity of a screening charge. It is this model that will be employed in this paper.

Another approach to the MA problem is based on *ab initio* band-structure calculations. RE systems are hard subjects to apply standard band-theory methods to, and one has to use approximations and model concepts here (for example, the atomic-sphere approximation, inclusion of *f* states into the core). Modern calculations [7, 8] consider the anisotropic contribution of conduction electrons in an atomic sphere centered on the RE ion in greater detail, and the remaining "lattice" contribution is calculated in a point-charge approximation with screened charge densities of other cells, which do not overlap the *f* shell. In actual fact, the atomic and lattice contributions are not independent and partially compensate one another. While the approaches based on full-potential energy calculations within the density functional method [8] yield a correct order-of-magnitude estimate of the anisotropy energy, no satisfactory quantitative agreement with the experiment has thus far been reached. Thus, despite the recent progress in band theory, one may still find a straightforward qualitative analysis based on the physically clear point-charge concept refined by introducing distance-dependent effective ionic charges useful.

1063-7834/00/4206-1087$20.00

1. SIMPLE CONDUCTION-ELECTRON SCREENING MODEL

Consider the MA formation taking into account spatial screening by conduction electrons.

The MA constants are derived from the angular dependence of the energy of magnetic ions

$$\delta\varepsilon_{cf} = K_1 \sin^2\theta + \ldots \quad (1)$$

We are considering a magnetic ion at point $\mathbf{r} = 0$ in the field of the surrounding ions. The contribution of a bare charge Q_0 at point $\mathbf{R}$ to the CF can be written as

$$V_{cf}(\mathbf{r}) = \frac{Q_0 + Q_{el}(\mathbf{R}-\mathbf{r})}{|\mathbf{R}-\mathbf{r}|}, \quad (2)$$

where the charge is measured in units of the electronic charge $|e|$, and $Q_{el}(\mathbf{R})$ is the charge of the conduction electrons screening the impurity ion. Expanding (2) in powers of r to terms of order r^2, one obtains for K_1 (cf. [4, 9])

$$K_1 = 3e^2\Lambda\langle r_f^2\rangle\alpha_J J(J-1/2). \quad (3)$$

Here $\langle r_f^2\rangle$ is the mean squared f-shell radius, J is the total angular momentum of the RE ion, α_J is the Stevens factor

$$\Lambda = \sum_{\mathbf{R}} Q^*(\mathbf{R})\frac{3\cos^3\theta_{\mathbf{R}} - 1}{2R^3}, \quad (4)$$

where the sum is run over the whole lattice, $\theta_{\mathbf{R}}$ is the polar angle of the vector $\mathbf{R}$, and $Q^*(\mathbf{R})$ are the corresponding screened ionic charges. (It should be noted that the factor of 2 in the denominator was erroneously omitted in [9].) One can see here the difference from the band-structure approaches (see, e.g., [7]), where one calculates, roughly speaking, the screening charge inside a sphere centered on a magnetic RE ion.

In the approximation of a spherical charge density distribution we obtain [9]

$$Q^*(\mathbf{R}) = Q_0 + Q_{el}(R) - \frac{4}{3}\pi R^3[Z(R) - RZ'(R)], \quad (5)$$

where $Q_{el}(R)$ is the charge of the conduction electrons inside a sphere centered at a point charge and having a radius R,

$$Q_{el}(R) = 4\pi\int_0^R \rho^2 d\rho Z(\rho), \quad (6)$$

$Z(R)$ is the charge density, and $Q'_{el}(R) = 4\pi r^2 Z(R)$. We readily see that the quantity $Q^*(\mathbf{R})$ explicitly includes, besides the total charge $Q_{el}(R)$, the charge density $Z(R)$ and its derivative $Z'(R)$. Such terms do not appear in the calculations [7] where the "lattice" charge density does not overlap the f shell. Note that the higher-order MA constants, which appear while calculating the terms of the next order in r, contain higher-order derivatives of $Z(R)$. It should be stressed that the expressions for different anisotropy constants contain different effective charges. This may turn out to be important when interpreting experimental data. To obtain a specific value of $Q^*(\mathbf{R})$, one should study charge screening for a given electronic spectrum. The single-center screening problem was considered in [9] in terms of a simple model of free conduction electrons ($E = k^2/2$) in a square potential well with thickness d and depth $E_0 = k_0^2/2$ [6]. This model permits one to calculate the conduction-electron charge distribution through the spherical Bessel and Neumann functions $j_l(kr)$ and $n_l(kr)$ ($r > d$) and the scattering-phase shifts η_l. The value of k_0 is determined for given k_F and d from the Friedel sum rule

$$Q_0 = \frac{2}{\pi}\sum_{l=0}^{\infty}(2l+1)\eta_l(k_F). \quad (7)$$

The parameter d depends on the lattice geometry near the impurity. In a study of impurities distributed in a silver matrix [6], d was taken equal to the Wigner-Seitz

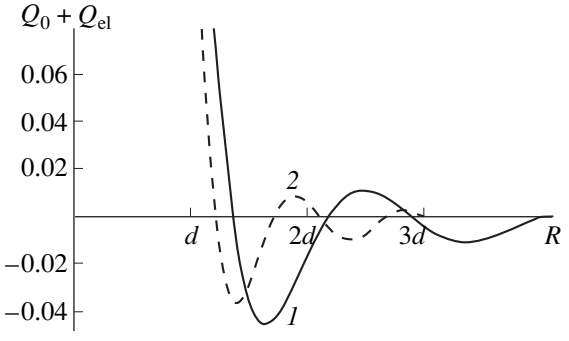

Fig. 1. The sum of the ion bare charge and of the screening electron charge $Q_0 + Q_{el}(R)$ ($Q_0 = 1$) as a function of distance for (*1*) $k_F d = 2$ and (*2*) $k_F d = 3$. Equation (7) yields $k_0 d = 1.46$ and 1.235 for these cases, respectively.

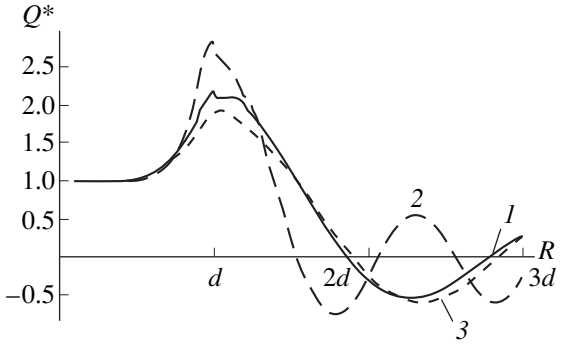

Fig. 2. Effective charge $Q^*(R)$ vs. distance (5) calculated (*1*, *2*) for the parameters of Fig. 1 and (*3*) for $k_F d = 1.5$ and $k_0 d = 1.61$.

radius, such that $k_F d = 2$. The calculations made for $Q_0 = 1$, $k_F d = 1.5$, 2, and 3 are shown in Figs. 1 and 2.

The model being discussed here is of a qualitative nature and is more applicable to impurities resulting in a strong charge-density perturbation (for instance, in RE systems containing hydrogen and nitrogen impurities, see Section 3). In the case of a periodical lattice, where the screening clouds of different centers interfere, the choice of d may naturally be different, and more complex models may become necessary. In metals, the ionic charge Q_0 may be taken equal to the charge in a sphere (for instance, in [7] one considered charge transfer in an atomic sphere), and it may not necessarily coincide with the nominal value for a free ion. Besides, the $Q^*(\mathbf{R})$ relation in the lattice may become anisotropic.

As seen from Fig. 2, for $R < d$ [excluding very small R where $Q^*(R)$ increases slightly], the term with the derivative in (5) gives rise to a growth of $Q^*(R)$ despite the increase of $|Q_{el}(R)|$. For $R \simeq d$, where Z' is the maximum, the consequence of the nonuniform electronic density distribution is that the effective charge Q^* is positive and greatly exceeds the bare value Q_0 (in our case, $Q_0 = 1$). The situation changes dramatically, however, as R continues to increase; indeed, Z' decreases to become negative, so that the ionic charge becomes "overscreened". At large distances, Q^* tends to zero, but the effective charge undergoes noticeable oscillations with sign reversal, which decay slowly. On the other hand, the quantity $Q_0 + Q_{el}(R)$ decreases monotonically up to $R \simeq d$, after which it tends very fast to zero with only very weak oscillations (Fig. 1). This agrees with the fact that band-structure calculations usually yield very low values for the charge transfer in the atomic sphere (see, e.g., [7]). Although Q^* drops rapidly at a distance d, the oscillation period and the position of the subsequent maxima and minima in the $Q^*(R)$ relation are only slightly sensitive to Q_0 and d and are primarily determined by the k_F parameter.

2. CHARGE SCREENING IN THE RCo_5 SYSTEM

To give here a simple enough yet practically interesting example, we consider the geometry of an RCo_5 lattice ($CaCu_5$ structure, Fig. 3) with $c \simeq 4$ Å and $a \simeq 5$ Å. The cobalt ions occupy two sites in two different hexagonal layers, namely, the 2c sites (CoI) in the layers containing RE ions with $R = a/\sqrt{3} \simeq 0.57a$ and 3g sites (CoII) in the RE-free layers with $R = \frac{1}{2}\sqrt{a^2 + c^2} \simeq 0.64a$. Although the sites of all RE ions are equivalent, the contributions to the CF at a given site, due to charges in the same (RI sites, $R = a$) and in the neighboring planes (RII sites, $R = c$), may be different,

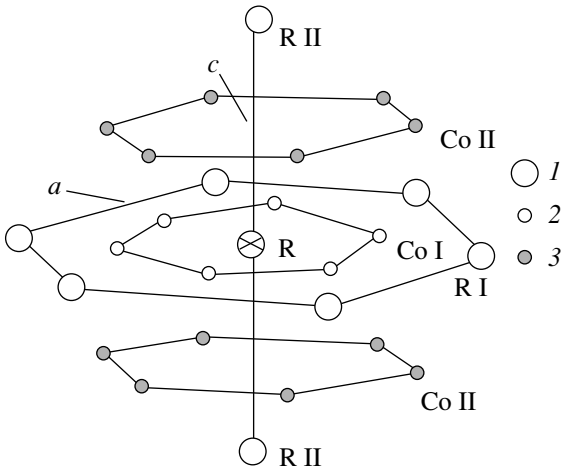

Fig. 3. Local environment of the R site in the RCo_5 lattice. (*1*) R ions, (*2*) CoI(2c) sites, (*3*) CoII(3g) sites.

because the effective charge depends on the distance between two sites. We can thus write (cf. [4])

$$\Lambda = 3a^{-3}\left(16\frac{2y^2-1}{(1+y^2)^{5/2}}Q^*_{\mathrm{CoII}} - 3^{3/2}Q^*_{\mathrm{CoI}} + \frac{2}{3}y^{-3}Q^*_{\mathrm{RII}} - Q^*_{\mathrm{RI}}\right), \quad (8)$$

where $y = c/a \simeq 0.8$. The contributions of the neighbors of site R in the same plane (I) and from other planes (II) have opposite signs. However, in contrast to pure RE metals with a hcp structure [1], no small factor of the type of $\sqrt{8/3} - c/a \sim 0.05$ appears here, so that the calculated value of K_1 turns out to be two orders of magnitude higher. The experimental data on the ratio c/a and the constant K_1 for RCo_{5+x} compounds obtained at low temperatures are given in Table 1. Note the monotonic growth of c/a in the RE series (with the exclusion of the quadrivalent cerium). One readily sees that the experimental values of K_1^{exp} for heavy RE metals and Sm agree with theory at $\Lambda a^3 \simeq 1$. Taking into account only the contribution of Co in (8) and assuming $Q^*_{\mathrm{CoI}} = Q^*_{\mathrm{CoII}} = \bar{Q}^*_{\mathrm{Co}}$, we find

$$\Lambda \simeq -\frac{11.7}{a^3}\bar{Q}^*_{\mathrm{Co}}. \quad (9)$$

Thus, for $\bar{Q}^*_{\mathrm{Co}} \sim 1$, the K_1 quantity has the wrong sign and is very large in magnitude (of the order of 1000 K). It should be noted that such large values of K_1 are not actually self-consistent; they would destroy the Russell-Sounders coupling and freeze out the total ion angular moments. The magnetic moments of light RE

Table 1. Total angular momentum J, Stevens factors α_J, mean squared f-shell radius $\langle r_f^2 \rangle$ (in a.u.) for free R ions, c/a ratio, and experimental values of K_1 (K/RE ion) for RCo_{5+x} systems (data of [10, 11] for light R, the contribution of the RE sublattice by [12] for heavy R elements)

RCo_{5+x}	$CeCo_5$	$PrCo_5$	$NdCo_5$	$SmCo_5$	$TbCo_{5.1}$	$DyCo_{5.2}$	$HoCo_{5.2}$	$ErCo_6$
J	5/2	4	9/2	5/2	6	15/2	8	15/2
$\alpha_J \times 100$	–5.7	–3.4	–7.1	4.1	–1.0	–0.63	–0.22	0.25
$\langle r_f^2 \rangle$	1.20	1.09	1.00	0.88	0.76	0.73	0.69	0.67
c/a	0.817	0.797	0.796	0.795	0.803	0.810	0.817	0.821
K_1^{exp}	–61	–44	–220	190	–96	–211	–203	80
$\bar{Q}_{Co}^*$	–0.015	–0.006	–0.01	–0.08	–0.04	–0.06	–0.2	–0.08

Note: The corresponding values of $\bar{Q}_{Co}^*$ were calculated using (9) and (3).

metals (Ce, Pr, Nd, and Sm) derived from magnetization measurements [13] are indeed noticeably reduced. In the case of cerium (which is assumed to be quadrivalent), the f electrons are partially itinerant, while for the other light RE metals, the strong CF and exchange coupling effects are important. On the other hand, the saturation magnetic moments in Tb, Dy, Ho, and Er are close to their values for free ions [14].

To compensate the large numerical factor in (9), one has to assume $\bar{Q}_{Co}^*$ to be negative and very small in magnitude (Table 1). While one cannot rule out the possibility that the Co ion separation corresponds to $Q^* < 0$, $|Q^*| \ll 1$ in Fig. 2, such a situation is fairly unusual. Therefore, the simple model assuming equal Co charges is hardly capable of accounting for the observed values of K_1, which requires a more detailed analysis of the screening.

It was conjectured that the main contribution to the CF is due to the R ions, while the Q_{Co}^* quantities may be neglected [11, 15]. The effective charges Q_R^* can be assumed to be close to unity, as in the case of pure rare earths, where this parameter is about 2 [9]. Then we shall obtain the correct sign and order of magnitude for K_1, because the RII ions provide a dominant contribution. However, the distances between the RE ions in RCo_5, c and a, are much larger than those in pure rare earths (about 3.5 Å), and therefore, the values of Q_R^* can be substantially smaller. Besides, the variation of effective charges in the RCo_5 series is considerably greater than that in the case of pure rare earths. This variation may originate from the contribution of the CoII sites, because the factor in the first term in the parentheses in (8) depends noticeably on $y = c/a$.

Let us now take into account the anisotropy in Co charge screening connected with that of the Fermi surface in a hexagonal lattice. Then the magnitude of the screening will be determined by the Fermi wave vector in a given direction. It may be conjectured that the effective values of k_F in the reciprocal-lattice directions corresponding to the hexagonal planes are smaller than those in the directions to the CoI sites. Therefore, the charge of the CoII ions becomes screened with distance more slowly than that for the CoI ions and can provide a dominant contribution to K_1 despite the larger distance and numerical factor in (8). This may cause also an additional (besides the purely geometrical) dependence of the anisotropy on y. It should be noted that calculations made for $SmCo_5$ [7] yield different values for a charge transfer in the cobalt atomic spheres q_{Co} (as well as for the magnetic moments of CoI and CoII): $q_{CoI} \simeq 0$ and $q_{CoII} \simeq -0.03$.

The experimental values of K_1 from Table 1 can be obtained, for instance, for $Q_{CoII}^* \simeq 4Q_{CoI}^* \simeq 0.3$, $Q_R^* = 0$, or for $Q_{CoII}^* \simeq 3Q_{CoII}^* \simeq 0.2$, $Q_R^* \simeq 1$ (in the latter case, the sign of K_1 is determined by the contribution of the R ions, which is partially compensated by that due to the Co ions). Thus, the accidental formation of very small values of Q_{Co}^* is not required here.

An analysis performed for the $R_2Fe_{14}B$ [16] showed that iron ions should be assigned small charges.

Similar calculations can be carried out for the impurity-induced local MA. Here, the small factor $1.633 - c/a$ for interstitial impurities in pure RE metals is absent, which results in a large value of the corresponding anisotropy constant [17].

3. DISCUSSION OF EXPERIMENTAL DATA ON THE HYDRIDES AND NITRIDES

Consider some important experimental data on the hydrides and nitrides of RE compounds obtained in the recent years. Already, MA studies of the simplest com-

pounds, namely, the cubic Laves phases RFe_2H_x (see, e.g., [18]), revealed a strong effect of interstitial hydrogen. This phenomenon was associated with the onset of a local uniaxial anisotropy with a local constant K_1 near the hydrogen ions of the order of 10^9 erg/cm^3, and estimates in the point-charge approximation yielded $Q_H \simeq -1$ for these ions. The negative value corresponds to the so-called anion model of hydrogen, put forward earlier in [19], a paper that discussed the formation of localized levels at the H impurity.

Strong effects are observed also in uniaxial crystals. The $R_2Fe_{17}(H, N)_x$ (rhombohedral Th_2Zn_{17} structure for light R and hexagonal Th_2Ni_{17} structure for heavy R) and $RFe_{11}Ti(H, N)_x$ (hexagonal $ThMn_{12}$ structure) compounds were studied in [20–23]. The contribution of the hydrogen and nitrogen was determined by subtracting the constants at $x = 0$. The MA constants were already observed to change noticeably at low concentrations of these impurities.

The contributions to the MA due to the RE and iron sublattices can be separated using data on Y_2Fe_{17}. The doping-induced variation of the contribution of the iron sublattice to K_1 may be neglected, because this quantity only starts to vary for hydrogen concentrations $x > 3$ [23] (this correlates with the behavior of the lattice parameter c, which starts to grow at these values of x).

The MA data on pure R_2Fe_{17} compounds are listed in Table 2. A comprehensive quantitative analysis is made difficult by the large scatter in the values of K_1 and, particularly, of K_2 (the observed orientation of the magnetization is determined by the linear combination $K_1 + 2K_2$). We believe the most likely result for Sm_2Fe_{17} to be the figure obtained in [26], $K_1 \simeq -8.1 \times 10^7$ erg/cm^3, and for Y_2Fe_{17}, $K_1 \simeq -2.3 \times 10^7$ erg/cm^3 [24]. Then the contribution of samarium ions to K_1 can be estimated as the difference between these values, i.e. -5.8×10^7 erg/cm^3. Using the corresponding data for the $RFe_{11}Ti$ system [22], 7.2×10^7 and 2×10^7 erg/cm^3 (the values at helium temperatures were obtained by extrapolation), we obtain now for the contribution of the samarium ion a figure of the opposite sign, 5.2×10^7 erg/cm^3. This is most likely due to the different signs of the geometric factor. At the same time, replacement of one of the Fe ions in the nearest environment of the Sm ion by a Ti ion can provide a substantial contribution to the MA. These data are of interest for determining the effective charges of the Fe and Ti ions in the systems under discussion. However, the calculation of the corresponding geometric factors in (4) is complicated by the large number of ionic sites.

The hydrides and nitrides are more convenient in this respect, because the contribution to the geometric factor Λ (4) due to impurities in the nearest-neighbor approximation is given by a simple expression. By

Table 2. Experimental values for the magnetic anisotropy constants (in units of 10^7 erg/cm^3) and the anisotropy field of the R_2Fe_{17} compounds

R	K_1	K_2	T, K	H_A, T	Ref.
Y	-2.3 ± 0.1	-1.1 ± 0.8	4.2	4	[24]
Y				4.2*	[25]
Y	–3.7	1.2	4.2		[26]
Y	–2.55		50	4	[25]
Y			78	4.7	[27]
Sm	1.25	–2	$\longrightarrow 0$		[21]
Sm	–1.2	~0	293	2.7	[28]
Sm	–3	<0.1	$\longrightarrow 0$		[29]
Sm	–1.75	<0.05	300		[29]
Sm	–8.1	3.7	4.2		[26]
Sm	–0.8	0.2	300		[26]
Sm	–6.3		78	9.8	[27]

* Single-crystal data.

[20], the crystal-field parameter as a function of impurity concentration can be written in the form

$$A_2^0(x) = A_2^0(0) + \frac{1}{2}xz(3\cos^2\theta - 1)\tilde{A}_2, \qquad (10)$$

where z is the number of nearest interstitial sites for a rare-earth ion, θ is the angle between the c axis and the direction to the interstice ($z = 3$, $\theta = \pi/2$ for R_2Fe_{17}, and $z = 2$, $\theta = 0$ for $RFe_{11}Ti$), and $K_1 \sim \alpha_J A_2^0$. The factor of the parameter $\tilde{A}_2$, which has opposite signs for our structures, corresponds to factor (4). Estimates based on the experimental data on the effect of nitrogen show [20] that, despite the strong difference between the values of K_1, the $\tilde{A}_2$ parameters for both structures under consideration are about equal, 200 K/a_0^2 (a_0 is the Bohr radius), so that the difference in geometries plays the dominant part. At the same time, an estimate of $\tilde{A}_2$ made in the point-charge approximation with $Q_N = -3$ for the $Sm_2Fe_{17}N_3$ yields a colossal figure $\tilde{A} = 4500$ K/a_0^2, which exceeds by about 20 times the experimental value. Thus, the nitrogen ion charge is very strongly screened to result in an effective value $Q_N^* = -0.15$. Note that the authors of [20] used the maximum experimental value of the K_1 constant; taking other data results in an even stronger decrease in Q_N^*. The strong screening of the negative charge in a metal, which can be called a cation effect, is far from a trivial phenomenon. For negative point charges, the screening corresponds to a decrease of the electron concentration in their vicinity. Therefore, within Daniel's model [6] the potential well must be a well for holes.

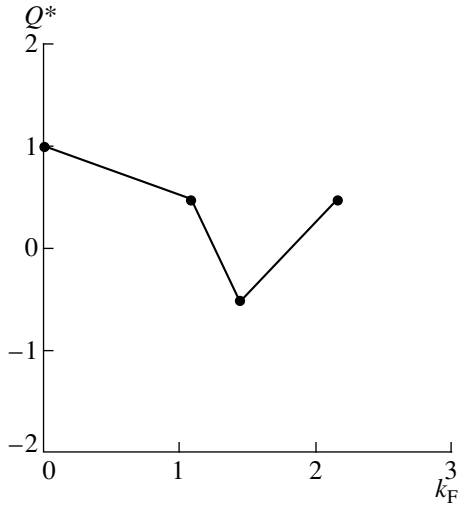

Fig. 4. Schematic dependence of the effective charge on the k_F parameter (Å^{-1}) corresponding to Fig. 2, calculated for d = 1.4 Å.

A typical illustration of the anion and cation effects is also provided by the $Ho_2Fe_{17}(H, N)_x$ hydrides and nitrides studied in [23]. The contributions of H and N to the K_1 constant (to be more precise, to the sum $K_1 + 2K_2$ of the Sm sublattice) obtained at $x = 2$ and $T = 80$ K are about 10^7 and -4×10^7 erg/cm^3, respectively, i.e., they are opposite in sign (results close to the latter value are obtained for $Dy_2Fe_{17}N_2$, despite the threefold larger value of α_J for Dy). The corresponding crystal-field parameters per hydrogen and nitrogen atom are estimated as 25 and –60 K/a_0^2, respectively. Because both impurities are characterized by the same geometry, this difference in the sign is due to the effective charges having opposite signs, namely, the hydrogen ion retains its cation properties, whereas the nitrogen ion behaves as the anion. In this case, in (3) we have $\Lambda = x/(2R^3)$, where $R \simeq 2.5$ Å is the R–N distance, so that from the data on K_1 one obtains $Q_H^* \simeq 0.02$ and $\simeq$–0.05. These results can be explained using Fig. 2.

In addition to $Q^*(R)$, we also consider the $Q^*(k_F)$ function in terms of the model [6]. This relation may be of use in explaining the concentration dependence of MA for RM_xT_y-type alloys [for instance, $Sm_2(FeTi)_{17}$], where the k_F parameter depends on the component concentrations x, y, as well as for hydrides and nitrides, where introducing impurities noticeably affects the lattice. The $Q^*(k_F)$ dependence is plotted in Fig. 4 for $1 < k_F < 2$ Å^{-1}. As before, d can be taken equal to the double Wigner-Seitz radius. In the case of a nitrogen impurity in Sm_2Fe_{17}, this radius can be estimated as the difference between the Sm–N separation and the radius of the trivalent Sm ion in the metal, which yields about 0.7 Å. This value coincides with the nitrogen bond length quoted in [20]. In a realistic situation, particularly in a uniaxial crystal, the Fermi surface is naturally strongly anisotropic, which calls for the generalization of the square-well model.

We readily see that the effective ionic charge can reverse sign with varying k_F (viewed from the physical standpoint, this effect is also related to the Friedel oscillations). This reversal first occurs when k_F becomes of the order of the inverse potential-well width near the impurity. Although the above reasoning is qualitative and based on the simplest possible model, this explanation of the small value of the effective charge and of its high sensitivity appears reasonable.

Let us now make a comparison with other theoretical methods. The screening charge distribution $Q_{cf}(R)$ was also studied [30] within the Thomas-Fermi model, whose region of validity is fairly limited. It was shown that there are negative contributions to Q_{cf}, which are due to the finite size of electronic cores of the surrounding ions. For the case of a nitrogen ion in the $Sm_2Fe_{17}N_3$ system, accepting $q = 3$ Å^{-1} for the screening parameter, one obtained $Q_{cf}(R = 2.5 \text{ Å}) = -9.2$, which provides a satisfactory agreement of the magnetic anisotropy constant K_1 with the experiment. Such a large value of $|Q_{cf}|$ is apparently connected with the fast (exponential) decrease of charge density in the Thomas-Fermi approach.

We could mention also a first-principles calculation of the band-structure of the $Sm_2Fe_{17}N_x$ system [31], where one found the number of screening electrons as a function of the distance to the nitrogen ion (unfortunately, only for distances below 1.5 Å). No Friedel-type oscillations were observed here.

The physical reason for all the above phenomena lies in the strong dependence of screening on the electrical potential gradient. Also, as pointed out in [20], the change in the potential occurring when crossing the boundary of the Wigner-Seitz cell, which appears in calculations (and can be fairly sharp in realistic conditions), may play a vital part.

The main conclusion of our consideration is that the impurity ion charges are strongly screened, with the nonuniformity of the conduction electron distribution being of crucial significance [the term with the derivative in the expression for the effective charge (5), which is disregarded in standard approaches]. This screening may result either in a sign reversal of the effective charge or in a substantial change of its magnitude.

ACKNOWLEDGMENTS

The authors are indebted to N. V. Mushnikov, E. A. Shcherbakova, S. A. Nikitin, and I. S. Tereshina for fruitful discussions.

Partial support of the Russian Foundation for Basic Research (grant no. 99-02-16268) is gratefully acknowledged.

REFERENCES

1. Yu. P. Irkhin, Usp. Fiz. Nauk **151** (2), 321 (1988).
2. V. Yu. Irkhin and Yu. P. Irkhin, *Electronic Structure. Correlation Effects and Physical Properties in d- and f-Transition Metals and their Compounds*, cond-mat/9812072.
3. K. H. J. Buschow, Rep. Prog. Phys. **54** (9), 1123 (1991).
4. Yu. P. Irkhin, E. I. Zabolotskiĭ, E. V. Rozenfel'd, and V. P. Karpenko, Fiz. Tverd. Tela (Leningrad) **15** (10), 2963 (1973) [Sov. Phys. Solid State **15** (10), 1976 (1973)].
5. S. Adam, Gh. Adam, and E. Burzo, J. Magn. Magn. Mater. **61** (3), 260 (1986).
6. E. Daniel, J. Phys. Radium **20** (10), 769 (1959).
7. M. Richter, P. M. Oppeneer, H. Eschrig, and B. Johansson, Phys. Rev. B **46** (21), 13919 (1992).
8. S. Buck and M. Fähnle, J. Magn. Magn. Mater. **166** (3), 297 (1997).
9. V. Yu. Irkhin and Yu. P. Irkhin, Phys. Rev. B **57** (5), 2697 (1998).
10. A. S. Ermolenko, in *Proceedings of the International Conference on Magnetism MKM-73, Moscow, 1973* (Nauka, Moscow, 1974), Vol. 1, p. 231.
11. S. G. Sankar, V. U. S. Rao, E. Segal, *et al.*, Phys. Rev. B **11** (1), 435 (1975).
12. A. S. Ermolenko, Fiz. Met. Metalloved. **53** (4), 706 (1982); A. S. Ermolenko and A. F. Rozhda, Fiz. Met. Metalloved. **54** (4), 697 (1982); **55** (2), 267 (1983).
13. E. Tatsumoto, T. Okamoto, H. Fujii, and C. Inoue, J. Phys. (Paris) **32** (C-1), 550 (1971).
14. T. Okamoto, H. Fujii, C. Inoue, and E. Tatsumoto, J. Phys. Soc. Jpn. **34** (3), 835 (1973).
15. J. E. Greedan and V. U. S. Rao, J. Solid State Chem. **6** (3), 387 (1973).
16. A. V. Andreev, A. V. Deryagin, N. V. Kudrevatykh, *et al.*, Zh. Éksp. Teor. Fiz. **90** (3), 1042 (1986) [Sov. Phys. JETP **63**, 608 (1986)].
17. Yu. P. Irkhin and V. Yu. Irkhin, Fiz. Tverd. Tela (St. Petersburg) **40** (7), 1298 (1998) [Phys. Solid State **40** (7), 1182 (1998)].
18. N. V. Mushnikov, V. S. Gaviko, A. V. Korolyov, and N. K. Zaikov, J. Alloys Compd. **218** (2), 165 (1995).
19. W. E. Wallace, S. K. Malik, T. Takeshita, *et al.*, J. Appl. Phys. **49** (3), 1486 (1978).
20. R. Skomski, M. D. Kuz'min, and J. M. D. Coey, J. Appl. Phys. **73** (10), 6934 (1993).
21. Y. Xu, T. Ba, and Y. Liu, J. Appl. Phys. **73** (10), 6937 (1993).
22. S. A. Nikitin, E. A. Ovchentsov, A. A. Salamova, and V. N. Verbetsky, J. Alloys Compd. **260** (1), 5 (1997); V. Yu. Bodriakov, T. I. Ivanova, S. A. Nikitin, and I. S. Tereshina, J. Alloys Compd. **259** (2), 265 (1997); S. A. Nikitin, T. I. Ivanova, and I. S. Tereshina, Neorg. Mater. **34** (5), 566 (1998); S. A. Nikitin, I. S. Tereshina, V. N. Verbetsky, and A. A. Salamova, in *Procedings of the Moscow International Symposium on Magnetism (MISM-99), Moscow, 1999* (in press); I. S. Tereshina and N. Yu. Pankratov, *ibid.*
23. S. A. Nikitin, E. A. Ovchentsov, A. A. Salamova, *et al.*, J. Alloys Compd. **261** (1), 15 (1997).
24. M. I. Averbuch-Pouchot, R. Shevalier, J. Deportes, *et al.*, J. Magn. Magn. Mater. **68** (2), 190 (1987).
25. B. Garsia-Landa, P. A. Algarabel, M. R. Ibarra, *et al.*, J. Magn. Magn. Mater. **140**–**144**, 1085 (1995).
26. S. Brennen, R. Skomski, O. Cugat, and J. M. D. Coey, J. Magn. Magn. Mater. **140**–**144**, 971 (1995).
27. A. Paoluzi and L. Pareti, J. Magn. Magn. Mater. **189** (1), 89 (1998).
28. M. Katter, J. Wecker, C. Kuhrt, *et al.*, J. Magn. Magn. Mater. **117** (3), 419 (1992).
29. O. Isnard, S. Miraglia, M. Guillot, and D. Fruchart, J. Appl. Phys. **75** (10), 5988 (1994).
30. R. Skomski, Philos. Mag. B **70** (2), 175 (1994); R. Skomski and J. M. D. Coey, J. Magn. Magn. Mater. **140**–**144**, 965 (1995).
31. Z. Zeng, Q. Zheng, W. Lai, and C. Y. Pan, J. Appl. Phys. **73** (10), 6916 (1993).

Translated by G. Skrebtsov

Physics of the Solid State, Vol. 42, No. 6, 2000, pp. 1094–1099. Translated from Fizika Tverdogo Tela, Vol. 42, No. 6, 2000, pp. 1062–1067.

MAGNETISM AND FERROELECTRICITY

Principal Mode of the Nonlinear Spin-Wave Resonance in Perpendicular Magnetized Ferrite Films

Yu. V. Gulyaev, P. E. Zil'berman, A. G. Temiryazev, and M. P. Tikhomirova

Institute of Radioengineering and Electronics, Russian Academy of Sciences, Fryazino, 141120 Russia

e-mail: tema@ms.ire.rssi.ru

Received November 18, 1999

Abstract—The paper reports a theoretical and experimental study of the nonlinear spin-wave resonance (SWR) modes in normally magnetized ferrite films. Particular attention is focused on the principal, lowest frequency, SWR mode. It is shown theoretically that, as the precession amplitude increases, the profile of the principal mode changes to make the excitation distribution across the film thickness more uniform. The nonlinear shift of the resonance field depends on the surface-spin pinning parameters. An experimental study has been made of YIG films with a strong uniaxial anisotropy field gradient over the film thickness, as well as of YIG films of submicron thickness. As the microwave power was increased, the principal-mode resonance field was observed undergoing a sublinear shift accompanied by a superlinear growth of absorbed power. This behavior is attributed to a change in the profile of the spatial distribution of ac magnetization. © *2000 MAIK "Nauka/Interperiodica".*

Studies of the nonlinear ferromagnetic resonance (FMR) carried out after the pioneering works of Suhl [1] and Weiss [2] showed that nonlinear phenomena occurring at large precession angles can be divided into two groups [3]. The first of them is associated with a decrease in the static component of the magnetization vector with increasing precession amplitude. This brings about a resonance frequency shift, an asymmetric distortion of the resonance line, and a bistability of microwave power absorption. Note that the latter phenomenon can be employed to develop bistable devices in the microwave range [4]. The second group of the nonlinear phenomena is due to the fact that, starting from a certain threshold level, spin vibrations become unstable against parametric decay. This instability gives rise to parametric excitation of short-wavelength spin waves, the onset of self-oscillations of the magnetization, and a reduced coupling between the pump microwave field and the original vibration [5]. As a result, the linear dependence between the pump field and the precession amplitude breaks down, and a further increase in the pumping does not produce a noticeable increase of the precession amplitude.

It thus becomes clear that parametric instability precludes reaching large precession angles and hinders the development of devices for which such angles are necessary, for example, of bistable microwave devices or magnetooptic elements for light control at microwave frequencies. To avoid the parametric instability, one has to excite the FMR at the frequency corresponding to the bottom of the spin-wave spectrum. In this case, there are no short-wavelength spin waves at the frequency of the original vibration. This regime can be realized under two conditions; namely, the ferromagnetic sample must have the shape of a thin plate or a film, and the external field must be directed along the film plane normal. Note that the parameters of such a resonance, including the shape of the ac magnetization distribution across the film thickness, depend substantially on the degree of film uniformity in thickness and the character of spin pinning at the surfaces. At the same time, theoretical studies on the nonlinear FMR (see, e.g., [6, 7]) are limited, as a rule, to analyzing the spatially uniform mode. In this work, we are going to consider spatially nonuniform modes of a ferromagnetic film excited in spin-wave resonance (SWR) [8] and to study the transformation of these modes with increasing pump level to nonlinear eigenmodes. The paper consists of two parts. The first part is a theoretical investigation of spin oscillations of an arbitrary amplitude in a ferromagnetic film placed in a normal saturating magnetic field. Various conditions of spin pinning at the film surfaces are considered. The analysis does not include the processes of parametric decay. The second part presents the results of an experimental investigation of a nonlinear SWR.

1. THEORY

Consider a ferromagnetic film in an external magnetic field **H**, which is aligned with the z axis coinciding with the film surface normal (Fig. 1). We assume the film dimensions to be unbounded along the x and y axes, and the film center to coincide with the $z = 0$ plane. The film is uniform, except for the near-surface layers, where spins may be pinned. The sample has the following parameters: the thickness d, saturation magnetization M_S, uniaxial anisotropy constant K_a, nonuni-

1063-7834/00/4206-1094$20.00

form exchange constant α, and gyromagnetic ratio $\gamma > 0$. We shall neglect the effects of dissipation.

The components of the magnetization vector **M** in polar coordinates are found from the relations $M_z = M_S\cos\theta$, $M_x = M_S\sin\theta\cos\varphi$, $M_y = M_S\sin\theta\sin\varphi$. The Landau–Lifshits equations can be written as

$$\begin{aligned}\dot\theta &= \alpha\gamma M_S(\sin\theta\varphi'' + 2\cos\theta\varphi'\theta'),\\ \sin\theta\dot\varphi &= \gamma\sin\theta(H - 4\pi M_{\text{eff}}\cos\theta)\\ &\quad - \alpha\gamma M_S(\theta'' - \sin\theta\cos\theta\varphi'^2),\end{aligned} \tag{1}$$

where the dot denotes the derivative with respect to time; the prime, with respect to coordinate z; and the effective magnetization M_{eff} is determined from the relation $4\pi M_{\text{eff}} = 4\pi M_S - K_a M_S$.

We note some specific features of small-amplitude oscillations. Let us introduce for convenience the circular magnetization component $m^+ = M_S\sin\theta e^{i\varphi}$. As is well known, after linearization, equation (1) has the following solution:

$$m^+(z, t) = [A\cos(kz) + B\sin(kz)]\exp(i\omega t), \tag{2}$$

where A and B are arbitrary constants, ω is the natural oscillation frequency, and k is the wave number, $k^2(\omega, H) = \delta H/\alpha M_S$, where $\delta H = \omega/\gamma - H + 4\pi M_{\text{eff}}$. A comparison of (2) with the expression for m^+, presented above in angular variables, shows that small-amplitude oscillations satisfy the conditions

$$\begin{aligned}\dot\theta &= 0,\\ \varphi' &= 0.\end{aligned} \tag{3}$$

Conditions (3) reflect the fact that the normal modes of a film at small amplitudes are standing waves.

We now turn to an analysis of normal modes of an arbitrary amplitude. We shall look for nonlinear solutions that also satisfy conditions (3) and are in this sense a generalization of standing waves in linear theory. The form of the solution we are looking for can naturally be justified only below the parametric instability threshold. In view of (3), the first relation in (1) is satisfied automatically, and the second can be cast in the form

$$\dot\varphi = \gamma(H - 4\pi M_{\text{eff}}\cos\theta) - \alpha\gamma M_S\frac{\theta''}{\sin\theta}. \tag{4}$$

The left-hand side of (4) depends only on t, whereas the right-hand one, on z only. This is possible only for $\dot\varphi = \omega$, where ω is a constant (frequency), which does not depend on t and z. With this in mind, equation (4) takes the form

$$\alpha M_S\theta'' + [\delta H - 4\pi M_{\text{eff}}(1 - \cos\theta)]\sin\theta = 0. \tag{5}$$

Note that (5) is equivalent to the equation of motion of a classical particle with "total energy"

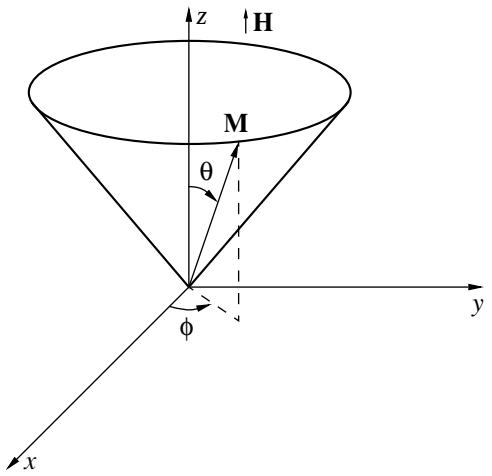

Fig. 1. Orientation of the basic vectors.

$$E = \frac{\theta'^2}{2} + U(\theta), \tag{6}$$

where the first term on the right-hand side is the kinetic energy, and the second, the potential energy

$$U(\theta) = \frac{1}{\alpha M_S}[(4\pi M_{\text{eff}} - \delta H)\cos\theta - \pi M_{\text{eff}}\cos 2\theta]. \tag{7}$$

Because the total energy E is the integral of motion, (i.e., in this case, it does not depend on z), (6) can be integrated one more time to yield a general solution of the problem. However, the solutions for a film must satisfy not only (5) and (6), but boundary conditions as well. Generalizing the mixed boundary conditions [9, 10]

$$\left.\frac{\partial m^+(z, t)}{\partial z^S} + \mu m^+(z, t)\right|_{z = \pm\frac{d}{2}} = 0 \tag{8}$$

to the case of oscillations of an arbitrary amplitude, we obtain (for more details, see [11])

$$\begin{aligned}&\left.\frac{\partial\varphi}{\partial z^S}\sin\theta\cos\theta\right|_{z = \pm\frac{d}{2}} = 0,\\ &\left.\frac{\partial\theta}{\partial z^S} + \mu\sin\theta\cos\theta\right|_{z = \pm\frac{d}{2}} = 0,\end{aligned} \tag{9}$$

where μ is a constant characterizing the spin pinning at the surfaces, and the derivative $\partial/\partial z^S$ is taken along the outward normal to the surface. The first condition in (9) is satisfied automatically, because, as follows from (3), $\varphi' = 0$. Only the second condition imposes limitations on the form of the solutions being looked for. In what follows, we assume the μ parameter to be the same on both film surfaces. Then, there will be independent

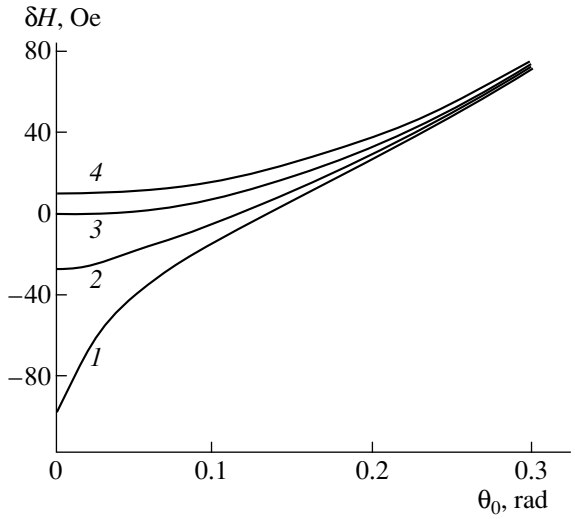

Fig. 2. Dependence of δH on precession angle θ_0 for the principal mode in a YIG film of thickness $d = 0.5$ μm calculated for different pinning parameters: (*1*) $\mu = -10\sqrt{\alpha}$, (*2*) $\mu = -5\sqrt{\alpha}$, (*3*) $\mu = 0$, and (*4*) $\mu = 10\sqrt{\alpha}$.

even and odd solutions for the film. Integrating (6) yields the even solutions

$$z = \pm\int_{\theta_0}^{\theta} \frac{d\bar{\theta}}{\sqrt{2(E - U(\bar{\theta}))}}, \qquad (10)$$

where θ_0 is found from the equality $U(\theta_0) = E$ and actually represents the precession angle at the film center. Thus, the θ_0 angle characterizes the level of excitation of the mode under consideration.

Relations (10) permit one to construct the profile of precession angle distribution over the film thickness. Using (6) and (9), one can find the θ angle at the surface, i.e., for $z = d$. Now substituting the angle thus found in (10) for $z = d$, one can determine the resonance condition, i.e., the $\delta H(\theta_0)$ function, which is the deviation of the resonance field for a given θ_0 from the field corresponding to uniform small-amplitude precession. We shall call the mode with the minimal frequency the principal mode. Note that the principal mode is nonuniform over the thickness, with the exclusion of the case of free spins at the surfaces, where $\mu = 0$. If $\mu > 0$, the maximum of $\theta(z)$ lies at the film center. The condition $\mu < 0$ corresponds to easy-plane surface anisotropy. In this case, the $\theta(z)$ function reaches a maximum at the surfaces. Figures 2 and 3 present the results of numerical calculations made for the principal mode in films with differently pinned spins at the surfaces. Note the following:

(i) The nonlinear shift of the principal-mode resonance field depends substantially on the spin-pinning conditions at the surfaces. As the precession amplitude increases, the effect of pinning on the resonance field decreases, and the fields themselves tend to the field of uniform resonance with the given amplitude.

(ii) The principal mode in a uniform film with free spins at the surfaces ($\mu = 0$) is unique in that its profile does not depend on precession amplitude. In the case of pinning ($\mu \neq 0$), the growth of the amplitude changes the profile. For large amplitudes, the profile of the principal mode becomes practically uniform, except narrow layers near the boundaries.

A more detailed theoretical analysis is given in [11], where one considers, in particular, higher order SWR modes and where one derives the nonlinear boundary conditions.

One should stress here once more the specific part played by the principal mode in a normally magnetized film. This mode has the lowest frequency; i.e., it forms the bottom of the spectrum. Therefore, the principal mode cannot undergo parametric decay. In order to observe the principal mode experimentally, one has to use films with well-resolved frequencies of adjacent

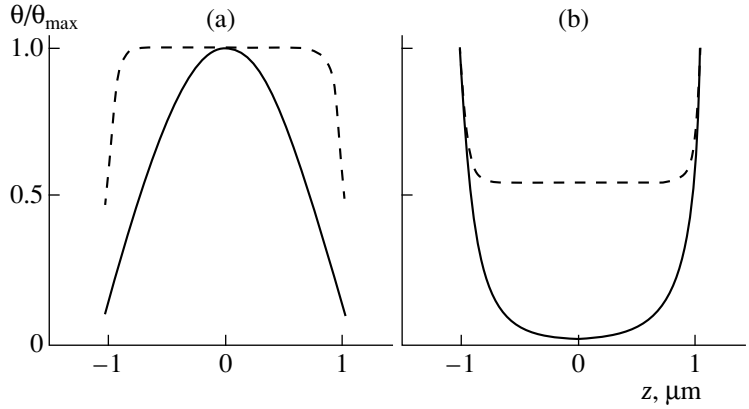

Fig. 3. Profiles of the principal mode in a YIG film of thickness $d = 2$ μm. The solid line relates to the maximum angle $\theta_{max} = 0.005$ rad; the dotted line, to $\theta_{max} = 0.3$ rad; (a) $\mu = 10\sqrt{\alpha}$, (b) $\mu = -10\sqrt{\alpha}$.

SWR modes. These can be either thin enough films or films with a substantial uniaxial anisotropy field gradient over the thickness. In the latter case, the frequency separation between adjacent resonances is determined not by the thickness of the film but rather by the extent of its nonuniformity.

2. RESULTS OF THE EXPERIMENT

The first series of experiments was carried out on YIG samples with a noticeable nonuniformity of the uniaxial anisotropy field over their thickness. We used specially grown YIG films 10–30 μm thick, where the gradient of the uniaxial anisotropy field reached 30 Oe/μm. The excitation and propagation of linear spin waves in such films were considered in detail in [12, 13]. The films were employed to prepare resonators with plane dimensions less than 1 mm, which were placed in a 3-cm reentrant microwave cavity resonator with a Q factor of about 1200. The pump frequency was 9240 MHz. The absorption spectrum of a film 23 μm thick is shown in Fig. 4. The spectrum can be divided into two regions denoted here by *A* and *B*. Region *B*, which lies at higher magnetic fields, contains SWR modes. The extreme absorption peak on the right corresponds to the principal mode. Because of the nonuniformity, the oscillation is localized within a layer less than 1 μm in thickness in the region of the anisotropy field minimum. The localization region expands as the peak number increases to finally extend throughout the film thickness. The excitation of the SWR modes in the spectrum stops here, and one observes a series of primarily dipole modes (region *A*) differing in the structure of ac magnetization distribution along the film surface. Compare the spectra in Figs. 4a and 4b, which were obtained at different microwave powers fed into the resonator. Note that these spectra were recorded at different receiving channel gains, which were chosen so as to permit the comparison of the resonance lines in the figure. One readily sees a substantial change of the relative amplitudes of the principal SWR mode and of the dipole spectrum. While at low power levels the amplitude of the principal mode is less than that of the dipole spectrum roughly by a factor of two, at high pumping this ratio reverses. It turns out that while the resonance saturates and the absorption level decreases by about 3 dB with respect to the linear dependence in the dipole spectrum, the amplitude of the principal SWR peak grows with increasing power superlinearly. The deviation from the linear dependence is about 3 dB.

It may be conjectured that the reason for the superlinear growth of the amplitude lies in a change in the structure of the ac magnetization distribution. An increase of the precession angle results in an extension of the layer in which the oscillation is localized. Such a change in the mode profile increases the coupling of this mode to the external uniform pump field and, hence, results in enhanced absorption. Note that the results of a calculation made within the model of a uniform film with spin pinning at the surface (Fig. 3) show that, in this case, one would also expect a superlinear growth of the amplitude, because the precession angle distribution over the thickness becomes more uniform.

Figure 5 plots the field shift ΔH of the principal SWR mode vs. power. This relation is essentially nonlinear, whereas the theory developed for uniform FMR predicts a linear dependence. The reason for the deviation from linearity may consist in the principal mode being spatially nonuniform. As seen from Fig. 2, a linear dependence $\delta H(P_{in})$ can be expected to hold only for a uniform mode under the condition $\mu = 0$ (curve *3*

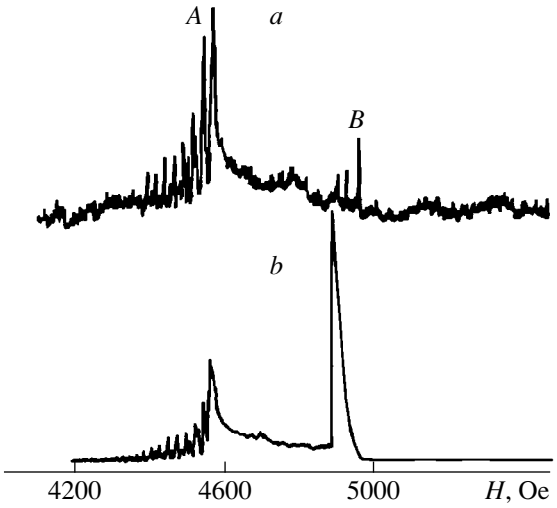

Fig. 4. Absorption spectra of a nonuniform YIG film measured with decreasing magnetic field. (*a*) P_{in} = 7 μW, (*b*) P_{in} = 27 mW.

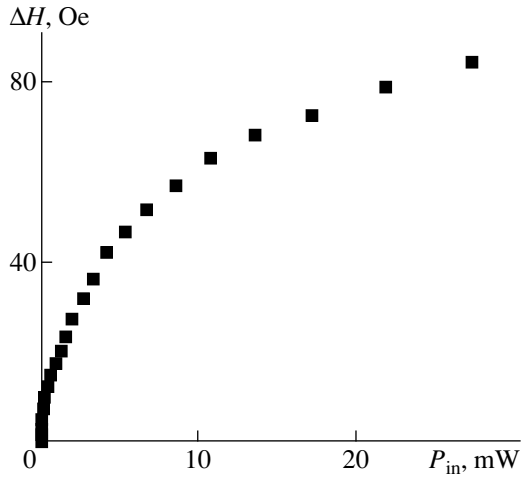

Fig. 5. The shift of the principal-mode resonance field with increasing microwave power input.

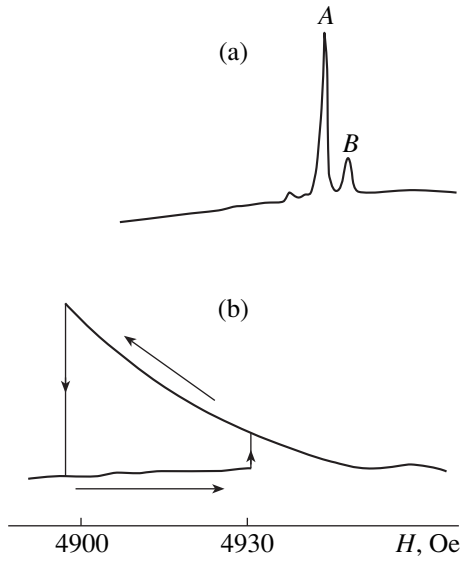

Fig. 6. Absorption spectra of a YIG film of thickness d = 0.5 μm. (a) P_{in} = 27 μW, (b) P_{in} = 27 mW.

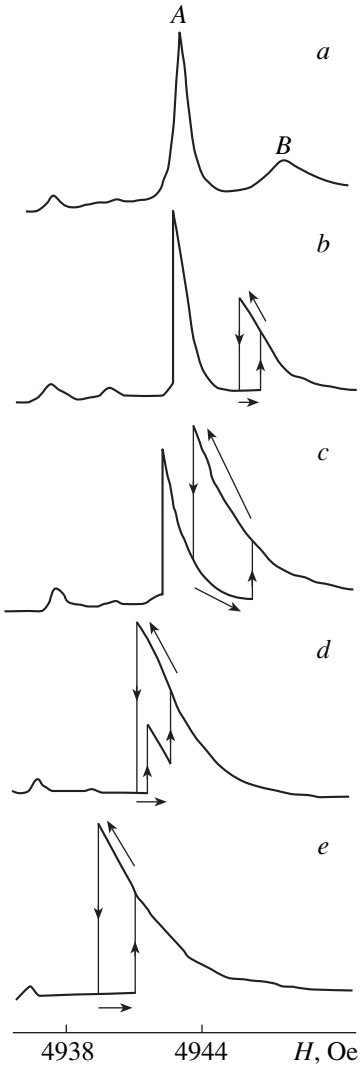

Fig. 7. Absorption spectra of a YIG film of thickness d = 0.5 μm. P_{in} (μW): (*a*) 27, (*b*) 135, (*c*) 215, (*d*) 615, (*e*) 1030.

in Fig. 2). For this curve, $\delta H \sim \theta_0^2$. At the same time, it is seen that for any other pinning parameter the dependence will be nonlinear. Note that a nonlinear behavior of the $\Delta H(P_{in})$ dependence was observed experimentally earlier in FMR studies [14], but the interpretation of the experiment was based on the assumption of the dissipation parameter being dependent on the precession amplitude.

Note that the spectra presented in Fig. 4 were obtained with decreasing magnetic field. The direction in which the field changes determines, to a considerable extent, the shape of the nonlinear resonance. This is seen from Fig. 6, which shows absorption spectra of a resonator made of a 0.5 μm thick YIG film. The conditions chosen for the epitaxial growth of this film did not include special measures to make the film properties intentionally nonuniform. Nevertheless, as seen from Fig. 6a, the spectrum taken at a low pump power contains a weaker peak *B* near the strong peak *A*. This weaker peak is apparently due to the presence of a near-surface layer such that the spins at the film surface are not free, and $\mu < 0$. Thus, in the linear regime, a near-surface mode is excited in the film, which has a low absorption intensity (provided the layer is thin enough) and a small detuning from the mode localized in the bulk of the film (if the parameters of the layer are close to those of the material in the bulk of the film). Nevertheless, by the terminology used earlier, it is peak *B* that corresponds to the principal mode resonance, because it lies at a higher magnetic field; i.e., it corresponds to the minimum frequency at a fixed field. An increase of the pump power results in a substantial change in the spectrum (Fig. 6b). Here, one absorption peak forms whose width and amplitude depend on the direction of the magnetic-field variation. The sample exhibits hysteresis within a certain range of power and magnetic field; i.e., the level of absorption depends on the direction of the magnetic field sweep. The existence of this hysteresis indicates that it is possible to use such films to develop bistable microwave devices. We are going to show that it is peak *B*, corresponding to the principal mode resonance, that serves as a nucleus for a broad nonlinear-absorption peak to grow. Figure 7 presents initial stages of the development of a nonlinearity in this film. As the pump power increases, the relative peak amplitudes are seen to change. The growth of peak *B* in amplitude is accompanied by the formation of a part with hysteresis which broadens to absorb peak *A*. At the same time, a characteristic shoulder appears at the left-hand edge of peak *A*, but no hysteresis sets in. As the pump power increases (Fig. 7*e*), the spectrum takes on the shape typical of a single nonlinear resonance.

This specific example shows that nonlinear resonance can develop out of an absorption peak that has a very small amplitude in the linear regime. It may be conjectured that, in some samples, such a peak would be unresolvable against the background of a closely

lying peak with a larger amplitude. In this case, the formation of the observed nonlinearity would look like a direct transition from peak *A* in Fig. 7*a* to the spectrum of Fig. 7*e*. Nevertheless, some nonlinear-resonance parameters, in particular, the threshold for the onset of the hysteresis, can depend on the position of the principal mode. This point requires further study.

In conclusion, we note that our experiments have revealed a specific role played by the principal SWR mode in the formation of nonlinear spin-wave resonance. Under certain conditions of spin pinning at the surface, or if the film properties are nonuniform over the thickness, the nonlinearity of the principal mode may manifest itself in a superlinear growth of absorbed power. This conclusion has a theoretical validation based on the variation of the spatial distribution of ac magnetization with increasing precession angle. Besides, a theoretical analysis of the normal nonlinear film modes shows that the nonlinear resonance-field shift depends substantially on the character and degree of spin pinning at the film surface.

ACKNOWLEDGMENTS

The authors are indebted to A. V. Maryakhin for providing samples of nonuniform YIG films.

Support of the Russian Foundation for Basic Research (grant no. 97-02-16055) is gratefully acknowledged.

REFERENCES

1. H. Suhl, J. Phys. Chem. Solids **1** (4), 209 (1957).
2. M. T. Weiss, Phys. Rev. Lett. **1** (7), 239 (1958).
3. B. Lührmann, M. Ye, H. Dötsch, and A. Gerspach, J. Magn. Magn. Mater. **96**, 237 (1991).
4. Y. K. Fetisov, P. Kabos, and C. E. Patton, Electron. Lett. **32**, 1894 (1996).
5. A. G. Gurevich and G. A. Melkov, *Magnetic Oscillations and Waves* (Nauka, Moscow, 1994).
6. G. V. Skrotskiĭ and Yu. A. Alimov, Zh. Éksp. Teor. Fiz. **35** (6), 481 (1958).
7. G. V. Skrotskiĭ and Yu. A. Alimov, Zh. Éksp. Teor. Fiz. **36** (4), 1267 (1959) [Sov. Phys. JETP **9** (4), 899 (1959)].
8. C. Kittel, Phys. Rev. **110**, 1295 (1958).
9. G. T. Rado and J. R. Weertman, J. Phys. Chem. Solids **11**, 315 (1959).
10. N. M. Salanskiĭ and M. Sh. Erukhimov, *Physical Properties and Applications of Magnetic Films* (Nauka, Novosibirsk, 1975).
11. Yu. V. Gulyaev, P. E. Zil'berman, A. G. Temiryazev, and M. P. Tikhomirova, Radiotekh. Élektron. (Moscow) **44**, 10 (1999).
12. A. G. Temiryazev, M. P. Tikhomirova, and P. E. Zilberman, J. Appl. Phys. **76**, 5586 (1994).
13. P. E. Zil'berman, A. G. Temiryazev, and M. P. Tikhomirova, Zh. Éksp. Teor. Fiz. **108** (1), 281 (1995) [JETP **81**, 151 (1995)].
14. Chen, C. E. Patton, G. Srinivasan, and Y. T. Zhang, IEEE Trans. Magn. **25**, 3485 (1989).

Translated by G. Skrebtsov

Physics of the Solid State, Vol. 42, No. 6, 2000, pp. 1100–1105. Translated from Fizika Tverdogo Tela, Vol. 42, No. 6, 2000, pp. 1068–1072.

MAGNETISM AND FERROELECTRICITY

Quantum Transformation of Spin Structure of a Fe_8 Nanocluster in Ultrastrong Magnetic Fields

A. K. Zvezdin, V. I. Plis, and A. I. Popov

Moscow State Institute of Electronic Engineering (Technical University), Zelenograd, Moscow oblast, 103498 Russia

Received July 16, 1999; in final form, November 25, 1999

Abstract—The transformation of the spin structure of a high-spin Fe_8 cluster in a strong magnetic field has been investigated. The magnetization and magnetic susceptibility of the material are calculated at different external magnetic fields and temperatures. It is shown that the magnetic field induces transformation of the spin structure of a Fe_8 cluster from the quasi-ferrimagnetic structure with an average magnetic moment of 20 μ_B per molecule to the quasi-ferromagnetic structure with a magnetic moment of 40 μ_B. Unlike a similar transformation of a Néel ferrimagnet, which is continuous and occurs through an intermediate angular phase, this process in Fe_8 at low temperatures manifests itself as a cascade of discrete quantum jumps, each being the transition accompanied by an increase in the spin number of the complex. At high temperatures, the behavior of the magnetic cluster approaches the cluster behavior described by the classical theory. The nature of quantum jumps is discussed in terms of the magnetic-field-induced energy level crossing in the ground state of a magnetic cluster.

1. INTRODUCTION

At present, intensive studies have been conducted with molecular crystals consisting of high-spin organic clusters with transition metal ions ($Mn_{12}Ac$, Fe_6, Fe_8, F_{10}, etc.) [1–11]. Magnetic interactions between clusters in these molecular crystals are negligibly weak. In terms of magnetism, they represent a set of virtually noninteracting magnetic subsystems and offer interesting possibilities in studies of quantum laws for systems with intermediate (mesoscopic), but well-defined dimensions. In this respect, particular attention has been given to the properties observed in magnetic clusters such as the bistability, quantum hysteresis, macroscopic quantum tunneling of magnetization, and giant quantum fluctuations [2–5, 8, 12]. By a molecular bistability is meant that the molecular cluster can exist in two different states, provided the external parameters change in a certain range. The molecular bistability is of obvious interest for development of information technologies [11]. The macroscopic quantum tunneling is closely connected with the properties of molecular bistability and holds considerable physical interest with respect to the fundamental problems of the quantum theory and, quite possibly, the problem of applying quantum methods to data processing. The magnetic clusters exhibit an intermediate-type behavior with the classical features (characteristic of bulk magnetic materials) and the specific quantum features, which are similar to those of individual atoms and molecules [9, 13].

In the present work, we investigated the Fe_8 cluster. The structure of this cluster is schematically shown in Fig. 1. Its general formula is $[(tacn)_6Fe_8O_2(OH)_{12}]$, where (*tacn*) is the so-called triazacyclopentane. The symmetry of the Fe_8 cluster is close to D_2. In weak fields, the cluster in the ground state has the total spin $S_t = 10$. This value is the result of antiferromagnetic exchange interactions between Fe^{3+} ions. Hence, this cluster can be considered a ferrimagnet on the molecular level. The most important characteristics of magnetic clusters are the exchange integrals specifying a particular magnetic structure of the cluster. Recently, it was shown with the $Mn_{12}Ac$ magnetic cluster as an example that the measurement of the transformation of the magnetic structure from ferrimagnetic to ferromagnetic is the efficient direct method for determining the exchange parameters of clusters. The measurements of the magnetic susceptibility of a $Mn_{12}Ac$ cluster upon transformation were carried out in megagauss magnetic fields with the use of MK-1 magnetic explosion generators. It is known that the classical ferrimagnet transforms into the angular phase with an increase in the magnetic field, and subsequently, the angular phase transforms into the ferromagnetic phase. These phase transitions are continuous for isotropic systems. However, in the case of magnetic clusters with antiferromagnetic exchange interaction between the magnetic ions, the transition from the ferrimagnetic state to the ferromagnetic state qualitatively differs from the classical transition. Specifically, this transition represents a sequence of quantum jumps in magnetization, each being accompanied with an increase in the spin number of the complex [9]. In the present work, we studied a similar transformation of the spin structure of a Fe_8 cluster in ultrastrong magnetic fields. The behavior of magnetization and magnetic susceptibility of the cluster was investigated at different field strengths and temperatures.

1063-7834/00/4206-1100$20.00

2. HAMILTONIAN, BASIS FUNCTIONS, AND MATRIX ELEMENTS

The Hamiltonian for the Fe_8 magnetic cluster can be represented in the form (Fig. 1) [10]

$$H = J_{12}(\mathbf{S}_1\mathbf{S}_2) + J_{13}(\mathbf{S}_1\mathbf{S}_3 + \mathrm{S}_2\mathbf{S}_3 + \mathbf{S}_2\mathbf{S}_4 + \mathbf{S}_1\mathbf{S}_4) + J_{15}(\mathbf{S}_1\mathbf{S}_5 + \mathbf{S}_1\mathbf{S}_8 + \mathbf{S}_2\mathbf{S}_7 + \mathbf{S}_2\mathbf{S}_6) \quad (1)$$

$$+ J_{35}(\mathbf{S}_3\mathbf{S}_5 + \mathbf{S}_3\mathrm{S}_7 + \mathbf{S}_4\mathbf{S}_6 + \mathbf{S}_4\mathbf{S}_8) + 2\mu_B H\sum_{i=1}^{8} S_{iz},$$

where $S_i = 5/2$.

This Hamiltonian comprises the matrix $6^8 \times 6^8$ in the space of spin states, which considerably complicates the direct numerical analysis of this system. For this reason, we use the hierarchy of exchange integrals in Hamiltonian (1) in order to analyze the energy spectrum of the system. According to [10], in Hamiltonian (1),

$$J_{12} = 25,\ J_{13} = 140,\ J_{15} = 17,\ J_{35} = 48\ \mathrm{cm}^{-1}. \quad (2)$$

Rewrite (1) in the form

$$H = H_0 + H', \quad (3)$$

where

$$H_0 = H_{01} + H_{0z}$$

$$= J_{13}(\mathbf{S}_1\mathbf{S}_3 + \mathbf{S}_2\mathbf{S}_3 + \mathbf{S}_2\mathbf{S}_4 + \mathbf{S}_1\mathbf{S}_4) + 2\mu_B H\sum_{i=1}^{4}\hat{S}_{iz}, \quad (4)$$

and the Hamiltonian H' involves the exchange interactions J_{12}, J_{15}, and J_{35}, and the remaining part of the Zeeman interaction.

Let us derive the eigenfunctions and energy levels of the Hamiltonian H_{01} It is easily seen that H_{01} can be represented as

$$H_{01} = J_{13}(\mathbf{S}_1\mathbf{S}_3 + \mathbf{S}_2\mathbf{S}_3 + \mathbf{S}_2\mathbf{S}_4 + \mathbf{S}_1\mathbf{S}_4) = J_{13}(\mathbf{S}_1 + \mathbf{S}_2)(\mathbf{S}_3 + \mathbf{S}_4). \quad (5)$$

It follows from (5) that the eigenfunctions of the H_{01} Hamiltonian correspond to the following scheme of summation of the angular momenta:

$$(\mathbf{S}_1 + \mathbf{S}_2) = \mathbf{S}_{12},\quad (\mathbf{S}_3 + \mathbf{S}_4) = \mathbf{S}_{34},\quad (\mathbf{S}_{12} + \mathbf{S}_{34}) = \mathbf{S}. \quad (6)$$

In (6), the S_{12} and S_{34} quantities can be equal to 0, 1, …, 5 in accord with $S = 0, 1, \ldots, 10$.

Thus, the eigenstates of Hamiltonian (5) are equal to the eigenstates of operators $\hat{S}_1^2$, $\hat{S}_2^2$, $\hat{S}_3^2$, $\hat{S}_4^2$ ($S_i = 5/2$), $\hat{S}_{12}^2$, $\hat{S}_{34}^2$, $\hat{S}^2$, and S_z. These eigenstates take the form

$$|S_1S_2(S_{12})S_3S_4(S_{34})SM_S\rangle$$

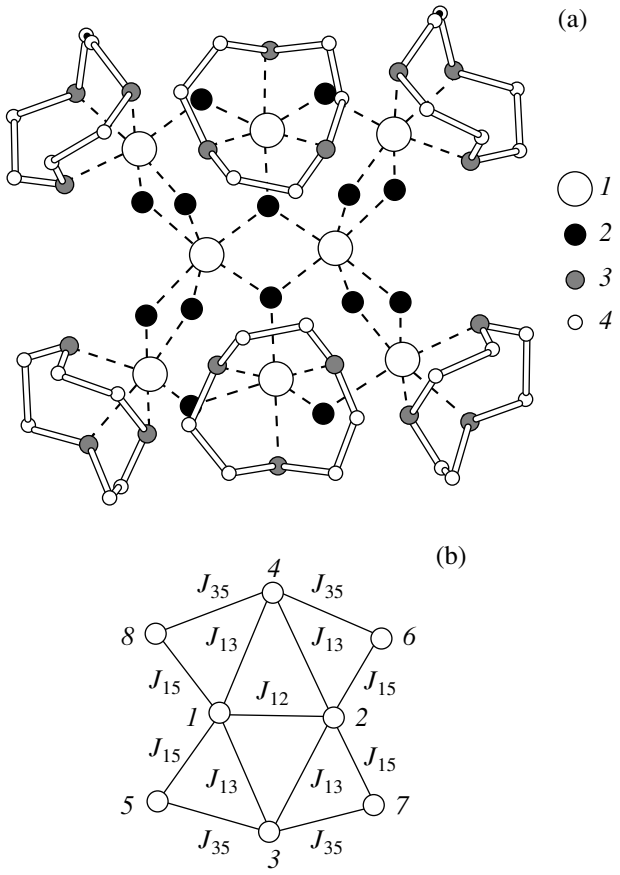

Fig. 1. (a) Structure of a Fe_8 cluster: (*1*) Fe_8, (*2*) O, (*3*) N, and (*4*) C ions. (b) Scheme of the exchange coupling of iron ions in a Fe_8 cluster.

$$= \sum C^{SM_S}_{S_{12}M_{12}S_{34}M_{34}} C^{S_{12}M_{12}}_{S_1m_1S_2m_2} C^{S_{34}M_{34}}_{S_3m_3S_4m_4} \times |S_1m_1\rangle|S_2m_2\rangle|S_3m_3\rangle|S_4m_4\rangle. \quad (7)$$

The energy levels of the Hamiltonian H_{01} have the form

$$E_{01}(S_{12}, S_{34}, S) = \frac{J_{13}}{2}[S(S+1) - S_{12}(S_{12}+1) - S_{34}(S_{34}+1)]. \quad (8)$$

In order to investigate the behavior of cluster magnetization, we will use only the actual states with $S_{12} = S_{34} = 5$ and $M_S = -S$, because, at a given S value, the states that correspond to the S_{12} and S_{34} values different from 5 lie substantially above ($\Delta E \geq 5J_{13} = 700\ \mathrm{cm}^{-1}$) and their thermal population can be neglected. Hereafter, we will omit the indexes S_{12}, S_{34}, and S_i ($i = 1, \ldots, 4$) in the notation of the eigenstates and energy levels [see expressions (7) and (8)]. The ground state of the Fe_8 cluster in weak fields is characterized by the total spin $S = 10$. This value can be achieved (at $J_{13} > 0$) solely on the condition that the ground states of ions 5–8 are the states with $|S_jm_j\rangle$ ($j = 5, \ldots, 8$) $S_j = 5/2$, $m_j = -5/2$.

Thus, as a first approximation, the actual states of the cluster as a whole can be written as

$$\Psi^{(0)}(S) = |SM_S = -S\rangle\prod_{j=5}^{8}|S_j m_j = -5/2\rangle. \quad (9)$$

Let us now calculate the mean energy of states (9). We invoke the condition that, for states (9),

$$\mathbf{S}_1\mathbf{S}_2 = \frac{S_{12} - S_1(S_1+1) - S_2(S_2+1)}{2} = \frac{25}{4},$$

$$\left(S_{12} = 5, S_1 = S_2 = \frac{5}{2}\right),$$

$$\langle S(-S)|S_{iz}|S(-S)\rangle = -\frac{S}{4} \quad (i = 1, \ldots, 4)$$

and find that

$$E^{(0)}(S, H) = \langle\Psi^{(0)}(S)|H|\Psi^{(0)}(S)\rangle$$
$$= \frac{J_{13}}{2}S(S+1) + (J_{15} + J_{35})\frac{5S}{2} - 2\mu_B HS - 20\mu_B H. \quad (10)$$

In relationship (10), we omitted the terms independent of both the quantum number S and H, because they lead to the shift of energy levels $E^{(0)}(S, H)$ by the same value and, consequently, can be ignored. It is worth noting that $J_{13} > J_{15}, J_{35}$ [see relationship (2)]. Nonetheless, for small S ($S = 0, 1, 2$), the second term in expression (10) either exceeds the first term or is comparable to it. Therefore, the use of states (9) as the first approximation functions is incorrect in the calculation of the energy spectrum of the Fe_8 cluster at small S values. In order to find the actual energy levels, we introduce the notation

$$\varphi_n^k([m_j]) = \varphi_{m(n)}^k(m_5, m_6, m_7, m_8)$$
$$= \frac{1}{\sqrt{N_k}}\sum_p\left(\prod_{j=5}^{8}|S_j m_j\rangle\right)_n^k, \quad (11)$$

where p are the nontrivial permutations of m_j, N_k is their number, $n = m + 10$ ($n = 0, 1, \ldots, 10 - S$); $m = \sum_{j=5}^{8} m_j$ is the sum of the magnetic moments of the quantum numbers of states for ions 5, …, 8; k index varies from 1 to r; and r is the number of different sets of m_j, (j = 5, …, 8), for which m remains constant. The states $\varphi_n^k([m_j])$ are the eigenfunctions of the operator $\sum_{j=5}^{8} S_{jz}$, that is,

$$\left\langle \varphi_n^k([m_j])\left|\sum_{j=5}^{8} S_{jz}\right|\varphi_n^k([m_j])\right\rangle = m = n - 10. \quad (12)$$

The operators $\sum_{j=5}^{8} S_{jz}$ and $\hat{H}$ commute. Consequently, only the following states of interest can be related to each other:

$$\Psi_n^k(S) = |(S+n)(-S-n)\rangle\varphi_n^k([m_j]). \quad (13)$$

They correspond to the same value of the total spin $S_{iz} = -S - 10$. Let us choose functions (13) as the initial basis functions for determination of the energy spectrum of the Fe_8 cluster.

The diagonal matrix elements of Hamiltonian (1) in basis set (13)

$$H_{nn}(S) = \langle\Psi_n^k(S)|H|\Psi_n^k(S)\rangle$$
$$= W_n(S) - 2\mu_B SH - 20\mu_B H, \quad (14)$$

$$W_n(S) = \frac{J_{13}}{2}(S+n)(S+n+1)$$
$$+ \frac{(J_{15} + J_{35})}{4}(S+n)(10-n). \quad (15)$$

The off-diagonal matrix elements can be calculated from the relationship

$$\langle S(-S)|\langle S_j(m_j - 1)|\mathbf{S}_i\mathbf{S}_j|S_j m_j\rangle|S+1(-S-1)\rangle$$
$$= \frac{\sqrt{35}}{16}f(S)C^{\frac{5}{2}m_j - 1}_{\frac{5}{2}m_j 1 - 1}, \quad (16)$$

where

$$f(S) = \sqrt{\frac{(S+12)(10-S)(S+1)}{2S+3}}, \quad (17)$$

which was derived from the relationships of the angular momentum theory [14]. In (16), index i takes any value from 1 to 4, and index j, from 5 to 8.

In order to elucidate the physical properties of the cluster in strong magnetic fields, it is sufficient to investigate the influence of the magnetic field on the behavior of low-lying energy levels, which are specified by the diagonalization of the matrices $H_{(nk)(n'k')}(S, H = 0)$ ($S = 0, 1, \ldots, 10$) with the ranks in the range from 60 (at $S = 0$) to 1 ($S = 10$).

Nonetheless, this problem is rather cumbersome. However, the analysis demonstrates that, even for the J_{ij} quantities given in (2), it is possible to use the perturbation theory and to obtain the analytical expressions for the actual energy levels of the Fe_8 cluster, which depend on the parameters J_{ij} and H.

3. ENERGY LEVELS IN A MAGNETIC FIELD

In the basis functions

$$\Psi_1 = |S, -S\rangle\varphi_0^{(1)}\left(\left[-\frac{5}{2} - \frac{5}{2} - \frac{5}{2} - \frac{5}{2}\right]\right),$$

$$\Psi_2 = |S+1, (-S-1)\rangle\varphi_1^{(1)}\left(\left[-\frac{3}{2}-\frac{5}{2}-\frac{5}{2}-\frac{5}{2}\right]\right),$$

$$\Psi_3 = |S+2, (-S-2)\rangle\varphi_2^{(1)}\left(\left[-\frac{1}{2}-\frac{5}{2}-\frac{5}{2}-\frac{5}{2}\right]\right),$$

$$\Psi_4 = |S+2, (-S-2)\rangle\varphi_2^{(2)}\left(\left[-\frac{3}{2}-\frac{3}{2}-\frac{5}{2}-\frac{5}{2}\right]\right)$$

the matrix $H_{pt} = H_{(nk)(n'k')}(S)$ takes the form

$$\|H\| = \begin{Vmatrix} W_0 & H_{12} & 0 & 0 & . \\ H_{21} & W_1 & H_{23} & H_{24} & . \\ 0 & H_{32} & W_2 & 0 & . \\ 0 & H_{42} & 0 & W_2 & . \\ . & . & . & . & . \end{Vmatrix}. \quad (18)$$

In this case, $H_{1t} = H_{2t} = 0$, $t = 5, 6, \ldots, r$, where r is the rank of the $H_{pt}(S)$ matrix,

$$H_{12} = \frac{1}{2}\sqrt{\frac{5}{2}}f(S)(J_{15} + J_{35}),$$

$$H_{23} = \frac{1}{2}f(S+1)(J_{15} + J_{35}), \quad (19)$$

$$H_{24} = \frac{\sqrt{15}}{4}f(S+1)(J_{15} + J_{35}),$$

$f(S)$ are defined by expression (17), and the W_i quantities ($i = 0, 1, 2$) are determined by formula (15). For small S ($S = 0, 1$) and the aforementioned values J_{ij} [see relationship (2)], the off-diagonal matrix element H_{12} is comparable to $W_1(0) - W_0(0)$. Specifically, at $S = 0$ and $H_{12} = 325$ cm^{-1}, $W_1(0) - W_0(0) = 286$ cm^{-1}. Hence, we perform the following transformations. Let us diagonalize the matrix

$$\begin{Vmatrix} W_0(S) & H_{12}(S) \\ H_{21}(S) & W_1(S) \end{Vmatrix}.$$

The eigenvalues and eigenvectors of this matrix are determined as

$$\tilde{E}_{12}^{(0)} = \frac{1}{2}[W_1(S) + W_0(S) \pm \sqrt{[W_1(S) - W_0(S)]^2 + 4H_{12}^2(S)}],$$

$$\tilde{\Psi}_1 = \tilde{C}_1(S)\Psi_1 - \tilde{C}_2(S)\Psi_2, \quad (20)$$

$$\tilde{\Psi}_2 = \tilde{C}_2(S)\Psi_1 + \tilde{C}_1(S)\Psi_2,$$

$$\tilde{C}_{1,2}(S) = \frac{1}{\sqrt{2}}\sqrt{1 \pm \frac{W_1(S) - W_0(S)}{\sqrt{(W_1(S) - W_0(S))^2 + 4H_{12}^2(S)}}}.$$

In the basis set formed by the functions $\tilde{\Psi}_1$, $\tilde{\Psi}_2$, Ψ_3, Ψ_4, …, the matrix $\|H\|$ takes the form

$$\|H\| = \begin{Vmatrix} \tilde{E}_1^{(0)} & 0 & -\tilde{C}_2H_{23} & -\tilde{C}_2H_{24} & . \\ 0 & \tilde{E}_2^{(0)} & C_1H_{23} & C_1H_{24} & . \\ -\tilde{C}_2H_{23} & C_1H_{23} & W_2(S) & 0 & . \\ -C_2H_{24} & C_1H_{24} & 0 & W_2(S) & . \end{Vmatrix}.$$

For $J_{13} = 140$ cm^{-1}, $J_{15} = 17$ cm^{-1}, and $J_{35} = 48$ cm^{-1}, even at $S = 0$, the value $W_2(S) - \tilde{E}_1^{(0)}(S) = 872$ cm^{-1} substantially exceeds the off-diagonal components $\tilde{C}_2H_{23}(0) = 121$ cm^{-1} and $\tilde{C}_2H_{24}(0) = 234$ cm^{-1}. In this case, within the approximation linear in $\chi = \frac{V}{W_2 - \tilde{E}_1^{(0)}} \ll 1$ ($V = \tilde{C}_2H_{24}, \tilde{C}_2H_{23}$), we obtain

$$E_0(S) = \tilde{E}_1^{(0)}(S) + \frac{\tilde{C}_2^2(H_{24}^2 + H_{23}^2)}{W_2(S) - \tilde{E}_1^{(0)}(S)}. \quad (21)$$

Numerical values of $E_0(S)$ ($S = 0, 1, \ldots, 10$) at the aforementioned values J_{ij} are listed in the table. The behavior of the actual levels in the field is defined by the expression

$$E_0(S, H) = E_0(S) - 2\mu_B SH - 20\mu_B H. \quad (22)$$

It follows from the table and formula (20) that an increase in the field strength leads to the sequential crossings of low-lying energy levels, which correspond to the different values of S and $M = -S - 10$ (M is the magnetic quantum number of the cluster as a whole). The field strengths, at which the change of states characterized by quantum numbers S and $S + 1$ takes place, can be determined from the expression

$$2\mu_B H_S = E_0(S+1) - E_0(S). \quad (23)$$

The H_S values for the J_{ij} exchange integrals determined in (2) are given in the table.

Energy levels of a Fe_8 cluster and magnetic fields of energy level crossings in the ground state

S	0	1	2	3	4	5	6	7	8	9	10
$E_0(S)$, cm^{-1}	–292	55	536	1153	1920	2808	3835	5000	6302	7745	9325
H_S, T	371	515	662	827	950	1099	1258	1393	1544	1698	

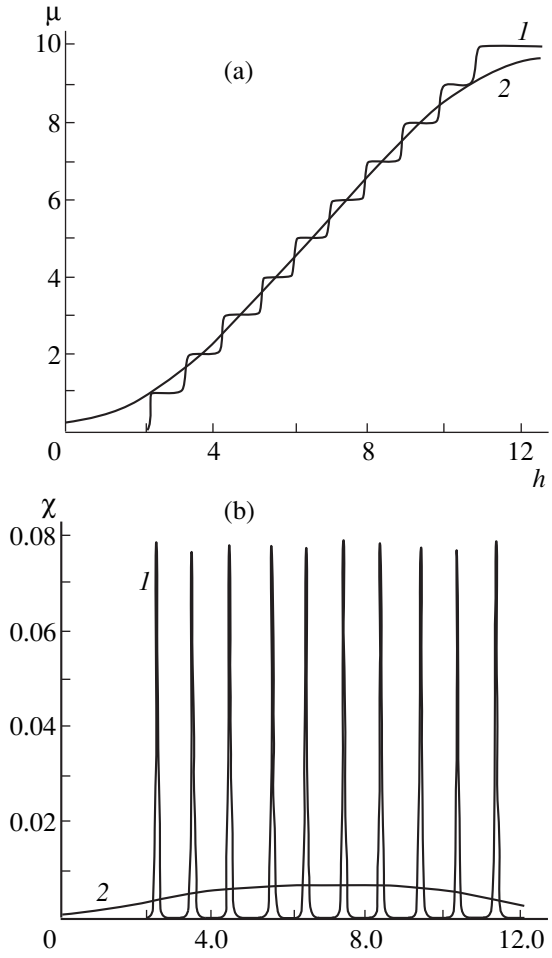

Fig. 2. Dependences of (a) the relative magnetization and (b) the relative magnetic susceptibility of a Fe_8 cluster on the magnetic field h. $h = 2\mu_B H/J_{13}$, (*1*) $\tau = kT/J_{13} = 0.02$ ($T = 4.2$ K) and (*2*) $\tau = 1.4$ ($T = 300$ K).

4. MAGNETIZATION AND MAGNETIC SUSCEPTIBILITY OF THE Fe_8 CLUSTER

The dependence of the cluster magnetization on the field strength and temperature is determined by the expression

$$M(H) = 2\mu_B \frac{\sum_{S=0}^{10} S\exp[-(E_0(S) - 2\mu_B SH)/kT]}{\sum_{S=0}^{10} \exp[-(E_0(S) - 2\mu_B SH)/kT]} + 20\mu_B, \quad (24)$$

where $E_0(S)$ are defined by formulas (21). Let us analyze the magnetic properties of the Fe_8 cluster. It is convenient to pass on to the dimensionless quantities $h = 2\mu_B H/J_{13}$, $\tau = T/J_{13}$, $\varepsilon_0(S) = E_0(S)/J_{13}$, and $\mu = M/2\mu_B$. Then, expression (24) takes the form

$$\mu(h, \tau) = \tilde{\mu}(h, \tau) + S_0,$$

$$\tilde{\mu}(h, \tau) = Z^{-1}\sum_{S=0}^{10} S\exp\left(-\frac{\varepsilon_0(S) - hS}{\tau}\right), \quad (25)$$

$$Z = \sum_{S=0}^{10} \exp\left(-\frac{\varepsilon_0(S) - hS}{\tau}\right),$$

$S_0 = 10$ is the spin of the ground state in weak magnetic fields.

From expression (25), we can easily derive the formula for the dimensionless magnetic susceptibility

$$\chi(h, \tau) = (\partial\mu(h, \tau)/\partial h)_\tau = \tau^{-1}\left\{Z^{-1}(h, \tau)\sum_{S=0}^{10} S^2\exp\left(-\frac{\varepsilon_0(S) - hS}{\tau}\right) - \tilde{\mu}^2(h, \tau)\right\}.$$

Figure 2 demonstrates the dependences of the magnetization (Fig. 2a) and magnetic susceptibility (Fig. 2b) for the cluster Fe_8 on the external magnetic field. The dependences were calculated at $J_{12} = 25$, $J_{13} = 140$, $J_{15} = 17$, and $J_{35} = 48$ cm^{-1} for low temperature $T_1 = 4.2$ K ($\tau_1 = 0.02$) and high temperature $T_2 = 300$ K ($\tau_2 = 1.4$).

Thus, we theoretically studied the magnetic-field-induced transformation of the spin structure of the Fe_8 magnetic cluster. It was shown that the transition from the ferrimagnetic structure to the ferromagnetic one is realized through a set of ten quantum jumps with a jump amplitude equal to $1\mu_B$. All the jumps occur in a megagauss field. The first three jumps can be measured with the modern MK-1 generators [15]. The measurements of the other jumps require ultrastrong fields above 10 MG.

ACKNOWLEDGMENTS

This work was supported by the Russian Foundation for Basic Research (project no. 97-02-17-972a), the Foundation for Basic Natural Sciences of the Ministry of Education of the Russian Federation (project no. 97-0-7.036), the International Scientific and Technical Program (MNTP) (project no. 97-1071), and the Federal Program “Integration” (project no. K-0573).

REFERENCES

1. D. Gatteschi, A. Caneschi, L. Pardi, and R. Sessoli, Science (Washington, D. C.) **265**, 1054 (1994).
2. R. Sessoli, D. Gatteschi, A. Caneschi, and H. A. Novak, Nature (London) **356**, 141 (1993).
3. J. R. Friedman, M. P. Sarachik, J. Tejada, and R. Ziolo, Phys. Rev. Lett. **76**, 3830 (1996).
4. L. Thomas, F. Lionti, R. Ballou, *et al.*, Nature (London) **383**, 145 (1996).

5. V. V. Dobrovitski and A. K. Zvezdin, Europhys. Lett. **38**, 377 (1997).
6. R. Sessoli, Hin-Lien Tsai, A. R. Shake, *et al.*, J. Am. Chem. Soc. **115**, 1804 (1993).
7. A. Caneschi, D. Gatteschi, and R. Sessoli, J. Am. Chem. Soc. **113**, 5872 (1991).
8. L. Gunther, Europhys. Lett. **39**, 1 (1997).
9. A. K. Zvezdin and A. I. Popov, Zh. Éksp. Teor. Fiz. **109**, 2115 (1996) [JETP **82**, 1140 (1996)].
10. A. I. Barra, P. Debrunner, D. Gatteschi, *et al.*, Europhys. Lett. **35**, 133 (1996).
11. O. Kahn and C. Jay Martínez, Science (Washington, D.C.) **279**, 44 (1998).
12. A. K. Zvezdin, V. V. Dobrovitski, B. N. Harmon, and M. I. Katsnelson, Phys. Rev. B **58**, R14733 (1998).
13. A. K. Zvezdin, in *Field-Induced Phase Transitions in Ferrimagnets. Handbook of Magnetic Materials*, Ed. by K. H. J. Buschov (Elsevier, Amsterdam, 1995), Vol. 9, p. 405.
14. D. A. Varshalovich, A. N. Moskalov, and V. K. Khersonskiĭ, *Quantum Theory of Angular Momentum* (Nauka, Leningrad, 1975).
15. A. D. Sakharov, Usp. Fiz. Nauk **88**, 725 (1966) [Sov. Phys. Usp. **9**, 294 (1966)].

Translated by N. Korovin

Physics of the Solid State, Vol. 42, No. 6, 2000, pp. 1106–1109. Translated from Fizika Tverdogo Tela, Vol. 42, No. 6, 2000, pp. 1073–1076.

MAGNETISM AND FERROELECTRICITY

Self-Oscillations of an Ordered Magnetic Structure

S. K. Godovikov*, V. P. Petukhov*, Yu. D. Perfil'ev, and A. I. Firov*****

**Institute of Nuclear Physics, Moscow State University, Vorob'evy gory, Moscow, 119899 Russia*

***Chemical Department, Moscow State University, Vorob'evy gory, Moscow, 119899 Russia*

****A. A. Baĭkov Institute of Metallurgy and Materials Science, Russian Academy of Sciences, Leninskiĭ pr. 49, Moscow, 117911 Russia*

Received August 10, 1999; in final form, December 6, 1999

Abstract—The first observation of self-oscillations of an ordered magnetic structure is reported. They were detected by the Mössbauer effect in the $Tb_{0.8}Y_{0.2}Fe_2$ ferrimagnetic compound and occur with a period of several days. The oscillations were initiated by a single electric-field pulse (~10^8 kV cm^{-1} s^{-1}). A phenomenological model of the phenomenon is proposed. © *2000 MAIK "Nauka/Interperiodica".*

The $TbFe_2$ ferrimagnetic compound was studied intensely by various physical methods. It is known to possess a record-high magnetic anisotropy and magnetostriction at T = 293 K [1]. Its Mössbauer parameters, corresponding to two magnetically inequivalent positions of the Fe atom in the RFe_2 structure, were investigated in considerable detail. In 1997, a Mössbauer study of $Tb_{0.8}Y_{0.2}Fe_2$ ($TbFe_2$ with an Y nonmagnetic impurity) revealed long-time relaxation (on the scale of days and months) of an ordered magnetic structure [2, 3]. It consists in that, after application of a magnetic-field pulse (~3 ms, up to 250 kOe) to a sample, part of the Fe atoms change orientation, thereafter slowly and aperiodically returning to the initial state after several days or weeks. The diversity of the extremal physical properties of this magnet is not apparently limited to the above manifestations. It is known [1] that the magnetic anisotropy in rare-earth magnets is of an electrostatic nature. This has inspired our attempt at probing the relaxation properties of the $Tb_{0.8}Y_{0.2}Fe_2$ magnetic structure with a pulse of the field with the Mössbauer effect. This time the field is electric.

1. TECHNIQUE AND RESULTS OF THE EXPERIMENT

The experiment with the electric field had a number of specific methodological features. The sample was a polycrystalline Mössbauer absorber, 0.2 mm thick and 25 mm in diameter, deposited from a powder suspension in a glue on a Mylar substrate. All operations with the sample and measurements were performed at T = 293 K. The disk sample, insulated by 0.1 mm thick teflon washers, was clamped between the plates of a specially designed, variable-gap capacitor. The voltage (16–18 kV) was supplied to the capacitor from a high-voltage power pack of a REIS-I x-ray emitter. An electric pulse ~0.3 μs long was produced by closing the capacitor plates, one of them being grounded. The rate of electric-field variation was ~10^8 kV cm^{-1} s^{-1}, and the field was applied in a single pulse. The measurements were carried out with a Co^{57} Mössbauer source in Cr on a Perseĭ setup, which is capable of providing Doppler shifts of an object to within 0.001 mm s^{-1}. The x-ray structural analysis was made with a DRON-3 diffractometer.

Several series of Mössbauer measurements were carried out immediately after the electric-field application. The time taken to obtain a spectrum was ~12 h, with an interval between measurements of one to two days. The spectrum can be decomposed into two sextets of lines with different magnetic hyperfine fields (H_1 and H_2), isomer shifts (δ_1 and δ_2), quadrupole splittings (Q_1 and Q_2), linewidths (Γ_1 and Γ_2), and populations of the sextets A_1 and A_2 (A_1/A_2). While, within the realm of traditional concepts, an electric field cannot affect these parameters in any way, the experiment showed the reverse to be true. Figure 1 presents the A_1/A_2, H_1 and H_2, Q_1 and Q_2 parameters as functions of time during a period covering ~40 days. The initial points correspond to the original state of the sample. One clearly sees that the A_1/A_2 parameter (as well as Q_2 and H_2) does depend on time and that this relation is oscillatory. During the initial period of time (of up to two weeks) the oscillation period of A_1/A_2 is ~5 days, then it decreases to 2–3 days, after which the oscillations take on a somewhat irregular, stochastic character. Measurements of an unperturbed sample, as well as of a sample subjected to the slowly (~10 min) decreasing electric field, revealed no changes in the hyperfine coupling parameters. X-ray measurements made at T = 293 K showed that the cubic structure of $Tb_{0.8}Y_{0.2}Fe_2$ is rhombohedrally distorted and that the rhombohedron angle α = 89.88°.

1063-7834/00/4206-1106$20.00

2. DISCUSSION OF RESULTS

The oscillations seen in Fig. 1 reflect self-oscillations of the atomic magnetic structure of the material. This is the first time the phenomenon has been observed. The fact that they were revealed in this particular magnet is associated with a unique combination of its structural and magnetic properties. Figure 2 shows a fragment of the $TbFe_2$ structure (the Laves phase). The Tb atoms form a diamond lattice, whose unit cell contains four Fe tetrahedra arranged identically with the one shown in the figure. The easy magnetization axis is [111]. The ϑ angle between the magnetic moment of an Fe atom and the electric-field gradient axis assumes two values, $\vartheta = 0$ and $70°32'$, and it is this that accounts for the magnetic difference between Fe atoms as a result of combined magnetic dipole and electric quadrupole interaction, as well as of the anisotropic hyperfine interaction. As is evident from Fig. 2, in a normal state, $A_1/A_2 = 3$, and this is exactly what is initially observed (Fig. 1). One can readily understand how deviations from the normal state arise. For this to occur, the ϑ angle for at least one of the Fe atoms in Fig. 2 must change. For instance, a moment flip of the type of $70°32' \longrightarrow 0°$ would result in $A_1/A_2 = 2 : 2 = 1$ and that of the type $0° \longrightarrow 70°32'$, in $A_1/A_2 = 4 : 0$, i.e. destruction of the magnetic inequivalence. If structural defects of the latter type appear in at least one of the three cells, this will yield an average value $A_1/A_2 = 5$, which is close to the experimental one (Fig. 1). The absence of uniformity in the rotation of the moments and the preferred nature of individual Fe atoms are apparently accounted for by their closeness to Y nonmagnetic atoms, whose concentration relative to Fe is 1 : 10.

The electric field was applied to the metallic sample under study for $\sim 10^{-6}$ s. This is equivalent to the action of an electromagnetic wave with a frequency of the order of a few MHz during this time. The skin-layer thickness here is ~0.1 mm, so the field penetrates completely into the absorber particles, whose dimensions are ~0.01 mm. The magnetic field of the displacement currents in this experiment is $\sim 10^{-3}$ Oe, and it does not affect the magnetic structure in any way. Recalling the results of the experiment with a smooth decrease of the field in the capacitor, one can thus consider it to be established that the observed physical phenomena are caused by a sudden drop of the electric field E^0 to zero, i.e., by the derivative dE^0/dt becoming as high as 10^8 kV cm^{-1} s^{-1}.

The electric-field pulse displaces the lattice ions. The energy of this displacement, the energy of magnetoelastic interaction, and the energy of rhombohedron formation should be of the same order of magnitude, because they are actually based on the electrostatic interaction producing the magnetic anisotropy. The energy of rhombohedron formation can be calculated

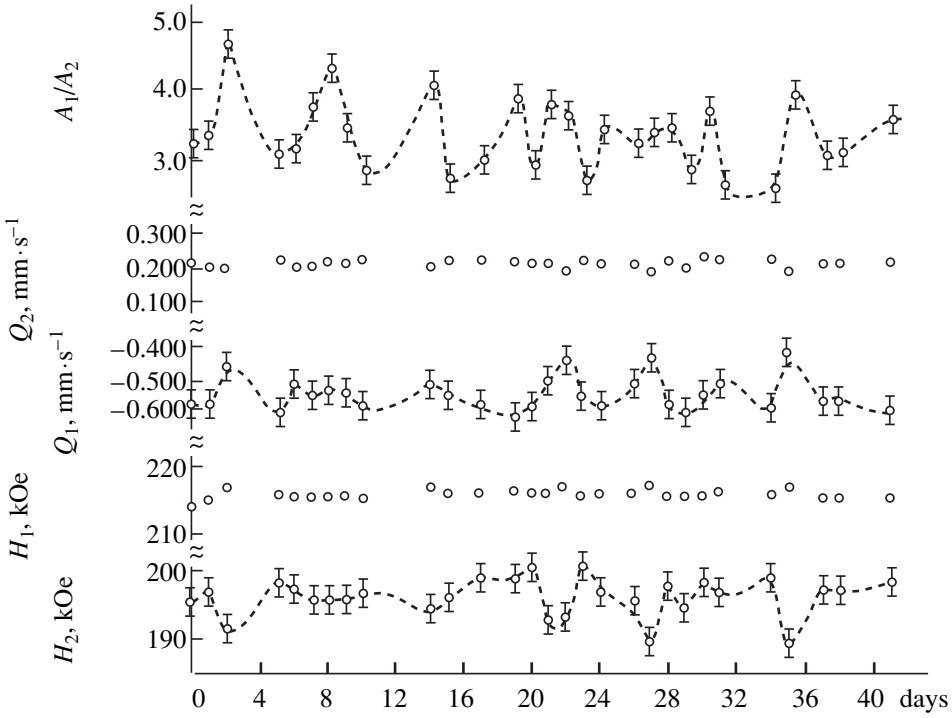

Fig. 1. Temporal dependences of the parameters of $Tb_{0.8}Y_{0.2}Fe_2$ Mössbauer spectra: A_1/A_2 (relative sextet population), Q_1 and Q_2 (quadrupole splittings), and H_1 and H_2 (magnetic hyperfine fields).

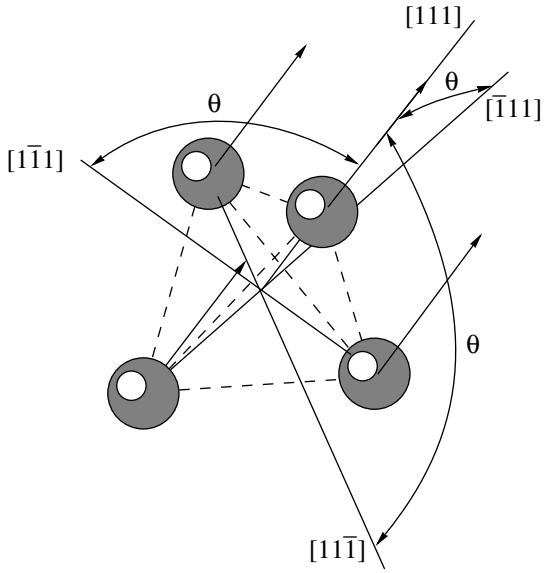

Fig. 2. Fe atom arrangement in the $TbFe_2$ structure. The arrows depict Fe magnetic moments.

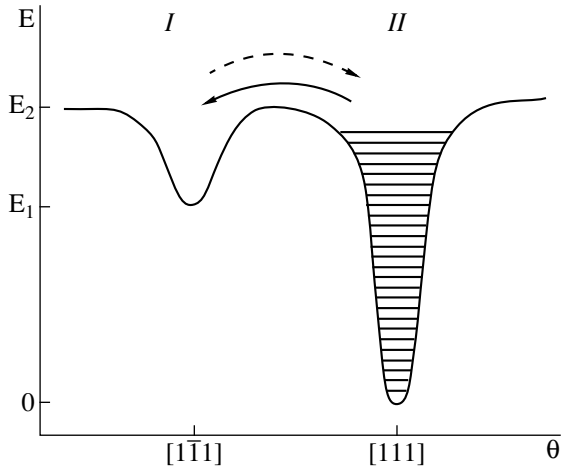

Fig. 3. Energy scheme of the process of self-oscillations of the magnetic moments of Fe atoms.

as the work done to displace the ions so as to deform the cube faces through an angle $\Delta\alpha \sim 0.12°$. It is ~0.01 eV/ion. While the accuracy of the x-ray structural analysis (0.001 Å) turned out to be not high enough to establish the possible change of the lattice parameter, a change of $\Delta\alpha$ is conceivable. That the ion displacement process is real is also indicated by the fact that the isomer shift parameter δ_1 changed after the field application by ~0.06 mm s^{-1}, and the Q_2 parameter changed by ~0.15 mm s^{-1}, i.e., quite significantly. This means that the lattice received an ion displacement energy, which is subsequently transformed into the energy of magnetic perturbation $\Delta E \sim 0.01$ eV/ion.

Consider now the oscillation process as a whole. The energy ΔE creates, in a part of unit cells, one more direction of moment orientation of the [111] type, which differs from the one already available in the given cell, for instance, $[1\bar{1}1]$. This is possible if the $[1\bar{1}1]$ axis and the direction of deformation coincide. As a result, part of the moments make a flip of the type $0° \longrightarrow 70°32'$, which brings about a growth of A_1/A_2, as described above. Figure 3 presents an energy scheme used in the subsequent discussion. It consists of two mutually coupled potential wells I and II, connected conventionally with the $[1\bar{1}1]$ and [111] directions, respectively. Well I is more shallow than well II, apparently by at least a factor of three. It is this depth ratio that would fit the observed maximal values of the A_1/A_2 parameter (Fig. 1). The depth E_2 of well II is ~0.01 eV/ion, as can be inferred from the exchange interaction intensity for $TbFe_2$, whose Curie point is 682 K.

We introduce an average angle $\vartheta_{av}(t)$, which characterizes the degree of moment flips to the $[1\bar{1}1]$ axis as a function of time, in the form

$$\vartheta_{av}(t) = 70°32' \cdot N_{[1\bar{1}1]}(t)/[N_{[1\bar{1}1]}(t) + N_{[111]}(t)], \quad (1)$$

where $N_{[1\bar{1}1]}(t)$ and $N_{[111]}(t)$ are the numbers of moments in wells I and II, respectively. The true angle ϑ assumes only two discrete values, but ϑ_{av}, which characterizes the change of the magnetic structure of the sample as a whole, varies smoothly. The growth of $N_{[1\bar{1}1]}(t)$ implies an increase of $\vartheta_{av}(t)$ and of the associated energy, which can be expressed as $\xi\vartheta_{av}(t)$, where ξ is a normalization factor of proportionality. On the other hand, a change in the orientation of an individual moment brings about a change of the magnetic flux and creates additional energy proportional to the rate of this change. This additional term can be expressed through ϑ_{av} as $\tau d\vartheta_{av}/dt$, where τ is the relaxation time of the system of magnetic moments. The ϑ_{av} change is driven by the energy E_2 of moments in well II and by the energy of the magnetic perturbation ΔE. Thus, the energy balance equation for the motion of magnetic moments can be written as

$$\xi(\tau d\vartheta_{av}/dt + \vartheta_{av}) = E, \qquad E = E_2 + \Delta E. \quad (2)$$

For the initial stage of ϑ_{av} variation, equation (2) has a solution of the form

$$\vartheta_{av}(t) = E/\xi[1 - \exp(-t/\tau)]. \quad (3)$$

Equation (3) permits an estimate that the time Δt_1 for the transfer of a moment into well I does not exceed, in order of magnitude,

$$\Delta t_1 \sim \tau \ln[(E - E_1)/(E - E_2)]. \quad (4)$$

The quantity ΔE is not constant. After well I is completely filled, it reverses its sign sharply, and, because E_2 and ΔE are approximately equal in magnitude, equation (2) takes on a substantially different form

$$\tau d\vartheta_{av}/dt + \vartheta_{av} = 0. \quad (5)$$

The physical meaning of this is that well I is filled to a greater extent than well II, which initiates a reverse transfer of magnetic moments with a characteristic time

$$\Delta t_2 = \tau \ln E_2/E_1. \quad (6)$$

Thus, the period of the total process Δt is

$$\Delta t = \Delta t_1 + \Delta t_2. \quad (7)$$

The filling of well II means a return to the initial state, where $\Delta E > 0$, and conditions (2) and (3) are met. Therefore, the process repeats, and a new cycle of the oscillation begins. The sign reversal of ΔE is due to the fact that this quantity includes the change in the crystal-field energy induced by the moment rotation, during which the moment direction passes through the region of the hard-magnetization axis [100], where the sign of the magnetic anisotropy constant K_1 is opposite to that of the initial state. The form of the differential equations (2) and (5) indicates that the oscillations have a relaxation character. They are essentially self-oscillations drawing on the energy of the initial lattice deformation, which gradually goes into temporal magnetoelastic processes.

Let us now estimate the Δt parameter. It is known [3] that the characteristic time of aperiodic relaxation of magnetic moments in the system under study $\tau \sim$ 7 days. Whence, according to (4), $\Delta t_1 \approx 2$ d, while by (6) $\Delta t_2 \approx 2.8$ d, i.e., $\Delta t \approx 4.8$ d. This is close to the experimentally observed periodicity of the initial part of the A_1/A_2 dependence on time, which is ~5 d (Fig. 1). The Δt parameter is very critical to the value of E_1, i.e., to the depth of well I. According to (4) and (6), an increase of E_1 results in a decrease of Δt. This effect becomes manifest at times above two weeks (Fig. 1), when the amplitude of A_1/A_2 oscillations has decayed with time, which is equivalent to a decrease of the depth of well I. Besides, Δt is very sensitive to the magnitude of ΔE. If ΔE is very small (a weak perturbation), then, by (4), $\Delta t_1 \longrightarrow \infty$; i.e. an aperiodic process sets in. Such cases were indeed observed in preliminary experiments with electric-field application [4].

An analysis of the flipping of moments on the microscopic scale suggests that it occurs by the cluster mechanism, and that, for the observed relaxation times, the cluster size should be ~20 Fe magnetic moments [3]. This accounts for the stochastic character of the oscillations at long times (>25 d), when the perturbation centers become apparently scattered over the crystal. This hinders the formation of large clusters, while small ones are known [3] to decay within a very broad time spectrum, from a few minutes to several days.

Consider now the behavior of the H_1, H_2, Q_1, and Q_2 parameters (Fig. 1). The temporal stability of the H_1 and Q_1 parameters is due to the fact that they relate to the large part of Fe atoms that are not adjacent to Y atoms and are stable against perturbation. On the other hand, the H_2 and Q_2 parameters are connected with that part of the Fe atoms whose moments flip in at least one of three unit cells. This process brings about a slight perturbation of the local magnetic and atomic structure and, hence, of the H_2 and Q_2 parameters, which should be opposite in phase, and that is exactly what is expected in the case of combined hyperfine interaction.

ACKNOWLEDGMENTS

Support of the "Universities of Russia: Basic Research" program (grant no. 5363) is gratefully acknowledged.

REFERENCES

1. K. P. Belov, *Rare-Earth Magnets* (Nauka, Moscow, 1980).
2. S. K. Godovikov, Yu. D. Perfiliev, Yu. F. Popov, and A. I. Egorov, in *Abstracts of the International Conference on Applications of Mossbauer Effect, Rio de Janeiro, 1997*, P.MO.T8.PO4.
3. S. K. Godovikov, Yu. D. Perfil'ev, Yu. F. Popov, and A. I. Firov, Fiz. Tverd. Tela (St. Petersburg) **40**, 508 (1998) [Phys. Solid State **40**, 467 (1998)].
4. S. K. Godovikov, Yu. D. Perfil'ev, and V. P. Petukhov, in *Abstracts of the All-Russian Conference on Applications of Methods of Nuclear Physics in the Magnetism and Materials Sciences, Izhevsk, 1998*, p. 39.

Translated by G. Skrebtsov

Physics of the Solid State, Vol. 42, No. 6, 2000, pp. 1110–1115. Translated from Fizika Tverdogo Tela, Vol. 42, No. 6, 2000, pp. 1077–1082.

MAGNETISM AND FERROELECTRICITY

Thermal-Expansion and Magnetostriction Anomalies in Phase Transitions in $La_{1-x}Sr_xMnO_3$

A. M. Kadomtseva*, Yu. F. Popov*, G. P. Vorob'ev*, K. I. Kamilov*, V. Yu. Ivanov, A. A. Mukhin**, and A. M. Balbashov*****

**Moscow State University, Vorob'evy gory, Moscow, 119899 Russia*

e-mail: popov@plms.phys.msu.su

***Institute of General Physics, Russian Academy of Sciences, ul. Vavilova 38, Moscow, 117942 Russia*

****Moscow Power Institute, Krasnokazarmennaya ul. 14, Moscow, 111250 Russia*

Received in final form, December 14, 1999

Abstract—A study is reported on phase transitions in the $La_{1-x}Sr_xMnO_3$ system, both spontaneous and induced by a pulsed magnetic field of up to 250 kOe, accompanied by anomalies in magnetoelastic properties. The temperatures of the polaron (charge) and magnetic ordering, as well as those of structural transitions, are observed to be in good agreement with the results obtained by other methods. Jumps in the field dependence of longitudinal and transverse magnetostriction associated with field-induced orbital ordering have been found. A strong temperature dependence of the corresponding threshold fields is observed. © *2000 MAIK "Nauka/Interperiodica".*

In the recent years, immense interest has been focused on the investigation of substituted oxides in the $La_{1-x}Sr_xMnO_3$ system, which is primarily due to the observation of the colossal magnetoresistance effect in them. Studies have revealed a number of new and interesting phenomena in these materials, which are associated with carrier localization and charge ordering of the Mn^{3+}/Mn^{4+} ions, orbital ordering of the Mn^{3+} ions, as well as with magnetic-field-induced magnetic and structural phase transitions and semiconductor–metal-type phase transitions [1–4].

The mechanism of these phenomena is connected, on one hand, to the strong ferromagnetic exchange coupling appearing when the crystal is doped by divalent ions Sr^{2+} and Ca^{2+} (Zener's double exchange). On the other hand, as shown by recent theoretical studies, an important part is played here by lattice distortions caused by the Jahn–Teller effect at the Mn^{3+} ions and by the formation of magnetic polaron states [5], as well as by structural inhomogeneities associated with the substitution of divalent Sr^{2+} (Ca^{2+}) for the rare-earth ion.

Although doped manganites exhibit a direct correlation between structural distortions, magnetic ordering, and transport properties, studies on spontaneous and magnetic-field-induced structural phase transitions in these compounds are relatively scant.

This work was aimed at studying the magnetic properties, thermal expansion, and magnetostriction in strong pulsed magnetic fields of up to 250 kOe in $La_{1-x}Sr_xMnO_3$ single crystals (the results obtained were partially published in [6]). $La_{1-x}Sr_xMnO_3$ single crystals (x = 0, 0.1, 0.125, 0.15, 0.175, 0.2, 0.25) were grown by zone melting. X-ray diffraction analysis showed the grown crystals to be single phase and, as a rule, twinned. The magnetization $M(T, H)$ and magnetic susceptibility $\chi_{ac}(T)$ were measured in static fields H = 12 kOe at T = 4.2–300 K. The magnetostriction was measured with a quartz probe, pasted to the sample, in pulsed magnetic fields of up to 250 kOe within the temperature interval of 10–300 K. Thermal expansion was determined with a conventional strain gauge in the range from 78 to 350 K.

In pure $LaMnO_3$ [7, 8] with a distorted perovskite structure, the spins of Mn^{3+} are ordered below T_N = 140 K antiferromagnetically along the b axis of the rhombic crystal and possess a weak transverse ferromagnetic moment along the c axis (A_yF_z-type layered magnetic structure). The weak ferromagnetic moment and the transverse susceptibility at T = 4.2 K are m_0 = 4.2 ± 0.emu/g and $\chi_\perp = (1.8 \pm 0.3) \times 10^{-4}$ cm^3/g, respectively.

The longitudinal magnetostriction $\lambda_\parallel$ of $LaMnO_3$ was measured in a magnetic field oriented along the b axis in one of the twin types. Figure 1 illustrates the $\lambda_\parallel(H)$ dependence for several temperatures. As seen from Fig. 1, at $H = H_{cr} \sim 200$ kOe, one observes a jump against a background of a smooth variation of magnetostriction, which we assign to a spin reorientation of the weak ferromagnetic moment from the c to b axis of the crystal (A_yF_z–A_zF_y) in the corresponding twin type. This transition is accompanied by a hysteresis in the behavior of the $\lambda(H)$ relation. The threshold field of the transition can be found from expression [9]

$$H_{cr} = -H_D + (H_D^2 + 2H_AH_E)^{1/2},$$

1063-7834/00/4206-1110$20.00

where $H_E = M_0/2\chi_\parallel \approx 330$ kOe is the isotropic exchange field, $H_D = m_0/\chi_\perp \approx 23$ kOe is the antisymmetric exchange field, $H_A = K_{cb}/M_0$ is the anisotropy field in the *bc* plane and K_{cb} is the corresponding anisotropy constant, and $M_0/2$ is the sublattice magnetization. The threshold field in our experiment decreased by ~30 kOe with increasing temperature by about 100 K. Using the antiferromagnetic resonance frequency value for $LaMnO_3$ [7, 10]

$$\hbar\omega = g\mu_B(2H_AH_E)^{1/2} \approx 17\text{–}19 \text{ cm}^{-1}$$

at $T < 50$ K ($g = 2$), we obtain an estimate for H_{cr} of 180–200 kOe, which is in good agreement with our experiment.

All the substituted compounds studied by us exhibited anomalies in the temperature dependence of thermal expansion $\frac{\Delta l}{l}(T)$ and in the field dependence of magnetostriction $\lambda(H)$ which are due to magnetic and structural phase transitions.

The temperature dependence of thermal expansion obtained in the zero magnetic field is presented in Fig. 2.

For the $x = 0.1$ composition, one observed clearly pronounced anomalies near the temperatures of polaron (charge) ordering ($T_p = 130$ K) and of the structural ($T_s' = 300$ K) phase transition from the orthorhombic (Jahn–Teller) phase *O*' to the weakly distorted orthorhombic (pseudocubic) phase *O** [11].

For $x = 0.125$, a negative jump in thermal expansion during the polaron (charge) ordering at $T_p = 150$ K was observed, as well as a sharp increase of thermal expansion near the *O*'–*O** structural transition at $T_s' = 250$–270 K [11].

For $x = 0.15$, the thermal expansion decreased near $T_p = 200$ K and increased again in the 210–240 K interval, where magnetic ordering and the *O*'–*O** structural transition occur.

For the $x = 0.175$ composition, where there is no polaron (charge) ordering, we associate the thermal-expansion anomaly near 200 K with a structural phase transition from the rhombohedral *R* to rhombic (pseudocubic) *O** structure, and the slight bend in the $\frac{\Delta l}{l}(T)$ curve near 290 K is due to the ferromagnetic ordering at the Curie point [11].

The $x = 0.2$ and 0.25 compositions, which, according to the phase diagram of [11], do not undergo any phase transitions in the temperature region studied, do not exhibit anomalies in the temperature dependence of thermal expansion.

Particular attention in this work was focused on the magnetostriction of substituted $La_{1-x}Sr_xMnO_3$ compo-

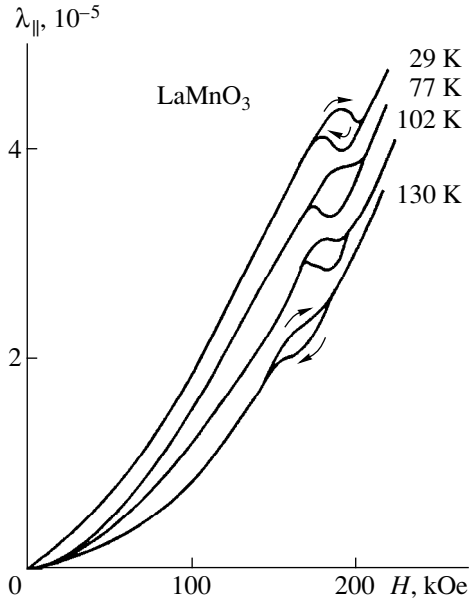

Fig. 1. Field dependences of longitudinal magnetostriction for $LaMnO_3$.

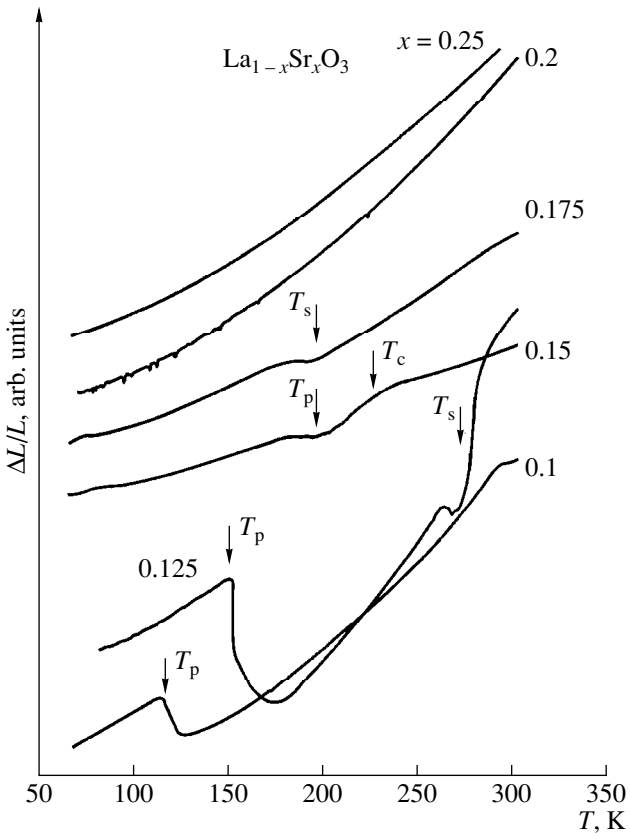

Fig. 2. Thermal expansion of $La_{1-x}Sr_xMnO_3$ for $x = 0.1$, 0.125, 0.15, 0.175, 0.2, and 0.25. The arrows here and in other figures identify the temperatures of magnetic and structural transitions.

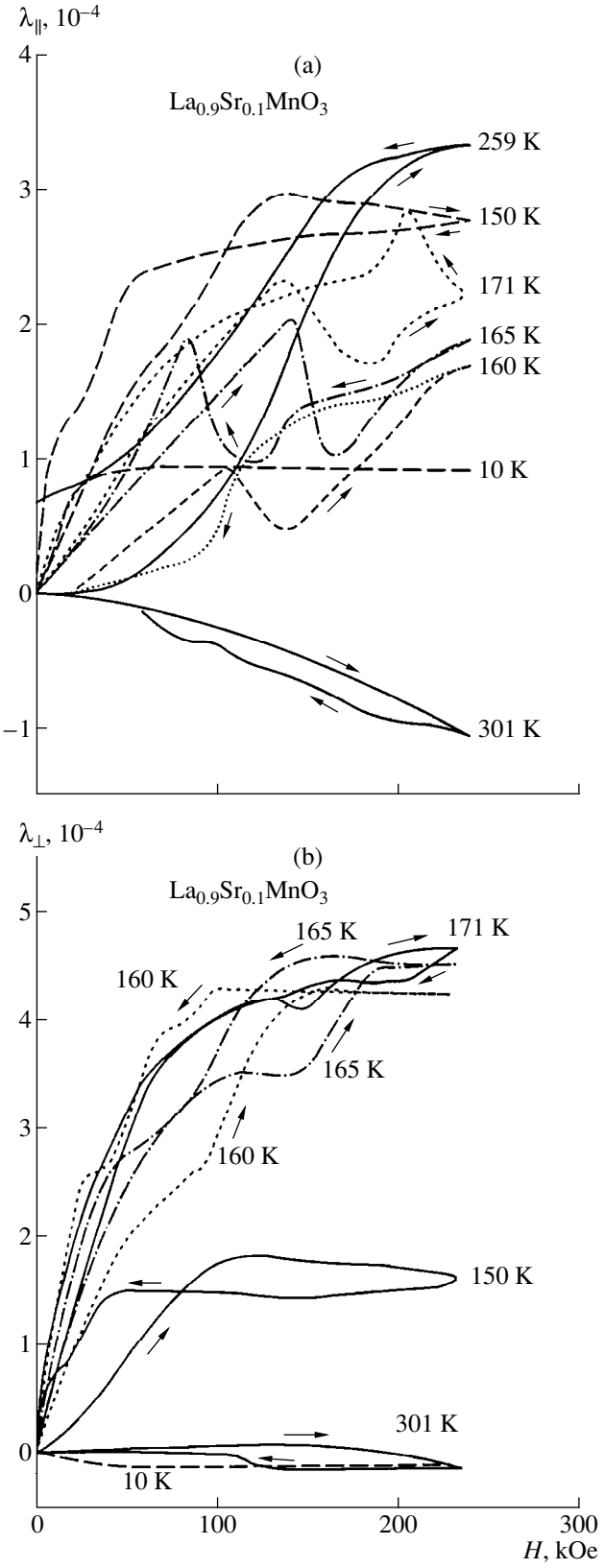

Fig. 3. Field dependences of (a) longitudinal $\lambda_{\parallel}$ and (b) transverse $\lambda_{\perp}$ magnetostriction of $La_{0.9}Sr_{0.1}MnO_3$ obtained at different temperatures.

sitions (x = 0.1, 0.125, 0.15), for which, as already pointed out, a large variety of phase transitions occur.

The field dependence of longitudinal magnetostriction for the x = 0.1 composition (Fig. 3a), for which T_p = 130 K, T_c = 160–170 K, and T_s = 300 K [11], had no anomalies at $T < T_p$, and the saturated magnetostriction was $\sim 1 \times 10^{-4}$. As the temperature increased above T_p, one observed a substantial growth of magnetostriction (see, e.g., the curve for 150 K), with a sharp break evident at 150 K in the $\lambda_{\parallel}(H)$ curve. As the temperature increased further (curves at 160 and 171 K), the breaks in the $\lambda_{\parallel}(H)$ curves were replaced by dips with a sharp falloff and subsequent increase of magnetostriction. These anomalies indicate the existence of phase transitions, their threshold fields increasing with increasing temperature. Unusual phase transitions were earlier observed in these compounds in the same temperature region $T_p < T < T_c$, and they were accompanied by jumps in magnetization and a positive jump in magnetoresistance [12, 13]. These transitions were assigned to field-induced orbital ordering. As seen from Fig. 3a, such transitions are also accompanied by strong magnetoelastic anomalies, with a substantial field hysteresis. Above T_c, another structural phase transition takes place between the Jahn–Teller orthorhombic phase O' and the orthorhombic (pseudocubic) phase O^* at a temperature T_s'. As one approaches the temperature of the structural transition T_s', magnetostriction decreases and reverses its sign (the curve at 301 K).

Similar features were observed in the field dependence of transverse magnetostriction $\lambda_{\perp}(H)$ (Fig. 3b), which likewise argues for the existence of field-induced magnetic and structural phase transitions. A distinctive feature of the behavior of transverse magnetostriction $\lambda_{\perp}(H)$ at x = 0.1 is its large magnitude, which exceeds the longitudinal magnetostriction $\lambda_{\parallel}$ at some temperatures by nearly twofold and has the same sign. This accounts for the large magnitude of volume magnetostriction $\left(\frac{\Delta V}{V} \approx 10^{-3}\right)$ for this composition.

In $La_{0.875}Sr_{0.125}MnO_3$ (T_p = 150 K, T_c = 200 K, and T_s' = 250–270 K), as well as for the x = 0.1 composition, one observes an increase of both the longitudinal and transverse magnetostriction $\lambda_{\parallel,\perp}(H)$ near T_p (see the curves for 160 K in Figs. 4a, 4b). The behavior of $\lambda_{\parallel,\perp}(H)$ reveals, however, some new features; namely, after an increase of the magnetostriction near T_p, one can see a decrease and sign reversal of $\lambda_{\parallel}(H)$ and $\lambda_{\perp}(H)$ in weak fields (the curves for 188 and 259 K in Fig. 4a and for 182 and 259 K, in Fig. 4b).

The $La_{0.85}Sr_{0.15}MnO_3$ composition (T_p = 190–200 K, $T_c \sim T_s' \sim$ 220–230 K) revealed a similar increase of $\lambda_{\parallel}(H)$ to 7×10^{-4} at temperatures $T_p < T < T_c$. However, that increase occurred without any jumps.

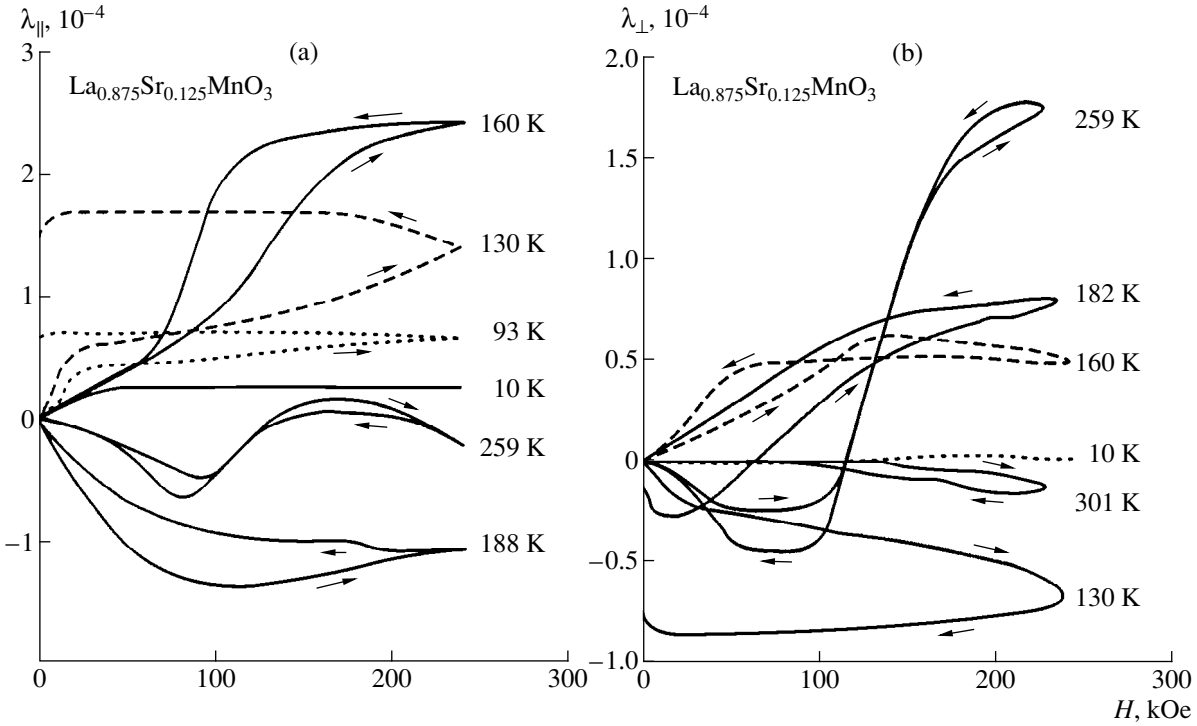

Fig. 4. Field dependences of (a) longitudinal $\lambda_{\parallel}$ and (b) transverse $\lambda_{\perp}$ magnetostriction for the $x = 0.125$ composition.

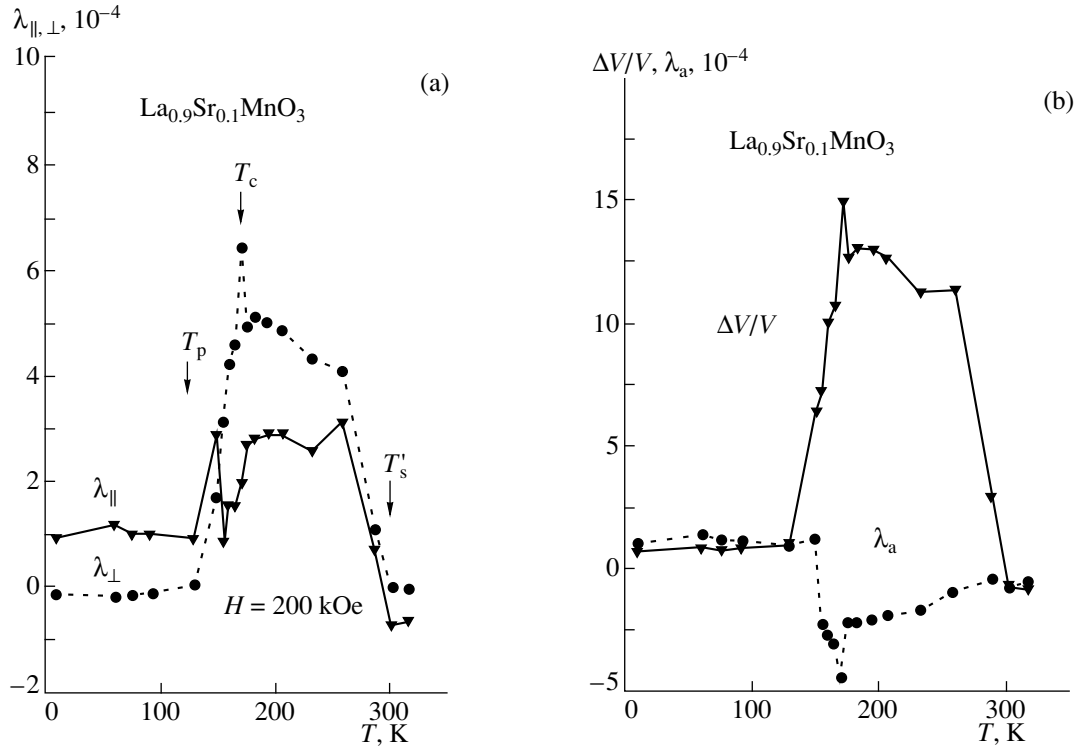

Fig. 5. Temperature dependence of (a) longitudinal, $\lambda_{\parallel}$, and transverse, $\lambda_{\perp}$, magnetostriction, and (b) volume and anisotropic magnetostriction of $La_{0.9}Sr_{0.1}MnO_3$ obtained at 200 kOe.

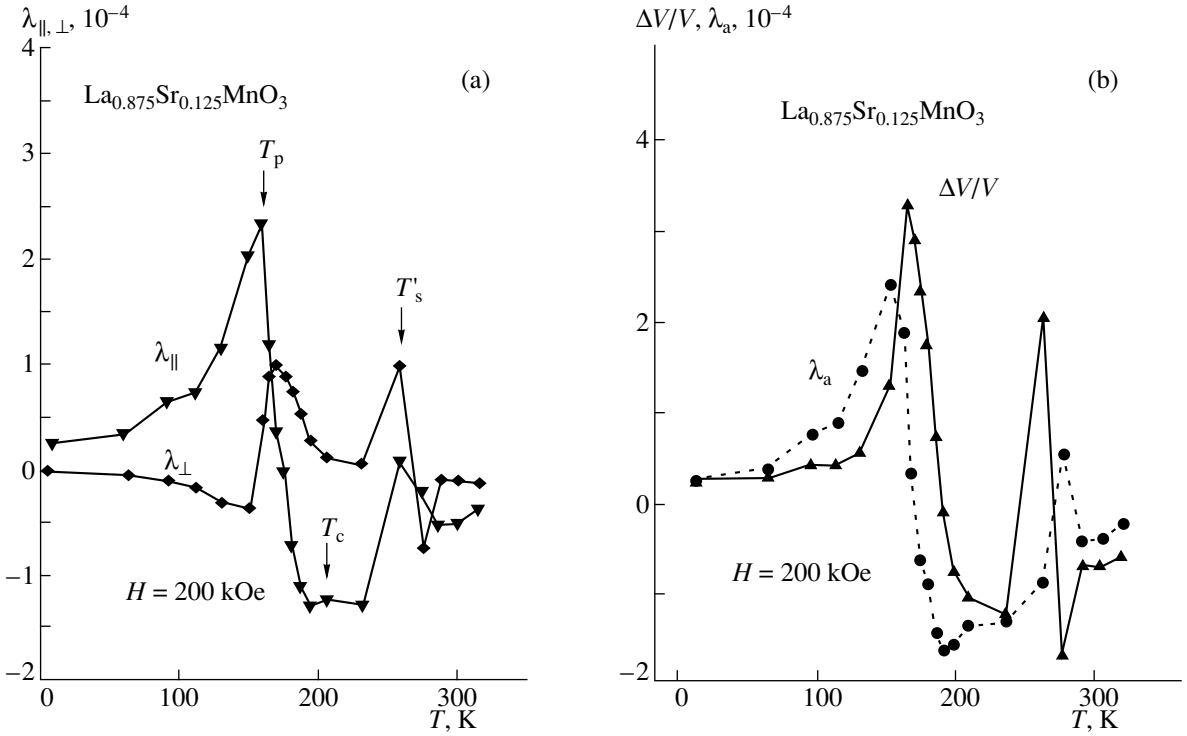

Fig. 6. Temperature dependences of (a) longitudinal and transverse magnetostriction, and (b) volume and anisotropic magnetostriction of $La_{0.875}Sr_{0.125}MnO_3$ obtained at 200 kOe.

Magnetoelastic properties exhibit well-pronounced anomalies near magnetic and structural phase transitions in the temperature dependence of magnetostriction measured at a fixed magnetic field. Figures 5a, 5b, 6a, and 6b present temperature dependences of $\lambda_{\parallel,\perp}(H)$, as well as of the volume magnetostriction $\frac{\Delta V}{V} = \lambda_\parallel + 2\lambda_\perp$ and anisotropic magnetostriction $\lambda_a = \lambda_\parallel - \lambda_\perp$, obtained for the $x = 0.1$ and 0.125 compositions at a fixed field of 200 kOe. We found a distinct correlation of the temperatures of the observed anomalies in $\lambda_{\parallel,\perp}(T)$ at H = const with the spontaneous transitions occurring at T_p, T_c, and T'_s. Note that at temperatures near T_p, the field-induced longitudinal magnetostriction is positive and comparatively large for all compositions, whereas near T_c, the $\lambda_\parallel(T)$ relation exhibits a decreasing trend and a sign reversal for $x = 0.1$, becoming negative for the $x = 0.125$ composition.

These features in the behavior of magnetostriction can be associated with suppression of the Jahn–Teller phase O' in the magnetic field inducing a transition to a new state with another type of orbital ordering and, hence, with another magnitude of effective exchange coupling. The negative magnetostriction in the vicinity of T_c can be connected with the trend to field-induced charge delocalization, which, by [14], is accompanied by the onset of negative magnetostriction.

The $x = 0.1$ and 0.125 compositions also revealed anomalies in the temperature dependence of magnetostriction accompanied by a second sign reversal near T'_s, the temperature at which the O'–O^* structural phase transition takes place.

To sum up, our studies on thermal expansion and magnetostriction reveal the existence of a strong connection between the magnetoelastic properties of $La_{1-x}Sr_xMnO_3$ crystals and the magnetic and crystalline structures and can be used to probe various transformations in such systems.

ACKNOWLEDGMENTS

Partial support of the Russian Foundation for Basic Research (grant no. 96-02-17350) is gratefully acknowledged.

REFERENCES

1. R. von Helmolt, J. Wecker, B. Holzapfel, *et al.*, Phys. Rev. Lett. **71**, 2331 (1993).
2. A. Urushibara, Y. Moritomo, T. Arima, *et al.*, Phys. Rev. B **51**, 14103 (1995).
3. A. Asamitsu, Y. Moritomo, Y. Tomioka, *et al.*, Nature **373**, 407 (1995).
4. Y. Tomioka, A. Asamitsu, H. Kuwahara, *et al.*, Phys. Rev. B **53**, R1689 (1996).

5. A. J. Millis, P. B. Littlewood, and B. I. Shaiman, Phys. Rev. Lett. **74**, 5144 (1995).
6. Yu. F. Popov, A. M. Kadomtseva, G. P. Vorob'ev, *et al.*, J. Appl. Phys. **83** (11), 7160 (1998).
7. F. Moussa, M. Hennion, J. Rodríguez-Carvajal, *et al.*, Phys. Rev. B **54**, 15149 (1996).
8. E. O. Wollan and W. C. Kohler, Phys. Rev. **100**, 545 (1955).
9. K. P. Belov, A. K. Zvezdin, A. M. Kadomtseva, and R. Z. Levitin, *Orientational Transitions in Rare-Earth Magnets* (Nauka, Moscow, 1979).
10. V. Yu. Ivanov, V. D. Travkin, A. A. Mukhin, *et al.*, J. Appl. Phys. **83** (11), 7180 (1998).
11. A. A. Mukhin, V. Yu. Ivanov, V. D. Travkin, *et al.*, Pis'ma Zh. Éksp. Teor. Fiz. **68** (4), 356 (1998) [JETP Lett. **68** (4), 356 (1998)].
12. H. Nojirii, K. Koneko, M. Motokawa, *et al.*, in *Abstracts of III International Conference on Physical Phenomena at High Magnetic Fields, Tallahassee, Florida, 1998*, p. 203.
13. M. Paraskevopoules, J. Hemberger, A. Loidl, *et al.*, cond-mat/9812305.
14. M. R. Ibarra, P. A. Algarabet, C. Marqina, *et al.*, Phys. Rev. Lett. **75** (19), 3541 (1995).

Translated by G. Skrebtsov

Physics of the Solid State, Vol. 42, No. 6, 2000, pp. 1116–1119. Translated from Fizika Tverdogo Tela, Vol. 42, No. 6, 2000, pp. 1083–1086.

MAGNETISM AND FERROELECTRICITY

Influence of Mobile Charged Defects on the Dielectric Non-Linearity of Thin Ferroelectric PZT Films

B. M. Gol'tsman, V. K. Yarmarkin, and V. V. Lemanov

Ioffe Physicotechnical Institute, Russian Academy of Sciences, Politekhnicheskaya ul. 26, St. Petersburg, 194021 Russia

e-mail: B.Goltsman@shuvpop.ioffe.rssi.ru

Received November 23, 1999

Abstract—The capacity–voltage (C–V) characteristics of thin ferroelectric PZT films are investigated, varying the rate of change of the control voltage in a wide range. It is established that the distance between the maxima of the C–V characteristics decreases as the rate of the voltage change is decreased. This effect is caused by the decrease of the coercive field due to the spatial separation of mobile charge carriers under the action of the control field and the accumulation of charged defects in the near-electrode regions of the films. Parameters characterizing the formation of the bulk charge in the films (concentration and mobility of oxygen vacancies) are estimated. The estimations made are consistent with the literature data. *© 2000 MAIK "Nauka/Interperiodica".*

The strong dependence of the dielectric function of ferroelectric materials on the electric field strength (dielectric nonlinearity) is of interest for science and applications. The investigations of the physical nature of the dielectric nonlinearity and its possible practical uses (see, e.g., [1]) are based on the determination of "quasi-static" C–V characteristics, that is, the dependencies of the capacitance C of ferroelectric capacitor structures on a slowly varying (at a rate of change of less than 1 V/s) bias voltage (which is called the control voltage V in what follows). The capacitance of the structures is determined by applying an alternating high-frequency voltage (its frequency exceeds 100 kHz) creating an electric field of small strength (1–5 kV/cm), while the control voltage corresponds to a much stronger field (tens or hundreds of kilovolts per centimeter).

The C–V characteristic of ferroelectric structures can also be determined by differentiation of a ferroelectric hysteresis loop $P(V)$, where P is the polarization and V is the voltage applied across the structure. The voltage corresponds to the control voltage at a direct measurement of C–V characteristics. This possibility follows from the expression determining the relative dielectric function

$$\varepsilon = 1 + \frac{1}{\varepsilon_0} dP/dE,$$

which leads to the relationship

$$C(E) \sim dP/dE$$

(ε_0 is the dielectric constant of vacuum) at large values of ε typical of ferroelectrics. Hence, we have

$$C(V) \sim dP/dV.$$

Ferroelectric materials have hysteresis-like C(V) dependencies with two maxima. The appearance of these maxima is due to polarization switching. The distances between these maxima on the voltage scale as determined from the "quasi-static" C–V characteristics are 1.5–2 times smaller than that found from ferroelectric hysteresis loops (see, e.g., [2, 3]) which are usually measured at much higher rates of the control voltage change (more than 100 V/s). In order to elucidate the physical nature of the difference pointed out, we developed a method for determining the "dynamic" C–V characteristics by means of the direct measurement of the capacitance. The method differs from the "quasi-static" one by the essentially larger rates of the control voltage change (up to 10^4 V/s). We determined the distances ΔV_m between the maxima of the $C(V)$ dependence measured by this method and compared them with the values of ΔV_m found by differentiating the ferroelectric hysteresis loops at the same rates of the control voltage change.

1. EXPERIMENTAL

Capacitor sandwich-type structures based on PZT thin films 200 nm thick were investigated. The $Pb(Zr_{0.52}Ti_{0.48})O_3$ films were produced by the sol gel method on the surface of platinized (100)Si plates with an adhesive titanium sublayer. The plates were covered by a 500 nm thick thermal oxide layer. The upper nickel electrodes 0.2 nm in diameter and 100 nm in thickness were deposited on the surface of the PZT film by thermal evaporation through a mask. The method of preparation of capacitor structures was earlier described in detail in [4].

When determining the "quasi-static" C–V characteristic, the capacitance of the structures was measured

1063-7834/00/4206-1116$20.00

at an ac voltage amplitude of 0.04 V and a frequency of 200 kHz and a rate of the control voltage change of 0.065 V/s. The hysteresis loops were measured by means of a Sawyer-Tower circuit at frequencies of 500 Hz and 1 kHz.

The "dynamic" C–V characteristics were measured by applying a periodic saw-tooth alternating control voltage $V(t)$ of a frequency of 500 Hz or 1 kHz, which caused a periodic change in the structure capacitance $C(t)$. To determine $C(t)$, a voltage of a frequency of 10 MHz was applied across the capacitor structure and a load resistor connected in series. This voltage produced a capacitive current, which was modulated by the voltage $V(t)$ owing to the structure nonlinearity. The voltage across the load resistor was proportional to $C(t)$ under the condition that the magnitude of the load resistor was much smaller than the capacitive resistance of the structure. The $V(t)$ and $C(t)$ dependencies were registered simultaneously.

2. RESULTS AND DISCUSSION

Figure 1 shows (a) a ferroelectric hysteresis loop obtained at a sinusoidal voltage with a frequency of 1 kHz, (b) a C–V characteristic obtained by differentiating this hysteresis loop, and (c) a "quasi-static" C–V characteristic, typical of the structures investigated.

The earlier mentioned difference in the distances between the maxima of the $C(V)$ dependence on the voltage scale obtained by the methods pointed out above can be seen in Figs. 1b and 1c. Some shift of the hysteresis loop and C–V characteristics to the region of negative voltage is also observed. This shift takes place due to the "built-in" electric field, whose origin was discussed in [4].

Figure 2 illustrates the "dynamic" method of measuring the C(V) dependence. The C–V characteristics of the capacitor structures investigated are shown in Fig. 2a. Figure 2b presents time diagrams of the control voltage and the envelope of the modulated voltage across the load resistor corresponding to these dependencies; these diagrams were observed on the screen of an oscilloscope. It is seen that the positions of the envelope minima (points A and D) coincide with that of the extreme points of the control voltage in time, while the envelope maxima (points C and F) lag behind the instants of zero control voltage (points B and E). As is seen from Figs. 2a and 2b, this delay is due to the shift of the maxima of the $C(V)$ dependence with respect to zero voltage (the shifts are the voltages V_m^+ and V_m^- corresponding to points C and F in Figs. 2a and 2b). The fact that the delay of the maxima is not caused by an imperfection of the measuring circuit has been tested in the following way. When a ceramic ferroelectric capacitor characterized by a capacitance and nonlinearity close to the corresponding parameters of the capacitor structures and having a C–V characteristic with a single maximum located at zero control voltage was placed in the circuit instead of the structures, the maxima coincided in time with zero values of the control voltage.

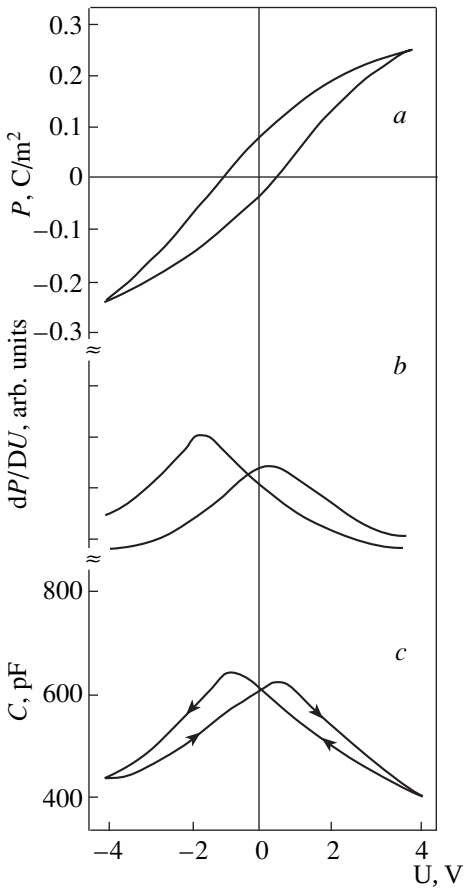

Fig. 1. (*a*) Hysteresis loop, (*b*) C–V characteristic obtained from the hysteresis loop, and (*c*) "quasi-static" C–V characteristic of a capacitor structure based on a PZT film. The discontinuities of the C(V) dependence at the limiting values of V in Fig. 1b can be explained by the polarization not being saturated at these values. When the polarization is saturated, the derivatives dP/dV for the upper and lower branches of a hysteresis loop coincide.

Thus, the distance between the maxima of the C–V characteristic, which is equal to $\Delta V_m = \left|V_m^+\right| + \left|V_m^-\right|$ can be directly determined as the magnitude of the interval GH on the voltage axis (see Fig. 2b). The ΔV_m measurements at different frequencies of the control voltage $V(t)$ are given in the table. The corresponding values

The values of the parameter ΔV_m in volts obtained from the "quasi-static" and "dynamic" C–V characteristics, and from hysteresis loops at different frequencies of the control voltage

"Quasi-static" C–V	"Dynamic" C–V		Hysteresis loops	
0.004 Hz	500 Hz	1000 Hz	500 Hz	1000 Hz
1.0	1.3	1.8	1.4	2.2

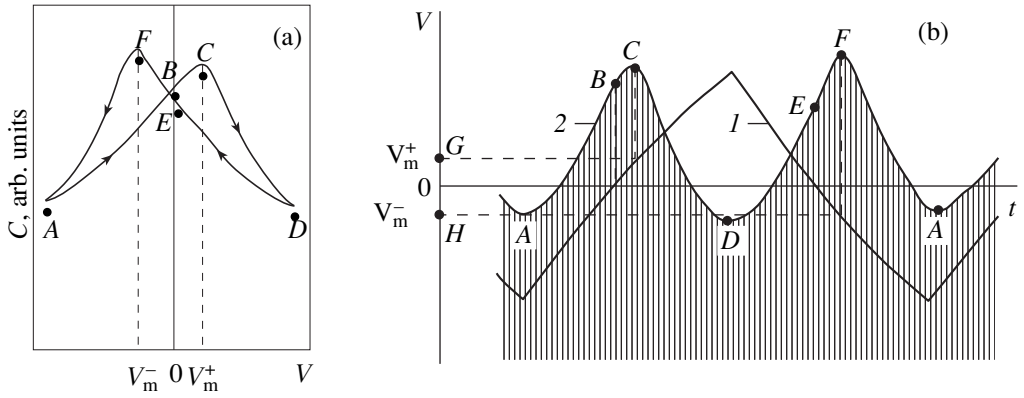

Fig. 2. (a) Schematic representation of the C(V) dependence; and (b) the time diagram of the control voltage (*1*) and the envelope of the voltage across the load resistor (*2*) used in the "dynamic" method of the determination of the C(V) dependence. The frequency of the control voltage is 1 kHz and the frequency of the capacitance measurement voltage is 10 MHz.

obtained from the "quasi-static" C–V characteristic and from the ferroelectric hysteresis measurements are also listed in the table. The accuracy of ΔV_m measurement is approximately ±10%. It should be noted once again that the appearance of the maxima in a C–V characteristic and their positions on the V scale are related with the polarization switching caused by the control voltage. The capacitance-measurement voltage, which is much smaller in magnitude, does not essentially influence the value of ΔV_m.

It can be concluded from the data given in the table that the value of ΔV_m grows with increasing rate of change of the bias voltage, regardless of the method by which the C–V characteristic is measured. The earlier mentioned difference is also seen between the values of ΔV_m obtained by the "quasi-static" method and those determined from the hysteresis loop. It is also evident from the table that the values of ΔV_m determined by the "dynamic" method and from the hysteresis loop at the same frequencies are close to each other.

The dependence of ΔV_m on the rate of the control voltage change cannot be due to a finite rate of the polarization switching in the capacitor structures investigated, the switching time in which does not exceed 1 ns [5]. The observed decrease in ΔV_m with decreasing the rate of the control voltage change can be explained in terms of the displacement of mobile charged defects (for example, doubly charged oxygen vacancies [6]) and of free charge carriers (electrons and holes) in the film under the influence of the control voltage. Since the metallic electrodes block the exchange between the film and the surrounding atmosphere with oxygen atoms [6], this leads to the accumulation of the bulk charge in the near-electrode regions and hence, according to Maxwell's equation

$$\mathrm{div} D = \rho$$

($D = \varepsilon\varepsilon_0 E$ is the electric induction and ρ is the space charge density), to the significantly increased control field strength E in these regions [7]. This circumstance favors the formation of nuclei of domains in the bulk-charge region. Since the energy of domain nucleus formation is much higher than the energy of domain growth, the polarization switching is facilitated and occurs at a much weaker external field [8]. As a result, the distance between the maxima of the C–V characteristic decreases.

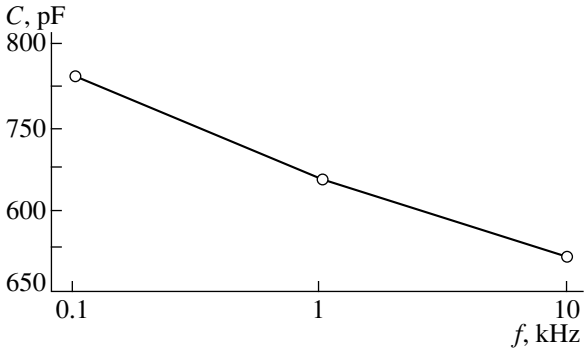

Fig. 3. The frequency dependence of the capacitance of the capacitor structure based on PZT films. The amplitude of the capacitance measurement voltage is 2 V.

The frequency dependence of the structure capacitance shown in Fig. 3 is an argument in favor of this explanation. The capacitance is seen to grow as the frequency decreases. This fact can be explained in terms of the increase in the bulk charge in the near-electrode regions. The analogous regularities were obtained in [9] for $BaTiO_3$ films.

Let us estimate some parameters characterizing the formation of the bulk charge. The mobility μ of charged defects can be determined from the relationship

$$\mu = 2L/ET,$$

where L is the displacement of the defects during a half-period $T/2$ of the control voltage with an amplitude V under the action of the field $E = V/d$ (d is the width of

the film). Using the values $L \cong d = 2 \times 10^{-7}$ m, $V = 4$ V, and $T \cong 10^{-3}$ s, we obtain the estimate $\mu \cong 10^{-11}$ m^2/Vs, which agrees with the data cited in [10] for oxygen vacancies in PZT. Supposing that the polarization P caused by the formation of the bulk charge in the near-electrode regions is comparable with the total polarization of the film, we put $P \cong 10^{-1}$ C/m^2. Then, estimating the concentration of mobile defects N from the relationship

$$P = qNL,$$

where $q = 3.2 \times 10^{-19}$ C is the charge of oxygen vacancies, we find that N is approximately equal to 10^{24} m^{-3}. This result is consistent with the estimates obtained for PZT films from both the C(V) dependence [3] and the dependence of the coercive field of the films on their width [8].

Thus, the regions of the bulk charge characterized by an elevated electric field strength are formed as a result of spatial separation of mobile charge carriers under the influence of the control field in the film near the electrodes. This field facilitates the formation of the domain nuclei during polarization switching. As a result, the coercive fields defining the positions of the maxima of the C–V characteristics become smaller, and the distance between the maxima decreases.

ACKNOWLEDGMENTS

This work was supported by the Russian Foundation for Basic Research, project no. 99-02-18022.

REFERENCES

1. *Ferroelectrics in Microwave Engineering*, Ed. by O. G. Vendik (Nauka, Moscow, 1979).
2. K. A. Vorotilov, M. I. Yanovskaya, and O. A. Dorokhova, Integr. Ferroelectr. **3** (1), 33 (1993).
3. C. Brennan, Integr. Ferroelectr. **8** (3-4), 335 (1995).
4. V. K. Yarmarkin, N. V. Zaĭtseva, S. V. Shtel'makh, and A. V. Motornyĭ, Fiz. Tverd. Tela (St. Petersburg) **37** (2), 324 (1995) [Phys. Solid State **37** (2), 176 (1995)].
5. P. K. Larsen, R. Cuppens, and G. A. C. M. Spierings, Ferroelectrics **128**, 265 (1992).
6. T. Baiatu, R. Waser, and K.-H. Hardtl, J. Am. Ceram. Soc. **73** (6), 1663 (1990).
7. V. M. Fridkin, *Ferroelectric Semiconductors* (Nauka, Moscow, 1976).
8. A. K. Tagantsev, Cz. Pawlaczyk, K. Brooks, and N. Setter, Integr. Ferroelectr. **4** (1), 1 (1994).
9. S.-J. Lee, K.-Y. Kang, and S.-K. Han, Appl. Phys. Lett. **75** (12), 1784 (1999).
10. S. D. Bernstain, T. Y. Wong, Y. Kisler, and R. W. Tustison, J. Mater. Res. **8** (1), 12 (1993).

Translated by A. Pushnov

Physics of the Solid State, Vol. 42, No. 6, 2000, pp. 1120–1125. Translated from Fizika Tverdogo Tela, Vol. 42, No. 6, 2000, pp. 1087–1091.

LATTICE DYNAMICS AND PHASE TRANSITIONS

Computer Simulation of Crystal Structure Formation upon Transition from Amorphous State

V. A. Lagunov and A. B. Sinani

Ioffe Physicotechnical Institute, Russian Academy of Sciences, Politekhnicheskaya ul. 26, St. Petersburg, 194021 Russia
e-mail: alfred@mdiab.ioffe.rssi.ru

Received in final form, November 15, 1999

Abstract—The structure of a solid has been studied by the molecular dynamics technique upon transition from the amorphous state to the crystalline state. The influence of initial conditions in the simulation of an amorphous sample and the temperature of its heating on the resulting structure is examined. It is found that structures of two types can be formed in the sample: single crystals consisting of face-centered cubic (fcc) and hexagonal close-packed (hcp) cells with a small number of pentahedral cells in the boundary region of the sample and block crystals with an ordered pentahedral structure composed of fcc, hcp, pentahedral, and icosahedral cells. Linear chains of vacancies are revealed at the boundaries of blocks. *© 2000 MAIK "Nauka/Interperiodica".*

Earlier [1], we showed that the structure of a solid is formed by four types of crystal cells spontaneously arising in the computer experiment. This result was obtained with a single sequence of random numbers in the simulation of the initial sample.

Of special interest was to investigate a larger set of initial conditions used in simulation of samples and different procedures of their heat treatment upon transition from the amorphous state to the crystalline state. Moreover, the problem concerning the structure of block boundaries upon crystallization remained to be solved.

The force interaction between atoms was specified by the modified Lennard-Jones potential [2]. The simulation of the initial sample, integration of the equations of atomic motion, and determination of the atomic configuration stable at a low temperature were performed according to the procedure described in [1, 3].

It was necessary to elucidate how the structure of a solid changes with a variation in the sampling of atomic coordinates. For this purpose, random numbers were generated by the specially devised procedure, which made it possible to precisely reproduce their sequence at any instant of time. The order of priority of random numbers was determined by the ordinal number of the sequence. Correction of the shape and dimensions of the sample was carried out with a sequence identical to that employed in the initial simulation of the sample.

Characteristics of studied samples

Sample	T	N	P/N	fcc	hcp	ph	ico	asym	$K = 11$	$K = 10$	$K = 13$	$g1$, %	$g2$, %
fcc	0	763	5.452	415	0	0	0	0	0	0	0	0.58	–
hcp	0	749	5.452	0	408	0	0	0	0	0	0	–	0.81
1	0	717	5.206	15	39	10	0	50	56	11	16	6.61	8.96
2	0	728	5.208	31	32	2	0	56	51	16	8	6.64	7.19
3	0	712	5.185	14	23	16	1	55	62	10	8	10.57	9.42
4	0	711	5.174	0	7	8	1	63	59	17	10	–	11.49
1a	0.5	745	5.437	118	231	63	1	0	0	0	0	3.32	3.73
2a	0.5	756	5.452	299	109	5	0	0	0	0	0	0.77	1.16
3a	0.5	748	5.445	248	147	13	0	0	0	0	0	1.17	1.63
4a	0.5	733	5.251	14	46	22	0	56	55	17	15	7.49	9.49
1b	1	742	5.423	237	141	2	0	6	8	0	0	2.19	3.33
2b	1	752	5.406	265	95	4	0	5	13	3	0	2.17	3.75
3b	1	743	5.426	277	97	10	0	6	7	0	0	1.25	2.81
4b	1	750	5.444	144	216	23	2	0	0	0	0	1.97	2.71

1063-7834/00/4206-1120$20.00 © 2000 MAIK "Nauka/Interperiodica"

Figure 1 displays the selected data obtained in the computer experiments, namely, the dependences of the mean energy of atoms U_a (expressed in terms of the dissociation energy D) after cooling the sample on the ordinal number of treatment stage. The dependences were obtained at different random sequences of atomic coordinates and two temperatures of an intermediate heating of the sample. Curve *1* in Fig. 1a corresponds to the data reported in [1].

The results obtained in the investigation of all the samples, including theoretical crystals built up of the face-centered cubic (fcc) and hexagonal close-packed (hcp) cells with geometrical dimensions identical to those for the studied samples, are summarized in the table. In particular, the table presents the mean initial kinetic energy of an atom T (in terms of the dissociation energy D), which specifies the temperature of samples, and the number of atoms in the spherical sample with a diameter of ten interatomic distances after all treatment stages. The table also lists the mean potential energy of atoms P/N (in terms of D); the numbers of fcc, hcp, pentahedral (ph), and icosahedral (ico) cells; the number of asymmetric (asym) cells (different from the fcc and hcp cells) with a coordination number of 12; the numbers of cells with different coordination numbers K; and the degrees of tetragonal distortion of fcc ($g1$) and hcp ($g2$) cells for the studied sample.

It is assumed that the atomic energy depending on the mutual arrangement of crystal cells should reflect the structural state of the sample. Figure 1 illustrates the evolution of the energy during heat treatment of different initial samples. As before, the samples were heat-treated according to the following procedure. Prior to each heat treatment stage, we corrected distortions of the shape and dimensions of the sample, which were caused by atomic displacements at the preceding stage. To accomplish this, the spherical shape of the sample with a specified size was recovered by eliminating distant atoms and randomly placing them in the regions of structural sparseness. Moreover, we alternated the stages of pure cooling and the stages with a short (during the course of about twenty periods of lattice vibrations) initial heat treatment of the sample at a higher temperature. Note that Figs. 1a and 1b correspond to different temperatures of sample heating. The initial heat treatment temperature corresponds to 0.5D per atom in Fig. 1a and 1D per atom in Fig. 1b.

A comparison of the curves obtained in different computer experiments shows that the heat treatment of the sample at a higher temperature brings about a more rapid transition to the final solid state, which subsequently remains unchanged. In the process, the energy of atoms rapidly approaches the theoretical values for infinite crystals made up of the fcc or hcp cells. The designations of points that correspond to different initial thermal energies of atoms (including deep annealing of the sample that leads to breakdown of the resulting structure) are given in the figure caption.

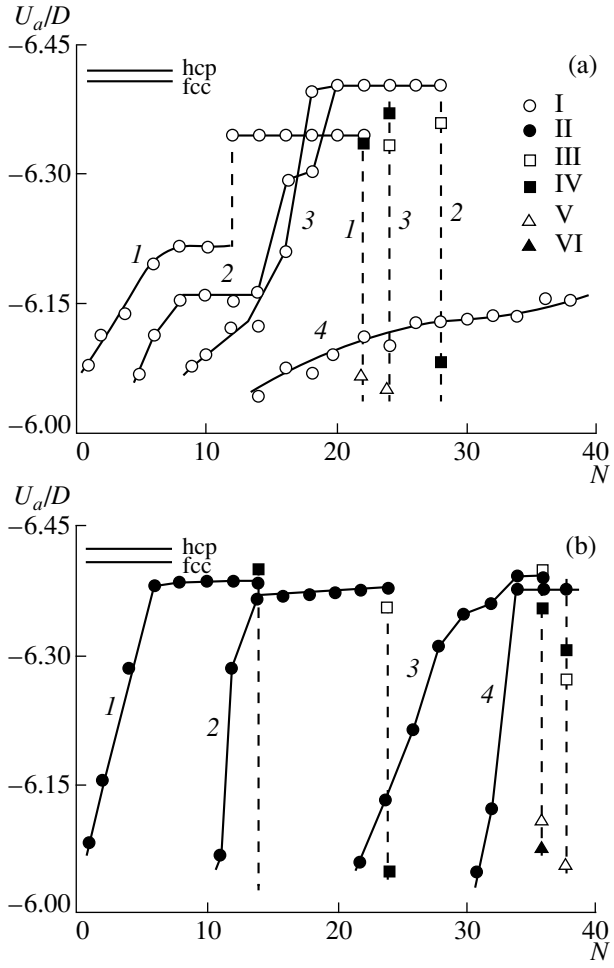

Fig. 1. Evolution of the energy U_a per atom in a cell for four samples at different heat treatment conditions. Initial thermal energy per atom: (a) (I) 0.5D and (b) (II) 1D. Heat treatment corresponds to (III) 2.00D, (IV) 2.13D, (V) 2.26D, and (VI) 2.40D. D is the dissociation energy of atom pair. N is the ordinal number of treatment stage. Curves *2*, *3*, and *4* are shifted along the abscissa axis.

According to the computer experiments, a complex structure represents an ordered combination of linear crystals comprised of pentahedral cells with a fivefold symmetry axis [4, 5]. This structure is observed in two out of eight cases. Figure 2 demonstrates two projections of the spontaneously formed structure consisting of pentahedral cells and two icosahedral cells (sample 4*b* in table) designated by asterisks. This structure is similar to that observed earlier in [1]. In Fig. 2, identical symbols denote the cells belonging to the same linear crystal. It can be seen that the length of these crystals between intersection points is equal to seven interatomic distances as before. For a better pictorial representation, the sample was preliminarily rotated so that the linear crystal between icosahedra was located perpendicularly to the plane of the first projection.

The structure of sample 4*b* (Fig. 2) involves several groups of the fcc and hcp cells with the same orienta-

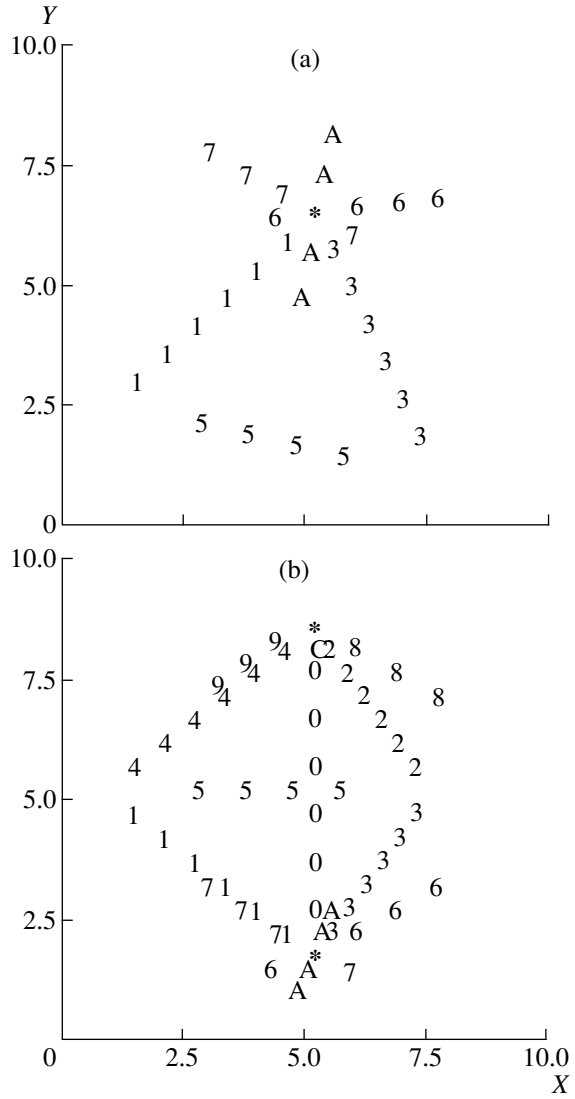

Fig. 2. Arrangement of pentahedral and icosahedral cells in sample 4*b* upon formation of a large number of pentahedral cells.

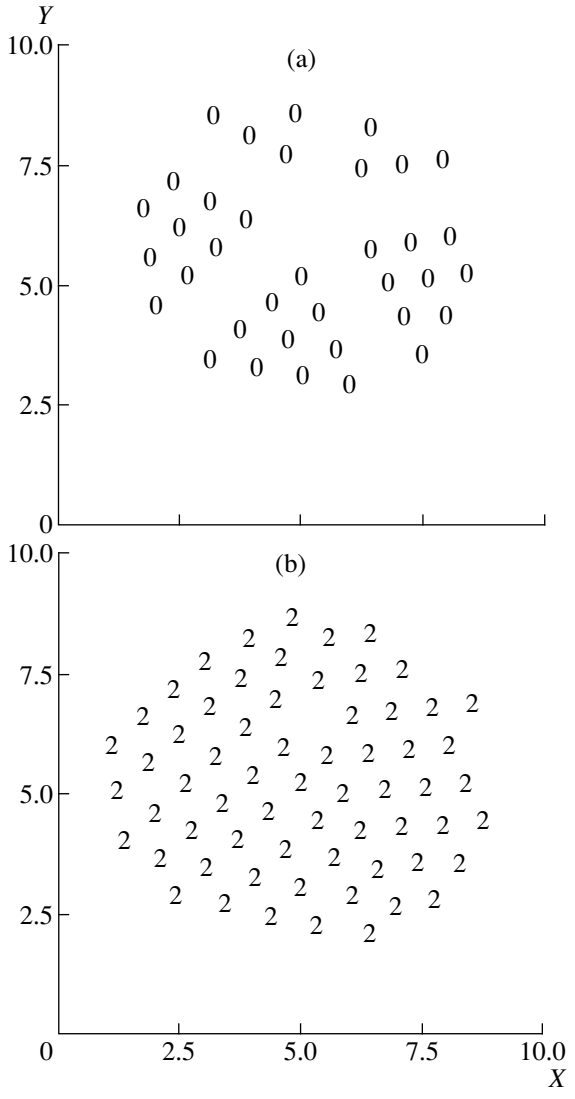

Fig. 3. Arrangement of (a) fcc and (b) hcp cells for the largest fcc and hcp nuclei in sample 4*b* with a large number of pentahedral cells.

tion. The largest groups of cells have the axes oriented parallel to the axis of the whole crystal with a precision of less than 0.1°. Their arrangement is shown in Fig. 3. It is worth noting that the identically oriented fcc cells are spatially separated in such a way that the whole sample exhibits a fivefold symmetry axis coinciding with the axis of the linear crystal. This fact suggests an orientation of the sample as a whole.

A simpler structure formed by fcc and hcp cells with a small number of linear crystals consisting of pentahedral cells is observed in other cases. A typical example of such a structure—an oriented single crystal—is given in Fig. 4 (sample 2*a*). This single crystal represents a combination of fcc, hcp, and pentahedral cells. The arrangement of the fcc and pentahedral cells is depicted in Fig. 4a, and the arrangement of the hcp and pentahedral cells is displayed in Fig. 4b. The resulting structure of the sample involves a bulk fcc crystal comprised of atoms located only in the fcc cells, several single-layer lamellas aligned with the crystal, and a tubular structure of the hcp cells with a fivefold symmetry axis, the latter structure surrounding the linear crystal.

Despite a large number of heat treatment stages, the sample does not undergo crystallization in one of eight cases (see Fig. 1a, curve *4*). However, the computer experiment with the same pseudorandom sequence of atomic coordinates upon simulation of the sample with an increase in the temperature of intermediate annealing led to a rapid formation of the structure (Fig. 1b, curve *4*) similar to that described in [1] and shown in Figs. 2 and 3.

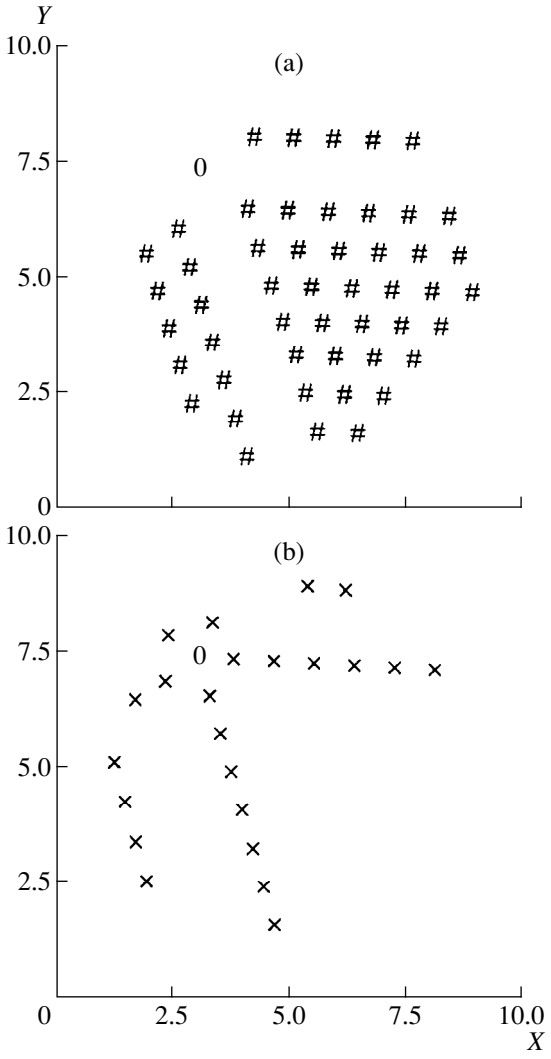

Fig. 4. Arrangement of (a) fcc and pentahedral cells and (b) hcp and pentahedral cells in sample 2*a* with a small number of pentahedral cells.

Additional information on the shape of the fcc and hcp cells formed in the computer experiment can be extracted from Figs. 3 and 4. In particular, the observed deviation of hexagons from a regular shape in the cells, one axis of which is perpendicular to the projection plane, indicates the presence of tetragonal distortions in these cells. As can be seen from Fig. 3b, the shape of hexagons in the hcp cells substantially changes, which suggests a varying degree of tetragonal distortions. In this respect, we made the quantitative evaluation of these distortions.

The degree of tetragonal distortion g in the cell was calculated as the difference between unity and the ratio of the maximum distance a_{max} to the minimum distance a_{min} of the central atom to the other atoms in the cell, that is, $g = a_{max}/a_{min} - 1$. The mean values of g for all the studied samples are given in the table. Note that the g value is equal to zero for infinite theoretical fcc and hcp crystals, whereas the samples of finite dimensions exhibit a slight tetragonality after the relaxation (see table).

Figure 5 shows the distributions of the degree of tetragonal distortion of the fcc and hcp cells in sample 4*b* with a complex crystal substructure. These data demonstrate that, first, tetragonal distortions of the order of 1–3% arise in both fcc and hcp cells, and, second, the distributions of the degree of distortion are split for cells of both types. The latter finding indicates a change in the tetragonality of the fcc and hcp cells.

For comparison, similar distributions for sample 2*a* are displayed in Fig. 6. It can be seen that the tetragonal distortions of cells in this sample are considerably smaller. Specifically, the degree of tetragonal distortion of the fcc cells is equal to 0.4%. This value only slightly differs from the distortions observed for the theoretical crystal with the same free surface.

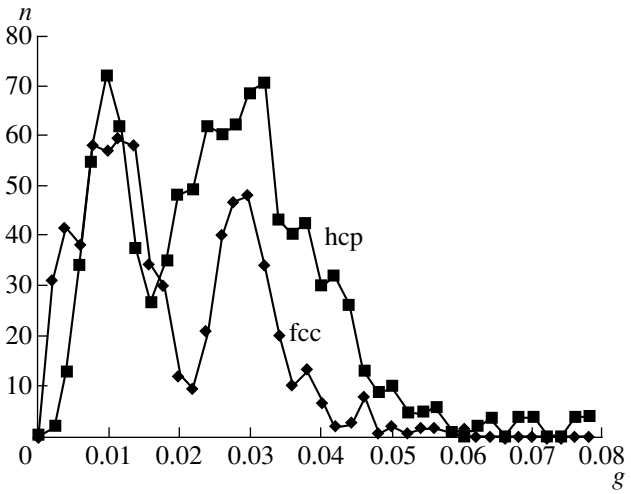

Fig. 5. Distribution of the degree of tetragonal distortion g of the fcc and hcp cells for sample 4*b* with a large number of pentahedral cells (n is the number of cells with a particular distortion).

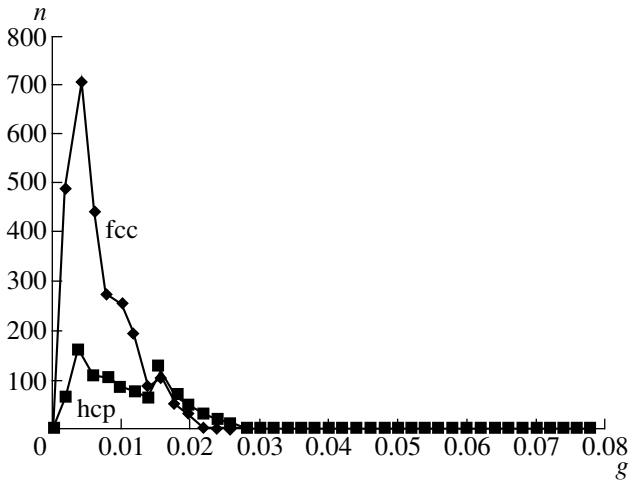

Fig. 6. Distribution of the degree of tetragonal distortion g of the fcc and hcp cells for sample 2*a* with a small number of pentahedral cells.

The resolved splitting of the distribution is observed only for the hcp cells. A special simulation revealed that, in this sample, the hcp cells with large tetragonal distortions are concentrated in a pentahedral tunnel around the linear crystal and also in the boundary region of the sample. This is supported by the data shown in Fig. 7, which represents the arrangement of the hcp and pentahedral cells in two projections. In this figure, the hcp cells with a high degree of tetragonal distortion (more than 1.4%) are designated by crosses.

The state of boundary surfaces of crystallites is of particular interest. In [1], it was found that, upon formation of a two-dimensional structure, the central part of the sample contains only atoms whose coordination number is twelve, even though there are boundaries between the blocks. This suggests that vacancies and interstitial atoms do not participate in the formation of block boundaries. No atoms with a coordination number differing from twelve are observed in other samples obtained at a lower temperature of the initial heat treatment.

However, quite a different situation arises as the heat treatment temperature increases. This is illustrated by the data shown in Fig. 8, which depicts the projection of sample 3*b*. This sample is characterized by the formation of two parallel linear crystals that consist of pentahedral cells and are separated by only two interatomic distances. As can be seen from the figure, in addition to the pentahedral cells, two parallel columns composed of cells with a coordination number of 11 and a column comprised of asymmetric cells (in which sites are nonequivalent) with a coordination number of 12 are also formed in this case. The presence of cells with a coordination number of 11 suggests the formation of vacancy chains in the sample, which reduce the lattice distortions upon structure formation.

Therefore, the formation of pentahedral cells is observed in all the cases. At a small number of pentahedral cells, when they arise, for the most part, in the boundary region of the sample, the number of the fcc cells is approximately two or three times larger than that of the hcp cells. In this case, the fcc and hcp cells are joined together with a misorientation angle of the order of 0.1° and, as a rule, form a perfect single crystal.

At a large number of pentahedral cells, the formation of a rather complex structure with a fivefold symmetry axis is accompanied by the formation of the hcp cells, whose number is 1.5–2 times larger than that of the fcc cells, and isolated pentahedral cells. This pro-

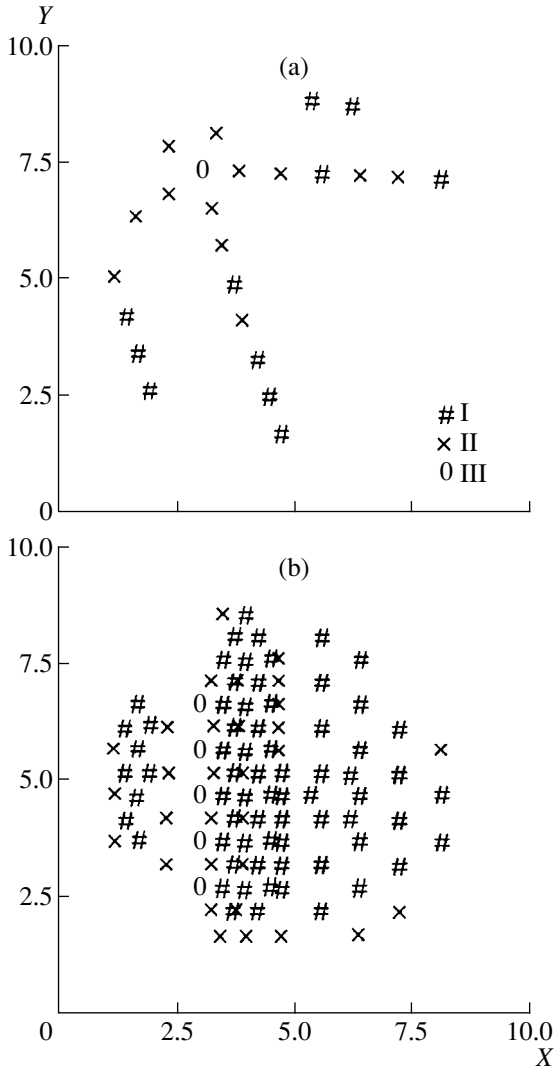

Fig. 7. Arrangement of (I, II) tetragonally distorted hcp cells and (III) pentahedral cells in sample 2*a* with a small number of pentahedral cells. Degree of tetragonal distortion: (I) less than 1.4% and (II) more than 1.4%.

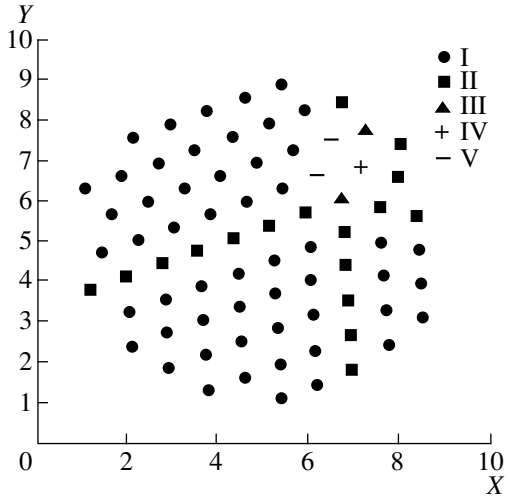

Fig. 8. Arrangement of atomic cells in sample 3*b*: (I) fcc cell, (II) hcp cell, (III) pentahedral cell, (IV) asymmetric cell with the coordination number $K = 12$, and (V) "vacancy" cell with $K = 11$.

cess, as a rule, leads to the formation of a single crystal with a block structure.

The vacancy chains at the block boundaries arise when the structure is formed upon heat treatment at a higher temperature.

REFERENCES

1. V. A. Lagunov and A. B. Sinani, Fiz. Tverd. Tela (S.-Peterburg) **40** (10), 1919 (1998) [Phys. Solid State **40** (10), 1742 (1998)].
2. V. A. Lagunov and A. B. Sinani, Fiz. Tverd. Tela (S.-Peterburg) **38** (6), 1791 (1996) [Phys. Solid State **38** (6), 987 (1996)].
3. V. A. Lagunov, Fiz. Tverd. Tela (Leningrad) **28** (11), 3466 (1986) [Sov. Phys. Solid State **28** (11), 1950 (1986)].
4. D. Shechtman, I. Blech, D. Gratias, and J. W. Cahn, Phys. Rev. Lett. **53** (20), 1951 (1984).
5. I. A. Ovid'ko, *Defects in Condensed Matter* (Obshchestvo "Znanie," St. Petersburg, 1991).

Translated by O. Borovik-Romanova

Physics of the Solid State, Vol. 42, No. 6, 2000, pp. 1126–1133. Translated from Fizika Tverdogo Tela, Vol. 42, No. 6, 2000, pp. 1092–1099.

LATTICE DYNAMICS AND PHASE TRANSITIONS

On the Nature of Metal–Semiconductor Phase Transition in Vanadium Dioxide

E. B. Shadrin and A. V. Il'inskiĭ

Ioffe Physicotechnical Institute, Russian Academy of Sciences, Politekhnicheskaya ul. 26, St. Petersburg, 194021 Russia
e-mail: shadr.solid@pop.ioffe.rssi.ru

Received November 16, 1999

Abstract—The method of coercive temperature distribution function is used to prove that the metal–semiconductor temperature-induced phase transition in vanadium dioxide manifests itself as a Mott electronic transition. © *2000 MAIK "Nauka/Interperiodica".*

Vanadium dioxide remains an object of considerable interest, both for theorists and for applications.

As regards applications, the interest in this material is due to the possibility of synthesis of thin-film interferometers based on VO_2 and used as a reversible medium for recording holograms, as well as modulators of IR radiation. The theoretical interest is due to the as yet unclear origin of temperature-induced "metal–semiconductor" phase transition in VO_2.

It is well known [1] that the metal–semiconductor phase transition in VO_2 is a first-order transition occurring ar T_c = 67°C: above T_c, VO_2 is a metal with a tetragonal lattice symmetry, while below T_c it is a semiconductor with a monoclinic lattice symmetry and a gap width approximately equal to 0.7 eV. The fundamental question whether the given phase transition is an electron Mott transition accompanied with structural changes, or a Peierls-type transition in which structural changes dominate, and the rearrangement of the electron subsystem is an auxiliary process, remains unanswered.

Here we will prove that advances in determining the type of the phase transition in VO_a can be made by studying the fine structure of the temperature hysteresis loop of the metal–semiconductor phase transition (MSPT) occurring in vanadium dioxide films.

1. SAMPLES AND EXPERIMENTAL TECHNIQUE

Our experiments were based on an analysis of optical and electrical loops of the temperature hysteresis for the given phase transition.

For optical measurements, we synthesized on a 0.8–1 mm-thick silicon or sapphire substrate and 20 × 20 mm area interference structures comprising a high-reflectivity aluminum mirror of thickness 300–600 Å, deposited directly on the substrate and carrying a 700–1000 Å-thick VO_2 film. The second mirror of the interferometer was deposited on the film. The interference structure was synthesized according to the standard technique [2, 3].

Such a construction of the interferometer was dictated by the fact that the jump of the reflectivity in VO_2 films during a MSPT is small and amounts to only a few percentage points [2]. For this reason, it is convenient to study optical hysteresis loops by the method of interference enhancement of the contrast, in which a VO_2 film is placed between the mirrors of a Fabry–Perot interferometer. As a result, the jump in the reflectivity during the phase transition is not less than 50%, due to the shift of the interference minimum of the interferometer reflectivity towards shorter waves. This is due to the fact that a phase transition gives rise to jumps in the optical constants (the refractive index at λ = 6328 Å changes from 2.5 to 2.0, while the extinction changes from 0.4 to 0.6 in the semiconducting and metallic phases, respectively) as well as in the resistivity of the material (from 10^{-6} to 10^{-1} $\Omega \cdot$ m).

The hysteresis in the optical properties of vanadium dioxide generates a hysteresis in the reflectivity of the interferometer. Experiments show that the temperature hysteresis loops for VO_2 single crystals and film differ dramatically: the loops for single crystals are vertical relative to the temperature scale, while the ascending and descending branches of the loop for films are extended in temperature. Such "blurring" is accounted for by the fact that the VO_2 film is formed by a large number of microscopic crystals, each of which is characterized by its own phase-transition temperature and its own width of the hysteresis loop, the loops being distributed in a certain way according to their widths and positions on the temperature scale. A mathematical description of this distribution can be carried out with the help of a two-dimensional coercive temperature distribution function (CTDF) which was first used by Merkulov [4] to describe the properties of vanadium dioxide.

1063-7834/00/4206-1126$20.00

The CTDF can be determined experimentally as follows.

One chooses for the investigation a physical parameter of the material that is a linear function of the concentration of microscopic regions in the bulk of the sample, in which the phase transition has occurred. Then the internal structure of the main hysteresis lop is studied by recording the total array of particular hysteresis loops. After this, the obtained loops are differentiated with respect to two variables: the temperature corresponding to the beginning of a particular loop and the current temperature. The result of such a processing is the coercive temperature distribution function. In the case of vanadium-oxide interferometer, the parameter displaying a linear dependence on the concentration of the new phase in the bulk of the old phase is its reflectivity [4].

Apart from the optical loops, we also studied the loops of temperature hysteresis of the electrical conductivity of a VO_2 film (in direct current). It should be noted that electrical conductivity is not a quantity depending linearly on the concentration of the nuclei of the new phase in the bulk of the old phase, and one has to resort to the concepts of the percolation theory providing the relation between the temperature dependence of the concentration of the phase that has experienced the phase transition and the electrical conductivity of the sample for determining the CTDF experimentally [5]. This relation is not linear, and deviations from linearity should be taken into account in an analysis of experimental results. In spite of its cumbersomeness, the procedure of experimental measurement of the CTDF does not involve any fundamental difficulties, both for optical and electrical hysteresis loops, and is described comprehensively in [6].

It was noted above that this procedure requires the knowledge of the complete array of particular hysteresis loops reflecting the fine structure of the main loop (within which the reflectivity of the interferometer as well as the conductivity of the VO_2 film are functions of two variables: the temperature corresponding to the beginning of a particular loop and the current temperature [4]), as well as the possibility of differentiating the array of particular loops with respect to these variables with any step required.

To be able to differentiate the array of particular loops step by step, we approximated the total family of optical hysteresis loops (both principal and particular) by functions of the form

$$R(T) = A(T_s) + B(T_s)/T + D(T_s)F(T),$$

where T is the current temperature and T_s is the temperature corresponding to the beginning of a particular hysteresis loop [1], $R(T)$ is the reflectivity of the interferometer, $F(T) = 1/\{1 + \exp[-(T - T_{av})/T^*]$, T_{av} is the temperature corresponding to the midpoint of a branch of the loop, and the functions $A(T_s)$, $B(T_s)$, and $D(T_s)$ have the same form as $R(T)$, but the coefficients A, B, and D in them are constants.

The experimental accuracy of determining these constants is quite high: the error amounts to less than 0.1% since the fitting process use was associated with the substitution of the exponent into the exponent of another exponential (this is readily seen from the formula for $R(T)$).

In experiments devoted to the study of electrical conductivity of vanadium dioxide, the VO_2 film was deposited on a substrate made of ZrO_2 : Y, viz., a superionic conductor serving simultaneously as an electrode of the measuring cell and an oxygen-ion pump injecting to or extracting from the VO_2 film a fraction of oxygen ions by changing the polarity of the applied voltage.

The vanadium-oxide interferometer was also used in experiments on passive intracavity control of the parameters characterizing the radiation emitted by a pulsed solid-state laser. The interferometer was used as the cavity end mirror of the Nd:YAG laser, and the possibility of giant pulse generation, as well as of passive synchronization of its modes was investigated.

2. DISCUSSION OF RESULTS

The main idea underlying this work is to demonstrate the possibility of separating the electron and lattice contributions to the phase transition process, which can be done by studying the kinetics of the phase transition (phase-transition kinetics was studied by placing the vanadium-oxide interferometer into the cavity of a pulsed laser as the cavity end mirror), as well as by analyzing the evolution of the coercive temperature distribution function under various external factors acting on the sample. We classified these factors as the variation of the synthesis conditions, the bombardment by a moderate-energy (6–10 keV) electron beam, and the extraction of a fraction of oxygen from the sample followed by the backward injection of the same fraction of oxygen into the sample.

2.1. Variation of Synthesis Conditions

By varying the condition of synthesis of the interferometer, one can obtain temperature hysteresis loops of various shapes, both symmetric and asymmetric, to various degrees of asymmetry, which is determined, according to experiments, by the extent of oxygen deficiency in the VO_2 film (the variations of the synthesis conditions included the change in oxygen pressure in the reaction chamber, the substrate temperature, and the target sputtering rate).

It was found that a symmetric hysteresis loop has a two-dimensional coercive temperature distribution function with a single peak, while an asymmetric function has a peak split in the cross section reflecting the width distribution of elementary loops (Fig. 1a). The

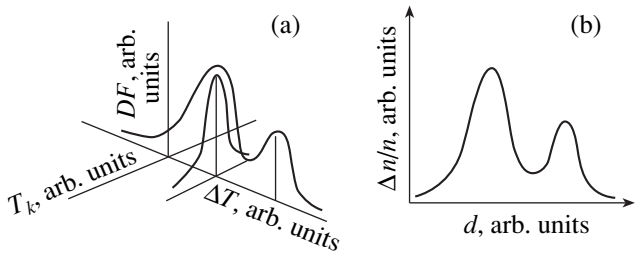

Fig. 1. Illustration of the correspondence between the CTDF features and the morphology of the VO_2 film: (a) the CTDF section by the planes reflecting the distribution of loops over their widths (ΔT) and positions on the temperature scale (T_k) for a hysteresis loop whose asymmetry is created by the variation of the conditions of the interferometer synthesis; *DF* is the CTDF amplitude; (b) the histogram of the size distribution of grain in the VO_2 film of the interferometer, $\Delta n/n$ is the relative number of crystallites of a given size, and *d* is the crystallite diameter.

other CTDF cross section reflecting the distribution of elementary loops over their positions on the temperature scale (thermoposition cross section) does not experience any changes upon a variation of the synthesis conditions.

It turned out that the reason behind the observed splitting lies in the martensite nature of the given phase transformation. This conclusion was drawn from the following considerations.

In a martensite transformation, a new phase appears in the bulk of the old phase in the form of thin seed plates oriented strictly along crystallographic directions. A nucleus starts growing when the energy deviates from the value corresponding to the thermodynamic equilibrium of the phases by a quantity inversely proportional to the square root of the characteristic size restricting the growth of the martensite plate. The characteristic size for a perfect single crystal is the distance to the adjacent nucleus, while for a film it is the diameter of a grain, since a single nucleus appears in a small grain [7].

The fact that the phase transition in vanadium dioxide is a martensite transformation is confirmed by the histogram of the size distribution of grains in the film (Fig. 1b) which exhibits for an asymmetric loop the same peculiarities as in the split cross section of the CTDF, thus confirming the applicability of the martensite model in the given case. Our processing of all the available data on the basis of this model confirms the validity of the conclusion concerning the martensite type of the metal–semiconductor phase transition in vanadium dioxide.

Thus, the elastic energy of the outer boundary of a grain, i.e., the quantity characterizing the state of the crystal lattice of the material, contributes greatly to the energy of transition owing to its realization through nucleation.

Returning to the fundamental question concerning the type of the given phase transformation, note that the Peierls nature of the transition, according to which the lattice cooled below the transition point undergoes distortions, such that its period at least doubles (which is the reason behind the emergence of the energy gap in the energy spectrum [2]), presumes the leading part of the lattice contribution to the transition energy. An increase in temperature above T_c eliminates these distortions, raising the lattice symmetry from monoclinic to tetragonal (this is determined by the symmetry of the thermodynamic potential) and removes the gap in the electron spectrum.

Conversely, the Mott nature of the transition presumes the presence of a gap in the electron spectrum in view of small widths of the energy *d* bands (including the conduction band). According to calculations [8], the Coulomb energy of repulsion between a free electrons and the electrons of the atomic core to which the free electron arrives in an attempt to drift over the conduction band and to ensure the electrical conduction of the material (the electron–electron correlation energy) is an order of magnitude higher than the width of the allowed conduction band, so that the electron is expelled in energy to the forbidden band, thus blocking the conduction. The material becomes a Mott-type insulator.

In this connection, it was interesting to study the effect of selective excitation of the crystal lattice of the material on the phase transition in the unconditional absence of any effect on its electron system, and conversely.

The experimental construction of the two-dimensional CTDF offers just such an opportunity because this allowed us to control the presence or absence of crystal lattice distortions under various external factors acting on the sample from the presence or absence of distortions in the corresponding measurement of the two-dimensional CTDF.

2.2. Oxygen Extraction–Injection with the Help of a Superionic Pump

The selective excitation of the lattice subsystem of the crystal that did not affect the electron subsystem was carried out as follows.

A superionic oxygen pump was used to extract a certain fraction of oxygen from the vanadium dioxide film (the construction of the pump is described in [9]). Oxygen extraction was carried out until the free carrier concentration increased by two orders of magnitude as a result of the formation of donor-type defects [2]. This is usually observed after the removal of oxygen ions due to the violation of the charge balance of the lattice (spontaneous restoration of the balance is accompanied by an increase in the conductivity).

The reversal of the supply voltage of the superionic pump resulted in the backward injection of oxygen to the sample leading to the complete restoration of the

initial value of conductivity and the return of the phase transition temperature, shifted towards lower temperatures after the extraction, to its previous value. The hysteresis loop was found to increase its width (from 4 to 25°C) after such an effect. As regards the CTDF, it was found that the first distribution of elementary loops (over their widths) became much broader, while the second (thermopositional) distribution did not change within the margin of experimental error.

As regards the process of defect formation, we can state that both oxygen extraction and injection occur through the region of contact between the crystallites of the film and the substrate playing the part of an oxygen pump, i.e., through the surface of the grains. The temperature at which the oxygen extraction, followed by injection, was carried out was approximately 200°C, which was determined by the standard operation conditions of the superionic pump. This temperature was far from the temperature of synthesis of the VO_2 film (470°C). Thus, the film was treated under strongly nonequilibrium conditions, the perturbation affecting the surface of crystallites through which the oxygen ion flow passed. The fact that the film conductivity returned to its initial low value after the termination of the injection indicates that donor-type defects emerging as a result of the extraction have been healed, while other types of defects (e.g., interstitial atoms) concentrated on the surface of the crystallites of the film continue to make an additional contribution to the energy of formation of martensite-type nuclei, leading to the formation of a large number of broadened elementary loops (reflected in the behavior of the CTDF) and, as a result, to a broadening of the principal hysteresis loop. Note that the charge that had to be passed through the superionic pump to restore the initial value of conductivity during the oxygen injection was an order of magnitude larger than for the extraction. This means that the efficiency of healing of donor-type defects amounts to less than one tenth of the efficiency of their formation. The remaining nine-tenths of oxygen ions arriving at the VO_2–ZrO_2 interface effectively perturbed the surface of crystallites in the VO_2 film.

The variation of the oxygen extraction–injection procedure revealed that it is impossible to induce a forced metal–semiconductor phase transition in VO_2 or noticeably change its position on the temperature scale by perturbing the lattice without changing the carrier concentration in it, and thus leaving the electron subsystem of the material unperturbed (which can be controlled unambiguously from the behavior of the corresponding cross section of the CTDF). In our opinion, this indicates an auxiliary role of lattice perturbations in the transition process.

2.3. Irradiation by Moderate-Energy Electron Flow

We succeeded in carrying out a selective excitation of the electron subsystem of the material leaving the lattice subsystem unaffected by introducing donor-type defects through irradiation of the VO_2 film by a moderate-energy electron flow.

It is well known that an electron bombardment generates donor-type defects in VO_2 films [10].

The mechanism of defect formation can be described as follows.

The flow of 7 keV electrons pierces a VO_2 film of thickness 1000 Å practically without any interaction and penetrates the substrate to a depth of the order of 1 μm according to estimates obtained by three different methods [11]. This intrusion induces, apart from heating, a cascade of secondary electrons with a broad energy spectrum [12]. Interacting with the VO_2 film, secondary electrons lead to defect formation in the bulk of grains in contrast to the case of oxygen extraction through the film–substrate interface.

The increase in the concentration of free carriers generated by donors shifts the phase-transition temperatures in the crystallites of the film towards lower temperatures.

The experiments demonstrated that such an increase in the concentration changes the other (temperature-position) measurement in the two-dimensional CTDF without affecting the first measurement, viz., the width distribution of loops (Fig. 2).

The principal hysteresis loop in this case acquires an asymmetry resembling that in the case of deficiency of oxygen introduced during the synthesis. However, the morphology of the obtained VO_2 films in these cases differs basically: in the former case, different sizes of grains display different extents of oxidation, leading to a transformation of the histogram of the width distribution of the region in the film grains occupied by vanadium dioxide and to a change in the shape of the transverse section of the CTDF; in the latter case, donor-type defects are formed, sharply elevating the free carrier concentration in the conduction band, without any transformation of the histogram or a change in the

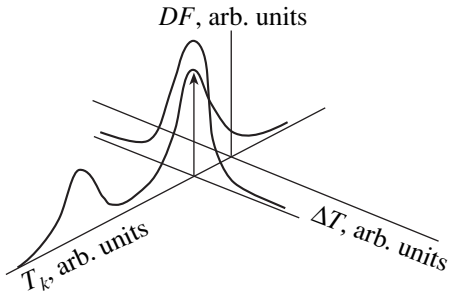

Fig. 2. Temperature-position and width sections of the CTDF for a VO_2 film whose hysteresis loop asymmetry is created by the bombardment of the initial sample with a symmetric loop by a moderate-energy (7 keV) electron flow; notation is the same as in Fig. 1.

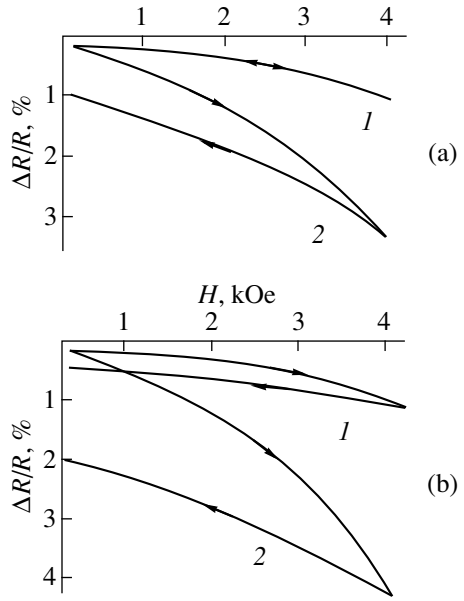

Fig. 3. Hysteresis phenomena in the negative magnetoresistance of a VO_2 film irradiated by electrons: the magnetic field direction is perpendicular (a) and parallel (b) to the film surface; *T*, K: (*1*) 4.2, (*2*) 1.2.

CTDF section reflecting the distribution of loops over widths, but with a change in the phase transition temperatures of individual crystallites forming the film, and hence the change in the temperature-position section of the CTDF.

The dependence of the transition temperature on the carrier concentration is a distinguishing feature of the Mott electron transition. According to our experiments, the introduction of donor-type defects through the bombardment by an electron flow does not cause a significant perturbation of the crystal lattice. Otherwise, the CTDF section reflecting the width distribution of loops and sensitive to elastic perturbations should undergo changes.

The proof of the possibility of generation of defects possessing the donor properties and perturbing the lattice only slightly is of principal importance for experiments with defect formation in vanadium dioxide because it allows one to selectively use the basic property of donors, i.e., the supply of carriers to the conduction band. It was found that the bombardment by an electron flow can transfer the VO_2 film to the metallic state by inducing a forced insulator–metal phase transition in a wide temperature range from T_c = 340 K (67°C) to T = 1.6 K, the invariability of the CTDF section reflecting the width distribution of the loops indicating the smallness of the perturbation of the lattice by the field of the defects formed as a result of irradiation.

This means that such an experiment permits the observation, in a pure form, of the electron phase transition in vanadium dioxide.

The electron bombardment of a VO_2 film makes it possible to observe a number of auxiliary effects.

It allows one to metallize the VO_2 film to such an extent that it preserves its metallic properties down to T_c = 1.6 K. We proved that under maximum exposure doses, the sample is a film-type semiconducting matrix pierced by a network of one-dimensional conducting filaments having a thickness of a few tens of angstroms [13]. It was also proved that a weak charge localization takes place in this case, owing to potential fluctuations that emerged as a result of the electron bombardment.

The existence of localization can be detected by placing the sample in a magnetic field in order to induce delocalization, which was actually done in our experiments. We investigated the magnetoresistance of VO_2 films bombarded by electrons in fields up to 35 kOe. Within the experimental error, the magnetoresistance did not depend on the sample orientation, which confirms the one-dimensional nature of current-carrying formations.

The magnetoresistance proved to be negative (NMR), its magnitude being on the average 2% at 4.2 K and 7% at 1.6 K.

The dependence of the negative magnetoresistance on the magnetic field strength was correctly described by the formula derived in the Aronov–Altshuler theory for the weak localization of charge carriers in one-dimensional conducting filaments [14]:

$$\Delta R_H/R_{H=0} = K\{[1 + (H/H_c)^2]^{-1/2} - 1\},$$

where K is a constant factor depending on temperature and sample geometry and H_c is the critical field of delocalization, which was found to be 50 kOe for an exposure dose of 10^{19} e/cm^2 and 95 kOe for 6×10^{19} e/cm^2.

Subsequent experiments proved that the negative magnetoresistance exhibited a hysteresis loop in the magnetic field, whose magnitude depended strongly on temperature (Fig. 3).

We also found that apart from hysteresis, the irradiated VO_2 samples also displayed a dependence of NMR on the time and past history of the sample (Fig. 4). For example, a sample that initially displayed no hysteresis (which was confirmed by the return of its resistance to the value in zero magnetic field after the field removal) exhibited an MNR drift towards higher values in a field of 20 kOe at 2 K, the NMR increasing by 25% in 40 minutes. After repeated applications of the magnetic field, the value of the NMR was found to be smaller (1% instead of 1.6%), the time drift persisted, and, besides, a hysteresis in magnetic field took place. The above effects disappeared after heating to room temperature.

Note that such behavior of conductivity as a function of time (slow drift without features of saturation) and magnetic field (hysteresis loop depending on sample previous history) is typical of spin glasses [15].

The existence of the glass state was predicted by us theoretically and observed experimentally in another series of experiments [16], which will be discussed elsewhere.

In our opinion, the results of the experiments with oxygen pump described above indicate an auxiliary role of lattice perturbations in the phase transition under investigation.

On the contrary, by perturbing the electron subsystem without affecting the crystal lattice, one can induce a metal–semiconductor phase transition in VO_2 in a very wide temperature range. We believe that this is evidence of the dominating role of the electron subsystem in the transition.

2.4. Generation of Passive Mode Synchronization Pulses

An additional argument in favor of the electronic nature of the given phase transition is the passive synchronization of the modes emitted by a pulsed IR laser with the help of a vanadium-oxide interferometer.

In this experiment, the VO_2 interferometer was used as the cavity end mirror in the cavity of a Nd:YAG laser ($\lambda = 1.06$ μm).

It was found that at the radiation energy density in the cavity of the order of 20 J/cm^2, a giant radiation pulse is formed at the output of the optical system due to a jump in the reflectivity of the mirror induced by the semiconductor–metal phase transition. The duration of the radiation pulse was approximately 60 ns and was determined by the rate of liberation of the latent heat of transition to the substrate of the interferometer [17].

Experiments proved that (in contrast to [18]) an order-of-magnitude decrease in the average energy in the cavity leads to the emergence at the cavity output of the passive mode synchronization pulses of duration 20–30 ps with fronts of 3–5 ps.

The interferometer stabilization temperature in our experiments was 22°C, the laser beam diameter was 1 mm, the reflection coefficient of the laser output mirror was 52%, the reflection coefficient of the cavity end mirror was 12% in the semiconducting state and 46% in the metallic state, and the output energy of the pulse was 112 μJ. An analysis of the oscillogram of the output pulses obtained under such conditions has made it possible to estimate the energy of the first (weakest) pulse of passive mode synchronization, which was found to be 0.4 μJ (4×10^{-7} J).

At the same time, taking the specific heat of vanadium dioxide equal to 80 J/mol K, the latent heat of phase transition equal to 1000 cal/mol, the temperature corresponding to the onset of nonlinear process as 55°C, the vanadium dioxide density as 4.7 g/cm^3, and the thickness of the VO_2 layer in the mirror at 1000 Å, we find that a transition to the metallic state under these conditions requires an energy supply of approximately

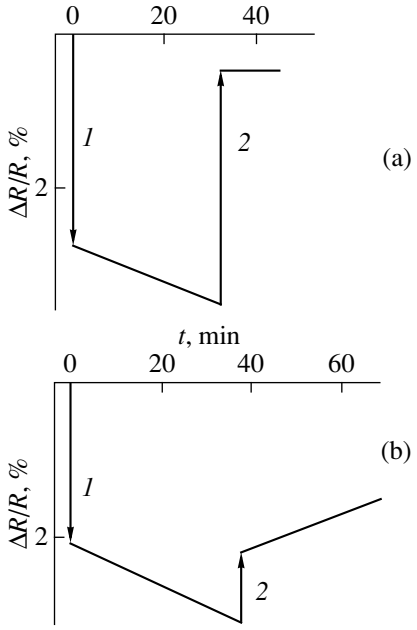

Fig. 4. Relaxation of the negative magnetoresistance of a VO_2 film ($T = 1.2$ K) exposed to a moderate-energy electron flow: (a) the first application of a magnetic field $H = 20$ kOe, (b) repeated application of a magnetic field of the same strength; the time interval between the states (a) and (b) is 20 min; (*1*) in the field, (*2*) in zero field.

4×10^{-5} J, i.e., the value two orders of magnitude higher than the energy in the first synchronization pulse.

Thus, we see that a monopulse of passive mode synchronization does not ensure conditions for a full-fledged phase transition of the VO_2 film to the metallic state, firstly, in view of the energy deficit of two orders of magnitude, and secondly, due to the fact that the release of the latent heat of phase transition to the substrate over a picosecond time interval is ruled out in accordance with the previous experience with the generation of a giant radiation pulse, during which a full-fledged semiconductor–metal phase transition occurred. In this case, the release of the latent heat of transition takes place during a time three orders of magnitude longer, namely, in nanoseconds (10^{-9} s).

According to estimates, the jump in the reflectivity of the vanadium-dioxide mirror cannot be attributed to the reaction of free carrier plasma either, since its concentration in a semiconductor such as VO_2 is too low to ensure a jump in the mirror reflectivity of 38%, which is determined by the properties of the semiconducting phase of vanadium dioxide [2]. The deficiency in this case is at least three orders of magnitude.

Finally, this effect could be associated with the fact that obtaining passive mode synchronization pulses is known to require just a 10%-variation of the reflectivity of the nonlinear mirror as compared to that required for the generation of a giant pulse [1]. Analysis leads to the rejection of this assumption also.

Indeed, simple estimation shows that the adiabatic heating of the VO_2 mirror from room temperature (22°C) at which experiments were made to the temperature corresponding to the onset of changes in the film reflectivity (55°C) requires approximately the same energy as that needed for a 100% phase transition of the mirror to the metallic phase at 55°C. This means that the energy in the monopulse of passive mode synchronization lowered by two orders of magnitude is *a fortiori* insufficient for heating the mirror from room temperature to the transition temperature and the more so, for initiating this transition.

It remains for us to assume that the nonlinear properties of the VO_2 mirror, which are manifested during its pumping by radiation with a wavelength of 1.06 μm (corresponding approximately to the edge of intrinsic absorption in vanadium dioxide [2]), are due to a selective response to the optical pumping of the electron subsystem of the material in a state preceding the full-fledged semiconductor–metal phase transition. The rearrangement of the crystal lattice, which is the final stage of the phase transition, lags behind in its response. Under such an assumption, a rapid (lasting for picoseconds) return of the mirror to the initial state in the passive mode synchronization is accounted for by the release of the excitation energy of the electron subsystem to the crystal lattice of the material, rather than to the substrate, as would be in the case of lattice excitation.

This statement fits with the conclusions formulated by Berger and Shuker [20], who proved that the effect of such short light pulses is too weak for an appreciable modulation of optical constants responsible for the observed laser radiation pulses. These authors noted that the crucial point in this case is the increase in the electron concentration in the conduction band. However, in their opinion, the mechanism causing the strong changes in optical constants due to such an increase requires further investigation.

We believe that the results of our experiments shed light on this mechanism.

As a matter of fact, an elevation of the concentration of free charge carriers leads to Coulomb screening of electron–electron correlations at the same lattice site, as is usually the case in a Mott electron transition [21]. This screening lowers the correlation energy in VO_2 approximately by an order of magnitude [8] so that free carriers get in energy into the conduction band, and the metal acquires a metal-type conductivity. The high-frequency permittivity (and hence the optical constants of the material) changes simultaneously. In other materials with a phase transition, such screening is observed only in the immediate vicinity of the phase-transition point, while the electron order parameter in vanadium dioxide is capable of changing significantly, according to our previous publication [16], starting from 8°C, i.e., at a temperature sixty degrees lower than the phase transition point. At room temperature (23°C), at which our experiments were made, the Coulomb screening can be quite noticeable.

This means that by absorbing a radiation pulse at a wavelength of 1.06 μm corresponding to the edge of the fundamental absorption in vanadium dioxide [2] and by generating free charge carriers most effectively, the electron subsystem goes over to an excited state. The free carrier concentration in the conduction band increases in the process of absorption of new and new optical quanta, and the process of the Mott electron phase transition begins. This is followed by a rearrangement of the crystal lattice, which tunes itself to the changes in the electron subsystem, and the crystal thermodynamic potential becomes higher than its minimum value. The described processes modify the optical constants. However, the crystal rapidly returns to the initial state corresponding to the minimum of the thermodynamic potential of the semiconducting phase because the energy absorbed by the material is insufficient to overcome the potential barrier separating the semiconducting and the metallic phases of the material, and the laser cavity responds to this by generating a passive mode synchronization pulse. In this case, a full-fledged phase transition accompanied by a rearrangement of the electron, as well as the lattice subsystems of the crystal, and by the fixation of the material in the new metallic state does not take place.

In other words, according to our concepts, the initial stage of the semiconductor–metal phase transition includes a rapid rearrangement of the valence electron subsystem of the material (in terms of [8, 21], the electron density transfer to the ligand), which is associated with an abrupt increase in the free carrier concentration in the conduction band of vanadium dioxide upon the absorption of the most intense radiation pulse emitted as a result of a Gaussian stochastic process in the laser cavity [19], preceding the passive mode synchronization phenomenon. This is observed at temperatures much lower (23°C) than the temperatures from the neighborhood of the phase transition point (67°C), which is due to the temperature dependence of the electron order parameter for VO_2 [16].

This process is similar to superfast vibronic phase transitions in ordinary superconductors of the Si, GaAs, or InSb type [22], the only difference being that the superfast phase transition in the above semiconductors requires the softening of the phonon spectrum, initiated by a high concentration of the plasma of free charge carriers. In our case, however, the phonon spectrum softens, irrespective of the concentration of the free charge carrier plasma as the temperature approaches the semiconductor–metal phase transition point [16], the softening beginning from 8°C, i.e., the temperature sixty degrees lower than the phase transition point. A detailed pattern of transformation, under the action of short laser pulses, of a superfast vibronic phase transition to a semiconductor–metal phase transition at a

temperature approaching the phase-transition point will be the subject of further investigations.

Thus, the results of experiments described above lead to the main conclusion of this work: the metal–semiconductor phase transition in vanadium dioxide acts as an electronic phase transition (at least in the given series of experiments) in the sense that its initial stage is the rearrangement of the electron subsystem of the material, and the changes in the crystal lattice inevitably accompanying this process are auxiliary because these changes form a stage of the process of sample transition from the semiconducting to the metallic state, which occurs immediately after the pumping of the electron subsystem of the material.

REFERENCES

1. A. A. Bugaev, B. P. Zakharchenya, and F. A. Chudnovskiĭ, *Metal–Semiconductor Phase Transition and Its Applications* (Nauka, Leningrad, 1979).
2. W. Bruckner, H. Opperman, W. Reichelt, *et al.*, *Vanadium Dioxide* (Akademie-Verlag, Berlin, 1983).
3. V. L. Gal'perin, I. A. Khakhaev, F. A. Chudnovskiĭ, and E. B. Shadrin, Zh. Tekh. Fiz. **61** (10), 194 (1991) [Sov. Phys. Tech. Phys. **36**, 1190 (1991)].
4. T. G. Lanskaya, I. A. Merkulov, and F. A. Chudnovskiĭ, Fiz. Tverd. Tela (Leningrad) **20**, 1201 (1978) [Sov. Phys. Solid State **20**, 193 (1978)].
5. B. I. Shklovskiĭ and A. L. Éfros, Usp. Fiz. Nauk **117**, 401 (1975) [Sov. Phys. Usp. **18**, 845 (1975)].
6. I. A. Khakhaev, F. A. Chudnovskiĭ, and E. B. Shadrin, Fiz. Tverd. Tela (St. Petersburg) **36** (6), 1643 (1994) [Phys. Solid State **36** (6), 898 (1994)].
7. A. L. Roĭtburd, Usp. Fiz. Nauk **113**, 69 (1974) [Sov. Phys. Usp. **17**, 326 (1974)].
8. T. Altanhan, J. Phys. C: Solid State Phys. **20**, L949 (1987).
9. S. E. Nikitin, I. A. Khakhaev, F. A. Chudnovskiĭ, and E. B. Shadrin, Fiz. Tverd. Tela (St. Petersburg) **35** (10), 2815 (1993) [Phys. Solid State **35** (10), 1393 (1993)].
10. A. Leone, A. Trione, and F. Junga, IEEE Trans. Nucl. Sci. **37** (6), 1739 (1990).
11. E. B. Shadrin, Author's Abstract of Doctorate's Dissertation (St. Petersburg, 1997).
12. A. R. Shul'man and S. A. Fridrikhov, *Secondary-Electron Investigation Methods of Solids* (Nauka, Moscow, 1977).
13. E. I. Nikulin, F. A. Chudnovskiĭ, E. B. Shadrin, and D. A. Myasnikov, Zh. Tekh. Fiz. **58** (12), 2411 (1988) [Sov. Phys. Tech. Phys. **33** (12), 1473 (1988)].
14. B. L. Al'tshuler and A. G. Aronov, Pis'ma Zh. Éksp. Teor. Fiz. **33** (10), 515 (1981) [JETP Lett. **33** (10), 499 (1981)].
15. V. S. Dotsenko, Usp. Fiz. Nauk **6** (1), 151 (1993).
16. V. S. Vikhnin, I. N. Goncharuk, V. Yu. Davydov, *et al.*, Fiz. Tverd. Tela (St. Petersburg) **37** (12), 3580 (1995) [Phys. Solid State **37** (12), 1971 (1995)].
17. A. A. Bugaev, V. V. Gudyalis, and A. V. Klochkov, Fiz. Tverd. Tela (Leningrad) **26** (5), 1463 (1984) [Sov. Phys. Solid State **26** (5), 887 (1984)].
18. I. A. Belashenkov, P. A. Solunin, I. A. Khakhaev, *et al.*, Fiz. Tverd. Tela (St. Petersburg) **36** (8), 2032 (1994) [Phys. Solid State **36** (8), 1347 (1994)].
19. J. Herrman and B. Wilhelmi, *Laser für Ultrakurze Lichtimpulse* (Academie-Verlag, Berlin, 1984; Mir, Moscow, 1986).
20. N. K. Berger and R. Shuker, Appl. Phys. Lett. **74** (19), 2770 (1999).
21. N. F. Mott, *Metal–Insulator Transitions* (Taylor and Francis, New York, 1990, 2nd ed.; Nauka, Moscow, 1979).
22. V. I. Emel'yanov and D. V. Babak, Fiz. Tverd. Tela (St. Petersburg) **41** (8), 1462 (1999) [Phys. Solid State **41** (8), 1338 (1999)].

Translated by N. Wadhwa

Physics of the Solid State, Vol. 42, No. 6, 2000, pp. 1134–1138. Translated from Fizika Tverdogo Tela, Vol. 42, No. 6, 2000, pp. 1100–1104.

LATTICE DYNAMICS AND PHASE TRANSITIONS

Effect of Hydrostatic Pressure and Temperature on the EPR Spectrum of the Mn^{2+} Ion in $Zn(BF_4)_2 \cdot 6H_2O$

G. N. Neĭlo, A. A. Prokhorov, and A. D. Prokhorov

Donetsk Physicotechnical Institute, National Academy of Sciences of Ukraine, Donetsk, 340114 Ukraine

e-mail: prohorov@pr.fti.ac.donetsk.ua

Received November 25, 1999

Abstract—A study of the effect of hydrostatic pressure and temperature on the EPR spectrum of the Mn^{2+} ion in $Zn(BF_4)_2 \cdot 6H_2O$ is reported. The break in the temperature dependence of the b_2^0 parameter at 196 K is evidence of the existence of a phase transition accompanied by a change in the thermal expansion coefficient. It is shown that pressure considerably affects the spectral parameters by reducing the axial parameter b_2^0 and increasing the cubic one, b_4^0. At 9 kbar, the b_2^0 parameter is temperature independent. A comparison of the pressure dependences of the spectra of $Zn(BF_4)_2 \cdot 6H_2O$, $ZnSiF_6 \cdot 6H_2O$, $ZnTiF_6 \cdot 6H_2O$, and $MgSiF_2 \cdot 6H_2O$ crystals suggests equal hydrogen-bond lengths in these compounds. A ligand hyperfine structure has been detected, which originates from the Zeeman interaction with the proton nuclei surrounding Mn^{2+} and manifests itself in the formation of satellites at each EPR line, their separation being proportional to the magnetic field. The nonlinear pressure dependence of the linewidth is related to the structural features of the crystal under study.

The $Zn(BF_4)_2 \cdot 6H_2O$ crystals belong to an isomorphic family in which the ion metal can be replaced by Co, Ni, Fe, Mn, and Mg ions, and Cl can occupy the place of B. There is considerable interest in these materials, because a number of phase transitions caused by weak orientational forces exist in them and because they therefore have a multi-site potential minimum. Determining the phase diagrams of such materials, complemented by an investigation of the microscopic properties in various phases, including an EPR study of the changes of the ground state of paramagnetic ions under the variation of an external pressure and of temperature, may provide an insight into the nature of the phase transitions occurring in these crystals.

The first crystallographic data on the perchlorates were presented in [1]. Comparative measurements of the lattice constants of the perchlorates and fluoroborates were made in [2]. X-ray diffraction data are also available on the zinc and nickel perchlorates [3, 4]. The arrangement of the ClO_4 tetrahedra and $M \cdot 6H_2O$ octahedra was found to be identical with that in $LiClO_4 \cdot 3H_2O$ [1, 4]. Unfortunately, more detailed crystallographic information on fluoroborates is lacking, but their internal structure can be revealed by studying the perchlorates.

Fluoroborates are dealt with in a number of EPR studies of the Mn^{2+} and Ni^{2+} ions [5–9]. The results reported in [5] and [6] are rather contradictory. While the authors of [6], as well as of [7–9], detected only one phase transition in $Zn(BF_4)_2 \cdot 6H_2O$ and $Ni(BF_4)_2 \cdot 6H_2O$ crystals in the 77–300 K temperature region (at ~180 K), which results in a break in the temperature dependence of the original splitting, similar to that observed in $ZnSiF_6 \cdot 6H_2O$ [10], Jain and Geoffroy [5] report observing several phase transitions. Besides, the values of the $D(b_2^0)$ parameter characterizing the Mn^{2+} ion splitting and quoted in [5] and [6] are substantially different.

This work describes an EPR study of the Mn^{2+} ion (0.5%) in the $Zn(BF_4)_2 \cdot 6H_2O$ crystal performed at temperatures from 77 to 320 K, as well as high pressure measurements, aimed at revealing specific features in the temperature and pressure dependences of the spectrum.

1. EXPERIMENTAL TECHNIQUES, SAMPLES, CRYSTAL STRUCTURE

EPR spectra were measured on a 3 cm superheterodyne radiospectrometer, which was provided by special white-sapphire resonators that enable us to study at high hydrostatic pressures within a broad temperature range. For a pressure generator, a self-contained high-pressure vessel of a nonmagnetic material (beryllium bronze) was used. The sample to be studied was mounted in the white-sapphire resonator which, in turn, was placed in the high-pressure vessel. The pressure-transmitting medium was a mixture of equal parts dehydrated transformer oil and kerosene. Particular attention was placed on making sure that the pressure

was indeed hydrostatic. For this purpose, a thin teflon cap filled with dehydrated benzine, which remains liquid up to 20 kbar, was put on the sapphire resonator. The resonator was coupled with the spectrometer waveguide through a thin coaxial line. The pressure was measured throughout the temperature range covered by a manganin transducer simultaneously with the measurement of temperature with a calibrated copper-resistance thermometer. A nichrome heater was wound on the high-pressure vessel to obtain the desired temperature, and the construction as a whole was isolated by a thin vacuum gap. An electronic control system allowed us to stabilize the temperature to within 0.1 K and to vary it smoothly.

$Zn(BF_4)_2 \cdot 6H_2O$ single crystals with an addition of 0.5% Mn^{2+} were grown from a water solution by two methods, namely, by slowly lowering the thermostat temperature and by evaporating the solution at room temperature. In both cases, the crystals grow to become well-faceted hexahedral prisms, which facilitated their orientation. Unlike the crystals studied in [5], our samples were not hygroscopic and were stored in normal atmospheric conditions.

Like the perchlorate, the zinc fluoroborate has a pseudohexagonal structure ($P6_3mc$) exhibiting three-component orthorhombic twinning ($Pmn2_1$). The schematic representation of its structure can be found in more than one publication [5, 12] ($z = 2$, $a = 7.62$ Å, $b = 13.2$ Å, $c = 5.30$ Å).

The ion of the divalent metal is surrounded by six H_2O molecules, which make up an octahedral structure slightly distorted along the *c* axis. In its turn, the water octahedron is surrounded by six BF_4 tetrahedra, which also form an octahedral structure. The two water octahedra in the unit cell are turned with respect to one another by 60° about the *c* axis.

If the space group of the crystal is C_{2v}^7 ($Pmn2_1$), then the two metal cations in the cell occupy a position with C_s symmetry [11, 12]. If the four $(BF_4)^-$ ions are considered equivalent, they should sit at sites of C_1 symmetry.

The magnetic multiplicity, i.e., the number of spatially inequivalent EPR spectra for a divalent ion which can be observed in a structure with the above symmetry, is two. Note that the magnetic axes of both spectra coincide along the *a* axis, while the other two can be arbitrarily oriented. Because there are three blocks (or domains) turned through 120° with respect to one another, one should be able to observe six EPR spectra. To illustrate, one could present a Mn^{2+} EPR spectrum of $MgSiF_6 \cdot 6H_2O$ in the monoclinic phase $P2_1/c$ [13]. Because the crystal as a whole has pseudohexagonal symmetry, all spectra must coincide along the *c* axis.

2. TEMPERATURE DEPENDENCE OF THE SPECTRUM

The EPR spectrum observed at normal pressure throughout the temperature range studied can be approximated with satisfactory accuracy by the axial spin Hamiltonian

$$\hat{H}\beta\mathbf{B}g\hat{S} + \frac{1}{3}b_2^0O_2^0 + \frac{1}{60}b_4^0O_4^0 + \hat{S}A\hat{I}, \qquad (1)$$

where g is the spectroscopic splitting factor tensor, β is the Bohr magneton, **B** is the magnetic induction vector, $\hat{S}$ is the spin operator, O_2^0 and O_4^0 are the Stevens operators, and A is the hyperfine interaction tensor. The parameters of the Hamiltonian were obtained by processing experimental spectra using a special program. The g factor and the hyperfine interaction parameters are isotropic to within experimental errors.

The Mn^{2+} spectrum was measured within a broad temperature region extending from 77 to 320 K. It consists of 30 absorption lines making up the fine and hyperfine structure (electronic spin $S = 5/2$, nuclear spin $I = 5/2$). The g factor and the hyperfine interaction parameters remain constant throughout the temperature region covered. The axial splitting parameter b_2^0 undergoes a noticeable variation. Figure 1 presents the temperature dependence of the difference between the fields of the high- and low-field EPR lines, which is proportional to the b_2^0 parameter.

This relation consists of two linear parts crossing at 196 K. Observation of such a break in the temperature dependence was reported earlier in [6]. A similar pattern was observed in the Mn^{2+} EPR spectrum of $ZnSiF_6 \cdot 6H_2O$ at a temperature very close to ours (200 K) [10]. These changes can be identified with a second-order phase transition accompanied by a change in the ther-

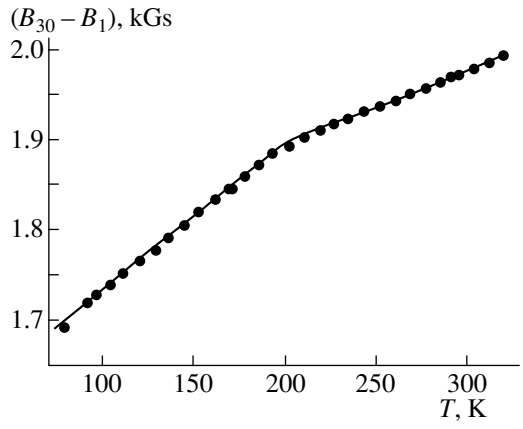

Fig. 1. Temperature dependence of the field difference between the first and last lines of the Mn^{2+} EPR spectrum for $Zn(BF_4)_2 \cdot 6H_2O$.

Parameters of the spin Hamiltonian (1) for 77 and 293 K

T, K	g	b_2^0, 10^{-4} cm^{-1}	b_4^0, 10^{-4} cm^{-1}	A, 10^{-4} cm^{-1}
77	2.001(1)	–140.0(1)	–3.1(2)	–89.6(8)
293	2.001(1)	–170.1(1)	–2.6(2)	–89.6(8)

mal expansion coefficient. In the temperature region of 77 to 196 K, $\Delta b_2^0/\Delta T = -0.189 \times 10^{-4}$ cm^{-1}/K, and at higher temperatures, from 196 to 320 K, $\Delta b_2^0/\Delta T = -0.113 \times 10^{-4}$ cm^{-1}/K. The nature of this transition remains unclear. It may, however, be conjectured that it is the same for the $ZnSiF_6 \cdot 6H_2O$ and $Zn(BF_4)_2 \cdot 6H_2O$ crystals.

Measurements carried out at the helium temperature let us determine the signs of the spin Hamiltonian parameters, which are listed in the table together with the values of the parameters for the two temperatures.

3. PRESSURE DEPENDENCE OF THE Mn^{2+} EPR SPECTRUM

The EPR spectrum of the Mn^{2+} ion in $Zn(BF_4)_2 \cdot 6H_2O$ was studied at high hydrostatic pressures of up to 15 kbar at room temperature and up to 12 kbar at the nitrogen temperature. The EPR spectrum is well approximated by the spin Hamiltonian (1). The parameters characterizing the electronic Zeeman (g tensor) and the hyperfine interaction with the nucleus (A tensor) do not vary within experimental error with increasing pressure. The b_2^0 parameter characterizing the deviation from a cubic crystal field undergoes the largest variation. Figure 2 presents the pressure dependence of the b_2^0 parameter obtained at room and nitrogen temperatures. The b_2^0 parameter decreases with increasing pressure, this dependence being steeper at room temperature ($\Delta b_2^0/\Delta P = 7.9 \times 10^{-4}$ cm^{-1}/kbar) than at liquid nitrogen ($\Delta b_2^0/\Delta P = 4.3 \times 10^{-4}$ cm^{-1}/kbar). At 9 kbar, the pressure plots, corresponding to different temperatures, cross to produce a unique situation where the b_2^0 parameter is temperature independent at the given pressure. Below 9 kbar, an increase in temperature gives rise to an increase in the b_2^0 parameter, and above 9 kbar, to its decrease.

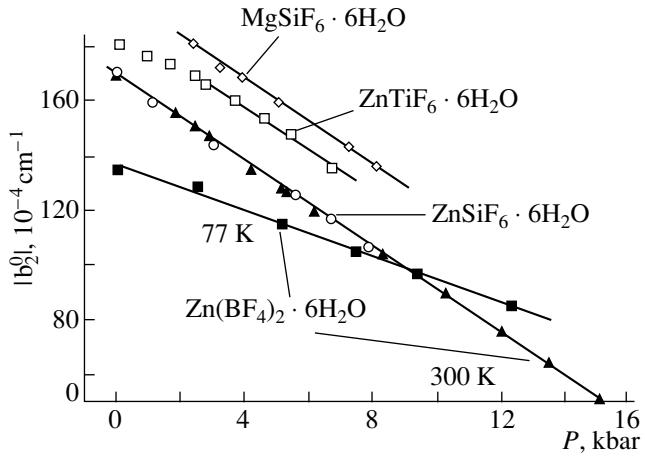

Fig. 2. Spin Hamiltonian parameter $|b_2^0|$ vs. pressure plot for various crystals.

The b_4^0 parameter, which characterizes the Mn^{2+} level splitting in a cubic crystal field, increases in absolute magnitude with increasing pressure at both room and nitrogen temperatures

$$b_4^0(293\ \text{K}) = -(2.6 + 0.055P) \times 10^{-4}\ \text{cm}^{-1}\ (P \text{ in kbar}),$$

$$b_4^0(77\ \text{K}) = -(3.1 + 0.051P) \times 10^{-4}\ \text{cm}^{-1},$$

which is close to the results obtained for zinc fluorosilicate [14].

A comparison of our data with the pressure dependences of the b_2^0 parameter in other crystals, $ZnSiF_6 \cdot 6H_2O$ [10], $ZnTiF_6 \cdot 6H_2O$ [15], and $MgSiF_6 \cdot 6H_2O$ [13] (Fig. 2) shows that the pressure coefficients for all these crystals practically coincide. This implies equal compressibilities of the water complexes in these crystals, despite the differences in the anions (SiF_6, TiF_6, BF_4) making up the second coordination shell, and in the space symmetry groups the crystals belong to, namely, $R\bar{3}$ for $ZnSiF_6 \cdot 6H_2O$ and $Pmn2_1$ for $Zn(BF_4)_2 \cdot 6H_2O$. The elastic properties are accounted for by the nearest environment of the divalent metal, i.e. the six H_2O molecules in our case, and by their coupling with the anion environment through the hydrogen bonds. According to the data obtained, this coupling is practically the same for all the above crystals.

4. EPR LINEWIDTH AND SHAPE

The measurements of the Mn^{2+} EPR linewidth and shape revealed two interesting features; namely, the line shape and width depend on the quantum number characterizing the transition, and the linewidth depends substantially on pressure. We will consider each of these two unusual properties in its own turn.

The low-field line belonging to the $\Delta M_s = \pm 1(-5/2, -3/2)$ and $\Delta m_I = 0(5/2, 5/2)$ transition has a width of 8 G and a Gaussian shape, whereas the high-field one, $\Delta M_s = \pm 1(5/2, 3/2)$ and $\Delta m_I = 0(5/2, 5/2)$, exhibits a clearly pronounced additional structure of two satel-

lites, higher and lower in field from the central line (Fig. 3). The width of each satellite is 4 G, and the absorption line can be approximated by three Lorentzians. Following from the measurements made on all thirty spectral lines, the satellite separation is proportional to the magnetic field in which each absorption line is observed. It is maximum for the last line ($B \approx$ 4.3 kG) and minimum for the first line ($B \approx 2.0$ kG), and in the first line, the satellites merge with the central peak.

The origin of the satellites can be explained by considering the extra terms of the spin Hamiltonian describing the ligand hyperfine structure. Each paramagnetic Mn^{2+} ion in $Zn(BF_4)_2 \cdot 6H_2O$ is surrounded by six water molecules, and each molecule contains two hydrogens; hence, the nearest environment of Mn^{2+} contains 12 protons with a magnetic moment ($I = 1/2$). The ligand hyperfine structure can be described by the following extra terms in the spin Hamiltonian

$$\sum_L \hat{S} A^L \hat{I}^L + \sum_L g_n \beta_n \mathbf{B} I^L, \qquad (2)$$

where $\hat{S}$ is the electronic spin operator, $\hat{I}^L$ is the ligand nuclear-spin operator, A^L is the ligand hyperfine interaction tensor, **B** is the magnetic-field induction vector, g_n is the proton spectroscopic splitting factor, and β_n is the Bohr magneton.

If we assume that all protons are equivalent and that the first term in Hamiltonian (2) dominant, one should observe 13 ligand structure lines with the following intensity ratios: 1:12 : 66 : 220 : 495 : 792 : 924 : 792 : 495 : 220 : 66 : 12 : 1. All the transitions preserve the nuclear quantum number $\Delta m_I = 0$. The spectrum observed experimentally is simpler: it has only two satellites. This becomes clear if one assumes the second term of the Hamiltonian (2), which describes the Zeeman interaction with the protons, to be considerably larger than the first one. This situation gives rise to the so-called flip-flop transitions, in which, besides the reversal of the electronic spin $\Delta M_s = \pm 1$, the nuclear spin also reverses, $\Delta m_I = \pm 1$. It is these transitions that produce the satellite lines shifted from the main transition H_0 by the amount corresponding to the Zeeman energy of the nuclear moment

$$B_\pm = B_0(1 \pm g_n \beta_n / g_e \beta_e),$$

where g_n and β_n are the g factor and the magneton for the nuclear moment, respectively, and g_e and β_e are the same quantities for the electronic moment. An increase in the magnetic field brings about an increase of the satellite splitting, which grows from the first to the last line of the Mn^{2+} ion spectrum. For the first line (2.0 kG), $\Delta B = 3$ G, and for the last one (4.3 kG), $\Delta B = 6.5$ G. A similar pattern was observed by us for the $ZnSiF_6 \cdot 6H_2O$ crystal, whereas deuterated $ZnSiF_6 \cdot 6D_2O$ did not produce any satellites at all, because the magnetic moment of deuterium is ~ three times smaller than that of the proton. The nature of these satellites was first explained in [16], which reported an observation of EPR spectra of irradiated acids. It should be pointed out that despite the large number of EPR studies of hydrated crystals, the absorption line structure we revealed was not mentioned anywhere.

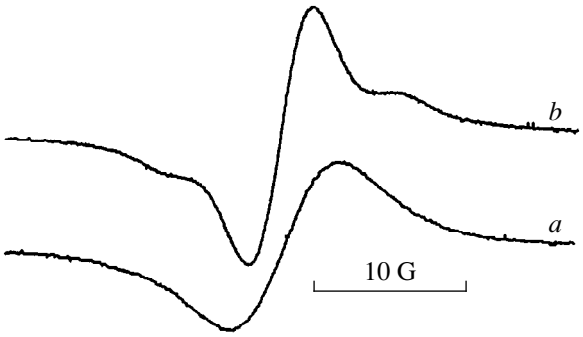

Fig. 3. Derivatives of the absorption lines in the Mn^{2+} EPR spectrum of $Zn(BF_4)_2 \cdot 6H_2O$: (a) low-field and (b) high-field lines.

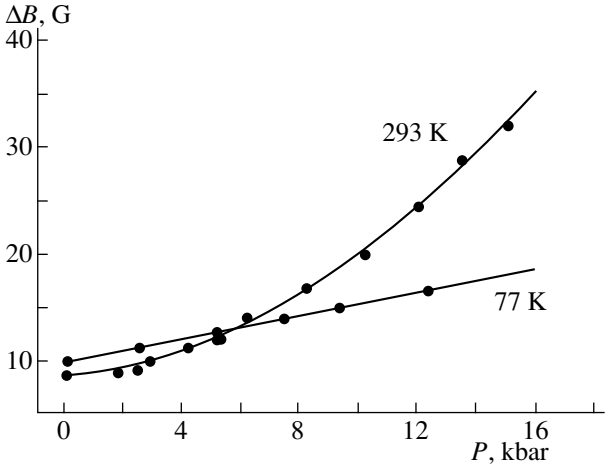

Fig. 4. Pressure dependence of the absorption linewidth measured at room (293 K) and nitrogen (77 K) temperatures.

An increase of pressure results in a broadening of the absorption line. The experimental data relate to the case of the external magnetic field being parallel to the c axis. The data presented in Fig. 4 relate to the low-field spectral line, with all the others behaving in a similar way. As seen from these data, the effect of pressure at $T = 293$ K is essentially nonlinear and can be approximated by a quadratic relation $\Delta B = 8.5 + 0.24P + 0.09P^2$ (B is in G, and P, in kbar). Also shown in Fig. 4 are data obtained at 77 K; at this temperature, the pres-

sure dependence of the linewidth is linear, $\Delta B = 9.8 + 0.54P$.

It should be noted that nothing like this has been observed in pressure studies of $ZnSiF_6 \cdot 6H_2O$ and $ZnTiF_6 \cdot 6H_2O$ and of other crystals. As a rule, nonlinear effects are not observed within the pressure range used here. We immediately stress that any deviation from the hydrostatic pressure pattern at the crystal must be ruled out, because, as mentioned in Section 1, the crystal is immersed in benzine, which solidifies above 20 kbar.

In our opinion, the reasons for this should be looked for in the internal structure of the crystal. As mentioned in Section 1, each spectral line is actually a sum of six lines coinciding in the **H** || *c* orientation. At normal pressure, the spectral axes deviate only slightly from the *c* direction, by ~1–2%, so that the lines of all six spectra are nearly at their extrema. In this direction, the scatter in the spin Hamiltonian parameters exerts the lowest effect on linewidth. If the angle between the *c* axis and the axis of the spectrum increases with increasing pressure, as is the case with the $ZnTiF_6 \cdot 6H_2O$ crystal [15], this will entail a line broadening, because the angular dependence of the absorption line is proportional to $(3\cos^2\vartheta - 1)$. It is also possible that internal stresses at twin boundaries increase with pressure. These conjectures cannot offer an exhaustive explanation for our observation, much less pinpoint the reason for the substantial difference between the relations obtained at different temperatures, but we hope to do this in our future studies by carrying out additional measurements of the absorption linewidth and shape.

Our results can be summed up as follows. Despite the different composition and symmetry of the $Zn(BF_4)_2 \cdot 6H_2O$, $ZnSiF_6 \cdot 6H_2O$, $MgSiF_6 \cdot 6H_2O$, and $ZnTiF_6 \cdot 6H_2O$ crystals, the compressibility of the $M^{2+}6H_2O$ complex they contain is the same, which implies equal bond lengths in these crystals.

It has been shown that the $Zn(BF_4)_2 \cdot 6H_2O$ crystal undergoes one second-order phase transition ($T_n = 196$ K) in the temperature range studied. At 9 kbar, the main spin-Hamiltonian parameter b_2^0 does not depend on temperature.

We have detected a ligand hyperfine structure associated with the Zeeman interaction among the protons surrounding the paramagnetic ion, and we have found the linewidth to depend quadratically on pressure.

ACKNOWLEDGMENTS

The authors are indebted to L. F. Chernysh and G. Ya. Samsonova for growing high-quality crystals, and to S. N. Lukin for determining the sign of the spin Hamiltonian b_2^0 parameter.

REFERENCES

1. C. D. West, Z. Kristallogr. **91**, 480 (1935).
2. K. C. Moss, D. S. Rassell, and D. W. A. Sharp, Acta Crystallogr. **14**, 330 (1961).
3. M. Ghosh and S. Ray, Z. Kristallogr. **145**, 146 (1977).
4. S. Ghosh, M. Mukherjee, A. Seal, and S. Ray, Acta Crystallogr. B **53**, 639 (1997).
5. A. K. Jain and M. Geoffroy, J. Phys. Chem. Solids **44**, 535 (1983).
6. E. D. Mauro and W. Sano, J. Phys. Chem. Solids **48**, 29 (1987).
7. W. Sano, S. Isotani, J. A. Ochi, and J. C. Sartorelli, J. Phys. Soc. Jpn. **46**, 26 (1979).
8. J. B. Domiciano, W. Sano, K. R. Juraitis, and S. Isotani, J. Phys. Soc. Jpn. **48**, 1449 (1980).
9. W. Sano, J. B. Domiciano, and J. A. Ochi, Phys. Rev. B **50**, 2958 (1994).
10. A. D. Prokhorov, Fiz. Tverd. Tela (St. Petersburg) **37**, 1362 (1995) [Phys. Solid State **37**, 740 (1995)].
11. M. B. Patel, Solid State Commun. **53**, 431 (1985).
12. M. L. Meĭl'man and M. I. Samoĭlovich, *Introduction to EPR Spectroscopy of Doped Crystals* (Atomizdat, Moscow, 1977).
13. G. N. Neĭlo and A. D. Prokhorov, Fiz. Tverd. Tela (St. Petersburg) **35**, 748 (1993) [Phys. Solid State **35**, 384 (1993)].
14. S. N. Lukin, Fiz. Tverd. Tela (St. Petersburg) **35**, 671 (1993) [Phys. Solid State **35**, 343 (1993)].
15. A. D. Prokhorov, Fiz. Tverd. Tela (St. Petersburg) **38**, 544 (1996) [Phys. Solid State **38**, 298 (1996)].
16. G. T. Trammel, H. Zeldes, and R. Livingstone, Phys. Rev. **110**, 630 (1958).

Translated by G. Skrebtsov

Physics of the Solid State, Vol. 42, No. 6, 2000, pp. 1139–1146. Translated from Fizika Tverdogo Tela, Vol. 42, No. 6, 2000, pp. 1105–1112.

LOW-DIMENSIONAL SYSTEMS AND SURFACE PHYSICS

Electron Transport in the Carbon–Copper Nanocluster Structure

L. V. Lutsev*, S. V. Yakovlev*, and V. I. Siklitskiĭ**

** Domen Research Institute, St. Petersburg, 196084 Russia*

*** Ioffe Physicotechnical Institute, Russian Academy of Sciences, Politekhnicheskaya ul. 26, St. Petersburg, 194021 Russia*

e-mail: siklitsky@pop.ioffe.rssi.ru

Received July 14, 1999; in final form, October 7, 1999

Abstract—The electron transport in hydrogenated amorphous carbon films *a*-C : H with copper nanocluster inclusions has been investigated. The conditions of cluster formation are derived. It is theoretically demonstrated that the energy band structure of the matrix substantially affects the conditions of cluster formation. The electron transport depends on the cluster structure. It is found that, below the percolation threshold (the case of isolated clusters), the transport current is governed by two components depending on the electric field strength. At low field strengths, the current is caused by electrons in the conduction band of amorphous carbon, which are thermally excited from copper clusters. At high field strengths, the transport current is provided by tunneling electrons from the Fermi level of copper clusters to the conduction band of *a*-C : H. The difference between the mobility edge of the conduction band of amorphous carbon and the Fermi level in copper clusters is determined from the temperature dependence of the resistance and proves to be equal to 0.48 eV. The temperature dependences of the resistance at low field strengths exhibit a fine structure. It is revealed that, above the percolation threshold, the electrical resistance of clusters is considerably contributed by the residual resistance, which is supposedly associated with the electron scattering by cluster surfaces. The temperature effect on the electron transport is examined using the spin-wave scattering technique at a frequency of 4.0 GHz. It is found that the spin wave in the yttrium iron garnet (YIG) film is predominantly affected by thermally excited electrons located above the mobility edge in the conduction band of *a*-C : H. © *2000 MAIK "Nauka/Interperiodica"*.

INTRODUCTION

The aim of the present work was to investigate the electron transport in the structure consisting of metallic clusters in an isolating matrix near the percolation threshold and to elucidate how the band structure of the matrix affects the transport processes. These investigations were carried out using hydrogenated amorphous carbon *a*-C : H with copper nanocluster inclusions. The *a*-C : H compound is an amorphous organic semiconductor whose band structure is determined and can change with the content of hydrogen in the sp^3 configurations [1]. The π valence band and the π^* conduction band in *a*-C : H are formed by π electrons and governed by the sp^2 bonds. The difference E_g (pseudogap) between the upper mobility edge of the π band and the lower mobility edge of the π^* band is equal to 1.5–4 eV depending on the hydrogen content. The elimination of hydrogen from *a*-C : H leads to an increase in the number of sp^2 configurations and a decrease in the pseudogap E_g. The possibility of varying the pseudogap renders the $(a\text{-C} : \text{H})_{1-x}\text{Cu}_x$ system convenient for revealing the main regularities in the influence of the band structure on the cluster formation and the electron transport.

The electrical properties of the $(a\text{-C} : \text{H})_{1-x}\text{Cu}_x$ system for small dc currents at room temperature were studied in [2]. It was noted that the current–voltage characteristic exhibits a linear behavior. The dependences obtained were interpreted within the classical percolation theory. The band structure of the matrix was not taken into account.

In Section 1, we consider the influence of the band structure and the Coulomb interaction on the formation of cluster structure from bulk metallic inclusions. The condition for the cluster formation is derived, and the applicability of the Fermi liquid model to metallic particles is assessed. The results of experimental investigations into the electrical properties of the $(a\text{-C} : \text{H})_{1-x}\text{Cu}_x$ system in the case of isolated clusters at low and high electric field strengths are described in Sections 2 and 3, respectively. The character of the conductivity depends on the field strength. At low field strengths, the current–voltage characteristic shows a linear behavior, and the current is determined by the electron scattering in the π^* conduction band of *a*-C : H. At high field strengths, the transport current is brought about by electron tunneling from the Fermi level of copper clusters to the π^* band of *a*-C : H. The electron transport in the cluster with sizes equal to the distance between the contacts is discussed in Section 4. The conductivity of the cluster exhibits a metallic behavior, the residual resistance being significant. In Section 5, we analyze the data on the influence of temperature on the electron

transport in the $(a\text{-C : H})_{1-x}Cu_x$ system at different x, which were obtained by the spin-wave scattering technique at a frequency of 4.0 GHz. It is shown that the thermally excited electrons located above the mobility edge in the π^* band of a-C : H make the main contribution to the spin wave in the yttrium iron garnet (YIG) film.

1. CONDITION FOR FORMATION OF CLUSTER STRUCTURE

In order to determine the conditions for the cluster structure formation, we consider electrons in a bulk metallic (copper) particle in the hydrogenated amorphous carbon matrix a-C : H (Fig. 1). The mean size of a copper particle is $l = 3$ nm [3]. The Fermi energy ε_F is defined by the relationship [4]

$$\varepsilon_F = \frac{h^2}{2m^*_{Cu}}\left(\frac{3n_{Cu}}{8\pi}\right)^{2/3}, \quad (1)$$

where m^*_{Cu} is the effective electron mass, and n_{Cu} is the electron concentration in the conduction band of copper. Taking into account that copper is univalent metal, the concentration of free electrons in it is equal to the concentration of atoms, that is,

$$n_{Cu} = \frac{\eta_{Cu}N_A}{M_{Cu}} = 0.849\times10^{23}\ \text{cm}^{-3}, \quad (2)$$

where $\eta_{Cu} = 8.96$ g/cm^3 is the density, N_A is the Avogadro number, and $M_{Cu} = 63.546$ g/mol is the atomic mass. By assuming that the effective mass of an electron m^*_{Cu} is equal to the mass of a free electron and using formulas (1) and (2), we obtain the Fermi energy $\varepsilon_F = 7.04$ eV.

Let us assess the applicability of the Fermi liquid model to the electrons in a copper particle. To accomplish this, we determine the discreteness of the energy spectrum $\Delta\varepsilon$, which is due to finite sizes of the potential well of a copper particle at $\varepsilon > \varepsilon_F$. The energy ε and the number of eigenvalues g_R in the unit layer of radius $R_n = (n_1^2 + n_2^2 + n_3^2)^{1/2}$ in the space of states are given by [4]

$$\varepsilon = \frac{h^2R_n^2}{8m^*_{Cu}l^2}, \quad g_R = \pi R_n^2. \quad (3)$$

After the differentiation of relationships (3), at $\Delta R_n = 1$, we have

$$\Delta\varepsilon = \frac{h^2R_n\Delta R_n}{4g_Rm^*_{Cu}l^2} = \frac{h^3}{8\pi m^{*3/2}_{Cu}(2\varepsilon)^{1/2}l^3}. \quad (4)$$

Near the Fermi level, $\Delta\varepsilon = 2.05$ meV. This value is considerably less than the Fermi energy ε_F, and $k_T = 25.8$ meV at $T = 300$ K, which, to a first approximation, justifies the applicability of the Fermi liquid model to the conduction electrons in a copper particle. According to the Fermi liquid model, the density of electronic states in a copper particle of volume $\nu^{(1)}$ is determined as [4]

$$g^{(1)}(\varepsilon) = \frac{8\pi m^{*3/2}_{Cu}\sqrt{2\varepsilon}\nu^{(1)}}{h^3}. \quad (5)$$

Now, we derive the condition for cluster formation. The formation of cluster structure essentially depends on the Coulomb interaction and, correspondingly, the capacitance of metallic particles forming the cluster. The capacitance of a spherical particle can be written as

$$C^{(1)} = 2\pi\varepsilon_0\varepsilon_{a\text{-C : H}}l,$$

where $\varepsilon_0 = 8.854\times10^{-12}$ F/m, and $\varepsilon_{a\text{-C : H}}$ is the permittivity of a-C : H. Since the capacitance $C^{(1)}$ is small, the escape of p electrons ($p < 0$) from the metallic particle or the appearance of p electrons ($p > 0$) in the particle can lead to a change in the band structure of the particle in the matrix (Fig. 1) and result in additional energy, that is,

$$V_c(\mathbf{r}) = \frac{V_p^{(1)}l}{2|\mathbf{r}|}, \quad (6)$$

where $V_p^{(1)} = pe^2/2C^{(1)}$, e is the electron charge, and $|\mathbf{r}| > l/2$ is the distance from the center of particle. Setting $\varepsilon_{a\text{-C : H}} = 2$, at $p = 1$, we obtain $V_p^{(1)} = 0.24$ eV.

Assume that fluctuations or current flow bring about the appearance of an electron in one of metallic particles. This frustrates the electroneutrality of the particle (Fig. 1) and results in a rise in the energy levels by $V_p^{(1)}$. If the probability of tunneling of one electron with the energy ε to the adjacent particle is designated as $w^{(1)}(\varepsilon)$,

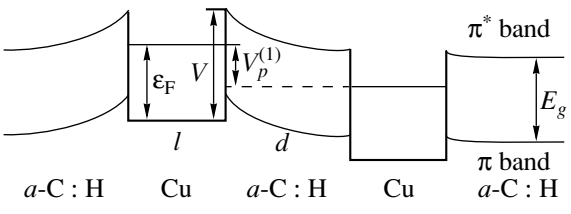

Fig. 1. Electronic band structure of a metallic particle in a-C : H.

the total probability of the tunneling with allowance made for relationship (5) is given by

$$W^{(1)} = \int_{\varepsilon_F - V_s^{(1)}(d)}^{\varepsilon_F} w^{(1)}(\varepsilon) g^{(1)}(\varepsilon) d\varepsilon,$$

where $V_s^{(1)}(d) = V_c(l/2) - V_c(d + l/2) = 2dV_p^{(1)}/2d + l$, and d is the distance between particles. If $W^{(1)} \geq 1$, this process brings about the delocalization of electron over two particles and the formation of a cluster composed of these particles. A further delocalization of the electron can result in the formation of a cluster consisting of q particles. To determine the condition for formation of the cluster consisting of q particles (hereafter, it will be referred to as the q cluster), we introduce the following designations: $C^{(q)}$ is the capacitance of the q cluster, $V^{(q)}$ is the volume of metallic particles in the q cluster, $g^{(q)}(\varepsilon) = g^{(1)}(\varepsilon)V^{(q)}/V^{(1)}$ is the density of electronic states per energy interval, $V_p^{(q)} = pe^2/2C^{(q)}$ is the Coulomb energy of the q cluster with p electrons, and $w^{(q)}(\varepsilon)$ is the probability of tunneling of one electron with the energy ε from the q cluster to the adjacent isolated metallic particle.

Then, the condition for the formation of the q cluster in an equilibrium state can be written as

$$W^{(q)} = \int_{\varepsilon_F - V_s^{(q)}(d)}^{\varepsilon_F} w^{(q)}(\varepsilon) g^{(q)}(\varepsilon) d\varepsilon \geq 1, \quad W^{(q+1)} < 1, \tag{7}$$

where $V_s^{(q)}(d) = 2dV_p^{(q)}/(2d + l)$.

If the matrix has no localized states lying below the bottom of the conduction band, then $w^{(q)}(\varepsilon)$, to a first approximation, can be represented as [5]

$$w^{(q)}(\varepsilon) = \exp\left\{-\frac{2}{\hbar}\int_0^d \left[2m^*_{\text{matrix}}\left(V - \frac{2r}{2r + l}V_p^{(q)} - \varepsilon\right)\right]^{1/2} dr\right\}.$$

In the amorphous semiconducting matrix, the Anderson localized states lying below the mobility edge of the conduction band play an important part [6, 7]. They can lead to a considerable increase in $w^{(q)}(\varepsilon)$ and, as a consequence, to an increase in the number of particles q forming the cluster. According to the estimates made for $(a\text{-C : H})_{1-x}Cu_x$ at $x = 0.16$, q is equal to several tens. The population of the Anderson localized states depends on the temperature. Hence, the second consequence of the presence of these states is the change in $w^{(q)}(\varepsilon)$ and the rearrangement of cluster structure with a variation in the temperature.

The formation of the cluster structure satisfying condition (7) causes the necessity of correcting certain statements of the classical percolation theory [7], which should be taken into account in the study of films containing metallic inclusions [8].

(1) The band structure of the matrix substantially affects the cluster formation by changing the probability of tunneling $w^{(q)}(\varepsilon)$.

(2) According to condition (7), the cluster size is limited. Therefore, the percolation threshold x_{perc} depends not only on the concentration x of metallic particles in the matrix, but also on the ratio between the cluster size and the distance between the contacts of the studied sample. For films, this can lead to the anisotropy of electrical properties: the percolation threshold along the film can be considerably larger than the percolation threshold across the thickness.

(3) Condition (7) is valid for the initial cluster structure without field but can be violated at high strengths of the applied electric field. This gives rise to a new cluster structure. It is experimentally found that the isolated cluster structure of $(a\text{-C : H})_{1-x}Cu_x$ at $x = 0.16$ transforms into the conducting structure at voltages $U > 20$ V (see Section 3).

The existence of the cluster structure is indirectly confirmed in the experiments by the data of small-angle X-ray scattering in $(a\text{-C : H})_{1-x}Cu_x$ [3]. A change in the structure of scattering objects is observed beginning with $x = 0.14$. These objects begin to acquire the fractal properties and, to a first approximation, can be considered fractal clusters [9]. There appears a "snowball"-type scattering object with a large fractal dimension ($D = 2.3$).

2. ELECTRON TRANSPORT IN THE CASE OF ISOLATED COPPER CLUSTERS AT LOW ELECTRIC FIELD STRENGTHS

At low electric field strengths, the electric conductivity is determined by carriers in the conduction band of amorphous carbon. As the concentration of carriers depends on the temperature, we measured the temperature dependences of the current–voltage characteristics. This enabled us to determine the difference $V - \varepsilon_F$ and the concentration of carriers.

The $(a\text{-C : H})_{1-x}Cu_x$ amorphous carbon film with copper clusters to be studied was prepared on a quartz substrate by the magnetron sputtering technique. The film thickness was 1.73 μm. The content of copper inclusions x was equal to 16 at. %. Contacts were evaporated onto the quartz substrate and onto the film. The structure of the $(a\text{-C : H})_{1-x}Cu_x$ film with the above copper content x, thickness, and geometry of contacts turned out to be close to the percolation threshold. We chose such a contact in which the conductivity of the film was below the percolation threshold (the case of isolated clusters). Figure 2 demonstrates the current–voltage characteristic at low voltages. At $U < 2V$, this

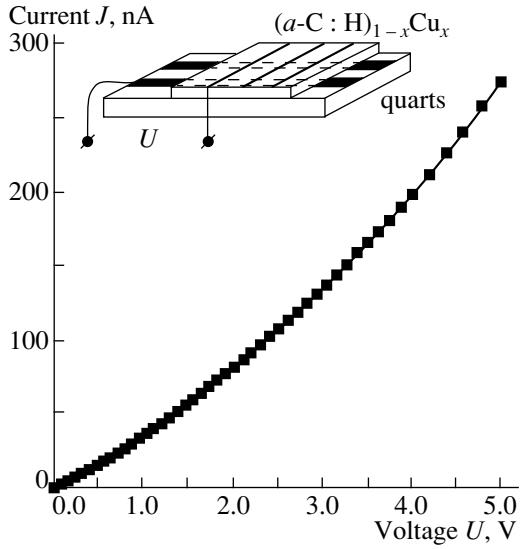

Fig. 2. Initial portion of the current–voltage characteristic for the $((a\text{-C : H})_{1-x}Cu_x$ film at $x = 0.16$ (isolated clusters).

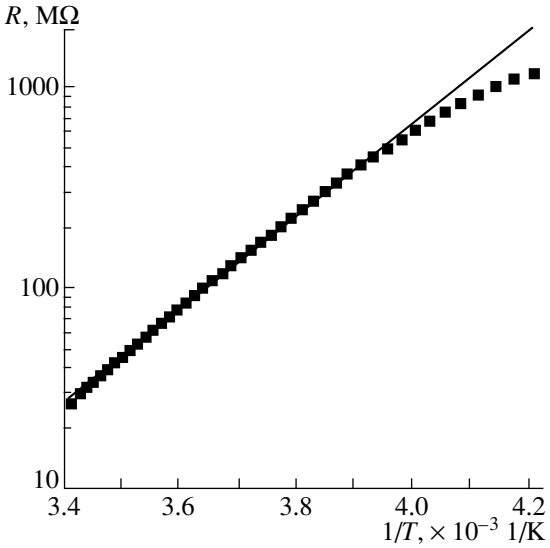

Fig. 3. Temperature dependence of the resistance for the $(a\text{-C : H})_{1-x}Cu_x$ film at $x = 0.16$ (isolated clusters).

characteristic is close to a linear dependence. The dependence of the logarithm of the resistance $\ln R$ on the reciprocal of temperature $1/T$ in the temperature range 230–293 K is depicted in Fig. 3. The applied voltage U is equal to 0.1 V. At $T < T_K = 248$ K ($1/T_K = 4 \times 10^{-3}$ K^{-1}), $\ln R$ linearly depends on $1/T$. At $T < T_K$, the tunneling effects begin to play a significant role. In order to interpret these temperature dependences, it is necessary to take into account the following factors: (1) near the percolation threshold, $q \gg 1$ and $V_1^{(q)} \longrightarrow 0$ for the q cluster; and (2) at $\varepsilon = V$, the Fermi distribution

$$f(\varepsilon) = \frac{1}{\exp[(\varepsilon - \varepsilon_F)/kT] + 1} \tag{8}$$

is well approximated by the Boltzmann distribution $\exp[-(V - \varepsilon_F)/kT]$. This makes it possible to determine the difference between the barrier height and the Fermi energy from two points in the linear portion of the temperature dependence

$$V - \varepsilon_F = \frac{k(\ln R_1 - \ln R_2)}{T_1^{-1} - T_2^{-1}} = 0.48 \text{ eV}. \tag{9}$$

The concentration of carriers in the conduction band of amorphous carbon at $T = 293$ K is as follows:

$$n_C = n_{Cu}\exp[-(V - \varepsilon_F)/kT] = 5.51 \times 10^{14} \text{ cm}^{-3}. \tag{10}$$

Figure 4 shows the fine structure of the temperature dependence of the relative resistance dR/RdT. One can see the quasi-periodicity with the period $\Delta T = 5.8$ K. The fine structure can be caused by one of two factors.

(1) The discreteness of levels in the energy spectrum of the potential well for the isolated metallic particle at $\varepsilon \sim V$. The electrons propagating in the conduction band of a-C : H can scatter by the potential wells of isolated particles. The resistance R is directly proportional to the effective cross-section $\sigma(\varepsilon)$ for scattering of electron by the well [10] and also to the number of electrons in the π^* conduction band of a-C : H

$$R \sim \sum_{i=1}^{N_n} \int_V^\infty f(\varepsilon)\sigma_i(\varepsilon)g_i^{(1)}(\varepsilon)d\varepsilon, \tag{11}$$

where $g_i^{(1)}(\varepsilon)$ is defined by formula (5), and N_n is the number of scattering centers. If the well has the discrete

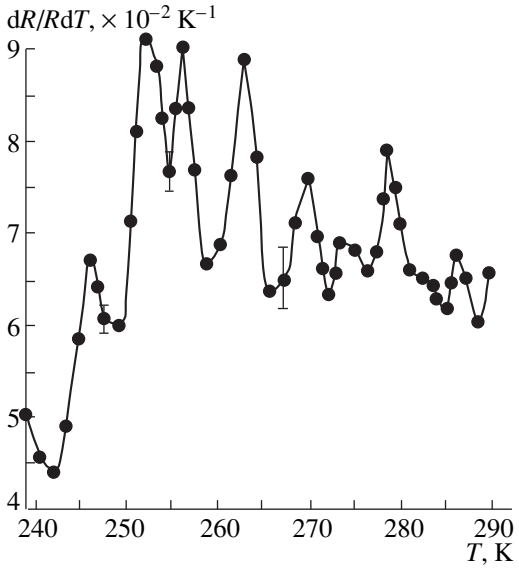

Fig. 4. Fine structure of the temperature dependence of the resistance for the $(a\text{-C : H})_{1-x}Cu_x$ film at $x = 0.16$.

levels at $\varepsilon \sim V$, the cross-section $\sigma(\varepsilon)$ shows the energy dependence due to these levels. The resonant scattering takes place at $\varepsilon \sim V$ [11]. Taking into account relationship (8), integral (11) involves the component quasi-periodic in T. From formula (4), at $\varepsilon = V$, we can estimate the period of the fine structure

$$\Delta T = \frac{\Delta\varepsilon}{kN_n}.$$

Since the scattering occurs in the regions between clusters near the percolation threshold, the number of scattering centers (isolated particles) cannot be very large. At $N_n = 4$, we have $\Delta T = 5.6$ K.

(2) The rearrangement of cluster structure. A change in the temperature results in a change in the population of the Anderson localized states lying below the mobility edge of the π^* band of a-C : H. This leads to a change of $w^{(q)}(\varepsilon)$ in condition (7) for cluster formation and, as a consequence, to a change in their relative positions and the resistance R.

The unique choice of the model for explaining the temperature oscillations calls for further investigations.

3. HIGH ELECTRIC FIELD STRENGTHS: TUNNELING EFFECTS

The tunneling mechanism of conductivity manifests itself at high electric field strengths E (Fig. 5). The tunneling current J is proportional to [5]

$$J \sim \int_0^{V+V_p^{(q)}} \{D(\varepsilon) f(\varepsilon)[1 - f'(\varepsilon)]g^{(q)}(\varepsilon) - D'(\varepsilon) f'(\varepsilon)[1 - f(\varepsilon)]g^{(q')}(\varepsilon)\} d\varepsilon, \quad (12)$$

where $D(\varepsilon)$ and $D'(\varepsilon)$ are the coefficients of tunneling through the potential barrier from the q cluster to the q' cluster and back; $g^{(q)}(\varepsilon)$ and $g^{(q')}(\varepsilon)$ are the corresponding densities of quantum states; and $f(\varepsilon)$ and $f'(\varepsilon)$ are the Fermi distributions in the q cluster and in the region where the electron tunnels. The highest field strength E between two isolated clusters arises in the region with the thinnest isolating gap. The resistance of the clusters themselves is considerably less than the resistance of the isolating region and can be ignored. Let $L = \sum_{i=1}^{s} d_i$ be the least thickness of all the isolating regions between clusters minus the sizes of metallic particles, which are located in the thinnest isolating intercluster region and do not enter into the cluster structure (Fig. 5). Then $E = U/L$, where U is the voltage across the contacts. If $eUd_1/L > V - \varepsilon_F$ (where d_1 is the distance between the cluster and the nearest isolated particle), then

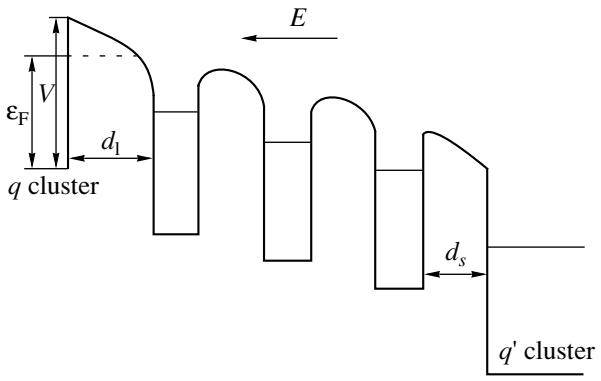

Fig. 5. Band structure illustrating the tunneling between clusters at high strengths of the applied electric field.

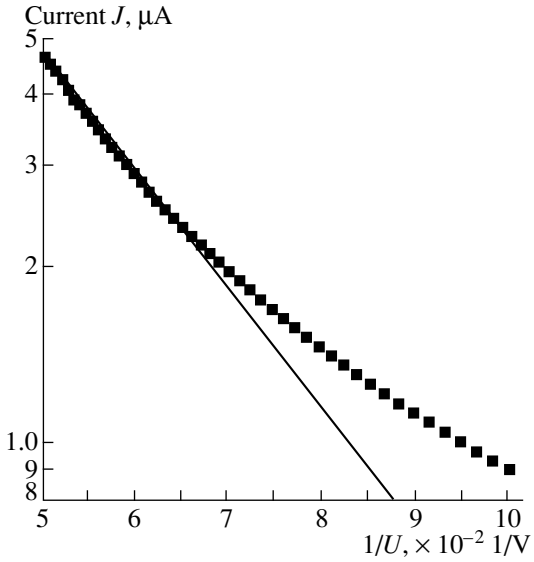

Fig. 6. Current–voltage characteristic for the $(a\text{-C} : \text{H})_{1-x}\text{Cu}_x$ film with $x = 0.16$ (isolated clusters) at high voltages.

(1) to a first approximation, ignoring the Anderson localized states [5],

$$D(\varepsilon) = D'(\varepsilon) = \exp\left[-\frac{4\sqrt{2m^*_{a\text{-C}:\text{H}}}}{3\hbar eE}(V - \varepsilon_F)^{3/2}\right];$$

(2) $f'(\varepsilon) \ll 1$ in the π^* band of a-C : H, and

(3) the electrons occupying the Fermi level of the q cluster make the main contribution to the tunneling.

In this case, from relationship (12), we obtain the approximate dependence of the tunneling current

$$J \sim \exp\left[-\frac{4L\sqrt{2m^*_{a\text{-C}:\text{H}}}}{3\hbar eU}(V - \varepsilon_F)^{3/2}\right]. \quad (13)$$

With allowance made for the Anderson localized states, the character of the dependence $J(U)$ remains

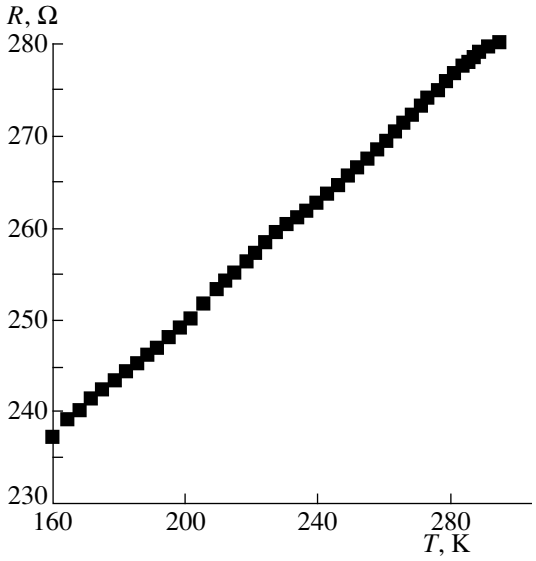

Fig. 7. Temperature dependence of the resistance for a conducting cluster in the $(a\text{-C : H})_{1-x}Cu_x$ film at $x = 0.16$.

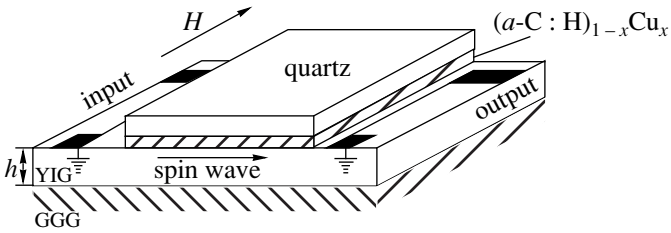

Fig. 8. Schematic representation of the measuring cell for studying the conductivity of a $(a\text{-C : H})_{1-x}Cu_x$ layer by the spin-wave scattering technique.

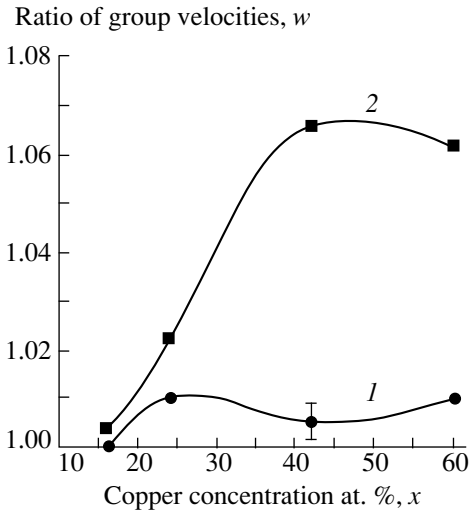

Fig. 9. Ratio of the group velocity of spin wave in the YIG film with a $(a\text{-C : H})_{1-x}Cu_x$ layer to the group velocity without $(a\text{-C : H})_{1-x}Cu_x$ layer as a function of the copper content x at temperatures of (*1*) 77 and (*2*) 293 K.

unchanged: $J \sim \exp[-\text{const}/U]$ [6, 8]. For comparison of relationship (13) with the experimental data, the dependence of $\ln J$ on U^{-1} at $U > 10$ V is constructed in Fig. 6. It can be seen that, at high voltages U, the dependence becomes close to linear. By ignoring the localized states, we can evaluate the tunneling distance L from two points of the linear dependence, when $m^*_{a\text{-C : H}}$ is equal to the mass of free electron, that is,

$$L = \frac{3\hbar e(\ln J_1 - \ln J_2)}{4\sqrt{2m^*_{a\text{-C : H}}}(V-\varepsilon_F)^{3/2}(U_2^{-1} - U_1^{-1})} = 24 \text{ nm}.$$

The rearrangement of the cluster structure is observed at $U > 20$ V. A group of isolated clusters transforms into one conducting cluster. This is attended by a decrease in the resistance across the contacts by five orders of magnitude. After a lapse of time, the conducting cluster relaxes to the initial state of isolated clusters.

4. ELECTRON TRANSPORT IN CONDUCTING CLUSTER

Figure 7 displays the temperature dependence of the resistance for the $(a\text{-C : H})_{1-x}Cu_x$ film at $x = 0.16$ in the case when one conducting cluster occurs between the contacts. As can be seen, the temperature dependence shows a metallic behavior. Hence, in order to interpret the experimental results, we invoke the basic statements of the theory of metals [12, 13]. The resistance R in metals is determined by the scattering of electrons at the Fermi level, primarily, by thermal acoustic phonons, impurities, boundaries, and defects. At $T \gg 0.1T_D$ (where T_D is the Debye temperature; for copper, $T_D = 347$ K), the temperature dependence of the resistance R_{ph} due to the scattering by acoustic phonons is linear ($\sim T$). The scattering by impurities, defects, and boundaries is temperature-independent and determines the residual resistance R_{res}

$$R = R_{ph} + R_{res}.$$

It is seen from the temperature dependence in Fig. 7 that the ratio between R_{res} and R_{ph} is sufficiently large

$$u = R_{res}/R_{ph}(0°\text{C}) = 185.6\ \Omega/88.5\ \Omega. \qquad (14)$$

The resistivity ρ is inversely proportional to the electron mean free path λ [12, 13]

$$\rho = \frac{m^*_{Cu}\nu_F}{n_{Cu}e^2\lambda}, \qquad (15)$$

where $\nu_F = (2\varepsilon_F/m^*_{Cu})^{1/2} = 1.57 \times 10^6$ m/s is the electron velocity on the Fermi surface. With the knowledge of the resistivity of pure copper $\rho_{ph} = 1.55 \times 10^{-6}\ \Omega$ cm ($T = 0°$C) [14], which is associated with the scattering by thermal acoustic phonons, and using relationships

(15) and (16), we can estimate the free path λ_{res} related to R_{res}

$$\lambda_{res} = \frac{m^*_{Cu}v_F}{n_{Cu}e^2\rho_{res}} = \frac{m^*_{Cu}v_F}{n_{Cu}e^2\rho_{ph}(0°C)^u} = 20 \text{ nm}.$$

The very low value of λ_{res} is likely explained by the fact that the scattering by the cluster surface considerably contributes to the electron scattering.

5. SPIN-WAVE SCATTERING

The electron transport in the ac electromagnetic field depends on the frequency ω of the applied field, the electronic structure, the concentration of carriers, and the presence of obstacles to free motion of electrons. According to formulas (2) and (10), $n_C \ll n_{Cu}$ in *a*-C : H amorphous carbon containing the copper clusters. In the copper clusters, the electron at the Fermi level make the main contribution to the interaction with the electromagnetic field. The boundaries of metallic particles constituting the cluster are the main obstacles to the free motion of electrons. In *a*-C : H, the thermally activated electrons of the π^* band interact with the electromagnetic field. By neglecting the scattering by clusters and defects, there are no barriers to motion of electrons in *a*-C : H.

The standard model of interaction between the electromagnetic field and free carriers in metals is applicable in the case when, during the period of ac electromagnetic field, the electron occupying the Fermi level in the copper clusters travels a distance of less than the size *l* of metallic particle [15, 16]. The constraints on the electron motion begin to manifest themselves at frequencies $\omega < \bar{\omega}$, where

$$\bar{\omega} = \frac{2\pi v_F}{l}, \quad \left(\bar{\lambda} = \frac{2\pi c}{\bar{\omega}} = 0.57 \text{ μm at } l = 3 \text{ nm}\right).$$

The total reflection of electromagnetic wave is observed in the frequency range $[\bar{\omega}, \omega_{pl}^{(Cu)}]$ [where $\omega_{pl}^{(Cu)}$ is the plasma frequency of copper]. At the frequencies $\omega < \bar{\omega}$, the transparency increases and the reflectivity of electromagnetic wave decreases. As the frequency of the electromagnetic field decreases, electrons in the conduction band of amorphous carbon begin to play a decisive part due to the constraints on the electron motion in clusters. The second plasma frequency is also associated with these electrons [15, 16]

$$\omega_{pl}^{(a\text{-C : H})} = \left(\frac{e^2 n_C}{\varepsilon_0 m^*_{a\text{-C : H}}}\right)^{1/2}.$$

Under the assumption that $m^*_{a\text{-C : H}}$ is equal to the mass of a free electron, at room temperature, we have $\omega_{pl}^{(a\text{-C : H})}/2\pi = 210$ GHz. At the frequencies $\omega < \omega_{pl}^{(a\text{-C : H})}$, the reflection of electromagnetic wave, depending on the temperature, can be determined by both electrons of copper clusters and the electrons in the π^* conduction band of amorphous carbon.

In order to determine the contributions from electrons of the cluster and carbon to the reflection, we examined the influence of the $(a\text{-C : H})_{1-x}Cu_x$ conducting layer on the group velocity of spin wave as a function of the copper percentage *x* in the carbon matrix. To put it differently, we investigated the elastic scattering of the spin wave by plasmons of electrons in the cluster and carbon. The measuring cell is schematically shown in Fig. 8. The $Y_3Fe_5O_{12}$ YIG film on the $Gd_3Ga_5O_{12}$ gadolinium gallium garnet (GGG) substrate had the thickness $h = 14$ μm. The surface spin wave was excited in the YIG film by a transmitting antenna. The thicknesses of receiving and transmitting antennas were equal to 50 μm. The distance between the antennas was 7.8 mm. The $(a\text{-C : H})_{1-x}Cu_x$ film was placed onto the surface of the YIG film from above. The thicknesses of the $(a\text{-C : H})_{1-x}Cu_x$ films were equal to 50 nm. The measurements were performed at a frequency of 4.0 GHz at temperatures of 77 and 293 K. The tangential magnetic field *H* was equal to 787 Oe at 293 K and 644 Oe at 77 K. The ac magnetic field of the spin wave excited the ac electric field in the $(a\text{-C : H})_{1-x}Cu_x$ conducting layer. A change in the conductivity of the layer led to a change in the spin wave spectrum (the amplitude–frequency characteristic). The group velocity of spin wave was determined from the spin wave spectrum. The ratios of the group velocity of spin wave in the YIG film with a $(a\text{-C : H})_{1-x}Cu_x$ layer to the group velocity without $(a\text{-C : H})_{1-x}Cu_x$ layer $w = v_g/v_{g(YIG)}$ as a function of the copper concentration *x* at temperatures of 77 and 293 K are displayed in Fig. 9. To a first approximation, the group velocity of spin wave is directly proportional to the conductivity of the $(a\text{-C : H})_{1-x}Cu_x$ layer.

The dependences obtained allow us to make the following conclusions.

(1) The contribution from electrons in the π^* conduction band of carbon to the elastic scattering of spin wave at a temperature of 293 K is sufficiently large in comparison with the contribution from the cluster electrons. At 77 K, the electrons in carbon are almost completely frozen, and the scattering is governed by electrons in the clusters. The electric conductivity between the clusters can result in a partial removal of obstacles to the electron motion and an increase in the contribution from the cluster electrons to the scattering of spin wave.

(2) Within the limits of experimental error, the data of the spin-wave scattering measurements indicate that the clusters and free electrons are absent in the conduction band of carbon when the copper percentage *x* is less than 14%. This is explained by the fact that the distances between metallic particles increase at small *x*, which leads to the violation of condition (7) for cluster formation. If the particles are not joined into the cluster,

then, for an isolated particle, the Coulomb term $V_p^{(1)}$ with $p < 0$ [formula (6)] should be added to the activation energy of electron $V - \varepsilon_F$ [formula (9)]. The presence of the $V_p^{(1)}$ term results in a drastic decrease in the concentration of electrons in the π^* band of *a*-C : H. For the cluster, a similar term $V_p^{(q)} \longrightarrow 0$ at $q \gg 1$.

(3) An increase in the carbon conductivity with an increase in the copper content from 16 to 42% in the carbon matrix and a further stabilization of the conductivity suggest that the free electrons in the π^* band of *a*-C : H are located near metallic particles of clusters. The thickness of the electron cloud near particles is comparable in the order of magnitude to the sizes of metallic inclusions. The form of the Coulomb energy $V_c(\mathbf{r})$ [formula (6), Fig. 1] and the Anderson localized states in the π^* band favor the localization of electrons in the neighborhoods of cluster particles.

The results of the investigations performed can be summarized as follows.

(1) The electron transport in the $(a\text{-C} : \text{H})_{1-x}\text{Cu}_x$ system essentially depends on the cluster structure. The condition of its formation is governed by the energy band structure of the matrix and the Coulomb interaction between metallic particles.

(2) The free electrons of the π^* conduction band of carbon are located in the neighborhoods of metallic particles forming the cluster.

(3) At low applied dc voltages, the electron transport is determined by the motion of carriers in the π^* conduction band of *a*-C : H.

(4) The fine structure revealed in the temperature dependence of the dc resistance near the percolation threshold can be brought about by the size quantization in metallic particles or the rearrangement of the cluster structure.

(5) At high applied dc voltages, the electron transport occurs through the tunneling mechanism. At voltages higher than the threshold voltage, the structure consisting of isolated clusters transforms into one conducting cluster. The relaxation to the initial state is also observed.

(6) Above the percolation threshold, the conductivity exhibits a metallic character, the residual resistance being significant. This large residual resistance can be due to the scattering of electrons by the surfaces of a conducting cluster.

ACKNOWLEDGMENTS

We are grateful to T.K. Zvonareva for preparing experimental samples and to V.I. Ivanov-Omskiĭ, T.A. Polanskaya, and L.V. Sharonova for helpful discussions and remarks.

This work was supported by the Russian Foundation for Basic Research (project no. 99-02-17071a). V.I. Siklitskiĭ acknowledges the support of the Russian Research Program "Fullerenes and Atomic Clusters" (grant "Film-2"), the Russian Foundation for Basic Research (project no. 98-07-90336), and the International Scientific and Technical Program "Physics of Solid-State Nanostructures."

REFERENCES

1. J. Robertson, Adv. Phys. **35** (4), 317 (1986).
2. V. I. Ivanov-Omskiĭ, A. B. Lodygin, and S. G. Yastrebov, Fiz. Tverd. Tela (S.-Peterburg) **37** (6), 1693 (1995) [Phys. Solid State **37** (6), 920 (1995)]; V. I. Siklitsky, S. G. Yastrebov, and A. B. Lodygin, Chaos, Solitons and Fractals **10** (12), 2067 (1999).
3. V. I. Ivanov-Omskiĭ, V. I. Siklitskiĭ, and S. G. Yastrebov, Fiz. Tverd. Tela (S.-Peterburg) **40** (3), 568 (1998) [Phys. Solid State **40** (3), 524 (1998)].
4. A. I. Ansel'm, *Fundamentals of Statistical Physics and Thermodynamics* (Nauka, Moscow, 1973).
5. A. S. Davydov, *Quantum Mechanics* (Nauka, Moscow, 1973).
6. N. F. Mott and E. A. Davis, *Electronic Processes in Non-Crystalline Materials* (Clarendon Press, Oxford, 1979; Mir, Moscow, 1982).
7. B. I. Shklovskiĭ and A. L. Efros, *Electronic Properties of Doped Semiconductors* (Nauka, Moscow, 1979; Springer-Verlag, New York, 1984).
8. B. Abeles, Ping Sheng, M. D. Coutts, and Y. Arie, Adv. Phys. **24** (3), 407 (1975).
9. B. M. Smirnov, *Physics of Fractal Clusters* (Nauka, Moscow, 1991).
10. P. S. Kireev, *Physics of Semiconductors* (Vysshaya Shkola, Moscow, 1975).
11. L. D. Landau and E. M. Lifshitz, *Quantum Mechanics: Non-Relativistic Theory* (Nauka, Moscow, 1974, 3rd ed.; Pergamon Press, Oxford, 1977, 3rd ed.).
12. E. M. Lifshitz and L. P. Pitaevskiĭ, *Physical Kinetics* (Nauka, Moscow, 1979; Pergamon Press, Oxford, 1981).
13. A. A. Abrikosov, *Fundamentals of the Theory of Metals* (Nauka, Moscow, 1987; North-Holland, Amsterdam, 1988).
14. *Physical Quantities*, Ed. by I. S. Grigor'ev and E. Z. Meĭlikhov (Énergoatomizdat, Moscow, 1991).
15. A. S. Davydov, *Theory of the Solid State* (Nauka, Moscow, 1976).
16. P. M. Platzman and P. A. Wolff, *Wave and Interactions in Solid State Plasmas*, Suppl. 13 (Academic Press, New York, 1973), translated under the title *Volny i vzaimodeĭstvie v plazme tverdogo tela* (Mir, Moscow, 1975).

Translated by O. Borovik-Romanova

Physics of the Solid State, Vol. 42, No. 6, 2000, pp. 1147–1153. Translated from Fizika Tverdogo Tela, Vol. 42, No. 6, 2000, pp. 1113–1119.

LOW-DIMENSIONAL SYSTEMS AND SURFACE PHYSICS

Microscale Deformations in a Two-Dimensional Lattice: Structural Transitions and Bifurcations at Critical Shear

É. L. Aéro

Institute of Problems in Machine Science, Russian Academy of Sciences, Vasil'evskiĭ ostrov, Bol'shoi pr. 61, St. Petersburg, 199178 Russia

Received July 14, 1999; in final form, November 11, 1999

Abstract—A two-dimensional model of a crystal lattice with an essentially nonlinear interaction between atoms for arbitrary mutual displacements under shear conditions is considered. The energy of deformation contains a periodic term and gradient terms. The equilibrium equation in the sine-Helmholtz form (with two characteristic coherence lengths) is solved exactly. It is shown that a large uniform shear deformation is unstable and is accompanied by periodic modulations emerging in the plane of the layer and leading to nonuniform extensions and compressions of atomic chains, i.e., to a change in the long-range order. The chain slip by a lattice half-period or a larger value changes the long-range order as well. The obtained relations connecting the unit cell size and the amplitude of the displacement field determine the conditions for the existence of a modulated structure. A bifurcation transition from a purely elastic deformation of the lattice to its elastoplastic deformation, as well as a transition to its disordered (amorphous-type) state, is observed. © *2000 MAIK "Nauka/Interperiodica".*

Some of the results of the theory were described in the brief communication [1]. This work not only provides a substantiation of these results, but also reveals the physical meaning of the structural transitions and bifurcation points.

In the theory of deformation of rigid bodies, including crystalline objects, the condition of conservation of the local topology in the process of structural transformation is postulated. According to this condition, the closest neighbors (within a small neighborhood of a material particle) remain the same, and force couplings between particles do not commute. Only the resistance offered by the body to a change in the distance between small, but macroscopic, volumes is taken into consideration. However, in actual practice, the long-and short-range translational orders in the crystal also change. These changes can be taken into account by introducing structural factors. To a certain extent, this was done long ago by M. Born and K. H. Huang in their famous works devoted to analyzing optical vibrational branches (true, only in the linear approximation). Microscopic displacements u of neighboring atoms relative to one another were presented as half-differences of the displacements of the sublattices. Macrodisplacements U responsible for acoustic vibrations corresponded to half-sums of the displacements. The analysis was confined to small displacements and purely dynamic effects.

In order to develop a more general theory, we take into account both the continual forces and the structural forces. The latter tend to preserve the periodic translational order in conformity with the internal structure of the body, while continual forces tend to violate this order. The structural degrees of freedom correspond to the lattice term in the elastic potential, which is a periodic function of microsidplacements u, while continual degrees of freedom correspond to the term that is a quadratic function of their gradients. The latter should be distinguished from the macropotential U of the acoustic field, which will not be analyzed here. It obeys the equations in the theory of elastic continuum, which are beyond the scope of the present paper. The equilibrium between the two factors is possible only in the limit of certain spatial scales intermediate between atomic and macroscopic scales. Therefore, we will deal with the theory considering mesoscopic modes in the motion of the atomic lattice.

Avoiding here the construction of a general theory of microdeformations (to be more precise, mesodeformations), we confine our analysis to the simplest version. We consider the static shear deformation along the y axis of a two-dimensional square lattice with a period b and nonlinear forces of interaction between atoms. The energy E of a region of a layer of thickness H and length $2B$ is taken in the form

$$E = \int_0^H \int_0^B [(1/2)k_1(\partial u/\partial x)^2 + (1/2)k_2(\partial u/\partial y)^2 + p(1-\cos u)]dxdy. \quad (1)$$

Here, u is the mutual microdisplacement of chains (in the units of b) along the layer (y axis), k_1 is the shear micromodulus, k_2 is the micromodulus of longitudinal extension of the lattice, and p is the amplitude of the periodic potential of particle interaction, as well as the

1063-7834/00/4206-1147$20.00

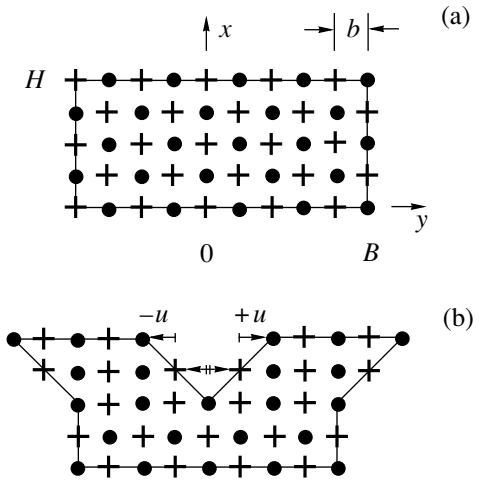

Fig. 1. Arrangement of atoms in a square lattice in the initial state (a) and after uniform twinning deformation ($u = \pm 2\pi$) (b). Crosses and circles distinguish the sublattices, demonstrating the effect of commutation of bonds.

amplitude (maximum value) of the adhesive force. Strictly speaking, micromoduli differ from the corresponding moduli in the macroscopic theory of elasticity.

The third term in (1) corresponds to the energy of uniform shear of rigid monolayers (chains), while the first two terms take into account their compliance or the elasticity of the two-dimensional lattice in the shear or extension along the *y* axis. In the case of rigid monolayers, the simple condition that the field of microdisplacement is constant indicates not a rigid displacement of the lattice as a hole, but its uniform shear microdeformation, which is essentially equal to the relative (in the *b* units) value of microdisplacement *u*. In the case of a rigid microscopic shear of adjacent chains by an atomic spacing, we obtain a uniform twinning deformation (Fig. 1).

The equilibrium equation corresponding to the minimum of functional (1) has the form

$$k_1(\partial^2 u/\partial x^2) + k_2(\partial^2 u/\partial y^2) - p\sin u = 0. \qquad (2)$$

This nonlinear equation, known as the sine-Helmholtz equation, obviously contains two characteristic coherence lengths of the lattice, i.e.,

$$l_1 = \sqrt{k_1/p}, \quad l_2 = \sqrt{k_2/p}. \qquad (3)$$

These lengths determine the mesoscopic scales which appear in the present theory, in contrast to the continual theory without any scale. On scales smaller than mesoscopic distances, the long-range translational order is completely violated by strain gradients. The lattice preserves a definite translational order only at large distances. It will be proved that coherence lengths in the nonlinear theory decrease and do not give an exact limit of existence of the order.

For $l_1 \longrightarrow 0$, we arrive at the one-dimensional Frenkel–Kontorova model, i.e., an elastic chain of atoms interacting with a periodic substrate. In our model, however, we consider the interaction of parallel chains with one another (and not with the substrate). The chains can slip relative to one another and can be deformed continuously. The first two terms in the equilibrium equation (2) correspond to continual forces smoothed on atomic scales, while the third nonlinear term takes into account interatomic structural forces. The case when continual forces vanish for zero gradients of microdisplacements is not trivial. In this case, the structural forces become self-balances if $u = 2n\pi$, which is a direct consequence of equation (2). For $u = 2\pi$, we are obviously dealing with the twinning deformation.

If equation (2) corresponds to the minimum of functional (1), the maximum corresponds to the equation with the opposite sign of the nonlinear term. It can be easily seen that their solutions u_+ and u_- are connected through a transformation (reversing the sign of the sine), i.e.,

$$u_-(x, y) = u_+(x, y) \pm \pi,$$
$$k_1(\partial^2 u_+/\partial x^2) + k_2(\partial^2 u_+/\partial y^2) + p\sin u_+ = 0. \qquad (4)$$

They differ in the translations of the structure by half the lattice period (in the *b* units). As a result, we go over from a stable to an unstable lattice configuration, for which some atoms are displaced from local minima to the peaks of potential barriers, while others, conversely, move from the peaks to the minima, which formally corresponds to the sign reversal of the quantity *p*, viz., the maximum force of the interaction between atoms. It is obvious that a change in the environment of the particles leads to a commutation of atomic bonds (the situation which is ruled out in the model of a continuous medium). In the case of rigid chains, commutation of bonds takes place over the entire layer. In the case of elastic systems, however, the commutation of bonds can be strongly localized, and then a transition through the extremal state again results in a stable, but excited state whose energy is associated with boundaries.

It would be interesting to consider a microdeformation in a layer with a critical shear $u = \pi$ or a twinning shear $u = 2\pi$ at the boundaries, the shear between boundaries being smaller (Fig. 2). The boundaries are conditional, since beyond them we have the same lattice separated (see below) into layers of the same thickness with the same microdeformation pattern in them. The thickness of the layers is not quite arbitrary, but is determined by the conditions of stability of a large shear.

We begin to study these effects from an analysis of the exact two-dimensional solution *u* of equation (2), which satisfies the boundary conditions of twinning

nonuniform(!) shear with commutation of bonds (Fig. 2a), i.e.,

$$u(0, y) = 0,\ u(|n|H, y) = 2\pi|n|,\ n = \pm 1, 2, \ldots . \quad (5)$$

We will also construct the solution u_- satisfying the critical shear conditions (Fig. 2b)

$$\begin{aligned} u_-(0, y) &= -\pi, \\ u_-(|n|H, y) &= (2|n| - 1)\pi, \quad n = \pm 1, 2, \ldots . \end{aligned} \quad (6)$$

In the latter case, we are speaking of the mutual shear of neighboring chains at the boundaries $x = 0$ and H (for $n = 1$) by π, i.e., half the period of the initial lattice in both directions. Leaving aside the case of large n, we note that the boundary atoms reach the peaks of the microscopic relief under the critical shear, while in the bulk of the layer (of thickness H) these shear strains are naturally smaller. Such a deformation can be rightfully referred to as purely elastic. We will prove that the corresponding limiting state of the lattice can be stable when deformations experience periodic modulations in the plane of the layer.

In the case of the first type of boundary conditions, we are dealing (for $n = 1$) with a rigid mutual shear of neighboring chains at the boundary $x = +H$ and $-H$ by an atomic spacing (to the left and to the right also). Note that, in contrast to the previous case, the mutual shear of chains at $x = 0$ is absent: the atoms are at the initial valleys of the microrelief and get into neighboring wells at the boundaries. The level $x = 0$ could be taken as the boundary with the "sticking" condition. Such a supercritical (elastoplastic) shear can be stable under special conditions and in a configuration homogeneous in the plane of the layer.

Clearly, the conditions of the first type take into account the effect of commutation of atomic bonds at the boundary of a layer of thickness $2H$, accompanied by the formation of a topological defect of the slip line type. In a large volume, however, the system of slip lines (for $n \geq 1$) generates a plastic shear of the entire volume according to a dislocation-free twinning mechanism, which naturally presumes a softness of the lattice. The slip of pairs of chains (involving the nearest neighbors of atoms) takes place not only at the above boundaries, but also in the bulk of the layer at a certain distance, i.e., a sort of plastic boundary regions (which will be considered at a later stage) are formed.

One can rightfully expect that these effects emerge under certain threshold conditions. In order to verify this, we must construct the corresponding solutions. These solutions are stable if we assume periodic boundary conditions along the y axis with a certain period $2B$ (see below). In order to construct exact solutions of equation (2), we will use the Lamb method of separation of variables for the sine-Helmholtz equation [2], according to which the solution is sought in the form

$$\tan(u/4) = Q_1/Q_2, \quad Q_1 = Q(x), \quad Q_2 = Q(y). \quad (7)$$

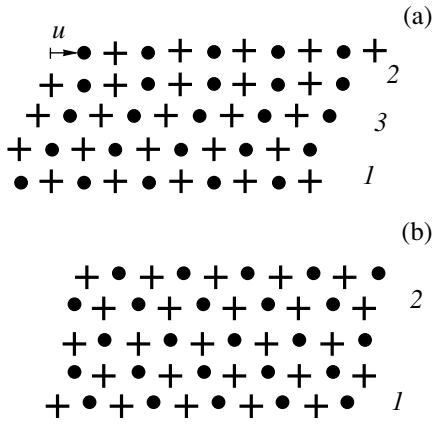

Fig. 2. Arrangement of chains under nonuniform elastoplastic (a) and elastic microscopic shear (b) at the boundary $x = 0$ (*1*), $x = H$ (*2*), and near the inner boundary between the elastic and plastic regions (*3*). In the latter case, the change of nearest neighbors can be seen.

Using this representation, we can divide the initial equation into two ordinary nonlinear differential equations in the partial functions Q_1 and Q_2:

$$\begin{aligned} (\partial Q_1/\partial x)^2 &= a^2(Q_1^2 + B_1)(Q_1^2 + C_1), \\ (\partial Q_2/\partial y)^2 &= a^2(Q_2^2 - B_2)(C_2 - Q_2^2). \end{aligned} \quad (8)$$

In the original work by Lamb [2], the right-hand sides of these equations contain three arbitrary integration constants which are selected beforehand to satisfy the initial equation. It is expedient to write, as was done for the first time in [3], the binomials on the right-hand side in terms of five constants (a, B_1, B_2, C_1, and C_2) and obtain [(by substituting (8) into (2)] the explicit form of two auxiliary relations connecting these constants:

$$B_1C_1 = B_2C_2, \quad a^2(B_1 + C_1) - a^2(B_2 + C_2) = 1. \quad (9)$$

Equations (8) can be solved in elliptical functions. The introduction of excess integration constants at the intermediate stage provides wider opportunities for choosing the required elliptical functions matching the preset boundary conditions. This choice is verified by using relations (9) that turn out to be the conditions for the existence of a solution.

The procedure of constructing the solution we are interested in is described in detail in [4, 5]. The solution has the form of the two-periodic function

$$\begin{aligned} \tan(u/4) &= \pm\tanh(q_1x)dn(q_2y)/Acn(q_2y), \\ A^2 &= \nu_2/\sqrt{1 - \nu_1^2}. \end{aligned} \quad (10)$$

Here, q_1 and q_2 are spatial elliptic frequencies

$$q_1 = K_1/H, \quad q_2 = K_2/B. \quad (11)$$

H and B are half-periods of the elliptic tangent tn, cosine cn, and the Jacobi delta function dn, respec-

tively, and K_1 and K_2 are complete elliptic integrals of the first kind, depending in the known way on their arguments, viz., moduli ν_1 and ν_2 [6]. The latter are defined on the interval from 0 and 1. The following asymptotic forms hold [6]:

$$\begin{gathered} K \longrightarrow \infty,\ \tanh \longrightarrow \sinh,\ dn \longrightarrow 1/\cosh,\ \nu \longrightarrow 1, \\ K \longrightarrow \pi/2,\ \tanh \longrightarrow \tan, \\ dn^2 \longrightarrow (1-\nu^2\sin^2),\ \nu \longrightarrow 0 \end{gathered} \tag{12}$$

Among other things, these relations indicate that the moduli ν_1 and ν_2, as well as K_1 and K_2 define the "extent of ellipticity" of the corresponding functions and the degree of their localization along relevant axes, and hence the gradients of displacements. The latter can, in principle, be indefinitely large for the bounded periods $2H$ and $2B$ or spatial frequencies of the displacement fields. In this case, soliton-like regions of localized deformations are formed.

Using (12), we can easily verify that solution (10) actually satisfies the boundary conditions (6) for all integral n, i.e., it generally exists in the entire plane, and the boundary shift increases linearly with the boundary number n. The boundary conditions (5) are satisfied by solution (4) which will be considered in detail later. It should be noted from the very start that the function u_+ in (4) is defined by the same formula (10), but with different values of A. Both solutions are periodic along the y axis (with a period $2B$) in view of the periodicity of the function dn. Since the latter function is positive (except in the limiting case of $\nu = 1$), all the cross sections of the layer are characterized by a complex displacement profile. Expression (10) is obviously a periodic solution along the x axis also with a period $2H$. The obtained solution shows that a translational order realized in the form of a domain superstructure is also possible in a deformed state, in which the critical shear conditions are observed at certain lines.

At the same time, a continuous increase in a mutual shear of chains from zero at $x = 0$ to 2π at the boundary $x = H$ takes place, in accordance with (5), within each unit cell of the superstructure (5), (10). In Fig. 2a, these levels are marked by *1* and *2*. Consequently, an intermediate value equal to π corresponding to the emergence of an atom at the top of the barrier is attained somewhere between these levels (level *3* in the same figure). The larger value of the shear strain corresponds to the plastic slip, viz., commutation of bonds and a change in the short-range order. Consequently, a region of elastic shear emerges near the center of each layer of thickness $2H$, while two plastic boundary layers are formed near the boundaries. Note that the inner interface between the elastic and plastic regions is not rectilinear as shown in Fig. 2a for the sake of simplicity. In actual practice, it oscillates with a period $2B$. The equation for the internal interface is given by (10) for $u = \pi$, when its right-hand side is equal to unity.

Continuing the analysis of the elastoplastic configuration (10), (5), let us consider the criteria for its existence. First of all, consider the fact that solution (10) satisfying the boundary conditions contains two arbitrary integration constants ν_1 and ν_2. In principle, they can be determined from relations (9), which should be referred to as dispersion relations since they impose constraints on the spatial frequencies q_1 and q_2. The latter can be expressed in terms of the above constants as follows:

$$(2-\nu_1^2)k_1q_1^2 - (1+\nu_2^2)k_2q_2^2 - p = 0, \tag{13}$$

$$k_1q_1^2 = A^2k_2q_2^2, \quad p \geq 0. \tag{14}$$

The first relation is a prototype of equation (2) itself and can be obtained by substituting solution (10) into it. The second term here corresponds to gradients of displacements along the layer, which are responsible for a nonuniform extension of the chains. It is significant that this term is negative in contrast to the first term. This means that a competition of corresponding forces establishing equilibrium takes place. Transverse gradients generate forces directed oppositely to the structural forces maintaining the order, while longitudinal extensions (compressions) of chains are acting in the same direction as the structural forces. Even the sign distribution in (13) indicates that the necessary condition for the fulfillment of this relation (the emergence of stable deformations) requires that the transverse shear gradients dominate over the longitudinal extension (compression).

The relation between these forces is given by the second dispersion relation (14) in terms of the parameter A which was defined initially in (10). Equation (14) attaches to it the simple meaning of the ratio of the characteristic energies of microscopic shear and microscopic extension. It plays a decisive role in the problems of stability of these deformations. The critical value of this parameter can be refined after the elementary transformation of (13) and (14) into the following two conditions:

$$S = A^2P_1 = P_2. \tag{15}$$

where

$$S = (A^2-1)(1-\nu_2^2/A^2). \tag{16}$$

In relation (15), we have introduced the quantities P_1 and P_2 defined as

$$P_1 = p/k_1q_1^2, \quad P_2 = p/k_2q_2^2. \tag{17}$$

In fact, conditions (15) separate the dispersion relations relative to spatial elliptic frequencies q_1 and q_2. In the nonlinear theory, the frequencies are expressed not only in terms of material constants, but are also functions of the parameter A.

In connection with new quantities (effective relative potentials) introduced into (17), note that they have the meaning of certain collective characteristics of interac-

tion between not individual atoms, but segments of chains of length $2B$ and $2H$ in the superstructure. Like the lattice potential p of an undeformed structure, these quantities are positive, which is equivalent to the stability of the superlattice. This, however, requires the fulfillment of the inequality $A \geq 1$ for which $S \geq 0$, and the dispersion relation in the form (15), i.e., the conditions for the existence of the solution, are satisfied. As mentioned above, the values of A smaller than unity, for which longitudinal gradients prevail, correspond to an unstable lattice configuration and negative values of the effective barriers $P_1$and P_2. The latter is equivalent to the fulfillment of the condition (4) of mutual shear of the chains by half the period of the undeformed lattice.

It will be proved below that a stable solution, but with new boundary conditions, can be constructed for values of the parameter $A \leq 1$ also; a transition to such a solution occurs at the point $A = 1$. For this reason, it would be interesting to consider the point $A = 1$ of the structural phase transition from a different point of view. It follows from (15) that this point also corresponds to the vanishing of the potential barrier, $p = 0$, say, due to temperature. In this case, structural forces vanish, and hence the translational order also disappears as a result of the loss of stability of the sublattices to shear. The model degenerates into two independent structureless continuums connected only through the boundary conditions. Indeed, in this case both fields (of micro- and macrodisplacements) obey the same equations in the classical theory of elasticity. Obviously, the condition $S = 0$ or $A = 1$ corresponds to the branching point of equation (2), and the quantity A has the meaning of the bifurcation parameter.

In fact, there is no need to modify the model itself upon an increase in the temperature of the body, which nullifies the barrier height p. In our case, a similar effect can be obtained due to the microstrain gradients, which also violate the translational order. True, the point $S = 0$ can be approached in this case only asymptotically by making the potential barriers P_1 and P_2 defined in (17) tend to zero. The role of the lattice potential is suppressed due to increasing strain gradients, so that the roles of transverse shear and longitudinal extension (compression) might interchange. As in the case when $p = 0$, the sign is reversed at S, i.e., in the gradient part of the equation due to a transition of the value of parameter A through unity. Naturally, the structural transition has another meaning: the stability of the deformed sublattices (superstructure) to the shear is lost, and a considerable rearrangement of a distorted translational order of the deformed configuration occurs. Consequently, the effective potentials, which are relative quantities, can be regarded as parameters of the distorted translational order in the deformed crystal.

A superstructure (and hence, a new translational order) appears again for $A \leq 1$, when a new stable microscopic field u_- is formed in accordance with (4). Let us refine the explicit form of the field u_+ in (4). It satisfies the equation in [2] which differs from (2) in the sign of the nonlinear term, which corresponds to the maximum of the functional (1). This unstable solution u_+ is also defined by formula (10), but with $A \leq 1$. As before, it satisfies the boundary conditions (5). The new stable solution u_- is defined by the first formula in (4) and obviously satisfies the boundary conditions (6) (see Fig. 2b). Therefore, in the case of microdeformations, we are dealing with a transition in the boundary conditions. An analogy is observed with the bifurcation point for large oscillations of a pendulum: in the upper position of an unstable equilibrium, the pendulum can move backwards or continue the motion in the same direction.

In contrast to (5), the new boundary conditions rule out plastic boundary regions, which is in accord with a reduced role of transverse shear for $A \leq 1$. In the new superlattice, there is no need for plastic accumulation of energy and commutation of bonds. The energy is redistributed in favor of the longitudinal deformation of the chains.

It should also be noted that such purely elastic displacements occur in a layer with half the thickness and with much smaller longitudinal periods $2B$.

Thus, the regions of purely elastic ($A \leq 1$) and elastoplastic ($A \geq 1$) deformations are separated by the bifurcation point $A = 1$, at which the transition is accompanied by a slip at the interface by half the period of the initial lattice.

In each of these regions, additional constrains are imposed. These constraints also follow from dispersion relations. In order to find them, one must eliminate the integration constants ν_1 and ν_2 from equations (13) and (14). Having determined these constants from (13) and (14) in terms of H and B, we obtain A as a function of the same quantities. It is more convenient to describe the relation between three quantities A, B, and H by a family of curves representing the dependence of H on B for various values of the bifurcation parameter A (Figs. 3 and 4).

Let us first consider the range of values $A \geq 1$ in which the solution if defined by (5) and (10). Each value of the parameter A corresponds to a curve in the plane (H, B) (see Fig. 3). It is close to a hyperbole with asymptotes

$$H \geq H_t, \quad H \leq \infty, \quad H_t = l_1(1 - 1/A^2)K_{11}, \qquad (18)$$

$$B \geq B_t, \quad B \leq \infty, \quad B_t = (\pi/2)l_2\sqrt{A^2 - 1}. \qquad (19)$$

Here, K_{11} is the value of the function $K_1(\nu_1)$ at the point $\nu_1 = \sqrt{(1 - 1/A^4)}$. These inequalities define the limiting values of the parameters of domains or unit cells of the superstructure. It can be easily seen that a uniform shear in the plane of the layer, for which $(1/B) \longrightarrow 0$, is in principle possible, but under the stringent condition $H = H_t$, which corresponds to an average

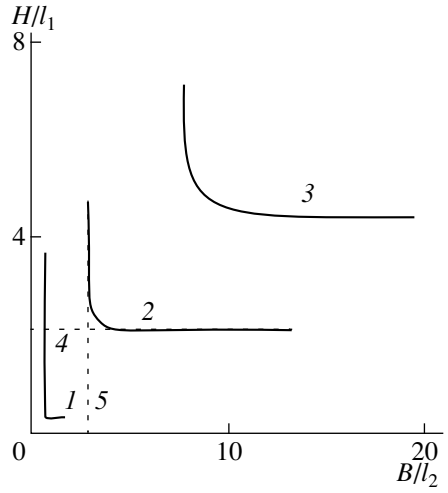

Fig. 3. Curves illustrating the existence of a stable lattice configuration for $A > 1$. Curve *1* corresponds to $A = 1.1$, *2* to $A = 2$, *3* to $A = 5$, *4* to $H = H_t$, and *5* to $B = B_t$.

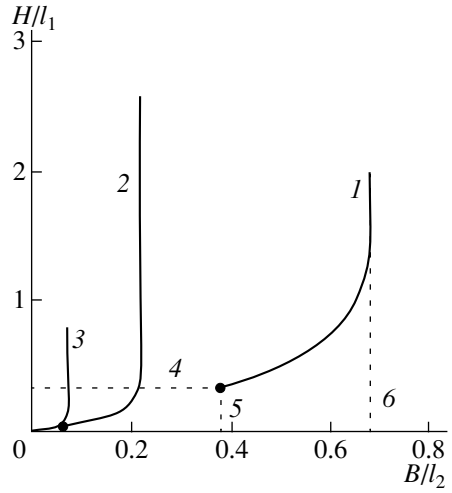

Fig. 4. Curves describing stable configurations for $A < 1$. Curve *1* corresponds to $A = 0.9$, *2* to $A = 0.99$, *3* to $A = 0.999$, *4* to $H = H_c$, *5* to $B = B_c$, and *6* to $B = B_i$.

deformation equal to b/H_t. However, for other thickness and strain values, a uniform shear is ruled out and is accompanied by modulations with periods $2B$.

Note that the magnitude of the threshold is determined by the coherence lengths l_1 and l_2, with coefficients depending on A. These coefficients effectively lead to a reduction of coherence lengths.

It follows from (18) and (19) that the solution with commutation of bonds at the boundaries, i.e., elastoplastic shear, is possible only in thick layers and in long unit cells. Otherwise, too large gradients of microscopic shear straons incompatible with a translational order appear in a layer.

This can be seen clearly if we present (18) and (19) in the form of energy relations with the coherence length defined by (3). This gives a different form of the conditions for the existence of an elastoplastic two-periodic field of microdisplacements or the condition for the emergence of a superstructure in the case of a slip of the chains:

$$p \geq k_1(K_{11}/H)^2(1-1/A^2)^2,$$
$$(1-1/A^2)^2 \leq P_1 \leq (1-1/A^2), \tag{20}$$

$$p \geq k_2\pi^2(A^2-1)/4B^2,$$
$$(A^2-1)^2/A^2 \leq P_2 \leq (A^2-1). \tag{21}$$

The first inequalities in (20) and (21) obviously indicate that a superstructure with slipping chains requires to maintain considerable structural potential barriers and bounded gradients violating the translational order in the lattice. If the former are too small and the latter too large, the conditions for the existence of the lattice are not satisfied. In this case, a disordered deformed structure is obviously formed, i.e., an order–disorder transition takes place, indicating that an amorphous-type structure can be formed under the action of large strain gradients (for low collective barriers). This problem cannot be solved completely in the framework of the given theory.

The second inequalities in (20) and (21) demonstrate the universal nature of limits for effective barriers determined only by the bifurcation parameter A. They vanish at the point of the boundary bifurcation.

Let us consider again the region $A \leq 1$, in which a stable configuration is defined by formulas (4) and (6), where the field u_+ (as well as u_-) is defined by relations (5) and (10), but for $A \leq 1$. It should be recalled that we are dealing here with a purely elastic microdeformation under the conditions of maximum possible shear at the boundaries. These boundaries are marked by *1* and *2* in Fig. 2b. The middle level at which microscopic displacements are equal to zero is marked by *4*. This level in fact oscillates, which is not reflected on the schematic diagram.

In the given case (Fig. 4), each curve on the same plane (HB) for a given value of A has only one asymptote $B = B_i$ and arrives at the final point H_c, B_c without reaching the origin, so that

$$H \geq H_c, \quad H \leq \infty, \quad B_c \leq B \leq B_i. \tag{22}$$

The values of these limits are as follows:

$$H_c = \pi l_1(1-A^2)/2A^2, \tag{23}$$

$$B_c = l_2(1-A^2)K_{22}, \quad B_i = \pi l_2\sqrt{1-A^2}/2. \tag{24}$$

Here K_{22} is the value of the function $K_2(\nu_2)$ at the point $\nu_2 = A^2$.

Comparing the scales on the coordinate axes in Figs. 3 and 4, we see that the unit cells of the super-

structure have become much smaller. Besides, as before, not all values of the parameters H and B are admissible because inequalities (21) and (22) impose obvious limitations.

However, in contrast to elastoplastic deformations, the entire region of large longitudinal scales B of superstructures, and hence a uniform shear, is eliminated completely. Indeed, the value of B does not exceed the coherence length with a factor depending on A, which may prove to be quite small for $A \longrightarrow 1$. The energy of uniform shear is too high and is transferred to longitudinal deformations to maintain stability. In the previous case, plastic deformation absorb the excess of elastic energy of uniform shear (true, under stringent limitations imposed on the layer thickness).

Thus, in small regions, only elastic distortions of translational order are possible. However, for a size of the unit cell of the superlattice smaller than the admissible values of H_c and B_c, we go beyond the region of existence of a solution, and a small-scale superstructure becomes impossible.

Inequalities (21) and (22) can be written in terms of the energy parameters as follows:

$$p \geq k_1(\pi/2H)^2(1-A^2)^2/A^2,$$
$$(1-A^2)^2/A^2 \leq P_1 \leq (1/A^2-1), \tag{25}$$

$$(\pi k_2/2B^2)(1-A^2) \geq p \geq (k_2/B^2)(1-A^2)^2K_{22}^2,$$
$$(1-A^2)^2 \leq P_2 \leq (1-A^2). \tag{26}$$

A considerable difference from the case of elastoplastic deformations is that the potential barrier is bounded not only from below, but also from above. In order to clarify this, we consider again the dispersion relation (13). A transition to the purely elastic case is formally reflected in the fact that the sum of the first two (gradient) terms has reversed its sign, which indicates a transition to a region in which parameter A becomes smaller than unity. In this case, however, longitudinal gradients must dominate, and domains cannot be too short (at the very least they must be much longer than atomic spacing). For this reason, too high potential barriers of the lattice cannot be overcome under such conditions. Therefore, a purely elastic critical shear emerges at the point of bifurcations of the values of p and B or gradients in accordance with (26).

As mentioned above, purely elastic, but large microstrains and their gradients are possible without a plastic unloading in the presence of another mechanism of unloading. It is realized owing to compensating (stabilizing) forces generated by microstrain gradients along a layer. As a matter of fact, extending (compressing) chains along the layer prevents the fall of particles to potential wells, since this would cause an extra extension (compression). In other words, the structures of adjacent chains become incompatible. As a result, instead of plastic deformations, high longitudinal gradients are generated, which absorb the excess energy of shear deformation. Such a redistribution of energy between microdeformation modes is realized in the small-scale (in the plane of the layer) modulated structure which is formed for $A \leq 1$. The nonconformity of the structure of adjacent chains is advantageous for stability only to a certain extent. If the chain length $2B$ is large, the energy of transverse shear is compensated insufficiently to ensure stability. For this reason, the length of purely elastic structure are limited in accordance with (22).

Thus, the nonlinear theory of microdeformations in a two-dimensional lattice, which is based on the exact solutions of the nonlinear sine-Helmholtz balance equation, predicts instability of a large nonuniform shear. It also makes it possible to take into account the effect of large gradients of microstains on the long-range translational order of the lattice in two cases of critical and twinning (supercritical) shear at the boundaries. In the latter case, the chains slip over a distance exceeding half the lattice period, which indicates the commutation of bonds and a change in the short-range order in the atomic arrangement. A two-dimensional superstructure with large periods is formed in the infinitely large space, i.e., the long-range translational order decreases. Two stable states of the microscopic field (critical and supercritical shear) separated by a bifurcation transition involving the commutation of atomic bonds, can form in domains or unit cells. The criteria for the existence of stable states limiting the values of strain gradients relative to the height of potential barriers of the initial undeformed structure of the lattice are formulated. The order parameters, viz., effective potential barriers vanishing asymptotically at the bifurcation point are established; this is interpreted as a complete loss of the long-range translational order.

ACKNOWLEDGMENTS

This research was carried out with the support of the Russian Foundation for Basic Research (project no. 98-01-01076).

REFERENCES

1. É. L. Aéro, Neorg. Mater. **8**, 1 (1999).
2. G. L. Lamb, *Elements of Soliton Theory* (Wiley, New York, 1980).
3. É. L. Aéro, Kristallografiya **40** (5), 889 (1995) [Crystallogr. Rep. **40** (5), 823 (1995)].
4. É. L. Aéro, Prikl. Mat. Mekh. **60** (1), 79 (1996).
5. É. L. Aéro, Izv. Ross. Akad. Nauk, Mekh. Tverd. Tela **1**, 182 (1998).
6. E. Jahnke, F. Emde, and F. Losch, *Tables of Higher Functions* (McGraw-Hill, New York, 1960, 6th ed.; Nauka, Moscow, 1977).

Translated by N. Wadhwa

Physics of the Solid State, Vol. 42, No. 6, 2000, pp. 1154–1159. Translated from Fizika Tverdogo Tela, Vol. 42, No. 6, 2000, pp. 1120–1124.

LOW-DIMENSIONAL SYSTEMS AND SURFACE PHYSICS

Investigation of Interaction between Lithium and Tantalum under a Silicon Film Coating by Electron-Stimulated Desorption Technique

V. N. Ageev and S. M. Solov'ev

Ioffe Physicotechnical Institute, Russian Academy of Sciences, Politekhnicheskaya ul. 26, St. Petersburg, 194021 Russia

Received April 1, 1999; in final form, June 12, 1999

Abstract—The electron-stimulated desorption of Li^+ ions from lithium layers adsorbed on the tantalum surface coated with a silicon film has been investigated. The measurements are performed using a static magnetic mass spectrometer equipped with an electric field-retarding energy analyzer. The threshold of the electron-stimulated desorption of lithium ions is close to the ionization energy of the Li 1*s* level. The secondary thresholds are observed at energies of about 130 and 150 eV. The threshold at an energy of 130 eV is approximately 30 eV higher than the ionization energy of the Si 2*p* level and can be associated with the double ionization. The threshold at 150 eV can be caused by the ionization of the Si 2*s* level. It is demonstrated that the yield of Li^+ ions does not correlate with the silicon amount in near-the-surface region of the tantalum ribbon and drastically increases at high annealing temperatures. The dependence of the current of Li^+ desorption on the lithium concentration upon annealing of the tantalum ribbon at $T > 1800$ K exhibits two maxima. The ions desorbed by electrons with energies higher than 130 and 150 eV make the largest contribution to the current of lithium ions after the annealing. The yield of lithium ions upon ionization of the Li 1*s* level at an energy of 55 eV is considerably lesser, but it is observed at higher concentrations of deposited lithium. The results obtained can be interpreted in the framework of the Auger-stimulated desorption model with allowance made for relaxation of the local surface field.

1. INTRODUCTION

Refractory metal–silicon junctions can be used in fabrication of high-temperature ohmic and rectifying contacts in high-temperature solid-state electronics [1]. However, the properties and mechanisms of formation of these junctions are still not clearly understood. Especially little is known about the kinetics of formation of refractory metal silicides upon silicon deposition [2–4]. Earlier [5], we employed the Auger electron spectroscopy to investigate the interaction between silicon and textured tantalum ribbons with the surface predominantly formed by the (100) face and revealed a number of sequential structural phase transitions. It was found that the kinetics of these transitions depends on the substrate temperature and amount of silicon deposited onto the surface. However, the Auger spectroscopy, like any electron spectroscopic technique, permits measurements of the concentration of elements contained in a substrate within the escape depth of electrons with a given energy whose minimum value is equal to several lattice constants [6].

For this reason, in the present work, we employed the electron-stimulated desorption technique in order to examine the processes occurring on the tantalum surface upon silicon adsorption. This method makes it possible to judge changes observed in the concentration and the state of silicon in the uppermost layer of the substrate from the data on desorption of alkali metal ions preliminarily adsorbed on the surface. Among all alkali metals, lithium is the most convenient for this purpose. Upon electron-stimulated desorption from silicon, lithium is eliminated only in the form of positive ions whose yield is sufficiently large and depends on the state of the silicon film [7].

2. EXPERIMENTAL TECHNIQUE

The measuring procedure and an experimental setup were described in detail earlier in [8]. Here, we only briefly recall the main parts of instruments and the features of their use. The measurements were carried out in an ultrahigh vacuum chamber at a residual gas pressure of 5×10^{-8} Pa. The ionic currents were measured using a static magnetic mass spectrometer equipped with an electric field-retarding energy analyzer. Textured tantalum ribbons ($40 \times 1.5 \times 0.01$ mm in size) with the surface predominantly formed by the (100) face served as samples. In order to provide the required orientation, the tantalum ribbon was heated by an alternating current at a temperature of 2400 K for 10 h. After this heating, the thermoionic work function turned out to be equal to the work function (4.2 eV) measured from the ionic current of surface ionization, which indicated an emission homogeneity of the surface.

The ribbon was cleaned from carbon by annealing in an oxygen atmosphere at a pressure of 1×10^{-4} Pa at

T = 1900 K for 3 h. After the evacuation of oxygen from the chamber, the finish cleaning of the ribbon from adsorbed gases was achieved by its heating up to $T >$ 1600 K for 5 s. Silicon was evaporated onto the sample from a small silicon bar with an antimony concentration of 5×10^{18} cm^{-2}). The bar $30 \times 1 \times 1$ mm in size was mounted parallel to the sample and then was heated by an electric current. The concentration of deposited silicon was determined from the evaporation time at a constant flux. The intensity of silicon flux was measured with a quartz balance [9]. The deposition of a silicon monolayer led to an increase in the work function up to 4.7 eV, which was measured by the method of contact potential difference with respect to a tungsten filament. The deposition of silicon was accompanied by the release of fluorine, which was most likely a technological impurity. To reduce the contamination of tantalum by fluorine, the ribbon was treated with an electron current of ~1 mA at an electron energy of 200 eV. Lithium was deposited from an evaporator filled with a mixture of Li_2CO_3, CaO, and an aluminum powder. The evaporator was heated through passage of electric current. The concentration of deposited lithium was determined from the deposition time at a constant flux. The intensity of lithium flux was measured from the total current of surface ionization on the tantalum ribbon. The surface ionization coefficient of lithium was calculated on the basis of the measured work function for the tantalum surface and temperature. The lithium concentration on the surface during the deposition was checked against the change in the work function measured by the contact potential difference technique.

3. RESULTS

Figure 1 demonstrates the dependences of the yield of lithium ions on the temperature of annealing the film for two electron energies. The annealing time at each temperature was equal to 3 min. It is seen that the yield of Li^+ ions increases with an increase in the electron energy and nonmonotonically changes with an increase in the annealing temperature of the silicon film. Curve *3* in Fig. 1 represents the dependence of the intensity of the silicon Auger signal (92 eV) on the temperature of annealing the silicon film deposited onto the tantalum substrate at T = 300 K [5]. As follows from comparison of the dependences, no correlation is observed between the intensity of the silicon Auger signal and the yield of Li^+ ions upon electron-stimulated desorption. The intensity of the silicon Auger signal gradually decreases with an increase in the annealing temperature, whereas the yield of Li^+ ions increases in the temperature range T = 700–1200 K, passes through a maximum at T = 1200 K, again increases at $T >$ 1600 K, and reaches a saturation at $T >$ 2100 K. Since the intensity of the silicon Auger signal is proportional to the silicon concentration in near-the-surface region, the absence of correlation between the intensity of the Auger signal and the yield of lithium ions implies that the annealing brings about a change in the cross-section of the electron-stimulated desorption of Li^+ ions.

The distribution of silicon in near-the-surface region of the tantalum ribbon depends on the amount of silicon initially deposited onto the surface. The dependences of the yield of Li^+ ions upon electron-stimulated desorption on the temperature of annealing the tantalum ribbon with different amounts of silicon deposited onto the surface are depicted in Fig. 2. It can be seen that the

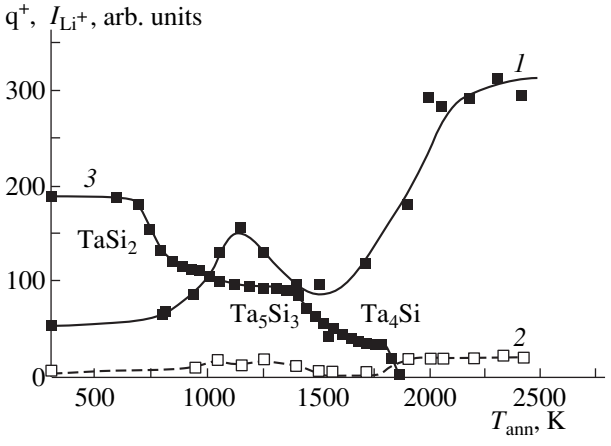

Fig. 1. Dependences of (*1*, *2*) the current of Li^+ ions upon electron-stimulated desorption from the Ta–Si surface at different energies of bombarding electrons and (*3*) the intensity of Auger signal on the temperature of annealing the surface. Energy of bombarding electrons E_p (eV): (*1*) 194 and (*2*) 70.

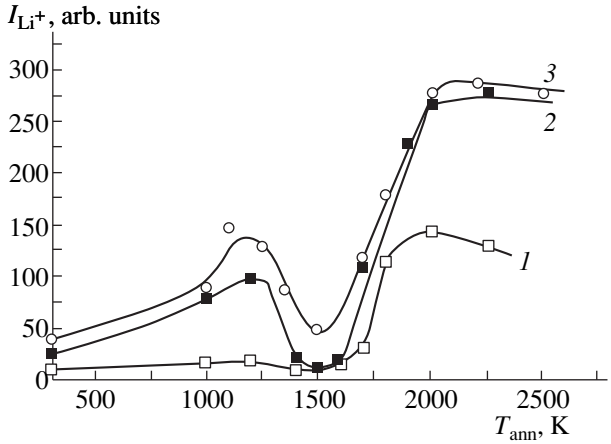

Fig. 2. Dependences of the current of Li^+ ions upon electron-stimulated desorption from the Ta–Si surface on the temperature of preliminary annealing of the surface at different silicon coverages Θ (ML): (*1*) 0.2, (*2*) 1, and (*3*) 6. (ML = monolayer).

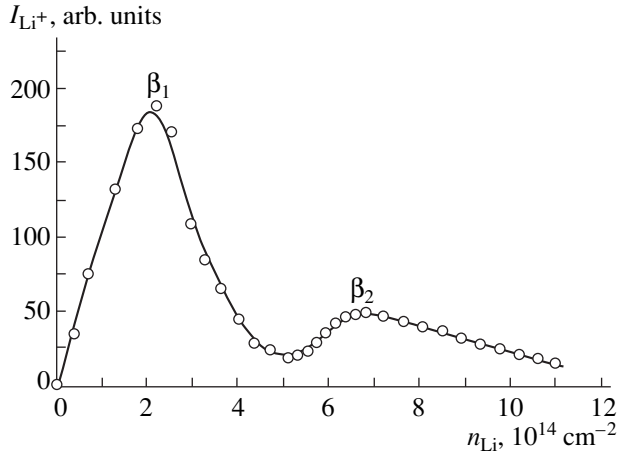

Fig. 3. Dependence of the yield of Li^+ ions upon electron-stimulated desorption from the Ta–Si surface annealed at T = 2500 K on the concentration of lithium deposited onto the surface. Intensity of lithium flux is 11.6×10^{13} cm^{-2} s^{-1}.

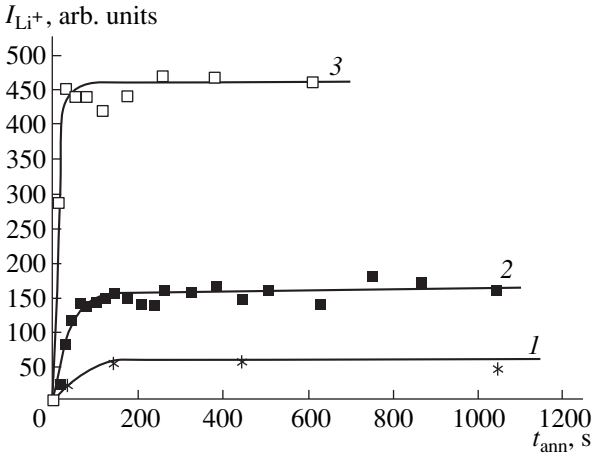

Fig. 4. Dependences of the maximum yield of Li^+ ions in the β_1 phase upon electron-stimulated desorption on the time of annealing the Ta–Si surface at different temperatures (K): (*1*) 1800, (*2*) 1950, and (*3*) 2400.

yield of lithium ions considerably changes in the range of annealing temperatures T = 300–1500 K only in the case when the concentration of deposited silicon is less than a monolayer. At T > 1500 K, a further increase in the temperature leads to an increase in the yield of lithium ions up to a saturation, irrespective of the concentration of deposited silicon. This observation provides support for the inference that a silicon monolayer is the stable coating and persists upon formation of silicides in the bulk [5]. Figure 3 displays the dependence of the yield of Li^+ ions on the concentration of lithium deposited at T = 300 K onto tantalum preliminarily coated with silicon and annealed at T = 2000 K for 120 s. The dependence exhibits two peaks. The height of these peaks depends on the temperature and duration of the preliminary annealing of the tantalum ribbon, the deposition temperature, and the intensity of lithium flux. Hereafter, the peak at short times of the lithium deposition corresponds to the β_1 phase of lithium upon electron-stimulated desorption, and the peak at long times of the lithium deposition is attributed to the β_2 phase of lithium.

The dependences of the maximum yield of Li^+ ions in the β_1 phase on the time of preliminary annealing of the tantalum ribbon at different temperatures prior to the deposition of lithium at T = 300 K are displayed in Fig. 4. As the annealing temperature increases, the maximum yield of lithium ions in the β_1 phase drastically increases and reaches a saturation. A further increase in the annealing temperature leads to an increase in the current of lithium ions at the saturation. The yield of Li^+ ions in the β_2 phase only slightly depends on the temperature and the duration of annealing. A decrease in the intensity of lithium flux causes the yield of lithium ions to increase in the β_1 phase and to decrease in the β_2 phase. It is seen from Fig. 5 that an increase in the temperature of lithium adsorption produces the same effect on the yield of lithium ions in both phases. As the temperature of lithium adsorption increases, the yield of lithium ions in the β_1 phase increases and reaches a saturation, whereas their yield in the β_2 phase tends to zero. The appearance of two maxima in the dependence of the yield of Li^+ ions on the concentration of adsorbed lithium is accompanied by changes in the dependence of the yield of Li^+ ions on the bombarding electron energy. This is illustrated by the curves shown in Fig. 6 for two lithium concentrations in the β_1 and β_2 phases. The threshold of the desorption of Li^+ ions is equal to approximately 55 eV, irrespective of the concentration of deposited lithium. Within the limits of experimental error and with allowance made for the contact potential difference between an electron emitter and the tantalum ribbon, this value is close to the ionization energy of the Li 1*s* core level [6]. As the concentration of deposited lithium increases, the yield of Li^+ ions at the bombarding electron energy E_p = 100 eV passes through a maximum at a lithium concentration of about 1.2×10^{14} cm^{-2} (Fig. 7). The lithium ions at electron energies above 133 eV make the main contribution to the current of Li^+ ions in the β_1 phase. The feature at an energy of 133 eV was earlier observed upon electron-stimulated desorption of Li^+ ions from tungsten coated with a silicon film. This feature was interpreted as a result of the double ionization of silicon due to the "detachment" of the valence electron [10]. In this energy range, the dependence of the yield of lithium ions takes the form of a sharp peak, which indicates the resonance character of the bond breaking (Fig. 6). The threshold at an ionization energy of 150 eV corresponds to the ionization of the Si 1*s* level [6].

The yield of Li^+ ions at bombarding electron energies above 133 eV reaches a maximum at a lithium concentration of 2.2×10^{14} cm^{-2}, which is considerably higher than the lithium concentration corresponding to the maximum yield of Li^+ ions near the threshold of the onset in the desorption of Li^+ ions. The current of lithium ions in the β_2 phase is associated with the excitation of lithium near the threshold of the onset in the electron-stimulated desorption. Since the experiments on silicon evaporation, annealing of the deposited film, cooling of the sample down to $T = 300$ K, and lithium deposition require the sufficiently long time, even at a residual gas pressure below 10^{-8}Pa, the possibility of contaminating the tantalum ribbon by residual gases cannot be ruled out. Among the residual gases, particular attention should be given to carbon oxide, which possesses a large sticking coefficient and dissociates on the tantalum surface [11]. In this respect, we measured the yield of Li^+ ions upon electron-stimulated desorption after the preliminary adsorption of hydrogen, oxygen, and carbon. The adsorption of hydrogen virtually does not affect the yield of Li^+ ions, and the current of H^+ ions upon electron-stimulated desorption tends to zero already at $T \sim 1200$ K. The adsorption of oxygen decreases the yield of Li^+ ions by almost an order of magnitude, but shifts the threshold of the desorption of lithium ions to 25 eV, which can be readily observed in the experiments. The adsorption of carbon even in small amounts substantially reduces the yield of lithium ions but leaves the threshold of the desorption of Li^+ ions unchanged. The adsorption of carbon oxide also leads to a decrease in the yield of Li^+ ions.

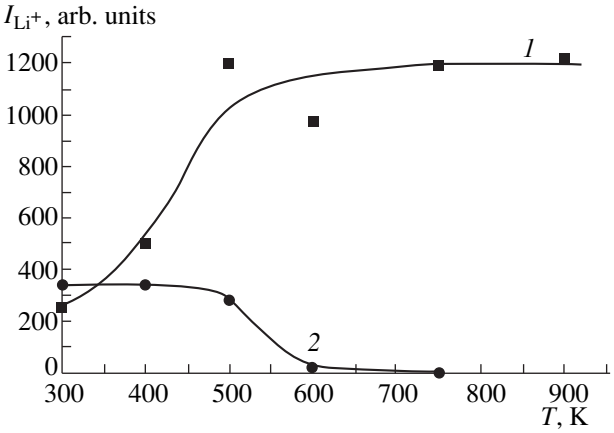

Fig. 5. Dependences of the maximum yield of Li^+ ions in (*1*) β_1 and (*2*) β_2 phases on the temperature of lithium adsorption on the Ta–Si surface.

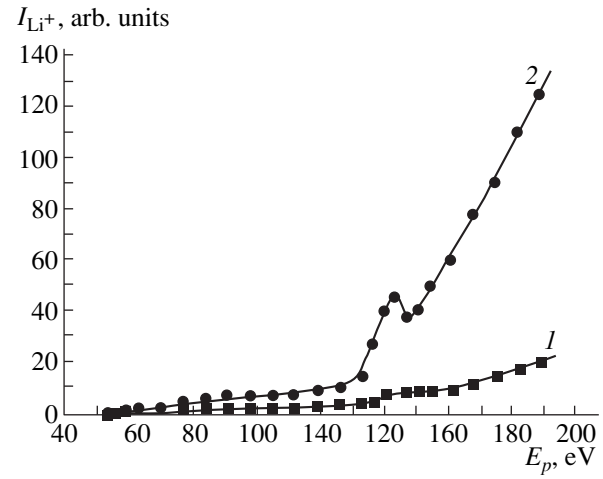

Fig. 6. Dependences of the current of Li^+ ions upon electron-stimulated desorption from the Ta–Si surface on the bombarding electron energy for different lithium concentrations at the surface: (*1*) 0.5×10^{14} and (*2*) 2.2×10^{14} cm^{-2}.

4. DISCUSSION

The majority of the results obtained for the electron-stimulated desorption of Li^+ ions can be interpreted in the framework of the model according to which the excitation of the adsorption bond begins with the Auger decay of core holes in silicon or lithium. Note that, in the case when ions move away from the surface, it is necessary to take into consideration the relaxation of the local surface field. Within this model, the desorption of Li^+ ions is caused by the Coulomb repulsion from Si^+ or Si^{2+} ions formed on the ribbon surface due to the intraatomic and interatomic Auger processes. During the desorption of lithium ions from the surface, the silicon ions regain their original charge at the expense of substrate electrons, and the Li^+ ions occur in the field of image forces. When the kinetic energy acquired by the Li^+ ions prior to relaxation of the charge on silicon ions becomes higher than the potential energy of the image forces, the lithium ions leave the surface; otherwise, they revert to the adsorbed state.

A silicon monolayer adsorbed on the Ta(100) face increases the work function by 0.3 eV, and, hence, the silicon atoms acquire the negative charge at this surface. On the other hand, the lithium adsorption decreases the work function of tantalum coated with silicon, and, correspondingly, the lithium atoms adsorb in the form of positive ions. The absence of correlation between the intensity of the silicon Auger signal and the current of Li^+ ions upon electron-stimulated desorption after the annealing of the tantalum ribbon (Fig. 1) suggests that changes in the silicon concentration in near-the-surface tantalum layer cannot be primarily responsible for the yield of lithium ions upon electron-stimulated desorption. Actually, at $T > 700$ K, the silicon concentration in near-the-surface layer decreases, whereas the yield of Li^+ ions increases, which is likely due to the formation of the $TaSi_2$ silicide in this temperature range. The electric resistivity of $TaSi_2$ is higher

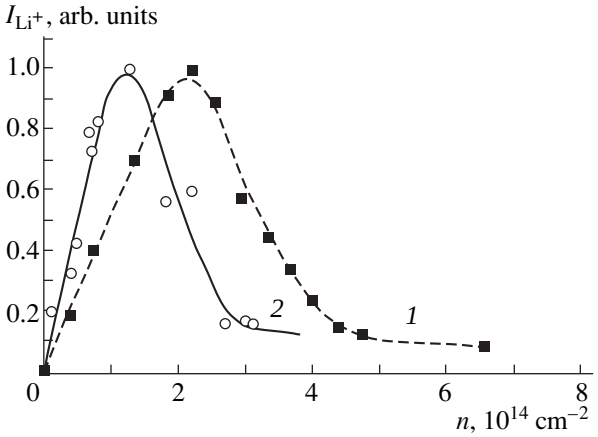

Fig. 7. Dependences of the normalized yield of Li^+ ions on the lithium concentration at the surface for different energies of bombarding electrons (eV): (*1*) 190 and (*2*) 100.

than that of amorphous silicon films, and, correspondingly, the cross-section of the electron-stimulated desorption of lithium ions increases owing to an increase in the relaxation time of the charge on positive ions of silicon. A decrease in the yield of Li^+ ions at $T > 1200$ K agrees well with both the onset of the thermal decomposition of the $TaSi_2$ silicide and the formation of the Ta_5Si_3 silicide whose electric conductivity should be higher than the conductivity of $TaSi_2$. Finally, at $T > 1600$ K, the formation of the Ta_4Si silicide is completed, and its decomposition proceeds at $T > 1800$ K, which is attended by the diffusion of silicon into the bulk of tantalum and the desorption [5]. It seems likely that, at such high temperatures, the silicon atoms can occupy nonequilibrium sites, which are retained upon rapid cooling of the substrate down to $T = 300$ K. Lithium adsorbed on these atoms possesses a high yield of ions upon electron-stimulated desorption. Note that the concentration of these silicon atoms is relatively low, because they cannot be detected by the Auger electron spectroscopy. As a result of this process, the tantalum surface becomes inhomogeneous in the work function. This is evidenced by the difference of about 0.6 eV between the thermoionic work function and the work function and also by the appearance of two peaks in the dependence of the yield of Li^+ ions upon electron-stimulated desorption on the concentration of deposited lithium (Fig. 3). A decrease in the flux of lithium atoms and an increase in the temperature of the ribbon upon lithium adsorption lead to the fact that all lithium atoms arrived at the surface have managed to find their way to the sites characterized by the highest binding energy, from which the electron-stimulated desorption of Li^+ ions in the β_1 phase likely occurs.

Of particular interest is the fact that the yield of Li^+ ions upon electron-stimulated desorption near the threshold of the onset in the desorption (~55 eV) and above additional thresholds (133 and 150 eV) reaches a maximum at different concentrations of deposited lithium (Fig. 7). The yield of Li^+ ions near a threshold of 55 eV reaches a maximum at a lithium concentration of 1.2×10^{14} cm^{-2}, whereas the maximum yield of Li^+ ions above additional thresholds is observed at a lithium concentration of 2.2×10^{14} cm^{-2}. These findings can be accounted for by the specificity of the Li^+ motion in these cases. In the former case, the Li^{2+} ion formed after the ionization of the Li^+ ion begins to move toward the surface due to an increase in the image forces and a weakening of the exchange repulsion.

The interatomic Auger process occurs at the distance X^*. As a result, the Li^{2+} ion again becomes the Li^+ ion, and the Si^- ion transforms into the Si^+ ion. The Coulomb repulsion between the Si^+ and Li^+ ions brings about the desorption of the Li^+ ion. Owing to the repulsion between the adsorbed atoms, the equilibrium distance X_0 between adsorbed atoms and the surface increases with an increase in the lithium concentration. This is accompanied by a decrease in the X^* distance due to an increase in the kinetic energy of the Li^{2+} ion, which it acquires in the field of image forces prior to the Auger process. In the general case, it is quite possible that the X^* distance does not correspond to the point of the closest approach of the Li^{2+} ion and the surface, and, therefore, the Li^+ ion after the interatomic Auger decay can continue to migrate toward the surface. A decrease in the X^* distance with an increase in the lithium concentration should lead to an increase in the probability of the yield of Li^+ ions upon electron-stimulated desorption owing to an enhancement of the repulsion between the Li^+ and Si^+ ions [12]. However, this pattern is not observed. It seems likely that the above effect is less pronounced than a decrease in the lifetime of the Si^+ ion due to the metallization of the adsorbed lithium layer with an increase in its coverage. A different situation arises in the vicinity of additional thresholds at 133 and 150 eV. The feature at ~133 eV in the dependence of the yield of Li^+ on the energy of primary electrons (Fig. 6) can be interpreted as a consequence of the double ionization of the Si^- ion followed by the Auger process [10]. In this case, the Si^- ion transforms into the Si^{2+} ion and begins to displace the Li^+ ion away from the equilibrium distance X_0. About the same situation is observed after the ionization of the Si 2*s* level and the subsequent cascade Auger process.

An increase in the lithium concentration gives rise to the narrow half-filled band of electronic states of lithium. As a consequence, the double ionization of the Si^- ion leads to an increase in the probability of the transfer of an electron to this band during its detachment, which brings about the appearance of the resonance peak at about 133 eV.

At high concentrations of adsorbed lithium, the band of free states becomes wider, and the resonance

peak disappears. As the concentration of adsorbed lithium increases, the equilibrium distance X_0between the adsorbed layer and the surface increases because of repulsion of the adjacent dipoles, which by itself leads to a decrease in the yield of Li^+ ions due to the weakening of the Coulomb repulsion from the Si^{2+} ions [10]. Moreover, the metallization of the adsorbed lithium layer brings about an increase in the probability of the neutralization of the Si^{2+} ions at the expense of collective electrons in the layer. Upon ionization of silicon, the Si^{2+} ions repel the Li^+ ions, and, therefore, the yield of Li^+ ions decreases at a higher concentration of adsorbed lithium as compared to the ionization of a Li^+ ion when the Si^+ ions participate in the repulsion. Apparently, in this case, the charge of the repelling ion plays no significant part in the electron-stimulated desorption process, which is contradictory to the results obtained in the work [13] concerned with the ion recharging on a metallic surface.

Finally, let us discuss the nature of the β_2 phase of Li^+ ions. This phase appears at a threshold of ~55 eV and exhibits no additional features at higher energies of electrons. The maximum yield of Li^+ ions in this phase does not correlate with a change in the silicon amount on the surface upon heating of the ribbon and the silicon deposition. However, the current of Li^+ ions reversibly changes in the range of substrate temperatures from 300 to 800 K. This fact allows us to assume that the β_2 phase of Li^+ ions is associated with carbon atoms, which are displaced by silicon into the bulk of tantalum and, in the regions free of silicon, can reversibly penetrate into the bulk of tantalum or transfer onto the surface with a change in the temperature [14].

ACKNOWLEDGMENTS

This work was supported by the "Surface Atomic Structures" Program of the Ministry of Science and Technology of the Russian Federation (project no. 4.5.99) and, in part, by the Russian Foundation for Basic Research (project no. 99-02-17972).

REFERENCES

1. S. P. Murarka, *Silicides for VLSI Applications* (Academic Press, New York, 1983; Mir, Moscow, 1986).
2. V. G. Lifshits, A. A. Saranin, and A. V. Zotov, *Surface Phases on Silicon: Preparation, Structures, and Properties* (Wiley, New York, 1994).
3. E. Kampshoff, N. Walchli, and K. Kern, Surf. Sci. **406**, 103 (1998).
4. J. H. Weaver, V. L. Moruzzi, and F. A. Schmidt, Phys. Rev. B **23**, 2916 (1981).
5. V. N. Ageev and E. Yu. Afanas'eva, Fiz. Tverd. Tela (S.-Peterburg) **39** (8), 1484 (1997) [Phys. Solid State **39** (8), 1318 (1997)].
6. *Practical Surface Analysis by Auger and X-ray Photoelectron Spectroscopy*, Ed. by D. Briggs and M. Seah (Wiley, New York, 1983; Mir, Moscow, 1987).
7. V. N. Ageev and B. V. Yakshinskiĭ, Fiz. Tverd. Tela (S.-Peterburg) **37** (2), 483 (1995) [Phys. Solid State **37** (2), 261 (1995)].
8. V. N. Ageev and B. V. Yakshinskiĭ, Fiz. Tverd. Tela (Leningrad) **27** (1), 99 (1985) [Sov. Phys. Solid State **27** (1), 57 (1985)].
9. V. N. Ageev, E. Yu. Afanas'eva, N. R. Gall', *et al.*, Poverkhnost **5**, 7 (1987).
10. V. N. Ageev, A. M. Magomedov, and B. V. Yakshinskiĭ, Pis'ma Zh. Tekh. Fiz. **15**, 6 (1989) [Sov. Tech. Phys. Lett. **15**, 234 (1989)].
11. Yu. K. Ustinov, Zh. Tekh. Fiz. **41** (2), 411 (1971) [Sov. Tech. Phys. **16**, 311 (1971)].
12. V. N. Ageev, O. P. Burmistrova, and B. V. Yakshinskii, Surf. Sci. **194**, 101 (1988).
13. M. A. Cazalilla, M. Lorente, R. Díez Muino, *et al.*, Phys. Rev. B **58** (20), 13991 (1998).
14. E. V. Rut'kov, Author's Abstract of Doctoral Dissertation in Mathematical Physics (Ioffe Physicotechnical Institute, St. Petersburg, 1995).

Translated by O. Borovik-Romanova

Physics of the Solid State, Vol. 42, No. 6, 2000, pp. 1160–1163. Translated from Fizika Tverdogo Tela, Vol. 42, No. 6, 2000, pp. 1125–1128.

LOW-DIMENSIONAL SYSTEMS AND SURFACE PHYSICS

DC Electric-Field-Induced Heterophase Structure on the Surface of a Peierls Metal

A. L. Semenov

Ulyanovsk State University, Ulyanovsk, 432700 Russia

e-mail: semenov@quant.univ.simbirsk.su

Received June 29, 1999

Abstract—A theoretical study has been made of the formation of a heterostructure of alternating metallic and semiconducting phases in atomic chains of a Peierls-metal surface monatomic layer placed in an electrostatic field normal to the surface. It is shown that an increase in the electric field results in an increase in the critical temperature of the metal–semiconductor phase transition on the sample surface, an increase in the temperature interval within which the heterostructure exists, a decrease in its spatial period, and an increase in the depth of spatial modulation of the gap in the electronic spectrum. *© 2000 MAIK "Nauka/Interperiodica".*

The Peierls system considered in the present paper is a chain of atoms, with one outer shell electron on each. The Peierls model theoretically describes a number of phenomena occurring in quasi-one-dimensional materials, namely, the metal–semiconductor phase transition and the structural transition taking place simultaneously [1, 2]; the formation and propagation of charge density waves [3, 4]; a shift of the critical temperature of the metal–semiconductor phase transition induced by pressure [5], by doping with substitutional impurities [6–9], by amorphization [2], or by adsorption of molecules from the gas phase, etc. [10]; the strain-induced effect at a phase transition [11]; photoinduced semiconductor–metal phase transition [12]; resonator-less optical bistability with increasing absorption [13–15]; the formation of a photoinduced superstructure with a spatially modulated gap in the electronic spectrum [16–18]; the onset of temporal oscillations of the system parameters under irradiation [19–21], etc.

When a dc electric field is applied to a Peierls dielectric along the chain of atoms, with each having $p \neq 1$ outer shell electrons, a phase transition may occur to a state with a propagating charge-density wave, which is characterized by a high nonlinear electrical conductivity and periodic oscillations of the system parameters in time [3, 22]. If $p = 1$, such a transition does not occur, but, at high electric fields, a semiconductor–metal phase transition may take place [23].

This paper considers a film (or a plane plate) made of a Peierls metal such that the atomic chains are parallel to the film surface. When an external dc electric field is applied perpendicular to the film, the number p of electrons per atom of a chain on the surface becomes other than unity ($\Delta p = p - 1 \neq 0$). In this case, the critical temperatures of a structural phase transition at the surface, T_c, and in the bulk, T_0, are different. As will be shown later, if p deviates from unity little enough, the inequality $T_0 < T_c$ holds, and at temperatures $T \in (T_0, T_c)$a one-dimensional, spatially periodic heterostructure of alternating metallic and semiconducting phases forms in the monatomic layer of a Peierls metal.

1. ELECTRONIC SPECTRUM

The electronic part of the Hamiltonian of an atomic chain can be written in the tight-binding approximation as [2]

$$H = \sum_m B_{m,m+1}(a_m^+ a_{m+1} + a_{m+1}^+ a_m), \qquad (1)$$

where a_m^+ and a_m are the operators of creation and annihilation, respectively, of an electron at the mth atom; the summation in (1) runs over all N atoms of a unit chain length; and $B_{m,m+1}$ is the wave-function overlap integral of adjacent atoms.

For narrow-gap systems (in particular, for the Peierls model), the $r_{m,m+1}$ distances between adjacent atoms exceed the effective radius R of the atomic wave function of the electron severalfold. In this case, the wave-function overlap integral between adjacent atoms, $B_{m,m+1}$, can be approximately written as [24]

$$B_{m,m+1} \sim \exp(-r_{m,m+1}/R), \qquad (2)$$

where

$$r_{m,m+1} = x_{m+1} - x_m, \qquad (3)$$

and x_m is the coordinate of the mth atom along the chain, which, with the inclusion of possible structural

distortions, can be expressed in the form

$$x_m = mr_0 + \frac{R\xi}{2}\cos(\pi m) + \frac{R\zeta}{2}\cos(qm + \varphi). \quad (4)$$

Here, r_0 is the distance between adjacent atoms for an equidistant chain in the high-temperature metallic phase (where $\xi = \zeta = 0$), φ is the initial phase, ξ and ζ are the reduced amplitudes of structural distortions characterizing the pairwise approach of atoms and formation of a static phonon mode with a wave number $q = 2k_f = \pi p$ ($p \neq 1$), respectively, and k_f is the Fermi quasi-wave number of electrons.

Using the Bogolyubov canonical-transformation method [25] and taking (2)–(4) into account, we calculate the electronic spectrum ε_k of the Hamiltonian (1) for the case $\zeta = 0$ [13]

$$\varepsilon_k = -2b\,\mathrm{sgn}(\cos k)\sqrt{\cos^2 k + \sinh^2\zeta}, \quad (5)$$

where $k = 0, \pm 2\pi/N, \pm 4\pi/N, \ldots, \pm\pi$; and b is the wave-function overlap integral of adjacent atoms in the metallic phase ($\xi = \zeta = 0$). In the notation of (1), the wave-function phases are chosen such that b in (5) is positive. The electronic spectrum ε_k described by (5) has gaps of equal width at $k = \pm\pi/2$.

To calculate the electronic spectrum ε_k of the Hamiltonian (1) in the $\xi = 0$ case, where the Peierls system has a static phonon with the wave number $q = p\pi$, we expand the overlap integral (2)–(4) in a Taylor series in the parameter $\zeta \ll 1$ to terms that provide the contribution to ε_k to within ζ^2. As we turn to (1), to collective second-quantization Fermi operators c_k, c_k^+ in accordance with the expression

$$a_n = \frac{1}{\sqrt{N}}\sum_k c_k e^{ikn} \quad (6)$$

we obtain

$$H = \sum_k (E_k c_k^+ c_k + V_{k,k-q} c_k^+ c_{k-q} + V_{k,k+q} c_k^+ c_{k+q}), \quad (7)$$

where

$$E_k = -2b\left(1 + \frac{\zeta^2}{4}\sin^2\left(\frac{q}{2}\right)\right)\cos k, \quad (8)$$

$$V_{k,k\mp q} = \pm ib\zeta\sin\left(\frac{q}{2}\right)\exp(\pm i\varphi)\cos\left(k \mp \frac{q}{2}\right). \quad (9)$$

Using the equation-of-motion method [26], we find from (7) the electronic spectrum ε_k of the Hamiltonian (1) in an implicit form,

$$\varepsilon_k - E_k = \frac{|V_{k,k-q}|^2}{\varepsilon_k - E_{k-q}} + \frac{|V_{k,k+q}|^2}{\varepsilon_k - E_{k+q}}. \quad (10)$$

The electronic spectrum ε_k described by (10) has gaps of equal width at the points $k = \pm q/2, \pm(\pi - q/2)$.

In a general case of $\xi \neq 0$ and $\zeta \neq 0$ and far from the discontinuity points $k = \pm\pi/2, \pm q/2, \pm(\pi - q/2)$, we obtain the following expression for the ε_k spectrum from (5) and (10) to within terms quadratic in ξ and ζ:

$$\varepsilon_k = -2b\cos k - \frac{b\xi^2}{\cos k} - \frac{b\zeta^2\sin(q/2)}{4} \times\left[2\left(1 - \sin\frac{q}{2}\right)\cos k + \frac{1}{\sin(k + q/2)} - \frac{1}{\sin(k - q/2)}\right]. \quad (11)$$

Equation (11) is valid everywhere except close to the singularity points, where the first term on the right-hand side of (11) is no longer dominant.

2. BEHAVIOR IN THE VICINITY OF THE CRITICAL POINT

The free energy of the electronic subsystem of a unit-length atomic chain can be written as

$$F_e = \mu Np - k_B T\sum_k \ln\left(1 + \exp\left(-\frac{\varepsilon_k - \mu}{k_B T}\right)\right), \quad (12)$$

where μ is the chemical potential and k_B is the Boltzmann constant. The free energy of the phonon subsystem F_p can be cast in the harmonic and molecular-field approximations [2] as

$$F_p = \sum_m \frac{\gamma}{2}(r_{m,m+1} - r_0)^2 = \frac{A\xi^2}{2} + \frac{A\zeta^2\sin^2(q/2)}{4}, \quad (13)$$

where γ is the effective lattice stiffness coefficient and $A = \gamma R^2 N$.

The critical temperatures T_1 and T_c for the onset of instabilities of the metallic phase (state with equidistant atoms in the chain) against the formation of static phonon modes with wave numbers π and $p\pi$ are found, respectively, from the equations

$$\left.\frac{\partial^2 F}{\partial\xi^2}\right|_{\xi = \zeta = 0, T_1} = 0, \quad (14)$$

$$\left.\frac{\partial^2 F}{\partial\zeta^2}\right|_{\xi = \zeta = 0, T_c} = 0, \quad (15)$$

where $F = F_e + F_p$ is the total free energy of the Peierls system. Substituting (12) and (13) in (14) and (15) and using (5), (10), and (11), we come to

$$A + 4b^2\int_{-2b}^{2b}\frac{n(E, T_1)\nu(E)}{E}dE = 0, \quad (16)$$

$$A + \int_{-2b}^{2b}\left[E\left(1 - \cos\left(\frac{\pi\Delta p}{2}\right)\right) + \frac{4b^2 E\cos(\pi\Delta p/2)}{E^2 - \mu^2}\right] \times n(E, T_c)\nu(E)dE = 0, \quad (17)$$

where

$$\nu(E) = \frac{2N}{\pi\sqrt{4b^2 - E^2}} \tag{18}$$

is the electronic density of states of the Hamiltonian (1) in the metallic phase ($\xi = \zeta = 0$), and

$$n(E, T) = \left(1 + \exp\left\{\frac{E-\mu}{k_B T}\right\}\right)^{-1} \tag{19}$$

is the Fermi–Dirac distribution.

Taking (18) and (19) into account, we calculate the integrals in (16) and (17) assuming that $|\mu_0| < k_B T_0$ to find the following approximate expressions for the critical temperatures T_1 and T_c:

$$T_1 = T_0 \exp\left\{-\frac{1}{2}\left(\frac{\mu_0}{2k_B T_0}\right)^2 - \frac{1}{12}\left(\frac{\mu_0}{2k_B T_0}\right)^4\right\}, \tag{20}$$

$$T_c = T_0 \exp\left\{\frac{1}{6}\left(\frac{\mu_0}{k_B T_0}\right)^4 + \frac{1}{30}\left(\frac{\mu_0}{k_B T_0}\right)^6\right\}, \tag{21}$$

where

$$T_0 = \frac{2b}{k_B}\exp\left\{1 - \frac{\pi A}{4bN}\right\} \tag{22}$$

is the critical temperature for the metal–semiconductor phase transition in the bulk (where $p = 1$, $\mu = 0$) and

$$\mu_0 = 2b\sin(\pi\Delta p/2) \equiv \pi b \Delta p \tag{23}$$

is the chemical potential in the metallic phase.

A comparison of (20) and (21) leads one to the conclusion that, when a Peierls metal is cooled, first occurs the phase transition at T_c to the state with $\xi = 0$ and $\zeta \neq 0$ at the sample surface, to be followed by the phase transition at $T = T_0$ to the $\xi \neq 0$, $\zeta = 0$ state in the bulk.

The dependence of the order parameter ζ on temperature is given by the equation

$$\left.\frac{\partial F}{\partial \zeta}\right|_{\xi = 0, \zeta, T} = 0. \tag{24}$$

Substituting $F = F_e + F_p$ from (12) and (13) in (24) and assuming $T_c - T_0 \ll T_0$ and $\zeta < \pi|\Delta p|$, for the temperatures $T \in (T_0, T_c)$, we obtain

$$\zeta = \frac{2k_B}{b}\sqrt{T_c(T_c - T)}. \tag{25}$$

As is seen from (25), near the critical point T_c, the $\zeta(T)$ relation follows the pattern typical of second-order phase transitions.

3. HETEROSTRUCTURE IN THE SURFACE MONATOMIC LAYER

Thus, at temperatures $T_0 < T < T_c$, there is a monatomic layer consisting of parallel chains on the surface of a Peierls metal. In these chains, the distances $r_{m, m+1}$ between adjacent atoms, in accordance with (3) and (4), are given by the expression

$$r_{m, m+1} = r_0 - R\zeta\cos\left(\frac{\pi\Delta p}{2}\right) \times \cos\left(\pi\Delta p\left(m + \frac{1}{2}\right) + \varphi\right)\cos(\pi m). \tag{26}$$

In the case of $|\pi\Delta p| < k_B T_0/b \ll 1$ considered here, the structural distortions (26) are a spatially modulated pairwise approach of atoms in the chain with the spatial modulation period $\lambda = 2r_0/|\Delta p|$, which considerably exceeds the average interatomic separation r_0.

Consider a region of the chain whose size l satisfies the condition

$$r_0 \ll l \ll \lambda. \tag{27}$$

In this region, the pairwise approach of atoms may be approximately treated as uniform. Then, the Hamiltonian (1) can be diagonalized exactly and has the form of (5), and the "local" electronic spectrum depending on the coordinate x along the chain can be written as

$$\varepsilon_k(x) = -2b\,\mathrm{sgn}(\cos k) \times \sqrt{\cos^2 k + \sinh^2\left[\zeta\cos\left(\frac{\pi\Delta p}{2}\right)\cos\left(\pi\Delta p\left(\frac{x}{r_0} + \frac{1}{2}\right) + \varphi\right)\right]}. \tag{28}$$

The gap width E_g of the electronic spectrum (28) is given by

$$E_g(x) = 4b\sinh\left|\zeta\cos\left(\frac{\pi\Delta p}{2}\right)\cos\left(\pi\Delta p\left(\frac{x}{r_0} + \frac{1}{2}\right) + \varphi\right)\right|. \tag{29}$$

As is seen from (29), at a temperature $T \in (T_0, T_c)$, the monatomic surface layer of a Peierls metal is a heterostructure of alternating metallic and semiconducting phases with a spatial period

$$d = r_0/|\Delta p|, \tag{30}$$

which is inversely proportional to the number Δp of excess electrons at each surface atom.

4. NUMERICAL ESTIMATES AND DISCUSSION

To make numerical estimates, we recall that the excess number of electrons $\Delta p = p - 1$ per surface atom, which are induced by an electric field E, is given by the approximate expression

$$|\Delta p| = \frac{E r_0^2}{4\pi q}, \tag{31}$$

where q is the electronic charge. Equation (31) was derived under the assumption that the characteristic distance between all neighboring atoms at the surface is approximately equal to the average distance r_0 between the adjacent atoms in a chain.

We shall make numerical estimates for vanadium dioxide, the bulk sample of which undergoes a metal–semiconductor phase transition at $T_0 = 340$ K (formation of a gap at the Fermi level in a one-dimensional conduction band produced by the overlap of the vanadium 3d wave functions along the C crystal axis) accompanied by pairwise approach of vanadium atoms along the C crystal axis [1].

Setting the numerical values of the parameters characteristic of VO_2 [1]: $r_0 \approx 3 \times 10^{-8}$ cm, $b \approx 0.25$ eV, and putting $E \approx 4 \times 10^7$ V/cm $\approx 1.3 \times 10^5$ CGSE, from (31), (30), (23), (21), (25), and (29) we obtain, respectively, $|\Delta p| \approx 1.9 \times 10^{-2}$, the heterostructure period $d \approx 1.6 \times 10^{-6}$ cm, $|\mu_0| \approx 1.7 \times 10^{-2}$ eV, the temperature interval within which the heterostructure exists at the surface of a Peierls metal

$$T_c - T_0 \cong \frac{T_0}{6}\left(\frac{\mu_0}{k_B T_0}\right)^4 \approx 7 \text{ K},$$

the maximum value of the order parameter $\zeta_0 = \zeta(T = T_0) \approx 3 \times 10^{-2}$, and the maximum gap width at the center of a semiconducting heterostructure domain $E_{g0} = \max\{E_g(T = T_0)\} \approx 3.3 \times 10^{-2}$ eV.

In conclusion, we note that the formation of a heterostructure of alternating metallic and semiconducting phases in a surface monatomic layer of a Peierls metal within the temperature region $T_0 < T < T_c$, considered in this work, is essentially based on the fact that $T_0 < T_c$ in (21). This result is a consequence of keeping nonlinear terms in the expansion of the overlap integral $B_{m,m+1}(\zeta)$, given by (2)–(4), in the ζ parameter.

The critical temperature T_0 of the metal–semiconductor phase transition in vanadium dioxide was experimentally observed to increase by $\Delta T \approx 2$ K in a corona discharge of both polarities [10]. The effective uniform electrostatic field estimated from the Stark shift was found to be $E \sim 10^8$ V/cm. Thus, this experimental result supports the theoretical conclusion drawn in this work that an electrostatic field, irrespective of its polarity, should increase T_0.

REFERENCES

1. A. A. Bugaev, B. P. Zakharchenya, and F. A. Chudnovskiĭ, *The Metal–Semiconductor Phase Transition and Its Applications* (Nauka, Leningrad, 1979).
2. L. N. Bulaevskiĭ, Usp. Fiz. Nauk **115** (2), 263 (1975) [Sov. Phys. Usp. **18**, 131 (1975)].
3. G. Grüner, Rev. Mod. Phys. **60** (4), 1129 (1988).
4. S. N. Artemenko, A. F. Volkov, and S. V. Zaĭtsev-Zotov, Usp. Fiz. Nauk **166** (4), 434 (1996) [Phys. Usp. **39**, 403 (1996)].
5. V. I. Emel'yanov, N. L. Levshin, and A. L. Semenov, Vestn. Mosk. Univ., Ser. 3: Fiz., Astron. **30** (5), 52 (1989).
6. V. I. Emel'yanov, N. L. Levshin, and A. L. Semenov, Fiz. Tverd. Tela (Leningrad) **31** (10), 261 (1989) [Sov. Phys. Solid State **31** (10), 1803 (1989)].
7. V. I. Emel'yanov, N. L. Levshin, and A. L. Semenov, Vestn. Mosk. Univ., Ser. 3: Fiz., Astron. **31** (5), 99 (1990).
8. A. L. Semenov, Fiz. Tverd. Tela (St. Petersburg) **36** (7), 1974 (1994) [Phys. Solid State **36** (7), 1079 (1994)].
9. A. L. Semenov and S. V. Sukhov, Izv. Vyssh. Uchebn. Zaved. Fiz., No. 6, 120 (1996).
10. V. I. Emel'yanov, N. L. Levshin, S. Yu. Poroĭkov, and A. L. Semenov, Vestn. Mosk. Univ., Ser. 3: Fiz., Astron. **32** (1), 63 (1991).
11. A. L. Semenov, Fiz. Tverd. Tela (St. Petersburg) **39** (5), 925 (1997) [Phys. Solid State **39** (5), 826 (1997)].
12. A. L. Semenov, Fiz. Tverd. Tela (St. Petersburg) **40** (11), 2113 (1998) [Phys. Solid State **40** (11), 1915 (1998)].
13. A. L. Semenov, Zh. Éksp. Teor. Fiz. **111** (4), 1398 (1997) [JETP **84**, 774 (1997)].
14. H. Gibbs, *Optical Bistability: Controlling Light with Light* (Academic Press, New York, 1985; Mir, Moscow, 1988).
15. A. L. Semenov, Zh. Éksp. Teor. Fiz. **114**, 1407 (1998) [JETP **87**, 764 (1998)].
16. A. L. Semenov, Zh. Éksp. Teor. Fiz. **115** (4), 1297 (1999) [JETP **88**, 716 (1999)].
17. K. F. Berggren and B. A. Huberman, Phys. Rev. B **18** (7), 3369 (1978).
18. V. V. Kapaev, Yu. V. Kopaev, and S. N. Molotkov, Mikroélektronika **12** (6), 499 (1983).
19. Yu. V. Kopaev, V. V. Menyaĭlenko, and S. N. Molotkov, Zh. Éksp. Teor. Fiz. **89**, 1404 (1985) [Sov. Phys. JETP **62**, 813 (1985)].
20. I. M. Suslov, Pis'ma Zh. Éksp. Teor. Fiz. **39** (12), 547 (1984) [JETP Lett. **39** (12), 670 (1984)].
21. V. B. Stopachinskiĭ and I. M. Suslov, Zh. Éksp. Teor. Fiz. **91**, 314 (1986) [Sov. Phys. JETP **64**, 183 (1986)].
22. V. E. Minakova, Yu. I. Latyshev, and V. A. Volkov, Pis'ma Zh. Éksp. Teor. Fiz. **62** (5), 442 (1995) [JETP Lett. **62** (5), 455 (1995)].
23. I. V. Krive and A. S. Rozhavskiĭ, Zh. Éksp. Teor. Fiz. **81**, 1811 (1981) [Sov. Phys. JETP **54**, 959 (1981)].
24. O. Madelung, *Introduction to Solid State Theory* (Springer-Verlag, Berlin, 1978; Nauka, Moscow, 1985).
25. N. N. Bogolyubov and N. N. Bogolyubov, Jr., *Introduction to Quantum Statistical Mechanics* (Nauka, Moscow, 1984; World Scientific, Singapore, 1982).
26. C. Kittel, *Quantum Theory of Solids* (Wiley, New York, 1963; Nauka, Moscow, 1967).

Translated by G. Skrebtsov

Physics of the Solid State, Vol. 42, No. 6, 2000, pp. 1164–1169. Translated from Fizika Tverdogo Tela, Vol. 42, No. 6, 2000, pp. 1129–1133.

LOW-DIMENSIONAL SYSTEMS AND SURFACE PHYSICS

Metal–Semiconductor Transitions Induced by Adsorption of Alkali Metals on the Si(001) Surface

S. Yu. Davydov

Ioffe Physicotechnical Institute, Russian Academy of Sciences, Politekhnicheskaya ul. 26, St. Petersburg, 194021 Russia

Received August 5, 1999; in final form, October 11, 1999

Abstract—The changes in the electronic structure of the surface layer of a semiconductor substrate have been studied with allowance made for the indirect and dipole–dipole interactions between adatoms. The conditions for the formation and suppression of gaps in the energy band of surface states of the substrate are determined as a function of the adatom coverage of the surface. The results obtained are used in the interpretation of the metal–semiconductor transitions upon adsorption of cesium and sodium atoms on the Si(001) surface. © *2000 MAIK "Nauka/Interperiodica".*

1. INTRODUCTION

In recent years, particular attention has been focused on investigations into the adsorption of alkali metals on the semiconductor surface [1–5]. By now, the adsorption of alkali metals on the (001) surface of silicon is best understood, because this system is a convenient model in studies of the metallization of a semiconductor surface. However, it has become common practice to begin almost all publications concerning this problem with the statement that, despite all efforts, there is no consensus of opinion among researchers regarding the geometry of the Si(001) surface, the most favorable adsorption sites, the coverage corresponding to a monolayer, and the character of an adsorbate–substrate interaction. In our opinion, a similar assertion is too pessimistic. Actually, the majority of researchers have believed that the Si(001) upper layer is formed by rows of the Si–Si asymmetric dimers, which, in turn, make up the 2×1 structure at room temperature. Sodium, potassium, and cesium atoms are adsorbed at the *T3* and *HH* sites (Fig. 1; see [6, 7] and references cited therein). A monolayer coverage corresponds to two alkali metal atoms per a 2×1 surface unit cell (according to the Abukawa–Kono double-layer model [8]) when all the *T3* and *HH* sites are occupied. It should be noted that another geometry of the adsorbed layer can also be realized upon adsorption of lithium atoms [9, 10], as is the case of the low-temperature adsorption of sodium [11] and cesium [12] atoms. As regards the nature of the alkali metal–adsorbate bonding, some controversies as to whether this bond is covalent or ionic are not a specific problem of alkali metal adsorption on silicon but go back to Ishida's work [13] concerned with the adsorption of alkali metals on metals. We suppose that the seemingly essential difference in the description of the adatom–adsorbate bond as a polarized covalent bond [7, 13, 14] and a heteropolar (ionic) bond [15–17] proposed in the classical Gurney work [18] arises from the incorrectly defined concept of effective charge of an adatom. Since the adsorption of alkali metals on the semiconductor surface leads to a considerable decrease in the work function of the adsorption system (see, for example, [9, 11, 16]), it is reasonable to believe that the adatom–adsorbate bond is ionic in nature.

Among the most intriguing effects brought about by adsorption of alkali metals are the metal–semiconductor phase transitions ($M \longrightarrow S$). For example, in the Na/Si(001) and Cs/Si(001) systems, these transitions occur with a variation in the adatom concentration on the surface [19–21]. Similar transitions are also observed on other substrates: Na (Cs)/Si(111) [22], GaAs(110) [23], and silicon carbide [24–27].

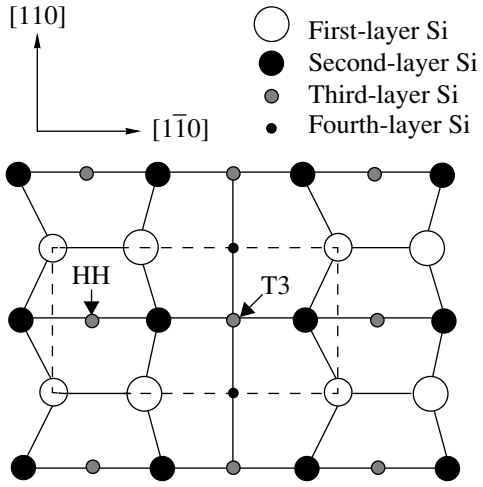

Fig. 1. The Si(001)-(2×1) structure with asymmetric dimers (taken from [7]). The dashed line represents a surface unit cell.

1063-7834/00/4206-1164$20.00

It is well known that the surface states play a crucial role in the adsorption on silicon [1–5]. These states are located in the bulk forbidden energy band and form two bands separated by a gap. These bands arise as a result of the π-interaction between the dangling sp^3 orbitals and correspond to the bonding and antibonding states. At $T = 0$, the low-lying π band is filled, and the higher-energy π* band is empty. In the problem on adsorption, we can restrict ourselves to the case of only the empty π* band by assuming that the occupation of the π band in the course of adsorption does not undergo substantial changes [16]. In this formulation, the problem on adsorption onto the semiconductor substrate differs not at all from the problem on adsorption onto a narrow-band-gap metal, which will be used in the subsequent consideration.

As a rule, the metal–semiconductor transitions are interpreted in the framework of the Hubbard model [6–10, 12], in which the formation of the energy gap in a continuous band is explained by the intraatomic Coulomb repulsion U of electrons on surface atoms of a substrate. In the present work, without invoking many-particle effects, we demonstrated that the energy gap opens as a result of the indirect (through a substrate) electron exchange between adatoms [28]. Moreover, taking into account the dipole–dipole interaction between the adatoms, we determined the conditions for suppression ("collapse") of the gap.

2. INDIRECT EXCHANGE AND DIPOLE–DIPOLE REPULSION IN ADSORBED LAYER

The indirect interaction between one-electron atoms adsorbed on a metallic surface was considered in our earlier works [29, 30]. In [29], it was shown that the integral density of states (i.e., the density of states for the structureless layer of adatoms) in the surface layer of a substrate ρ_s is determined by the relationship

$$\rho_s(\omega) = (1/\pi D)F(\omega),$$
$$F(\omega) = \arctan\{[\omega + D - \theta V^2/(\omega - \varepsilon_a)]/\gamma\} - \arctan\{[\omega - D - \theta V^2/(\omega - \varepsilon_a)]/\gamma\}. \quad (1)$$

Here, ω is the energy; D and γ are the parameters of the density of states of the initial substrate ρ_s^0 [31], which can be represented as a combination of the parallel $\rho_{s\parallel}^0$ and perpendicular $\rho_{s\perp}^0$ components

$$\rho_{s\parallel}^0 = \begin{cases} 1/2D, & |\omega| \le D, \\ 0, & |\omega| > D, \end{cases} \qquad \rho_{s\perp}^0 = \frac{1}{\pi}\frac{\gamma}{\omega^2 + \gamma^2}, \quad (2)$$

V is the matrix element of the adatom–substrate interaction; ε_a is the energy of the adatom level; and θ is the coverage ($0 \le \theta \le 1$). The energy is reckoned from the center of the band of the initial substrate. Relationships (2) were deduced under the assumption that $\theta \ne 0$.

Let us now take into account the dipole–dipole repulsion of adatoms and assume that this repulsion leads to a nonuniform distribution of electron density in the adsorbed layer, i.e., to an alternation of charges of the adjacent adatoms $Z_\pm = Z(1 \pm c)$, where the order parameter c is the number determined in a self-consistent way [32]. This results in the formation of the (+) and (–) sublattices of adatoms. It can be shown that the energy of the adatom level ε_a, in this case, is split and transforms to

$$\varepsilon_a^\pm = \varepsilon_a' \pm \delta, \quad \delta = c\nu\xi\theta^{3/2}Z,$$
$$\varepsilon_a' = \varepsilon_a - \xi\theta^{3/2}Z, \quad \xi = 2e^2l^2N_{\mathrm{ML}}^{3/2}A_0, \quad (3)$$

where the dimensionless parameters A_0 and ν are determined by the geometry of the adatom lattice [32], e is the elementary electronic charge, l is one-half the arm of a surface dipole formed by an adsorbed ion and its image in the substrate, and N_{ML} is the concentration of adatoms in the monolayer. Substitution of $\varepsilon_a^\pm$ for ε_a in formulas (1) gives the density of states $\rho_s^\pm$ This state of the adsorbed layer and the surface layer of the substrate will be referred to as the nonuniform charge distribution (NCD). In the case of uniform charge distribution (UCD), i.e., at $c = 0$, the energies of levels $\varepsilon_a^\pm$ transform to ε_a'.

In order to illustrate how the density of states of the adsorption system changes under the action of an indirect exchange and the dipole–dipole repulsion of adatoms, we consider the simple example. As follows from expressions (2), in the limit $\gamma \longrightarrow 0$, the band of the clean (free of adatoms) substrate becomes two-dimensional: the density of its states is represented by a rectangle with the height $(2D)^{-1}$ in the energy range $-D \le \omega \le D$. This model corresponds to the simplest description of the π* band of surface states in the Si(001) substrate.

It follows from relationship (1) that, in the case of uniform charge distribution, there are four characteristic points of the type $(\varepsilon_a' - D \pm R_-')/2$ and $(\varepsilon_a' + D \pm R_+')/2$ on the energy scale. Here, $R_\pm' = \sqrt{(\varepsilon_a' \pm D)^2 + 4\theta V^2}$, which determines the boundaries of subbands (see below). For the nonuniform charge distribution, when each ε_a' level is split into two levels $\varepsilon_a^\pm$ [32], the number of these points is doubled. Depending on the ratio between the energy parameters entering into these expressions, the characteristic points on the energy scale can be arranged in a different order.

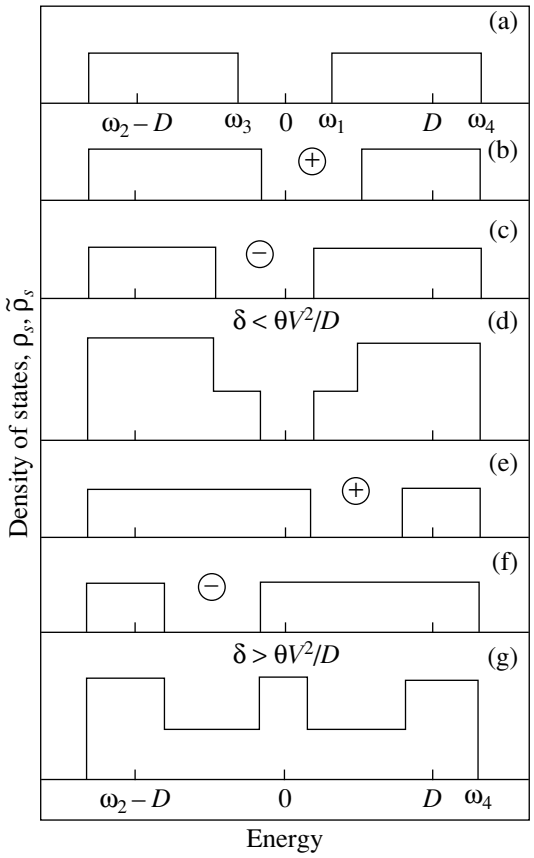

Fig. 2. Evolution of the density of states of the substrate surface upon transition from (a) the state with a uniform charge distribution to (b–g) the state with a nonuniform charge distribution in the limit $4\theta(V/D)^2 \ll 1$. Density of states: (a) ρ_s, (b, e) ρ_s^+, (c, f) ρ_s^-, and (d, g) $\tilde{\rho}_s = \rho_s^+ + \rho_s^-$. Parameter δ: (b, c, d) $\delta < \theta V^2/D$ and (e, f, g) $\delta > \theta V^2/D$. Densities of states ρ_s and $\tilde{\rho}_s$ correspond to the monoatomic and diatomic surface unit cells, respectively. Designations (±) refer to the (±) sublattices of adatoms.

Now, we consider the limit

$$4\theta(V/D)^2 \ll (1 \pm \varepsilon_a'/D)^2 \tag{4}$$

and assume that $\varepsilon_a' = 0$. Then, according to relationships (3), we can write $\varepsilon_a^\pm = \pm\delta$.

At the uniform charge distribution, the density of states of the substrate ρ_s is split into two subbands (Fig. 2a, in which $\omega_{1,3} = \pm\theta V^2/D$ and $\omega_{2,4} = \mp D \mp \theta V^2/D$. The gap in the spectrum is $\Delta = \omega_1 - \omega_2 = 2\theta V^2/D$. The widths of both bands $W_{41} = \omega_4 - \omega_1$ and $W_{32} = \omega_3 - \omega_2$ are equal to D.

The densities of states $\rho_s^\pm$ at the nonuniform charge distribution are depicted in Figs. 2b–2g. The sign "plus" (Figs. 2b, 2e) refers to the density of states ρ_s^+ of surface atoms of the adatom sublattice with the charges $Z_+ = Z(1 + c)$, and the sign "minus" (Figs. 2c, 2f) refers to the density of states ρ_s^- of surface atoms of the adatom sublattice with the charges $Z_- = Z(1 - c)$. In this case, the parameters ω_k are transformed to $\omega_k^\pm$ (where $k = 1, \ldots, 4$), that is,

$$\omega_1^\pm = \pm\delta + \theta V^2/D, \quad \omega_2^\pm = -D - \theta V^2/D,$$
$$\omega_3^\pm = \pm\delta - \theta V^2/D, \quad \omega_4^\pm = D + \theta V^2/D, \tag{5}$$
$$\tilde{W}_{41}^\pm = |D \mp \delta|, \quad \tilde{W}_{32}^\pm = |D \pm \delta|, \quad \Delta = 2(\theta V^2/D - \delta).$$

From formulas (5), it follows that the gap Δ exists only with the constraint

$$\delta < \theta V^2/D, \tag{6}$$

This corresponds to Fig. 2d, which depicts the total density of states $\tilde{\rho}_s = \rho_s^+ + \rho_s^-$ of the unit cell consisting of two atoms in the case of the nonuniform charge distribution. At the condition

$$\delta \geq \theta V^2/D \tag{7}$$

the energy gap is absent (Fig. 2g). Substitution of the δ parameter from relationship (3) into expression (7) gives the condition for the collapse of the gap

$$\theta \geq \theta_C = (V^2/Dc\nu\xi Z)^2. \tag{8}$$

Here, one additional remark is necessary. As was shown earlier in [32], the state with a nonuniform charge distribution arises only under certain conditions, specifically in the case when the coverage θ exceeds some critical value θ_b. Therefore, the sufficient condition for the gap collapse is the fulfillment of the inequality

$$\theta_b \leq \theta_C \leq \theta, \tag{9}$$

whereas relationship (8) corresponds only to the necessary condition. It is clear that the gap collapse also becomes possible in a more general case when $|\varepsilon_a'| \ll D$.

Let us consider the three-dimensional case under the assumption that $\gamma \neq 0$. By using relationship (1) and replacing ε_a by $\varepsilon_a^\pm$, it is easy to show that, at $\omega \longrightarrow \varepsilon_a^+$, the density of states

$$\rho_s^\pm \longrightarrow \frac{2\gamma}{\pi\theta^2 V^4}(\omega - \varepsilon_a^\pm)^2, \tag{10}$$

that is, the minima of the density of states ρ_s correspond to the energies $\varepsilon_a^\pm$. The maxima of ρ_s take place at the energies

$$\Omega_{1,2}^\pm = (\varepsilon_a^\pm \mp R^+)/2,$$
$$R^\pm = \sqrt{(\varepsilon_a^\pm)^2 + 4\theta V^2}, \tag{11}$$

where subscripts 1, 2 correspond to signs $\mp$ before the radical $R^{\pm}$. Therefore, the band is split into two subbands for each sublattice: the upper subband (antibonding) with maxima at $\omega = \Omega_2^{\pm}$ and the lower subband (bonding) with maxima at $\omega = \Omega_1^{\pm}$. The separation between the maxima of the densities of states $\rho_s^{\pm}$ for the $Z^{\pm}$ sublattices is equal to $R^{\pm}$. Consequently, allowance made for the three-dimensionality leads only to the smearing (smoothing) of the densities of states ρ_s, $\rho_s^{\pm}$, and $\tilde{\rho}_s$.

The sufficient condition for the gap collapse in the three-dimensional spectrum is the overlap of the minimum of the density of states of one sublattice with the maximum of the density of states of the other sublattice

$$\varepsilon_a^+ = \Omega_2^-, \quad \varepsilon_a^- = \Omega_1^+. \tag{12}$$

It can be easily shown that a set of equations (12) possesses a solution only with the constraint $\varepsilon_a^+ + \varepsilon_a^- = 0$, which results in $\varepsilon_a' = 0$ and $\varepsilon_a^{\pm} = \pm\delta$. Substituting the δ parameter from relationship (3), we obtain

$$\theta_C = V\sqrt{2}/c\nu\xi Z. \tag{13}$$

It is interesting to note that, unlike the purely two-dimensional case [see relationship (8)], criterion (13) does not involve the D parameter, which is a consequence of the smearing of the density of states.

3. METAL–SEMICONDUCTOR TRANSITION IN THE ALKALI METAL/SI(001) SYSTEM

Let us apply the above results to the interpretation of the experimental data obtained by Lee and Chung [19], who studied the adsorption of Cs and Na atoms on the Si(001) surface. These authors [19] revealed that, at small coverages, the Si(001)-(2×1) surface becomes metallic; i.e., the semiconductor–metal transition takes place. As the coverage θ increases, there occurs the metal–semiconductor transition, which is attended by the structural rearrangement of the adsorbed layer: the adsorption of sodium leads to the formation of the (4×1) structure, and the adsorption of cesium gives rise to the (2×3) structure. A further increase in the concentration of sodium atoms does not change the semiconductor properties of the Si(001) surface, whereas an increase in the cesium concentration again leads to the semiconductor–metal transition.

Before proceeding to the application of the above theoretical results for the explanation of the experimental data, it is necessary to evaluate the model parameters for the Na/Si(001) and Cs/Si(001) systems. As is known, the electron affinity of silicon χ is equal to 3.99 eV [33]. From the data obtained in [7, 34], we find the location of the center of the π^* band, that is, $E_s \cong -4.4$ eV with respect to vacuum, and, according to [16], assume that $D = 0.17$ eV. Since the ionization potentials I for cesium and sodium are known (3.89 and 5.14 eV, respectively [35]), it is possible to calculate the locations of atomic levels for cesium ($\varepsilon_a^0 = 0.51$ eV) and sodium ($\varepsilon_a^0 = -0.74$ eV) with respect to the center of the π^* band. To take into account the Coulomb shift of the atomic level ($e^2/4l$) [36], we multiply it into the dielectric correction $(\varepsilon_0 - 1)/(\varepsilon_0 + 1)$ [37], where the dielectric constant ε_0 for silicon is equal to 11.7 [25]. The first principles calculations for the Na/Si(001) and K/Si(001) systems [20] showed that the distance between the adatom and the midpoint of the Si–Si dimer at coverages $\theta < 0.5$ is very close to the value of ionic radii r_i for sodium and potassium, whereas at larger coverages, this distance is close to their atomic radii r_a. In this respect, for simplicity, we assume that one-half the arm of a dipole l is equal to the half-sum of radii r_i and r_a; i.e., $l = (r_a + r_i)/2$, which gives $l = 2.24$ and 1.39 Å for Cs and Na, respectively [35]. Then, we obtain $\varepsilon_a = 1.86$ eV for cesium and $\varepsilon_a = 1.44$ eV for sodium. It immediately follows that, at coverages close to zero, when the interaction between adatoms can be ignored, the electrons transfer from the high-lying energy levels of adatoms to the empty π^* band. Consequently, the semiconductor–metal transition takes place, which is actually observed in the experiments [19–21]. As the adatom concentration increases, the indirect exchange results in the formation of two subbands, and, according to relationship (3), the dipole–dipole interaction leads to a shift of the centers of gravity of these subbands. Further estimations require the knowledge of the dipole shift parameter ξ and the charge Z of adatoms in the state with a uniform charge distribution.

The structure of alkali metal films on the Si(001) surface is complex. It is assumed that, at small coverages $\theta \le 0.5$, the adatoms occupying the *T3* sites form chains, whereas at $\theta > 0.5$, the adatoms begin to fill the *HH* sites (Fig. 1). For the calculation of the ξ parameter defined by relationship (3), let us assume that $A_0 = 9$, which corresponds to a square lattice [38]. By using the lattice constant for silicon, taken from [39], we find $N_{\mathrm{ML}} = 6.78 \times 10^{14}$ cm^{-2}. Then, according to formula (3), the values of ξ for Cs and Na are equal to 22.97 and 8.85 eV, respectively. The ν parameter required to estimate the splitting of the band in the state with a nonuniform charge distribution [see relationships (3)] can be found by the direct calculation: $\nu = 0.5$.

The charge Z of adatoms and the location of their quasi-levels ε_a' can be determined from the data on the change in the work function $\Delta\phi$ of the Si(001) surface upon adsorption of cesium and sodium [16, 19, 40]. It is known (see, for example, [41, 42]) that the value of $\Delta\phi$ can be calculated by the relationship

$$\Delta\phi = -\theta Z\Phi, \quad \Phi = 4\pi e^2 l N_{\mathrm{ML}}. \tag{14}$$

As a result, we obtain $\Phi = 27.48$ and 17.06 eV for cesium and sodium, respectively. Unfortunately, in the majority of recent works (the exception is the work of Kato *et al.* [16]), the data on $\Delta\phi$ are given depending on the time (or dose) of deposition of the adsorbed film rather than on the coverage θ. Clearly, this decreases the accuracy of evaluating the charge Z from formula (14). By using the data taken from [16, 19] and assuming that, at $\theta = 0.1$, the decrease in the work function $\Delta\phi$ is equal to ~–2 eV for cesium and ~–1 eV for sodium, we obtain $Z \approx 0.7$ and ≈0.59 for Cs and Na, respectively. In this case, ε_a'(Cs) ≈ 1.3 eV, and ε_a'(Na) ≈ 1.2 eV. Under the assumption that, at $\theta = 0.25$, $\Delta\phi$ ~ –3 eV for Cs and ~–2 eV for Na, we find $Z \approx 0.4$ and ≈0.5 for Cs and Na, respectively. Then, ε_a'(Cs) ≈ 0.6 eV, and ε_a'(Na) ≈ 0.9 eV. Therefore, at intermediate coverages, the quasi-levels of sodium and cesium are located, as before, considerably higher than the center of the band. Consequently, according to relationship (13), the transition to the gap-free state is impossible (this can also be easily shown for the two-dimensional case). Thus, the Na/Si(001) and Cs/Si(001) systems gain the gap in the spectrum due to the indirect exchange and retain the semiconductor state at intermediate coverages. The energy gap Δcan be very roughly evaluated as the difference between the maxima of the density of states ρ_s, i.e., as being equal to R [see formula (11)], which naturally leads to an overestimated value of Δ Setting $V = D$, we arrive at $R \approx 0.6$ eV and ≈1.0 eV for cesium and sodium, respectively ($\theta = 0.5$). The experimental value of Δ is equal to 0.2 eV for Cs and 0.6 eV for Na [19]. Taking into account that $\Delta < R$, our result should be treated as satisfactory.

Now, we consider the case when $\theta \sim 0.5$. Putting $\Delta\phi$ ~ –3 eV for Cs and ~–2 eV for Na, we obtain $Z \approx 0.2$ for Cs and Na, and, correspondingly, ε_a'(Cs) ≈ 0 eV and ε_a'(Na) ≈ 0.68 eV. Note that the cesium quasi-level ε_a' lying above the sodium quasi-level at zero coverage becomes below it at larger coverages. This is due to the larger parameter of the dipole–dipole shift ξ for cesium as compared to that for sodium. Since the quasi-level of sodium is located, as before, substantially higher than the center of the π^* band, the gap in the spectrum of the Na/Si(001) system is retained. In this case, $\Delta < R \approx$ 1 eV. On the other hand, the quasi-level of cesium overlaps with the center of the π^* band, i.e., satisfies criterion (13). Consequently, if the transition from the state with a uniform charge distribution to the state with a nonuniform charge distribution is possible in the Cs/Si(001) system at large coverages, it will be accompanied by the semiconductor–metal transition.

In order to reveal the possibility of the transition from the state with a uniform charge distribution to the state with a nonuniform charge distribution, it is necessary to demonstrate that the state with nonzero order parameter c determining the difference in the charges of adatoms in the ($\pm$) sublattices takes place (it can be shown that, if the state with a nonuniform charge distribution is possible, this state is favorable [32]). With the relationship for the density of states ρ_s of an adatom at $\theta = 1$, taken from [29] (with the appropriate replacement of ε_a by $\varepsilon_a^\pm$), we obtain the densities of states $\rho_a^\pm$ of adatoms in the sublattices

$$\rho_a^\pm(\omega) = [V^2/\pi D(\omega - \varepsilon_a^\pm)^2]F(\omega), \tag{15}$$

where $F(\omega)$ is defined by expression (1). When only the low-lying ($\pm$) subbands are filled, we have (in the limit $\gamma \longrightarrow 0$)

$$n_a^\pm = \frac{V^2}{\pi D}\frac{\varepsilon_F - \omega_2^\pm}{(\varepsilon_F - \varepsilon_a^\pm)(\omega_2^\pm - \varepsilon_a^\pm)}, \tag{16}$$

where ε_F is the energy of the Fermi level. Since the π^* band is initially empty, the location of the Fermi level should be self-consistently determined from the condition for conservation of the number of electrons in the system, which can be written as

$$n_s + n_a = 1, \quad n_{s,a} = (n_{s,a}^+ + n_{s,a}^-)/2, \tag{17}$$

where $n_{s(a)}$ is the mean occupation number of the surface band (of an adatom) per one surface atom. On the other hand, reasoning from the form of the density of states of the two-dimensional substrate (Fig. 2), it can be easily shown that

$$n_s = (\varepsilon_F - \omega_2^+)/\tilde{W}_{32}^+ + (\varepsilon_F - \omega_2^-)/\tilde{W}_{32}^-. \tag{18}$$

By determining ε_F from relationships (17) and (18) and substituting its value into formula (16), we obtain the self-consistent equations for determination of the occupation numbers of the bands (adatoms). The charge order parameter $c \neq 0$ is found from the equation

$$\begin{aligned} 2cZ = (V^2/\pi D)[&(\varepsilon_F - \omega_2^-)/(\varepsilon_F - \varepsilon_a^-)(\omega_2^- - \varepsilon_a^-) \\ &- (\varepsilon_F - \omega_2^+)/(\varepsilon_F - \varepsilon_a^+)(\omega_2^+ - \varepsilon_a^+)]. \end{aligned} \tag{19}$$

Since $n_a = 0.77$, $n_s = 0.23$, and $\varepsilon_a^\pm = \pm\delta$, we obtain (under the assumption that $V = D$) $\delta = 0.30$ ($c = 0.32$), which corresponds to the fulfillment of inequality (7). Therefore, the transition from the state with a uniform charge distribution to the state with a nonuniform charge distribution takes place and, in the two-dimensional case, leads to the collapse of the energy gap in the π^* band. In the three-dimensional case, according to expression (13), we have $\theta_C \approx 0.4$, which is in good agreement with the initial assumption $\theta \sim 0.5$. This implies that the transition from the state with a uniform charge distribution to the state with a nonuniform charge distribution and the semiconductor–metal transition occur in the Cs/Si(001) adsorption system at large coverages, which was observed in the experiments [19–21].

The above (rather approximate) estimates demonstrate that, in principle, the metal–semiconductor transitions in the Na/Si(001) and Cs/Si(001) systems can be explained by the indirect and dipole–dipole interactions between atoms in the adsorbed layer rather than by the intraatomic Coulomb repulsion U of electrons at an adatom (the Hubbard model). At the same time, a rather large number of physically "transparent" but difficultly determined parameters involved in our model make it impossible to unambiguously argue that it is this mechanism of the interaction between adatoms that is responsible for the transitions observed. The solution of this problem calls for further experimental and theoretical investigations.

ACKNOWLEDGMENTS

This work was supported by the "Surface Atomic Structures" Program of the Ministry of Science and Technology of the Russian Federation (project no. 4.5.99).

REFERENCES

1. D. Haneman, Rep. Prog. Phys. **50** (8), 1045 (1987).
2. F. J. Himpsel, Surf. Sci. Rep. **12** (1), 1 (1990).
3. S. Pick, Surf. Sci. Rep. **12** (3), 99 (1991).
4. *Theoretical Approaches to Metal–Semiconductor Interfaces*, Ed. by A. Hiraki (Ohmsha Ltd., Tokio, 1995).
5. G. P. Srivastava, Rep. Prog. Phys. **60** (5), 561 (1997).
6. H. Hamamatsu, H. W. Yeom, T. Yokoyama, *et al.*, Phys. Rev. B **57**, 11883 (1998).
7. K. Kobayashi, Y. Morikawa, K. Terakura, and S. Blügel, Phys. Rev. B **45**, 3469 (1992).
8. T. Abukawa and S. Kono, Phys. Rev. B **37**, 9097 (1988).
9. C. Y. Kim, K. S. Shin, K. D. Lee, and J. W. Chung, Surf. Sci. **324**, 8 (1995).
10. K. D. Lee, C. Y. Kim, and J. W. Chung, Surf. Sci. **366**, L709 (1996).
11. Y.-J. Ko, K. J. Chang, and J.-Y. Yi, Phys. Rev. B **51**, 4329 (1995).
12. Y.-C. Chao, L. S. O. Johansson, and R. I. G. Uhrberg, Phys. Rev. B **56**, 15446 (1997).
13. H. Ishida, Phys. Rev. B **38**, 8006 (1988).
14. H. Ishida and K. Terakura, Phys. Rev. B **40**, 11519 (1989).
15. S. Ciraci and I. P. Batra, Phys. Rev. Lett. **56**, 877 (1986).
16. T. Kato, K. Ohtomi, and M. Nakayama, Surf. Sci. **209**, 131 (1989).
17. I. P. Batra, Phys. Rev. B **43**, 12322 (1991).
18. R. W. Gurney, Phys. Rev. **47**, 479 (1935).
19. K. D. Lee and J. W. Chung, Phys. Rev. B **55** (19), 12906 (1997).
20. Y.-C. Chao, L. S. O. Johansson, and R. I. G. Uhrberg, Phys. Rev. B **54**, 5901 (1996).
21. Y.-C. Chao, L. S. O. Johansson, and R. I. G. Uhrberg, Phys. Rev. B **55**, 7198 (1997).
22. K. D. Lee and J. W. Chung, Phys. Rev. B **57** (4), R2053 (1997).
23. N. J. DiNardo, T. M. Wong, and E. W. Plummer, Phys. Rev. Lett. **65** (17), 2177 (1990).
24. O. Pankratov and M. Scheffler, Phys. Rev. Lett. **70** (3), 351 (1993).
25. O. Pankratov and M. Scheffler, Phys. Rev. Lett. **71** (17), 2797 (1993).
26. V. Yu. Aristov, L. Douillard, O. Fauchoux, and P. Soukiassian, Phys. Rev. Lett. **79** (19), 3700 (1997).
27. J. E. Northrup and J. Neugebauer, Phys. Rev. B **57** (8), R4230 (1998).
28. O. M. Braun and V. K. Medvedev, Usp. Fiz. Nauk **157** (4), 631 (1989) [Sov. Phys. Usp. **32**, 328 (1989)].
29. S. Yu. Davydov, Fiz. Met. Metalloved. **47** (3), 481 (1979).
30. S. Yu. Davydov, Poverkhnost **8**, 17 (1991).
31. M. Tsukada, J. Phys. Soc. Jpn. **41** (3), 899 (1976).
32. S. Yu. Davydov, Fiz. Tverd. Tela (S.-Peterburg) **41** (9), 1543 (1999) [Phys. Solid State **41** (9), 1413 (1999)].
33. T. Bechshtedt and R. Enderlein, *Semiconductor Surfaces and Interfaces: Their Atomic and Electronic Structures* (Academie-Verlag, Berlin, 1988; Mir, Moscow, 1990).
34. P. Krüger and J. Pollmann, Phys. Rev. Lett. **74** (7), 1155 (1995).
35. *Physical Quantities: A Handbook*, Ed. by I. S. Grigor'ev and E. Z. Meĭlikhov (Énergoatomizdat, Moscow, 1991).
36. J. W. Gadzuk, Phys. Rev. B **1** (5), 2110 (1970).
37. L. D. Landau and E. M. Lifshitz, *Electrodynamics of Continuous Media* (Nauka, Moscow, 1982; Pergamon Press, Oxford, 1984).
38. C. E. Carrol and J. W. May, Surf. Sci. **29** (1), 60 (1972).
39. Ch. Kittel, *Introduction to Solid State Physics* (Wiley & Sons, New York, 1976, 5th ed.; Nauka, Moscow, 1978).
40. M. Tikhov, G. Boishin, and L. Surnev, Surf. Sci. **241** (1), 103 (1991).
41. S. Y. Davydov, Appl. Surf. Sci. **140** (1), 52 (1999).
42. S. Y. Davydov, Appl. Surf. Sci. **140** (1), 58 (1999).

Translated by O. Borovik-Romanova

Physics of the Solid State, Vol. 42, No. 6, 2000, pp. 1170–1175. Translated from Fizika Tverdogo Tela, Vol. 42, No. 6, 2000, pp. 1134–1140.

LOW-DIMENSIONAL SYSTEMS AND SURFACE PHYSICS

Formation of Intercalate-Like Systems of Graphite–Ytterbium Monolayers on the Ni(111) surface

A. M. Shikin, M. V. Poĭgin, Yu. S. Dedkov, S. L. Molodtsov, and V. K. Adamchuk

Institute of Physics (Petrodvorets Branch), St. Petersburg State University, Petrodvorets, 198904 Russia

e-mail: shikin@snoopy.phys.spbu.ru

Received in final form, December 1, 1999

Abstract—The ytterbium intercalation under a graphite monolayer formed on the Ni(111) surface has been studied by Auger electron and angle-resolved photoelectron spectroscopy. The features of the electronic structure of the intercalate-like thin-film compound formed in this process are analyzed. It is shown that the energy shift of the π and σ states in the valence band toward higher binding energies (by ~2 and ~1 eV, respectively) can be described in terms of hybridization of the carbon π states in the graphite monolayer with the *d* states of the underlying metal. © *2000 MAIK "Nauka/Interperiodica".*

1. INTRODUCTION

The present state of science and technology can be supported only by a continuous search for and the development of new low-dimensional systems with strongly differing properties. Particular attention among these systems is focused on intercalate-like layered thin-film structures based on graphite monolayers, grown on ordered substrates, and monolayers of different metals intercalated under the graphite monolayer [1–6]. On the one hand, these systems possess all the properties characteristic of bulk intercalate-like systems (strongly anisotropic properties, high conductivity, including superconductivity, etc. [7, 8]). On the other hand, due to the smallness of their transverse dimensions (on the order of a few monolayers), these systems should also exhibit a number of features inherent in low-dimensional structures.

The aim of the present work was to study the possibility of forming intercalate-like thin-film structures based on a graphite monolayer (MG) grown on the Ni(111) surface by carbon-containing gas cracking and monolayers of ytterbium (a rare-earth metal with an *s*-type valence band) intercalated under this monolayer, as well as to analyze the specific features of the electronic structure of the systems thus formed by photoelectron and Auger-electron spectroscopy (AES).

This work was stimulated by the studies of the formation and specific features of the electronic structure of bulk intercalate-like systems based on rare-earth metals (REM) and graphite single crystals [9–13]. As was shown in these publications, bulk intercalates of rare-earth metals with an *s*-type valence band (Yb, Eu) can be formed by diffusion of Yb and Eu atoms from the films of these metals deposited onto a graphite surface in the course of annealing of these systems at 250–300 and 350–400°C, respectively. The electronic structure of the REM intercalates thus formed is similar to that of the classical alkali metal intercalates [7, 8, 14] and can be adequately described in terms of charge transfer from the Yb and Eu intercalated atoms to empty π* states of the graphite matrix [10, 11, 13].

In this paper, we present the results obtained in the study of the intercalation of thin Yb layers under a graphite monolayer on the Ni(111) surface and the specific features in the electronic structure of intercalate-like thin-film compounds formed in these processes. This study has demonstrated that deposition of thin Yb layers onto the surface of a MG/Ni(111) system with the subsequent annealing in the temperature range 300–400°C results in the intercalation of Yb under the graphite monolayer on Ni(111) to form an intercalate-like thin-film layered system. The changes in the electronic structure of the systems thus formed (an energy shift of the graphite π and σ states in the valence band toward higher binding energy compared to graphite by 2 and 1 eV, respectively) can be described in terms of hybridization of the carbon π states in graphite with the *d* states of the substrate and filling of a part of the π* states near the Fermi level in these processes. The above interaction differs from that of an intercalated metal with the graphite matrix in bulk Yb intercalates, in which the electronic structure can be treated primarily within the concept of straightforward charge transfer from metal atoms to free π* states of graphite.

2. EXPERIMENTAL DETAILS

The experiments were carried out on two independent setups. The photoemission studies of the valence-band structure and the dispersion of the corresponding electronic states were made on an ARIES photoelectron spectrometer (Vacuum Science Workshop), capable of angular resolution and equipped with a hemispherical analyzer mounted on a double-axis goniometer. The measuring chamber also contained a diffractometer

1063-7834/00/4206-1170$20.00

with a four-grid electron optics used for recording the low-energy electron diffraction (LEED) patterns. As a radiation source for photoemission measurements, we used the monochromatic beam in a TGM-4 output channel of the storage ring at the BESSY-I Synchrotron Radiation Center (Berlin, Germany). The radiation was incident on the sample at an angle of 45° to its surface. The AES studies were performed on an electron spectrometer including a four-grid retarding-field analyzer, which was also employed in the LEED measurements. The spectra were recorded under normal incidence of 1000-eV primary electrons on the sample.

Graphite monolayers on the Ni(111) surface were formed by the technique developed in our previous work [4–6], which was based on the propylene (C_3H_6) cracking at a sample temperature of 500°C and a pressure of 1×10^{-6} Torr. Keeping a Ni(111) sample in the above conditions for four min was sufficient for a graphite monolayer to form.

Before the propylene cracking, the Ni(111) surface was cleaned by the standard technique involving successive annealing in oxygen and hydrogen at a pressure of about 5×10^{-8} Torr and a temperature of 500 and 230°C, respectively. The sample temperature was monitored with a CrNi–AlNi thermocouple. The LEED pattern of the MG/Ni(111) system thus formed had a hexagonal (1×1) structure characteristic of the (0001) surface of single-crystal graphite.

The Yb layers were deposited onto the MG/Ni(111) surface by thermal evaporation of a metal piece placed in a special crucible made of tungsten wire and heated directly by electric current. The thickness of the deposited layers was derived from the frequency shift of a quartz-crystal resonator (silica microbalances).

Ytterbium was intercalated under the graphite monolayer by heating the MG/Ni(111) system with the deposited Yb layers. The annealing temperatures of the system were varied within the range 100–450°C, with the sample kept at each temperature for 10 min. It was established that the intercalation of Yb under the graphite monolayer is most efficient at annealing temperatures of 300–400°C. An increase in the anneal temperature of the system above 450–500°C destroys the graphite monolayer.

The LEED patterns obtained after the Yb intercalation also had a graphite-like structure with a stronger diffuse background and reflections diffused to a larger extent than those of the MG/Ni(111) system.

The base pressure in the measuring chambers did not exceed 1×10^{-10} Torr during the experiments.

3. RESULTS AND DISCUSSION

3. 1. Intercalation of Yb under MG on Ni(111)

The intercalation of Yb under the graphite monolayer was studied by Auger electron spectroscopy by measuring the Auger peak intensities of the components of the system in the course of its formation.

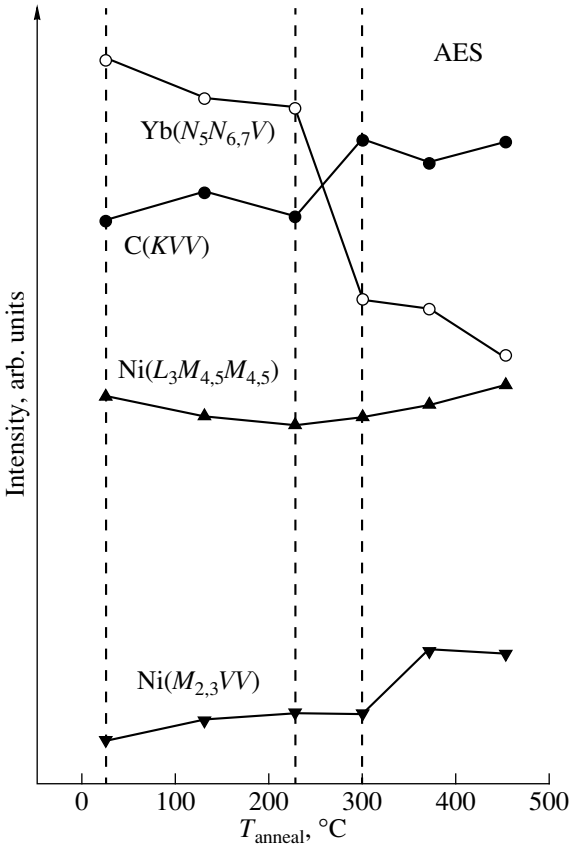

Fig. 1. Variations in the intensity of the Yb($N_5N_{6,7}V$), C(KVV), Ni($L_3M_{4,5}M_{4,5}$), and Ni($M_{2,3}VV$) Auger peaks at energies of 175, 272, 61, and 840 eV, respectively, during the annealing of a system made up of an Yb thin layer (~7 Å) predeposited onto a graphite monolayer on the Ni(111) surface. The annealing time at each temperature is 10 min.

Figure 1 presents the corresponding changes in the intensity of the Yb($N_5N_{6,7}V$), C(KVV), Ni($M_{2,3}VV$), and Ni($L_3M_{4,5}M_{4,5}$) Auger peaks (at energies of 175, 272, 61, and 840 eV, respectively) observed after deposition of a ~7-Å-thick Yb layer on to the MG/Ni(111) surface and subsequent annealing at different temperatures. As is seen from the figure, the intensity of the carbon Auger peak increases and that of the ytterbium peak decreases with an increase in the annealing temperature. An increase in the carbon peak intensity and a decrease in the Yb peak intensity are maximum at an annealing temperature of 300°C, which can be due to reaching the maximum rate of Yb diffusion under the graphite monolayer. This temperature coincides with that observed in the formation of bulk Yb intercalates by diffusing Yb into the bulk of the graphite matrix [10–13]. It is known [10–13] that heating of bulk Yb intercalates above 300°C results in an intense desorption of Yb atoms from the surface of the system. However, as is evident from Fig. 1, the Yb + MG/Ni(111) system also exhibits the Yb($N_5N_{6,7}V$) and Ni($M_{2,3}VV$)

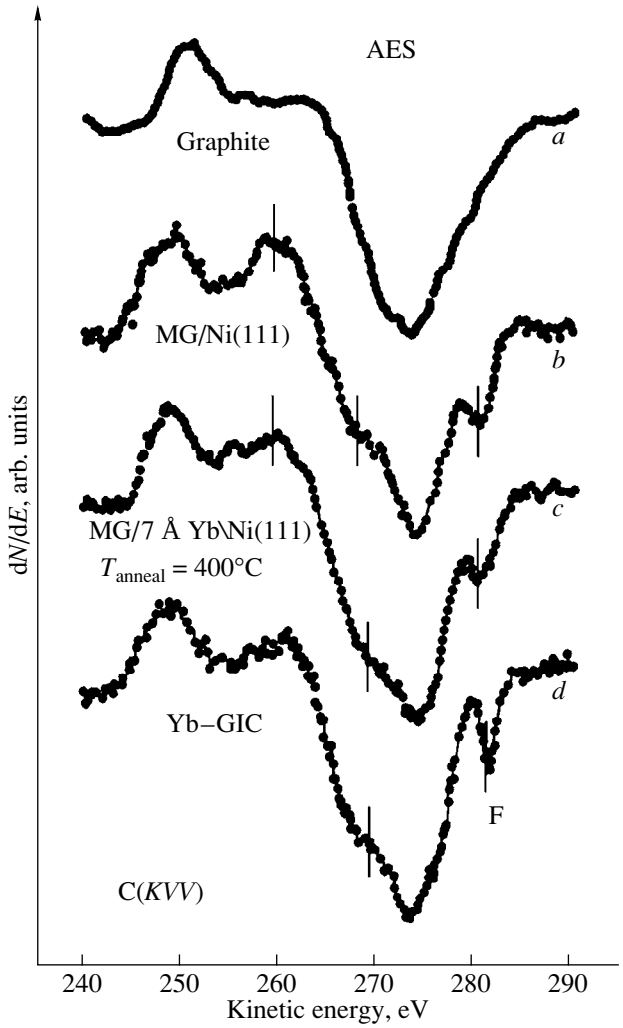

Fig. 2. The C(*KVV*) Auger line shapes for (*a*) graphite single crystal and a graphite monolayer on the Ni(111) surface (*b*) before and (*c*) after Yb intercalation (T_{anneal} ~ 400°C) in comparison with (*d*) line shape for bulk Yb-intercalated graphite. Spectra (*a*) and (*d*) are taken from [11].

Auger peaks after heating above 300°C, at a level comparable in intensity to the Auger peaks of carbon and nickel. Upon heating in the range 300–400°C, these peaks vary little in intensity, and only heating the system above 450–500°C gives rise to noticeable changes in both shape and intensity of the corresponding Auger peaks in the spectra. The fact that the nickel Auger intensity remains unaffected by the heating of the system while those of carbon and ytterbium change can indicate that the number of ytterbium and carbon atoms in the surface layer does not change; i.e., the Yb and C atoms only interchange without diffusing into the Ni substrate or desorbing from the surface of the system. In other words, we draw the conclusion from the above observations that Yb atoms are intercalated under the graphite monolayer. Annealing of the Yb + MG/Ni(111) system in the temperature range from 300 to 400°C forms an Yb intercalate under the graphite monolayer on the Ni(111) surface; i.e., the formation of the MG/Yb/Ni(111) system takes place. Figure 2 displays the C(*KVV*) Auger electron spectra for the MG/Yb/Ni(111) system in comparison with the spectra of bulk samples of single-crystal graphite and bulk Yb intercalate (Yb–GIC : Yb, where GIC is the graphite intercalation compound) taken from [10, 11] and a spectrum of MG/Ni(111) obtained in this work. It is known that the C(*KVV*) structure of the Auger electron spectrum can be described in a first approximation as a self-convolution of the local density of C(2*p*) electronic states in the valence band [11, 12, 15, 16]. Therefore, the C(*KVV*) Auger electron spectrum contains information on the variation of the population of C(2*p*)-type states and can serve as an indicator of the chemical interactions taking place in the system under study. An analysis of the C(*KVV*) Auger spectra presented in Fig. 2 shows that the shape of the spectra for the MG/Ni(111) and MG/Yb/Ni(111) systems changes substantially compared to that of single-crystal graphite. The fine structure of the spectrum also changes, and additional features appear at ~260 and ~268 eV. The most interesting of them is the clearly pronounced feature in the high-energy part of the spectrum at an energy of ~281 eV (the *F* feature). A similar feature was observed in the C(*KVV*) Auger spectra of alkali metal intercalates [15, 16], as well as of Yb–GIC, whose Auger spectrum is presented in Fig. 2. (This feature was associated in [11, 15, 16] with the filling of the graphite π^* states by charge transfer from atoms of an alkali metal to carbon atoms in the graphite matrix.) The C(*KVV*) spectra of MG/Ni(111) and MG/Yb/Ni(111) are practically of the same character.

Figure 3 shows the variations in the photoemission spectra obtained at photoelectron takeoff angles close to the surface normal (i.e., at the Γ point of the Brillouin zone) during the deposition of a thin Yb layer (~4 Å thick) onto the MG/Ni(111) surface, followed by the annealing of the whole system at ~400°C. Also shown for comparison are the spectra of a clean Ni(111) surface and a graphite monolayer on the Ni(111) surface. The spectra exhibit features that correspond to the graphite π_{1v} and σ_{1s} states (at binding energies of ~10 and 22.5 eV, respectively), Ni *d* states (0.5 and 1.5 eV), and Yb 5*p* and 4*f* states (24, 3, and 1 eV, respectively). An analysis of the spectra shows that the features corresponding to the graphite π_{1v} and σ_{1s} states and *d* states of nickel become weaker immediately after the Yb deposition, so that the spectra are dominated by the Yb 5*p* and 4*f* states. After annealing, the features due to the 5*p* and 4*f* states of Yb decrease substantially in intensity. They overlap with the C(σ_{1s}) and Ni(*d*) states to become nearly unresolvable from them. Annealing increases the intensity of the graphite π_{1v} states to a level comparable to that of the corresponding features characteristic of a clean surface of the MG/Ni(111) system. This is accompanied by their slight shift toward

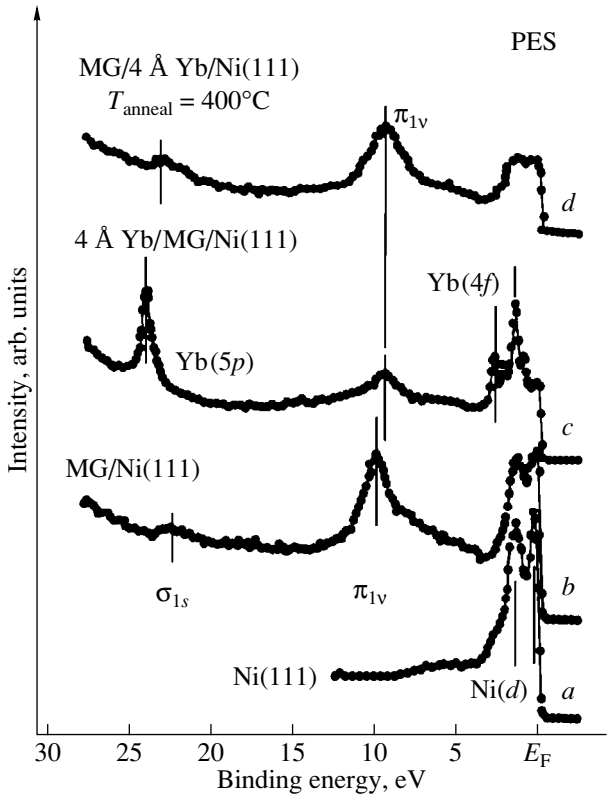

Fig. 3. Variations in the valence-band photoelectron spectra ($h\nu$ = 35 eV) of (*a*) Ni(111) and (*b*) the MG/Ni(111) system and in the spectra obtained (*c*) during the deposition of Yb thin layers (~4 Å) onto the MG/Ni(111) surface and (*d*) annealing of the system as a whole at 400°C for 10 min.

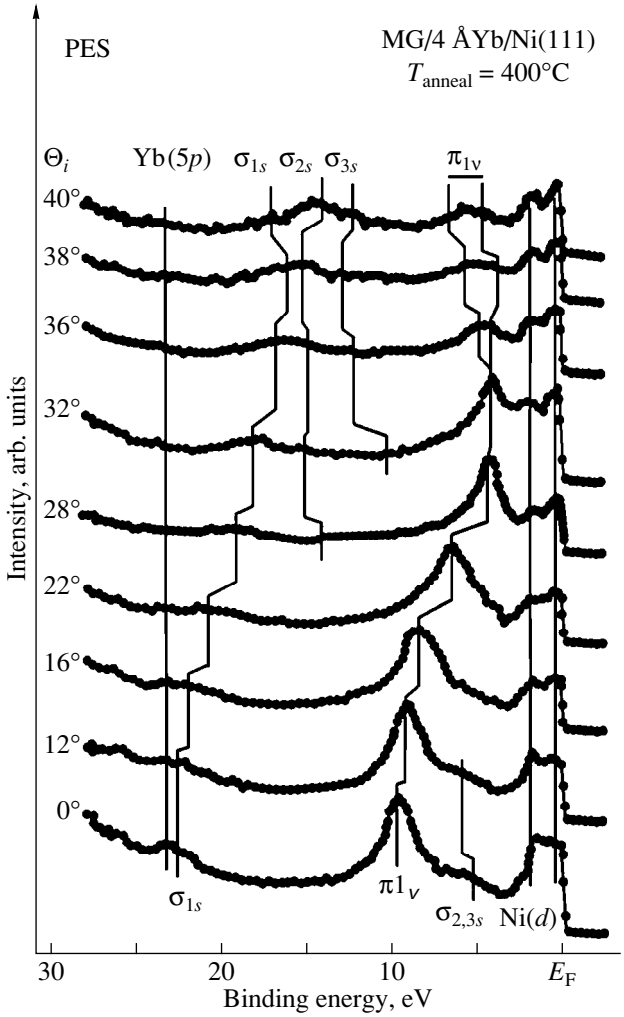

Fig. 4. Valence-band photoelectron spectra ($h\nu$ = 50 eV) of a thin-film intercalate-like compound made up of graphite and ytterbium monolayers for different photoelectron polar takeoff angles relative to the surface normal. The compound was formed on the Ni(111) surface by deposition of a 4-Å-thick Yb layer onto a graphite monolayer and annealing of the system at 400°C. The main spectral features denoted by σ_{1s}, σ_{2s}, σ_{3s}, π_{1v}, Yb(5*p*), and Ni(*d*) are connected by the corresponding lines.

lower binding energies. Similar spectral variations are observed in the case of a predeposited Yb layer of a different thickness (~12 Å), which was annealed at ~300–400°C (not shown in Fig. 3). The above variations in the photoelectron spectra are in excellent agreement with the conclusion drawn from analysis of the Auger peak intensities that the Yb intercalation under a graphite monolayer occurs upon heating the system in the temperature range from 300 to 400°C. The recovery of the feature corresponding in intensity to the graphite π_{1v} states and its energy shift indicate not only removal of Yb atoms from the surface of the system, but also a modified interaction of the graphite monolayer with the substrate as a result of Yb intercalating under the graphite monolayer.

3. 2. Electronic Structure of MG/Yb/Ni(111)

The valence-band electronic structure of the Yb-based intercalate-like thin-film compound prepared in this work was studied by angle-resolved photoelectron spectroscopy. Figure 4 shows the photoelectron spectra of a MG/Yb/Ni(111) system prepared by depositing a 4-Å-thick Yb layer onto the surface of the MG/Ni(111) system and its subsequent annealing at $T \cong 400$°C (i.e., under the conditions favoring Yb intercalation under the graphite monolayer). The spectra were measured for different photoelectron polar takeoff angles Θ in the ΓK direction of the surface Brillouin zone of graphite. The variation of the main features in energy is specified by the corresponding lines. The photoelectron spectra obtained for the system with a 12-Å-thick Yb layer follow a similar same pattern (not shown in Fig. 4). Figure 5 displays the dispersion relations $E(k_\parallel)$ for the main energy bands derived from analysis the photoelectron spectra by using the well-known expression

$$E(k_\parallel) \sim 0.51\sqrt{E_{kin}}\sin\Theta_i,$$

where $k_\parallel$ is the parallel component of quasi-momentum in the Brillouin zone, E_{kin} is the photoelectron kinetic

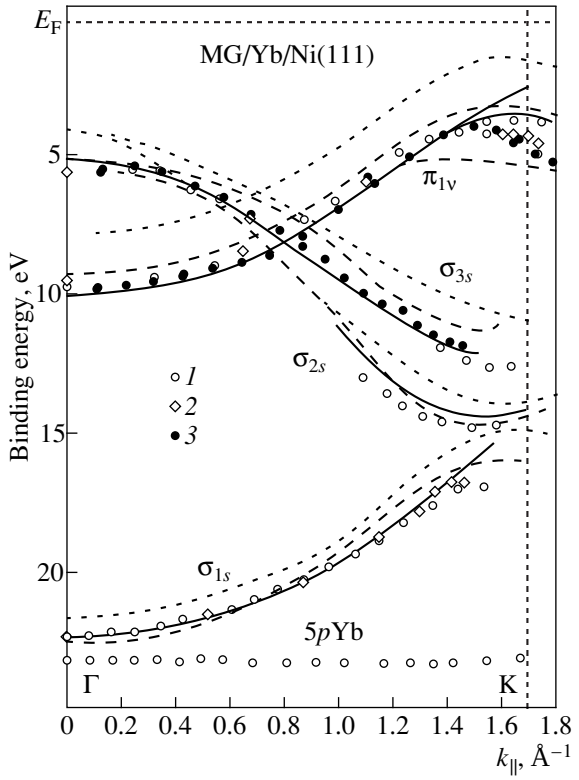

Fig. 5. Dispersion relations $E(k_{||})$ of the main graphite-like branches of the σ_{1s}, σ_{2s}, σ_{3s}, and π_{1v} electronic states for MG/Yb/Ni(111) systems obtained after deposition of (*1*, *3*) 4- and (*2*) 12-Å-thick Yb layer on the MG/Ni(111) surface and annealing at 400°C for 10 min. The figure contains data obtained for exciting radiation energies $h\nu$ = (*3*) 33 eV and (*1*) 50 eV. Shown for comparison are the corresponding dispersion relations for the MG/Ni(111) system (solid lines), graphite single crystal [10] (dotted lines), and bulk Yb intercalate [11] (dashed lines).

energy, and Θ is the photoelectron polar takeoff angle relative to the surface normal.

Figure 5 demonstrates the data obtained for the MG/Yb/Ni(111) system with an Yb layer of different thickness (4 and 12 Å) at different energies of the exciting radiation ($h\nu$ = 33 and 50 eV). Shown for comparison are the corresponding dispersion relations for the MG/Ni(111) system. The dashed lines are plots of the dispersion relations for Yb-intercalated bulk graphite taken from [11]. The dispersion relations given in [10] for single-crystal graphite are presented in Fig. 5 by dotted lines. As follows from a comparison of the data in Fig. 5, the spectra of the MG/Yb/Ni(111) system also exhibit all the branches of electronic states characteristic of graphite (σ_{1s}, $\sigma_{2,\,3s}$, and π_{1v}). However, in contrast to graphite, the graphite π and σ states are shifted toward higher binding energies by ~1 eV for the σ states and by ~2 eV for the π states. All graphite-like states of the MG/Yb/Ni(111) system lie substantially closer to the energies characteristic of the MG/Ni(111) system. The Yb intercalation under the graphite monolayer on Ni(111) results only in a small energy shift of these states toward lower binding energies. A comparison of the photoelectron spectra obtained (and the dispersion relations) with the corresponding spectra (and dispersion relations) of bulk Yb intercalates [10, 11] shows that it is in the π_{1v} branch that the valence-band features differ most in energy. Indeed, the bulk Yb intercalate exhibits a noticeably smaller energy shift of these states than is the case with the MG/Yb/Ni(111) system relative to pure graphite. For instance, the π_{1v} electron binding energy for the Yb bulk intercalate at the Γ point is ~9 eV, which is less by ~1 eV than that for the MG/Yb/Ni(111) system. An interesting feature of the spectra observed for the MG/Yb/Ni(111) system is the splitting of the π_{1v} band at the *K* point into two branches. As the $k_{||}$ component increases and transfers to the second Brillouin zone, one of these branches tends to a ~3.5-eV energy level. The other branch splits off from the first one and shifts gradually toward higher binding energies with an increase in the *k* value. Interestingly, the MG/Ni(111) system exhibits a similar behavior of the π_{1v} states in the vicinity of the *K* point of the Brillouin zone (see solid lines in Fig. 5). In this case, however, the binding energies of both branches of the split π_{1v} states are lower. Theoretical calculations made for the MG/Ni(111) system also reveal the presence of such a splitting in the second Brillouin zone upon transfer from the *K* point to the *M* point [17].

Thus, an analysis of all the data displayed in Figs. 4 and 5 suggests that the valence-band structure and the behavior of the main features for the MG/Yb/Ni(111) system are more similar to those observed in the MG/Ni(111) system than in Yb–GIC. This implies, in turn, that the type of interaction of the graphite monolayer with the substrate is mostly preserved after Yb intercalation. An analysis was made of the different energy shifts of the π and σ states in the valence band for a graphite monolayer on the Ni(111) surface [1, 18]. The results obtained led to the assumption [18] that the observed changes in the electronic structure of the MG/Ni(111) system are due to the hybridization of the π orbitals of the graphite monolayer with the *d* orbitals on the Ni(111) surface. This hybridization gives rise to a charge density redistribution from the bonding π to antibonding π* states, whose binding energy increases as they become admixed to the substrate states. Because of the substantially weaker coupling of the Ni *d* electrons with the σ states of graphite, the energy of the latter states changes to a considerably smaller extent than that of the π states. It appears of interest to consider from this standpoint the formation of the feature in the high-energy part of the C(*KVV*) Auger peak at ~281 eV (Fig. 2). As noted above, a similar feature is observed in the C(*KVV*) Auger spectra of bulk alkali metal intercalates, in which it is assigned to the filling of a part of the graphite π* states near the Fermi level as a result of the charge transfer from the intercalated metal atoms to the graphite matrix [15, 16]. An analysis of the energy shift of the MG/Ni(111) electronic struc-

ture made in [19] also assumed, by analogy with these systems, an ionic type of bonding between the graphite monolayer and the Ni substrate with a charge transfer from the *d* orbitals in the Ni(111) plane to free π* states of the graphite monolayer. However, if this assumption is correct, approximately equal energy shifts of the π and σ states should be observed in the valence band, as this occurs in the alkali metal intercalates [15, 16] and Yb(Eu)–GIC [10, 11]. However, as already mentioned, the MG/Ni(111) and MG/Yb/Ni(111) systems exhibit a substantially different shift of the π and σ states in the valence band. This gives grounds to suggest that it is in terms of the hybridization between the *d* orbitals of the substrate and the π orbitals of graphite that one could most likely describe the main features in the energy structure of the MG/Ni(111) and MG/Yb/Ni(111) systems and the corresponding structural changes in the photoelectron and Auger electron spectra.

It appears interesting to consider from this standpoint the energy position of the band features for the MG/Ni(111) and MG/Yb/Ni(111) systems near the *K* point of the Brillouin zone (Fig. 5). The binding-energy difference of these states for the MG/Ni(111) and MG/Yb/Ni(111) systems can be assigned to different binding energies for *d*-type states of Ni and Yb. For Ni, the binding energy of these states is lower than that for Yb (atomic Yb has no filled *d* orbitals). As a result, the corresponding (*d*–π) hybridized orbitals in the MG/Ni(111) system should have a higher binding energy. Thus, an analysis of the above features in the electronic structure of the MG/Yb/Ni(111) system, as compared to intercalate-like systems based on Yb and alkali metals, permits a conjecture that the process underlying MG interaction with an Yb intercalated layer is, similar to the MG/Ni(111) system, the (*d*–π) hybridization. However, judging from the energy shift of the graphite-like branches in the valence band, the strength of the coupling in these two systems is somewhat different.

Thus, we showed by Auger-electron and photoelectron spectroscopy that the deposition of Yb thin layers onto the surface of a graphite monolayer prepared on Ni(111) by propylene cracking, followed by annealing of the system at temperatures from 300 to 400°C, results in intercalation of Yb under the graphite monolayer and formation of a thin-film intercalate-like compound. The different energy shift of the π and σ states of this system compared to graphite (by ~2 and ~1 eV, respectively) in the valence-band electronic structure can be understood in terms of the hybridization of the carbon π states in graphite with the substrate *d* states and the filling of a part of the π* states near the Fermi level in these processes. The above interaction differs from the intercalated metal–graphite matrix coupling in bulk Yb intercalates, where the main features of the electronic structure can be described primarily in terms of the formation of ionic bonding, i.e., simple charge transfer from metal atoms to free graphite π* states.

ACKNOWLEDGMENTS

The authors are grateful to Prof. C. Laubschat and coworkers (Dresden Technical University) and the St. Petersburg Joint Use Center for providing scientific equipment for the experiments. Particular gratitude is expressed to the administration and personnel of the BESSY-I Synchrotron Radiation Center, who provided the necessary equipment and beam operating time to perform our studies with the synchrotron radiation at the BESSY-I storage ring.

This work was supported by the Science & Technology State Programs "Surface Atomic Structures" (project no. 2.1.99), "Fullerenes and Atomic Clusters" (project no. 98052), and the Joint Russian–German RFBR–NNIO Program (project nos. 96-02-00045 and 98-03-04071).

REFERENCES

1. A. Nagashima, N. Tejima, and C. Oshima, Phys. Rev. B **50**, 17487 (1994).
2. A. Ya. Tontegode and E. V. Rut'kov, Usp. Fiz. Nauk **163** (11), 57 (1993) [Phys. Usp. **36**, 1053 (1993)].
3. N. R. Gall, S. N. Mikhailov, E. V. Rut'kov, and A. Ya. Tontegode, Surf. Sci. **226**, 381 (1990).
4. A. M. Shikin, D. Farias, and K. H. Rieder, Europhys. Lett. **44**, 44 (1998).
5. A. M. Shikin, G. V. Prudnikova, V. K. Adamchuk, *et al.*, Surf. Sci. **331**–**333**, 517 (1995).
6. Yu. S. Dedkov, A. M. Shikin, V. K. Adamchuk, *et al.*, Phys. Rev. B (in press).
7. M. S. Dresselhaus and G. Dresselhaus, Adv. Phys. **30**, 139 (1981).
8. *Intercalation in Layered Materials*, Ed. by M. S. Dresselhaus (Plenum Press, New York, 1986).
9. A. M. Shikin, S. L. Molodtsov, C. Laubschat, *et al.*, Phys. Rev. B **51**, 13586 (1995).
10. S. L. Molodtsov, C. Laubschat, M. Richter, *et al.*, Phys. Rev. B **53**, 16621 (1996).
11. A. M. Shikin, G. V. Prudnikova, V. K. Adamchuk, *et al.*, Phys. Low-Dimens. Semicond. Struct. **7**, 79 (1997).
12. A. M. Shikin, S. L. Molodtsov, G. V. Prudnikova, and V. K. Adamchuk, Poverkhnost **8**–**9**, 66 (1998).
13. S. A. Gorovikov, A. M. Shikin, G. V. Prudnikova, *et al.*, Phys. Low-Dimens. Semicond. Struct. **10**–**11**, 29 (1995).
14. N. Gunasekara, T. Takahashi, F. Maeda, *et al.*, Z. Phys. B: Condens. Matter **70**, 349 (1988).
15. J. S. Murday, B. I. Dunlap, F. L. Hutson II, and P. Oelhafen, Phys. Rev. B **24**, 4764 (1981).
16. M. Lagues, D. Marchand, and C. Fretigny, Solid State Commun. **59**, 583 (1986).
17. Y. Souzu and M. Tsukada, Surf. Sci. **326**, 42 (1995).
18. C. Oshima and A. Nagashima, J. Phys.: Condens. Matter **9**, 1 (1997).
19. K. Yamamoto, M. Fukushima, T. Osaka, and C. Oshima, Phys. Rev. B **45**, 11358 (1992).

Translated by G. Skrebtsov

Physics of the Solid State, Vol. 42, No. 6, 2000, pp. 1176–1181. Translated from Fizika Tverdogo Tela, Vol. 42, No. 6, 2000, pp. 1141–1146.

FULLERENES AND ATOMIC CLUSTERS

On Fractal Nature of the Structure of Nanoporous Carbon Obtained from Carbides

É. A. Smorgonskaya[1], R. N. Kyutt[1], S. K. Gordeev[2], A. V. Grechinskaya[2], Yu. A. Kukushkina[3], and A. M. Danishevskiĭ[1]

[1] *Ioffe Physicotechnical Institute, Russian Academy of Sciences, Politekhnicheskaya ul. 26, St. Petersburg, 194021 Russia*
[2] *Central Research Institute of Materials, St. Petersburg, 121014 Russia*
[3] *All-Russia Research Center of Applied Chemistry, St. Petersburg, 197198 Russia*

Received December 3, 1999

Abstract—The curves describing small-angle x-ray scattering at *npor*-C nanoporous carbon samples obtained from polycrystalline α-SiC, TiC, and Mo_2C and a 6*H*-SiC single crystal have been analyzed. An algorithm is developed for taking into account the corrections to experimental curves for the intensity of the primary beam transmitted through the sample and the height of the inlet slit in these measurements. Two systems of nanoclusters observed in the *npor*-C structure differ in the type of stacking of structural elements: small-scale mass fractals of a dimension $1 < D_2 < 3$ and a size $L_2 = 50$–90 Å, which depend on the type of the initial carbide, and large-scale nanoclusters having a size $L_1 > 550$ Å. In most samples, large-scale nanoclusters can be regarded as objects with a fractal surface and a dimension $2 < D_1 < 13$, which also depends on the type of the initial carbide. Large-scale nanoclusters in *npor*-C obtained from Mo_2C prove to be mass fractals with a dimension $D_1 > 2$. Peculiarities of the structure formation of nanoporous carbon obtained from various carbides are discussed.

Recent studies of the structure of many porous materials revealed that nanoscale structural elements (clusters, pore, or their interfaces) constituting such materials are of a fractal type. An analysis of the structure based on the small-angle x-ray scattering (SAXS) method in a certain range of scattering vector modulus $s' < s < s''$ ($s \equiv 4\pi\sin\theta/\lambda$, where 2θ is the scattering angle and λ is the radiation wavelength) gives an exponential decrease in the scattering intensity $I(s) \propto s^{-\alpha}$ with a nonintegral exponent $\alpha < 4$ [1–3]. (The value $D = 4$ corresponds to the well-known Porod law describing the asymptotic behavior of the intensity of SAXS at homogeneous particles with a linear size L and a smooth surface for $sL \gg 2\pi$ [4].) This law of decrease of $I(s)$ for $3 < \alpha < 4$ is typical of scattering at nanoparticles with a fractal (rough) surface of dimension $6 - \alpha$ [1] and is observed, for example, in a porous silicate glass of the Vycor type [3], and some porous coals (lignites) [1]. For $1 \le \alpha < 3$, the exponential decrease of $I(s)$ is typical of scattering at fractal aggregates of nanoparticles (clusters of the mass fractal type) of dimension $D = \alpha$ in the range $L_0^{-1} \gg s \gg L^{-1}$, where L_0 and L are the minimum size of an individual particle in a cluster and the cluster size, respectively [5]. Fractal nanoclusters of this type are formed, for example, in porous silicon [2], their dimension being heavy dependent on the parameters of the electrolytic etching of silicon during the formation of a porous film. Mass (bulk) or surface fractals are observed in a number of systems based on solid-state carbon, namely, in the above-mentioned porous coals [1], shungites [6], ultradisperse diamond [7], and amorphous carbon with copper nanoclusters [8].

The formation of definite fractal carbon structures is determined by the conditions of obtaining and processing of the material. In turn, fractal parameters of the existing structures can determine many physical and physicochemical properties of carbon. In this work, the concept of fractals is used for analyzing the results of investigation of SAXS at nanoporous carbon (*npor*-C) obtained from polycrystalline powders of carbides α-SiC, TiC, and Mo_2C as well as from 6*H*-SiC single crystals by the removal of noncarbon atoms by high-temperature chlorination [9, 10]. The interest in *npor*-C is due to its unique properties that are useful for a number of technical applications [11], as well as due to the general increase in the interest in solid-state nanostructures of various types. According to the SAXS data obtained earlier [12], *npor*-C is a system of scattering particles with the most probable characteristic size $2R_g \sim 10$ Å (R_g is the radius of inertia) and the average size $2R_g^{av} = 12$–25 Å depending on the type of the initial carbide. Most of the volume (85–90%) is occupied by the finest nanoparticles with a radius of inertia smaller than $2R_g^{av}$, the remaining volume being filled by coarser nanoparticles with a size of up to ~100 Å. The results presented below indicate that on a certain scale of lengths, nanoclusters in *npor*-C can be

regarded as fractals whose type and parameters also depend on the type of the initial carbide.

The technology of preparing *npor*-C samples and the experimental setup for SAXS studies were described by us earlier [11, 12]. The SAXS intensity as a function of the scattering angle $I_{exp}(2\theta)$ was measured in the through mode of transmission of an x-ray beam through the sample (2θ scanning) in the angular range $0 < 2\theta < 8°$. It should be noted that the signal recorded by the detector gives a $I_{exp}(2\theta)$ curve differing in shape from the true SAXS curve $I(2\theta)$. In our case, the distortions of the true SAXS curve appeared mainly for two reasons.

First, in the range of the smallest angles ($2\theta < 0.65°$), the diverging primary beam transmitted through the sample and attenuated to a certain extent by a small absorption in it (the attenuation factor was 1.8–2.4 cm^{-1} [12]) contributed to the $I_{exp}(2\theta)$ signal recorded by the detector. In order to compensate the error emerging due to this contribution, we introduced the corresponding correction to $I_{exp}(2\theta)$ taking into account the true profile $i_0(2\theta)$of the primary beam and its absorption in the material:

$$I^*_{exp}(2\theta) \cong I_{exp}(2\theta) - [I_{exp}(0)/i_0(0)]i_0(2\theta)/\cos 2\theta. \quad (1)$$

The quantity $I^*_{exp}(2\theta)$ is the intensity of the scattered radiation only. For $2\theta < 0.65°$, the factor $1/\cos 2\theta \cong 1$ takes into account the true path of the beam in the sample.

Second, the signal $I_{exp}(2\theta)$ detected with a slit collimation of the scattered beam for a given 2θ was in fact the result of integration over the angular interval $(2\theta, 2(\theta + \Delta\theta))$, where $\Delta\theta$ is determined by the slit size and by the separation d between the sample and the detector ($d = 20$ cm in our case) and is a function of the scattering angle 2θ itself (see Fig. 9.1 from [4]). The slit collimation is normally used to increase the intensity of the recorded signal instead of the pinhole collimation, although the latter allows one to determine the scattering angle with a considerably higher accuracy. In our case, the width of the inlet slit was quite small (0.5 mm), ensuring a high resolution in the scattering angle (0.16°). However, the slit height h was 2.0 mm. It follows from the geometrical considerations that the interval of signal integration by the inlet slit is

$$2\Delta\theta = \sqrt{(2\theta)^2 + \psi_m^2} - 2\theta, \quad (2)$$

where $\psi_m \sim h/2d \ll 1$ is the angle at which the half-height of the slit is seen at a distance d from the sample. (We have used here the smallness of the angles 2θ and ψ_m.) Expression (2) shows that as the scattering angle 2θ decreases, the integration interval $2\Delta\theta$ increases, becomes comparable with 2θ for $2\theta \lesssim 2°$, and exceeds considerably 2θ as $2\theta \longrightarrow 0$: $2\Delta\theta \longrightarrow \psi_m \gg 2\theta$. For large values of scattering angle in the interval under investigation ($2\theta \geq 5°$), it is found that $2\Delta\theta \ll 2\theta$, and we can assume that the slit collimation gives a result close to that for the pinhole collimation, i.e., the true SAXS curve $I(2\theta)$ virtually coincides with the experimental curve: $I(2\theta) \cong I^*_{exp}(2\theta)$ (if we disregard absorption in the sample).

The correction to $I^*_{exp}(2\theta)$ to the slit height was introduced as follows. The intensity of the detected scattering signal after the subtraction of the primary beam in (1) is given by

$$I^*_{exp}(2\theta) \propto \int_0^{\psi_m} I(\sqrt{(2\theta)^2 + \psi^2})d\psi, \quad (3)$$

so that the problem of determining the true function $I(2\theta)$ from the experimental function $I^*_{exp}(2\theta)$ obtained taking into account the correction to the primary beam in (1) essentially boils down to solving the integral equation (3). Going over in (3) to new coordinates, we obtain

$$I^*_{exp}(2\theta) \propto \int_{2\theta}^{\sqrt{(2\theta)^2 + \psi_m^2}} I(\varphi)\frac{\varphi d\varphi}{\sqrt{\varphi^2 - (2\theta)^2}}. \quad (4)$$

In the general case, the integral on the right-hand side of (4) cannot be evaluated analytically. If, however, we assume for simplicity that the true SAXS intensity in a certain range of scattering angles 2θ decreases according to a power low with the exponent n, i.e.,

$$I(2\theta) \propto (2\theta)^{-n} \ (n > 0), \quad (5)$$

the function $I^*_{exp}(2\theta)$ from equation (4) can be evaluated analytically and has the form

$$I^*_{exp}(2\theta) \propto \frac{1}{2(n-1)\Gamma\left(\frac{n}{2}\right)}(2\theta)^{-n}\Bigg[(n-1)\sqrt{\pi}\Gamma$$

$$\times\left(\frac{n-1}{2}\right)(2\theta) - 2\Gamma\left(\frac{n}{2}\right)(2\theta)^n((2\theta)^2 + \psi_m^2)^{\frac{1-n}{2}} \quad (6)$$

$$\times {}_2F_1\left(\frac{1}{2}; \frac{n-1}{2}; \frac{n+1}{2}; \frac{(2\theta)^2}{(2\theta)^2 + \psi_m^2}\right)\Bigg].$$

Here Γ is the gamma-function and ${}_2F_1$ is a hypergeometrical function. Comparing the function $I^*_{exp}(2\theta)$ calculated from (6) with the experimental function from (1) in a certain angular interval of 2θ, we can define the exponent n of the presumed exponential decrease of the true $I(2\theta)$ curve as a parameter ensuring the best agreement between the theory and experiment in the given interval of 2θ.

An analysis of expression (6) indicates that, as the scattering angle approaches zero, the dependence

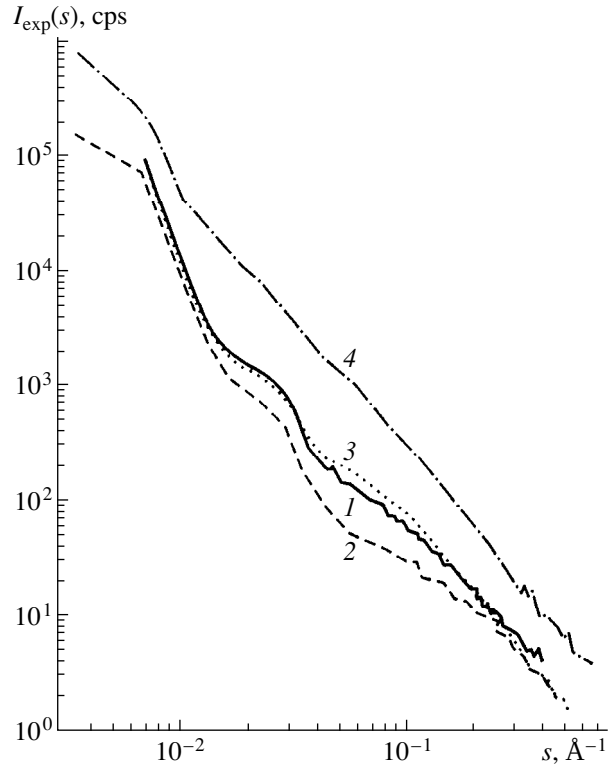

Fig. 1. SAXS curves $I_{exp}(s)$ recorded in experiments on *npor*-C samples obtained from polycrystalline α-SiC (curve *1*), TiC (curve *2*) and Mo_2C (curve *3*) and a 6*H*-SiC single crystal (curve *4*).

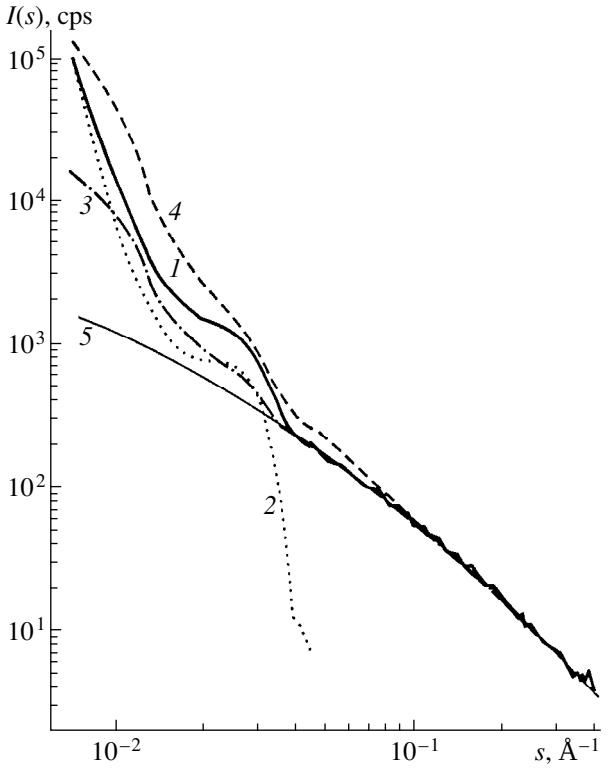

Fig. 2. True SAXS curve $I(s)$ for *npor*-C⟨α-SiC⟩ (curve *4*) reconstructed from the experimental curve $I_{exp}(s)$ (curve *1* in Fig. 1) taking into account the corrections to the intensity of the primary x-ray beam passing through the sample without scattering and to the height of the inlet slit. The angular distribution $i_0(s)$ of intensity of the beam incident on the sample (curve *2*), the experimental SAXS curve $I^*_{exp}(s)$ taking into account the correction to the primary beam intensity (curve *3*) and the distribution of SAXS intensity calculated by formula (6) for $n = 2$ (curve *5*) are also plotted in the figure.

$I^*_{exp}(2\theta)$ becomes close to a power-low dependence with the exponent $-n + 1$. Indeed, the integration of the true SAXS exponential function with the exponent $-n$ in a wide range of angles $\psi_m \gg 2\theta$ must lead to an increase in the exponent by unity, i.e., to the corresponding decrease in the observed steepness of the descend of the scattering curve as compared to the true curve. On the other hand, for large angles 2θ, the asymptotic behavior of the calculated function $I^*_{exp}(2\theta)$ corresponds to an exponential decrease with the exponent $-n$, i.e., coincides with the predicted variation of the true scattering function $I(2\theta)$ as expected. Thus, according to calculations, in the case of an exponential decrease of the true SAXS curve (5), for the observed behavior of the scattering curve (taking into account the correction to the primary beam) we have

$$I^*_{exp}(2\theta) \propto \begin{cases} (2\theta)^{-n+1}, & 2\theta \longrightarrow 0; \\ (2\theta)^{-n}, & 2\theta \longrightarrow \infty. \end{cases} \qquad (7)$$

For intermediate values of 2θ, the observed behavior of the scattering intensity $I^*_{exp}(2\theta)$ calculated by formula (6) differs from the exponential variation and can be written as

$$I^*_{exp}(2\theta) \propto (2\theta)^{-n+\Delta n(2\theta)}, \qquad (8)$$

where $0 < \Delta n(2\theta) < 1$, so that the observed local steepness of the descent of the scattering function $I^*_{exp}(2\theta)$ is always lower than that of the true SAXS curve in the case of the pinhole collimation of the scattered beam.

Figure 1 shows on the log–log scale the experimental SAXS curves $I_{exp}(s)$ for all the *npor*-C samples under investigation ($s \cong 4\pi\theta/\lambda$ for small angles). In Fig. 2, the reconstruction of the true SAXS curve $I(s)$ (curve *4*) from the $I_{exp}(s)$ (curve *1*) is illustrated in detail for an *npor*-C⟨*poly*-SiC⟩ sample obtained from polycrystalline α-SiC. At first, in accordance with (1), a correction is introduced to the attenuated primary beam whose initial profile $i_0(s)$ at the moment of incidence on the sample is also shown in Fig. 2 (curve *2*). As noted above, the obtained intermediate result $I^*_{exp}(s)$ (curve *3*)

corresponds to the observed intensity of scattering in pure form. For large values of s ($s > 0.15$ Å^{-1}) it was found that $I^*_{exp}(s) = I_{exp}(s) \propto s^{-2}$ for our sample, and according to the above analysis, such an exponential decrease in the given interval can be regarded as true, i.e., $I_{exp}(s) \cong I(s) \propto s^{-n}$ for $n \cong 2$. However, the calculations based on formula (6) with $n = 2.0$ show that, as expected, the calculated function $I^*_{exp}(s)$ (curve *5* in Fig. 2) does not coincide with the experimental curve $I^*_{exp}(s)$ determined from expression (1) (curve *3*) for $s < 0.04$ Å^{-1}. Consequently, the true $I(s)$ curve cannot be described by an exponential decrease with the same exponent 2 in the entire range of s under investigation. In this case, dividing the entire interval into a finite number of narrower intervals and using formula (6), we can find the values of n for which the best agreement between the calculated function $I^*_{exp}(s)$ (6) and the experimental function $I^*_{exp}(s)$ (1) in the steepness of the descent is attained in each of the intervals. Consistently joining the calculated values of $I^*_{exp}(s)$ at the boundaries of the intervals starting from the lower boundary $s = 0.15$ Å^{-1} of the final interval $s = 0.15$–0.4 Å^{-1}, in which the true SAXS function $I(s)$ for *npor*-C⟨*poly*-SiC⟩ coincides with the observed $I^*_{exp}(s)$, one can reconstruct the required function $I(s)$ (curve *4*) from $I_{exp}(s)$ (curve *1*) in the entire range of s.

Figure 3 shows on the log–log scale the true SAXS curves $I(s)$ reconstructed with the help of the above-described procedure for all the *npor*-C samples under investigation. It can be seen that all the curves contain two rectilinear segments with various slopes, indicating the exponential decrease in the scattering intensity

$$I(s) \propto \begin{cases} s^{-\alpha_1}, & s < s_1; \\ s^{-\alpha_2}, & s > s_2, \end{cases} \qquad (9)$$

with the exponents α_1 and α_2 of a larger and a smaller magnitude ($\alpha_1 > \alpha_2$) for relatively small and large values of s, respectively. These segments are connected through a transient region of width $s_2 - s_1 = 0.02$–0.03 Å^{-1}. For samples obtained from polycrystalline α-SiC, TiC, and Mo_2C, a steeper exponential decrease in $I(s)$ is observed for $s < s_1 \cong 0.05$ Å^{-1} and a slower one, for $s > s_2 \cong 0.08$ Å^{-1}. For the *npor*-C sample prepared from the 6*H*-SiC single crystal, a more rapid descent is transformed into a slower one for $s_1 \cong s_2$ close to 0.12 Å^{-1}. The values of α_1 and α_2 we determined from the true SAXS curves for all types of samples (Fig. 3) are given in the table.

An important feature of all the curves is the absence of a segment with a slope equal to 4. The violation of the Porod laws indicates that an increase in the value of s in experiments leads to the resolution of finer and finer elements of the structure, so that the asymptotic form of scattering at coarser particles is not seen as we go over to a smaller scale since the scattering from finer particles is superimposed on it. In this case, the shape of the observed scattering curve can be treated as the sum of the partial curves describing the scattering at particles of various size in a polydisperse medium. Such an approach was exactly used for determining the size distribution of scattering particles [12]. However,

Parameters of the fractal structure of nanoporous carbon

Initial material	*poly*-SiC	*poly*-TiC	*poly*-Mo_2C	6*H*-SiC
α_1	3.03	3.43	2.70	3.29
D_1	2.97	2.57	2.70*	2.71
l_1, Å	140	140	140*	60
L_1, Å	≥550			
α_2	1.97	1.64	2.36	2.34
D_2	1.97	1.64	2.36	2.34
l_2, Å	<10–15			
L_2, Å	75	60	90	50

* The dimension and size correspond to a large-scale mass fractal.

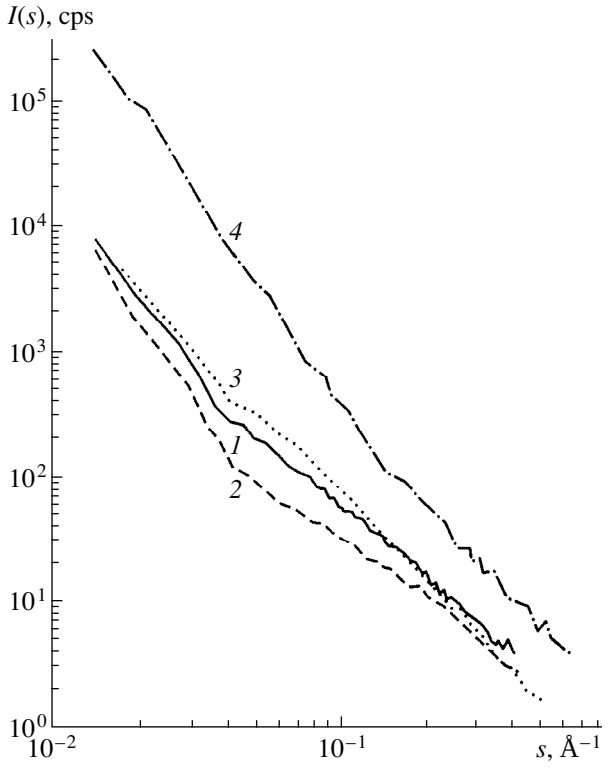

Fig. 3. True SAXS $I(s)$ curves for *npor*-C samples obtained from polycrystalline α-SiC (curve *1*), TiC (curve *2*), and Mo_2C (curve *3*) and a 6*H*-SiC single crystal (curve *4*).

the line of reasoning can be different; indeed, fine elements of the structure resolved for relatively small values of s are components of coarser particles which are not characterized by a smooth and continuous internal distribution of electron density or by a smooth surface any longer. The above-mentioned Porod law does not hold for scattering at such loose particles either, or this law is observed only in a narrow interval of s.

The exponential decrease of $I(s)$ (9) with $1 < \alpha_2 < 3$, which we observed on all the types of *npor*-C samples for $s > s_2$, indicates a fractal stacking of finest carbon nanoparticles into clusters. The dimension D_2 ($\equiv \alpha_2$) of such small-scale fractal nanoclusters is also given in the table. The lower boundary of the fractal stacking mode on the s scale, i.e., s_2, provides an estimate for the size L_2 of a fractal cluster having the given dimension D_2: $L_2 \cong 2\pi/s_2$ (see the table). It can be seen that mass fractals formed in *npor*-C obtained from polycrystalline carbides have a slightly larger size than those formed in a sample prepared from the 6*H*-SiC single crystal. Generally speaking, the size l_2 of the finest particles constituting a cluster can be estimated roughly from the upper boundary of the fractal region in which a transition from the fractal mode to the Porod law observed for $sl_2 \gg 2\pi$ takes place. Such a transition takes place, for example, for porous silicon [2]. In our case, however, the value of l_2 in a cluster cannot be determined in view of the absence of the Porod asymptotic form in the range of s under investigation. It can only be stated that the size l_2 for various samples is at any rate smaller than 10–15 Å, which actually corresponds to the highest value of s attained in the experiments. Typically, the dimension of small-scale fractals in the *npor*-C⟨*poly*-SiC⟩ sample is close to two, indicating the formation of virtually planar carbon fragments with a typical size $L_2 \sim 75$ Å.

The table also contains the values of the exponent α_1 in the power law (9) describing the decrease of $I(s)$ for $s < s_2$. The range of s under investigation corresponds to larger-scale aggregates. Note that, while determining α_1 in this interval, we disregarded the initial segment of the SAXS curve ($s < 0.01$ Å^{-1}, $2\theta < 0.2°$), in which the accuracy of the reconstruction of the true function $I(s)$ from experimental data is not high enough. For all the samples except *npor*-C⟨*poly*-Mo_2C⟩, the value of α_1 lies between 3 and 4. It follows that SAXS in these samples for $s < s_1$ is determined by the fractal surface of large-scale nanoclusters, whose dimension is $D_1 = 6 - \alpha_1$ [1]. The values of D_1 noticeably exceed the value of 2 for ordinary smooth surfaces, indicating a considerable extent of unevenness (roughness) of the surface of large-scale nanoclusters. From this point of view, the surface of nanoclusters in a *npor*-C⟨*poly*-SiC⟩ sample for which D_1 is close to three is the most rugged. The minimum scale of the length l_1 on the fractal surface of nanoclusters, estimated from the upper boundary of s_1 of the corresponding linear segment (see Fig. 3), is found to be ~140 Å in *npor*-C⟨*poly*-SiC⟩ and *npor*-C⟨*poly*-TiC⟩ samples and ~60 Å in a *npor*-C⟨6*H*-SiC⟩ sample. For *npor*-C⟨*poly*-Mo_2C⟩, $\alpha_1 = 2.70 < 3$, and mass fractals with the dimension $D_1 = \alpha_1 = 2.70$ and the minimum size $l_1 \sim 140$ Å of particles constituting them play the part of large-scale scattering aggregates. The determination of the maximum scale of lengths L_1 over which the fractal structure of the surface or the bulk of large-scale clusters is preserved for the dimensions D_1 indicated above is limited by the discontinuity of the experimental SAXS function $I_{exp}(s)$ for small s. According to our results, $L_1 \geq 550$ Å.

The conclusion concerning the fractal nature of the surface of large-scale nanoclusters for *npor*-C⟨*poly*-SiC⟩ cannot be regarded as unambiguous, as the error in the estimates of the value of D_1 (± 0.15) does not allow one to rule out, for example, the three-dimensional nature of homogeneous large-scale clusters in the form of a homogeneous sphere (the sphere can be treated as a mass fractal of dimension $D = \alpha = 3$). Besides, the exponential decrease of $I(s)$ with $\alpha_1 \cong 3$ can be treated as the Porod law for the asymptotic form of scattering at large-scale two-dimensional objects for $sL_1 \gg 2\pi$. However, as the value of s increases further, the exponential decrease with $\alpha_1 \cong 3$ is replaced by a decrease with $\alpha_2 \cong 2$. This means that, as mentioned above, fine two-dimensional structural elements with a size $L_2 \cong 75$ Å contained in the system are resolved. At the same time, the exponential decrease with $\alpha_2 \cong 2$ can be interpreted as a manifestation of the Porod law for one-dimensional objects (filaments or rods). In the case of carbon, the formation of two-dimensional and even one-dimensional structural elements of nanometric size appears quite probable. Indeed, such elements composed, for example, of stacks of fragments of graphen layers more or less oriented in space are observed in the known forms of solid-state carbon, such as glass carbon or carbon fibers [13].

The results described above lead to the following conclusions concerning the nature of fractal nanostructure of *npor*-C samples under investigation. First of all, the shape of all the true SAXS curves (see Fig. 3) suggests that the hierarchy of nanostructural elements in *npor*-C contains at least two clearly separable groups of clusters, each characterized by its own law of bulk or surface organization, viz., small-scale nanoclusters of size L_2 and large-scale clusters, in which the minimum length scale approximately corresponds to the scale l_1 more or less close to L_2. It can be seen from the table that small-scale nanoclusters in *npor*-C obtained on the basis of different initial carbides are of the form of mass fractals with greatly different dimensions. This means that the microscopic mechanism of aggregation of the finest carbon particles with a size smaller than 10–15 Å into clusters strongly depends on the type of carbide-forming atoms removed in the course of the chemical reaction, and apparently, on the crystalline structure of

the initial carbide. For example, when the initial material is TiC with a cubic structure of the NaCl type, the nanoclusters formed have a very loose structure with a dimension $D_2 < 2$. In the case of other carbides (Mo_2C and 6*H*-SiC with a hexagonal structure), these are tighter and more homogeneous objects with a fractal dimension $D_2 > 2$. A special situation occurs when *npor*-C is obtained from polycrystalline α-SiC: in this type of *npor*-C, almost two-dimensional and probably even one-dimensional clusters are formed. One can assume that the presence of six-carbon rings in the (0001) plane of the hexagonal α-SiC facilitates the formation of the elements of graphen layers, which are similar to those existing in graphite in the (0002) plane. However, the formation of two- or one-dimensional clusters apparently requires a free discharge of the reaction products, which is realized in the case of *poly*-SiC due to micropores in the region of grain boundaries of the initial powder. However, in the bulk 6*H*-SiC single crystal, this supplementary condition is not satisfied, plane fragments in *npor*-C being formed undergo considerable distortions, and the fractal growth is terminated in this case for a smaller size $L_2 \sim 50$ Å of the cluster being formed.

The SAXS at large-scale nanoclusters in *npor*-C⟨*poly*-TiC⟩ and *npor*-C⟨6*H*-SiC⟩ is determined by the fractal interface between clusters and pores. The extent of roughness of the interfaces also depends on the type of the initial carbide. A *npor*-C⟨*poly*-Mo_2C⟩ sample contains quite large mass fractals, by their formation, starting from the size $l_1 \sim 140$ Å, is accompanied by a change in the particle stacking regularity with the formation of a denser structure: $D_1 > D_2$. In a *npor*-C⟨*poly*-SiC⟩ sample, large scale nanoclusters of size $L_1 >$ 550 Å are two- dimensional formations or three-dimensional aggregates with an extremely uneven fractal surface on a scale >140 Å. Such nanoclusters are composed of smaller two- or one- dimensional carbon fragments. In our opinion, this feature accounts for a high specific surface and adsorbability of *npor*-C obtained from polycrystalline α-SiC [11]. The problem of dimension of nanoclusters in *npor*-C⟨*poly*-SiC⟩ has no unique solution in the SAXS method. This question calls for supplementary methods of investigation which would make it possible to judge about the type of valence bonds and the structure of short-range order in the environment of carbon atoms.

ACKNOWLEDGMENTS

This research was carried out with the support of the Russian Foundation for Basic Research (grant no. 99-02-17984) and the Ministry of Science of the Russian Federation, under the program "Fullerenes and Atomic Clusters" (grant no. 98-059).

REFERENCES

1. H. D. Bale and P. W. Schmidt, Phys. Rev. Lett. **53** (6), 596 (1984).
2. P. Goudeau, A. Naudon, R. Herino, and G. Bomchil, J. Appl. Phys. **66**, 625 (1989).
3. J. C. Li and D. K. Ross, J. Phys.: Condens. Matter **6**, 351 (1994).
4. D. I. Svergun and L. A. Feĭgin, *X-ray and Neutron Small-Angle Scattering* (Nauka, Moscow, 1986).
5. R. Jullien, Usp. Fiz. Nauk **157** (2), 339 (1989) [Comments Condens. Matter Phys. **13** (4), 177 (1987)].
6. N. Yushkin, Dokl. Akad. Nauk **337**, 603 (1994) [Phys. Dokl. **39**, 562 (1994)].
7. M. V. Baĭdakova, A. Ya. Vul', V. I. Siklitskiĭ, and N. N. Faleev, Fiz. Tverd. Tela (St. Petersburg) **40** (4), 776 (1998) [Phys. Solid State **40** (4), 715 (1998)].
8. V. I. Ivanov-Omskii, V. I. Siklitsky, and M. V. Baidakova, in *Diamond-Based Composites and Related Materials*, Ed. by M. A. Prelas *et al.*, NATO ASI Series, 3. High Technology (Kluwer, Dortrecht, 1997), Vol. 38, p. 197.
9. US Patent No. 3066099 (1962).
10. N. F. Fedorov, G. K. Ivakhnyuk, and D. N. Gavrilov, Zh. Prikl. Khim. **55** (1), 272 (1981).
11. S. K. Gordeev and A. V. Vartanova, Zh. Prikl. Khim. **66** (7), 1080 (1994); **66** (8), 1375 (1994).
12. R. N. Kyutt, É. A. Smorgonskaya, S. K. Gordeev, *et al.*, Fiz. Tverd. Tela (St. Petersburg) **41** (5), 891 (1999) [Phys. Solid State **41** (5), 808 (1999)]; Fiz. Tverd. Tela (St. Petersburg) **41** (8), 1484 (1999) [Phys. Solid State **41** (8), 1359 (1999)].
13. Thomas W. Ebbesen, in *Carbon Nanotubes: Preparation and Properties* (CRC Press, Boca Ratón, 1997).

Translated by N. Wadhwa

Physics of the Solid State, Vol. 42, No. 6, 2000, pp. 1182–1185. Translated from Fizika Tverdogo Tela, Vol. 42, No. 6, 2000, pp. 1147–1150.

FULLERENES AND ATOMIC CLUSTERS

Paramagnetic Relaxation Kinetics of the Cation Radical C_{60}^+ in C_{60} Powder

G. G. Fedoruk

Institute of Applied Physical Problems, 220064 Minsk, Belarus

e-mail: fedoruk@zakaz.unibel.by

Received November 23, 1999

Abstract—The kinetics of spin–lattice and phase relaxation of C_{60}^+ radicals in C_{60} powder has been studied at room temperature by pulsed EPR. It is found that the kinetics can be described by the relation $\exp(-a\sqrt{t})$ characteristic of the case in which the paramagnetic centers are distributed over relaxation times. It is concluded that the observed kinetics are due to the presence of oxygen molecules, which act as a fast-relaxing impurity and accelerate the relaxation of the C_{60}^+ radicals. The results obtained offer an explanation for a number of features of C_{60}^+ relaxation in fullerites discovered earlier. © *2000 MAIK "Nauka/Interperiodica".*

1. INTRODUCTION

EPR signals are not likely to be observed in ideal fullerene-based solids (fullerites). Nevertheless, EPR signals are detected even in well-purified fullerites, and this can be explained to be due to their structural imperfections, as well as to impurities left after their synthesis and purification [1–4]. The C_{60} fullerite powder most frequently exhibits EPR signals with g = 2.0027(3), which is identified with the cation radical C_{60}^+ [1–3]. This signal is a single structureless line of width $\Delta B_{pp} \approx 0.15$ mT (between the extrema of the absorption signal derivative) and is observed in the temperature range from 1.7 to 300 K.

Relaxation parameters (the spin–lattice relaxation time T_1 and the phase relaxation time T_m) provide more detailed information on these radicals. References to publications on the relaxation of paramagnetic centers in C_{60} solutions can be found in [1]. As regards to the relevant studies in the solid-phase C_{60}, it was found [1] that paramagnetic relaxation of the C_{60}^+ radicals follows a double-exponential law. The fast component ($T_1 \approx 25$ μs, $T_m \approx 0.3$ μs) is practically independent of temperature. The slow component (T_1 = 400–700 μs, T_m = 1.4–2.6 μs) depends relatively weakly on temperature in the interval T = 4.2–90 K range studied here. Besides, T_1 decreases with increasing temperature much more slowly than according to the standard spin–lattice relaxation mechanisms involving one-phonon, Raman, or Ohrbach relaxation processes. The nature of the double-exponential relaxation kinetics remains unclear. A temperature dependence of T_1 for the C_{60}^+ radicals in a fullerite, which is anomalous from the standpoint of standard spin–lattice relaxation mechanisms, was also observed in [2] at T = 1.7–15 K. However, the low-temperature results obtained in [1] and [2] differ very strongly quantitatively. The relaxation times of C_{60}^+ radicals obtained in [2] for fullerite samples by continuous saturation at higher temperatures appear strange. For example, the values of T_1 presented in [2] (2 μs at 77 K and 0.5 μs at 300 K) turned out to be smaller than those of T_m (about 13 μs) determined by the same authors. Nutation EPR spectroscopy studies [4] revealed that the magnitude of T_1 of C_{60}^+ radicals found for fullerene-containing powders is considerably larger than the values obtained in [2] and exceeds 30 μs at room temperature. Besides, there are indications that the relaxation processes depend on the thermal treatment of fullerite samples [2], as well as on the surrounding gaseous medium [4].

In this paper, we present the results of an investigation of the spin–lattice and phase relaxation kinetics for C_{60}^+ radicals in C_{60} powder, carried out at room temperature by the pulsed EPR technique.

2. EXPERIMENTAL TECHNIQUE AND SAMPLES

The nonstationary EPR signals (nutation [5], double-pulse delayed nutation [6], nutation echo [6], and double-pulse electron spin echo) were produced by pulses of a polarizing magnetic field [6]. This technique is a magnetic counterpart of the method of Stark pulses used in optical resonance studies [7]. The nonadiabatic ($dB/dt \gg \gamma B_1^2$) onset of resonance conditions

$$\omega = \gamma B_0 = \gamma(B_s + \Delta B)$$

1063-7834/00/4206-1182$20.00

was achieved by varying the polarizing magnetic field B at fixed frequency ω and amplitude B_1 of the magnetic component of the microwave field. Here, γ is the gyromagnetic ratio, B_s is the dc component of the polarizing magnetic field, and ΔB is the amplitude of the polarizing magnetic-field pulses.

The studies were carried out on a 3-cm pulsed EPR spectrometer [6]. The maximum value of B_1 at the sample was about 0.054 mT, and it was high enough to produce nutation signals with a frequency $\omega_1 = \gamma B_1$ up to 1.52 MHz, $\Delta B = 0.12$ mT, and the rate of variation of the polarizing magnetic field was about 1.2 mT/μs. Nonstationary EPR signals with a rise time of 150 ns could be detected.

Nonstationary EPR signals were produced by two pulses with durations of t_1 and t_2, respectively, separated by a time interval τ. The spin–lattice relaxation kinetics were measured by the double-pulse delayed nutation method [6, 7], which permits one to study the dependence of the initial nutation signal amplitude during the second pulse on the pulse separation τ. We also used the nutation echo to probe spin–lattice relaxation, and we used double-pulse echo to investigate phase relaxation.

High-purity powder C_{60} samples (≥99.9%) were used in the measurements. Prior to being measured, the samples were annealed at $T = 150$°C for five hours in a dynamic vacuum of about 10^{-2} Torr and evacuated.

3. EXPERIMENTAL RESULTS

Stationary EPR spectra of all the samples studied displayed a symmetric EPR line of the C_{60}^+ radicals with $g = 2.0027(2)$ and $\Delta B_{pp} \approx 0.15$ mT. After annealing, the linewidth decreased.

The kinetics of spin–lattice relaxation measured by double-pulse delayed nutation on an evacuated sample are shown in Fig. 1. While the pattern of kinetics was similar for all samples, the relaxation rate was somewhat different and increased when air was admitted to the samples.

If, for instance, the process is described by one spin–lattice relaxation time T_1, the dependence shown in Fig. 1 should obey the relation [6, 7]

$$\nu(\tau) = \nu_0\left[1 - \exp\left(-\frac{\tau}{T_1}\right)\right], \qquad (1)$$

where ν_0 is the maximum amplitude of the nutation signal measured during the first pulse. However, the dependence (1) was not observed in the samples studied by us. One could attempt to approximate the kinetics in Fig. 1 by a double-exponential decay curve. The curve in Fig. 1 is such an approximation with relaxation times of 15 and 85 μs. Note that it is a double-exponential approximation that was employed for data processing in [1]. As already mentioned, however, such kinetics cannot be explained in this case.

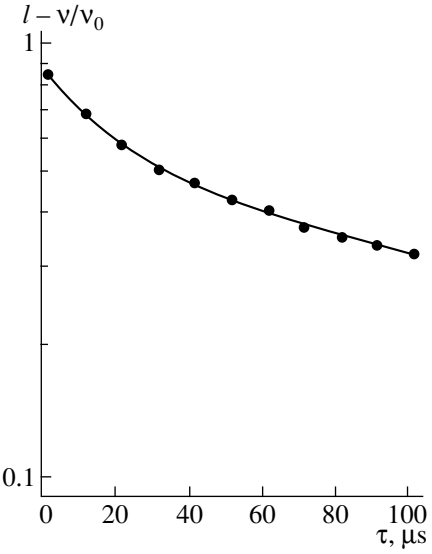

Fig. 1. Spin-lattice relaxation kinetics of an evacuated C_{60} sample. The curve is a semilogarithmic anamorphosis corresponding to the sum of two exponentials.

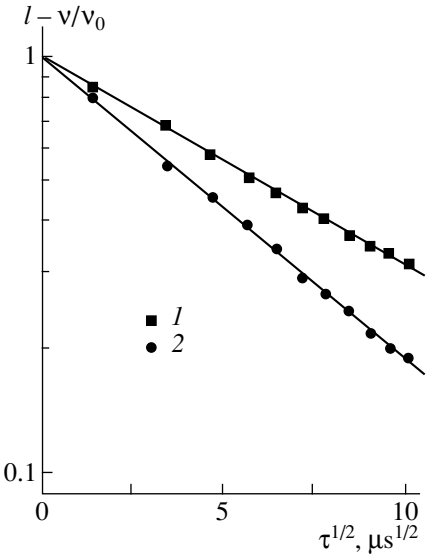

Fig. 2. Spin-lattice relaxation kinetics of an evacuated (*1*) and a nonevacuated (*2*) C_{60} sample. The lines are semilogarithmic anamorphoses of the kinetics described by Eq. (2).

The spin–lattice relaxation kinetics of the same sample measured by us in a vacuum and in air is presented in Fig. 2 in the $\log(\nu/\nu_0) - \tau^{1/2}$ coordinates. The measurements in air were performed 30 min after admitting air to the sample. As seen from Fig. 2, the

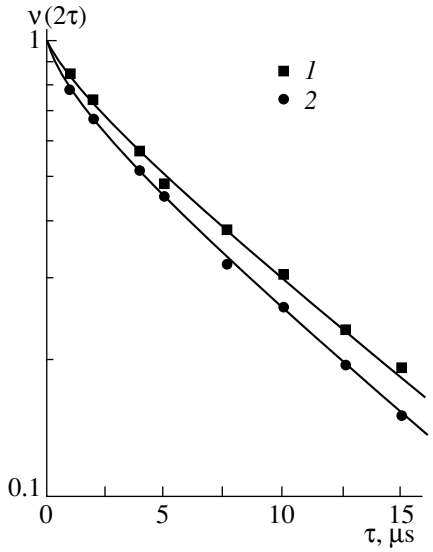

Fig. 3. Phase relaxation kinetics of an evacuated (*1*) and a nonevacuated (*2*) C_{60} sample.

experimental data can be approximated within measurement error by a dependence of the type

$$\nu(\tau) = \nu_0\{1 - \exp(-a\sqrt{\tau})\}. \quad (2)$$

These kinetics are typical of the case where paramagnetic centers are distributed over times T_1 [8]. The most probable spin–lattice relaxation time is

$$T_1^m = \frac{2}{d^2}. \quad (3)$$

The values of a derived from the data in Fig. 2 are 0.115(15) and 0.166(17) $\mu s^{-1/2}$ for the samples in a vacuum and in air, respectively. The values of T_1^m obtained for these samples from (3) are 151(15) and 73(7) μs.

The spin–lattice relaxation kinetics measured by the nutation echo technique for $\tau \gg t_1$ = const was approximated by the relation

$$\nu(\tau) \propto \exp(-a\sqrt{\tau}). \quad (4)$$

The values of the parameter a determined by nutation echo and double-pulse delayed nutation were found to coincide.

Figure 3 shows the double-pulse echo decay for the sample whose spin–lattice relaxation kinetics are shown in Fig. 2. The echo was formed by two identical pulses of duration 0.2 μs at ω_1 = 1.52 MHz.

4. DISCUSSION OF RESULTS

The kinetics of type (2) can be observed in magnetically dilute solids in the cases where the sample is characterized by a distribution of spin–lattice relaxation times. In particular, a spread in T_1 may be due to rapidly relaxing additional impurities which act as sinks of the spin system energy to the lattice [8]. The dependence of the relaxation rate of C_{60}^+ radicals on the presence of air around a sample indicates that the observed kinetics are related with the existence of paramagnetic oxygen molecules in the samples. Compared to the radicals, these molecules are fast-relaxing impurities. The parameter a is expected to be proportional to the impurity concentration. It was also pointed out in [2] that at 4.2 K, T_1 of the C_{60}^+ radicals increased by an order of magnitude after annealing, while their concentration remained practically unchanged. This led to the conclusion that annealing changed the pattern of the local radical distribution toward a decrease in the size of exchange interacting aggregates. The conclusions made in [2] are not convincing in the absence of an analysis of a possible effect of oxygen and of a reliable determination of T_m as well as the local radical concentration from the saturation of steady state spectra, particularly in the case of relaxation kinetics of type (2). Recall the paradoxical nature of relaxation times ($T_1 < T_m$) obtained in [2]. The data obtained in steady-state saturation in [2] were processed using a semiphenomenological approach based on the model of noninteracting spin packets of Lorentzian shape. For the case of the relaxation kinetics of type (2), it was shown [9] that such an approach may result in a substantial (by a few orders of magnitude) error in the estimates of the dipole–dipole interaction.

It can be easily seen that the values of T_1 obtained in this work are larger than those found for fullerite powders at room temperature by the continuous saturation technique [2] by two orders of magnitude. They are smaller only by a factor of three than the values obtained in [2] by pulsed EPR technique at low temperatures (20–90 K) for unannealed samples in air. The spin–lattice relaxation time of C_{60}^+ radicals in solid-phase fullerenes is found to be comparable to T_1 of the substituting nitrogen in such an allotropic modification of carbon as diamond [10] and of nitrogen atoms embedded in the C_{60} molecule in solutions of $N@C_{60}$ endohedrals [11].

Because the concentration of magnetic nuclei in C_{60} is low, it can be expected that the phase relaxation kinetics of C_{60}^+ in the presence of oxygen molecules will follow the relation

$$\nu(2\tau) = \nu(0)\exp(-2b\tau - a\sqrt{\tau}). \quad (5)$$

The first term in the argument of the exponential describes phase relaxation caused by the dipole–dipole interaction between radicals by the mechanism of instantaneous diffusion, while the second term corresponds to the mechanism of spectral diffusion due to the dipole–dipole interaction between C_{60}^+ and the oxy-

gen molecules. The lines in Fig. 3 show the kinetics (5) for $a = 0.115(15)$ and $0.166(17)$ $\mu s^{-1/2}$, respectively, and $b = 0.042$ μs^{-1}.

This value of b can be used to estimate the local radical concentration N. The highest possible decay rate of the primary echo signal due to the dipole–dipole interaction among the spins distributed in a random manner over the lattice can be written as [8]

$$b = \frac{4\pi^2\gamma^2\hbar N}{9\sqrt{3}}. \quad (6)$$

According to (6), $N < 9 \times 10^{16}$ cm^{-3} for our samples.

Besides accounting for multiexponential kinetics, spectral diffusion caused by fast-relaxing impurities may also give rise to a temperature dependence of the spin–lattice and phase relaxation, which would appear anomalous from the standpoint of standard mechanisms [8]. This possibility was disregarded in the analysis of experimental data in [1, 2].

ACKNOWLEDGMENTS

The author expresses his gratitude to V. F. Stel'makh for fruitful discussions and to A. G. Soldatov for kindly providing the samples.

REFERENCES

1. S. K. Hoffman, W. Hilczer, W. Kempin'ski, and J. Stankowski, Solid State Commun. **93** (3), 197 (1995).
2. I. M. Zaritskiĭ, S. S. Ishchenko, A. A. Konchits, *et al.*, Fiz. Tverd. Tela (St. Petersburg) **38** (2), 419 (1996) [Phys. Solid State **38** (2), 231 (1996)].
3. F. Pozploch, S. Jagielski, L. Nowak, *et al.*, Mol. Phys. Rep. **18**/**19**, 131 (1997).
4. G. G. Fedoruk, S. M. Pancovetz, V. D. Shimanovich, *et al.*, in *Abstract of the XVII Conference on Radio- and Microwave Spectroscopy, Specialized Colloque AMPERE/RAMIS'97, Poznan, 1997*, p. 4.
5. H. C. Torrey, Phys. Rev. **76** (8), 1059 (1949).
6. G. G. Fedoruk, Zh. Prikl. Spektrosk. **65** (3), 405 (1998).
7. R. Shoemaker, in *Laser Coherence Spectroscopy*, Ed. by J. Steinfeld (Plenum, New York, 1978; Mir, Moscow, 1982).
8. K. M. Salikhov, A. G. Semenov, and Yu. D. Tsvetkov, *Electron Spin Echo and Its Applications* (Nauka, Novosibirsk, 1976).
9. V. V. Kurshev, A. M. Raĭtsimring, and Yu. D. Tsvetkov, Teor. Éksp. Khim. **5**, 520 (1989).
10. R. C. Barklie and J. Guven, J. Phys. C: Solid State Phys. **14**, 3621 (1981).
11. C. Knapp, R.-P. Dinse, B. Pietzak, *et al.*, Chem. Phys. Lett. **272** (5–6), 433 (1977).

Translated by G. Skrebtsov

Physics of the Solid State, Vol. 42, No. 6, 2000, pp. 991–1008. Translated from Fizika Tverdogo Tela, Vol. 42, No. 6, 2000, pp. 961–978.

REVIEW

Low-Temperature Pyroelectricity

V. K. Novik and N. D. Gavrilova

Moscow State University, Vorob'evy gory, Moscow, 119899 Russia

e-mail: novikmp@orc.ru

Received October 14, 1999; in final form, December 14, 1999

Abstract—The current state of the set of problems associated with the study and application of the pyroelectric effect at low ($T < 30$ K) temperatures is outlined. The reasons for the qualitatively different temperature dependences of the total pyroelectric coefficient $\gamma^{\sigma}(T)$ in linear pyroelectrics and ferroelectrics are discussed. An analysis is given of the reasons why the theoretical temperature dependences obtained for the primary pyroelectric coefficient $\gamma^{\varepsilon}(T)$ adequately describe the experimental $\gamma^{\sigma}(T)$ dependences for all materials studied. In this connection, the correctness of determining the secondary pyroelectric coefficient $\gamma^{\delta}(T)$ from the macroscopically measured coefficients of thermal expansion is considered. The potential of thermodynamically nonequilibrium polar media and low-temperature pyroelectric materials is substantiated. The review consists of the following sections: (1) an introduction; (2) the theory of low-temperature pyroelectricity; (3) experimental procedures; (4) discussion of the experimental data: (A) perfect single crystals, (B) the problem of the secondary pyroelectric coefficient, (C) imperfect single crystals; (5) pyroelectric materials for low-temperature applications; and (6) a conclusion. © *2000 MAIK "Nauka/Interperiodica".*

1. INTRODUCTION

The pyroelectric effect is a change in the zero-field electric dipole moment of a unit volume (spontaneous polarization) of a single- or polycrystal dielectric when its temperature is varied uniformly over this volume. This effect refers to a large class of thermoelectric phenomena that manifest themselves as electrification of the dielectric when the temperature is varied. The spontaneous electric polarization is characteristic of crystals that belong to one of the following ten polar crystal symmetry classes: 1, 2, *m*, *mm*2, 3, 3*m*, 4, 4*mm*, 6, and 6*mm*. According to various estimates, the class of polar dielectrics (organic for the most part) covers more than a million compounds, which is about a fifth of all crystal solids.

At room and higher temperatures, pyroelectricity of linear pyroelectrics and ferroelectrics is well understood, and each of the stages in the traditional sequence—physics of the phenomenon, methods for controlling the properties, materials science, and practical applications—is realized. Pyroelectric transducers are currently used in various thermal radiation detectors, infrared imaging matrices, chromatographic detectors, thermometers, derivatograph sensors, anemometers, shock-wave sensors, etc. All these devices are manufactured by firms in Russia and other countries.

Low-temperature pyroelectricity is interesting because this effect is believed to have simple features universal for a wide variety of solids at $T \longrightarrow 0$. At the same time, the studies of low-temperature pyroelectricity are viewed as a basis for its applications. The total amount of information, accumulated in those studies, is the foundation for this review.

In the review, we discuss the set of problems associated with the study and applications of the pyroelectric effect at low temperatures ($T < 30$ K). Our primary purpose is to outline (1) the basic mechanisms determining the temperature dependences of the pyroelectric coefficients of both perfect and imperfect single crystals in the temperature range $1.5 < T < 30$ K, (2) the methods for controlling the properties of these materials, and (3) the fundamentals of the pyroelectric-materials science. The upper limit of the temperature range is that above which the typical low-temperature mechanisms commonly cease to operate, while the lower limit separates the range in which the reliable experimental data are unavailable. In what follows, the $T < 1.5$ K range is referred to as that of ultralow temperatures.

2. THEORY OF LOW-TEMPERATURE PYROELECTRICITY

A quantitative measure of the pyroelectric effect is the pyroelectric coefficient (PEC)

$$\boldsymbol{\gamma}_i^{\sigma}(T) = (\partial \mathbf{P}_s/\partial T)_{E_i} = (\partial P_s/\partial T)\mathbf{p} + (\partial \mathbf{p}/\partial T)P_s$$

$$\mathbf{p} = \mathbf{P}_s/P_s,$$

where $\boldsymbol{\gamma}_i^{\sigma}(T)$ is the PEC at a fixed mechanical stress $\sigma = 0$; $\mathbf{P}_s(T)$ is the spontaneous polarization; T is the temperature; and $E_i \cong 0$ is the electric field in the pyroelectric.

The spontaneous polarization and the PEC are vectors. However, since these quantities are measured on

1063-7834/00/4206-0991$20.00

samples with a fixed crystallographic orientation *i*, we shall drop the index and vector notation when discussing the theoretical results.

Using the thermodynamic relationships for the pyroelectric effect, it was shown that the PEC at a constant mechanical stress, $\gamma^{\sigma}(T)$, consists of two components,

$$\gamma^{\sigma}(T) = \gamma^{\varepsilon}(T) + \gamma^{s}(T), \quad (1)$$

where $\gamma^{\varepsilon}(T)$ is the primary PEC, which could have been measured if the crystal's shape and size had not been varied, that is, if there had been no thermal expansion (ε = const = 0); and $\gamma^{s}(T)$ is the secondary PEC, $\gamma^{s}(T) = d_{ijk}^{T,E}(T)\, c_{jklm}^{T,E}(T)\, \alpha_{lm}^{\sigma,E}(T)$.

Here, $d_{ijk}^{T,E}$, $c_{jklm}^{T,E}$, and $\alpha_{lm}^{\sigma,E}$ are the piezoelectric coefficients, the elastic stiffness constants, and the coefficients of thermal expansion, respectively; the repeated indices are understood to be summed over; and the index *i* corresponds to the direction of the spontaneous polarization.

General phenomenological theories can be developed only for the component $\gamma^{\varepsilon}(T)$. The other component, $\gamma^{s}(T)$, consists of a large number (especially for lower symmetry) of temperature-dependent terms and reflects the individual properties of the crystal. Only at $T \le 6$ K, where $\alpha_{lm}^{\sigma,E}(T) \sim T^3$ [1], can the component $\gamma^{s}(T) \sim T^3$ be *a priori* included.

The conditions for the thermodynamic stability (integrity) of the crystal [2] and the third law of thermodynamics [3] impose restrictions on the form of the $\gamma^{\varepsilon}(T)$ dependence as $T \longrightarrow 0$ (for $T \le 0.1\Theta_D$, where Θ_D is the Debye temperature). According to [2],

$$|\gamma^{\varepsilon}(T)| < \beta T, \quad (2)$$

where β is a constant. According to [3], the dependence must satisfy the condition

$$|\gamma^{\varepsilon}(T)| \sim T^n \text{ with } n \ge 3. \quad (3)$$

Hence, in thermodynamically equilibrium polar media, the primary PEC must vary as the cubic or a higher power of temperature when $T \longrightarrow 0$. In thermodynamically nonequilibrium polar media, this coefficient may tend to a constant as $T \longrightarrow 0$ [4],

$$\gamma^{\sigma}(T) = \text{const}. \quad (4)$$

There is also a general thermodynamic relation [5] between $\gamma^{\varepsilon}(T)$ and the specific heat at constant volume $C_v(T)$. Since the spontaneous polarization at constant strain P_s^{ε} and the total internal energy U are single-valued functions of temperature, they can be related to each other. Expanding the temperature-dependent part of the total internal energy ΔU in powers of ΔP_s^{ε}, we can write $\Delta U = a_1 \Delta P_s^{\varepsilon}$ plus terms proportional to $(\Delta P_s^{\varepsilon})^2$, $(\Delta P_s^{\varepsilon})^3$, etc. Dropping the higher order terms, we have, at $T \longrightarrow 0$,

$$C_v(T) = (\partial U/\partial T)_v \sim (\partial P_s^{\varepsilon}/\partial T) = \gamma^{\varepsilon}(T). \quad (5)$$

The proportionality takes place between the individual contributions to the specific heat and the PEC from every vibrational mode involved in the variation of P_s^{ε}, as well as from any other pyroelectrically active process [6] (see also (6f), (6g) and [7]).

In all the theories of low-temperature pyroelectricity that agree with the experiment, it is assumed that the temperature variation of each component of the total dipole moment of a unit volume [spontaneous polarization $P_s^{\varepsilon}(T)$] at constant volume and shape of the sample is solely due to the spatial displacements of the charges that compose dipoles; the charges themselves are assumed to be unchanged with any variations in temperature. Although there is no experimental data arguing against this assumption, we shall cite, for completeness, a theoretical paper [8] in which the contribution to pyroelectricity from dipoles with temperature-dependent charges is considered. These charges may be associated with any charged structural units of the crystal lattice: individual ions, molecules, or molecular complexes.

The experimental data suggest that there are only two typical fundamental mechanisms of low-temperature displacements of charged structural units: (a) anharmonic acoustic and optical lattice vibrations and (b) displacements of charged structural units in asymmetric potential wells. Particular mechanisms of low-temperature structural and magnetic phase transitions that reveal themselves in the pyroelectric effect will not be discussed in this section, because they are still little understood and there are no commonly accepted theories developed for them. The relevant experimental data will be presented later.

(a) Anharmonic Lattice Vibrations and Canonical Dependences

We shall refer to the temperature dependence of the pyroelectric coefficient as the canonical one if it is due to anharmonic vibrations of charged structural units of the crystal lattice.

The temperature dependence of the PEC caused by collective anharmonic acoustic vibrations is given by the expression [6, 9–11]

$$\gamma^{\varepsilon}(T) = AD(\Theta_D/T), \quad (6a)$$

while the temperature dependence due to individual anharmonic polar optical modes is [9–13]

$$\gamma^{\varepsilon}(T) = \sum B_i E(\Theta_{Ei}/T), \quad (6b)$$

where $\gamma^{\varepsilon}(T)$ is the primary PEC; A and B_i are constants; $D(\Theta_D/T)$ and $E(\Theta_{Ei}/T)$ are the Debye and Einstein func-

tions, respectively, for the specific heat at constant volume; and Θ_D and Θ_{Ei} are the corresponding characteristic temperatures.

It should be noted that, even in 1922, Born pointed out [14] that experimental data for the temperature range extending down to liquid helium temperature were required for the general theory of pyroelectricity to be constructed. For a wide temperature range, Born derived the expression [10]

$$\gamma^{\varepsilon}(T) = AD(\Theta_D/T) + \sum B_i E(\Theta_{Ei}/T). \qquad (6c)$$

(b) Displacements of Charged Structural Units in Asymmetric Potential Wells

At low and ultralow temperatures, the thermal and electrical properties of polar crystals strongly suggest that the potential relief has features characterized by an energy gap of $\delta \sim 1$ meV (Figs. 1a, 1b). In particular, if there are two or several potential wells with a difference in depth like that for the units of the lattice structure, the average spatial arrangement of these units must vary with a decrease in temperature because of their ordered localization in the potential wells.

To describe this mechanism, the Ising model in the mean-field approximation was used [15]. The $\gamma^{\varepsilon}(T)$ dependence was calculated in this model when the structural units are ordered in a double-well potential with an energy gap $\delta(T)$ (Fig. 1a). At minima *1* and *2*, the dipole moment p of a unit makes angles ξ_1 and ξ_2, respectively, with the direction of the spontaneous polarization of the matrix; the binding energies between the crystal lattice and the structural unit (element) at minima *1* and *2* differ by S. The calculated dependence is

$$\gamma^{\varepsilon}(T) = Np(\cos\xi_1 - \cos\xi_2) \times \frac{\ln^2[(1-w)/w]}{b\ln[(1-w)/w] + (bw-a)/w(1-w)}, \qquad (6d)$$

where

$$a = \frac{1}{k_b}\left[\frac{8\pi}{3}p(\cos\xi_1 - \cos\xi_2)(Np\cos\xi_2 \pm \pm P_s(T=0)) + S\right],$$

$$b = \frac{8\pi}{2k_b}Np^2(\cos\xi_1 - \cos\xi_2)^2;$$

$$T = (bw-a)/\ln[(bw-a)/w], \qquad (6e)$$

$$W(T) = \frac{1}{1+\exp(-\delta(T)/k_bT)},$$

$$\delta(T) = k_b[a - bW(T)],$$

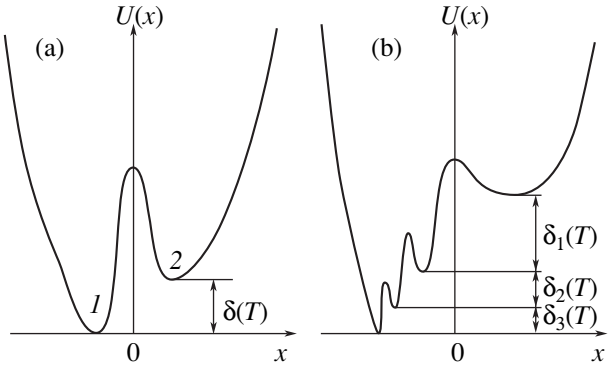

Fig. 1. Potential field in which a localizing particle moves: (a) an asymmetric double-well potential and (b) a hypothetical multiwell potential; $\delta(T)$ is the energy gap.

k_b is the Boltzmann constant; $W(T)$ is the probability of the occupation of position *1* ($W = 1$ at $T = 0$, and $W = 0.5$ at $T \longrightarrow \infty$); and N is the number of ordering structural elements per unit volume. If the microscopic quantities δ, N, p, ξ_1, ξ_2, S, and P_s have all been known, one could have calculated a and b and thus obtained the $\gamma^{\varepsilon}(T)$ dependence in an explicit form. Unfortunately, it is unlikely to experimentally determine this set of quantities and, therefore, a and b should be considered to be adjustable parameters.

Expression (6d) is universal and adequately describes both the low-temperature [16] and high-temperature (about 50 to 250 K) $\gamma^{\sigma}(T)$ dependences (e.g., in cancrinite and nepheline, see [17]).

The influence of ordering dipoles on the value of the energy gap $\delta(T)$ is of fundamental importance [see the term $(-bW(T))$ in (6e)] and should be taken into account when describing the high-temperature dependences. Physically, this means that the ordering charged structural unit itself, as well as the neighbor atoms of the crystal lattice, participates in the formation of the double-well potential.

In the case of low-temperature pyroelectricity, the double-well potential with an energy gap of $\delta \sim 1$ meV is simply the initial single-well potential slightly distorted by, say, defects of the crystal lattice. In this case, the ordering structural element (proton) cannot significantly affect the value of $\delta(T)$ and, at $T \leq 4$ K, one can put $\delta(T) = \text{const} = \delta(0) = ak_b$. The validity of this approximation is confirmed by calculations from formula (6d) using the experimental data [16]; for doped triglycine sulphate, we thus obtain $a \cong 5.2$ K, $b = 0$, and hence $\delta(0) \cong 0.23$ meV.

With the condition $b = 0$, the cumbersome expression (6d) is much simplified and becomes

$$\gamma^{\varepsilon}(T) = \frac{k_b}{\delta}Np(\cos\xi_1 - \cos\xi_2)\left(\frac{\delta/2k_bT}{\cosh(\delta/2k_bT)}\right)^2. \qquad (6f)$$

In the same case, the temperature dependence of the specific heat, determined by the process of ordering, is

given by

$$C_v(T) = Nk_b\left(\frac{\delta/2k_bT}{\cosh(\delta/2k_bT)}\right)^2. \quad (6g)$$

Thus, we have the proportionality $C_v(T) \sim \gamma^\varepsilon(T)$, in agreement with (5).

The model of the temperature-dependent displacement of the structural unit in a double-well potential, considered above, can be easily generalized to the case (a) of simultaneous displacements of several structural units in the corresponding potential wells or (b) of successive displacements of the structural unit in a multiwell potential. Most likely, these generalizations will be realized by numerical methods and will be the first step on the road to a comprehensive theory of pyroelectric materials at temperatures $T \ll 1.5$ K.

3. EXPERIMENTAL PROCEDURES

For a quantitative analysis of the $\gamma^\sigma(T)$ dependences for specific types of a single crystal, one should use experimental dependences obtained on highly perfect crystals and in temperature ranges starting from 1.5–2 K. Technically pure monocrystalline samples, unfortunately, show marked individual features (Fig. 5a, curves *1* and *2*).

The experimentally measured $\gamma^\sigma(T)$ curves under the conditions indicated above will allow one (1) to establish the fundamental relation between pyroelectricity and the lattice dynamics; (2) to employ these curves as the reference when comparing with $\gamma^\sigma(T)$ dependences in similar crystals with defects in order to study the influence of defects on these dependences; and (3) to determine the contribution to the $\gamma^\sigma(T)$ dependence from the lowest frequency modes, with wavenumbers 5–15 cm^{-1}, which can be correctly identified only at $T \geq 1.5$ K.

The choice of the appropriate experimental procedure for low-temperature measurements of the pyroelectric coefficient is of fundamental importance. When determining the numerical value of the PEC by this procedure, the result must be very carefully corrected for spurious signals and interference in each measurement act. Only after this *prior* "refinement" should the numerical data be subjected to a statistical treatment.

Among numerous well-known methods, only the static technique meets the requirements indicated above, in which a running record is made of the pyroelectric current pulse during a stepwise increase in temperature ΔT from one steady-state value T_1 to another steady-state value T_2.

The time dependences of the pyroelectric current and of some accompanying effects (thermodepolarizing and electret currents) with a stepwise increase in temperature are qualitatively different. A running record allows one to extract the pyroelectric pulse current with a required accuracy and then to determine the released pyroelectric charge ΔQ by integration of this current. Given ΔT and ΔQ in each measurement act, one can immediately calculate the PEC γ^σ for the temperature T by the formula

$$\gamma^\sigma(T) = \Delta Q/S\Delta T,$$

where S is the electrode area of the sample; $\Delta T = T_2 - T_1$; $T = (T_1 + T_2)/2$; $\Delta T \ll T$.

Making repeated measurements near selected temperature values (for both an increase $T_1 \longrightarrow T_2$ and a decrease $T_2 \longrightarrow T_1$), as well as on heating and cooling runs, one can obtain the required data array for the subsequent mathematical treatment.

It is well to bear in mind that, at $T = 1.5$–2 K, the steps should be as small as $\Delta T \approx 0.05$–0.15 K. At these temperatures, the typical values of the PEC are $\gamma^\sigma \sim 5 \times 10^{-14}$ C cm^{-2} K^{-1}, that is, six orders of magnitude smaller than those at room temperature. Charge signals can be measured with reasonable accuracy if $\Delta Q \geq 10^{-13}$ C. For charge signals to be as large as these values, the surface area of samples must be large, $S \approx 5$–7 cm^2.

An experimental technique that meets the requirements indicated above is very delicate [18]. In the process of measurements, samples should be mechanically free and have no temperature gradients. Their thickness must be about 2–3 mm to ensure against strains caused by the tension of sputtered electrodes. The electric circuit transmitting the pyroelectric signal from the low-temperature zone must have a minimal thermal electrification (less than 10^{-15} C), with its insulation resistance being $\sim 10^{14}$ Ω.

When investigating the mechanisms specific to low-temperature pyroelectricity, the $\gamma^\sigma(T)$ dependences must also be measured in the directions that are nonpolar at room temperature. The component of the spontaneous polarization along these directions may become nonzero on cooling because of the symmetry reduction of the crystal lattice.

Reliable experimental data on the $\gamma^\sigma(T)$ dependence require a great deal of the unified efforts of experimental physicists and experts in crystal growth. That is why there is a relatively small number of correct papers on low-temperature pyroelectricity.

4. DISCUSSION OF THE EXPERIMENTAL DATA

A. Perfect Single Crystals

Expressions (6a) and (6c) agree surprisingly well with the correctly measured $\gamma^\sigma(T)$ dependences for a wide range of linear pyroelectrics [11, 17, 19, 20–24], and expression (6b) does so for ferroelectrics of various types [11, 13, 16, 17, 25–30]. Expressions (6a)–(6c) are valid for both binary (II–VI) compounds and single crystals having tens or hundreds of atoms per unit cell (tourmaline, triglycine sulphate, boracites). Some examples are presented in Table 1.

Table 1. Approximations to the experimental $\gamma^\sigma(T)$ dependences given by (6a), (6b), and (6c)

Compound	Temperature range, K		Approximation parameters Θ_D, K; ν_{Ei}, cm^{-1}	References
	measurements of $\gamma^\sigma(T)$	approximations to $\gamma^\sigma(T)$		
Linear pyroelectrics				
ZnO	5–300	5–300	240 K, 436	[17]
CdS	5–300	5–300	120 K, 292	[17]
Pink tourmaline	5–900	5–850	220 K, 486, 3560	[17]
Resorcinol $C_6H_2(OH)_2$	5–350	5–320	115 K, 177, 520	[17]
$(C_3H_5O_4)Na$	4.2–350	5–350	200 K, 818	[21]
$(C_3H_5O_4)K$	10–350	10–350	250 K, 375	[21, 22]
$(C_3H_5O_4)Pb$	10–350	10–350	140 K, 319	[21, 22]
$Li_2SO_4 \cdot H_2O$	5–350	5–300	265 K, 325, 1200	[17, 24]
$Li_2SO_4 \cdot H_2O$	1.5–350	1.5–325	275 K, 100, 189, 765	[23]
Ferroelectrics				
LTT, $T_C \cong 13$ K	5–100	5–11	13.9; 29.8	[17, 30]
TGS, $T_C = 322$ K	5–330	7–270	50.4; 173; 615; 1535	[17]
TGS, $T_C = 322$ K	1.5–330	1.5–100	10; 47.2; 154	[16, 30]
KDP + Cr^{3+}, $T_C = 122$ K	5–130	5–100	33.4; 129; 500	[17, 24]
KDP, $T_C = 122$ K	1.5–330	1.5–100	30.5; 130; 546	[27, 29, 30]
DKDP, $T_C = 213$ K	1.5–220	1.5–55	76.5; 197	[27, 29, 30]
$LiNbO_3$, $T_C = 1470$ K	5–500	5–350	50; 79.3; 230	[17, 24]
$LiNbO_3$, $T_C = 1470$ K	1.5–80	1.5–80	81.9; 161	[16]
$LiTaO_3$, $T_C = 890$ K	10–200	10–200	81; 218	[13]
$LiTaO_3$, $T_C = 890$ K	1.5–80	1.5–80	80.5; 171	[16]
$KTiOPO_4$, $T_C = 165$ K	5–80	14–80	96.2	[25]

The single crystals indicated in this table as those for which measurements were carried out in a range from 1.5 K are perfect samples or, if not perfect those of the highest quality attainable by today's standards. The others are technically pure. The sample of tourmaline is a mineral.

Both the highly perfect and technically pure samples of the group of polar dielectrics in Table 1 show qualitatively similar behavior (see $Li_2SO_4 \cdot H_2O$, TGS, KDP, $LiNbO_3$, $LiTaO_3$), differing only in the numerical values of the approximation parameters. Clearly, the presence of defects in the samples, the limitations of the measuring techniques, and the value of the lowest temperature of the approximation have some effect on the approximation parameters, but they cannot radically alter the form of the approximation. Noteworthy is the small number of terms in the approximations describing the $\gamma^\sigma(T)$ dependences in wide temperature ranges. Therefore, even in multiatomic single crystals, such as tourmaline and triglycine sulphate (TGS), a highly limited number of polar optical modes are involved in the temperature variation of the spontaneous polarization.

A great body of experimental data [11, 13, 16, 17, 19–30] shows that the $\gamma^\sigma(T)$ dependences are adequately described in terms of the theories developed for $\gamma^\varepsilon(T)$ and that the pyroelectric properties of various materials at $T \longrightarrow 0$ are described by similar formulas within each of two groups of polar dielectrics: linear pyroelectrics, formulas (6a) and (6c), and ferroelectrics, (6b). In the first group, the $\gamma^\sigma(T)$ dependence at $T \longrightarrow 0$ is due to the anharmonism of acoustic vibrations [(6a), (6c)], while in the second group, it is due to anharmonism of optical vibrations, (6b), or, more precisely, due to that of the lowest polar mode (Fig. 2).

Expression (6b) describes the low-temperature behavior of $\gamma^\sigma(T)$ of ferroelectrics of various symmetry and chemical composition, intrinsic and improper ones, hydrogenous (LTT [16], KDP [17, 27, 29], DKDP [27, 29], TGS [16, 17, 26]), oxygen-octahedron ($BaTiO_3$ [17], $LiNbO_3$ [11, 16, 17], $LiTaO_3$ [13, 16], boracites [17, 24]), and oxygen-free ones (Ag_3AsS_3 [17, 31], $TlInS_2$ [28]), with phase-transition points from 13 K (lithium thallium tartrate, LTT) to 1470 K ($LiNbO_3$).[1]

[1] In the context of this general conclusion, it is of interest to measure $\gamma^\sigma(T)$ of the ferroelectric phase ($T_C \cong 47$ K) of monocrystalline BCCD, which undergoes fifteen structural transformations [32] above this transition.

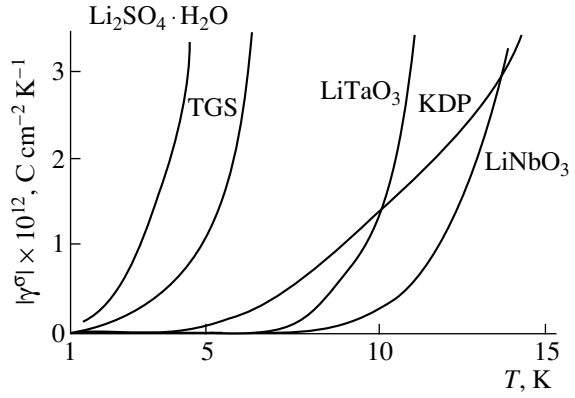

Fig. 2. Low-temperature portions of the $\gamma^\sigma(T)$ dependences of perfect single crystals. Curves: $Li_2SO_4 \cdot H_2O$ [22]; TGS (triglycine sulphate) [15]; $LiTaO_3$ [15]; KDP (potassium dihydrogen phosphate) [26, 28]; and $LiNbO_3$ [15]. Experimental dots are dropped. For single crystals of $Li_2SO_4 \cdot H_2O$, the relation $\gamma^\sigma(T) \sim T^3$ holds in a range of 1.5–6 K [22].

The Debye temperatures Θ_D of linear pyroelectrics determined from pyroelectric measurements (Fig. 3) agree with those obtained from calorimetry data and from elastic-constant measurements, while the quantities $\Theta_{Ei} = \hbar\omega_{Ei}/k_b$ correspond closely to the wavenumbers ν_i of experimentally observed modes in the vibrational spectra of linear pyroelectrics and ferroelectrics. The procedure of determining Θ_D and Θ_{Ei} is clear from Fig. 3.

For all linear pyroelectrics that have been studied up to now and for which the temperature dependence of the specific heat $C_{p,E}(T) \cong C_v(T)$ has been measured, relation (5) is valid in the low-temperature range. The proportionality $C_{p,E}(T) \sim \gamma^\sigma(T)$ takes place for II–VI compounds up to temperatures $T \geq 100$ K [11, 19], for $Li_2SO_4 \cdot H_2O$ up to 20 K [23], and for $C_6H_2(OH)_2$ (resorcinol) samples up to 85 K [16]. It is noteworthy that, in spite of the fact that these single crystals are so distinct from each other, the ratio of the pyroelectric coefficient to the molar specific heat varies within relatively narrow limits (Fig. 4),

$$\left|\partial\gamma^\sigma/\partial C_{p,E}\right| = (0.92\text{–}3.2) \times 10^{-10} \text{ C mol cal}^{-1} \text{ cm}^{-2}.$$

The formation of ferroelectric components in the plane perpendicular to the polar axis of linear pyroelectrics (Ag_3AsS_3 [31], NH_4HSeO_4 [33], $LiKSO_2$ [34]) radically alters the canonical dependence (6c) of the PEC along the polar axis, especially in the vicinity of the phase transition points. Such a combination, "a ferroelectric in a linear pyroelectric," is likely to be a fairly common phenomenon.

The formation of an orthogonal polarization component with no evidence of ferroelectricity is less known and not at all understood. Such a component occurs in single crystals of $Li_2SO_4 \cdot H_2O$ below 110 K [23]. One might expect similar features in single crystals of linear pyroelectric $Ba(NO_2)_2 \cdot H_2O$, in which the $\gamma^\sigma(T)$ dependence is anomalous, with the PEC changing its sign twice, at 22.5 and 158 K. This distinctive polar state is likely to be due to [35] loss of ergodicity in the water molecule subsystem during a glasslike phase transition. In ferroelectrics, the reasons for the departure of the $\gamma^\sigma(T)$ dependence from the canonical dependences (6a)–(6c) at $T > 1.5$ K are known to be as follows:

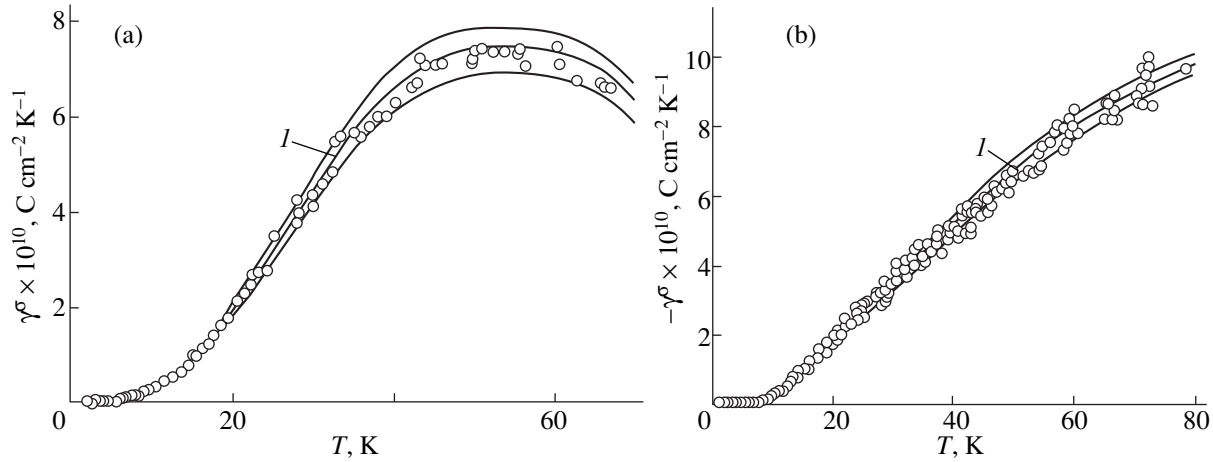

Fig. 3. Approximations to the experimental $\gamma^\sigma(T)$ dependences of perfect single crystals: (a) the $\gamma^\sigma(T)$ dependence of a polar cut of a single crystal of $Li_2SO_4 \cdot H_2O$ in a range of 1.5–325 K, which is described by the expression $\gamma^\sigma(T) = [3.3D(275\text{ K}) - 2.3E(144\text{ K}) - 8.8E(272\text{ K}) - 22.7E(1102\text{ K})] \times 10^{-9}$ C cm^{-2} K^{-1}; the characteristic temperatures Θ_D and Θ_E are determined from the middle curve *1* of the "corridor" containing all experimental dots between the curves $\gamma^\sigma(T) = AD(\Theta_D \pm 5\%) + \Sigma B_i E(\Theta_{Ei} \pm 5\%)$; this figure presents a fragment of a general curve [22] in a range of 1.5–70 K. (b) The $\gamma^\sigma(T)$ dependence of a polar cut of a single crystal of TGS in a range of 1.5–100 K, which is described by the expression $\gamma^\sigma(T) = [-1.49E(14.5\text{ K}) - 437E(68\text{ K}) - 1100E(22\text{ K}) \times 10^{-12}$ C cm^{-2} K^{-1}; the characteristic temperatures Θ_{Ei} are determined from the middle curve *1* of the corridor containing all experimental dots between the curves $\gamma^\sigma(T) = \Sigma B_i(\Theta_{Ei} \pm 5\%)$; this figure presents a fragment of a general curve [15] in a range of 1.5–80 K.

(1) The occurrence of low-temperature structural phase transitions, such as those that occur in single crystals of $Ca_2Sr(C_2H_5CO_2)_6$ [36] and $(CH_3NH_3)HgCl_3$ [37];

(2) The low-temperature ordering of structural units of the single crystal (for instance, of protons in KDP [30]) not associated with a phase transition (see below);

(3) The occurrence of low-temperature magnetic phase transitions. Giant anomalies of the PEC associated with these transitions were observed in ferroelectrics $BaNiF_4$ [7], Cu–Br, Co–I, and Fe–Br boracites [24, 38], Fe_3O_4 magnetite [39, 40], and $KNiPO_4$ [41]. The proportionality between the temperature-dependent "magnetic" component of the PEC and the corresponding component of the specific heat was observed in [7], which illustrates the generality of relationship (5).

B. The Problem of the Secondary Pyroelectric Coefficient

The fact that the experimental temperature dependence of the total PEC $\gamma^\sigma(T)$ is adequately described in terms of the theories developed for the primary PEC $\gamma^\varepsilon(T)$ casts some doubt on the applicability of these theories to the $\gamma^\varepsilon(T)$ dependence, and the question of the role of $\gamma^s(T)$ arises [see (1)]. The question of separating the total PEC into two components was posed as early as 1899 [42], when J. Curie, P. Curie, and W. Röntgen called the existence of primary pyroelectricity into question. In [42], using techniques in which the errors of absolute measurements of γ^σ and γ^s had no influence on the result, it was found that $|[\gamma^\varepsilon(22.2°C)/\gamma^\sigma(22.2°C)]| \cong 0.2$ for samples cut from the same single crystal of tourmaline.

In [43], it was experimentally established that the total PEC of tourmaline is negative. Nowadays, this result is known to be universal. X-ray structural analysis and pyroelectric measurements showed that the spontaneous polarization decreases with increasing temperature (at elevated temperatures) in all polar dielectrics studied, including the compounds, such as $Ba(NO_2)_2 \cdot H_2O$ [44, 45], in which $\gamma^\sigma(T)$ repeatedly changes its sign at low temperatures.

There are many papers in which there occurred a separation into two components at some temperatures or in some narrow temperature ranges, following [42], on the basis of the quantity $\alpha_{lm}^{\sigma, E}(T)$ [according to (1)], considering it to be macroscopically measured. The results are discussed in the review articles [46, 47] and presented in the following papers: for $Li_2SO_4 \cdot H_2O$, in [48]; for α-$Cu(IO_3)_2$, $Nd(IO_3)_3 \cdot H_2O$, and $LiClO_4 \cdot 3H_2O$, in [49]; for $LiKSO_4$, in [50]; and for thin films (~1 μm thick) of PZT ceramics and of single crystals of $PbTiO_3$ and ZnO, in [51]. However, as far as we know, there are only two papers (ZnO [52] and CdS [53]) where the $\gamma^\varepsilon(T)$ dependences are calculated in the range 10 to 260 K from the $\alpha_{lm}^{\sigma, E}(T)$ dependences experimentally measured in this range. Although the accuracy of measurements in [46–53] was much lower than in [42], the data presented allow certain general inferences to be drawn. Let us consider the data on the relationship between $\gamma^\sigma(T)$, $\gamma^\varepsilon(T)$, and $\gamma^s(T)$ in combination with the experimentally measured $\alpha_{lm}^{\sigma, E}(T)$ dependences, keeping in mind that the $\gamma^\sigma(T)$ dependences are adequately described in terms of the theories constructed for $\gamma^\varepsilon(T)$ for all materials studied.

Linear pyroelectrics. The relation between the primary and secondary pyroelectric coefficients (including both their magnitudes and signs) depends on the temperature [50, 52, 53]. At room temperatures, the primary PEC is much higher in magnitude than the secondary one in crystals whose structural units are reoriented [45, 48, 49].

In some pyroelectrics, the thermal expansion coefficients are negative in some temperature ranges; in single crystals of ZnO and CdS, $\alpha_{lm}^{\sigma, E}(T) < 0$ at $T < 125$ K [54, 55], while in single crystals of $Li_2SO_4 \cdot H_2O$, $\alpha_{33} < 0$ at room temperature [48]. The change of the sign of $\alpha_{lm}^{\sigma, E}(T)$ does not reveal itself in the $\gamma^\sigma(T)$ dependences for those single crystals at the corresponding temperatures.

In ZnO, the $\alpha_{lm}^{\sigma, E}(T)$ dependences are closely approximated in the temperature range 8–300 K by two Einstein functions (having opposite signs) with wavenumbers $\nu_{E1} = 76$ and $\nu_{E2} = 410$ cm^{-1}, respectively [54]. The first mode does not manifest itself in the $\gamma^\sigma(T)$ dependence, while the second is close to the mode with a wavenumber of 436 cm^{-1} (see Table 1). The low-temperature Debye component [1] is suppressed in the $\alpha_{lm}^{\sigma, E}(T)$ dependence for ZnO (within the limits of approximation error) [54] but is dominant in the $\gamma^\sigma(T)$ dependence [11, 17]. The calculated $\gamma^\varepsilon(T)$ dependences for ZnO and CdS [52, 53] do not agree with the canonical dependences (6a)–(6c).

Thus, based on the data presented in [46–53], one can conclude that there is no tendency toward a unified relationship between $\gamma^\sigma(T)$, $\gamma^\varepsilon(T)$, and $\gamma^s(T)$ even when the linear pyroelectrics are monotonically dependent.

Ferroelectrics. The primary PEC of ferroelectrics was measured only at room temperatures, where, as a rule, it is 5–50 times higher than the secondary PEC [46, 47, 51]; hence, the contribution from acoustic vibrations through thermal expansion is very small at these temperatures. In the $\gamma^\sigma(T)$ dependences measured in ferroelectrics in a range from 1.5 K (Fig. 2), this contribution [the Debye term (6a)] is completely absent.

To explain these experimental data, it has been proposed [11] that, in ferroelectrics, the contribution to $\gamma^\sigma(T)$ from acoustic vibrations [the term $D(\Theta_D/T)$ in (6c)] is

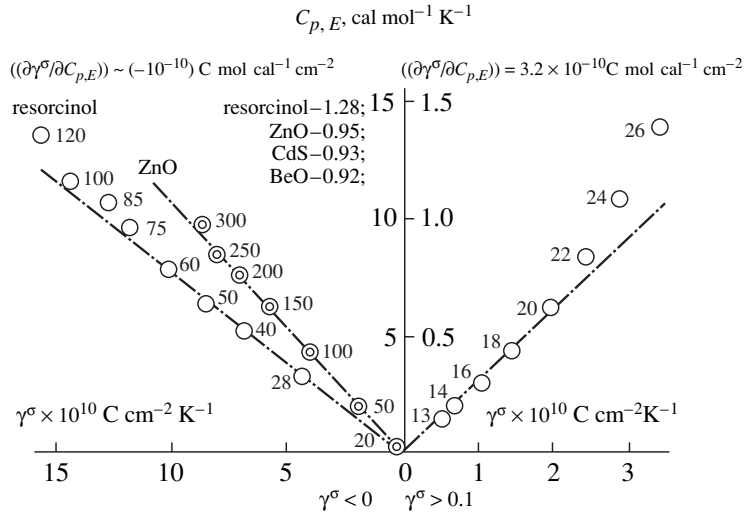

Fig. 4. Dependence $C_{p,E} = f(\gamma^\sigma)$ for some linear pyroelectrics. The absolute temperatures are indicated near the dots.

small in comparison with that from optical modes [the term $E(\Theta_{Ei}/T)$ in (6c)]. However, high-precision measurements on perfect single crystals of $LiNbO_3$ and $LiTaO_3$ [16] showed that $\gamma^\sigma < 10^{-14}$ C cm^{-2} K^{-1} in a wide range of 1.5–7 K; that is, there are no low-lying excitations (Fig. 2). For comparison, we note that, in the linear pyroelectric $Li_2SO_4 \cdot H_2O$, $\gamma^\sigma(3\text{ K}) \cong 1 \times 10^{-12}$ C cm^{-2} K^{-1} (Fig. 2).

Measurements of the $C_p(T)$ dependence for single crystals of $BaTiO_3$ and KDP [56], $LiNbO_3$, $LiTaO_3$, $NaNO_2$, $BaTiO_3$, and TGS [57] in a range from 0.5 K showed that $C_p(T) \sim T^3$ at $T < 6$ K. Clearly, $C_p = f(\gamma^\sigma)$ curves, constructed in a range of 1.5–7 K for KDP, $LiNbO_3$, and $LiTaO_3$, showed no linear dependences, as was also the case with single crystals of TGS [16]. It will be recalled that C_p and γ^σ are proportional to each other in linear pyroelectrics (Fig. 4).

In the context of the experimental data, the question arises of whether the acoustic vibrations can participate in the formation and temperature variation of the spontaneous polarization of a ferroelectric. The proportionality $\gamma^\sigma(T) \sim C_p(T)$ (Fig. 4) in linear pyroelectrics at low temperatures suggests that all atoms of the lattice are involved in the formation and temperature variation of the polar state through acoustic vibrations of the lattice. It is reasonable to infer that the result of the influence of acoustic vibrations on the polar properties of linear pyroelectrics is (1) the single orientation of the spontaneous polarization everywhere over the crystal, (2) the fact that the spontaneous polarization cannot be reversed (reoriented) by an external field, and (3) its persistence when the temperature is increased up to the destruction point.

We note that the nonpolar-phase–linear-pyroelectric phase transition in a solid contradicts the Neumann principle, and the consistency of the ferroelectric phase transitions with this principle was also a widely debated topic at one time until hemihedry (hemimorphism) of single-domain ferroelectrics was experimentally discovered [58].

It is well known that theories of ferroelectric phase transitions are based on the concept of the optical soft mode, which is associated with a rearrangement of only a few atoms in the unit cell; the positions of the other atoms, forming the lattice and responsible for the lattice component of the specific heat, remain unchanged [59].

In other words, a ferroelectric can be considered, structurally, to consist of a nonpolar (electrically neutral) frame and a reversible ferroelectric dipole component within it. Clearly, anharmonism of acoustic vibrations of the nonpolar frame cannot make a contribution to any component of the PEC. If we assume that anharmonism of long-wave acoustic vibrations is responsible for the formation of $\mathbf{P}_s$ in ferroelectric domains polarized in opposite directions and that $\mathbf{P}_s$ can be reversed by an external field, then we must leave room for the change in the direction of anharmonism of the entire spectrum of acoustic branches of individual domains or, in the case of polarization switching of a single-domain crystal, for the change in the direction of anharmonism of vibrations of all atoms. Taking the deformations that accompany such processes into account, it is unlikely that the single crystal will remain intact under these hypothetical conditions.

However, this does not rule out the contribution of acoustic vibrations to macroscopically measured (by dilatometry) $\alpha_{lm}^{\sigma,E}(T)$ dependences, which are determined fundamentally by the thermal expansion of the electrically neutral frame. The authors failed to find experimental data on $\alpha_{lm}^{\sigma,E}(T)$ dependences of single crystals of TGS, KDP, $LiNbO_3$, and $LiTaO_3$ at liquid helium temperatures. However, there is no doubt that the dependence $\alpha_{lm}^{\sigma,E}(T) \sim T^3$ [1] takes place, if only for

one of these four monocrystalline ferroelectrics, and this power-law component should have revealed itself in the $\gamma^{\sigma}(T)$ dependences, as is the case with $Li_2SO_4 \cdot H_2O$ (Fig. 2). However, for some reason, there is no contribution from this component to $\gamma^{\sigma}(T)$ for each of the four classic model ferroelectrics, which are very distinct from each other.

A similar situation also occurs at higher temperatures. A strong anomaly of $\alpha_{33}(T)$ in $LiNbO_3$ at 60 K [60] does not manifest itself in the $\gamma^{\sigma}(T)$ dependence [11]. The changes of the sign of $\alpha_{lm}^{\sigma, E}(T)$ in single crystals of KDP at 108 and 117 K [59] do not affect the $\gamma^{\sigma}(T)$ dependence of single crystals of KDP + Cr^{3+} [27, 29]. No contribution from acoustic vibrations was observed in the $\gamma^{\sigma}(T)$ dependence of the ferroelectric component, appearing in the matrix of the linear pyroelectric Ag_3AsS_3, in the direction perpendicular to the polar axis [17].

These facts suggest that the physical meaning of the term $\alpha_{lm}^{\sigma, E}(T)$ in (1) should be refined, because it is this term that determines the temperature dependence of $\gamma^{\varepsilon}(T)$. [There are many experimental papers in which it was shown that $d_{ijk}^{T, E}(T) \cong$ const and $c_{jklm}^{T, E}(T) \cong$ const.] When calculating $\gamma^{\varepsilon}(T)$, one may (a) use the macroscopically measured thermal expansion coefficients $\alpha_{lm}^{\sigma, E}(T)$ or (b) take into account only those components of the macroscopically measured $\alpha_{lm}^{\sigma, E}(T)$ that are associated with the physical mechanisms and structural elements directly responsible for pyroelectricity in a given crystal lattice.

These typical facts concerning the lack of correlation between the temperature dependences of $\gamma^{\sigma}(T)$ and macroscopically measured $\alpha_{lm}^{\sigma, E}(T)$ imply that, if we accept the variant (a), the $\gamma^{\sigma}(T)$ dependence will not be described in terms of the theory developed for $\gamma^{\varepsilon}(T)$. This is not the case. Therefore, this variant is ruled out.

Let us consider the other variant. The total pyroelectric coefficient $\gamma^{\sigma}(T)$ is the sum of n terms due to different physical mechanisms (collective anharmonism of acoustic vibrations, anharmonism of individual polar modes, the process of ordering of structural elements, process of magnetic ordering), each of which also contributes to the free energy and, hence, to the specific heat $C_{vn}(T)$ [see (5)]. These contributions also determine the corresponding components of the thermal expansion coefficient, such that we have $[\alpha_{lm}^{\sigma, E}(T)]_n \sim C_{vn}(T)$ [61]. From (5), it follows that $\gamma_n^{\varepsilon}(T) \sim C_{vn}(T) \sim [\alpha_{lm}^{\sigma, E}(T)]_n$ and, hence, the nth components of the primary PEC and of the thermal expansion coefficient have the same temperature dependence.

Therefore, the temperature dependence of the total PEC

$$\gamma^{\sigma}(T) = \sum_{1}^{n} \{\gamma_n^{\varepsilon}(T) + [d_{ijk}^{T, E} c_{jklm}^{T, E} \alpha_{lm}^{\sigma, E}(T)]_n\}$$

will be described in terms of the theories developed for the primary PEC.

This result was first obtained in [6] for the specific case of linear pyroelectrics. The assumption about the term $\alpha_{lm}^{\sigma, E}(T)$ in (1) is of fundamental importance and provides the explanation of why the experimental $\gamma^{\sigma}(T)$ dependences of all materials studied are adequately described in terms of the theories developed for $\gamma^{\varepsilon}(T)$.

As yet, it is not clear how to extract the pyroelectrically active components from the macroscopically measured $\alpha_{lm}^{\sigma, E}(T)$ dependences. Perhaps this can be done (using the relationship between thermal expansion and other properties of polar dielectrics) by the methods discussed in [61, p. 34].

C. Imperfect Single Crystals

Along with the successful application of the canonical dependences for describing the $\gamma^{\sigma}(T)$ behavior, noticeable deviations from these dependences, including the change of the sign of the PEC, were also observed at $T < 30$ K in [11, 17, 62, 63] and later papers [16, 25, 27–30, 64–66] in both linear pyroelectrics and ferroelectrics (Figs. 5–7).

In [11, 17], it was suggested that these deviations are due to defects of single crystals. Later, after the amount of experimental evidence of this common phenomenon became large enough, it was proposed [16, 66] to consider the spontaneous polarization of a crystal $\mathbf{P}_s$ as consisting of two components: the spontaneous polarization of the matrix $\mathbf{P}_{s, m}$ and an additional component $\mathbf{P}_{s, ad}$, which is due to physical mechanisms other than anharmonism of lattice vibrations. Typically, $|\mathbf{P}_{s, ad}|/|\mathbf{P}_s| \sim 10^{-6}$–$10^{-4}$.

Thus, $\mathbf{P}_s(T) = \mathbf{P}_{s, m}(T) + \mathbf{P}_{s, ad}(T)$, and the total PEC can be written as

$$\boldsymbol{\gamma}^{\sigma}(T) = \frac{\partial}{\partial T}[\mathbf{P}_{s, m}(T) + \mathbf{P}_{s, ad}(T)] = \boldsymbol{\gamma}_m^{\sigma}(T) + \boldsymbol{\gamma}_{ad}^{\sigma}(T)$$

or, in terms of the projections on the crystallographic axes, $\gamma_i^{\sigma}(T) = \gamma_{m_i}^{\sigma}(T) - \gamma_{ad_i}^{\sigma}(T)$.

The physical mechanism of the additional component of the PEC can be identified using its temperature dependence, which can be found as the difference of the experimentally measurable dependences $\gamma_i^{\sigma}(T)$ and $\gamma_{m_i}^{\sigma}(T)$, namely, $\gamma_{ad_i}^{\sigma}(T) = \gamma_i^{\sigma}(T) - \gamma_{m_i}^{\sigma}(T)$. In this difference, the term $\gamma_i^{\sigma}(T)$ represents the temperature dependence of the PEC of the real (defect) single crystal,

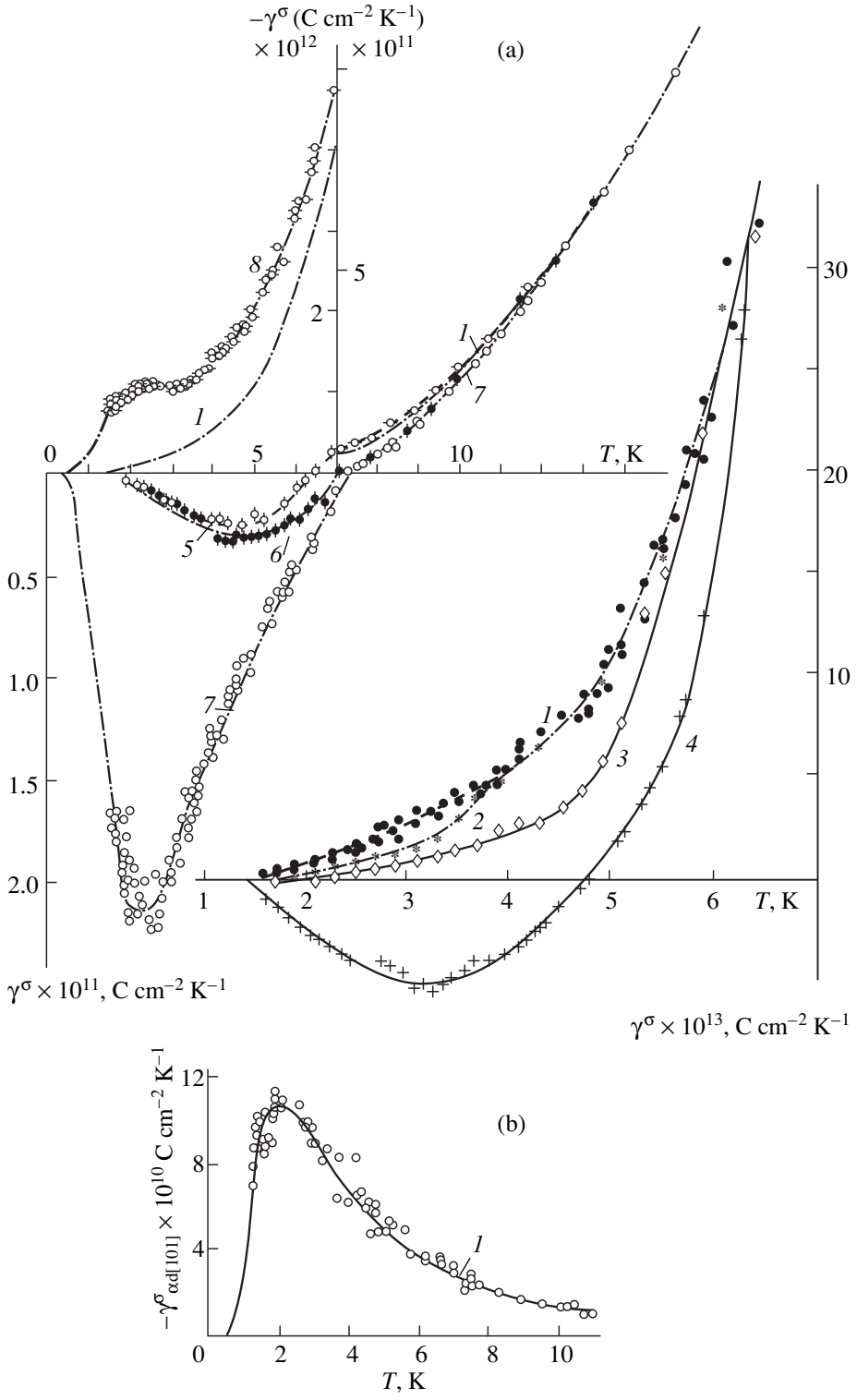

Fig. 5. Temperature dependences $\gamma^{\sigma}(T)$ of perfect and impurity single crystals of TGS: (a) the $\gamma^{\sigma}(T)$ dependences of polar cuts of single crystals of TGS-based compounds; curves: (*1*) the purest, perfect single crystal; (*2*) a technically pure single crystal; (*3*) TGS + L, α alanine ≈ 0.02 wt % (ATGS); (*4*) TGS + L, α alanine ≈ 0.08 wt % + Cr^{3+} ≈ 0.08 wt % (ATGS + Cr^{3+}); (*5*) TGS + L, α alanine ≈ 0.06 wt % + Cu^{2+} ≈ 0.04 wt % (ATGS + Cu^{2+}); (*6*) TGS + L, α alanine ≈ 0.06 wt % + Fe^{3+} ≈ 0.04 wt % (ATGS + Fe^{3+}); (*7*) TGS + Cr^{3+} ≈ 0.03 wt % (TGS + Cr^{3+}); and (*8*) TGS + L, α alanine ≈ 0.01 wt % + P^{3+} ≈ 0.1 wt % (ATGSP); the dot-and-dash line (coinciding with curve *1*) is a theoretical approximation (curve *1* in Fig. 3b). (b) The $\gamma^{\sigma}_{ad}(T)$ dependence of a nonpolar [101] cut of a single crystal of TGS + Cr^{3+}; curve *1* is the approximation by (6f) with $b = 0$, $a = 5.2$ K, and $\delta = 0.23$ meV.

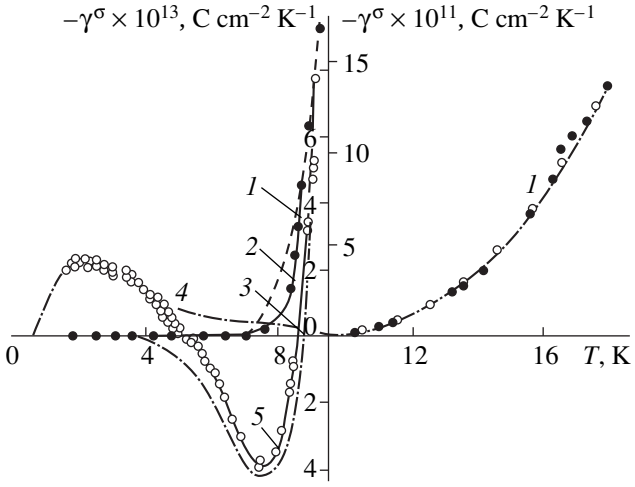

Fig. 6. Temperature dependences $\gamma^\sigma(T)$ of polar cuts of a high-quality single crystal and an impurity single crystal of $LiTaO_3$. Curves: (*1*) the approximation by (6b); (*2*) a high-quality single crystal; (*3*) $LiTaO_3 + Rh^{3+} \approx 1.5$ wt %; (*4*) the approximation to the $\gamma^\sigma_{ad_i}(T)$ dependence by (6f) with $b = 0$, $a \approx 5$K, and $\delta \approx 0.25$ meV; and (*5*) the difference of curves *3* and *4*.

while $\gamma^\sigma_{m_i}(T)$ is the PEC of a perfect, defect-free sample, the temperature dependence of which is described by the canonical relations (6a)–(6c).

Figures 5 and 6 illustrate the typical evolution of the $\gamma^\sigma_i(T)$ dependences of crystals of the highest quality with the introduction of various impurities into them.

The temperature dependence of $\gamma^\sigma(T)$ along the polar axis of the single crystals of TGS that were grown from a starting material recrystallized three times at a temperature above the Curie point can be taken to be the reference for low-temperature pyroelectric properties of ferroelectrics (curve *1* in Fig. 5a). The parameters of its approximation by expression (6b) are listed in Table 1. The technically pure sample has a noticeably different temperature dependence (curve *2* in Fig. 5a). Impurities produce a component $\gamma^\sigma_{ad}(T)$ opposite in sign (curves *2–7* in Fig. 5a) to $\gamma^\sigma_m(T)$ (curve *1*) or of the same sign (curve *8* in Fig. 5a).

High-quality single crystals of $LiTaO_3$ are not as perfect as those of TGS, but their $\gamma^\sigma(T)$ dependences (curves *1*, *2* in Fig. 6) share common features. In impurity single crystals of $LiTaO_3 + Rh^{3+}$, there appear (curve *3* in Fig 6) two different components, $\gamma^\sigma_{ad_1}(T)$ and $\gamma^\sigma_{ad_2}(T)$. The first component is associated with OH^- hydroxyl groups [16] and described by (6f) (curve *4* in Fig. 6). The second component, $\gamma^\sigma_{ad_2}(T)$, which can be obtained by subtracting curves *1* and *4* from curve *3*, is associated with structural elements heavier than a proton. These structural elements are not identified. Noteworthy are the identical positions ($T = 2.2$ K) of the peaks in $\gamma^\sigma_{ad_1}(T)$ that are associated with proton ordering (curves *7*, *8* in Fig. 5a; curve *4* in Fig. 6).

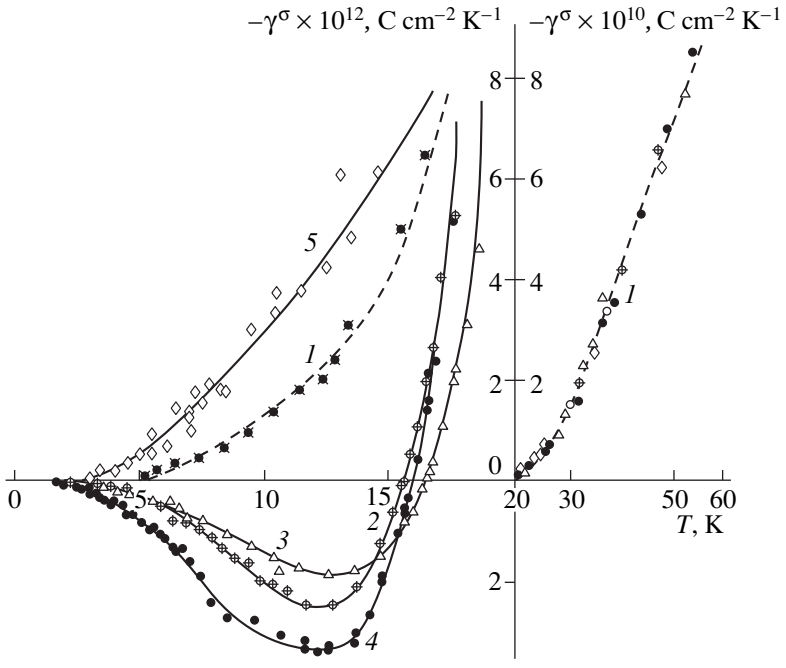

Fig. 7. Temperature dependences $\gamma^\sigma(T)$ of polar cuts of single crystals of KDP. Curves: (*1*) the approximation by (6b) to the $\gamma^\sigma(T)$ dependence of a highly perfect single crystal annealed at 180°C; (*2*) the highly perfect single crystal; (*3*) a single crystal with numerous bubbles; (*4*) a technically pure single crystal; and (*5*) KDP + $Cr^{3+} \approx 0.05$ wt %.

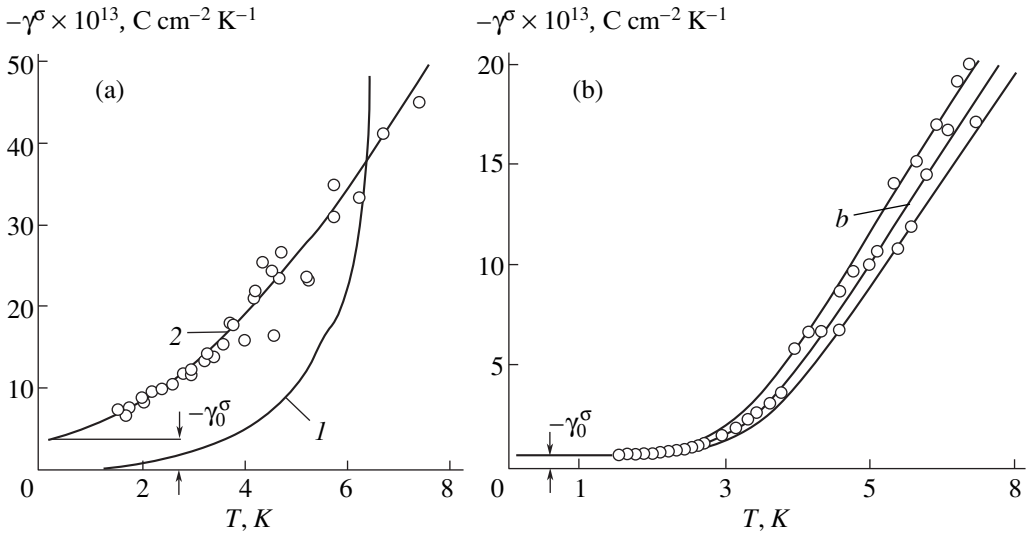

Fig. 8. Constant component in the $\gamma^\sigma(T)$ dependence of ferroelectrics containing a glasslike phase: (a) single crystals of TGS-based compounds; curves: (*1*) a perfect single crystal of TGS (curves *1* in Figs. 3b, 5a); (*2*) a single crystal of ATGSP irradiated with γ-rays, dose 35 Mrad, the approximation by the expression $\gamma^\sigma(T) = (3.6 + 1.43T^{1.709} + \ldots) \times 10^{-13}$ C cm^{-2} K^{-1}. (b) Ferroelectric ceramics of the TsTS-40 type; curve *1* is the approximation by the expression $\gamma^\sigma(T) = [0.5 + E(24\text{ K}) + \ldots] \times 10^{-13}$ C cm^{-2} K^{-1}.

The $\gamma_{ad}^\sigma(T)$ components are observed in a limited temperature range; no matter what their nature, all $\gamma^\sigma(T)$ curves of defect single crystals merge with the $\gamma_m^\sigma(T)$ curves (curves *1* in Figs. 5a, 6) in a range of 10–15 K.

To grow a perfect, defect-free single crystal for the measurement of reference $\gamma_m^\sigma(T)$ dependences is a very laborious problem in and of itself. Growing a single crystal of a stoichiometric compound (with respect to hydrogen) with short, strong H bonds is an even more complicated problem. The nonstoichiometry, which is likely to be due to the noncongruence of the growth process and should be considered to be a natural structure imperfection, makes a very large contribution to low-temperature anomalies of electrical properties of polar single crystals [23, 27, 67, 68, 70]. The $\gamma^\sigma(T)$ dependence becomes even more complicated when this natural imperfection combines with a low-temperature ordering of the proton subsystem of the lattice. This situation is typical for single crystals of KDP (Fig. 7). Figure 7 shows the $\gamma^\sigma(T)$ dependences of a highly perfect single-domain KDP sample (curve *2*), of a sample with numerous bubbles (curve *3*), of a technically pure sample (curve *4*), and of a sample of KDP + Cr^{3+} (curve *5*). In the samples represented by curves *2–4*, protons are in a natural free state. The experimental points of curve *1* represent the $\gamma^\sigma(T)$ dependence of a highly perfect single-domain sample annealed at 180°C for two hours. Annealing at a temperature higher than the tetragonal–monoclinic phase transition point blocks free proton movement (this can be explained by a number of reasons [27, 29, 30]), which leads to the restoration of (a) the characteristic λ peak of the dielectric permittivity at the ferroelectric phase transition and (b) the canonical $\gamma^\sigma(T)$ dependence (curve *1* in Fig. 7) described by (6b) with parameters presented in Table 1. The different levels and signs of the $\gamma_{ad}^\sigma(T)$ dependences obtained by subtracting curve *1* from curves *2–5* is noteworthy. In the KDP matrix doped with chromium (curve *5*), it is seen that the contribution from protons disappears and a new component of the opposite sign arises. At $T > 20$ K, curves *1–5* coincide, which supports the general conclusion that the component $\gamma_{ad}^\sigma(T)$ occurs in a limited temperature range. The KDP case can probably be described [30] in terms of expressions (6d) and (6f) generalized to the case where all protons of the unit cell are displaced in their potential wells. However, such a generalization has not been developed. It should be noted that protons make a contribution [30] to well-known anomalies of the dielectric permittivity and of the pyroelectric coefficient of KDP, which is confirmed by the fact that the λ peak in $\varepsilon_{33}(T)$ changes into a plateau under hydrostatic compression in a single crystal of KDA (isomorphic to KDP) [69].

Various investigations into the mechanisms of the formation of the component $\gamma_{ad_i}^\sigma(T)$ due to defects revealed that one common feature is the displacement of a charged structural element of the crystal in the double-well or multiwell potential with an energy gap between the bottoms of the wells $\delta \le 1$ meV.

Such a situation can be created in a single crystal by introducing impurities or exposing it to light (Ag_3AsS_3 [24, 31]) or penetrating radiation [16, 26, 66]; it may also be caused by nonstoichiometry with respect to hydrogen [27, 62, 67], or it may be due to water molecules, which are loosely bound to the crystal frame

[22]. The appearance of nonzero polarization components along the crystallographic directions that are nonpolar at $T \sim 300$ K is strong evidence of the operation of the mechanism involving the ordering of the relevant crystal structural elements at low temperatures [16, 23, 26, 66].

The above-mentioned external actions on the body of a single crystal produce distortions in the initial potential relief of the polar matrix and create new charged mobile or rotatable structural elements (ions, dipoles). By now, only one mobile structural element, the proton, has been reliably identified at $T \leq 15$ K. This property of the proton is likely due to its extremely small mass and high mobility.

Let us consider the case where the distorted potential relief is characterized by a double-well potential and the double wells are similar and uniformly distributed over the volume of the single crystal, i.e., $\delta(x, y, z) = \text{const}$. As the temperature is decreased, the temperature-dependent process of the localization of charged structural elements in the double wells will proceed and there will appear an additional component in the spontaneous polarization, $\mathbf{P}_{s,\,ad}(T)$, the orientation of which will be constant with respect to the crystal axes. In this case, the temperature dependences of the projections of the PEC onto the coordinate axes, $\gamma^{\sigma}_{ad_i}(T)$, will be proportional to each other and can be described by expression (6f) (Fig. 5b). Such dependences, associated with the localization of protons on distorted hydrogen bonds in single crystals of TGS + Cr^{3+}, ATGS + Fe^{3+}, ATGS + Cu^{2+}, ATGSP (curves *5–8* in Fig. 5a) and of protons of OH^- hydroxyl groups adsorbed by single crystals of $LiTaO_3$ from the atmosphere during their growth (Fig. 6), were observed in [16, 26, 66] and were also adequately described by expression (6f).

However, as one would expect, the case of similar and uniformly distributed distortions is the exception rather than the rule. This case merely demonstrates that there is a physical model that can be generalized and employed to explain (and, if need be, to realize) the occurrence of $\gamma^{\sigma}_i(T) \neq 0$ at $T \ll 4$ K. The broad extrema of $\gamma^{\sigma}_{ad_i}(T)$ in single crystals of ATGS and ATGS + Cr^{3+} (curves *3*, *4* in Fig. 5a) [16], $LiNbO_3$ + Fe^{3+}, $LiTaO_3$ + Rh^{3+} (curve *5* in Fig. 6) [14, 66], and KDP (curves *2–4* in Fig. 7) [27, 61], which are not described by (6f), can be explained in terms of this model by a nonuniform distribution of the energy gap $\delta(x, y, z)$ corresponding, in general, to localizing structural elements of different types. In all these single crystals, the pyroelectric coefficient $\gamma^{\sigma}_{ad_i}(T)$ begins to increase at $T \geq 1.5$ K, from which the inference can be drawn that the variable values of δ are also of the order of 1 meV. It should be noted that the lower limit $T \geq 0.5$ K is only characteristic of the localizing proton (the cases of ATGS, ATGS + Cr^{3+}, KDP). In the case of heavier localizing structural elements, this limit is higher; for a single crystal of $LiNbO_3$ + Fe^{3+}, we have $T > 5$ K, and for a single crystal of $LiTaO_3$ + Rh^{3+}, we have $T > 4$ K (curve *5* in Fig. 6) [16].

The relationship, following from (6f), between δ and the low-temperature limit above which the PEC begins to increase is illustrated by curves *7* (Fig. 5a) and *1* (Fig. 5b). In this case, we have $T \approx 0.5$ K, and the corresponding energy gap is $\delta \approx 0.23$ meV.

These results, the model itself, and the assumption that the broadening of the extrema of $\gamma^{\sigma}_{ad_i}(T)$ is due to spatial variations of the energy gap were verified experimentally [26]. Different imperfect crystals of TGS were exposed to γ-rays, with doses being close to those at which the crystal lattice is disintegrated. Under these conditions, most of the hydrogen bonds are disrupted and the protons are localized in potential wells with energy gaps $\delta(x, y, z)$ varying in a wide range from zero to δ_{max}.

Based on the results of investigations of TGS exposed to γ-rays [71], one can infer that the depths of the wells [and, accordingly, the values of $\delta(x, y, z)$] are much smaller than those in the initial imperfect lattice. Indeed, only in this case can protons transfer through the body of the crystal and come out as free hydrogen atoms.

If protons are indeed localized in a well with $\delta(x, y, z)$ ranging from zero to δ_{max}, then the low-temperature extrema of the $\gamma^{\sigma}_i(T)$ dependence of impurity single crystals of TGS must be broadened toward $T \longrightarrow 0$ and the temperature dependence can be roughly approximated by a constant or something like this in the range $T \leq 1.5$ K. The temperature dependence of this new component (which can no longer be considered as an additional one in view of distortions of the entire lattice) must reflect the appearance of a variety of temperature-dependent electric dipoles having different volume concentrations and orientations in space. The temperature variation of the magnitude of the dipole moments is determined by the particular value of the space-dependent energy gap ranging from extremely small ($\delta \ll 1$ meV) values. When integrated over volume, the polarization component due to these dipoles is nonzero because of the orienting effect of the residual spontaneous polarization of the matrix.

The measurements on single crystals of ATGSP irradiated with γ-rays revealed the presence of a constant component in the $\gamma^{\sigma}_i(T)$ dependences (Fig. 8a). This result gives reasons to expect that, at $T \ll 1.5$ K, the value of the PEC in single crystals irradiated with γ-rays will also be of the order of 10^{-13} C cm^{-2} K^{-1}, whereas for perfect single crystals of TGS, we have $\gamma^{\sigma} < 10^{-14}$ C cm^{-2} K^{-1} even at $T = 1.5$ K (Fig. 2). The fact that $\gamma^{\sigma}_i \neq 0$ at $T \longrightarrow 0$ does not violate the third law of thermodynamics in this case, because a single crystal exposed to γ-rays is a thermodynamically nonequilibrium system. The effect of irradiation with γ-rays on the

Table 2. Evolution of the $\gamma^{\sigma}(T)$ dependences of a single crystal of ATGSP under γ-ray irradiation

Dose, Mrad	Approximation parameters to $\gamma^{\sigma}(T)$ dependences						
	$\gamma_0^{\sigma} \times 10^{13}$, C cm^{-2} K^{-1}	n	a, K	wavenumbers of active modes, cm^{-1}			
0	–	–	7	10.4	34	50.6	140
8	–	–	–	10.1	30.6	46.5	113
15	4.34	2.06	–	–	25.8	45	108
25	4.5	1.86	–	–	–	43.6	104
35	3.6	1.709	–	–	–	41.6	83.5

Note: γ_0^{σ} is the constant component; n is the exponent of the power-law term in the approximation to $\gamma^{\sigma}(T)$; a is the parameter of the model in [15], an expression for which is given by (6d).

$\gamma_i^{\sigma}(T)$ dependences of single crystals of TGS containing various impurities was experimentally investigated in [26].

Since this effect is of immediate interest in the search for new pyroelectric materials used at $T \ll 4$ K, we shall discuss it in greater detail. Low and moderate doses ($D \leq 5$ Mrad) only slightly affect the magnitude of $\mathbf{P}_s(0)$. As one would expect at such doses, H bonds are ruptured and new bonds are formed in impurity crystals. The component $\mathbf{P}_{s,\,ad}(T)$ is determined by these two processes.

We separate three types of response of impurity crystals to elevated γ-ray doses ($D \cong 10$ Mrad): (1) The magnitude of $\gamma_{ad_i}^{\sigma}(T)$ is drastically reduced as compared to its initial value, and its temperature dependence is changed. (2) The value and temperature dependence of $\gamma_{ad_i}^{\sigma}(T)$ remain practically unchanged. (3) The magnitude of $\gamma_{ad_i}^{\sigma}(T)$ increases, and its temperature dependence is changed.

The response of single crystals of TGS + Cr^{3+} and ATGSP is of the first type. In these single crystals, $\gamma_{ad_i}^{\sigma}(T)$ is due to a highly ordered sublattice of protons produced by impurities. Irradiation with γ-rays destroys this sublattice by rupturing preexisting H bonds and forming new ones that have no long-range order. As a consequence, the $\gamma_{ad_i}^{\sigma}(T)$ dependence is radically altered at a dose of 10 Mrad: (a) In single crystals of TGS + Cr^{3+}, the component $\gamma_{ad_i}^{\sigma}(T)$ along the x and z axes disappears, while the component along the polar direction becomes an order of magnitude smaller than its initial values (curve *7* in Fig. 5a). (b) In single crystals of ATGSP, the sign and the temperature dependence of $\gamma_{ad_i}^{\sigma}(T)$ along the polar direction are changed, while the components along the x and z axes remain unaltered.

The response of single crystals of ATGS + Cr^{2+} and ATGS + Fe^{3+} to irradiation is of the second type. The temperature dependences of $\gamma_{ad_i}^{\sigma}(T)$ along the polar direction is changed only slightly as compared with its initial dependences (curves *5*, *6* in Fig. 5a). Some balance in the processes of rupture of preexisting bonds and the formation of new bonds is also noteworthy.

The response of single crystals of ATGS + Cr^{3+} to irradiation is of the third type. The $\gamma_{ad_i}^{\sigma}(T)$ curve for these single crystals confines a minimal area (curve *4* in Fig. 5a); that is, $P_{s,\,ad}(0)$ is a minimum for ligands of this type in comparison with other impurity samples. As the dose is increased, the $\gamma_{ad_i}^{\sigma}(T)$ curve merges with the group of $\gamma_{ad}^{\sigma}(T)$ curves for samples having other impurity compositions. The different effect of γ-ray irradiation on the $\gamma_{ad_i}^{\sigma}(T)$ dependences of differently doped samples, which then gives way to the similarity of these dependences for larger doses, may be due to different initial amounts of deformation (compression along the polar direction) of doped samples compared to undoped ones, which decrease with an increasing dose because of the expansion of the samples along this direction. The amount of compression increases along the series TGS + Cr^{3+}, ATGS + Cu^{2+}, and ATGS + Cr^{3+}, as suggested by the values of the equivalent displacement fields [26].

The variability in the response to irradiation of single crystals opens up fresh opportunities for the control of their properties. Irradiation of single crystals of the TGS family with γ-rays results in a change in the additional component $\gamma_{ad_i}^{\sigma}(T)$ and also affects the low-temperature dependence of the PEC of the polar crystal matrix, reducing the frequencies of the modes involved in the formation of $\gamma^{\sigma}(T)$ (Table 2).

Table 2 lists the values of the parameters characterizing an approximation (in the range of 0–80 K) of experimental temperature dependences of γ^{σ} of single crystals of ATGSP measured along the polar axis in a range of T = 1.5–100 K for progressively increased doses 0 ⟶ 8 ⟶ 15 ⟶ 25 ⟶ 35 Mrad. The data of Table 2 illustrate the basic tendencies in the response of hydrogenous impurity ferroelectrics to γ-ray irradiation. They were partly discussed above, but it should be

emphasized that the data show tendencies rather than quantitatively determined properties of impurity crystals even of the particular type. This conclusion is based on the fact that, in the matrix of a TGS crystal irradiated with γ-rays, there are both unit cells with various damages and those retaining the original structure. We have no data on the dose dependence of the relationship between the amounts of the former and latter unit cells, as well as on the state of protons and radiolysis products in the former ones. Hence, we are forced to consider the numerical results in Table 2 as some average data characteristic of single crystals of TGS-based compounds. Nonetheless, we can indicate the following common features:

(1) As the dose is increased from zero to 8 Mrad, the impurity component of the PEC is suppressed and the wavenumbers of pyroelectrically active modes become smaller, but the canonical dependence (6b) remains valid.

(2) When the dose is raised from 8 to 15 Mrad, the $\gamma^{\sigma}(T)$ dependence qualitatively changes; there appears a constant component and a power-law component. The latter hampers the observation of the lowest mode ≈ 10 cm^{-1} (its presence or absence should be established in other experiments). The modes observed have lower wavenumbers.

(3) At 15–35 Mrad doses, the situation remains the same, but the exponent n of the power-law component monotonically decreases. The linear extrapolation of the dose dependence $n(D)$ to $n = 1.5$ yields $D \approx 46$ Mrad, while the extrapolation to $n = 1$ gives $D \approx 75$ Mrad; these doses are so high that a hydrogenous crystal must disintegrate.

(4) The range 25–35 Mrad appears to be critical; the polar properties of the crystal matrix begin to degrade, and its polarizing effect on the crystal components is reduced, which results in a decrease of the constant component of the PEC.

The appearance of a constant component $\gamma_0^{\sigma}(T) \neq 0$ at $T \longrightarrow 0$ (Fig. 8a) when the dose is increased is apparently the first experimental verification of the prediction [4] that this component is characteristic of pyroelectric and polar glasses, i.e., materials still possessing translational symmetry, even though they have a relatively small amount of some randomly oriented or irregularly distorted structural elements. This prediction was based on the general statement that the third law of thermodynamics breaks down in disordered systems. In [4], one of the possible mechanisms of the predicted feature was considered, namely, it was assumed that the linear expansion coefficient $\alpha_{lm}^{\sigma, E}(T)$ is nonzero at $T \longrightarrow 0$, which leads to $\gamma^{\varepsilon}(T) \neq 0$ and, hence, $\gamma^{\sigma}(T) \neq 0$ at $T \longrightarrow 0$. In our opinion, the interpretation of the secondary PEC presented above provides an explanation for the relation between the $\gamma^{\varepsilon}(T) \neq 0$ and $\gamma^{\sigma}(T) \neq 0$ dependences, and only the possible physical mechanism responsible for the constant component of the PEC should be elucidated.

It is our opinion that the presence of the component $\gamma_0^{\sigma}(T)$ in the $\gamma^{\sigma}(T)$ dependences of single crystals of ATGSP at doses $D \geq 15$ Mrad may have much to do with the formation of a glasslike phase and the electret state in samples. But the dominant formation mechanism of the constant and power-law components in a hydrogenous ferroelectric is the temperature-dependent proton localization in the potential well that we discussed above. In this case, the value of the exponent n characterizes the specific collection of broken hydrogen bonds in the particular crystal matrix, rather than being a manifestation of a general fundamental law.

We believe that the power-law $\gamma^{\sigma}(T)$ dependence with the changeable exponent n in hydrogenous crystals irradiated with γ-rays is an indication of the formation of a glasslike polar phase spatially homogeneous on a scale of several unit cells. This property distinguishes the case that we consider here from the formation of a glasslike phase at grain boundaries in ferroelectric ceramics.

In [72], it was assumed that, in ferroelectric ceramics of a complex composition of the TsTS-40 type, the low-temperature range of the $\gamma^{\sigma}(T)$ dependence is described by the relation $\gamma^{\sigma}(T) \sim T$. However, using the same experimental data (Fig. 8b), this dependence can be more closely approximated in a range of 1.5–6 K by the expression

$$\gamma^{\sigma}(T) = \left[0.5 + E\left(\frac{24\ \mathrm{K}}{T}\right) + \ldots\right] \times 10^{-13}\ \mathrm{C\ cm^{-2}\ K^{-1}}.$$

The constant component and the Einstein-function terms in this approximation (in the absence of a power-law component) can be identified with the contributions to the $\gamma^{\sigma}(T)$ dependence from an ideal glasslike phase (grain boundaries) and an ideal ferroelectric phase (ceramic grains), respectively; hence, the contribution from the intermediate phase (defects) is absent. If the relationship

$$\left|\{\gamma^{\sigma}(T)/C_p(T)\}\right| = \text{const}$$

takes place in ceramics of this type [73] in a temperature range of $T < 2.5$ K, then we have $C_p(T) \sim T^n$ with $n \ll 1$, which contradicts the two-level tunneling model for atoms or groups of atoms in a double-well potential with a constant density of excited states [74]. It seems likely that this glasslike-state model is inadequate for ceramics. There are no currently available methods for producing a defect structure with a constant density of excited states in hydrogenous polar single crystals.

5. PYROELECTRIC MATERIALS FOR LOW-TEMPERATURE APPLICATIONS

The low-temperature range is preferable for practical applications of pyroelectric transducers owing to higher signal-to-noise ratios and a radically new feature, namely, the possibility to enhance signals at the thermal stage [75]. Since pyroelectric materials science has much to do with the development of methods for controlling material properties, we outline the potentialities of currently available materials.

(1) The dielectrics in a thermodynamically equilibrium polar state, having a high value of the PEC at liquid helium temperatures. Among them are (a) intrinsic ferroelectrics or their solid solutions undergoing phase transitions at low temperatures (LTT [17, 30, 76], $KTa_{0.992}Nb_{0.008}O_3$ [77], Ag_3AsS_3 [31], $Pb_{0.57}Ba_{0.43}Nb_2O_6$ [78]; (b) ferroelectrics with impurities giving rise to low-temperature PEC anomalies [16] (Figs. 5–7); and (c) single crystals undergoing low-temperature magnetic phase transitions that are accompanied by the emergence of magnetoelectric polarization [38–41, 79]. These materials can be used in a limited range, 2–8 K below the Curie point or the anomaly temperature, because the PEC sharply falls off for fundamental reasons, as seen from (6b) and (6f). The working temperature can be reduced to $T < 1.5$ K by choosing appropriate dopants [16] or temperatures of magnetic phase transitions (see references in [79]) or by combining the pyroelectric and thermodielectric effects (the work under an external electric field, see [77]). It is also of interest, from a conceptual point of view, to search for pyroelectrics whose dipolar structural elements have temperature-dependent charges [8].

(2) The dielectrics in a thermodynamically nonequilibrium polar state, having a high value of the PEC at liquid helium temperatures. Among these are materials in which the noticeable volume fraction is structurally disordered, such as (a) single crystals of TGS-based compounds irradiated with γ-rays with a dose higher than 15 Mrad [26], (b) polarized polymer films [80], (c) standard ferroelectric ceramics [72, 73] and polarized glass ceramics [81], and (d) quenched polarized ferroelectric glasses [82].

The pyroelectric properties of the materials indicated above are understood to a varying extent.

The properties of single crystals of TGS-based compounds irradiated with γ-rays were discussed above. Solid experimental data on the $\gamma^\sigma(T)$ dependences at $T \geq 1.5$ K, obtained by different methods are available only for these materials. These data allow one to predict the properties of the materials at ultralow temperatures and to express the factors that determine these properties and that should be provided by processing.

Among these factors is the presence of a double-well or multiwell potential relief of H bonds with a small difference in the well depth ($\delta \sim 1$ meV) and with temperature-dependent proton displacements being in the same direction at all these bonds. Both the variants of the potential relief are of technological interest.

In choosing the initial single-crystal matrices, one can take hydrogenous ferroelectrics or linear pyroelectrics with short (≅2.5 Å) strong hydrogen bonds. Long (≅2.8 Å) weak hydrogen bonds, characteristic of crystalline hydrates, are prone to being quickly re-established after their rupture under γ-ray irradiation, even at doses as high as 20 Mrad [23].

Polymer films, polarized through mechanical deformation and the application of an electric field, are a combination of a mechanoelectret and an electroelectret, and their polarization has a large nonequilibrium electret component. The temperature variation of the total polarization is characterized [72] by large enough values of the PEC, $\gamma^\sigma(3\text{ K}) \cong 3 \times 10^{-12}$ C cm^{-2} K^{-1}. There are no data available in the literature on the electret component of the PEC of the films at low temperatures; in our opinion, this component can be enhanced by processing to the values sufficient for operating at $T \ll 1.5$ K.

The first investigation [73] of low-temperature (from 1.18 K) pyroelectric properties of ceramics was conducted solely with the aim of estimating the parameters of deeply frozen pyroelectric detectors. Even for randomly chosen samples of PZT ceramics ($\tan\delta \cong 0.005$ and $\varepsilon \cong 200$ at $T = 1.2$ K), the result was quite good: NEP $= 2.95 \times 10^{-11}$ W Hz$^{-1/2}$ cm$^{-3/2}$. This result can be improved by optimizing the material, which is routinely performed by decreasing the permittivity and dielectric losses [67] and increasing the PEC. Also, it is desirable to investigate the induced polar properties of the glasslike phase at grain boundaries.

The properties of glass ceramics are still only partially understood [81], but they are promising in low-temperature applications primarily due to their strong mechanoelectret state, which becomes more pronounced with decreasing temperature because of mutual thermal deformations of the components of the glass ceramics.

Information on the properties of quenched polarized ferroelectric glasses [82] is more comprehensive. At room temperature, the values of the PEC and permittivity of $LiNbO_3$ and $LiTaO_3$ glasses are the same as in the original single crystals, but the dielectric losses are much lower, $\tan\delta \cong 0.005$. At $T = 5$ K, for both materials, we have $\varepsilon \cong 25$, while the dielectric losses are the same or lower; hence, the level of intrinsic noise is substantially lower than that in single crystals. As indicated in [82], the pyroelectric properties of these glasses are due to their electret, rather than spontaneous, polarization and, therefore, one might expect these properties to be enhanced further at $T < 1.5$ K.

6. CONCLUSION

This paper is the first review of low-temperature pyroelectricity; we have outlined the current state of the problem. In closing, we have analyzed methods for

controlling the low-temperature properties of pyroelectrics. The necessity of such an analysis stems from the fact that these materials are coming into use in new high technologies having considerable promise. We separated the following subjects of future investigations: (a) nonequilibrium polar media, which allow one to surmount the fundamental limitations on the applications in a range of $T < 1.5$ K, and (b) low-temperature magnetic phase transitions that are accompanied by the formation of a polar phase.

We hope that this overview of the results of studies on low-temperature pyroelectricity will favor further investigations in this field of solid state physics.

REFERENCES

1. M. Born and K. Huang, *Dynamical Theory of Crystal Lattices* (Clarendon Press, Oxford, 1954).
2. P. J. Grout, N. H. March, and T. L. Thorp, J. Phys. C: Solid State Phys. **8** (13), 2167 (1975).
3. R. Radebaugh, Phys. Rev. Lett. **40** (9), 572 (1978).
4. P. J. Grout, N.H. March, and Y. Ohmura, Appl. Phys. Lett. **32** (8), 453 (1978).
5. B. Szigetti, Phys. Rev. Lett. **37** (12), 792 (1976).
6. B. Szigetti, Phys. Rev. Lett. **35** (22), 1532 (1975).
7. A. M. Glass, M. E. Lines, M. Eibschutz, *et al.*, Commun. Phys. **2** (4), 103 (1977).
8. Y. Ohmura, P. J. Grout, and N. H. March, J. Phys. Chem. Solids **42** (4), 323 (1981).
9. S. Boguslawski, Phys. Z. **15** (17/18), 805 (1914).
10. M. Born, in *Atomtheorie des Festen Zustandes (Dynamik der Kristallgitter*) (Berlin, 1923), p. 686.
11. N. D. Gavrilova, E. G. Maksimov, V. K. Novik, and S. N. Drozhdin, Ferroelectrics **100**, 223 (1989).
12. S. Boguslawski, Phys. Z. **15** (11), 569 (1914).
13. M. E. Lines and A. M. Glass, Phys. Rev. Lett. **39** (21), 1362 (1977).
14. M. Born, Phys. Z. **23** (4), 125 (1922).
15. V. Yu. Galitskiĭ, Fiz. Tverd. Tela (Leningrad) **23** (3), 815 (1981) [Sov. Phys. Solid State **23** (3), 463 (1981)].
16. V. N. Novikov, V. K. Novik, A. B. Esengaliev, and N. D. Gavrilova, Ferroelectrics **118**, 59 (1991).
17. N. D. Gavrilova, S. N. Drozhdin, V. K. Novik, and E. G. Maksimov, Solid State Commun. **48** (2), 12 (1983).
18. V. N. Novikov, V. K. Novik, and G. I. Kaleva, Prib. Tekh. Éksp., No. 6, 187 (1988).
19. G. Heiland and H. Ibach, Solid State Commun. **4** (3), 353 (1966).
20. R. Poprawski, Yu. Shaldin, and S. Matyjasik, Phys. Status Solidi A **90** (1), 167 (1985).
21. R. Poprawski, S. Matyjasik, and Yu. V. Shaldin, Mater. Sci. **13** (1/2), 203 (1987).
22. R. Poprawski, S. Matyjasik, and Yu. Shaldin, Solid State Commun. **62** (4), 257 (1987).
23. A. B. Esengaliev, V. K. Novik, V. N. Novikov, and N. D. Gavrilova, Fiz. Nizk. Temp. **18** (4), 395 (1992) [Sov. J. Low Temp. Phys. **18** (4), 268 (1992)].
24. V. K. Novik, Author's Abstract of Doctoral Dissertation (Rostov. Gos. Univ., Rostov-na-Donu, 1984).
25. Yu. V. Shaldin and R. Poprawski, J. Phys. Chem. Solid **51** (2), 101 (1990).
26. A. B. Esengaliev, V. K. Novik, V. N. Novikov, *et al.*, Fiz. Nizk. Temp. **18** (4), 386 (1992) [Sov. J. Low Temp. Phys. **18** (4), 262 (1992)].
27. A. B. Esengaliev, V. K. Novik, V. N. Novikov, *et al.*, Fiz. Nizk. Temp. **18** (9), 1022 (1992) [Sov. J. Low Temp. Phys. **18**, 718 (1992)].
28. A. B. Esengaliev, F. M. Salaev, and V. K. Novik, Fiz. Tverd. Tela (St. Petersburg) **34** (10), 3276 (1992) [Sov. Phys. Solid State **34** (10), 1754 (1992)].
29. A. B. Esengaliev, V. K. Novik, V. N. Novikov, *et al.*, Ferroelectrics **167**, 151 (1995).
30. V. K. Novik, A. M. Kousainov, A. B. Esengaliev, *et al.*, Ferroelectrics **170**, 37 (1995).
31. N. D. Gavrilova, V. A. Koptsik, V. K. Novik, and T. V. Popova, Ferroelectrics **20**, 199 (1978).
32. L. G. Vieira, J. L. Ribeiro, A. Almeida, *et al.*, J. Phys.: Condens. Matter **9** (50), 11195 (1997).
33. R. Poprawski, J. Dziedzic, and Yu. V. Shaldin, Solid State Commun. **55** (1), 39 (1985).
34. R. C. de Sousa, J. A. C. de Paiva, J. Mendes Filho, and A. S. B. Sombra, Solid State Commun. **87** (10), 959 (1993).
35. A. Kliič and M. Marvan, Czech. J. Phys. **48** (4), 457 (1998).
36. V. M. Varikash, S. N. Drozhdin, T. A. Zarembovskaya, and V. K. Novik, Kristallografiya **20** (2), 435 (1975) [Sov. Phys. Crystallogr. **20** (2), 267 (1975)].
37. M. Taya, T. Asaji, and D. Nakamura, Phys. Status Solidi A **114** (1), 157 (1989).
38. B. I. Al'shin, D. N. Astrov, L. N. Baturov, *et al.*, Tr. Vses. Nauchno-Issled. Inst. Fiz.-Tekh. Radiotekh. Izmer. **32** (62), 109 (1977).
39. Y. Miyamoto, M. Kobayashi, and S. Chikazumi, J. Phys. Soc. Jpn. **55** (2), 660 (1986).
40. Y. Miyamoto, Ferroelectrics **161**, 117 (1994).
41. M. Lujan, J.-P. Rivera, I. S. Kizhaev, *et al.*, Ferroelectrics **161**, 77 (1994).
42. W. Voigt, Ann. Phys. (Leipzig) **66** (13), 1030 (1898).
43. W. Voigt, in *Lehrbuch der Kristallphysik (mit Ausschluss der Kristalloptik)* (Berlin, 1910), p. 247.
44. R. Poprawski and Yu. V. Shaldin, Solid State Commun. **68** (5), 487 (1988).
45. R. Liminga, S. C. Abrahams, A. M. Glass, and Å. Kvick, Phys. Rev. B **26** (12), 6896 (1982).
46. A. S. Bhalla and R. E. Newham, Phys. Status Solidi A **58** (1), K19 (1980).
47. A. S. Bhalla and L. E. Cross, Ferroelectrics **38**, 935 (1981).
48. H. Jaffe, Phys. Rev. **75** (10), 1625 (1949).
49. R. Liminga, S. Chomnilpan, and S. C. Abrahams, J. Appl. Crystallogr. **11**, Part 2, 128 (1978).
50. B. Mroz, T. Krajewski, and T. Breczewski, Acta Phys. Pol. A **63** (4), 445 (1983).
51. Chian-Ping Ye, T. Tamagawa, and D. L. Polla, J. Appl. Phys. **70** (10), 5538 (1991).
52. V. K. Novik, I. B. Kobyakov, S. N. Drozhdin, *et al.*, Pis'ma Zh. Tekh. Fiz. **1** (7), 344 (1975) [Sov. Tech. Phys. Lett. **1** (7), 163 (1975)].

53. N. D. Gavrilova, I. B. Kobyakov, V. K. Novik, and A. V. Solodukhin, Zh. Tekh. Fiz. **50** (3), 631 (1980) [Sov. Phys. Tech. Phys. **25** (3), 379 (1980)].
54. H. Ibach, Phys. Status Solidi **33** (1), 257 (1969).
55. V. S. Oskotskiĭ, I. B. Kobyakov, and A. V. Solodukhin, Fiz. Tverd. Tela (Leningrad) **22** (5), 1478 (1980) [Sov. Phys. Solid State **22** (5), 861 (1980)].
56. M. C. Foote and A. C. Anderson, Ferroelectrics **62**, 11 (1985).
57. R. Villar, E. Gmelin, and H. Grimm, Ferroelectrics **69**, 165 (1986).
58. H. Mueller, Phys. Rev. **57** (9), 829 (1940).
59. R. Blinc and B. Žekš, *Soft Modes in Ferroelectrics and Antiferroelectrics* (North-Holland, Amsterdam, 1974).
60. J. S. Browder and S. S. Ballard, Appl. Opt. **16** (12), 3214 (1977).
61. S. I. Novikova, *Thermal Expansion of Solids* (Nauka, Moscow, 1974).
62. S. Vieira, C. de las Heras, and J. Gonzalo, Solid State Commun. **31** (3), 175 (1979).
63. A. M. Glass and M. E. Lines, Phys. Rev. B **13** (1), 180 (1976).
64. S. P. Bravina, L. S. Kremenchugskiĭ, N. V. Morozovskiĭ, and A. A. Strokach, Ukr. Fiz. Zh. **33** (7), 1065 (1988).
65. Yu. V. Shaldin and S. Matyyasik, Fiz. Tverd. Tela (Leningrad) **33** (6), 1878 (1991) [Sov. Phys. Solid State **33** (6), 1056 (1991)].
66. A. B. Esengaliev, V. K. Novik, V. N. Novikov, and N. D. Gavrilova, Fiz. Nizk. Temp. **17** (4), 523 (1991) [Sov. J. Low Temp. Phys. **17** (4), 276 (1991)].
67. A. B. Esengaliev, V. K. Novik, V. N. Novikov, *et al.*, Vestn. Mosk. Univ., Ser. 3: Fiz., Astron. **33** (5), 91 (1992).
68. J. C. Holste, W. N. Lowless, and G. A. Samara, Ferroelectrics **11**, 337 (1976).
69. T. Hikita, Ferroelectrics **159**, 67 (1994).
70. H. Motegi, K. Kuramoto, and E. Nakamura, J. Phys. Soc. Jpn. **52** (4), 1131 (1983).
71. E. V. Peshikov, *Effect of Radiation on Ferroelectrics* (Fan, Tashkent, 1972).
72. A. B. Esengaliev, V. K. Novik, V. N. Novikov, and A. G. Segalla, Vestn. Mosk. Univ., Ser. 3: Fiz., Astron. **33** (4), 90 (1992).
73. F. Bordoni, P. Carelli, I. Modena, and G. L. Romani, Infrared Phys. **19** (6), 653 (1979).
74. *Amorphous Solids Low Temperature Properties*, Ed. by W. A. Phillips (Berlin, 1981), p. 38.
75. A. A. Belov, N. D. Gavrilova, and V. K. Novik, Pis'ma Zh. Tekh. Fiz. **12** (16), 1008 (1986) [Sov. Tech. Phys. Lett. **12** (8), 416 (1986)].
76. K. É. Khaller, A. A. Khaav, V. K. Novik, and N. D. Gavrilova, Fiz. Tverd. Tela (Leningrad) **30** (1), 88 (1988) [Sov. Phys. Solid State **30** (1), 47 (1988)].
77. T. E. Pfafman, M. LeGros, E. Silver, *et al.*, J. Low Temp. Phys. **93** (3/4), 721 (1993).
78. R. Guo, A. S. Bhalla, C. A. Randall, and L. E. Cross, J. Appl. Phys. **67** (10), 6405 (1990).
79. Y. Koyata, H. Nakamura, N. Iwata, *et al.*, J. Phys. Soc. Jpn. **65** (5), 1383 (1996).
80. R. W. Newsone and E. Y. Andrei, Phys. Rev. B **55** (11), 7264 (1997).
81. W. Xie, Z. Ding, and P. Zhang, J. Am. Ceram. Soc. **79** (12), 3336 (1996).
82. A. M. Glass, M. E. Lines, K. Nassau, and J. W. Shiever, Appl. Phys. Lett. **31** (4), 249 (1977).

Translated by Yu. Epifanov